

Accessible Sites at Bimetallic Complexes and Clusters

MAXIMILIAN MUHR

Vollständiger Abdruck der von der TUM School of Natural Sciences der Technischen Universität München zur Erlangung eines

Doktors der Naturwissenschaften (Dr. rer. nat.)

genehmigten Dissertation.

Vorsitz: Prof. Dr. Shigeyoshi Inoue

Prüfer der Dissertation:

1. Prof. Dr. Dr. h. c. Roland A. Fischer
2. Prof. Dr. Jean-Yves Saillard

Die Dissertation wurde am 15.11.2022 bei der Technischen Universität München eingereicht und durch die TUM School of Natural Sciences am 05.12.2022 angenommen.

Für Mama.

Perfection belongs to narrated events, not to those we live.

Primo Levi, *The Periodic Table*

*Annuntio vobis gaudium magnum:
Habemus Niccolum-Gallium!*

Danksagung

Ohne die Unterstützung zahlreicher Menschen, wäre diese Arbeit so nicht möglich gewesen. Ebenso wären die letzten Jahre nicht so schön gewesen und hätten mir nicht so viel Spaß gemacht. Obwohl es eine enorm anstrengende und fordernde Zeit war, musste ich nie mit einem ‚unguten Gefühl im Bauch‘ zur Arbeit kommen – das ist sicherlich nicht selbstverständlich. Darüber hinaus haben viele von Euch, in den letzten Jahren, einen prägenden Einfluss auf meine persönliche und wissenschaftliche Entwicklung genommen.

Zu Beginn möchte ich meinem Doktorvater **Prof. Dr. Roland Fischer** danken! Neben einem spannenden Promotionsthema haben Sie mir vor allem stets Vertrauen geschenkt. Auch als nach zwei Jahren noch fast nichts lief, haben Sie mich nie unter Druck gesetzt, sondern immer ermutigt weiterzumachen. Dabei haben Sie mir völligen wissenschaftlichen Freiraum gelassen und mir nie eine Kooperationsmöglichkeit verweigert. Durch die tollen inter-(nationalen) Forschungsaufenthalte, die Sie mir ermöglicht haben, konnte ich nicht nur meinen Horizont erweitern, sondern habe auch das besondere akademische AMC-Umfeld noch mehr zu schätzen gelernt. Neben einem vollausgestatteten Labor und einem einzigartigem Massenspektrometer, ist vor allem die Zusammensetzung des Lehrstuhls wunderbar. Sie haben es geschafft, dass es für fast jedes Thema einen Experten gibt und eine enorm unterstützende Atmosphäre zwischen den Untergruppen herrscht! Die große Unterstützung habe Sie mir selbstverständlich in Form von **Dr. Christian Gemel** zu Seite gestellt!

Lieber **Christian**, für deine Unterstützung bin ich Dir unendlich dankbar! Du warst stets für mich da und hast Dir immer Zeit für meine Probleme genommen. Ob beinahe täglich im Büro, um über Ergebnisse oder Sonstiges zu diskutieren, oder auch mal am Wochenende um zusammen an der X-ten Version des Ni/Ga Papers zu schreiben. Mit Deiner ausgeglichenen Art hast du es geschafft, die schlechtesten Ergebnisse gar nicht so wild aussehen zu lassen und nach ‚großen Entdeckungen‘ auf dem Boden zu bleiben. Deine Begeisterung für Cluster Chemie ist auf jeden Fall ansteckend und dein Engagement beeindruckend! Es war wirklich Urleiwand mit Dir, Danke!

Further I would like to thank all associated researchers and members of the ‘Mitellbau’. At some point, everyone of you helped me somehow, either with manuscript proof-reading, experimental advice, or data interpretation – and some nice chats for sure. Thanks to **PD Dr. Alexander Pöthig, Dr. Julien Warnan, Dr. Gregor Kieslich, Dr. Dominik Halter, Dr. Soumya Mukherjee, Dr. Markus Drees** and **Dr. Gabriele Raudaschl-Sieber**.

Ein besonderer Dank gilt außerdem **Dr. Mirza Cokoja**. Ich hatte immer viel Spaß mit Dir, egal ob zu ratschen und zu twittern! Außerdem hast du mit deinen tollen Vorlesungen meine Begeisterung für die metallorganische Chemie bereits im Studium geweckt und standest mir auch während der Promotion mit Rat und Tat zur Seite.

Desweiteren möchte ich **Dr. Julius Hornung** danken, welcher mich in den Lehrstuhl und die Cluster Chemie eingeführt und bis heute noch ein offenes Ohr für mich hat. Ich hätte mir keine besseren Betreuten als Dich vorstellen können und konnte mir einiges von Dir abschauen! Für viele Lacher und offene Arme in meiner Anfangszeit, danke ich zudem **Dr. Konstantin Epp**!

Ich möchte **Dr. Ralf Karch** für das Mentoring danken, mit Ihren kritischen Kommentaren haben Sie den Finger immer direkt in die Wunde und mich zum Nachdenken angeregt.

I'm very thankful to **Prof. Dr. Shigeyoshi Inoue** for taking the chairman position in my defense.

I'm deeply thankful to the 'Rennes-Team' for their theory support. With your calculations, you significantly enriched my thesis and it simply felt great to have such experts in my back! Merci beaucoup à **Dr. Samia Kahlal**, **Dr. Franck Gam** et **Hao Liang**! I'm extraordinary thankful to the one and only **Prof. Dr. Jean-Yves Saillard**! I really enjoyed our meetings and my time in Rennes, including the trip to Mont Saint Michel and the visit at the 'farmers market' (vine fair). Apart from teaching me about the bonding in my compounds, you also sparked my interest for delicious wine. I'm also very grateful that you took over a seat in my examination committee.

I received additional theory support from Brazil and want to thank **Prof. Dr. Juarez da Silva** and his group in São Carlos! I'm thankful for your kind hosting and convinced that our developed approach will be the fundament of for the next years of research. Obrigado!

Moreover, I would like to thank **Prof. Dr. János Mink** for making our Ni/Ga clusters object of his research and for contributing a fascinating spectroscopy study!

Zudem möchte ich **Brigitte Breitenstein**, **Prof. Dr. Konstantin Karaghiosoff** und vor allem **Dr. Lars Allmendinger** für ihre großzügige Unterstützung bei meinen VT-2D-NMR Messungen danken. Tage lag ein NMR an einer ‚fremden Uni‘ zu blockieren, ist nicht selbstverständlich!

Ebenso haben sich **Dr. Tanja Kunz** und **Prof. Dr. Andreas Schnepf** meinen Dank verdient. Meine zwei Aufenthalte in Tübingen an der ‚KoKo‘ waren sehr interessant.

Ein großer Dank geht auch an **Mathias Linden** und **Dr. Bernhard Linden** für ihren konstanten LIFDI Support und die großartige Kooperation bei der Verbindung des LIFDIs and die Glovebox. Es war immer sehr lustig mit Euch!

Neben Externen hatte ich auch großartige interne Kooperationspartner und Unterstützer. Für tatkräftige Mitwirkung durch Durchführung der Elementaranalysen möchte ich **Ulrike Amiri** und **Bircan Dliki** danken, sowie **Maria Matthews** für VT-NMR Messungen. **Jürgen Kudermann** danke ich für die rigorose Instandhaltung der Zentralanalytik, für verlässliche Messungen und lustige Gespräche. Außerdem danke ich **Dardan Ukaj** für zahlreiche Raman Messungen. Ein großer Dank geht an **Dr. Christian Jandl** für die zuverlässige Messung und Verfeinerung von Einkristallen – man konnte Dir blind vertrauen, ein hohes Gut für jeden Metallorganiker. Außerdem danke ich dem Makro-NMR Team (vor allem **Matthias Nobis** und **Andreas Saurwein**) für die NMR-Messungen meiner Katalysen

Bevor ich zu den ‚Engsten‘ komme, möchte ich allen aktuellen und ehemaligen Mitgliedern des **Lehrstuhls für Anorganische und Metallorganische Chemie** danken. Ich hatte besondere vier Jahre mit euch!

Besonders aber möchte ich allen Mitgliedern der ‚**OM-Gruppe**‘ danken. Es war mir eine große Freude mich mit **Dr. Patricia Weishäupl** durch die Promotion zu kämpfen. **Dr. Max Schütz** möchte ich für die schöne Zeit in Brasilien danken, Einkristall Messungen und dafür, dass er mir die Möglichkeit gegeben hat seine Cluster zu berechnen. Ebenso danke ich **Dr. Lena**

Staiger, auch wenn wir sicherlich unsere Phasen hatten, sind wir beide Gestärkt aus der Ni/Ga Geschichte hervorgegangen und können uns noch in die Augen schauen.

Zu besonders großem Dank bin ich meinen Freunden **Raphael Bühler** und **Johannes Stephan** verpflichtet. Es war mir eine große Ehre, dass ihr mir die Betreuung eures Masterprojekts anvertraut habt und eine noch größere Freude mit Euch zusammen zu arbeiten! Ihr habt wirklich großen Anteil, dass mir die Arbeit im Labor so viel Spaß gemacht hat und werdet mir besonders fehlen! All eure Beträge sind hier einfach nicht aufzulisten.

Aber nicht nur mit euch hatte ich Glück, sondern auch mit einen Bachelorstudenten und Forschungspraktikanten! Vielen Dank an **Kara Müller**, **Anton Fischbacher**, **Alexander Thomas**, **Johannes Stephan**, **Jonas Gilch**, **Tobias Weng**, **Robert Wolf** und **Fabrizio Napoli**. Ich hoffe ihr konntet was von mir lernen und wünsche Euch nur das Beste für Euern weitem Weg!

Als besondere Highlights bleiben die Reisen zu den verschiedenen Konferenzen in meinen Erinnerungen. Auch wenn wir vermutlich aus Münster Corona eingeschleppt haben, war der Kurztrip zur DGMS mit **Patricia** sehr lustig – vermutlich haben wir alle LIFDI User getroffen... Trotz OC-Überschwemmung und straffem ‚Bach Programm‘, war die Photochemie Konferenz in Halle zusammen mit **Raphael** ein großer Spaß und eine interessante Abwechslung. Getoppt wurde alles nur von der ACS in San Diego. Die Reisegruppe hat einfach perfekt zusammengepasst und ich hatte eine Wahnsinns-Woche mit euch in Cali. Vielen Dank an **Kathrin Kollmannsberger**, **Johanna Haimerl**, **Silva Kronawitter**, **Karina Hemmer** und **Philip ‚Stingray Stan‘ Stanley**! Last but not least war natürlich auch die Zeit in Rimini unvergesslich und kulinarisch ungeschlagen. Vielen Dank an **Johannes**, **Raphael**, **Fabrizio**, **Ivan Antsiurov**, **Richard ‚double-J‘ Weininger** und **Sarah Dummert**.

Hinter all dem Spaß (und manchmal auch Ernst) steht an der Uni natürlich auch eine Menge Bürokratie. Für deren Erledigung möchte ich **Dr. Dana Weiß** und **Martin Schellerer** danken.

Wenn ich in den letzten Jahren auch viel Zeit an der Uni verbracht habe, war die Zeit mit Freunden und Familie umso wichtiger! Ihr habt mir auf unterschiedlichste Wegen einen Ausgleich ermöglicht und mich auf eure eigene Art und Weise unterstützt. Auch wenn ich nicht jedem persönlich danken kann, bin ich mir über die große Anzahl an Menschen bewusst.

An der Schnittstelle von Freundschaft und Uni standen **Dr. Alexander Urstöger**, **Dr. Dominik Huber** und **Jonas Müller**. Ich bedanke mich für echt eine unvergessliche Zeit zwischen Uni, Urlaub und Unfug (manchmal auch alles drei gleichzeitig). Selbst die Zeit mit **Jonas** hat in der Regel ‚scho bassd‘. Außerdem danke ich **Dominik** für das Design des Dalton Covers! Dazu danke ich **Wilhelm Gottschall** für das spontane proof-reading dieser Arbeit.

Meine Eltern **Karl-Heinz** und **Ursula Muhr** haben mich auf meinem gesamten Lebensweg begleitet und mich in allen Entscheidungen unterstützt. Ich weiß, dass ich immer auf euch zählen kann und ihr immer hinter mir steht! Der Dank ist nicht in Wort zu fassen.

Zu guter letzte danke ich meiner Freundin **Ina Fürnrohr**, die fast die ganze Promotion miterlebt habt und mich immer unterstützt hat. Du hast all meine Up and Downs direkt miterlebt, mich aufgeheitert und motiviert weiterzumachen. Dabei hast du all meine Launen ertragen und gewusst, dass manchmal zuhören einfach die beste Medizin ist – und vielleicht ein erzwungener Tag Pause... Vielen Dank, ich liebe Dich.

Abstract

The presented work deals with the synthesis and characterization of 'Hume-Rothery inspired complexes and clusters' of the general formula $[TM_xE_y](R)_z$ (TM = transition metal; E = group 13 metal; R = organic ligand). The central objective of the project is the enhancement of the cluster reactivity through better accessible sites at the clusters. A special focus is set on the application of liquid injection field desorption ionization mass spectrometry (LIFDI-MS) as well as a density functional theory (DFT) calculations assessment of the clusters, regarding their structure and bonding situation.

Apart from common organometallic structure elucidation techniques (single crystal X-ray diffraction, NMR, MS), an advanced DFT screening approach is presented to identify the structure of the synthesized clusters. The methodology is applied to an inseparable and co-crystallizing ensemble of closely related cluster of the formula $[Ni_{6/7/8}Ga_{6/7}](Cp^*)_6$ and reveals an octahedral $(NiCp^*)_6$ shell around a central metal core as common structural feature. The identification of structures associated with the presence of naked Ni atoms within some of the cluster cores, allows to target these reaction center and selectively react individual clusters with substrates. Treatment of the ensemble with terminal alkynes leads to the isolation of pure $[Ni_8Ga_6](Cp^*)_6(acetylide)_2$. Cp^* transmetalation from Ga to Ni is identified as driving force for the cluster formation. The cluster $[Ni_4Ga_3](Cp^*)_3(dvds)_2$ is isolated as a reaction intermediate on the way to the ensemble and contains $GaCp^*$ as well as $NiCp^*$ moieties.

To avoid Cp^* transmetalation from Ga to Ni, as in the case of the ensemble, the alternative $GaTMP$ is employed, leading to the remarkably reactive cluster $[Ni_3Ga_7](TMP)_7$. In presence of H_2 the cluster forms different (poly-)hydride species, which are active in semihydrogenation catalysis of alkynes. The selectivity is reasoned by a cooperative effect between Ni and Ga. The structures of the (poly-)hydrides are elucidated by a combination of 2D NMR and DFT calculations. The cluster's structure and its catalytic selectivity are in strong relation to the solid Hume-Rothery phase Ni_5Ga_3 , strengthening the perception of clusters as molecular models for their solid-state counterparts.

An alternative strategy to form reactive sites at clusters is the partial removal of the protective ligand shell of the cluster. Under hydrogenolytic conditions a undercoordinated $[RuGa_3](Cp^*)_3$ species is formed, which subsequently activates H_2 and $HSiEt_3$ (Si-H) or toluene (C-H). The resulting species are used to perform bonding analysis on the Ru-Ga bond. Through photochemically induced reductive elimination of H_2 and $HSiEt_3$ from $[RuGa_3](Cp^*)_3(SiEt_3)(H)_3$, the transient $[RuGa_3](Cp^*)_3$ can be reformed and trapped as diphosphine adduct in form of $[RuGa_3](Cp^*)_3(dppe)$. The highly reactive $[RuGa_3](Cp^*)_3$ intermediate is proven to be catalytically active in the hydrogenation catalysis of 3-hexyne and it could further be shown to act as seeds for cluster growth reactions.

Mass spectrometry is the central analytical method in this work. The progress in this work is based on the advancement in fully inert mass spectrometry. A high-resolution orbitrap with LIFDI is coupled to an inert atmosphere glovebox, enabling MS under fully inert conditions. The improvement is demonstrated by a testing the setup to notoriously sensitive reaction.

Zusammenfassung

Die vorliegende Arbeit befasst sich mit der Synthese und Charakterisierung von "Hume-Rothery-inspirierten Komplexen und Clustern" der allgemeinen Formel $[TM_xE_y](R)_z$ (TM = Übergangsmetall; E = Metall der Gruppe 13; R = organischer Ligand). Das Hauptziel des Projekts ist die Steigerung der Reaktivität der Cluster durch besser zugängliche Stellen an den Clustern. Ein besonderer Schwerpunkt liegt dabei auf der Anwendung der ‚Liquid Injection Field Desorption Ionization‘-Massenspektrometrie (LIFDI-MS) sowie Dichtefunktional-Theorie (DFT) Berechnung der Cluster hinsichtlich ihrer Struktur und Bindungssituation.

Neben den klassischen metallorganischen Strukturaufklärungstechniken (Einkristall-Röntgendiffraktometrie, NMR, MS) wird ein innovativer DFT-Screening-Ansatz zur Identifizierung der Struktur der synthetisierten Cluster vorgestellt. Die Methode wird auf ein untrennbares und Co-kristallisierendes Ensemble von eng verwandten Clustern der Formel $[Ni_{6/7/8}Ga_{6/7}](Cp^*)_6$ angewandt und zeigt eine oktaedrische $(NiCp^*)_6$ -Schale um einen zentralen Metallkern als gemeinsames Strukturmerkmal. Die Identifizierung von Strukturen, die mit der Anwesenheit von nackten Ni-Atomen in einigen der Clusterkerne verbunden sind, ermöglicht es, diese Reaktionszentren anzusteuern und einzelne Cluster selektiv mit Substraten umzusetzen. Die Behandlung des Ensembles mit endständigen Alkinen führt zur Isolierung von reinem $[Ni_8Ga_6](Cp^*)_6(Acetylid)_2$. Die Cp^* -Transmetallierung von Ga zu Ni wurde als treibende Kraft für die Clusterbildung identifiziert. Der Cluster $[Ni_4Ga_3](Cp^*)_3(dvds)_2$ wird als Reaktionszwischenprodukt auf dem Weg zum Ensemble isoliert und enthält sowohl $GaCp^*$ - als auch $NiCp^*$ -Einheiten.

Um die Cp^* -Transmetallierung von Ga zu Ni zu vermeiden, wie im Fall des Ensembles, wird der Alternativligand GaTMP verwendet, woraus der bemerkenswert reaktive Cluster $[Ni_3Ga_7](TMP)_7$ resultiert. In Gegenwart von H_2 bildet der Cluster verschiedene (Poly-) Hydrid-Spezies, die aktive Katalysatoren für die Semihydrierung von Alkinen darstellen. Die Selektivität ist auf einen kooperativen Effekt zwischen Ni und Ga zurückzuführen. Die Struktur der (Poly-)Hydride wird durch eine Kombination von 2D-NMR und DFT-Berechnungen aufgeklärt. Die Struktur des Clusters und seine katalytische Selektivität stehen in enger Beziehung zur Hume-Rothery-Festphase Ni_5Ga_3 , wodurch die Interpretation von Clustern als molekulare Modelle für ihre Festphasenäquivalente geschärft wird.

Eine alternative Strategie zur Schaffung reaktiver Stellen an Clustern ist die partielle Entfernung der schützenden Liganden Hülle des Clusters. Unter hydrogenolytischen Bedingungen wird eine unterkoordinierte $[RuGa_3](Cp^*)_3$ -Spezies gebildet, die anschließend H_2 und $HSiEt_3$ (Si-H) oder Toluol (C-H) aktiviert. Die resultierenden Spezies werden zur Analyse der Ru-Ga-Bindung verwendet. Durch photochemisch induzierte reduktive Eliminierung von H_2 und $HSiEt_3$ aus $[RuGa_3](Cp^*)_3(SiEt_3)(H)_3$ kann das transiente $[RuGa_3](Cp^*)_3$ wieder gebildet werden und als Diphosphin-Addukt in Form von $[RuGa_3](Cp^*)_3(dppe)$ stabilisiert werden. Das hochreaktive $[RuGa_3](Cp^*)_3$ -Zwischenprodukt ist in der Hydrierungskatalyse von 3-Hexin katalytisch aktiv, und es konnte zudem gezeigt werden, dass es als Keim für Clusterwachstumsreaktionen dienen kann.

Massenspektrometrie stellt die zentrale Analysemethode in dieser Arbeit dar. Der Fortschritt dieser Arbeit beruht auf den Fortschritten in der Massenspektrometrie unter komplettem Luftausschluss. Ein hochauflösendes Orbitrap-Gerät mit LIFDI wurde mit einer Inertatmosphären-Glovebox gekoppelt, wodurch MS unter vollständig inerten Bedingungen ermöglicht. Die Verbesserung wird durch einen Test des Aufbaus an einer bekanntermaßen empfindlichen Reaktion demonstriert.

Table of Contents

1.	Introduction & Theory	1
1.1	Heterobimetallic Metal Interactions in Molecules and Solids	1
1.1.1	Principles of Metals Bonds	1
1.1.2	Hume-Rothery Phases	3
1.1.3	Hume-Rothery Inspired Nanoparticles	5
1.1.4	Defined Bimetallic TM/E Complexes	6
1.1.5	Hume-Rothery Inspired Atom Precise Clusters.....	12
1.2	The Wet Chemical Synthesis of Metallic Clusters	16
1.2.1	Why Clusters?.....	16
1.2.2	Basic Electronics of Clusters	17
1.2.3	Synthesis Principles of Ligand Stabilized Clusters	18
1.2.4	Hume-Rothery Inspired Clusters	19
1.2.5	Dendrimer Supported Multimetallic Clusters	21
1.3	Accessible Sites at Bimetallic Complexes and Clusters	24
1.3.1	Prologue	24
1.3.2	Concluding remark on the three challenges	27
1.3.3	Mass spectrometry in cluster research.....	28
1.3.4	Ni/Ga: Cp* transmetalation as root for a mixture in a crystal.....	29
1.3.5	Reactive sites by ligand removal	31
1.3.6	The influence of R on reactive sites	33
1.3.7	Epilogue	35
1.4	References	38
2.	Main Part.....	42
2.1	Formation of a propeller-shaped Ni ₄ Ga ₃ cluster supported by transmetalation of Cp* from Ga to Ni.	43
2.1.1	Abstract	44
2.1.2	Main Text.....	45
2.1.3	References.....	53
2.1.4	Additional Data and Information	57
2.2	Investigating Inseparable Cluster Ensembles: A Ni/Ga Case Study.....	100
2.2.1	Abstract	101
2.2.2	Main Text.....	102

2.2.3	References.....	111
2.2.4	Additional Data and Information	113
2.3	C-H and Si-H Activation Reactions at Ru/Ga Complexes: a Combined Experimental and Theoretical Case Study on the Ru-Ga Bond.....	165
2.3.1	Abstract	166
2.3.2	Main Text.....	167
2.3.3	References.....	174
2.3.3	Additional Data and Information	177
2.4	Photochemically Generated Reactive Sites at Ruthenium/Gallium Clusters: Catalysis vs. Cluster Growth.	204
2.4.1	Abstract	205
2.4.2	Main Text	206
2.4.3	References.....	210
2.4.4	Additional Data and Information	212
2.5	Alkyne Semihydrogenation with Polyhydride Ni/Ga Clusters.....	239
2.5.1	Abstract	240
2.5.2	Main Text.....	241
2.5.3	Reference	246
2.5.4	Additional Data and Information	249
2.6	Enabling LIFDI-MS measurements of highly air sensitive organometallic compounds: A combined MS/glovebox technique.	283
2.6.1	Abstract	284
2.6.2	Main Text.....	285
2.6.3	References	290
2.6.4	Additional Data and Information	293
2.7	Experimental Details.....	301
2.7.1	General Remarks	301
2.7.2	Single Crystal X-Ray Diffractometry	301
2.7.3	NMR Spectroscopy	302
2.7.4	Mass Spectrometry	302
2.7.5	Infrared Spectroscopy	302
2.7.7	UV-Vis Spectroscopy	303
2.7.9	Computational Methods	303
2.7.10	Common starting reagents.....	303
2.7.11	References.....	304

3. Conclusion.....	305
4. Appendix	306
4.1 List of Abbreviations	306
4.2 List of Publications	308
4.3 Reprint Permissions	309
5. Eidesstattliche Erklärung.....	333

1. Introduction & Theory

1.1 Heterobimetallic Metal Interactions in Molecules and Solids

1.1.1 Principles of Metals Bonds

Metals are crucial for most catalytic chemical transformations. In industry, typically monometallic systems are employed. The catalytically active metals are, however, often supported by a second metal e.g., on metal oxides (Cu@ZnO for methanol synthesis from CO₂ and H₂)^[1], and sometimes doped with small amounts of other metals (Potassium in the Fe-based Haber-Bosch catalyst for the ammonia synthesis from the elements)^[1]. These non-innocent influences derive from cooperative effects between the metals, which result in improved catalytic performance and make the utilization of the catalysts (even more) viable. On the other side, it is difficult to elucidate the role of the metal-metal interactions on the atomic level and at the reactive site. Indeed, this is a major challenge in heterogenous catalysis because the rational improvement of the catalyst is related to a precise understanding of the catalytic reaction steps on the molecular level.^[2] In contrast, there are well-understood monometallic examples with innocent support, such as platinum on carbon for the catalytic hydrogenation.^[3] Carbon as a support is chemically innocent and solely accounts for a good Platinum dispersion by preventing Pt agglomeration. It is thus a classical example for a transition metal on an innocent support. On the molecular level, a dihydrogen molecule is split into two hydrides and the electrons for the bond cleavage (oxidative addition to Pt in the words of a molecular chemist) are taken from the conductive band of the Platinum. After adsorption of the alkene on Pt, it is subsequently hydrogenated to the respective alkane. As a matter of fact, 'chemistry is a local event: bond breaking and bond making are confined to the catalytically active site(s)'^[4], it thus might be feasible to look at molecular compounds, with a chemical environment close to the catalytically active sites. In this regard, the conductive band of an 'infinite' solid becomes a directed metal-metal bond in a molecular assembly.

From the perception of molecular metal-metal bonds, hydrogen activation on solid metal is in a way reminiscent to the addition of H₂ to a homometallic TM-TM multiple bond in a molecular complex. Similar to unsaturated bonds in organic chemistry, multiple TM-TM bonds are prone to oxidative additions. The complex [Mo₂{HC(N-2,6-*i*Pr₂C₆H₃)₂}₂] (*i*Pr = *iso*-propyl) activates H₂ along its quintuple Mo-Mo bond, yielding the *trans*-dihydride and a quadruple Mo-Mo bond (Figure 1a)^[5]. This phenomenon is reversible. In a heuristic view, multiple metal-metal bonds may represent an ‘electron reservoir’ that can also be found in metal clusters and is promising for reactivity.

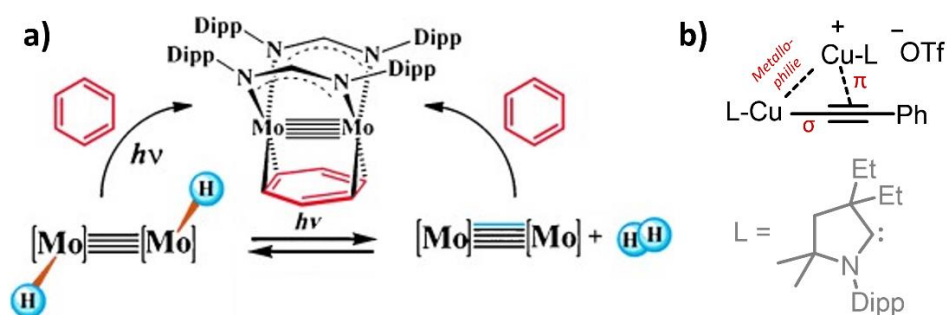


Figure 1: a) Schematic representation of the reversible reaction between a quintuple and a quadruple Mo-Mo bond with hydrogen. Reprinted with permission.^[5] b) Intermediate of the copper catalyzed azide alkyne cycloaddition, featuring metallophilic Cu-Cu interactions.

In general, metal-metal bonds in molecules possess a broad scope of reactivities. Among other factors, their reactivity depends on the nature of the two metals (or one metal for the homometallic case), the associated polarity of the bond, the bond order and the nature of the substrate which is again coupled the related activation pathway(s).^[6] In molecules, reaction intermediates are typically easier to characterize, as in solid-state materials. Even metal-metal interactions with a formal bond order smaller than one exist and can be studied in molecules and can be studied on the atomic level. Such a metallophilic Cu-Cu interaction plays a key role in the catalytic cyclization of alkynes with azides, known from click chemistry. The identified reaction intermediate could be stabilized by using tailored carbene ligands (Figure 1b). The alkyne is activated in a σ,π -acetylido complex with one σ - and one π -interaction to each Cu atom, along a Cu-Cu bond.^[7] Further detailed information about fundamentals, reactivities and current developments in homometallic bonds can be found in recent overview articles.^[6] Despite the apparent relevance of homometallic bonds to the chemical sciences, polarized heterobimetallic bonds show a fascinating chemistry – in materials as well as in molecular compounds.

Heterobimetallic bonds between late transition metals and main group metals are polarized, in solid-state materials as well as in molecules.^[8] The different nature of the metal atoms often assigns them to a different role in their reactivity. Especially compounds with bonds between late TMs and the more electropositive group 13 elements E (E = B, Al, Ga, In) are a combination, which keeps attracting interest, due to their supreme catalytic properties. Apart from the above briefly introduced factors as bond order and polarity, the type of assembly featuring the TM-E bond is pivotal. With increasing molecular size, the compounds can be defined as molecular complexes, atom precise clusters, nanoparticles and bulk-phase intermetallics. In the following, the role of TM-E interactions in compounds of different size regimes are discussed.

1.1.2 Hume-Rothery Phases

Hume-Rothery phases (Figure 2) consist of metal combinations between a TM and electropositive main group metal E, from group 12, 13, 14 (Sn, Pb). The borders between different types of intermetallics are, however, blurry and depend on multiple factors, such as atomic radii ratio, electronegativity difference and the ‘electron concentration’. A detailed and comprehensive assessment of Hume-Rothery phases as well as a discrimination to other intermetallic phases can be found in the dissertation of Jana Weßing.^[9]

Solid-state intermetallic Hume-Rothery phases are investigated as heterogeneous catalysts.^[10] They are a low-cost alternative to precious metal-based catalysts, due to their supreme catalytic properties. It should be noted that solid-state Hume-Rothery phases are

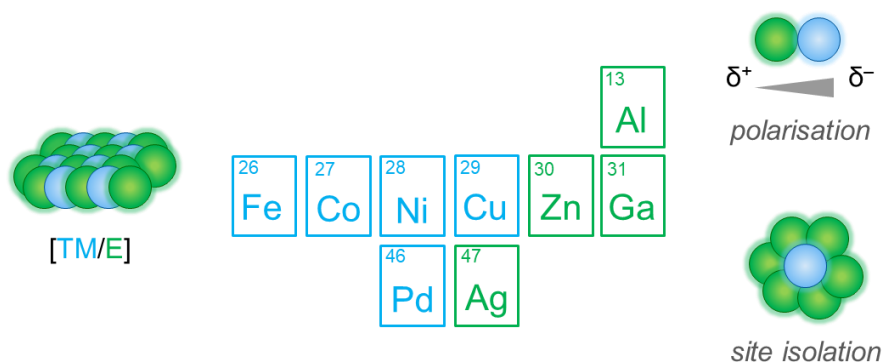


Figure 2: Schematic representation of a Hume-Rothery phase (left), an especially relevant section of elements for Hume-Rothery phases (middle; note the ‘blurry’ lines between the metals - Ag is sometimes employed as E, e.g. in PdAg) and important characteristics of Hume-Rothery phases (right).

infinite, but highly ordered solids, from which single crystals can be obtained.^[11] In contrast, alloys show a randomized atom distribution. The stoichiometric PdGa phase is well-studied and therefore a good example to understand bimetallic cooperativity in intermetallic phases.^[11-12] PdGa nicely reflects the so-called site isolation concept, where a single TM atom or TM atom ensemble is surrounded by E atoms and distinct and isolated TM sites are formed. In PdGa every atom is surrounded by seven Ga atoms. The Pd atoms show only negligible contacts with each other, indicated by the relatively long Pd-Pd distances (3.016 Å or longer). In contrast Pd-Ga interactions are much shorter (2.543 and 2.712 Å), pointing to bonding interaction.^[11] In addition to isolating the catalytically active TM atom(s), the electropositive Ga atoms alter the electronic situation of the Pd, another reason for the beneficial catalytic properties. This is supported by X-Ray photoelectron spectroscopy (XPS), that shows a shifted Pd signal in PdGa, compared to metallic Pd and indicates some sort of covalent bonding interaction between Pd and Ga.^[11] Apart from electronic 'fine tuning', the second metal simply offers an alternative binding partner for the substrate of a catalytic process. For the semihydrogenation reaction (acetylene to ethylene) this may increase the selectivity. Calculations on the active centers of the Pd₂Ga phase show, that active sites with a triangular arrangement of one Pd and two Ga atoms, bind differently to acetylene and ethylene: acetylene forms di-σ bonds bridging along the Ga-Ga site, in contrast ethylene weakly binds to Pd in a π-manner (such alkyne-metal interactions remind as well of the copper catalyzed azide alkyne cycloaddition). Due to the strong acetylene interactions with the surface, it gets hydrogenated, whereas for ethylene desorption is easier, than further hydrogenation.^[13] Especially studying molecular defined substrate interactions under catalytic conditions is experimentally very challenging and a lot relies on advanced computations. Molecules, in contrast, are by far easier to study under reaction conditions and reaction intermediates can sometimes be isolated.

An in-depth discussion on bimetallic Hume-Rothery phases in the application of (semi-)hydrogenation catalysis as well as their relation to atom precise complexes and clusters can be found in the dissertation of Julius Hornung.^[14] It should though be emphasized, that local and atomically defined active centers have pivotal influence on the substrate interaction and therefore on the catalytic selectivity – irrespective of 'less local' processes such as hydrogen migration and the fact, that under realistic conditions, materials suffer from defects sites on their surface.

1.1.3 Hume-Rothery Inspired Nanoparticles

The reactivity of Hume-Rothery nanoparticles (NPs) basically relies on the same principles as in solid-state intermetallics: site isolation of TMs, subtle changes of the electronic situation of the TM and additional reaction centers in form of E sites. Despite the non-trivial synthesis of phase pure NPs, they are crystalline and therefore well-ordered on the molecular level.^[15] The smaller the NP becomes, the less order is intrinsically possible. Benefit of NPs is the higher surface-to-volume ratio, which is promising for increased substrate interaction and therefore higher activity. On the other side, surfaces are always prone to form defects and other irregularities, their number is thus increased. Moreover, agglomeration of such nanophases has to be hampered by using surfactants, which act as protecting groups and are located on the surface of the nanoparticle. Without the choice of the right surfactant often amorphous metallic agglomerates are obtained. Ideally the surfactants are bound to the E atoms, while the TM centers remain well-accessible. In a way, this introduces some diffusion limitation, which however should not be too high in the homogenous phase, if sufficient substrate is present. Colloidal NPs in a surfactant shell are typically soluble and can therefore be regarded as 'quasi-homogenous'.^[16] Alternatively NPs can be deposited on a stabilizing support.^[17]

Yet, there is not a big number of publications on Hume-Rothery NPs. This is most likely due to their difficult synthesis: non-noble metals have a different redox potential than noble metals, which typically precludes co-reduction approaches - the established procedure in the synthesis of monometallic NPs.^[18] A standard procedure to phase pure Hume-Rothery NPs is still not developed and once more emphasizes the difficulties in forming TM-E bonds. The 'organometallic approach' (Figure 3), which involves organometallic precursors as the TM and E source, recently allowed to access different TM/E NPs with rather narrow size-distributions: controlled decomposition of organometallic precursors in presence of stabilizing agents (e.g. ionic liquids) produced catalytically active Ni/Ga and Cu/Zn NPs.^[19] The use of the σ -donating E(I) ligands, that coordinates the TM in solution, leads to small and uniformly distributed TM/E NPs, via smaller clusters and was successfully demonstrated for Ni/Al, Pd/Ga and Fe/Al.^[20]

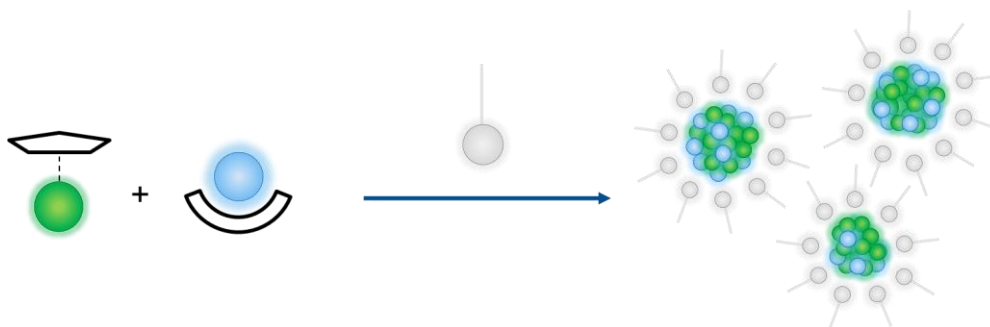


Figure 3: Schematic representation of the 'organometallic approach' towards bimetallic nanoparticles. In the presence of a surfactant (grey), a TM (blue) and an E (green) precursor form (ideally a narrow size distribution of) different surfactant-stabilized TM/E particles. The reaction is typically triggered by temperature or microwave irradiation.

Especially detailed theoretical studies shedding light on cooperative effects in Hume-Rothery NPs are missing to date. This would be of high interest, especially due to a possible combination of experimental observation and theoretical findings. Colloidal nanoparticles may be regarded as nano cut-outs of intermetallics, being in solution and quasi-homogenous at the same time. This opens up the use of a pool of analytical methods that cannot be used in the solid-state. Despite it should be noted, that nanoparticles are not atom precise and always formed in mixtures. An in-depth discussion on bimetallic Hume-Rothery nanoparticles and their application in (semi-)hydrogenation catalysis can be found in the dissertation of Lena Staiger.^[21]

1.1.4 Defined Bimetallic TM/E Complexes

1.1.4.1 Bonding principles

Following the order of size regimes, atom precise clusters would have to be discussed here. In the interest of this thesis, clusters are skipped for the moment and heterobimetallic complexes, the 'smallest' molecules (in terms of metal atom number), are introduced. Whereas the study of TM/E-substrate interaction in the solid-state is highly complicated, requires sophisticated *in-operando* techniques and modern quantum computational approaches,^[2] molecular compounds offer much more analytical techniques and thus better accessible and more precise information about such interactions. Information gained from atom precise molecular complexes may provoke a structure-reactivity-relationship that can be transferred to solid-state intermetallics.^[14] The more accurate the knowledge about structures and processes at the active site is, the higher the chances to improve the catalytic properties of the material.

The formation of bonds between TM and E, independent of being based on covalent or coordinative interactions, is very difficult and often such bonds are not stable – this is also well-known in chemistry bimetallic clusters and nanoparticles.^[22] In contrast, solid phases are formed by ‘simple’ alloying of two metals in the correct stoichiometry. Especially in the last decade, multi-dentate pincer-type ligands were recognized as scaffolds to bring TM and E atoms in sufficient proximity to each other. Here, the transition metal is typically in the oxidation state 0 and is coordinated by phosphines. The group 13 element is formally in its most stable oxidation state +3, either coordinated by amides or alkyls.^[22] Interactions between TM and E can be explained by the electron richness of the TM atom and electron deficient situation at the E atom. They act as Lewis-base (TM) and Lewis-acid (E) pair. So, E(III) is considered to be a Z-type ligand: the filled d-orbitals of the TM donate electron density into the empty p-orbitals of the E in a dative σ -type bond.^[23] This withdraw of electron density alters the electronic situation of the TM and thus changes its catalytic properties. The type of interaction is somewhat reminiscent to the situation in frustrated Lewis pairs.^[24] The σ -acceptor properties of E ligands are in sharp contrast to common organic L-type ligands applied in TM chemistry (Figure 4): phosphines are strong σ -donors and weak π -acceptors, whereas especially the π -accepting properties increase for ligands like carbon monoxide.^[25]

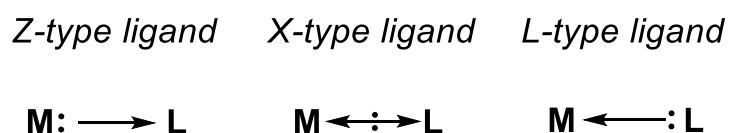


Figure 4: Schematic representation of different metal-ligand interactions.

Besides beneficial electronic influence, another advantage of TM-E bonds in (catalytic) bond activation is the non-innocent part of the E atom. Often substrates are activated along the TM-E bond and both elements participate. Metal-Ligand-Cooperation (MLC) (Figure 5) is especially attractive for polarized substrates $A(\delta^+) - B(\delta^-)$, which are coordinated by the $TM(\delta^-) - E(\delta^+)$ in inverse manner.^[26]

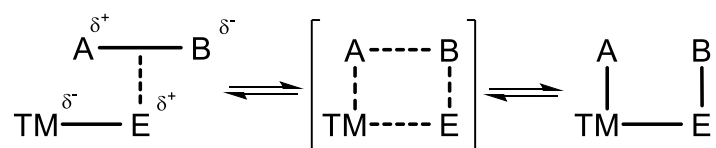


Figure 5: Simplified example for metal-ligand-cooperativity.

1.1.4.2 Pincer ligands as scaffolds for TM-E bonds

The probably best studied TM-E (E = group 13 element) bond is the bond between TM and Boron (Braunschweig 2001,2010).^[27] Metalloid boron effectively alters the electronic situation of the TM, due to its high Lewis-acidity and therefore good Z-type ligand properties.^[28]

A breakthrough example how to employ TM-E bonds in a pincer scaffold for catalysis, was the hydrogenation of styrene and 3,3-dimethylbut-1-ene to the respective alkane, with a Nickel-Boron pincer complex.^[29] The sterically unshielded Ni atom heterolytically activates the hydrogen in cooperativity with the adjacent Boron atom (Figure 6). The spectroscopically observed hydride bearing complex features a terminal hydride (Ni-H) and a bridging hydride between Ni and B (Ni-H-B). It is suggested that the Lewis acidic Boron accepts the H⁻ and the Lewis basic Ni accepts the H⁺.^[29] Moreover, the Boron atom helps to overcome the typical instability of monomeric Ni systems with two terminal hydrides, which typically results in instant reductive elimination of H₂.^[30]

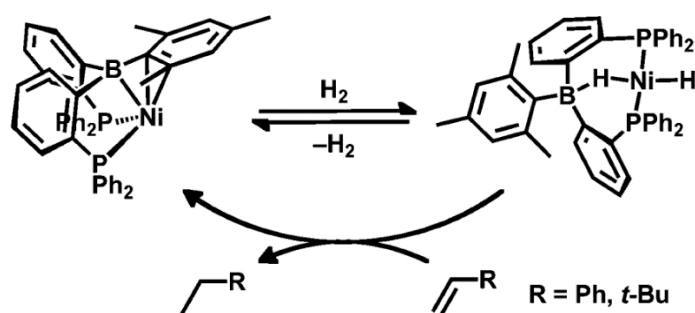


Figure 6: Cooperative hydrogen activation by a Ni-B pincer complex enables catalytic hydrogenation of alkenes. Reprinted with permission.^[29]

Similar cooperative H bridging between TM and B has been observed in Pd-B complexes, using KH as hydride source and can be catalytically exploited in the hydrodechlorination of aryl chlorides.^[31] In the latter example, the ‘intermediate’ hydride bearing complex can even be crystallographically characterized. Fixed atom positions are known, and defects or irregularities as in the solid-state materials do not exist.

Flexible incorporation of the heavier group 13 congeners and the use of different ‘true’ main group metals Al, Ga and In as ligands is by far more difficult, due to their high Lewis acidity and reactivity. A prime example is the hydrogenation of alkenes to alkanes with a Ni/E (E = Al, Ga, In) series in a 3-fold N,P-multidentate scaffold (Figure 7).^[32] Though a different scaffold is used, this can be placed in context of the above-described hydrogenation with a Ni/B complex.

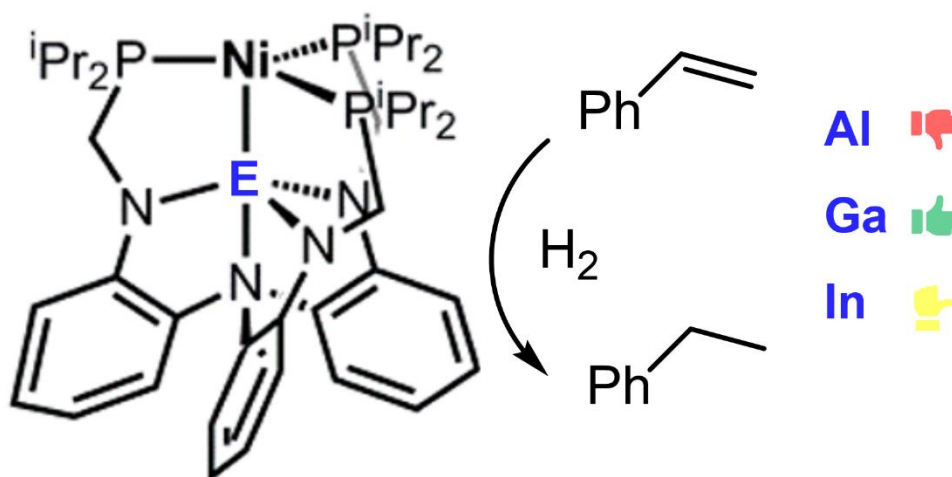


Figure 7: Bimetallic pincer complex. Activity of the catalytic hydrogenation depends on the choice of Al (no catalysis), In (low activity) and Ga (full conversion). Modified version reprinted with permission.^[32]

A series of Ni/E complex was prepared and tested for their catalytic activity. A stronger dative bonding from Ni to E can be observed with increasing ion size (In > Ga > Al), which results in a more electron deficient Ni. Whereas the Ni complex without E in proximity, as well as the Ni/Al complex show neither interaction with H₂ nor catalytic activity, the Ni/Ga and Ni/In analogues do. For Ni/In the H₂ adduct can be isolated, while for Ni/Ga it can only be observed spectroscopically. Interestingly, the Ni/Ga compound is 24 times more active in hydrogenation catalysis as the Ni/In compound. The reason for the significant difference in catalytic activity is not fully investigated, however experimental evidence suggests that H-H bond cleavage, as well as olefin coordination are associated with the rate determining step. Heuristically one might conclude that the remarkable stability of the dihydrogen Ni/In complex, which has been identified as resting state, intrinsically leads to a slow catalysis.

The same Ni/Ga complex was also tested in the hydrogenation of CO₂. While the pure Ni pincer complex shows no conversion of CO₂ to formate, the Ni/Ga compound is a highly active catalyst (initial turnover frequency 9700 h⁻¹).^[33] The reaction mechanism elucidates the essential role of the Z-type Ga ligand: Upon H₂ pressure the dihydrogen complex is formed, which is deprotonated by a base and forms the anionic complex H-NiGa⁻, featuring a terminal hydride (Figure 8). The CO₂ inserts into the Ni-H bond, resulting in an anionic Ni(0) formate adduct, with the protonated base as counter ion. Eventually, formate extrusion occurs under formation of [HCO₂][BaseH] and the parent Ni/Ga complex, which was identified to be rate determining step. Decisive for the catalysis to occur is the stabilization of the Ni-H, formed from deprotonation of the H₂-NiGa complex. This striking feature is only possible, because the

Ga atom withdraws electron density from the d_{10} Ni center. Solely adding GaCl_3 to the pure Ni complex yields no formate. This once more highlights the advantage of the molecular world: atom precise compounds together with multiple solution-based analytical techniques (including theoretical modelling, to access bond situations in molecules) even allow to understand subtle electronic changes and then to define catalytic cycles. Interestingly NiGa phases were shown to be active CO_2 hydrogenation catalysts.

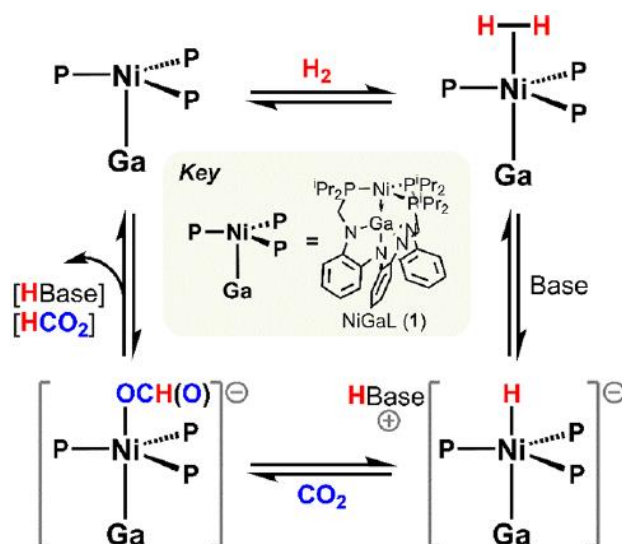


Figure 8: Proposed mechanism for the catalytic CO_2 conversion to formate using a Ni/Ga pincer complex. Reprinted with permission.^[33]

Even higher turnover frequencies in hydrogenation of CO_2 are reached with Co/Ga complexes. The entire series (Al, Ga and In) of Co/E complexes was tested, and again the Ga Z-type ligand is crucial for stabilization of the active Co(-I) species.^[34]

So far, the Z-type E ligands were placed in *trans* position to the reaction center, activated the TM, however, did not directly participate in the reaction. This is different in the Rh/Al catalyzed magnesiumation of aryl fluorides.^[35] In the *in-situ* generated catalyst, the Al acts as X-type ligand (two amide, one amine coordinating to Al – formally Al^{II}) and the Rh is only coordinated by two phosphines. Sterically this allows the aryl fluoride to coordinate along the Rh-Al bond (Figure 9). Calculations show that the F atom is directed to the Al atom, and upon C-F cleavage the aryl binds to the Rh. The catalyst can be renewed by reduction with Mg, which also leads to the magnesium aryl compound. The latter can then be converted to benzoic acid with CO_2 . Calculations on the mechanism clarify, that a Rh-only-centered C-F activation would energetically be extremely unfavored. Sadly, the authors did not perform an in-depth

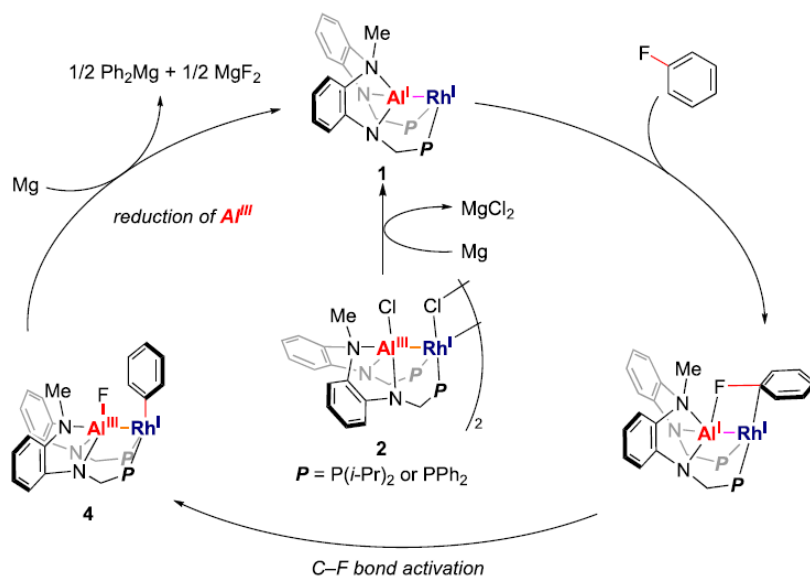


Figure 9: Proposed mechanism for activation of aryl fluorides along a Rh-Al bond. Reprinted with permission.^[35]

calculation on the Rh-Al bond in this complex. They propose rather an Al(I)-Rh(-I) interaction, but not too much is known about this.^[35-36]

The use of pincer-type ligands for bimetallic cooperativity is still its infancy and a young research field. Though, it nicely illustrates the power, as well as the richness of a transition metals in proximity to group 13 metals. It further allows to gain mechanical ideas of bimetallic cooperativity on the molecular defined level. An especially interesting aspect of these molecules is the fact, that their chemistry is not limited to bond activations: even catalytic transformations are possible. More fascinating examples of this intriguing chemistry, including ammonia synthesis from its elements^[37], can be found in a very recent review^[22], as well as a special issue^[38] in *Chemical Science*.

1.1.5 Hume-Rothery Inspired Atom Precise Clusters

Another class of molecules that lies between complexes and nanoparticles are clusters. Only a limited number of TM/E clusters has been found so far. Usually they all share subvalent E(I)R (R = organic ligand) L-type ligands. The unpaired electrons resemble a lone pair with 2S character, making these ligands strong σ -donors. A common R group is Cp* (Cp* = C₅Me₅), due to its good shielding properties and flexible binding modes. ECp* (E = Al, Ga, In) is thus isolobal to more classical ligands such as carbon monoxide, phosphine and N-heterocyclic carbenes (Figure 10). This has been proven by extensive substitution chemistry^[39] and theoretical investigation on their bonding properties^[39a, 40].

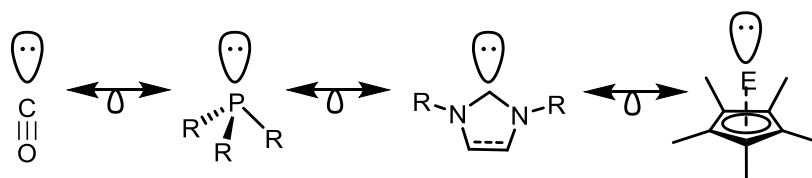


Figure 10: Isolobal relation between ECp and the common ligands, carbon monoxide, phosphines and N-heterocyclic carbenes (from left to right).*

Compounds resulting from reaction with TM precursors range from ‘classical’ complexes, that can be explained by the 18 valence electron rule^[39, 41], up to large intermetalloid superatoms^[41-42]. The intrinsic donor properties of ER ligands create direct TM-E bonds, without the need of elaborated scaffolds, such as multidentate pincer ligands. Indeed, often the strong σ -donation of the ER ligands leads to high electron density at the TMs, which in turn is promising for reactivity. Several bond activations have been reported within this compound class and all can be related to a bimetallic cooperativity. Substrate activation usually is centered at the TM, which is activated by the σ -donation of the ER ligands. The driving force, however, is often associated to the irreversible oxidation of E(I) to E(III) and the formation of strong E-C bonds. This limits substrate activation to stoichiometric reactions so far. In solid-state compounds, also the TM plays the active role, while E takes over a supportive character.

A well understood example is the oxidative addition of aromatic C-H and Si-H bonds to the 16 VE intermediate [Ni(AlCp*)₃] (Figure 11).^[43] Interestingly, the Si-H bond activation takes place at the Ni and the hydride as well as the silyl are both bound to the Ni center, giving [(H)(SiEt₃)Ni(AlCp*)₃]. All Al(I) ligands are intact and the reversible reaction can be thermally induced. In contrast, the C-H bond is most likely activated at the Ni too, however the hydride

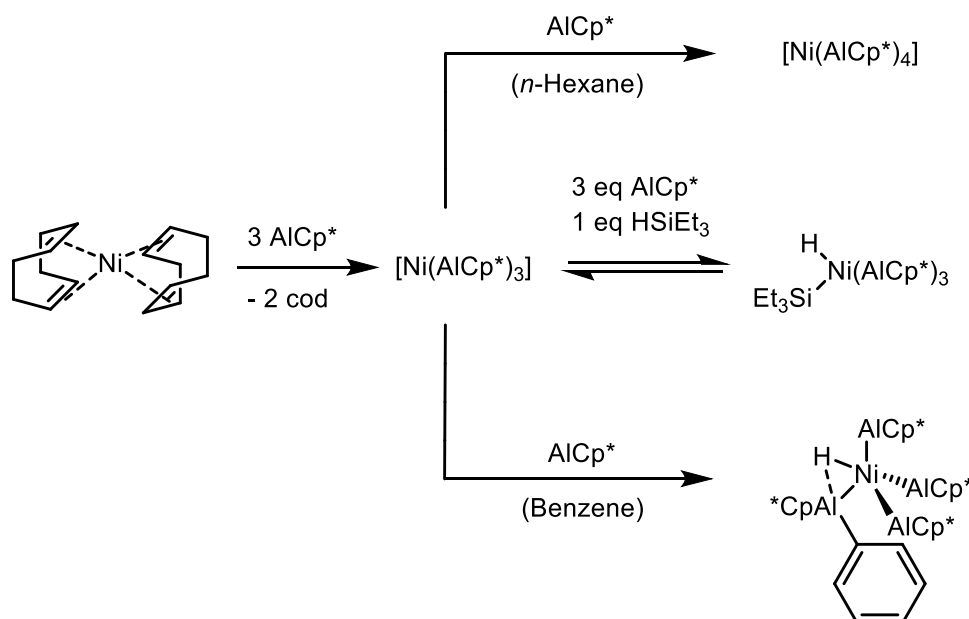


Figure 11: The intermediate $[\text{Ni}(\text{AlCp}^*)_3]$ in ir-/reversible bond activation.

is now in a μ^2 -bridging position between Ni and Al and the phenyl is completely transferred to an Al atom. The Al atom is formally oxidated to Al(III) and the reaction is thus irreversible.

Similar C-H activations have been observed in the AlCp* analogues of $\text{Fe}(\text{CO})_5$ and $\text{Ru}(\text{CO})_5$.^[44] Here the C-H bonds in two of the five Cp* ligands get intramolecularly activated, again resulting in μ^2 -bridging hydrides between Al and Fe/Ru and direct $\text{H}_2\text{C}-\text{Al}$ bonds. The complex $[\text{Cp}^*\text{Rh}(\text{CH}_3)_2(\text{GaCp}^*)]$ even shows a facile intramolecular C-C bond activation of Cp* under surprisingly mild conditions, yielding in the Ga(III) compound $[\text{RhCp}^*(\text{C}_5\text{Me}_4\text{Ga}(\text{CH}_3)_3)]$.^[45] Under hydrogenolytic conditions the $[\text{Ru}_2(\text{Ga})(\text{GaCp}^*)_7(\text{H})_3]$ cluster is formed, featuring hydrides from H_2 activation and a naked Ga from Cp* hydrogenolysis.^[46] Also, compounds with more than two TM atoms show interesting reactivity towards substrates. The hydride rich cluster $[(\text{H})_4\text{Cu}_6(\text{AlCp}^*)_6]$ forms the adimate $[(\text{PhHC}=\text{N})(\text{H})_3\text{Cu}_6\text{AlCp}^*_6]$ species in presence of benzonitrile via hydride migration: one hydride inserts into the C-N triple bond and reduces it to a formal double bond.^[47] An example of the diverse reactivity of bimetallic cluster is the radical $[\bullet\text{Cu}_7(\text{AlCp}^*)_6]$, which either incorporates another Cu atom, or activate C-H or Si-H bonds to get into a closed-shell configuration and to form $[\text{Cu}_8(\text{AlCp}^*)_6]$ or $[(\text{H})\text{Cu}_7(\text{AlCp}^*)_6]$ respectively.^[48] Notably, the large triradical $[\text{Cu}_{43}\text{Al}_{12}\text{Cp}^*_{12}]$ cluster shows no related reactivity, such as solvent activation. This can be explained by its uniformly coordinated protective Cp*₁₂ shell and its low solubility.^[42a] Most interestingly, the latter cluster already shows an electronic structure closely related to a conductive band, as common in bulk metals.

Hume-Rothery inspired atom precise clusters are indeed the link between molecules and the bulk phase. Several reports on the structural resemblance between Hume-Rothery inspired molecules and their respective solid-state counter parts can be found.^[47, 49] The metal core of the introduced Cu/Al cluster series $[(\text{H})_4\text{Cu}_6(\text{AlCp}^*)_6]$, $[\bullet\text{Cu}_7(\text{AlCp}^*)_6]$, $[(\text{H})\text{Cu}_7(\text{AlCp}^*)_6]$ and $[\text{Cu}_8(\text{AlCp}^*)_6]$ shows striking similarity to the nested polyhedral in the molecular structure of solid-state γ -brass (Figure 12).^[47] In this context, the hydride-bearing clusters might be regarded as a hydrogenated Cu/Al surface site, and the insertion reaction with benzonitrile as the first step of a hydrogenation reaction.

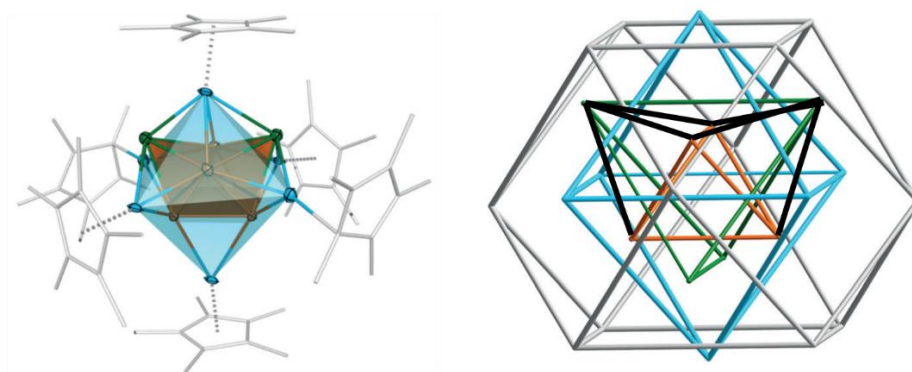


Figure 12: Molecular structure of $[(\text{Cp}^*\text{AlCu})_6\text{H}_4]$ (Cu atoms orange and green, Al atoms blue) (left) compared to the 26-atom nested polyhedral of γ -brass (right) with highlighted bicapped tetrahedron (black). Graphic adopted and reprinted with permission.^[47]

If clusters mimic the local structures of solid phases, can they also mimic their reactivities? A thought-provoking example, that not only the structure, but also the reactivity and associated selectivity of Hume-Rothery phases is reflected in clusters, is the DFT study on a series of Ni/Zn complexes (Figure 13).^[50] Ni/Zn phases were previously shown to be very selective in the semihydrogenation catalysis of acetylene to ethylene.^[10b] The complexes $[\text{Ni}(\text{ZnR})_4(\text{C}_2\text{H}_x)_2]$ ($\text{R} = \text{Cp}^*, \text{CH}_3; x = 2,4$) show a different coordination of acetylene or ethylene to the Ni/Zn center: Whereas ethylene solely coordinated to Ni (π -manner), the acetylene gets activated by coordination to Ni and Zn in a bridging fashion (σ -manner). The different coordination to Zn and Ni is indeed analogous to the solid-state Pd/Ga example introduced above: acetylene binds in a di- σ bond to two Ga sites, whereas ethylene solely shows a weak π -coordination. Despite a lot of effort has been made, such complexes were not isolated so far.^[14]

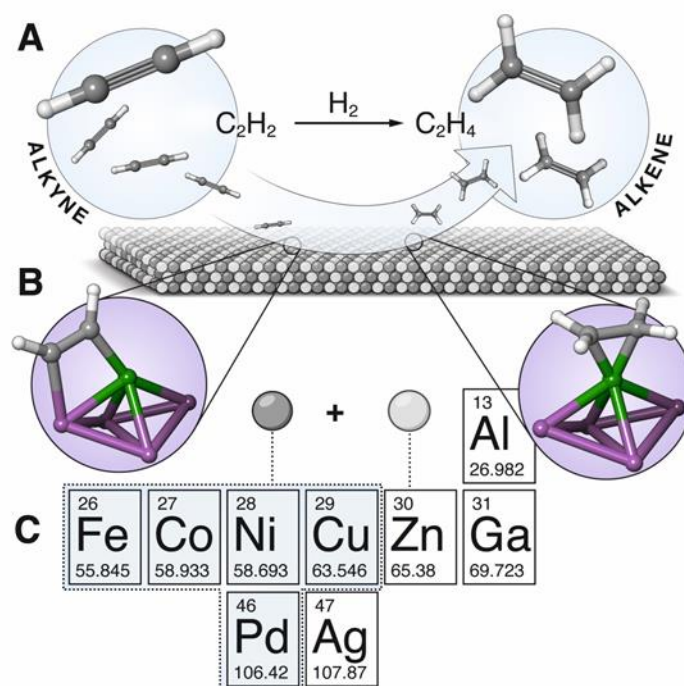


Figure 13: Concept figure for using atom precise compounds as cut-outs of surfaces. Reprinted with permission.^[50]

Clusters combine two interesting aspects: 1) they are atom precise, as the pincer complexes, which allows to follow bimetallic cooperativity and its influence on reactions on the molecular level - with all the advantageous analytical methods. 2) they resemble the structure and partly the reactivity of solid-state intermetallics, making them interesting model systems to understand the roles in metal cooperativity in solids.

The presented reactivities are interesting and the compound class is promising to exhibit unprecedented reactivities and/or bond activations. Being a link from the atom precise molecular world to materials chemistry at the same time, makes studying these compounds even more attractive. A controlled access to reactive sites at clusters, or smaller 'proto cluster species', would be essential to encounter novel reactivities. Inspired by solid-state phases, nanoparticles and pincer complexes, however, the question arises if L-type coordinated molecular defined clusters can participate in catalytic transformations? Can the observed reactivities be eventually related to the solid-state phases? And if yes, can conclusions be drawn conclusion from it, and how far can they advance knowledge about cooperativity?

1.2 The Wet Chemical Synthesis of Metallic Clusters

1.2.1 Why Clusters?

The world of metal aggregates ranges from infinite bulk materials over nanoparticles to metal containing molecules and complexes (Figure 14). Metal clusters are molecules and molecules are atom precise. Clusters are situated on the border to bigger and less defined materials, such as nanoparticles or even bulk metals. In the size regime of clusters (and molecules in general) 'every atom counts'. Clusters are very sensitive towards small changes of their composition and structure: the number of metal atoms and/or cluster geometry have pivotal influence on their physical and chemical properties, whereas materials are by far less affected by such subtle changes.^[51] Exemplary for this phenomenon, a Pt₁₂ cluster shows more than two-fold catalytic activity in the oxygen reduction reaction, compared to the one atom larger Pt₁₃ cluster.^[52] The difference between the reactivity of clusters and bulk is even engraved: bulk gold is notoriously noble and unreactive, whereas Au clusters are active catalysts for several reactions.^[53] The sensitive response to small changes makes metals clusters an interesting compound class. The directed synthesis of such molecules is, however, intrinsically difficult.

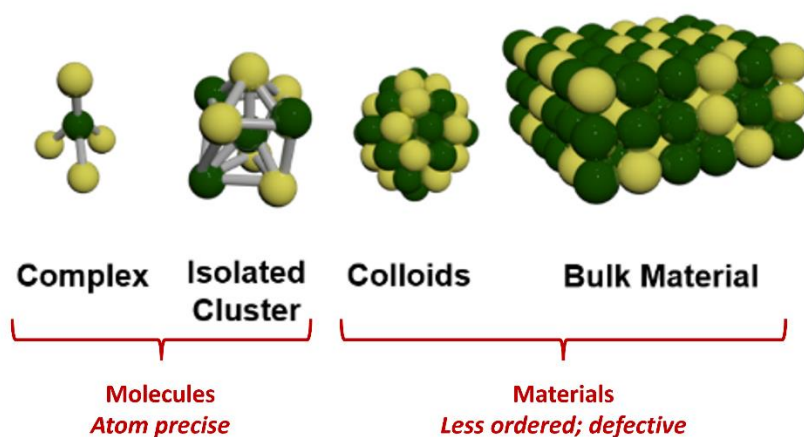


Figure 14: The world of metal aggregates - from molecules to materials.

1.2.2 Basic Electronics of Clusters

The altered and sometimes amplified reactivity of clusters compared to nano/bulk materials can be rationalized by the superior surface-to-volume ratio and therefore high number of surface atoms. Moreover, the electronic structure of clusters is crucial in determining the reactivity. Multiple simplifying theories have been developed to describe electronic situations of clusters. Especially for spherical clusters the jellium model, and with it the superatom concept was proven to be an appropriate description.^[54] This model presumes, that the positive nuclear charges are homogeneously distributed over the spherical cluster and the electrons are subject to the resulting potential field.^[55] This is reminiscent to an atom, where the central nucleus is surrounded by its electrons. Hereby jellium orbitals are occupied that again are similar to atomic orbitals (Figure 15).

The cluster Al_{13}^- (originally studied in the gas phase,^[56] later also prepared by wet chemical synthesis^[57]) is a well-studied example of a superatom, which reflects electronic structure as well as the reactivity of a single atom. The geometry of this superatom can be best described as a Al_{12} icosahedron, which is filled with one Al atom. The anionic species features 40 electrons ($13 \times 3 + 1$) and is thus in closed-shell 2P jellium configuration. The Al_{13}^- superatom shows striking similarity to halogenides: not only because of the closed P shell, but also the reactivity strongly reminds of that of a classical halide: when an ion stream of Al_{13}^- reacts with hydrogen iodide, IAl_{13}^- can be observed.^[56] Quantum chemical calculations reveal, that the Al_{13} kernel is still intact and binds to the iodine atom without significant structural changes. Therefore Al_{13}^- is regarded as a 'superhalogen'. Exemplarily by oxygen etching, the compounds $\text{I}_x\text{Al}_{13}^-$ ($x = \text{even number}$) can be observed, which are 'polyhalogenides'.^[58] Recently the Al_{13}^- cluster was also wet chemically prepared assisted by dendrimers (*vide infra*) and showed stunning stability, e.g., towards air.^[57]

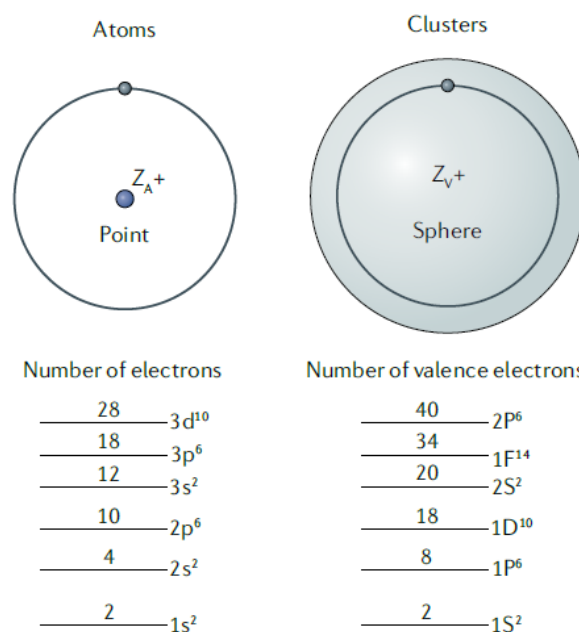


Figure 15: Electronic situation with respective orbitals of an atom (left) and a superatom (right). Reprinted with permission.^[55]

Clusters in the gas phase, are good models to study fundamental properties and reactivities. They show pronounced reactivity towards molecules, which are considered rather inert, such as methane.^[59] The high reactivity can be explained by the unprotected and ‘naked’ cluster surface, which is not shielded by protective ligands. Upscaling is however very limited and associated to support the clusters on solids, e.g., by soft landing methods.^[60] Wet chemical cluster chemistry also allows to study fascinating properties of clusters, maybe even under ‘more realistic’ conditions. Whereas gas phase clusters are typically produced by laser ablation and then mass selected, the selective wet chemical synthesis is by far more complicated. In addition, the synthesis of bi- and multimetallic cluster is more intricate in the gas phase by laser ablation.

1.2.3 Synthesis Principles of Ligand Stabilized Clusters

The wet chemical synthesis of ligand stabilized clusters can be divided into two approaches: 1) bottom-up - the clusters are formed from typically smaller compounds and 2) top-down - preformed clusters are extracted from solid phases.^[8b] The latter is the state-of-the-art procedure in Zintl cluster chemistry. Zintl phases are ordered and consist of elements with a high difference in electronegativity (not always, but often group 1/2 with group 14/15 elements).^[9, 61] By the use of strong coordinating organic molecules as solvents (liquid

ammonia, ethylene diamine), preformed polyhedral Zintl clusters are extruded from the solid-state into solution. Once in solution, the polyhedral entities can be regarded as clusters and subjected to chemical transformation such as functionalization or cluster growth – this is then somewhat reminiscent of the bottom-up approach.^[62]

In the bottom-up approach, clusters are build-up from smaller molecules, typically containing only one metal atom. For most metals, this relies on reduction of the metal(-organic) precursor. The stabilizing organic ligand, which is also one parameter to stir the growth process, can already part of the precursor or can be added to the reaction solution. The resulting metal cluster is then surrounded by a monolayer of the protective ligands. Most gold clusters are prepared accordingly to these principles and are commonly protected by phosphines and thiols.^[54c, 63] The latter are often reductant and protective ligand at the same time, giving disulfides and Au clusters as redox products.^[63]

1.2.4 Hume-Rothery Inspired Clusters

In a way reminiscent to the dual role of thiols in gold chemistry, σ -donating group 13 E(I)R (E = Al, Ga, In; R = Me, C₅Me₅) compounds can either act as reducing agent and/or stabilizing ligand for transition metals – eventually allowing to access bimetallic systems in a bottom-up fashion. As reactivity towards TM(0) complexes, typically coordination along with ligands substitution is observed. In particular weaker donors such as olefins, CO or phosphines are fully or partially replaced.^[39c, 39d] Here the chemical complexity is rather limited, and synthesis is plannable. So the cod (1,5-cyclooctadiene) ligands are fully replaced from Ni(cod)₂ by AlCp* giving Ni(AlCp*)₄^[43], whereas a full phosphine replacement from Ni(PEt₃)₄ is hampered by polarization effects and only Ni(AlCp*)₂(PEt₃)₂ is obtained.^[39e] Such reactions can generally be regarded as reversible processes. Due to the formal oxidation state +1, the subvalent E ligands are prone to oxidation (acting as reductant). E is often oxidized in presence of TM precursors where the formal oxidation state is higher than 0 (+1, +2, ...). Such disproportionation often give formal TM(0) and E(III) containing compounds and are irreversible. Regularly E(III) compounds are observed as by-products of the reduction, whereas the TM(0) atoms form clusters (by an metal agglomeration process) – sometimes stabilized by coordination of E(I)R ligands which did not participate in redox reaction. A suitable example for such processes is the formation of the superatomic M₅₅ Mackay-type cluster [Cu₄₃Al₁₂](Cp*₁₂), which is formed

from the reaction of AlCp^* with Cu(I)Mes (Mes = mesityl). Cu(I) is reduced by AlCp^* and incorporated into the cluster, with is stabilized by a protective icosahedral $(\text{AlCp}^*)_{12}$ shell.^[42a] Notably the reaction proceeds with low yields, pointing to a non-selective transformation. Depending on the choice of reaction conditions (stoichiometry, time, temperature, additives), also smaller Cu/Al clusters, which are potentially involved in the cluster growth process cluster up to $[\text{Cu}_{43}\text{Al}_{12}](\text{Cp}^*)_{12}$, via species like $[(\text{H})_4\text{Cu}_6(\text{AlCp}^*)_6]$, $[\bullet\text{Cu}_7(\text{AlCp}^*)_6]$, $[(\text{H})\text{Cu}_7(\text{AlCp}^*)_6]$ and $[\text{Cu}_8(\text{AlCp}^*)_6]$, as well as redox side products, e.g. AlMes_3 can be observed. In the isolated intermediate cluster $[\text{Cu}_4\text{Al}_4](\text{Cp}^*)_5(\text{Mes})$, Cu(I)Cp^* as well as Al(I)Mes can be identified as structural motives.^[48] This displays another possible reaction type: ligand exchange. Such a reaction is assumed to be irreversible (Cp^* binds stronger to 'soft' Cu, and Mes to hard Al). Depending on the respective example, however, it theoretically could be reversible, because no change of the formal oxidation state is involved. This for example is clearly different for the formal redox reaction of ligand (Cp^*) transmetalation from E(I) to TM(0) , leading to MCp^* and E . Such reactivity has been observed for late TM (e.g. Fe, Co, Ni, Cu) because of their tendency to form stable half-sandwich complexes.^[64] But similar reaction products are also known in the Cu/Al system, in form of the triangular $[\text{Cu}_2\text{Al}](\text{Cp}^*)_3$.^[48]

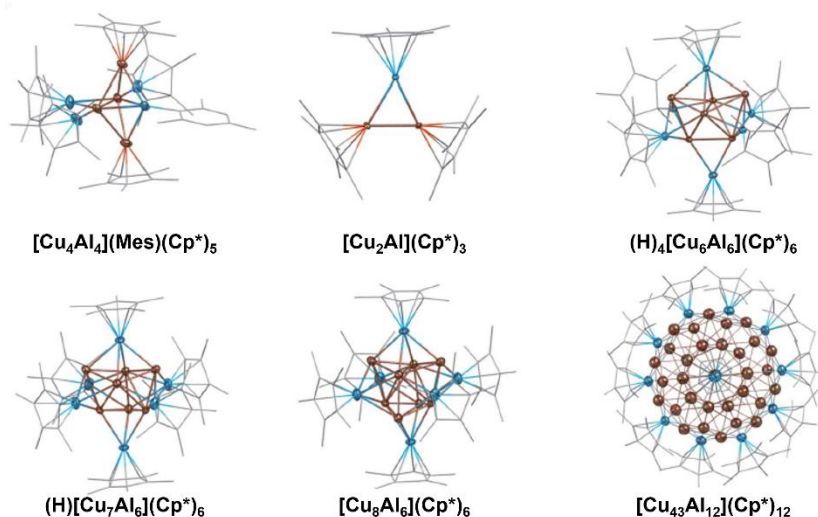


Figure 16: Isolated species of the 'Cu/Al family' as example for the chemical diversity in cluster solutions. Adopted and reprinted with permission.^[48]

In reality, all the described reactivities can (and often do) run parallel. Formed intermediate species are often transient and tend to engage in further reactions (again parallel with multiple possible reactivities). Therefore, it is hardly possible to follow cluster growth step by step, which would be a requirement to design planned synthesis procedures, as organic

synthesis uses the retrosynthetic approach. This remains so far illusive in preparative cluster chemistry – independent of mono vs. hetero metallic and top-down vs. bottom-up, etc. Findings usually relies on cluster which are confined to the ‘islands of stability’ (Figure 16): simply too many species in solution are too reactive to be isolated and only certain thermodynamic sinks (and/or kinetically controlled) can be accessed – and depending on the reaction conditions, they do not necessarily have to have a high concentration in the reaction solution. Heuristically, cluster chemists do not go out to reach ‘the desired island’, they rather explore a so far undiscovered ‘archipelago of unknown islands’. Especially bi- or even multi metallic clusters intrinsically possess a wide variety regarding their composition (number of atoms, stoichiometry) and their structure (geometry, isomerism) – and before being formed, the numerous intermediates follow multiple reaction pathways: every aspect (reactivity, formation, structure, etc.) is difficult or even impossible to control.

1.2.5 Dendrimer Supported Multimetallic Clusters

The use of dendrimers to form and stabilize clusters, is an approach (bottom-up) which offers an alternative to the established ‘trial and error’ strategy in solution. Metal salts (typically metal halides) are selective bound in dendrimers and eventually reduced (by common reductants as NaBH_4) to yield metal clusters supported within the dendrimer.^[55] Dendrimers are highly branched macromolecules, in which ‘multiple layers’ (typically four layers, also called generations or G) surround a central seed in a tree-like manner (Figure 17). Depending on the choice of dendrimer and the associated functional groups, metal salts can be selectively trapped in the dendrimer.^[55] State-of-the-art systems are phenylazomethine (DPA) and its derivatives: Lewis-basic imine units serve as coordination sites and the phenyl groups create a rigid π -system in the side chains. Interestingly, the Lewis-basicity decreases from the inner to the outermost sites and thus a ‘negative potential gradient’ is induced. This can be exploited for the selective coordination of metal salts: first the inner sites (G1) are coordinated, consecutively followed by the outer-next generations (G2-G4). The coordination thus is underling thermodynamic control. Modification of the dendrimer allows for coordination fine-tuning: attaching electron withdrawing fluorogroups at the phenyls next to an imine unit weakens the Lewis-basicity of the respective site and changes the order of coordination.^[65] Adding one pyridine moiety to the central dendrimer-seed (the dendrimer ‘grows’ in four

directions), also renders the complexation order.^[66] The pyridine moiety induces a kind of polarity into the dendrimer, now allowing to add two metals more, where the pyridine site and the adjacent one could potentially be regarded as G-1 and G-0.^[51b] Despite this dendrimer has only one site more, it does not follow the original core-shell-shell-shell like 4-8-16-32 series and heuristically also allows for ‘asymmetric cluster growth’. Also, the rigid π -system in the side chains was shown to be important for a controlled stepwise complexation. Dendrimers without this feature lead to a distorted growth due to the flexibility of the side chains.^[55, 67]

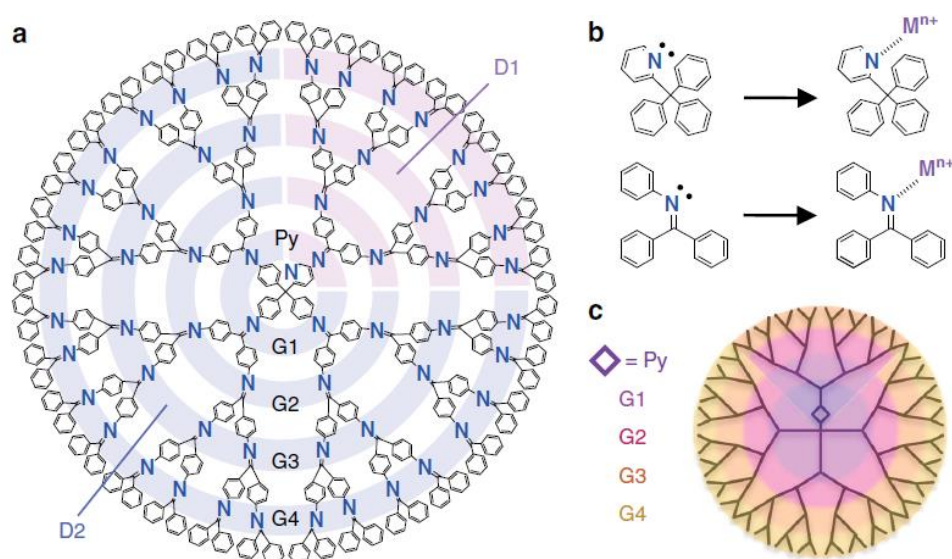


Figure 17: The pyridine modified DPA dendrimer template as example. a) Molecular structure b) Complexation of metal salts at the imine and pyridine sites c) Potential gradient in the dendrimer with an addition G-0 site (= Py). (purple: higher electron density, yellow: lower electron density). Reprinted with permission.^[55]

The counter part to the Lewis-basic imine sites are the Lewis-acidic metal salts. If heterometallic clusters are prepared, the order of complexation is influenced by the metal salt: stronger Lewis-acids (e.g., $\text{FeCl}_3 > \text{GaCl}_3 > \text{AuCl}_3 > \text{SnCl}_2$) bind to the stronger Lewis-basic sites close to the dendrimer-seed – in a way this is common in ‘simple acid-base reactions’.^[67]

The use of dendrimers allows for a controlled cluster synthesis and is thus an impressive tool. Nevertheless, it still has its inherent limitations: stronger acids will always choose the innermost stronger basic sites, preventing to build up heterometallic cluster structures with central elements coming from elements with typical Lewis basic salts (especially relevant for clusters with $M > 12$). Despite, this eventually may be overcome by extensive and laborious fine-tuning of the dendrimers (selective attachment of electron withdrawing/donation groups

in the dendrimer) and ideal choice of metal salts (with the matching Lewis basicity). Irrespective of the exact arrangement within the dendrimer, it is very difficult to identify the exact 'molecular structure' of the cluster after reduction. Alloying of the different metals is clearly proven, e.g., by X-ray photoelectron spectroscopy, and also the sizes of the clusters can usually be estimated by high resolution transmission electron microscopy, nevertheless an exact molecular structure remains unrevealed.^[51b] Such questions are far from being solved, at least experimentally. Single crystal X-ray diffraction is probably the only technique that would allow for assessing such complex structures (up to six different metal elements in a M_{17} cluster) and is elusive for obvious reasons (cluster@dendrimer). A theoretical assessment, also taking the highly Lewis-basic dendrimer support into account, would probably be the most promising solution to solve the problem - at least being able to predict the most probably isomers. This research field, dominated by the Yamamoto group, at least seems to be aware of the synthetic challenges: recently they used a novel dendrimer-seed and coupled it via tritylium (triphenylcarbenium) ions to the tailored DPA branches, in the end allowing them to overcome the four-layer size limitation by accessing a Rh_{84} cluster.^[68]

Even though the several approaches are investigated in wet-chemical cluster synthesis, and innovative advances have been made, a retrosynthetic approach in analogy to organic chemistry is still elusive and by far not insight. The multiple parallel reactivity of (sub)nano compounds and species involved into their formation process are simply too complex and have to be studied in most cases individually per system.

1.3 Accessible Sites at Bimetallic Complexes and Clusters

1.3.1 Prologue

Synergistic effects between two different metal possess very interesting properties for bond activation and catalysis. Atom precise TM/E clusters (TM = transition metal; E = electropositive metal) may allow to study these effects experimentally on the molecular level. Therefore, a central objective of this thesis is to enforce accessible sites at bimetallic clusters and study their reactivity, with the ultimate goal, to study cluster-substrate interactions. To understand the challenges that go along with creating such reactive sites at clusters, first the key challenges of synthetic cluster chemistry have to be named. The chemistry of wet chemical accessible, ligand protected clusters always faces three major challenges: 1) directed synthesis of a targeted cluster; 2) making the structure of a specific cluster predictable and 3) predicting and/or steering the physical and chemical properties of a cluster (e.g., the reactivity). The three challenges are general and thus valid for any type of cluster, however, their details relate to the individual system. Presumably it will be more challenging in the case of multimetallic systems, because a larger set of variables has to be taken into account. For Hume-Rothery inspired TM/E clusters this may be defined as the following:

1) Directed synthesis. As outlined in chapter 1.2, clusters are confined to ‘islands of stability’ – not every agglomeration of metal atoms is stable. Stability is not only defined by composition, but also by geometry and the associated electronic structure. Though certain concepts (e.g. superatom theory) help to understand why certain clusters are stable. It is barely impossible to predict whether a cluster is stable or not. Especially the formation of TM-E bonds is difficult, mainly due to the different redox potentials of TM and E thus the instability of the bond (1.1). This leads to multiple reaction types, that might be involved into the TM/E cluster formation, which can run consecutive and/or parallel. It might also be possible that the same intermediate participates in competing reactions. This leads to multiple reaction products and the reaction outcome is difficult to control. If more than one metal is involved and the metals differ in their properties (e.g., redox potential, affinity for a ligand, possible coordination number), it is even more delicate to gain control over the synthesis outcome (1.2). In the chemistry of ligand protected TM/E clusters, typically the TM precursor gets either coordinated or reduced by ER. Same accounts for the formed intermediates. Whether the reaction steps are reversible (e.g., coordination) or irreversible (e.g., redox

processes) plays a decisive role, for the eventual product distribution, as well as for the possibility to steer a reaction in a desired manner. In contrast to the retrosynthesis concept in organic chemistry, a cluster synthesis cannot be designed 'from scratch'. A system rather must be screened for the existing clusters ('islands of stability') and the reaction might be optimized towards enriching a selected species.

This goes hand in hand with another challenge: *in-situ* quantification techniques to monitor reactions and enrichment of species are missing, because the common methods of organometallic chemistry fail. Exemplary, NMR gives only information about ligands and not about the metal nucleus. Moreover, fluxional processes often hamper clear assignment and heavier clusters suffer from bad solubility. This typically results in a 'trail-and-error' approach, where several reaction conditions are tested (usually without knowing details about species in solution), until 'something crystallizes'. In contrast, mass spectrometry is not a quantitative method, but a powerful tool to give the composition of a set clusters. Having knowledge of the possible reaction involved from previous work on similar systems, helps to understand and manage a new cluster synthesis.

2) Structure prediction. Predicting the structure of a cluster "from scratch" is usually very difficult. For clusters of a given elemental composition, there are many ways to arrange the atoms spatially, even under strong constraints such as a spatially optimal arrangement of the organic ligands at the surface of a core of metal atoms. Simple structure prediction models such as Wade-Mingo's rules based on counting valence electrons or framework electrons often fail for larger cluster compounds.^[55, 69] As a basic principle, a metal cluster aims to minimize its surface area. In gas phase chemistry it is somewhat established to conclude the structure of a pre-selected cluster: from its m/z value the composition can be assessed, further gas phase spectroscopies allow to identify structural motives and theoretical considerations give possible structures.^[56, 58-59, 70] The latter plays a key role in the structural prediction and demands a precise and well-fitting theoretical model (e.g. correct functional in DFT). To identify the most probable geometry, the lowest energy structures are matched to structural motives that can be concluded from experimental data (if such data exists) and eventually the one most likely structure can be predicted.

In ligand protected cluster chemistry the molecular structure is commonly revealed by SC-XRD. If a single crystal of sufficient quality is obtained, the geometry of the cluster can be

revealed, and the atom position are assigned. Notably, crystalline material is usually associated to enriched solutions of the respective compound. For TM/E clusters the metal assignment is sometimes more delicate: when working with metals with a similar electron density (e.g., Cu/Zn, Ni/Ga), it sometimes is difficult to distinguish between the metal types and only a metal framework can be deduced. In order to pin down the metal positions, the allocation is to be further supported by means of spectroscopy (e.g. NMR, IR) or theory (calculation the different isomers).^[42b] An '*ab initio*' prediction of wet chemical accessible bimetallic clusters based on mass spectrometry has only been performed on Au/Ag M₂₅ cluster, where certain Au atoms were replaced by Ag atoms, while maintaining the original M₂₅ skeleton.^[71]

3) Reactivity control. Gaining control over the reactivity of a cluster is challenging, because usually multiple reaction pathways are possible. Ligand stabilized metal clusters can be involved in various types of reactions. With respect to the reaction site (core or ligand periphery), distinction of two general types of reactions can be made: i) cluster growth or degradation: reaction with a metal source (e.g. metal complexes, clusters) can lead to an increase of the number of metals in the core (growth) while reaction with strongly binding ligands can lead to a decrease of the number of metals in the core (degradation)^[48] and ii) interaction of either the cluster core or the ligands with organic substrates (ligand coordination, substrate activation, etc.).^[43, 46] While cluster growth was discussed in 1.2, accessible reactive sites are essential for the latter reaction type. Many classical organometallic reactions are possible, ranging from simple ligand/solvent coordination to bond activation reactions. In monometallic cluster chemistry, the ligands are intrinsically the only instrument to influence the properties, and thus the reactivity of a cluster (assuming a predetermined cluster composition and geometry).^[72]

In bimetallic TM/E cluster chemistry, both metals have a major influence on the reactivity of the cluster. While the transition metal usually remains the active site, its electronic properties are also influenced by the electropositive E metal, either indirectly by changing the electronic situation of TM (frontier orbitals, polarization, etc...) or directly by acting as a second reaction center. The observation that E cooperatively alters the electronic situation of a TM center in a TM/E compound, and thus the selectivity of a reaction, has so far been limited to complexes.^[22] The involvement of E as a second reaction site in bond activation processes has also been documented: The highly reactive complex [Cp*Rh(CH₃)₂(GaCp*)], for example,

triggers intermolecular C-C bond activation of a C_5Me_5 ligand under unusually mild conditions.^[45] Intramolecular C-H bond activation is observed in Fe/Al and Ru/Al compounds. Intermolecular C-H and Si-H activation of C_6H_6 and $HSiEt_3$ is mediated by the intermediate $[Ni(AlCp^*)_3]$.^[43] This is a consequence of the high donor capacity of the ECp^* ligand, which leads to highly nucleophilic TM centers that are readily accessible for stoichiometric oxidative addition reactions. The thermodynamic driving force of these reactions can be partially attributed to the irreversible oxidation of the low valence Al(I) centers and the formation of strong Al-C bonds. Nevertheless, these reactions remain stoichiometric and non-reversible, which prevents their application in catalytic cycles. Another challenge is to keep the TM sites accessible in the cluster synthesis. There are numerous examples of transmetalation of Cp^* from ECp^* to TM, blocking the TM centers and preventing any substrate interaction.^[64a, 73] Several approaches have been investigated to prevent or circumvent the blocking of TM centers by ligands: Cp^*H elimination by hydrogenation^[46] or protolysis^[74], oxidative cleavage^[75], protolytic ligand replacement^[76], phosphine dissociation^[39e, 77], or additively controlled cluster synthesis^[78]. However, the examples prove to be rather difficult or not very general, remaining limited to the respective systems.

1.3.2 Concluding remark on the three challenges

While the three major challenges of cluster chemistry can be defined individually, in practice they are always interrelated and cannot be addressed independently. As indicated earlier, (1) the directed synthesis of a cluster, and most likely (2) its spatial structure depends on (3) controlling the reactivity of the cluster and its intermediates. This is why cluster chemistry is so complicated, difficult to understand, and probably under-researched. At the same time, it makes cluster chemistry a highly interesting field of research, characterized by chemical complexity and diversity. In the following, the three challenges of cluster chemistry will be discussed in the context of the research on which this thesis is based. Cross references to the one or multiple challenges in the respective context will be made be in brackets and in *italic*: e.g., synthesis (1); structure and reactivity (1, 3).

1.3.3 Mass spectrometry in cluster research

A prerequisite for assessing the composition of reaction solutions (1) and to follow the reactivity of the respective clusters (3), is an analytical method that allows the individual species to be observed directly in solution. Common solution techniques such as NMR fail in the study of clusters because they are limited to the analysis of the organic ligands bound to the cluster surface and do not provide sufficient information about the metal core (e.g., number of metal atoms). Mass spectrometry (MS), on the other hand, provides information on the overall cluster composition. The combination of a high-resolution molecular mass with its isotopic pattern ('fingerprint' of the elemental combination) allows to determine the exact composition of an ionized species or at least to propose a small number of suitable compositions. The determination of compositions is further facilitated if all possible reactants (type of metal atoms, ligands, additives and solvents) are known and can usually be pinned down to one species by labeling experiments.

For this purpose, an ionization method must be chosen that is sensitive enough not to decompose the cluster species during ionization. For charged gold as well as Zintl clusters, electrospray ionization (ESI) is the method of choice.^[79] For neutral Hume-Rothery inspired clusters, LIFDI-MS (Liquid Injection Field Desorption Ionization) has already been shown to yield the M^+ ion from pure substances in many cases.^[80] This method has its origin in the very sensitive ionization method field desorption (FD): a dissolved sample is placed on an electrically conducting emitter rod, which has a high surface dendrite structure. By applying a strong electric field in a vacuum, the weakest bound electron of a compound is removed - usually yielding the M^+ ion, even for sensitive organometallic compounds. The technique can be applied to moisture and air sensitive compounds by passing the liquid sample through a thin fused silica transfer capillary (LIFDI) by piercing the protective septum of the vial stored under an inert atmosphere.^[81] Regardless of the transition from FD to LIFDI, the inner surface of the transfer capillary, connecting the ionization chamber to the sample, is constantly exposed to moisture and air. When working with reaction solution and mixtures (in which several compounds are present only at low concentrations) of very moisture and air sensitive compounds (which decompose upon contact with the adsorbed water molecule on the capillary), it is necessary to ensure that each species "survives" transport to the emitter. Therefore, a setup was developed that combines a ThermoFisher Exactive Plus Orbitrap mass spectrometer (high resolution) with a liquid injection field desorption ionization source

connected directly to an inert atmosphere glovebox (2.6).^[81] Since the transfer capillary is constantly kept under inert atmosphere, much less decomposition is observed compared to the classical LIFDI setup. This is vividly illustrated by the observation of a series of highly reactive Cu/Al clusters^[48] or even a mixture of up to 24 Cu/Zn clusters^[80].

1.3.4 Ni/Ga: Cp* transmetalation as root for a mixture in a crystal

Leading research questions: How to deal with inseparable mixtures? Can structure be predicted from composition? Can reactive sites be selectively addressed?

The power of LIFDI-MS in monitoring different clusters in solution is also reflected the case study on the cluster ensemble $[\text{Ni}_x\text{Ga}_y(\text{NiCp}^*)_6]$ ($\text{Cp}^* = 1,2,3,4,5$ -pentamethylcyclopentadienyl) (Chapter 2.2). A mixture of at least five closely related clusters is obtained from the reaction of GaCp^* with Ni(olefin) complexes and can be isolated in form of a co-crystallate. All clusters consist of a distorted octahedral $(\text{NiCp}^*)_6$ shell, surrounding different Ga-rich cores, which may include Ni atoms (namely: Ga_6 , Ga_7 , NiGa_6 , NiGa_7 , Ni_2Ga_6). A directed synthesis (1) of a singular cluster species is never achieved, even though several reaction parameters were screened (temperature, time, stoichiometry, reactants, additives). The choice of Ni(olefin) precursor, however, influences the product distribution. LIFDI-MS is thus the only method showing the composition and chemical richness in these black crystals. Due to co-crystallization of the different species, a clear structural assignment was not possible by SC-XRD. Indeed, a structural prediction (2) 'from scratch' is possible in this case, applying an advanced DFT-based screening approach. In analogy to gas phase chemistry, structural information about the three most prominent clusters (serving as reference) in the ensemble are gained solely knowing the clusters composition from MS and assuming the Cp^* ligands are intact (spectroscopic evidence, *vide supra*). The design principle essentially relies on the combination of two independent strategies (see chapter 2.2 for details). Most interestingly, both strategies lead to very similar results. The theoretically predicted structural feature of the $(\text{NiCp}^*)_6$ shell in all clusters, is also reflected in several spectroscopic data (^{13}C MAS NMR, IR and Raman, EPR and SQUID). The theory-based prediction is thus validated by multiple experimental techniques (2). Having elucidated the structures allows for a detailed look into the bonding situation of the different clusters: it rationalizes why their synthesis is so difficult to control, and why they are always formed in mixtures (1). The superatomic $[\text{Ga}_6(\text{NiCp}^*)_6]$ cluster can be identified as

parent species. It is able to bind to Ni and Ga atoms simultaneously, however, in different bonding-manners. Simplified the parent $[\text{Ga}_6(\text{NiCp}^*)_6]$ cluster, may be regarded as a 'sponge' that randomly takes up either Ni and/or Ga atoms. This is also in line with the stirring tool to influence the product distribution: the olefin in the Ni precursor. Probably the olefin is crucial for the stabilization and respectively for the availability of Ni atoms in solution (1). Once formed, the clusters seem to be in a thermodynamic sink and cannot to take up more atoms or exchange them (1, 3).

The key difference between these electronically and structurally closely related species is the presence of naked Ni atoms in some of the cluster cores. This fact is reflected in the reactivity assessment (3) of the ensemble. Carbon monoxide (prone to bind to Ni) can be used as probe molecules and shows enhances reactivity (adduct formation, decomposition) towards the naked-Ni-containing clusters. Inspired by this selectivity, employing the stick-like triisopropylsilylacetylene (TIPSA) as substrate under irradiation (350 nm), allows to selectively react (3) it with $[\text{Ni}_2\text{Ga}_6(\text{NiCp}^*)_6]$. The product $[(\text{TIPSA})_2\text{Ni}_2\text{Ga}_6(\text{NiCp}^*)_6]$ (two naked Ni atoms, two activated TIPSA) can be isolated in pure form and analyzed by means of SC-XRD (2). It shows a distorted polyhedral structure, where all Cp^* ligands are attached to Ni atoms. The TIPSA ligands are bound to the Ga atoms, probably a result of a transfer from Ni (where TIPSA is presumably activated) to Ga. The detailed formation mechanism is still under investigation, however, these preliminary results perfectly match the proposed structures (2) of the individual cluster species. This underlines the value of the performed work: without elucidating the structure (2) of the individual species by DFT, the crystals would have been discarded, a striking example of chemical complexity in cluster chemistry (1) would have remained undiscovered and a planned follow-up chemistry (3) would not be possible.

Moreover, the Cp^* transmetalation from Ga to Ni, which is also foreseen by theory (2), could be identified as a major problem when aiming for cluster-substrate interactions. Transmetalation has experimentally been observed for Ni/Ga as well as other systems such as Fe/Al and Ni/Zn (1). It relies on the fact, that late transition metals are keen to form stable half-sandwich complexes. For the reaction yielding the cluster ensemble, a key 'intermediate' is isolated and characterized (see chapter 2.1).^[64] Starting from $[\text{Ni}_2(\text{dvds})_3]$ (dvds = 1,1,3,3-Tetramethyl-1,3-divinyldisiloxane) and GaCp^* , the compound $[(\mu^2\text{-GaCp}^*)(\text{Ni}_2)(\mu^2\text{-GaNiCp}^*)_2(\text{dvds})_2]$ is typically observed as byproduct on the way to the ensemble (1), following this route. It can be accessed in good yields from $[(\text{Cp}^*\text{Ga})\text{Ni}(\text{dvds})]$ in

a solid-state reaction with itself (1) and contains one GaCp*, as well as, two NiCp* units and is further stabilized by two dvds ligands (2). As a pure compound, containing both GaCp* and NiCp*, it serves as important reference compound for the spectroscopic investigations of the ensemble. Moreover, it shows how Cp* transfer seems to be important for cluster growth and how potent stabilizing ligands (flexibility of dvds, chelating ligand) can capture intermediates by blocking reactive centers (1, 3).

A key conclusion from studying the Ni(olefin)/GaCp* system, is the value that can be drawn from a mass spectrometric assessment in combination with advanced DFT calculations. Deriving complex molecular structures only from composition (2) and accessing different reactivities from closely related clusters (3) opens up novel perspectives to study cluster mixtures in solution without isolating singular clusters (1). It also well-illustrates the chemical complexity, which already exists 'within a crystal' and how minor changes (number of atoms, Ni vs. Ga) have pivotal on reactivity (1). Nevertheless it also questions the role of the Cp* ligand, probably a source for chemical complexity (1), however, blocking several potential reaction sites (3).

1.3.5 Reactive sites by ligand removal

Leading research questions: What is the role of the Ga in Ru/Ga mediated bond activation? Are undercoordinated species formed under hydrogenolytic conditions? Can reactive sites be generated by soft photochemical activation?

To overcome the blockage of TM centers by Cp* transfer and to be able to study the interactions between clusters and substrates, Cp* might be removed by hydrogenolysis. This has already been shown for the Ru/Ga system: The reaction of Ru(olefin) precursors with GaCp* under H₂ pressure leads to [Ru₂(Ga)(GaCp*)₇(H)₃]^[46]. The cluster contains a bare Ga atom, the formation shows free Cp*H, in addition to three hydride ligands (requires two molecules H₂). It is thus a good starting point for studying the reactivity of undercoordinated and/or hydride-rich Ru/Ga clusters (3). LIFDI-MS identifies the reaction products of Ru(olefin) precursors with GaCp* under hydrogenolytic conditions: The presence of the undercoordinated [Ru(GaCp*)₃] species, can be traced by the observation of [Ru(GaCp*)₃(C₇H₇)(H)₃] and [Ru(GaCp*)₃(SiEt₃)(H)₃] (see chapter 2.3).^[83] The species are the

result of activated H₂ (H-H activation) and solvent (triethylsilane or toluene; C/Si-H activation) (3). In the case of the thermodynamically favored Si-H activation, the reaction proceeds selectively and the product can be isolated (1) in high yields (70%). In contrast, the reaction in toluene leads to several toluene-containing species, and the target compound [Ru(GaCp*)₃(C₇H₇)(H)₃] can only be observed by MS (1). A combination of experimental data and DFT optimizations allows to determine the position of the hydrides and predict the structures (2). This is critical for the C-H activation product, as activation can potentially occur at four different positions (*ortho*, *meta*, *para*, benzylic). Ultimately, the aromatic C-H bonds are preferentially activated, but the exact position cannot be determined: the energy differences are so small that even the possibility of isomers in solution must be considered (1, 2, 3). Both species (C-H and Si-H activation) are isostructural and all Ga atoms are foreseen to remain in the formal oxidation state +1.

Interestingly, the Ru-phosphine equivalents of the described compounds are known in literature. Despite the preparation pathways differ significantly from the Ru/Ga complexes described above (3), they are good models to compare the Ru-Ga to the more established Ru-P bond. A major difference is indeed a slightly weaker covalent σ -donation and an enhanced polarization of the Ru(δ^-)-Ga(δ^+) bond, including ionic contributions. Theory also predicts that [Ru(GaCp*)₃(H)₂] is thermodynamically favored in the bond activation of both substrates, compared to P equivalent (3).

Irrespective of being far from undercoordinated (7-fold coordination), [Ru(GaCp*)₃(SiEt₃)(H)₃] could be reactive towards substrates because of its three hydrides. TM hydrides are well known to participate in insertion reactions e.g., into unsaturated hydrocarbons. Moreover, it could be possible to thermally induce a reductive elimination of silane from the complex and create a free coordination site, in analogy to [Ni(AlCp*)₃(SiEt₃)(H)]. It was thus surprising, that the complex did not show any of these reactivities (1, 3). Irradiation the yellowish complex at its absorption maximum, hydrogen and triethylsilane become liberated, along with the formation of [Ru(GaCp*)₃], [Ru(GaCp*)₃(SiEt₃)(H)] and [Ru(GaCp*)₃(H)₂] (3). This photochemical induced reductive elimination enables the selective removal of ligands at mild conditions (room temperature, no Cp* transfer to expected), reminiscent to concept of protective groups in organic chemistry (see chapter 2.4). To further stress this, the RuGa₃ species was trapped by using the chelating phosphine dppe (dppe = 1,2-bis(diphenylphosphino)ethane), giving [Ru(GaCp*)₃(dppe)]. The phosphine stabilized product is

the result of a double reductive elimination from Ru(VI) to Ru(0)(1,3). $[\text{Ru}(\text{GaCp}^*)_3(\text{SiEt}_3)(\text{H})_3]$ can also be photochemically activated in presence of alkynes and hydrogen, resulting in catalytic hydrogenation, predominately to alkanes (3). LIFDI-MS of catalytic reaction solutions reveals a $[\text{Ru}(\text{GaCp}^*)_3(\text{hexyne})(\text{hexene})]$ species, which can be interpreted as catalytic intermediate (3). Most interestingly, the catalytic conversions are never complete. When the amount of substrate (and stabilizing ligand at the same time) decreases, cluster growth emerges (1, 3). Indeed, unsaturated hydrocarbons can be used as additives (with or without presence of dihydrogen) to influence the outcome of the cluster growth reactions. Irradiating samples in presence of hydrogen and without any stabilizing ligands, leads to fast cluster growth (1, 3). To gain precise control over these mixtures is still under investigation, they seem to be highly reactive however: already the addition of toluene lead to severe changes of the species in cyclohexane solutions (3).

Employing hydrogenolytic conditions in the Ru/Ga system allows to form undercoordinated and thus highly reactive 'proto-cluster' species (1). Depending on the choice of substrate they engage in un-/directed bond activation reactions (3). Especially for the unselective reactions, DFT calculation are pivotal for the structural prediction (2) and help to rationalize the bond activations (3). Introducing a novel and soft activation strategy, by removing 'protective groups' from compounds illustrates the common competitive reactivities of undercoordinated species: substrate activation or cluster growth (3).

1.3.6 The influence of R on reactive sites

Leading research questions: Does avoidance of transmetalation lead to reactive sites? How to access the polyhydride structures? Can TM/E clusters participate in catalytic transformations? What is the relation of molecular clusters and the solid-state?

Especially the Ni/Ga case study shows that Cp^* transmetalation blocks potential active Ni sites and already occurs at temperatures slightly above ambient conditions.^[78] A strategy using alternative GaR sources^[84], would imply to sacrifice the superior shielding properties of Cp^* , its flexible binding modes (and the associated chemical variety) along with risk of leaving the rather established TM/ECp* chemistry. On the other side, a more robust E-R bond may avoid

transmetalation, and eventually lead to active TM(0) sites. To ensure that stable TM/E clusters are formed, R has to be bulky enough to shield the cluster and to avoid further metal agglomeration, but not too sterically demanding, that the metal agglomeration stops on the level of 18 VE complexes (1). When using GaTMP (TMP = 2,2,6,6-tetramethylpiperidienyl) instead of GaCp*, analogous to the reaction leading to the Ni/Ga ensemble, no transmetalation is observed. In contrast, the clusters $[\text{Ni}_2(\text{GaTMP})_7]$ is obtained. Following up on these results, the cluster $[\text{Ni}_3(\text{GaTMP})_7]$ could be synthesized in the stoichiometric reaction of GaTMP with $[\text{Ni}(\text{cod})_2]$ (see chapter 2.5). Its molecular structure can be best described (2) as a central Ni_3 triangle surrounded by GaTMP. Pressurizing the cluster with H_2 leads to a mixture of Ni_3Ga_7 di-, tetra- and hexahydrides. The species are formed by the addition of one, two or three H_2 molecules respectively, in a highly reversible reaction (3). DFT calculations were performed on a well-selected set of possible isomers of each species and several structures were found, with only small energetical differences (2). Combining the proposed structures with ROESY-NMR spectroscopy data, a defined structure for the di- and hexahydride can be validated respectively (2). These (poly-) hydridic clusters are active in hydrogenation catalysis. Internal alkynes are mainly converted to alkenes, with rather small amounts of alkanes. Interestingly, the clusters selectivity is fairly similar to the N_5Ga_3 phase, a semihydrogenation catalyst the is known to be well-balance between activity and selectivity. In addition, triangular Ni_3 sites were identified as the catalytically active centers. From a heuristic viewpoint, the cluster might be regarded as a cut out active site in solution and may also be in line with the site isolation concept. Such molecular mimics of Hume-Rothery phases were so far restricted to a structural resemblance only. Now having found an example with catalytic reactivity may eventually allow to transfer information gained from solution-based analytics (NMR in this case) to solid-state materials (Figure 18).

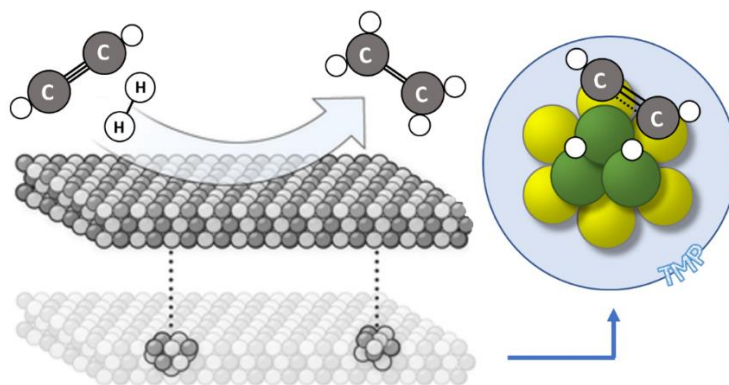


Figure 18: Schematic representation of clusters being local cut-outs of catalytically active surfaces.

1.3.7 Epilogue

Building on the previous discussions of TM/E interactions (synergistic effects; chapter 1.1), the difficulties in forming such bonds/interactions (unstable, involvement in redox processes; chapter 1.1) at the sub/nano scale, and the synthetic challenges for hetero/metal clusters (three problems of cluster chemistry; chapters 1.2 and 1.3), it can be concluded that a retrosynthetic approach to clusters, analogous to the retrosynthesis of organic molecules, would be highly desirable. This would meet the challenge of directed synthesis (1), thus allow isolation of pure material, which in turn would increase the chance of clearly interpretable spectroscopic and X-ray data, allowing the assignment of a unique spatial structure (2). From this point, structure-reactivity assessments could then be explored (3). Following this logic, a retrosynthetic approach to clusters may be called the "Holy Grail of cluster chemistry."

To put it bluntly: Let's assume that after an exhausting day (or even night) in the lab, Aladdin's genie appears and allows three freely chosen wishes (Figure 19). A passionate cluster chemist knows about the three challenges of cluster chemistry and will choose his wishes wisely, accordingly. Thus, the genie grants him a large Schlenk flask with a pure (1) and fully characterized (2) cluster that exhibits remarkable reactivity toward a desired substrate (3). But a really smart cluster chemist would probably want something else (health, happiness, and eternal research dollars aside): He would want the knowledge of a retrosynthetic concept that allows the synthesis of any cluster imaginable. A single cluster with intriguing reactivity may be fascinating, but it will not allow any general conclusions about structure/reactivity relationships. Because: to truly assess a structure-reactivity relationship, a large number of clusters with distinct structural differences would have to be tested with respect to their reactivity toward a substrate. Against this background, the previously described and highly desirable retrosynthetic approach to clusters (somewhat possible with the dendrimer approach; chapter 1.2) is in reality only partially desirable. Pharmaceutical research might be a good metaphor to illustrate this: Organic retrosynthesis provides access to a large number of similar organic molecules, each of which differs only slightly from the other. Here the challenge is not the synthesis, but to test all molecules for their efficacy against a specific disease, and thus to finally select the most effective substance.



Figure 19: Aladdin's genie allowing for three wishes. Genie graphic taken from <https://www.disneyclips.com/> with permission and extended with bubble and text.

It would therefore be interesting to evaluate the properties of clusters without their (laborious) isolation as pure substances - which is indeed reminiscent of screening strategies in pharmaceutical research. That is: the disadvantage of unselective cluster synthesis could thus perhaps be an opportunity for rapid cluster reactivity screening. By using 'tailored' mass spectrometry in combination with advanced theoretical predictions (chapter 2.2), clusters need not necessarily be isolated before structure-reactivity patterns can be investigated. Mixtures (which may contain highly reactive and therefore non-isolatable species) can be exposed to substrates, and the reactivity difference of the individual species can be studied. Cluster synthesis (cluster assembly/disassembly) would also benefit from such an approach. However, this does not necessarily preclude subsequent isolation of the clusters of interest: It may be possible to use a synthesis robot to sift through the experimental space of influencing parameters to enrich for a desired species. If this species still cannot be isolated by common separation methods (e.g., crystallization), tailored HPLC separation techniques are possible. This is already established for the separation of gold clusters.^[85]

Apart from 'bypassing' the three problems of cluster chemistry, the 'library approach' could eventually allow to support heterogenous catalysis researchers in elucidating the active catalyst sites on the molecular level (essential for rational catalyst design). Hume-Rothery inspired clusters show a significant resemblance, regarding structure and reactivity, to their solid-state counterparts. Connecting it to the thoughts, that a cluster reflects one defined site of a catalytically active surface (chapter 2.5), and that those solutions consist of multiple different clusters, a solution may be regarded as a 'dissolved surface' (Figure 20). Different clusters (or sites) show different reactivities and can be tested at the same time and conditions.

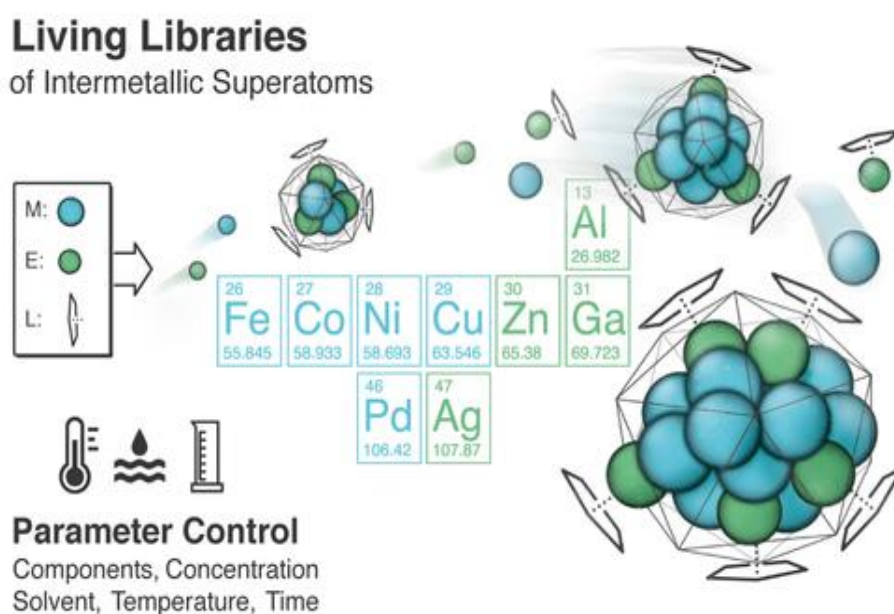


Figure 20: Schematic illustration of the 'Living Library' concept.

1.4 References

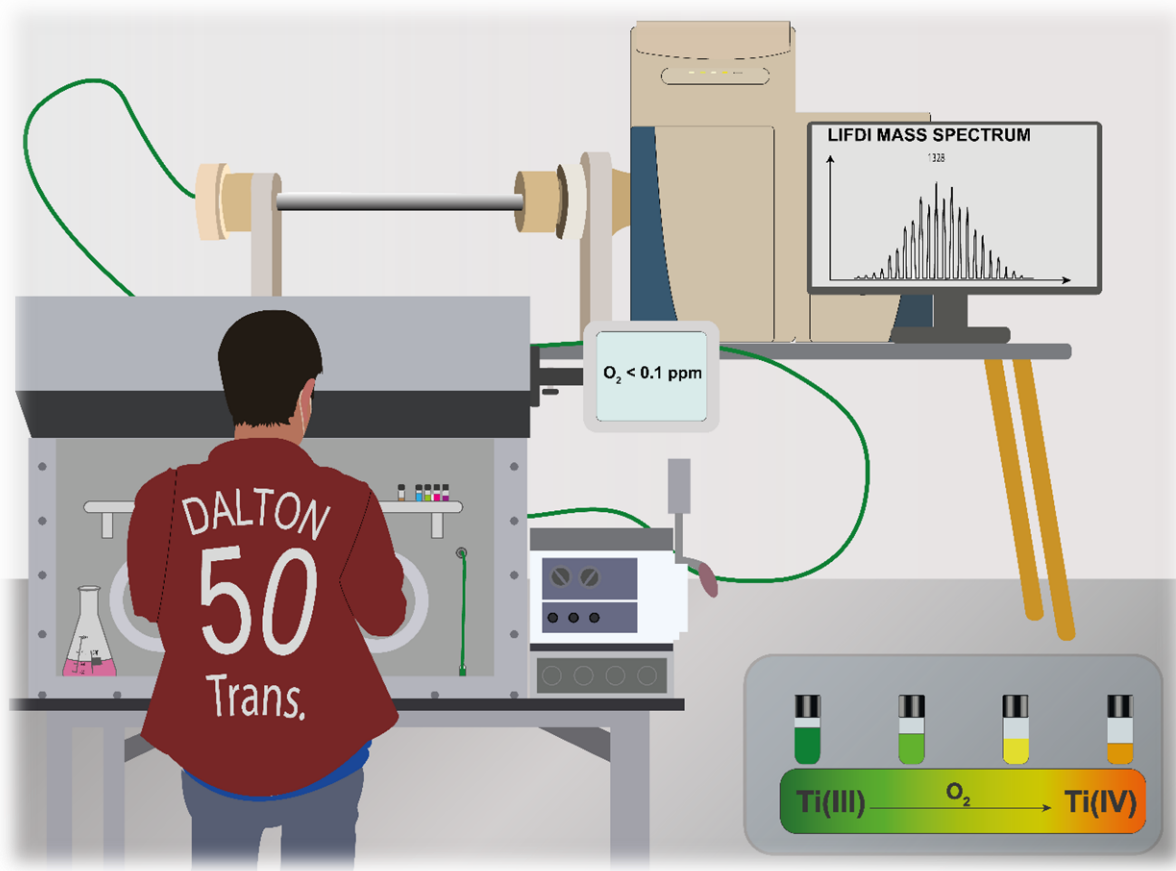
- [1] a) M. Bowker, *ChemCatChem* **2019**, *11*, 4238-4246; b) G. Ertl, *Angew. Chem.* **2008**, *120*, 3578-3590.
- [2] K. F. Kalz, R. Kraehnert, M. Dvoyashkin, R. Dittmeyer, R. Gläser, U. Krewer, K. Reuter, J.-D. Grunwaldt, *ChemCatChem* **2017**, *9*, 17-29.
- [3] S. Siegel, G. V. Smith, *J. Am. Chem. Soc.* **1960**, *82*, 6082-6087.
- [4] H. Schwarz, *Angew. Chem. Int. Ed.* **2015**, *54*, 10090-10100.
- [5] M. Carrasco, N. Curado, C. Maya, R. Peloso, A. Rodríguez, E. Ruiz, S. Alvarez, E. Carmona, *Angew. Chem. Int. Ed.* **2013**, *52*, 3227-3231.
- [6] a) D. C. Powers, T. Ritter, *Acc. Chem. Res.* **2012**, *45*, 840-850; b) I. G. Powers, C. Uyeda, *ACS Catal.* **2017**, *7*, 936-958.
- [7] L. Jin, D. R. Tolentino, M. Melaimi, G. Bertrand, *Sci. Adv.* **2015**, *1*, e1500304.
- [8] a) K. Mayer, J. Weßing, T. F. Fässler, R. A. Fischer, *Angew. Chem. Int. Ed.* **2018**, *57*, 14372-14393; b) M. Schütz, C. Gemel, W. Klein, R. A. Fischer, T. F. Fässler, *Chem. Soc. Rev.* **2021**, *50*, 8496-8510; c) M. Armbrüster, *Sci. Technol. Adv. Mater.* **2020**, *21*, 303-322.
- [9] J. Weßing, Technische Universität München (München), **2018**.
- [10] a) F. Studt, I. Sharafutdinov, F. Abild-Pedersen, C. F. Elkjær, J. S. Hummelshøj, S. Dahl, I. Chorkendorff, J. K. Nørskov, *Nat. Chem.* **2014**, *6*, 320; b) F. Studt, F. Abild-Pedersen, T. Bligaard, R. Z. Sørensen, C. H. Christensen, J. K. Nørskov, *Science* **2008**, *320*, 1320-1322; c) M. Armbrüster, K. Kovnir, M. Friedrich, D. Teschner, G. Wowsnick, M. Hahne, P. Gille, L. Szentmiklósi, M. Feuerbacher, M. Heggen, F. Girgsdies, D. Rosenthal, R. Schlögl, Y. Grin, *Nat. Mater.* **2012**, *11*, 690-693.
- [11] K. Kovnir, M. Armbrüster, D. Teschner, T. V. Venkov, F. C. Jentoft, A. Knop-Gericke, Y. Grin, R. Schlögl, *Sci. Technol. Adv. Mater.* **2007**, *8*, 420-427.
- [12] a) M. Armbrüster, R. Schlögl, Y. Grin, *Sci. Technol. Adv. Mater.* **2014**, *15*, 034803;) bM. Armbrüster, K. Kovnir, M. Behrens, D. Teschner, Y. Grin, R. Schlögl, *J. Am. Chem. Soc.* **2010**, *132*, 14745-14747.
- [13] M. Krajčí, J. Hafner, *J. Phys. Chem. C* **2014**, *118*, 12285-12301.
- [14] J. Hornung, Technische Universität München (München), **2019**.
- [15] M. Armbrüster, G. Wowsnick, M. Friedrich, M. Heggen, R. Cardoso-Gil, *J. Am. Chem. Soc.* **2011**, *133*, 9112-9118.
- [16] S. Vukojević, O. Trapp, J.-D. Grunwaldt, C. Kiener, F. Schüth, *Angew. Chem. Int. Ed.* **2005**, *44*, 7978-7981.
- [17] L. Shao, W. Zhang, M. Armbrüster, D. Teschner, F. Girgsdies, B. Zhang, O. Timpe, M. Friedrich, R. Schlögl, D. S. Su, *Angew. Chem. Int. Ed.* **2011**, *50*, 10231-10235.
- [18] Y. Liu, X. Liu, Q. Feng, D. He, L. Zhang, C. Lian, R. Shen, G. Zhao, Y. Ji, D. Wang, G. Zhou, Y. Li, *Adv. Mater.* **2016**, *28*, 4747-4754.
- [19] a) K. Schütte, H. Meyer, C. Gemel, J. Barthel, R. A. Fischer, C. Janiak, *Nanoscale* **2014**, *6*, 3116-3126; b) K. Schutte, A. Doddi, C. Kroll, H. Meyer, C. Wiktor, C. Gemel, G. van Tendeloo, R. A. Fischer, C. Janiak, *Nanoscale* **2014**, *6*, 5532-5544.
- [20] a) L. Staiger, T. Kratky, S. Günther, A. Urstoeger, M. Schuster, O. Tomanek, R. Zbořil, R. W. Fischer, R. A. Fischer, M. Cokoja, *Nanoscale* **2021**, *13*, 15038-15047; b) L. Staiger, T. Kratky, S. Günther, O. Tomanek, R. Zbořil, R. W. Fischer, R. A. Fischer, M. Cokoja, *ChemCatChem* **2021**, *13*, 227-234; c) M. Cokoja, H. Parala, M.-K. Schröter, A. Birkner, M. W. E. van den Berg, W. Grünert, R. A. Fischer, *Chem. Mater.* **2006**, *18*, 1634-1642.
- [21] L. Staiger, Technische Universität München (München), **2022**.
- [22] J. Takaya, *Chem. Sci.* **2021**, *12*, 1964-1981.

- [23] A. Amgoune, D. Bourissou, *Chem. Commun.* **2011**, 47, 859-871.
- [24] D. W. Stephan, G. Erker, *Angew. Chem. Int. Ed.* **2010**, 49, 46-76.
- [25] W. H. Harman, T.-P. Lin, J. C. Peters, *Angew. Chem. Int. Ed.* **2014**, 53, 1081-1086.
- [26] J. R. Khusnutdinova, D. Milstein, *Angew. Chem. Int. Ed.* **2015**, 54, 12236-12273.
- [27] a) H. Braunschweig, Q. Ye, K. Radacki, A. Damme, *Angew. Chem. Int. Ed.* **2012**, 51, 7839-7842; b) H. Braunschweig, R. D. Dewhurst, *Angew. Chem. Int. Ed.* **2010**, 49, 3412-3414; c) H. Braunschweig, M. Colling, *Coord. Chem. Rev.* **2001**, 223, 1-51.
- [28] a) A. F. Hill, G. R. Owen, A. J. P. White, D. J. Williams, *Angew. Chem. Int. Ed.* **1999**, 38, 2759-2761; b) J. R. Prat, R. C. Cammarota, B. J. Graziano, J. T. Moore, C. C. Lu, *Chem. Commun.* **2022**, 58, 8798-8801.
- [29] W. H. Harman, J. C. Peters, *J. Am. Chem. Soc.* **2012**, 134, 5080-5082.
- [30] I. Bach, R. Goddard, C. Kopsike, K. Seevogel, K.-R. Pörschke, *Organometallics* **1999**, 18, 10-20.
- [31] H. Kameo, J. Yamamoto, A. Asada, H. Nakazawa, H. Matsuzaka, D. Bourissou, *Angew. Chem. Int. Ed.* **2019**, 58, 18783-18787.
- [32] R. C. Cammarota, C. C. Lu, *J. Am. Chem. Soc.* **2015**, 137, 12486-12489.
- [33] R. C. Cammarota, M. V. Vollmer, J. Xie, J. Ye, J. C. Linehan, S. A. Burgess, A. M. Appel, L. Gagliardi, C. C. Lu, *J. Am. Chem. Soc.* **2017**, 139, 14244-14250.
- [34] a) M. V. Vollmer, J. Ye, J. C. Linehan, B. J. Graziano, A. Preston, E. S. Wiedner, C. C. Lu, *ACS Catal.* **2020**, 10, 2459-2470; b) M. V. Vollmer, J. Xie, C. C. Lu, *J. Am. Chem. Soc.* **2017**, 139, 6570-6573.
- [35] I. Fujii, K. Semba, Q.-Z. Li, S. Sakaki, Y. Nakao, *J. Am. Chem. Soc.* **2020**, 142, 11647-11652.
- [36] R. Seki, N. Hara, T. Saito, Y. Nakao, *J. Am. Chem. Soc.* **2021**, 143, 6388-6394.
- [37] a) J. S. Anderson, M.-E. Moret, J. C. Peters, *J. Am. Chem. Soc.* **2013**, 135, 534-537; b) J. S. Anderson, J. Rittle, J. C. Peters, *Nature* **2013**, 501, 84-87; c) J. Fajardo, J. C. Peters, *J. Am. Chem. Soc.* **2017**, 139, 16105-16108.
- [38] F. P. Gabbaï, C. Jones, C. C. Lu, *Chem. Sci.* **2021**, 12, 1961-1963.
- [39] a) W. Uhl, M. Benter, S. Melle, W. Saak, G. Frenking, J. Uddin, *Organometallics* **1999**, 18, 3778-3780; b) W. Uhl, M. Pohlmann, R. Wartchow, *Angew. Chem. Int. Ed.* **1998**, 37, 961-963; c) R. A. Fischer, J. Weiß, *Angew. Chem. Int. Ed.* **1999**, 38, 2830-2850; d) T. Steinke, C. Gemel, M. Winter, R. A. Fischer, *Chem. Eur. J.* **2005**, 11, 1636-1646; e) J. Hornung, J. Weßing, P. Jerabek, C. Gemel, A. Pöthig, G. Frenking, R. A. Fischer, *Inorg. Chem.* **2018**, 57, 12657-12664; f) A. Seifert, G. Linti, *Inorg. Chem.* **2008**, 47, 11398-11404.
- [40] a) J. Uddin, G. Frenking, *J. Am. Chem. Soc.* **2001**, 123, 1683-1693; b) J. Uddin, C. Boehme, G. Frenking, *Organometallics* **2000**, 19, 571-582; c) G. Frenking, N. Fröhlich, *Chem. Rev.* **2000**, 100, 717-774.
- [41] M. Schütz, M. Muhr, K. Freitag, C. Gemel, S. Kahlal, J.-Y. Saillard, A. C. H. Da Silva, J. L. F. Da Silva, T. F. Fässler, R. A. Fischer, *Inorg. Chem.* **2020**, 59, 9077-9085.
- [42] a) J. Weßing, C. Ganesamoorthy, S. Kahlal, R. Marchal, C. Gemel, O. Cador, A. C. H. Da Silva, J. L. F. Da Silva, J.-Y. Saillard, R. A. Fischer, *Angew. Chem. Int. Ed.* **2018**, 57, 14630-14634; b) K. Freitag, H. Banh, C. Gemel, R. W. Seidel, S. Kahlal, J. Y. Saillard, R. A. Fischer, *Chem. Commun.* **2014**, 50, 8681-8684.
- [43] T. Steinke, C. Gemel, M. Cokoja, M. Winter, R. A. Fischer, *Angew. Chem. Int. Ed.* **2004**, 43, 2299-2302.
- [44] T. Steinke, M. Cokoja, C. Gemel, A. Kempter, A. Krapp, G. Frenking, U. Zenneck, R. A. Fischer, *Angew. Chem. Int. Ed.* **2005**, 44, 2943-2946.
- [45] T. Cadenbach, C. Gemel, R. Schmid, R. A. Fischer, *J. Am. Chem. Soc.* **2005**, 127, 17068-17078.

- [46] T. Cadenbach, C. Gemel, R. Schmid, M. Halbherr, K. Yussenko, M. Cokoja, R. A. Fischer, *Angew. Chem. Int. Ed.* **2009**, *48*, 3872-3876.
- [47] C. Ganesamoorthy, J. Wessing, C. Kroll, R. W. Seidel, C. Gemel, R. A. Fischer, *Angew. Chem. Int. Ed.* **2014**, *53*, 7943-7947.
- [48] M. Schütz, C. Gemel, M. Muhr, C. Jandl, S. Kahlal, J.-Y. Saillard, R. A. Fischer, *Chem. Sci.* **2021**, *12*, 6588-6599.
- [49] a) T. Cadenbach, T. Bollermann, C. Gemel, M. Tombul, I. Fernandez, M. v. Hopffgarten, G. Frenking, R. A. Fischer, *J. Am. Chem. Soc.* **2009**, *131*, 16063-16077; b) K. Freitag, C. Gemel, P. Jerabek, I. M. Oppel, R. W. Seidel, G. Frenking, H. Banh, K. Dilchert, R. A. Fischer, *Angew. Chem. Int. Ed.* **2015**, *54*, 4370-4374.
- [50] J. Hornung, M. Muhr, C. Gemel, R. A. Fischer, *Dalton Trans.* **2019**, *48*, 11743-11748.
- [51] a) U. Heiz, F. Vanolli, A. Sanchez, W. D. Schneider, *J. Am. Chem. Soc.* **1998**, *120*, 9668-9671; b) T. Tsukamoto, T. Kambe, A. Nakao, T. Imaoka, K. Yamamoto, *Nat. Commun.* **2018**, *9*, 3873.
- [52] T. Imaoka, H. Kitazawa, W.-J. Chun, S. Omura, K. Albrecht, K. Yamamoto, *J. Am. Chem. Soc.* **2013**, *135*, 13089-13095.
- [53] B. Kumar, T. Kawawaki, N. Shimizu, Y. Imai, D. Suzuki, S. Hossain, L. V. Nair, Y. Negishi, *Nanoscale* **2020**, *12*, 9969-9979.
- [54] a) E. Roduner, *Phys. Chem. Chem. Phys.* **2018**, *20*, 23812-23826; b) Z. Luo, A. W. Castleman, *Acc. Chem. Res.* **2014**, *47*, 2931-2940; c) H. Hakkinen, *Chem. Soc. Rev.* **2008**, *37*, 1847-1859; d) H. Häkkinen, *Adv. Phys. X* **2016**, *1*, 467-491.
- [55] T. Tsukamoto, T. Kambe, T. Imaoka, K. Yamamoto, *Nat. Rev. Chem.* **2021**, *5*, 338-347.
- [56] D. E. Bergeron, A. W. Castleman, T. Morisato, S. N. Khanna, *Science* **2004**, *304*, 84-87.
- [57] T. Kambe, N. Haruta, T. Imaoka, K. Yamamoto, *Nat. Commun.* **2017**, *8*, 2046.
- [58] D. E. Bergeron, P. J. Roach, A. W. Castleman, N. O. Jones, S. N. Khanna, *Science* **2005**, *307*, 231-235.
- [59] J. F. Eckhard, T. Masubuchi, M. Tschurl, R. N. Barnett, U. Landman, U. Heiz, *J. Phys. Chem. A* **2021**, *125*, 5289-5302.
- [60] G. E. Johnson, Q. Hu, J. Laskin, *Annu. Rev. Anal. Chem.* **2011**, *4*, 83-104.
- [61] R. J. Wilson, N. Lichtenberger, B. Weinert, S. Dehnen, *Chem. Rev.* **2019**, *119*, 8506-8554.
- [62] a) Z.-M. Sun, Y.-F. Zhao, J. Li, L.-S. Wang, *J. Clust. Sci.* **2009**, *20*, 601-609; b) M. W. Hull, S. C. Sevov, *J. Am. Chem. Soc.* **2009**, *131*, 9026-9037.
- [63] P. Maity, S. Xie, M. Yamauchi, T. Tsukuda, *Nanoscale* **2012**, *4*, 4027-4037.
- [64] a) M. Muhr, J. Hornung, J. Weßing, C. Jandl, C. Gemel, R. A. Fischer, *Inorg. Chem.* **2020**, *59*, 5086-5092; b) B. Buchin, T. Steinke, C. Gemel, T. Cadenbach, R. A. Fischer, *Z. anorg. allg. Chemie* **2005**, *631*, 2756-2762; c) J. Weßing, C. Göbel, B. Weber, C. Gemel, R. A. Fischer, *Inorg. Chem.* **2017**, *56*, 3517-3525.
- [65] K. Yamamoto, M. Higuchi, S. Shiki, M. Tsuruta, H. Chiba, *Nature* **2002**, *415*, 509-511.
- [66] H. Kitazawa, K. Albrecht, K. Yamamoto, *Chem. Lett.* **2012**, *41*, 828-830.
- [67] K. Yamamoto, T. Imaoka, *Acc. Chem. Res.* **2014**, *47*, 1127-1136.
- [68] T. Tsukamoto, K. Tomozawa, T. Moriai, N. Yoshida, T. Kambe, K. Yamamoto, *Angew. Chem. Int. Ed.* **2022**, *61*, e202114353.
- [69] F. Lips, S. Dehnen, *Angew. Chem. Int. Ed.* **2011**, *50*, 955-959.
- [70] E. C. Tyo, S. Vajda, *Nat. Nanotechnol.* **2015**, *10*, 577-588.
- [71] C. Kumara, C. M. Aikens, A. Dass, *J. Phys. Chem. Lett.* **2014**, *5*, 461-466.
- [72] a) M. M. Shoshani, S. A. Johnson, *Nat. Chem.* **2017**, *9*, 1282-1285; b) M. M. Shoshani, J. Liu, S. A. Johnson, *Organometallics* **2018**, *37*, 116-126.

- [73] a) B. Buchin, C. Gemel, T. Cadenbach, R. A. Fischer, *Inorg. Chem.* **2006**, *45*, 1789-1794; b) M. Molon, C. Gemel, P. Jerabek, L. Trombach, G. Frenking, R. A. Fischer, *Inorg. Chem.* **2014**, *53*, 10403-10411.
- [74] B. Buchin, C. Gemel, T. Cadenbach, I. Fernández, G. Frenking, R. A. Fischer, *Angew. Chem. Int. Ed.* **2006**, *45*, 5207-5210.
- [75] M. Halbherr, T. Bollermann, C. Gemel, R. A. Fischer, *Angew. Chem. Int. Ed.* **2010**, *49*, 1878-1881.
- [76] J. Hornung, J. Weßing, M. Molon, K. Dilchert, C. Gemel, R. A. Fischer, *J. Organomet. Chem.* **2018**, *860*, 78-84.
- [77] P. Heiß, J. Hornung, X. Zhou, C. Jandl, A. Pöthig, C. Gemel, R. A. Fischer, *Inorg. Chem.* **2020**, *59*, 514-522.
- [78] P. Heiß, J. Hornung, C. Gemel, R. A. Fischer, *Chem. Commun.* **2022**, *58*, 4332-4335.
- [79] a) F. Pan, S. Wei, L. Guggolz, A. R. Eulenstein, F. Tambornino, S. Dehnen, *J. Am. Chem. Soc.* **2021**, *143*, 7176-7188; b) F. Pan, M. Lukanowski, F. Weigend, S. Dehnen, *Angew. Chem. Int. Ed.* **2021**, *60*, 25042-25047.
- [80] M. Schütz, Dissertation thesis, Technische Universität München (München), 2021.
- [81] J. H. Gross, *Eur. J. Mass Spectrom.* **2020**, *26*, 241-273.
- [82] M. Muhr, P. Heiß, M. Schütz, R. Bühler, C. Gemel, M. H. Linden, H. B. Linden, R. A. Fischer, *Dalton Trans.* **2021**, *50*, 9031-9036.
- [83] M. Muhr, R. Bühler, H. Liang, J. Gilch, C. Jandl, S. Kahlal, J.-Y. Saillard, C. Gemel, R. A. Fischer, *Chem. Eur. J.* **2022**, *28*, e202200887.
- [84] a) W. Uhl, W. Hiller, M. Layh, W. Schwarz, *Angew. Chem. Int. Ed.* **1992**, *31*, 1364-1366; b) A. Seifert, G. Linti, *Eur. J. Inorg. Chem.* **2007**, *2007*, 5080-5086; c) N. J. Hardman, B. E. Eichler, P. P. Power, *Chem. Commun.* **2000**, 1991-1992.
- [85] Y. Negishi, S. Hashimoto, A. Ebina, K. Hamada, S. Hossain, T. Kawawaki, *Nanoscale* **2020**, *12*, 8017-8039.

2. Main Part

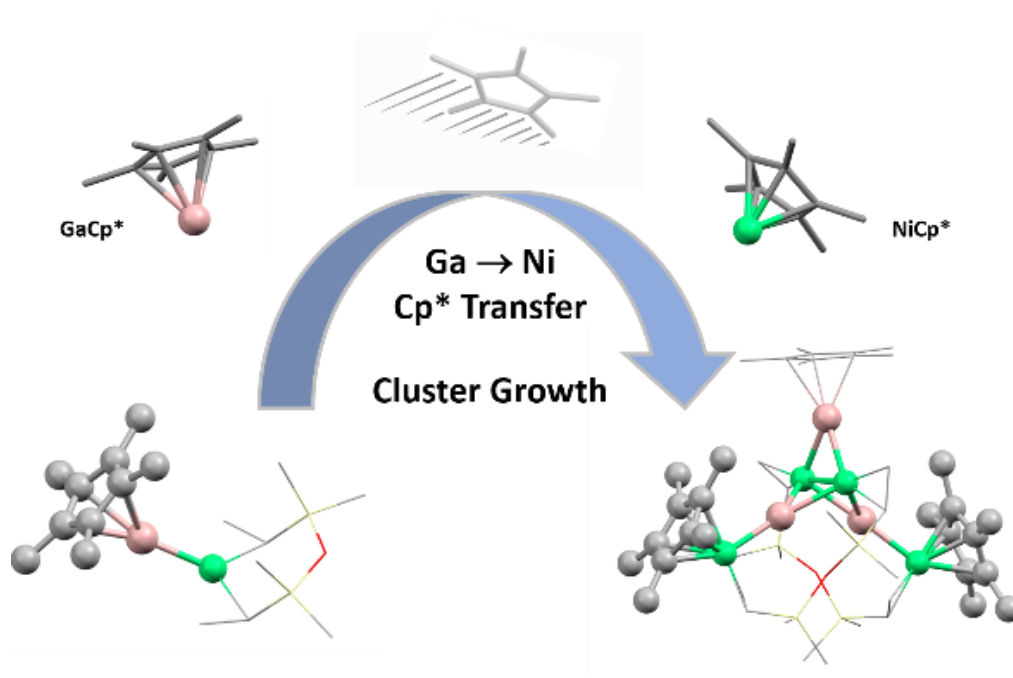


2.1 Formation of a propeller-shaped Ni₄Ga₃ cluster supported by transmetalation of Cp* from Ga to Ni.

Maximilian Muhr^{+, a}, Julius Hornung^{+, a}, Jana Weßing^a, Christian Jandl^a, Christian Gemel^a, Roland A. Fischer^{*, a}

[a] Chair of Inorganic and Metalorganic Chemistry, Department of Chemistry, Technical University Munich, Lichtenbergstraße 4, D-85748 Garching, Germany and Catalysis Research Center, Ernst-Otto-Fischer-Straße 1, D-85748 Garching, Germany.

[+] M.M. and J.H. equally contributed to this work



The following content has been published: *Inorg. Chem.*, **2020**, 59, 7, 5086–5092.

Reprinted with permission from Inorganic Chemistry. Copyright American Chemical Society.

Author contributions:

The manuscript was written by the two authors. Most experiments were planned by J.H. and mainly performed M.M.; J.W. performed initial experiments and C.J. supported with SCXRD measurements and evaluation. C.G. and R.A.F. supervised the research.

2.1.1 Abstract

The reactivity of GaCp* towards different Ni⁰ olefin complexes is investigated. The reaction of GaCp* with [Ni(cdt)] (cdt = all-*trans*-1,5,9-cyclododecatriene) leads to simple adduct formation and the 18 valence electron compound [Ni(GaCp*)(cdt)] (**1**). In contrast, [Ni₂(dvds)₃] (dvds = 1,1,3,3-tetramethyl-1,3-divinyldisiloxane) is converted to the undercoordinated and highly reactive 16 ve complex [Ni(GaCp*)(dvds)] (**2**), which represents an intermediate in the formation of the propeller-shaped M₇ cluster [Ni₄Ga₃](Cp*)₃(dvds)₂ (**3**). Extensive characterization of the latter compound by experimental and computational means reveals Cp* transfer from Ga to Ni. Therefore, the title compound can be best expressed by the structural formula [(μ₂-GaCp*)(Ni₂)(μ₂-GaNiCp*)₂(dvds)₂]. The flexible dvds ligands stabilize this arrangement via alkene-Ni and O-Ga interactions. Furthermore, compound **2** exhibits fast GaCp* ligand exchange with external GaCp*, which is rather unexpected for [TM(ECp*)_a] compounds, which usually do not undergo substitution reactions with two electron donor ligands like CO, phosphines or GaCp*.

2.1.2 Main Text

To date, experimental access to reactive intermetallic $[\text{TM}_a\text{E}_b]\text{L}_c$ (TM = transition metal; E = Ga, Al, Zn; L = stabilizing donor ligand) clusters remains a big challenge. While the synthesis of clusters of the general type $[\text{TM}_a\text{E}_b](\text{Cp}^*)_c$ ($a \leq 6$, $b > a$, $c \approx b$) follows established strategies and is comparably straightforward for many TM/E combinations^{1,2}, the generation of reactive sites at such cluster cores, which are subsequently available for substrate binding, remains elusive. We followed several strategies for creating vacant coordination sites on preformed TM/E clusters, e.g. Cp*H elimination by hydrogenation³ or protolysis⁴, protolytic ligand replacement⁵ or phosphine dissociation^{6,7}. The homoleptic compounds $[\text{TM}_2(\text{GaCp}^*)_5]$ (TM = Pd, Pt), so far represent exceptional cases which undergo reproducible and predictable ECp* exchange reactions leading to $[\text{TM}_2(\text{GaCp}^*)_3(\text{L})_2]$ (L = CO; PPh₃).¹ In general, TM-ECp* bonds are considered to be not inclined to substitution.⁸

However, none of the presented reaction pathways leading to accessible reactive sites can be considered as generally applicable and, in all cases, very specific requirements on the nature of the clusters limits their application. An alternative and potentially more general access to reactive TM/E clusters are compounds bearing labile olefin ligands. In contrast to PR₃ as stabilizing ligands which have been shown to become more inert when coordinated to TM/E clusters^{6,7}, the substitution of weaker olefin ligands seems feasible.

In this contribution we study the reaction of homoleptic $[\text{Ni}(\text{olefin})_n]$ complexes towards GaCp* with variation of the olefin ligands to

cdt (all-*trans*-1,5,9-cyclododecatriene) and dvds (dvds = 1, 1, 3, 3-tetramethyl-1, 3-divinyl-disiloxane). The use of GaCp* allows the application of mild synthetic conditions due to its high solubility even at low temperatures which is in contrast to the low solubility of AlCp*.⁹ Unlike the well-established $[\text{Ni}(\text{cod})_2]$, the alternative Ni⁰ sources $[\text{Ni}_2(\text{dvds})_3]$ and $[\text{Ni}(\text{cdt})]$ give access to a variety of Ni_aGa_b complexes and clusters featuring stabilizing olefin ligands. These results point towards the existence of a larger family of Ni_aGa_b clusters featuring different nuclearities and Ni/Ga ratios as well as potentially replaceable olefin ligands. Therefore, the new compounds reported herein represent promising starting points to explore the reactivity of Ni/Ga complexes and clusters towards unsaturated hydrocarbon substrates like e.g. alkynes or alkenes with relevance to catalytic hydrogenations.^{10,11}

Computational Details. Structures of the calculated molecules were optimized using the ORCA4.0²⁰ software package and Becke's exchange functional²¹ with Perdew's correlation functional²² (BP86). Grimme's Dispersion correction including Becke-Johnson damping (D3BJ)^{23,24} was used. After preoptimization and analytical calculation of the Hessian using Ahlrich's def2-SVP basis set, these structures were further optimized using the def2-TZVPP basis sets with subsequent frequency calculations.²⁵ Note: for compound **3** no frequency calculations were performed at the def2-TZVPP level, due to the system size. However, already the def2-SVP results show good agreement to the experimental results from single crystal XRD. The resolution of identity approximation (RI) was applied to speed up the calculations.²⁶

Synthetic protocols.

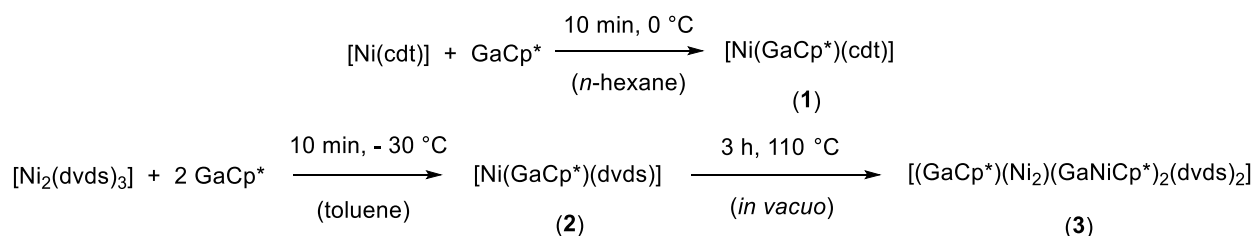
[Ni(GaCp*)(cdt)] (**1**). GaCp* (463 mg, 2.262 mmol) was added dropwise to a pre-cooled solution of [Ni(cdt)] (500 mg, 2.262 mmol) in *n*-hexane (10 mL) at 0 °C. The resultant orange suspension was stirred for 10 min before it was allowed to settle at -50 °C. Cannula filtration afforded **1** as an orange solid which was washed twice with a small amount of *n*-hexane and dried *in vacuo*. Further purification was achieved by re-crystallization of the compound from saturated toluene solutions at -30 °C. Yield: 0.771 g (1.810 mmol, 80 %). Dec. 167 °C. ¹H NMR (C₆D₆, r.t.): δ_H [ppm] = 4.37 (m, 6H, CH), 2.33 (m, 6H, CH₂), 1.95 and 1.92 (overlapping signals, 21H, Cp*/CH₂). ¹³C NMR (C₆D₆, r.t.): δ_C [ppm] = 113.57 (C₅Me₅), 102.86 (CH), 41.10 (CH₂), 9.97 ppm (C₅Me₅). IR (ATR, neat) [cm⁻¹]: 3004, 2961, 2938, 2880, 2837, 2816, 2789, 1508, 1470, 1413, 1366, 1312, 1296, 1262, 1231, 1187, 1164, 1016, 969, 935, 902, 878, 862, 840, 786, 585, 541, 499, 449, 408. LIFDI-MS [a.u.] m/z = 425.4 ([M]⁺, calc. 425.9). Anal. calc. for C₂₂H₃₃GaNi (M = 425.91 g/mol): C 62.04, H 7.81, Ga 16.37, Ni 13.78. Found: C 61.97, H 7.66, Ga, Ni not determined.

[Ni(GaCp*)(dvds)] (**2**). A solution of [Ni₂(dvds)₃] (600 mg, 0.89 mmol, 1.0 eq.) dissolved in toluene (1 mL) is cooled to -30 °C. Subsequently, a cooled solution (-30 °C) of GaCp* (366 mg, 1.78 mmol, 2.0 eq.) in toluene (0.5 ml) is added. After 10 min at -30 °C an orange precipitate is formed which is separated from the remaining solvent by cannula filtration. After drying *in vacuo*, 545 mg of [Ni(GaCp*)(dvds)] as an orange powder

are obtained (1.21 mmol, 68 %). Yellow crystals suitable for XRD analysis can be obtained from a toluene solution cooled to -30 °C. ¹H NMR (400 MHz, C₆D₆, 298 K): δ = 3.01 (m, 4H, CH₂), 2.69 (m, 2H, CH), 1.84 (s, 15H, GaCp*), 0.57 (s, 6H, Me), -0.05 (s, 6H, Me) ppm. ¹³C NMR (101 MHz, C₆D₆, 298 K): δ = 113.8 (s, C₅Me₅), 55.2 (s, C=C), 47.9 (s, C=C), 9.2 (s, C₅Me₅), 1.9 (s, CH₃), -0.4 (s, CH₃) ppm. IR (ATR, neat) [cm⁻¹]: 2962, 2912, 2856, 1604, 1522, 1473, 1410, 1379, 1297, 1241, 1203, 1097, 1066, 1035, 978, 859, 822, 765, 709, 615, 671, 565, 509, 433, 415. LIFDI-MS [a.u.] m/z = 450.0 [M]⁺ (calc.: 450.1) Elemental Anal. Calc. for C₁₈H₃₃NiGaSi₂O: C, 48.0; H, 7.4; Ni, 13.0; Ga, 15.5; Si, 12.5; found: C, 47.7; H, 7.6; Ni, 12.5; Ga, 14.5 %; Si, 12.5 %.

[Ni₄Ga₃](Cp*)₃(dvds)₂ (**3**). In the solid state [Ni(GaCp*)(dvds)] (**2**) (100 mg, 0.22 mmol) is heated to 110 °C for 2 h *in vacuo*, resulting in a black crystalline material, which is washed with cooled *n*-hexane (0.5 ml, -30 °C). After drying *in vacuo* 37 mg (0.12 mmol, 54 %) of the black solid is obtained. Single crystals with sufficient crystallinity for SC-XRD were obtained by recrystallization in cooled (-30 °C) *n*-hexane. ¹H NMR* (400 MHz, Tol-d₈, 298 K): δ = 3.77 – 2.53 (m, 12H, HC=CH₂), 2.06 (s, 15H, GaC₅(CH₃)₅), 1.91 – 1.82 (m, 30H, NiC₅Me₅), 0.49 – 0.10 (m, 24H, CH₃) ppm. ¹³C NMR* (101 MHz, Tol-d₈, 298 K): δ = 115.2 (s, GaC₅Me₅), 98.3 (s, NiC₅Me₅), 63.9 – 43.8 (s, C=C), 10.4, 4.6 – -2.7 (s, CH₃) ppm. IR (ATR, neat) [cm⁻¹]: 2945, 2907, 2855, 1461, 1245, 1293, 1379, 1200, 1173, 1152, 987, 822, 767, 713, 682, 623, 606, 551, 493, 469, 410. LIFDI-MS [a.u.] m/z = 1222.1 [M]⁺ (calc.: 1222.4). Elemental Anal. Calc. for C₄₆H₈₁Ni₄Ga₃Si₄O₂: found: C, 45.2; H, 6.7; Ni, 19.2; Ga, 17.1; Si, 9.2; O, 2.6; found: C, 42.0; H, 6.6; Ni, 18.1, Ga, 16.5; Si, 10.2.* (Only shifts of symmetric isomer).

Synthesis and characterization of
 $[Ni_1(GaCp^*)_1(olefin)_1]$



Scheme 1: Synthesis of Ni/Ga compounds (1-3) featuring stabilizing olefin ligands.

The Ni/Ga-olefin compound **1** can be selectively synthesized by the reaction (Scheme 1). The stable 18 ve complex is air and moisture sensitive but can be stored under an inert atmosphere for months without signs of decomposition. It is well soluble in non-polar organic solvents, like toluene or benzene. Characterization of **1** by 1H NMR spectroscopy gives rise to three signals at 4.37, 2.33 and 1.92 ppm corresponding to the CH, and the two chemically distinct hydrogen atoms of the CH_2 units of the cdt ligand, respectively. The latter signal coincides with an intense singlet at 1.95 ppm which is attributed to the $GaCp^*$ ligand. The ^{13}C NMR spectrum shows the expected sets of signals for the ring carbon atoms and methyl groups of the Cp^* ligand at 113.57 and 9.97 ppm, along with two additional peaks corresponding to the sp^2 and sp^3 -hybridized carbon atoms of the cdt ligand at 102.86 and 41.10 ppm. The overall composition of **1** was confirmed by mass spectrometric measurements using the mild liquid injection field desorption ionization (LIFDI) method which gives rise to the molecular ion peak $[M]^+$ at m/z 425.4 (calc. 425.9).

of equimolar amounts of $[Ni(cdt)]$ and $GaCp^*$ in n -hexane at $0^\circ C$ (

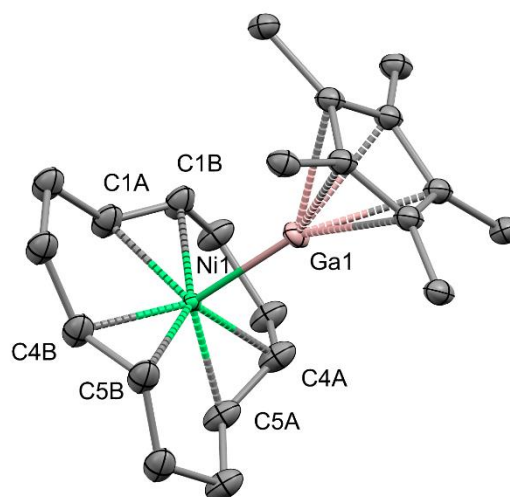


Figure 1: Molecular structure of $[Ni(cdt)(GaCp^*)]$ (**1**). Displacement ellipsoids are shown at the 50 % probability level, hydrogen atoms and disordered sites are omitted for clarity. Selected and averaged interatomic distances (Å) and angles (deg): Ni-Ga av. 2.308, Ga- Cp^*_{centr} av. 2.017, Ni-C av. 2.094, C=C av. 1.38, Cp^*_{centr} -Ga-Ni av. 167.6, $(C=C)_{centr}$ -Ni-Ga 104.6 - 111.7. Symmetry code to create equivalent atoms: $x, -y, z$.

The molecular structure of **1** (Figure 1) was determined by single crystal X-ray diffraction analysis of suitable crystals which were obtained from saturated toluene solutions at $-30^\circ C$ within several days. Compound **1** crystallizes as twinned, orange plates in the monoclinic space group Pm with four crystallographically independent molecules of **1** per unit cell. Its molecular structure features a central Ni

atom bearing one GaCp* as well as one disordered η^6 -coordinated cdt ligand, leading to a distorted tetrahedral coordination environment (counting each C=C bond and the GaCp* as ligator sites) which exhibits angles between 104.6 and 111.7° at the Ni center (with the centroids of each C=C bond as pivotal points of the tetrahedral axes; *Figure 1*). The average Ni-Ga bond length is 2.308 Å with an average Ga-Cp*_{centroid} distance of 2.017 Å. The Ni-C distances are 2.094 Å on average and the C=C bonds of the ethylene moieties are average 1.38 Å.

[Ni(GaCp*)(dvds)] (**2**) can be prepared in a similar manner by treatment of [Ni₂(dvds)₃] with two molar equivalents of GaCp* at -30 °C in toluene. At this temperature pure [Ni(GaCp*)(dvds)] crystallizes from the reaction solution as an orange crystalline solid. **2** decomposes slowly in solution as well as in solid state at ambient temperature and therefore has to be always handled at low temperatures. Prior to synthesis of **2**, single crystals of [Ni₂(dvds)₃] were obtained and analyzed (*Figure S1*). The compound however is of limited relevance for this work and therefore discussed in the supporting information.

The ¹H-NMR spectrum of freshly prepared solutions of **2** shows three doublets of doublets between 3.01 (vinylic, 4H) and 2.69 (vinylic, 2H), a singlet at 1.84 (GaCp*, 15H) and two singlets at 0.57 and -0.05 ppm (SiMe groups, 12H). The ¹³C NMR spectrum is consistent with the signals observed in the ¹H-NMR: The GaCp* signals are found at 113.8 and 9.2 ppm respectively, in accordance with other Ni-GaCp* compounds reported in literature.^{6,14,27} The signals of the dvds ligands

at 55.2, 47.5, 1.9 and -0.4 ppm are only slightly shifted compared to the starting material [Ni₂(dvds)₃].²⁸

Single crystals suitable for X-ray analysis were obtained from cooled toluene solutions at -30 °C after several days (*Figure*).

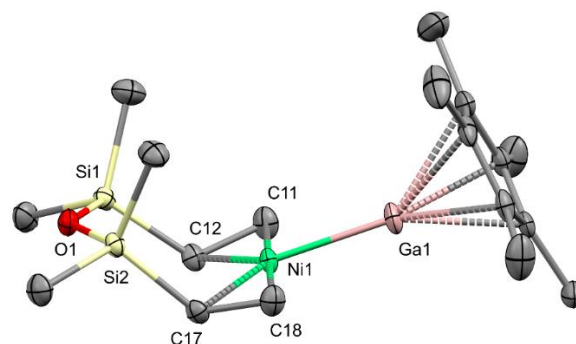


Figure 2: Molecular structure of [Ni(GaCp*)(dvds)] (**2**). Displacement ellipsoids are shown at the 50 % probability level and hydrogen atoms are omitted for clarity. Selected interatomic distances (Å) and angles (°): Ni-Ga: 2.2528(4), Ni-C(dvds): av. 2.00, C=C (dvds): av. 1.41, Ga-Cp*_{centroid}: 1.941, Si-O-Si: 129.07(9).

The Ni-GaCp* distance of 2.2528(4) Å is in the range of other Ni-GaCp* distances but slightly elongated compared to homoleptic [Ni(GaCp*)₄] (2.2188(5) Å), however shorter than in **1** (2.308 Å). The Ga-Cp*_{centroid} distance of 1.941 Å is somewhat shorter than in [Ni(GaCp*)₄] (2.003(4) Å) and **1** (2.017 Å) which is consistent with the electron poor nature of the Ni center and suggests a stronger dative Ga→Ni bond as in **1**.¹⁴ The dvds ligand adopts a chelating coordination mode as it is also found in [Ni₂(dvds)₃]. The Ni-C distance in **2** (av. 2.00 Å) is significantly shorter as in **1** (2.09 Å) and shorter as in [Ni₂(dvds)₃] (av. 2.05 Å), with expected effect for the C=C bonds. In **2** they are elongated (av. 1.41 Å) compared to [Ni₂(dvds)₃] (av.: 1.39 Å) and **1** (av. 1.38 Å) and distinctly longer than the C-C bonds of the related [Ni(cdt)(PR₂R')] (av. 1.31 Å).²⁹

Table 1. Crystallographic data for $[\text{Ni}_2\text{dvds}_3]$, **1**, **2** and **3** (for full details see SI).

	$[\text{Ni}_2\text{dvds}_3]$	1	2	3
formula	$\text{C}_{24}\text{H}_{34}\text{Ni}_2\text{O}_3\text{Si}_6$	$\text{C}_{22}\text{H}_{33}\text{GaNi}$	$\text{C}_{18}\text{H}_{33}\text{GaNiO}_2\text{Si}$	$\text{C}_{46}\text{H}_{81}\text{Ga}_3\text{Ni}_4\text{O}_2\text{Si}_4$
M_r [g/mol]	676.59	423.40	450.03	1222.39
crystal habit	yellow-orange fragment	orange fragment	yellow-orange fragment	black fragment
cryst syst	monoclinic	monoclinic	triclinic	triclinic
space group	$P 2/c$	$P m$	$P \bar{1}$	$P \bar{1}$
a [Å]	6.9926(8)	8.453(4)	9.5552(10)	12.844(14)
b [Å]	10.7321(12)	13.432(4)	10.9769(12)	13.324(17)
c [Å]	23.987(3)	17.910(6)	11.8382(13)	20.60(2)
α [°]	90	90	64.916(4)	86.12(4)
β [°]	94.064(4)	91.894(12)	80.903(4)	77.76(3)
γ [°]	90	90	72.007(4)	89.64(4)
V [Å ³]	1795.6(4)	2032.4(13)	1069.0(2)	3437(7)
Z	2	4	2	2
ρ_c [g cm ⁻³]	1.251	1.384	1.398	1.181
$F(000)$	724	890	472	1268
T [K]	100	100	100	100
μ [mm ⁻¹]	1.271	2.743	2.254	2.326
data / restrain / parameters	3678 / 39 / 184	7470 / 588 / 441	4210 / 0 / 217	13046 / 1424 / 936
GOF (F^2)	1.085	1.021	1.029	1.135
R_1^a, wR_2^b ($I > 2\sigma(I)$)	0.0346, 0.0787	0.0760, 0.1482	0.0245, 0.0548	0.0560, 0.1111

$$^a R_1 = \sum(|F_o| - |F_c|) / \sum |F_o|; \quad ^b wR_2 = \{\sum[w(F_o^2 - F_c^2)^2] / \sum[w(F_o^2)^2]\}^{1/2}$$

Cluster growth reaction and synthesis of $[(\text{Ni}_4\text{Ga}_3)(\text{Cp}^*)_3(\text{dvds})_2]$

When toluene solutions of $[\text{Ni}(\text{GaCp}^*)(\text{dvds})]$ are kept at ambient temperatures, their color readily changes from orange to black. Time and temperature dependent *in-situ* LIFDI-MS measurements of a heated toluene solution of $[\text{Ni}(\text{GaCp}^*)(\text{dvds})]$ indicate a conversion to a new species with 1222.1 m/z among with the formation of additional by-products. We found that heating an orange crystalline sample of **2** to 110 °C also leads to a color change to black. Analysis of the product confirms a highly selective solid-state reaction of **2** to **3** (yield > 95 %). After workup by recrystallization, the cluster $[(\mu\text{-GaCp}^*)(\text{Ni}_2)(\mu\text{-GaNiCp}^*)_2(\text{dvds})_2]$ (**3**) can be obtained in yields higher than 50 %. Single crystals suitable for X-ray crystallography were obtained by cooling a concentrated hexane solution to -30 °C. The single crystal structure (*Figure*) analysis unambiguously reveals a Cp* transfer reaction from Ga to Ni.

Displacement ellipsoids are shown at the 50 % probability level, hydrogen atoms and disordered sites are omitted for clarity. The carbon atoms are depicted in wireframe mode to highlight the M₇ cluster core. Selected interatomic distances (Å) and angles (°): Ni1-Ni2: 2.340(2), Ni1-Ga1: 2.389(3), Ni1-Ga2: 2.399(3), Ni1-Ga3: 2.402(3), Ni2-Ga1: 2.396(3), Ni2-Ga2: 2.430(3), Ni2-Ga3: 2.362(3), Ga2-Ni3: 2.347(3), Ga3-Ni4: 2.313(3), Ni3-Cp*_{centroid}: av. 1.78, Ni3-Cp*_{centroid}: av. 1.81, Ga1-Cp*_{centroid}: av. 2.01, Ni1-C1/2: 1.92-2.05, Ni2-C9/10: 2.02-2.09, C1-C2: av. 1.43, C9-C10: av. 1.48, C7-C8: 1.443(6), C15-C16: 1.441(8), Ga2-O1: 2.801(3), Ga3-O2: 2.887(3), Si-O-Si: 141-144. Average values or ranges are given due to disorder.

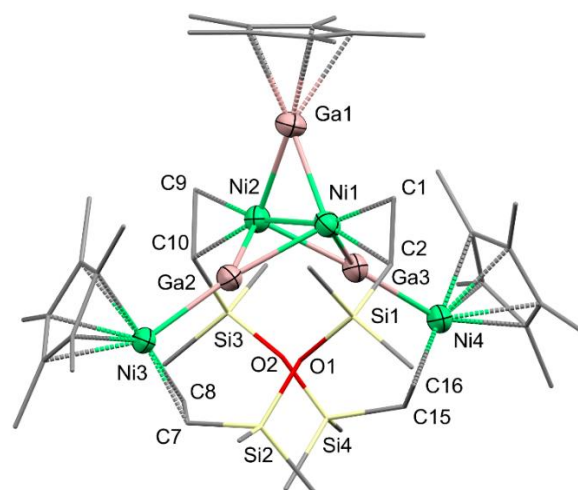


Figure 3: Molecular structure of $[(\mu\text{-GaCp}^*)(\text{Ni}_2)(\mu\text{-GaNiCp}^*)_2(\text{dvds})_2]$ (**3**).

The M₇ core of **3** is propeller-shaped and features a M₅ motif which is reminiscent of that found in $[\text{TM}_2(\text{ECp}^*)_5]$ complexes (TM = Ni, Pd, Pt; E = Al, Ga)^{1,30}. In these compounds the central TM₂ unit is bridged by three ECp* ligands and each TM atom is additionally coordinated by one terminal ECp* ligand. In **3**, the central Ni₂-unit is bridged by a single GaCp* ligand and two bare Ga atoms. Each of these two Ga atoms is bound to a NiCp*, resulting in a 'GaNiCp*' unit. The metal core structure is further stabilized by two dvds ligands each bridging two nickel centers, one of the central Ni₂-unit and one of the NiCp*. Moreover, stabilization is attributed to the short Ga-O distances of only 2.801(3)/2.887(3) Å between the bare Ga-atom of the GaNiCp* units and the O-atom of the dvds ligands. The Ga-O interaction is also supported by QTAIM calculations exhibiting a Ga-O bonding path (see SI *Figure S32*). The vinyl groups coordinated to the central Ni₂-unit are disordered with two positions. This suggests the existence of two isomers which differ in the relative orientation of these vinyl groups, one with a parallel, the other one with a perpendicular relative orientation (*Figure*). The intermetallic distances, including the

unprecedented formal $\text{Cp}^*\text{Ni}^{\text{I}}\text{-Ga}^0$ bond are all in the range of other Ni-Ga interactions.^{31,32} The $\text{M-Cp}^*_{\text{centroid}}$ distances are distinctly different for $\text{M} = \text{Ni}$ and Ga , with $\text{Ni-Cp}^*_{\text{centroid}}$ (av. 1.78/1.81 Å) being about 0.2 Å shorter than $\text{Ga-Cp}^*_{\text{centroid}}$ (av. 2.01 Å). Both distances are consistent with values found for comparable compounds in literature.³³⁻³⁵ The calculated bond distances at the BP86-D3/def2-TZVPP level of theory match well with the crystal structure. Different metal assignments were tested by DFT calculations, without successful convergence. This is further supported by NMR spectroscopy.

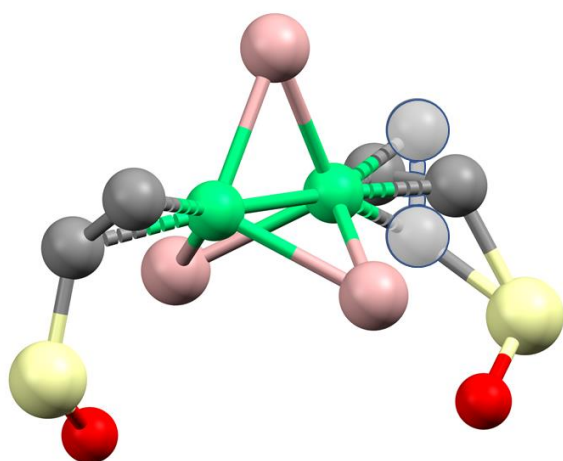


Figure 4: Schematic representation for possible coordination modes of the ethylene-moiety of *dvds* to the central Ni_2 -unit resulting in different isomers of **3**. (Ni = green, Ga = pink, C = gray, Si = yellow, O = red).

Based on the experimental crystal structure a definite assignment of the NMR-data (see SI Figure S9-S15) is possible. However, the unprecedented Cp^* transmetalation from Ga to Ni as well as the existence of at least two isomers drastically complicate the ^1H and ^{13}C NMR spectra.

The ^1H NMR of **3** shows several signals for the SiMe (0.43-0.12 ppm) and vinylic protons (3.75-2.53) of the *dvds* ligand. The large number of signals and their broad ppm range is in accordance with the observed disorder of

the *dvds* ligand leading to an unsymmetrical (C_1) isomer as well as an isomer of higher symmetry (C_2). The Si-Me groups lead to two sets of signals between 3.0 and -1.0 ppm. One set of signals gives rise to eight signals (3H each) and is assignable to a C_1 symmetric *dvds* coordination. The second signal set shows four singlets (6H each), i.e. corresponds to a *dvds* coordination exhibiting an element of symmetry (e.g. C_2 or C_s). Respective signals of *dvds* are consistent with the ^{13}C NMR. The M-Cp^* protons give rise to four singlets at 2.06 (GaCp^*), 1.90 and two overlapping signals at 1.84 and 1.83 ppm (all NiCp^*) with an integration ratio of 30:15:30:15. By 2D HMBC experiments the ^1H can be linked to ^{13}C shifts. The ^{13}C NMR spectra shows five peaks in the Cp^* range with the signals at 115.2 and 114.6 ppm attributed to GaCp^* and the peaks at 98.8, 98.6 and 98.3 ppm assigned to NiCp^* units. A tentative comparison of the peak integrals supports this assignment. Low temperature ^1H -NMR studies (see SI Figure S15) also confirm this assignment and reveal a decoalescence of the GaCp^* signal at -20°C into two distinct singlets with an integral ratio of 1:1.

This is well consistent with the existence of two isomers, that differ in their symmetry along the $\text{Ga-Cp}^*_{\text{centroid}}$ axis. However, a reproducible small ^1H NMR signal at 1.87 ppm (with integral 3 relative to 15H of one Cp^*), as well as ^{13}C NMR peaks at 114.3 and 99.0 ppm point to trace amounts of a third isomer, which could not be further identified.

Spectroscopic Investigations of Ligand Substitution in $[\text{Ni}(\text{GaCp}^)(\text{dvds})]$*

Since **2** represents a stable 16 ve complex, we were interested whether the corresponding 18 ve compound $[\text{Ni}(\text{GaCp}^*)_2(\text{dvds})]$ can be prepared or spectroscopically observed,

respectively. Addition of GaCp* to a freshly prepared solution of [Ni(GaCp*)(dvds)] and analysis via ¹H-NMR reveals coalescence of the signals for free GaCp* (1.93 ppm) and **2** (1.84 ppm) with a chemical shift of the coalesced signal which is consistent with a fast exchange of free and coordinated GaCp* (**Fehler! Verweisquelle konnte nicht gefunden werden.**). Down to -95 °C (see SI *Figure S16*) no splitting

of the coalesced signal is observed pointing to a very low barrier for the GaCp* exchange. Indeed, DFT calculations (BP86-D3/def2-TZVPP) on the 18 ve species [Ni(GaCp*)₂(dvds)], representing a plausible intermediate in an associative GaCp* exchange reaction, suggest a low barrier for the ligand exchange reaction by a very low energy difference of the two species. DFT calculations predict the [Ni(GaCp*)₂(dvds)] species being favored by 5 kcal/mol compared to [Ni(GaCp*)(dvds)] and free GaCp* (Gibbs free

enthalpy in vacuum). Interestingly the optimized structure of [Ni(GaCp*)₂(dvds)] shows two distinct GaCp* ligands with Ni-Ga distances of 2.31 and 2.41 Å, respectively.

Treatment of [Ni(GaCp*)(dvds)] with PEt₃ results in the formation of [Ni(PEt₃)(dvds)] (calculated: 363.3 m/z, observed: 362.9 m/z) as observed LIFDI-MS directly from the reaction solution (see SI *Figure S18*). DFT calculations confirm an elongation of the Ni-Ga bond in [Ni(PEt₃)(GaCp*)(dvds)] by 0.27 Å with respect to **2**, while the Ni-P distance (2.17 Å) is almost the same as in the corresponding 16 ve complex [Ni(PEt₃)(dvds)] (2.16 Å). The Ni-Ga bond seems to be more labile as the Ni-P bond. The observed lability of the Ni-GaCp* bond in **2** was unexpected and similar dissociation reactions have not been observed before. In fact, it has always been assumed that the TM-ECp* bonds are rather inert.⁸

Given the fact that substitution at 16 ve complexes might be more likely we followed

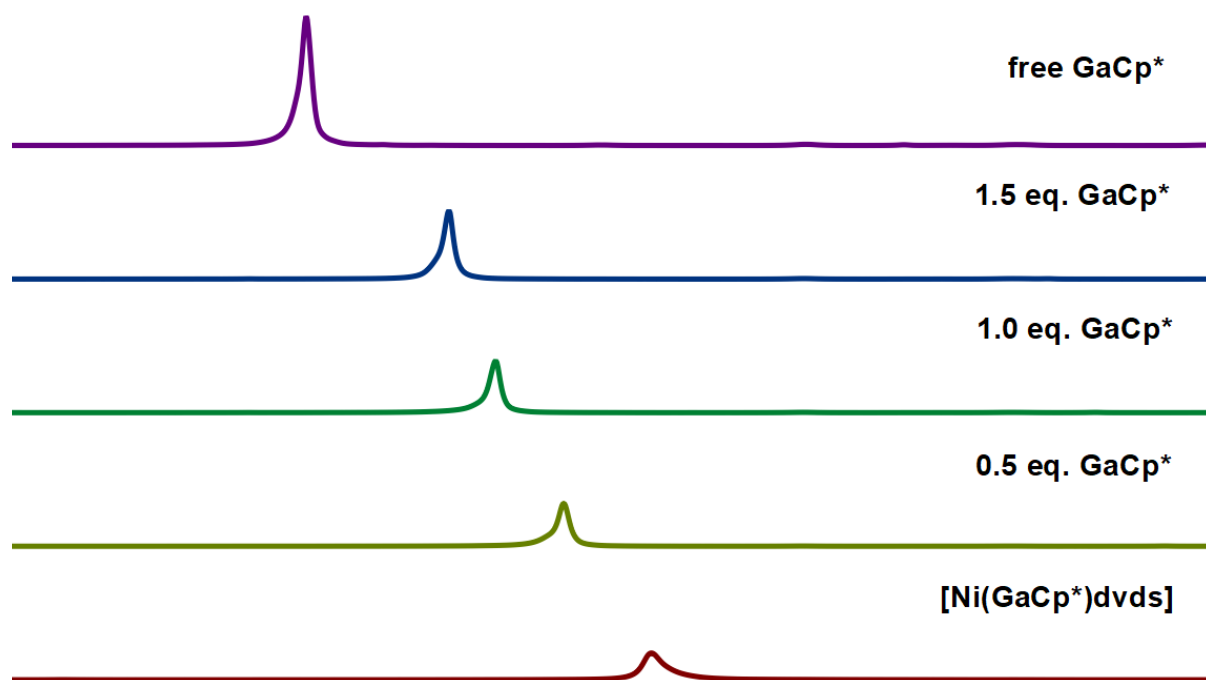


Figure 5: ¹H-NMR spectra of solutions of [Ni(GaCp*)(dvds)] (**1**) (bottom), GaCp* (top) and their mixtures with varying equivalents of GaCp* in C₆D₆. The pure samples exhibit the estimated signal for the GaCp* protons of [Ni(GaCp*)(dvds)] at 1.84 ppm and for GaCp* at 1.93 ppm. For the mixtures only a single signal can be observed indicating fast fluxional processes leading to the coalescence of the two signals.

the addition of an excess PEt_3 to a freshly prepared solution of the 18 ve compound $[\text{Ni}(\text{GaCp}^*)_2(\text{PEt}_3)_2]$ by ^{31}P NMR, confirming the formation of $[\text{Ni}(\text{GaCp}^*)(\text{PEt}_3)_3]$, supporting the lability of the Ni-GaCp* bond.

Conclusion

In this contribution we reported on three new Ni/Ga complexes with olefinic co-ligands. The existence of potentially labile olefinic co-ligands enables the introduction of organic substrates, which opens a link between TM/E clusters as reactivity models for TM/E intermetallic catalysts. However, selective removal of these olefinic groups by e.g. thermal treatment or under hydrogenolytic conditions proved challenging in preliminary experiments, leading to complex product mixtures in all cases. Mass spectrometric analysis of these complex mixtures as well as the identification of reaction conditions leading to well defined clusters are currently investigated and will be reported elsewhere.

An interesting result of this investigation is the role of the transmetalation reaction: While such Cp* ligand transfer reactions have been observed in various cases in mononuclear transition metal complexes³⁶, the NiCp* groups as well as the "naked" Ga centers resulting from the Cp* migration seem to be crucial for the formation of the higher nuclearity cluster **3**. However, at the same time the reactive Ni sites, that are vital for substrate binding are blocked by the Cp* groups. We therefore started to investigate the employment of Ga(I) ligands stabilized by bulky alkyl³⁷ or silyl³⁸ groups in order to suppress ligand transfer reactions.

As a long-term goal, we are curious to investigate the reactivity of catalytically relevant substrates (alkynes/alkenes, H_2 , CO,

CO_2 , ...) on complexes and clusters with different TM/E ratios in order to explore interesting substrate-cluster interactions (e.g. preferential alkyne vs. alkene coordination)³⁹ or to discover unexpected reaction behaviors as for example the C-H activation of benzene on a low-coordinated $[\text{Ni}(\text{AlCp}^*)_3]$ intermediate.⁸ The formation of such reactive transition metal centers in multinuclear intermetallic clusters remains a challenge.

Acknowledgement

This work was supported by the Deutsche Forschungsgemeinschaft (grant Fi 502/23-2) and TUM Graduate School. The authors thank Benjamin J. Hofmann for measuring VT-NMR of **3**.

2.1.3 References

1. Steinke, T.; Gemel, C.; Winter, M.; Fischer, R. A., The Clusters $[\text{M}_a(\text{ECp}^*)_b]$ (M=Pd, Pt; E=Al, Ga, In): Structures, Fluxionality, and Ligand Exchange Reactions. *Chem. Eur. J.* **2005**, *11* (5), 1636-1646.
2. Gemel, C.; Steinke, T.; Cokoja, M.; Kempter, A.; Fischer, Roland A., Transition Metal Chemistry of Low Valent Group 13 Organyls. *Eur. J. Inorg. Chem.* **2004**, *2004* (21), 4161-4176.
3. Cadenbach, T.; Gemel, C.; Schmid, R.; Halbherr, M.; Yussenko, K.; Cokoja, M.; Fischer, R. A., Substituent-Free Gallium by Hydrogenolysis of Coordinated GaCp*: Synthesis and Structure of Highly Fluxional $[\text{Ru}_2(\text{Ga})(\text{GaCp}^*)_7(\text{H})_3]$. *Angew. Chem. Int. Ed.* **2009**, *48* (21), 3872-3876.
4. Buchin, B.; Gemel, C.; Cadenbach, T.; Fernández, I.; Frenking, G.; Fischer, R. A., "Naked" Ga^+ and In^+ as Pure Acceptor Ligands: Structure and Bonding of $[\text{GaPt}(\text{GaCp}^*)_4][\text{BAR}^f]$. *Angew. Chem. Int. Ed.* **2006**, *45* (31), 5207-5210.

5. Hornung, J.; Weßing, J.; Molon, M.; Dilchert, K.; Gemel, C.; Fischer, R. A., Chemistry of Hume-Rothery inspired organometallics: Selective functionalization of $[M(\text{ZnCp}^*)_4(\text{ZnCH}_3)_4]$ ($M = \text{Ni, Pd, Pt}$) with terminal alkynes to yield $[M(\text{ZnCp}^*)_4(\text{ZnCCSiPr})_4]$. *J. Organomet. Chem.* **2018**, *860*, 78-84.
6. Hornung, J.; Weßing, J.; Jerabek, P.; Gemel, C.; Pöthig, A.; Frenking, G.; Fischer, R. A., Suppressed Phosphine Dissociation by Polarization Effects on the Donor–Acceptor Bonds in $[\text{Ni}(\text{PEt}_3)_{4-n}(\text{ECp}^*)_n]$ ($E = \text{Al, Ga}$). *Inorg. Chem.* **2018**, *57* (20), 12657-12664.
7. Heiß, P.; Hornung, J.; Zhou, X.; Jandl, C.; Pöthig, A.; Gemel, C.; Fischer, R. A., Combined Experimental and Theoretical Study on Hampered Phosphine Dissociation in Heteroleptic Ni/Zn Complexes. *Inorg. Chem.* **2020**, *59* (1), 514-522.
8. Steinke, T.; Gemel, C.; Cokoja, M.; Winter, M.; Fischer, R. A., AlCp^* as a directing ligand: C-H and Si-H bond activation at the reactive intermediate $[\text{Ni}(\text{AlCp}^*)_3]$. *Angew. Chem. Int. Ed.* **2004**, *43* (17), 2299-2302.
9. Ganesamoorthy, C.; Loerke, S.; Gemel, C.; Jerabek, P.; Winter, M.; Frenking, G.; Fischer, R. A., Reductive elimination: a pathway to low-valent aluminium species. *Chem. Commun.* **2013**, *49* (28), 2858-2860.
10. Armbrüster, M.; Kovnir, K.; Friedrich, M.; Teschner, D.; Wowsnick, G.; Hahne, M.; Gille, P.; Szentmiklósi, L.; Feuerbacher, M.; Heggen, M.; Girgsdies, F.; Rosenthal, D.; Schlögl, R.; Grin, Y., $\text{Al}_{13}\text{Fe}_4$ as a low-cost alternative for palladium in heterogeneous hydrogenation. *Nat. Mater.* **2012**, *11* (8), 690-693.
11. Studt, F.; Abild-Pedersen, F.; Bligaard, T.; Sørensen, R. Z.; Christensen, C. H.; Nørskov, J. K., Identification of Non-Precious Metal Alloy Catalysts for Selective Hydrogenation of Acetylene. *Science* **2008**, *320* (5881), 1320-1322.
12. Bogdanović, B.; Kröner, M.; Wilke, G., Übergangsmetallkomplexe, I. Olefin-Komplexe des Nickels(0). *Liebigs Ann. Chem.* **1966**, *699* (1), 1-23.
13. Krysan, D. J.; Mackenzie, P. B., A new, convenient preparation of bis(1,5-cyclooctadiene)nickel(0). *J. Org. Chem.* **1990**, *55* (13), 4229-4230.
14. Jutzi, P.; Neumann, B.; Reumann, G.; Stammler, H.-G., Pentamethylcyclopentadienylgallium (Cp^*Ga): Alternative Synthesis and Application as a Terminal and Bridging Ligand in the Chemistry of Chromium, Iron, Cobalt, and Nickel. *Organometallics* **1998**, *17* (7), 1305-1314.
15. *APEX suite of crystallographic software*, Version 2015-5.2; Bruker AXS Inc.: Madison, Wisconsin, USA, 2015.
16. *SAINT and SADABS*, Version 8.34A and Version 2014/5; Bruker AXS Inc.: Madison, Wisconsin, USA, 2014.
17. Sheldrick, G., SHELXT - Integrated space-group and crystal-structure determination. *Acta Crystallogr. A* **2015**, *71* (1), 3-8.
18. Sheldrick, G., Crystal structure refinement with SHELXL. *Acta Crystallogr. C* **2015**, *71* (1), 3-8.
19. Hubschle, C. B.; Sheldrick, G. M.; Dittrich, B., ShelXle: a Qt graphical user interface for SHELXL. *J. Appl. Crystallogr.* **2011**, *44* (6), 1281-1284.
20. Neese, F., The ORCA program system. *Wiley Interdiscip. Rev. Comput. Mol. Sci.* **2012**, *2* (1), 73-78.
21. Becke, A. D., Density-functional exchange-energy approximation with correct asymptotic behavior. *Phys. Rev. A* **1988**, *38* (6), 3098-3100.

22. Perdew, J. P., Density-functional approximation for the correlation energy of the inhomogeneous electron gas. *Phys. Rev. B* **1986**, *33* (12), 8822-8824.
23. Grimme, S.; Antony, J.; Ehrlich, S.; Krieg, H., A consistent and accurate ab initio parametrization of density functional dispersion correction (DFT-D) for the 94 elements H-Pu. *J. Chem. Phys.* **2010**, *132* (15), 154104.
24. Grimme, S.; Ehrlich, S.; Goerigk, L., Effect of the damping function in dispersion corrected density functional theory. *J. Comput. Chem.* **2011**, *32* (7), 1456-1465.
25. Weigend, F.; Ahlrichs, R., Balanced basis sets of split valence, triple zeta valence and quadruple zeta valence quality for H to Rn: Design and assessment of accuracy. *Phys. Chem. Chem. Phys.* **2005**, *7* (18), 3297-3305.
26. Neese, F.; Wennmohs, F.; Hansen, A.; Becker, U., Efficient, approximate and parallel Hartree-Fock and hybrid DFT calculations. A 'chain-of-spheres' algorithm for the Hartree-Fock exchange. *Chem. Phys.* **2009**, *356* (1), 98-109.
27. Molon, M.; Gemel, C.; von Hopffgarten, M.; Frenking, G.; Fischer, R. A., Molecular Hume-Rothery compounds $[M(ZnR)_n]$ and $[M(ZnR)_a(GaR)_b]$ ($a + 2b = n \geq 8$): relations of coordination polyhedra and electronic structure. *Inorg. Chem.* **2011**, *50* (24), 12296-12302.
28. Maciejewski, H.; Marciniak, B.; Kownacki, I., Catalysis of hydrosilylation: Part XXXIV. High catalytic efficiency of the nickel equivalent of Karstedt catalyst $\{[Ni(\eta\text{-CH}_2\text{CHSiMe}_2)_2\text{O}]_2\{\mu\text{-}(\eta\text{-CH}_2\text{CHSiMe}_2)_2\text{O}\}$. *J. Organomet. Chem.* **2000**, *597* (1), 175-181.
29. Wilke, G., Contributions to Organo-Nickel Chemistry. *Angew. Chem. Int. Ed.* **1988**, *27* (1), 185-206.
30. Gemel, C.; Steinke, T.; Weiss, D.; Cokoja, M.; Winter, M.; Fischer, R. A., $[M(GaCp^*)_4]$ ($M = Pd, Pt$) as Building Blocks for Dimeric Homoleptic Cluster Compounds of the Type $[MPt(GaCp^*)_5]$. *Organometallics* **2003**, *22* (13), 2705-2710.
31. Molon, M.; Bollermann, T.; Gemel, C.; Schaumann, J.; Fischer, R. A., Mixed phosphine and group-13 metal ligand complexes $[(PR_3)_aM(ECp^*)_b]$ ($M = Mo, Ni$; $E = Ga, Al$; $R = C_6H_5, \text{cyclo-C}_6H_{11}, CH_3$). *Dalton Trans.* **2011**, *40* (40), 10769-10774.
32. Molon, M.; Dilchert, K.; Gemel, C.; Seidel, R. W.; Schaumann, J.; Fischer, R. A., Clusters $[M_a(GaCp^*)_b(CNR)_c]$ ($M = Ni, Pd, Pt$): synthesis, structure, and Ga/Zn exchange reactions. *Inorg. Chem.* **2013**, *52* (24), 14275-14283.
33. Jutzi, P.; Neumann, B.; Schebaum, L. O.; Stämmler, A.; Stämmler, H.-G., Steric Demand of the Cp^*Ga Ligand: Synthesis and Structure of $Ni(Cp^*Ga)_4$ and of $cis\text{-}M(Cp^*Ga)_2(CO)_4$ ($M = Cr, Mo$). *Organometallics* **1999**, *18* (21), 4462-4464.
34. Shoshani, M. M.; Liu, J.; Johnson, S. A., Mechanistic Insight into H/D Exchange by a Pentanuclear Ni-H Cluster and Synthesis and Characterization of Structural Analogues of Potential Intermediates. *Organometallics* **2018**, *37* (1), 116-126.
35. Molon, M.; Gemel, C.; Jerabek, P.; Trombach, L.; Frenking, G.; Fischer, R. A., Hume-Rothery phase-inspired metal-rich molecules: cluster expansion of $[Ni(ZnMe)_6(ZnCp^*)_2]$ by face capping with $Ni^0(\eta^6\text{-toluene})$ and $Ni^I(\eta^5\text{-Cp}^*)$. *Inorg. Chem.* **2014**, *53* (19), 10403-10411.
36. Buchin, B.; Gemel, C.; Kempter, A.; Cadenbach, T.; Fischer, R. A., Reaction of iron and ruthenium halogenide complexes with $GaCp^*$ and $AlCp^*$: Insertion, Cp^* transfer

reactions and orthometallation. *Inorg. Chim. Acta* **2006**, *359*, 4833 - 4839.

37. Uhl, W.; Hiller, W.; Layh, M.; Schwarz, W., [Ga₄{C(SiMe₃)₃}₄] with a Tetrahedral Ga₄ Skeleton. *Angew. Chem. Int. Ed.* **1992**, *31* (10), 1364-1366.

38. Kehrwald, M.; Köstler, W.; Rodig, A.; Linti, G.; Blank, T.; Wiberg, N., Ga₁₀[Si(SiMe₃)₃]₆, [Ga₁₀(SitBu₃)₆]⁻, and [Ga₁₃(SitBu₃)₆]⁻-Syntheses and Structural

Characterization of Novel Gallium Cluster Compounds. *Organometallics* **2001**, *20* (5), 860-867.

39. Hornung, J.; Muhr, M.; Gemel, C.; Fischer, R. A., All-zinc coordinated nickel-complexes as molecular mimics for NiZn catalyst surfaces, a density functional theory study. *Dalton Trans.* **2019**, *48* (31), 11743-11748.

2.1.4 Additional Data and Information

Experimental Data

Comment on $[\text{Ni}_2(\text{dvds})_3]$ and adopted synthesis.

$[\text{Ni}_2(\text{dvds})_3]$ was synthesized from $[\text{Ni}(\text{cod})_2]$ in a classic ligand exchange reaction with an excess of dvds following a procedure described in literature, leading to an orange crystalline solid and not to an orange oil as described there.¹ After the reaction the ^1H NMR (Figure S) shows several multiplets in the range of $\delta = 4.05 - 2.94$ ppm, fitting to coordinated vinylic protons which are shifted compared to the free dvds ligand ($\delta = 5.38 - 4.89$ ppm). The broad splitting of the olefinic protons together with the six signals for the methyl group protons suggest an unsymmetrical coordination of the dvds ligand. The molecular structure of the higher homologue $[\text{Pt}_2(\text{dvds})_3]$ ² shows one dvds ligand bridging two $[\text{Pt}(\text{dvds})]$ units, which could be a potential explanation for the observed NMR signals of $[\text{Ni}_2(\text{dvds})_3]$. The mentioned methyl groups in $[\text{Ni}_2(\text{dvds})_3]$ exhibit six singlets ($\delta = 0.53 - -0.33$ ppm), each representing two methyl groups, and not just one singlet ($\delta = 0.26$ ppm) for all four CH_3 groups, as the free dvds does. This is supported by the ^{13}C NMR of $[\text{Ni}_2(\text{dvds})_3]$ showing 5 peaks, one with doubled intensity, in the range of $\delta = 67.1 - 68.5$ representing the C-atoms of the olefinic groups. The methyl group resonances are in the range of $\delta = -1.13 - 2.51$ ppm. Data match with literature values.¹ Indeed, single crystal X-ray diffraction analysis confirms the analogue molecular structure for $[\text{Ni}_2(\text{dvds})_3]$, featuring one bridging and two terminal dvds ligands, isostructural to the higher homologue $[\text{Pt}_2(\text{dvds})_3]$.

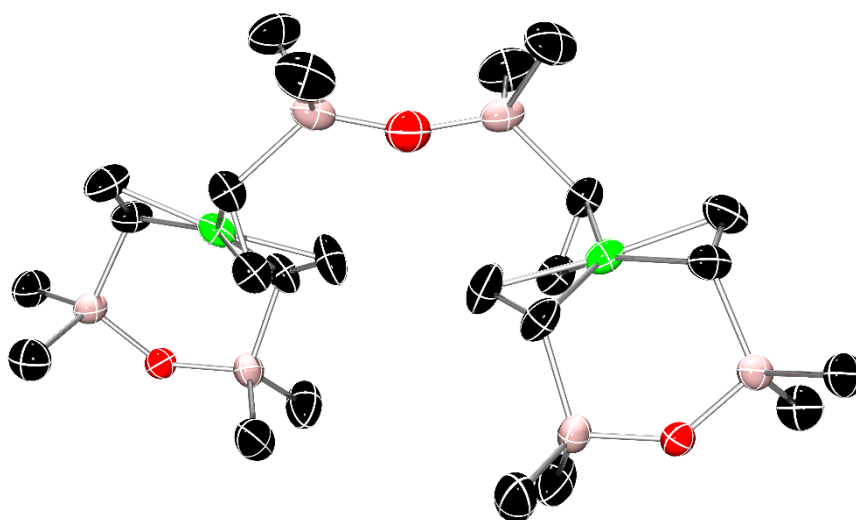


Figure S1: Molecular structure of $[\text{Ni}_2(\text{dvds})_3]$. Hydrogens and disordered sites omitted for clarity. Ellipsoids are drawn at 50% of probability. Symmetry code to generate equivalent atoms: $-x + 1, y, -z + 1.5$.

Single crystals, in shape of large orange needles, were grown within a week in hexane, cooled to $-30\text{ }^{\circ}\text{C}$. At first sight, there is no significant difference between a terminal and bridging dvds, according to the Ni-C_{olefin} distance. Both the Ni-C and C-C bond lengths are in similar ranges but will not be discussed in detail due to disorder. The crystallographic data of $[\text{Ni}_2(\text{dvds})_3]$ reveal the intrinsic flexibility of the dvds ligand, which is already obvious by its occurrence as terminal and bridging ligand within the same molecule. The torsion angles of the O-Si-bond with the C-C-double-bond of the terminal dvds are $-133.08(19)^{\circ}$ and $141.12(19)^{\circ}$, whereas for the bridging dvds they are around -174° and 22° (no exact values due to disorder). Further, the bond angle of the Si-O-Si-bond 'back bone' is $129.33(9)^{\circ}$ for the two terminal ligands, in contrast the bridging dvds has an angle of $159.77(19)^{\circ}$. This remarkable degree of flexibility enables a big overlap of the nickel and olefin orbitals and results in a good interaction, that exceeds other prominent olefin chelate ligands, as cod or cdt.

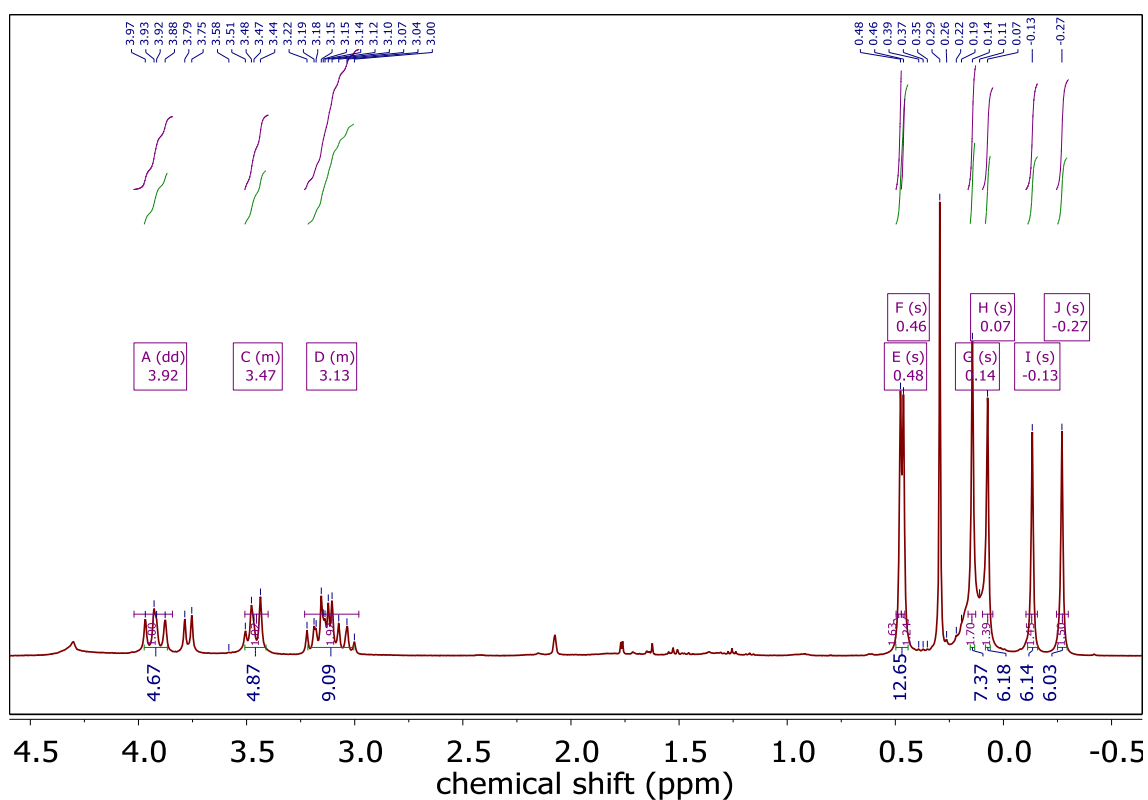


Figure S2: ^1H NMR of $[\text{Ni}_2(\text{dvds})_3]$.

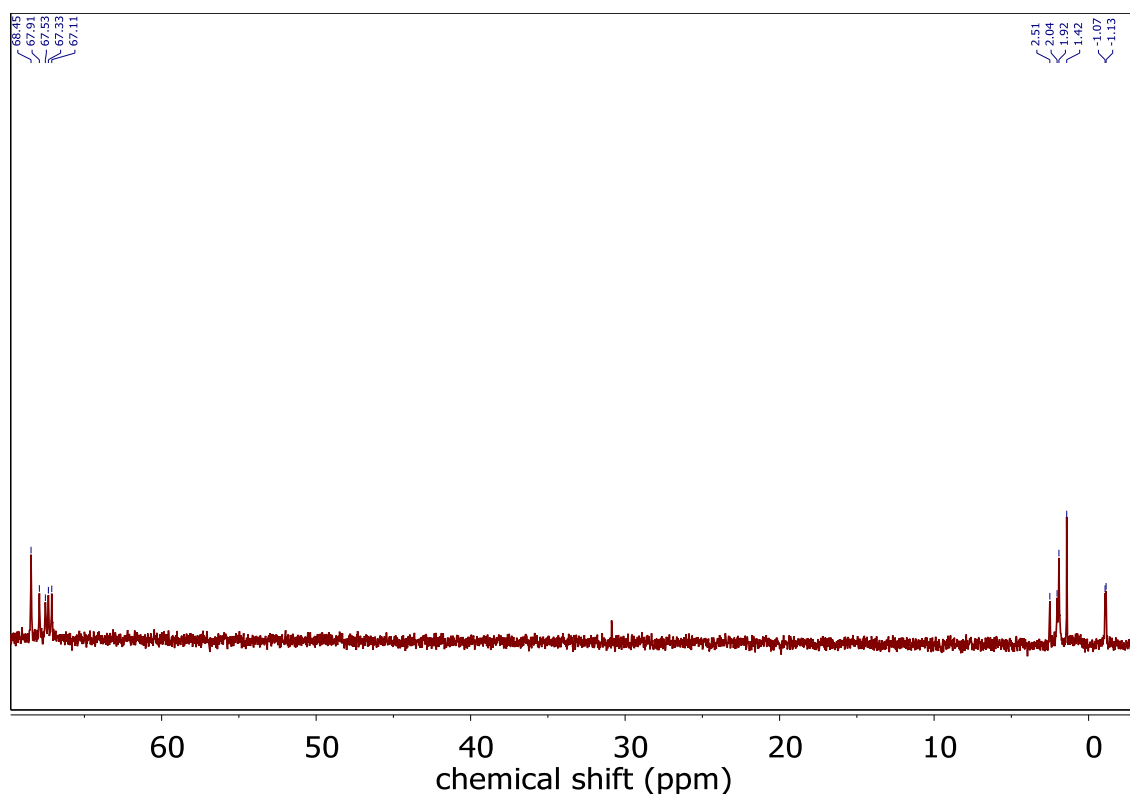


Figure S3: ^{13}C NMR of $[\text{Ni}_2(\text{dvds})_3]$.

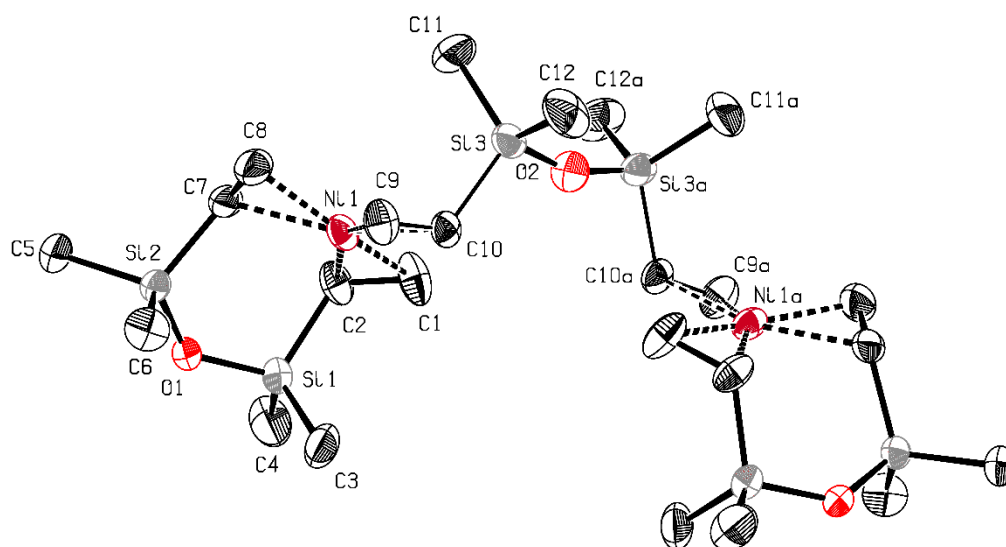
Synthetic protocol

$[\text{Ni}_2(\text{dvds})_3]$: $[\text{Ni}(\text{cod})_2]$ (4.00 g, 14.54 mmol, 1.0 eq.) is suspended in diethyl ether (45 mL), after addition of 1,3-divinyltetramethyldisiloxane (19.44 g, 104.27 mmol, 7.0 eq.) the orange reaction solution is stirred for 24 h at ambient temperature. Volatiles are removed *in vacuo*, the remaining brown oil is dissolved in *n*-hexane (20 ml), filtered over Celite® and washed with *n*-hexane (3x3 ml). After removing all volatiles, 4.92 g of $[\text{Ni}_2(\text{dvds})_3]$ as an orange powder are obtained (7.27 mmol, 50 %). Single crystals are grown in *n*-hexane at $-30\text{ }^\circ\text{C}$, in shape of large orange needles. ^1H NMR (400.0 MHz, C_6D_6 , 298 K): δ = 3.92 (dd, J = 20.7, 4H, CH_2), 3.77 (d, J = 13.0, 2H, CH), 3.51 – 3.40 (m, 4H, CH), 3.23 – 2.98 (m, 8H, CH_2), 0.48 (s, 6H, CH_3), 0.46 (s, 6H, CH_3), 0.14 (s, 6H, CH_3), 0.07 (s, 6H, CH_3), -0.13 (s, 6H, CH_3), -0.27 (s, 6H, CH_3) ppm. ^{13}C NMR (101 MHz, C_6D_6 , 298 K): δ = 68.5 (s, C=C), 67.9 (s, C=C), 67.5 (s, C=C), 67.3 (s, C=C), 67.1 (s, C=C), 2.5 (s, CH_3), 2.0 (s, CH_3), 1.9 (s, CH_3), 1.4 (s, CH_3), -1.1 (s, CH_3), -1.1 (s, CH_3) ppm. IR [cm^{-1}]: 2956, 2905, 2843, 1598, 1522, 1397, 1335, 1241, 1084, 1041, 1009, 990, 922, 828, 772, 778, 709, 678, 596, 559, 458, 409. Elemental Anal. Calc. for $\text{C}_{24}\text{H}_{54}\text{Si}_6\text{O}_3\text{Ni}_2$: C, 42.6; H, 8.1; Si, 24.9; Ni, 17.4; found: C, 41.6; H, 8.1; Si, 23.1; Ni, 15.7.

Comment on $[\text{Ni}_3\text{Ga}_4](\text{Cp}^)_4(\text{dvds})$*

In the LIFDI-MS spectra (Figure S21) of the reaction of $[\text{Ni}_2(\text{dvds})_3]$ with GaCp^* , the mass (m/z) 1181.8 a.u. is most probably related to $[\text{Ni}_3(\text{GaCp}^*)_4(\text{dvds})]$. The calculated isotopic pattern of $[\text{Ni}_3\text{Ga}_4](\text{Cp}^*)_4(\text{dvds})$ nicely fits to the experimental spectrum (Figure S21). Also, the existence of the analogous compound $[\text{Pd}_3(\text{GaCp}^{*\text{-Ph}})_4(\text{dvds})]$ that has already been extensively characterized² supports the assignment of the LIFDI-MS signal to $[\text{Ni}_3\text{Ga}_4](\text{Cp}^*)_4(\text{dvds})$. Performing DFT calculations (Figure S29) based on the already published structure of $[\text{Pd}_3\text{Ga}_4](\text{Cp}^*)_4(\text{dvds})$ results in a minimum and therefore both compounds could be isostructural.

[Ni₂dvd₃] (CCDC 1979648)



Diffractometer operator C. Jandl
scanspeed 1-5 s per frame
dx 50 mm
4179 frames measured in 16 data sets
phi-scans with delta_phi = 0.5
omega-scans with delta_omega = 0.5
shutterless mode

Crystal data

C₂₄H₅₄Ni₂O₃Si₆

$M_r = 676.59$

Monoclinic, P2/c

Hall symbol: -P 2yc

$a = 6.9926 (8) \text{ \AA}$

$b = 10.7321 (12) \text{ \AA}$

$c = 23.987 (3) \text{ \AA}$

$\beta = 94.064 (4)^\circ$

$V = 1795.6 (4) \text{ \AA}^3$

$Z = 2$

$F(000) = 724$

$D_x = 1.251 \text{ Mg m}^{-3}$

Melting point: ? K

Mo K α radiation, $\lambda = 0.71073 \text{ \AA}$

Cell parameters from 9557 reflections

$\theta = 2.6\text{--}27.5^\circ$

$\mu = 1.27 \text{ mm}^{-1}$

$T = 100 \text{ K}$

Fragment, yellow-orange

0.38 × 0.25 × 0.21 mm

Data collection

Bruker Photon CMOS
diffractometer 3678 independent reflections

Radiation source: TXS rotating anode 3393 reflections with $I > 2\sigma(I)$

Helios optic monochromator $R_{\text{int}} = \underline{0.046}$

Detector resolution: 16 pixels mm^{-1} $\theta_{\text{max}} = \underline{26.4}^\circ$, $\theta_{\text{min}} = \underline{2.6}^\circ$

phi- and ω -rotation scans $h = \underline{-8}$ 8

Absorption correction: multi-scan
SADABS 2014/5, Bruker $k = \underline{-13}$ 13

$T_{\text{min}} = \underline{0.666}$, $T_{\text{max}} = \underline{0.746}$ $l = \underline{-29}$ 29

88275 measured reflections

Refinement

Refinement on F^2 Secondary atom site location: difference
Fourier map

Least-squares matrix: full Hydrogen site location: inferred from
neighbouring sites

$R[F^2 > 2\sigma(F^2)] = \underline{0.031}$ H-atom parameters constrained

$wR(F^2) = \underline{0.080}$ $W = 1/[\Sigma^2(FO^2) + (0.0337P)^2 + 1.4479P]$
WHERE $P = (FO^2 + 2FC^2)/3$

$S = \underline{1.09}$ $(\Delta/\sigma)_{\text{max}} = \underline{0.001}$

3678 reflections $\Delta\rho_{\text{max}} = \underline{0.56}$ e \AA^{-3}

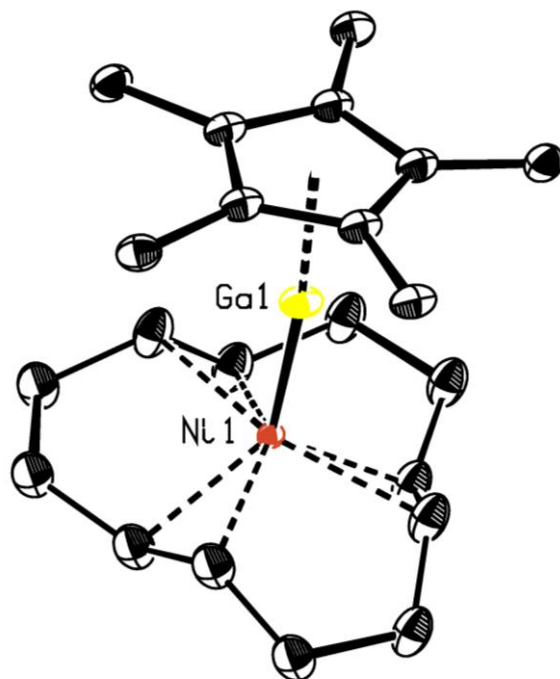
184 parameters $\Delta\rho_{\text{min}} = \underline{-0.44}$ e \AA^{-3}

39 restraints Extinction correction: none

0 constraints Extinction coefficient: -

Primary atom site location: intrinsic phasing

Compound 1 (CCDC 1829782)



Crystal data

$4(\text{C}_{12}\text{H}_{18}\text{GaNi}) \cdot 4(\text{C}_{10}\text{H}_{15})$

$M_r =$ 423.40

$D_x =$ 1.384 Mg m⁻³

Monoclinic, Pm

Melting point: ? K

Hall symbol: $P-2y$

Cu $K\alpha$ radiation, $\lambda =$ 1.54178 Å

$a =$ 8.453 (4) Å

Cell parameters from 9983 reflections

$b =$ 13.432 (4) Å

$\theta =$ 4.9–74.5°

$c =$ 17.910 (6) Å

$\mu =$ 2.74 mm⁻¹

$\beta =$ 91.894 (12)°

$T =$ 100 K

$V =$ 2032.4 (13) Å³

Fragment, orange

$Z =$ 4

0.22 × 0.13 × 0.08 mm

$F(000) =$ 890

Data collection

Bruker Photon CMOS
diffractometer 7470 independent reflections

Radiation source: IMS microsource 6266 reflections with $I > 2\sigma(I)$

Helios optic monochromator $R_{\text{int}} = ?$

Detector resolution: 16 pixels mm^{-1} $\theta_{\text{max}} = \underline{74.5^\circ}$, $\theta_{\text{min}} = \underline{3.3^\circ}$

phi- and ω -rotation scans $h = \underline{-10}$ 10

Absorption correction: multi-scan
TWINABS 2012/1, Bruker $k = \underline{0}$ 16

$T_{\text{min}} = \underline{0.640}$, $T_{\text{max}} = \underline{0.754}$ $l = \underline{0}$ 22

7470 measured reflections

Refinement

Refinement on F^2 Hydrogen site location: mixed

Least-squares matrix: full H atoms treated by a mixture of independent and constrained refinement

$R[F^2 > 2\sigma(F^2)] = \underline{0.061}$ $W = 1/[\Sigma^2(FO^2) + (0.0661P)^2 + 6.9187P]$
WHERE $P = (FO^2 + 2FC^2)/3$

$wR(F^2) = \underline{0.161}$ $(\Delta/\sigma)_{\text{max}} = \underline{0.003}$

$S = \underline{1.02}$ $\Delta\rho_{\text{max}} = \underline{0.97} \text{ e } \text{\AA}^{-3}$

7470 reflections $\Delta\rho_{\text{min}} = \underline{-1.15} \text{ e } \text{\AA}^{-3}$

588 parameters Extinction correction: none

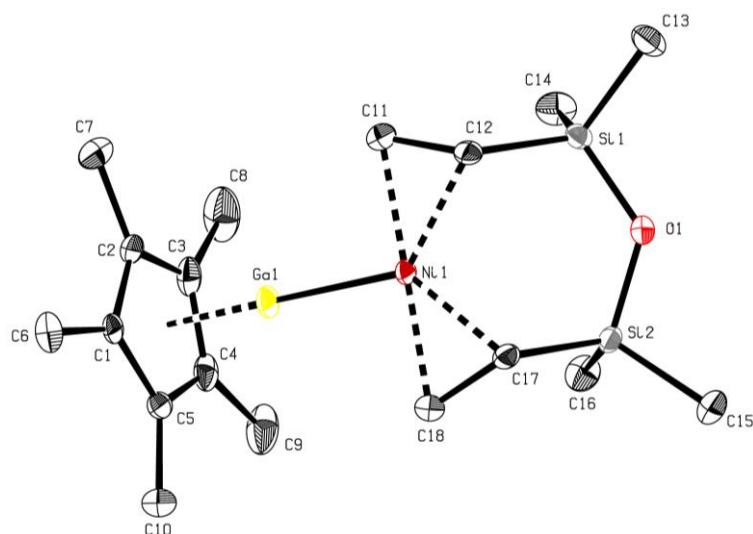
441 restraints Extinction coefficient: -

0 constraints Absolute structure: Flack^{C11,C12}

Primary atom site location: intrinsic phasing Absolute structure parameter: 0.11 (6)

Secondary atom site location: difference
Fourier map

Compound 2 (CCDC 1979647)



Diffraction operator C. Jandl
scanspeed 1-2 s per frame
dx 34 mm
1524 frames measured in 7 data sets
phi-scans with $\Delta\phi = 0.5$
omega-scans with $\Delta\omega = 0.5$
shutterless mode

Crystal data

$C_{18}H_{33}GaNiOSi_2$

$M_r = 450.03$

Triclinic, P

Hall symbol: $-P\ 1$

$a = 9.5552(10)$ Å

$b = 10.9769(12)$ Å

$c = 11.8382(13)$ Å

$\alpha = 64.916(4)^\circ$

$\beta = 80.903(4)^\circ$

$\gamma = 72.007(4)^\circ$

$V = 1069.0(2)$ Å³

$Z = 2$

$F(000) = 472$

$D_x = 1.398$ Mg m⁻³

Melting point: ? K

Mo $K\alpha$ radiation, $\lambda = 0.71073$ Å

Cell parameters from 9965 reflections

$\theta = 2.2\text{--}27.6^\circ$

$\mu = 2.25$ mm⁻¹

$T = 100$ K

Fragment, yellow-orange

$0.35 \times 0.26 \times 0.23$ mm

Data collection

Bruker Photon CMOS
diffractometer 4210 independent reflections

Radiation source: TXS rotating anode 3887 reflections with $I > 2\sigma(I)$

Helios optic monochromator $R_{\text{int}} = \underline{0.034}$

Detector resolution: 16 pixels mm^{-1} $\theta_{\text{max}} = \underline{26.0^\circ}$, $\theta_{\text{min}} = \underline{2.6^\circ}$

phi- and ω -rotation scans $h = \underline{-11}$ 11

Absorption correction: multi-scan
SADABS 2014/5, Bruker $k = \underline{-13}$ 13

$T_{\text{min}} = \underline{0.620}$, $T_{\text{max}} = \underline{0.746}$ $l = \underline{-14}$ 14

19885 measured reflections

Refinement

Refinement on F^2 Secondary atom site location: difference
Fourier map

Least-squares matrix: full Hydrogen site location: inferred from
neighbouring sites

$R[F^2 > 2\sigma(F^2)] = \underline{0.022}$ H-atom parameters constrained

$wR(F^2) = \underline{0.056}$ $W = 1/[\Sigma^2(FO^2) + (0.0212P)^2 + 0.8013P]$
WHERE $P = (FO^2 + 2FC^2)/3$

$S = \underline{1.03}$ $(\Delta/\sigma)_{\text{max}} = \underline{0.001}$

4210 reflections $\Delta\rho_{\text{max}} = \underline{0.37}$ e \AA^{-3}

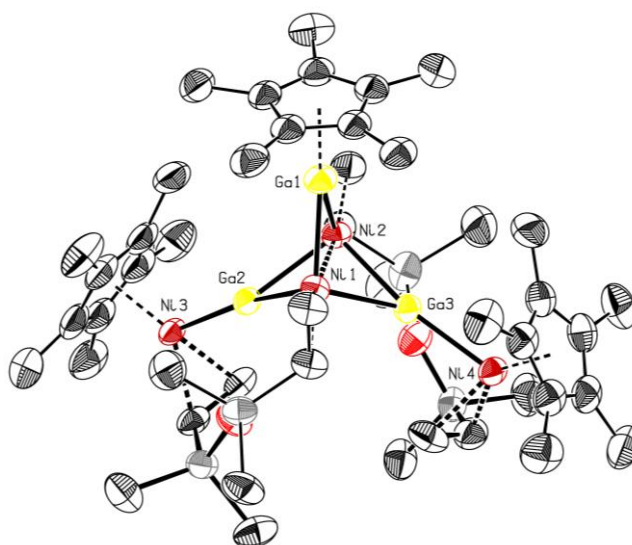
217 parameters $\Delta\rho_{\text{min}} = \underline{-0.34}$ e \AA^{-3}

0 restraints Extinction correction: none

0 constraints Extinction coefficient: -

Primary atom site location: intrinsic phasing

Compound 3 (CCDC 1979649)



Diffractometer operator C. Jandl
scanspeed 2-10 s per frame
dx 40 mm
1670 frames measured in 7 data sets
phi-scans with $\Delta\phi = 0.5$
omega-scans with $\Delta\omega = 0.5$
shutterless mode

Crystal data

$C_{46}H_{81}Ga_3Ni_4O_2Si_4$

$F(000) = 1268$

$M_r = 1222.39$

Triclinic, P

$D_x = 1.181 \text{ Mg m}^{-3}$

Hall symbol: $-P 1$

Melting point: ? K

$a = 12.844 (14) \text{ \AA}$

Mo $K\alpha$ radiation, $\lambda = 0.71073 \text{ \AA}$

$b = 13.324 (17) \text{ \AA}$

Cell parameters from 4207 reflections

$c = 20.60 (2) \text{ \AA}$

$\theta = 2.2\text{--}25.6^\circ$

$\alpha = 86.12 (4)^\circ$

$\mu = 2.33 \text{ mm}^{-1}$

$\beta = 77.76 (3)^\circ$

$T = 100 \text{ K}$

$\gamma = 89.64 (4)^\circ$

Fragment, black

$V = 3437 (7) \text{ \AA}^3$

$0.32 \times 0.31 \times 0.20 \text{ mm}$

$Z = 2$

Data collection

Bruker Photon CMOS
diffractometer 13046 independent reflections

Radiation source: TXS rotating anode 10404 reflections with $I > 2\sigma(I)$

Helios optic monochromator $R_{\text{int}} = \underline{0.076}$

Detector resolution: 16 pixels mm^{-1} $\theta_{\text{max}} = \underline{25.7^\circ}$, $\theta_{\text{min}} = \underline{2.2^\circ}$

phi- and ω -rotation scans $h = \underline{-15}$ 14

Absorption correction: multi-scan
SADABS 2014/5, Bruker $k = \underline{-16}$ 16

$T_{\text{min}} = \underline{0.570}$, $T_{\text{max}} = \underline{0.745}$ $l = \underline{-25}$ 25

77161 measured reflections

Refinement

Refinement on F^2 Secondary atom site location: difference
Fourier map

Least-squares matrix: full Hydrogen site location: inferred from
neighbouring sites

$R[F^2 > 2\sigma(F^2)] = \underline{0.043}$ H-atom parameters constrained

$wR(F^2) = \underline{0.119}$ $W = 1/[\Sigma^2(FO^2) + (0.0449P)^2 + 2.9018P]$
WHERE $P = (FO^2 + 2FC^2)/3$

$S = \underline{1.14}$ $(\Delta/\sigma)_{\text{max}} = \underline{0.002}$

13046 reflections $\Delta\rho_{\text{max}} = \underline{0.67}$ e \AA^{-3}

939 parameters $\Delta\rho_{\text{min}} = \underline{-0.66}$ e \AA^{-3}

1424 restraints Extinction correction: none

0 constraints Extinction coefficient: -

Primary atom site location: intrinsic phasing

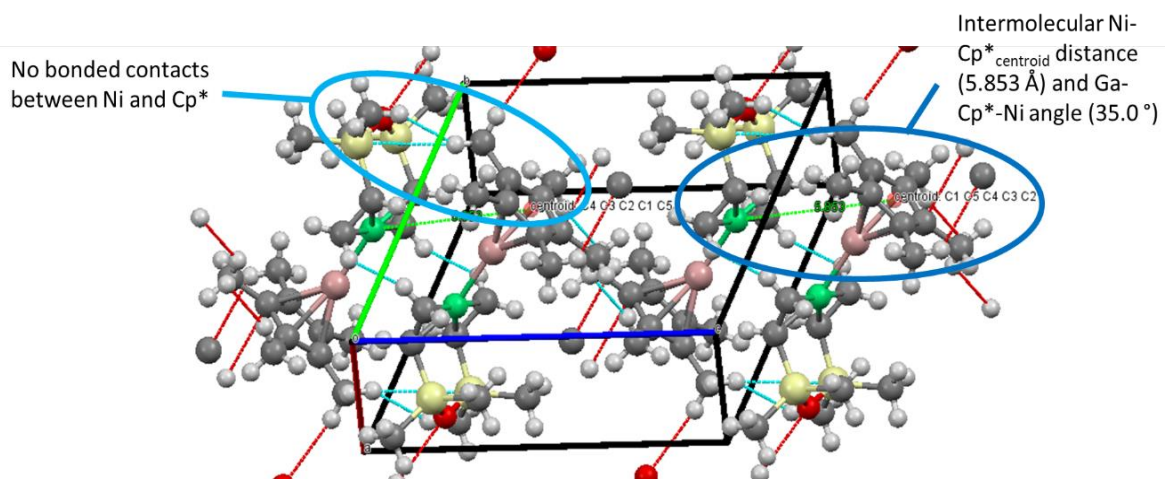


Figure S4: Packing of **2** with remarks highlighting non-bonding contacts – Ni (green), Ga (pink).

NMR spectra

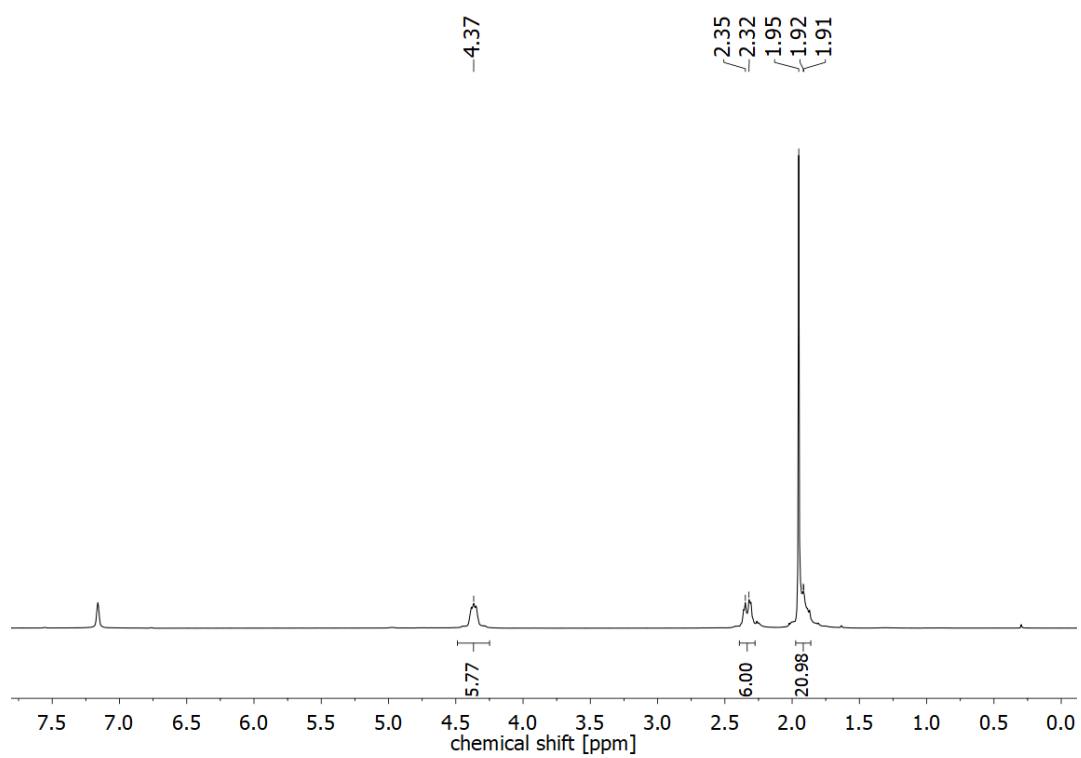


Figure S5: ^1H NMR of $[\text{Ni}(\text{GaCp}^*)(\text{cdt})]$ (**1**).

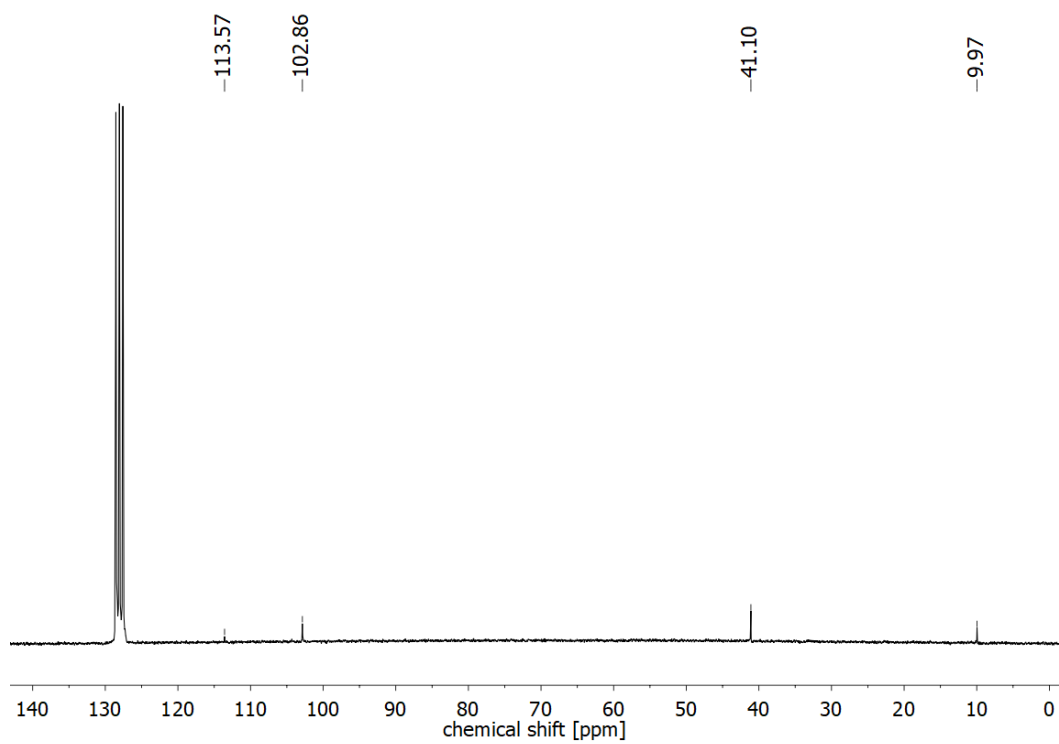


Figure S6: ^{13}C NMR of $[\text{Ni}(\text{GaCp}^*)(\text{cdt})]$ (**1**).

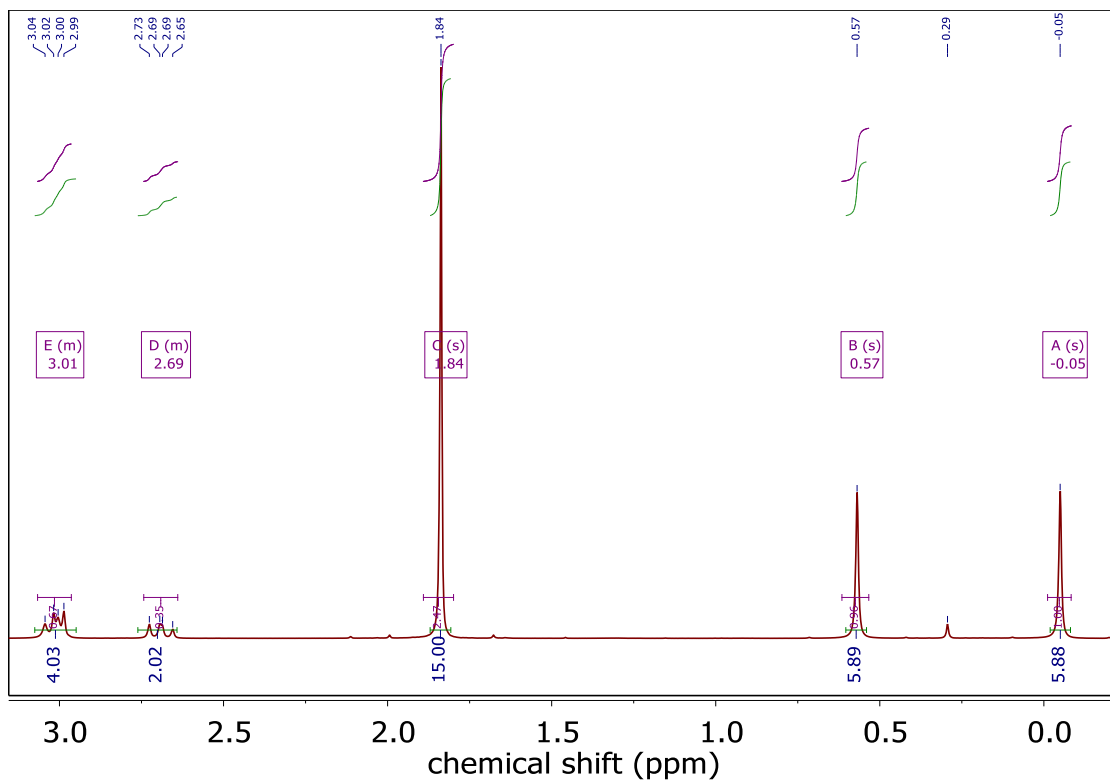


Figure S7: $^1\text{H-NMR}$ of $[\text{Ni}(\text{GaCp}^*)(\text{dvds})]$ (2).

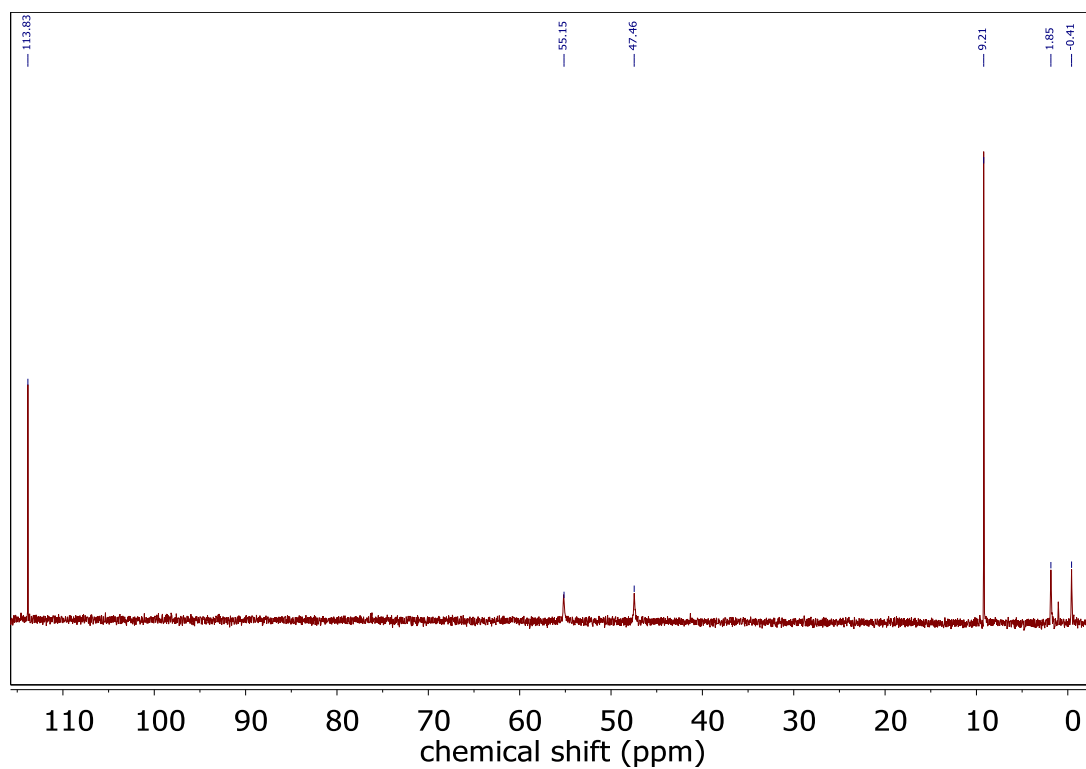


Figure S8: $^{13}\text{C-NMR}$ of $[\text{Ni}(\text{GaCp}^*)(\text{dvds})]$ (2).

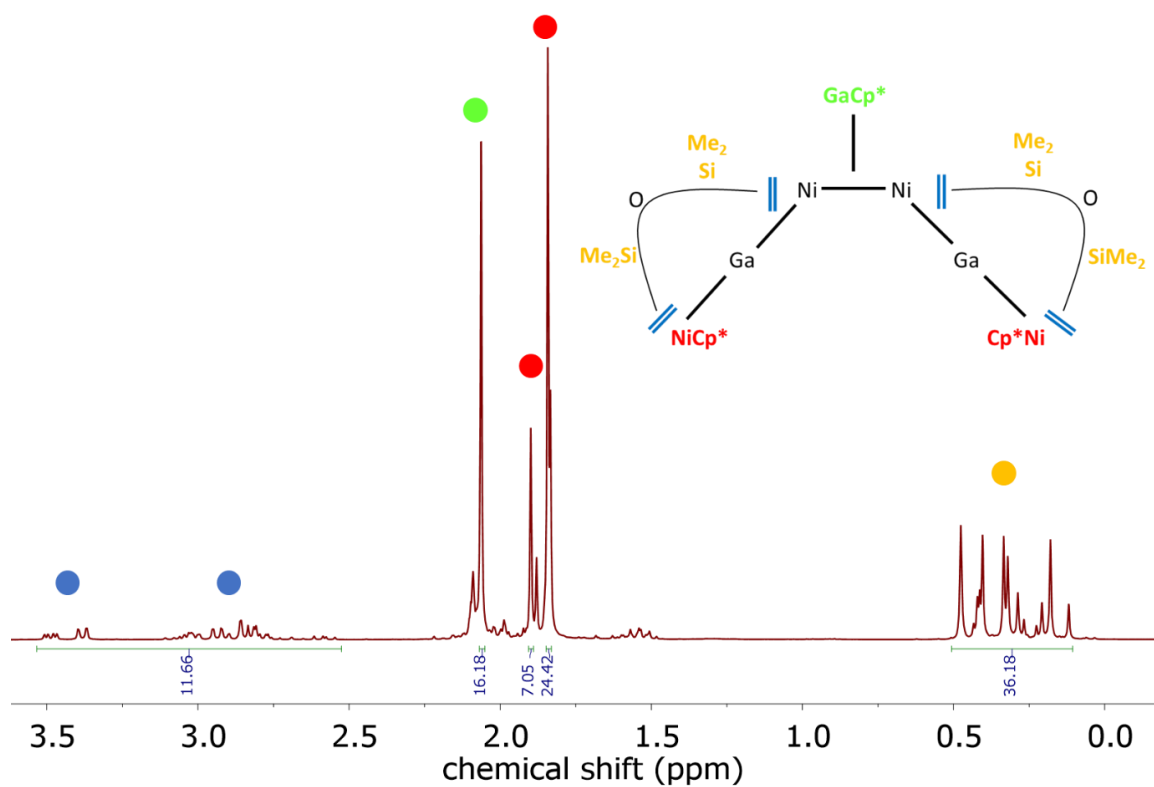


Figure S9: ^1H NMR of **3** with peak assignment by colors.

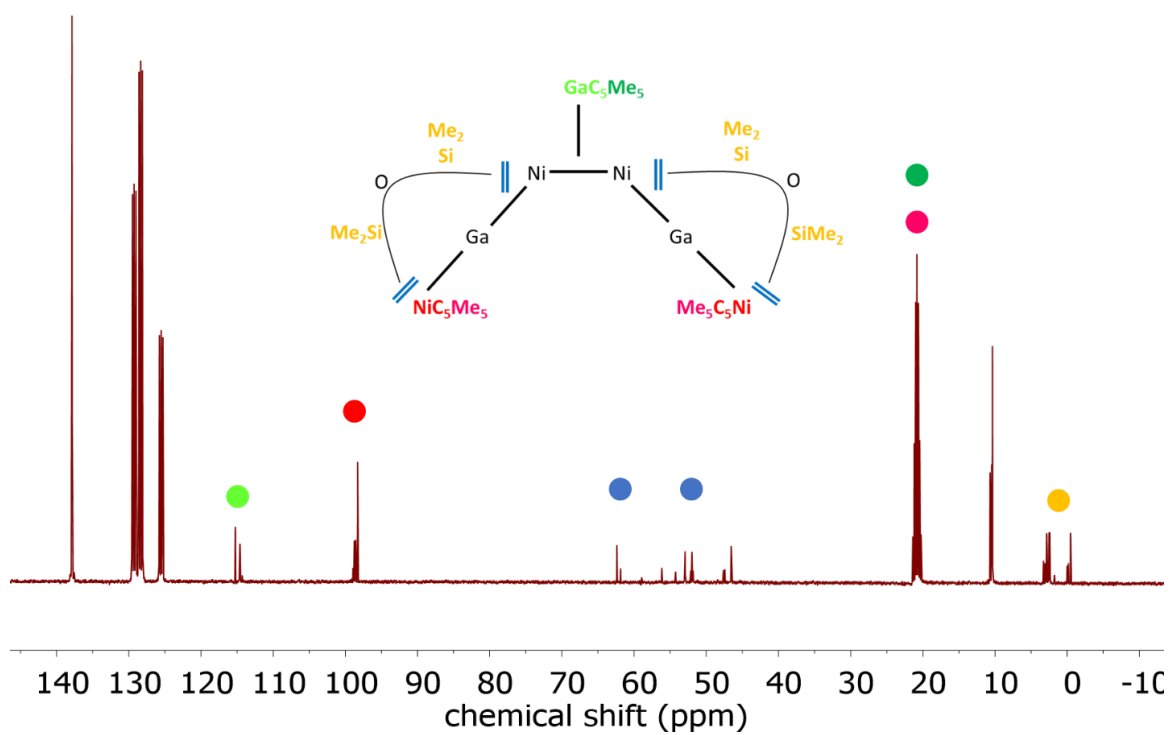


Figure S10: ^{13}C NMR of **3** with peak assignment by colors.

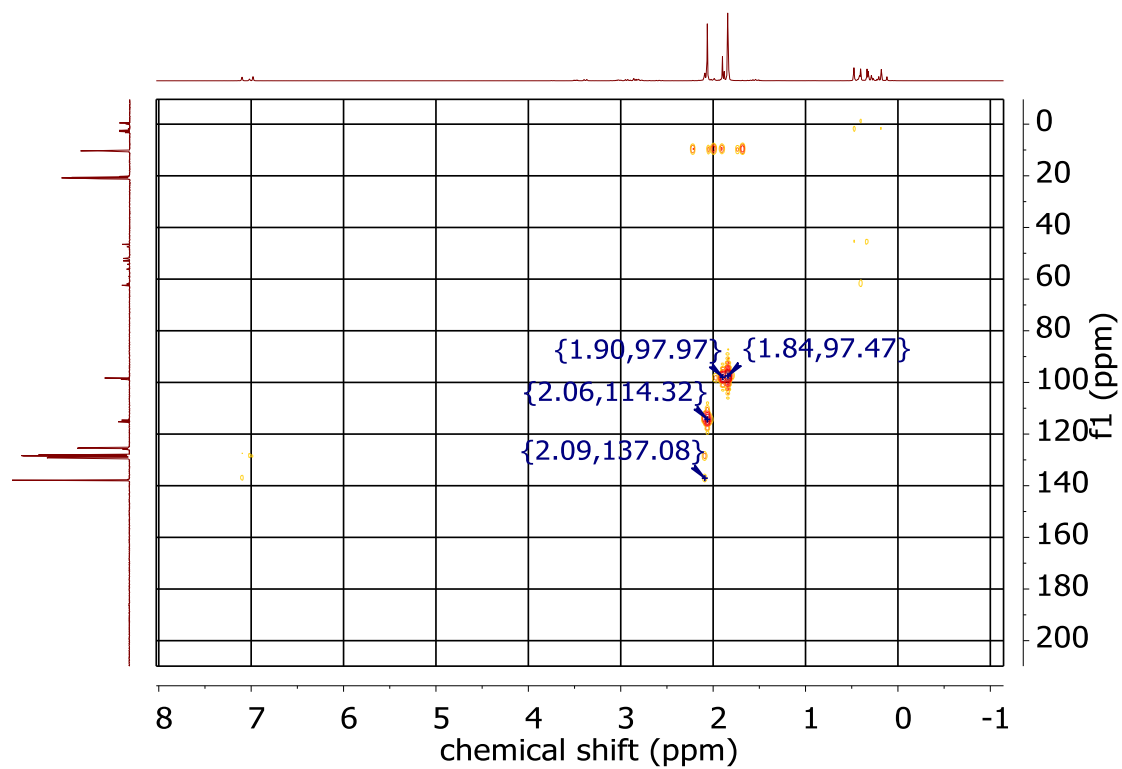


Figure S11: 2D HMBC NMR experiment of **3**.

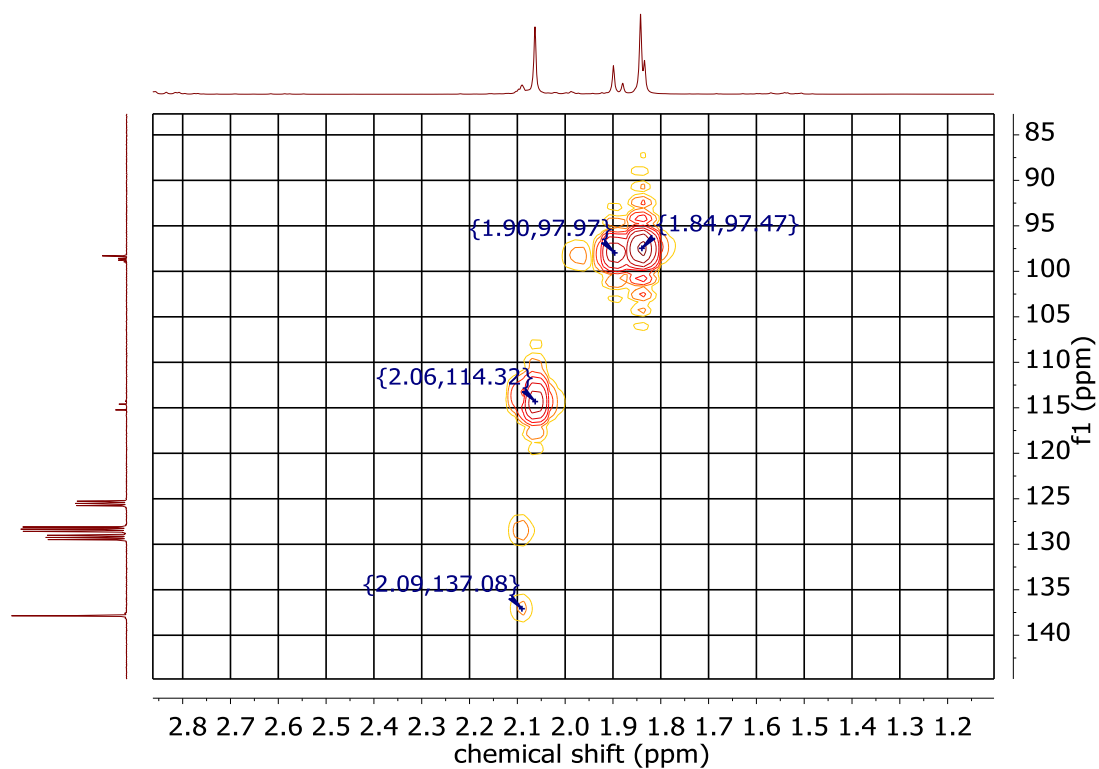


Figure S12 2D HMBC NMR experiment of **3**, assigning NiCp^* and GaCp^* shifts.

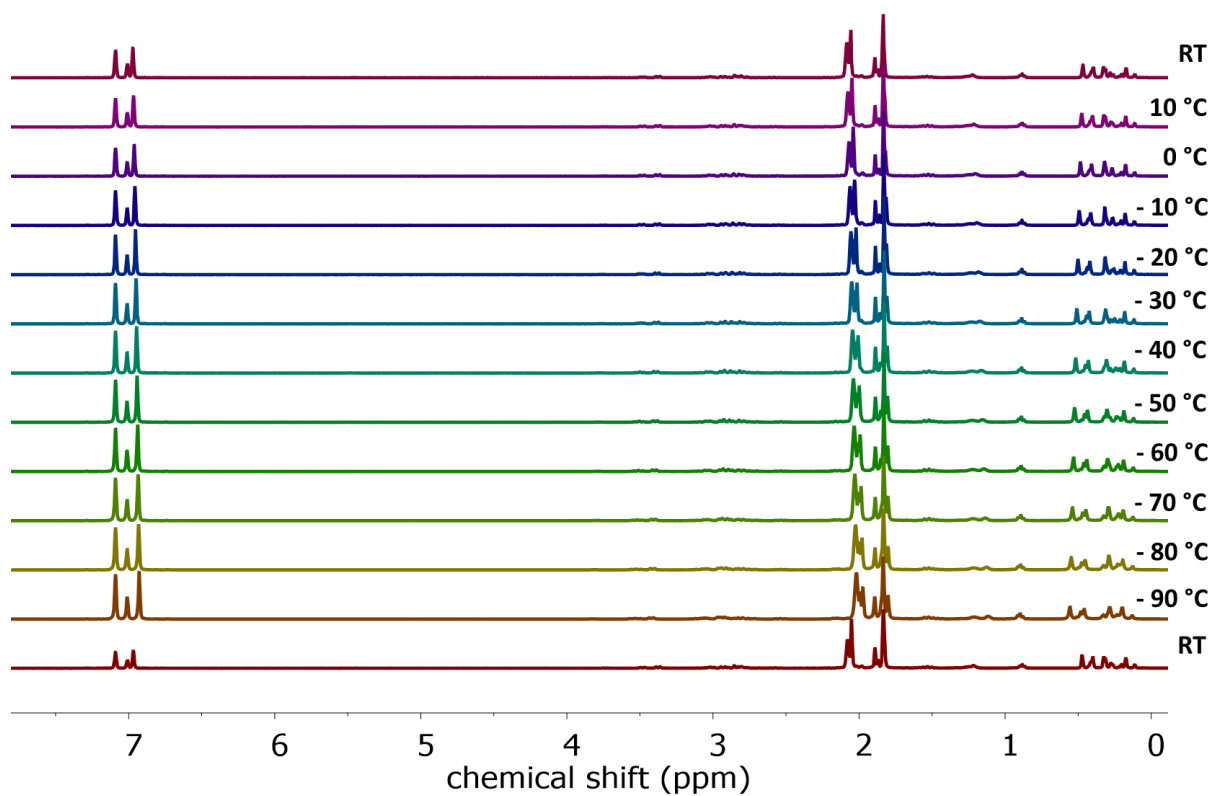


Figure S13: ^1H -VT-NMR spectrum of **3**, showing the coalescence of the GaCp* resonance.

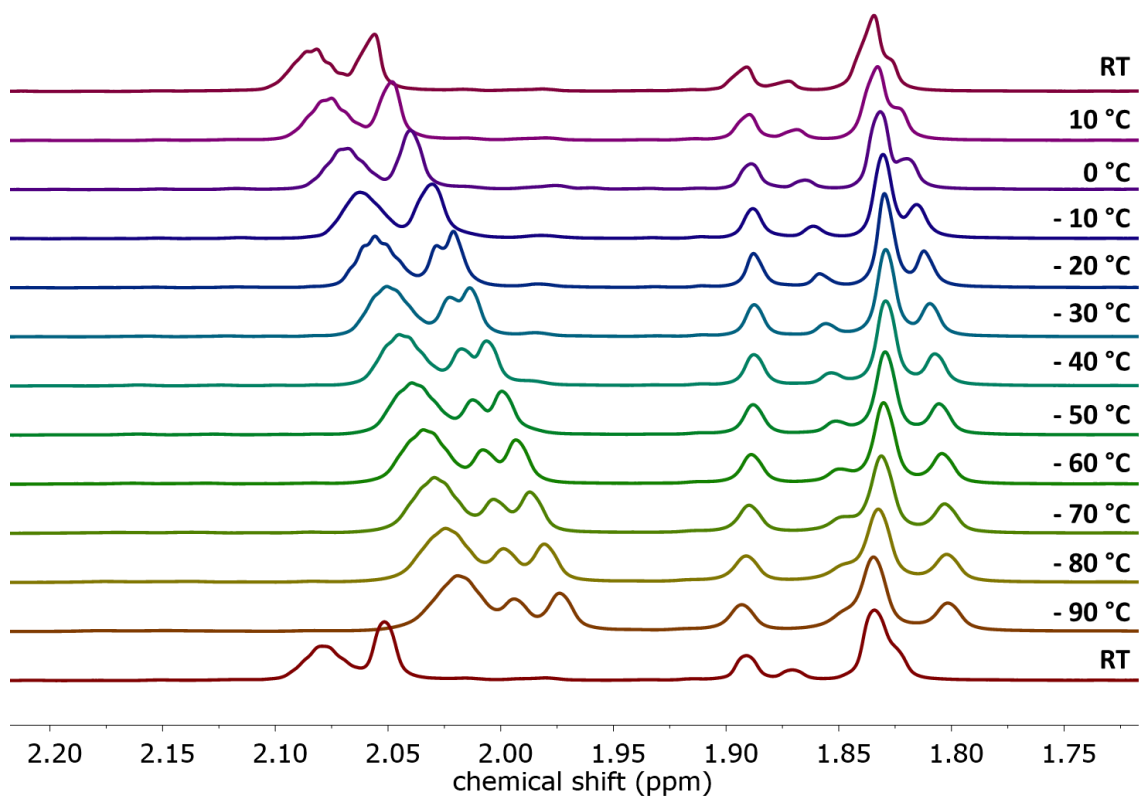


Figure S14: Zoomed ^1H -VT-NMR spectrum of **3**, showing the coalescence of the GaCp* resonance.

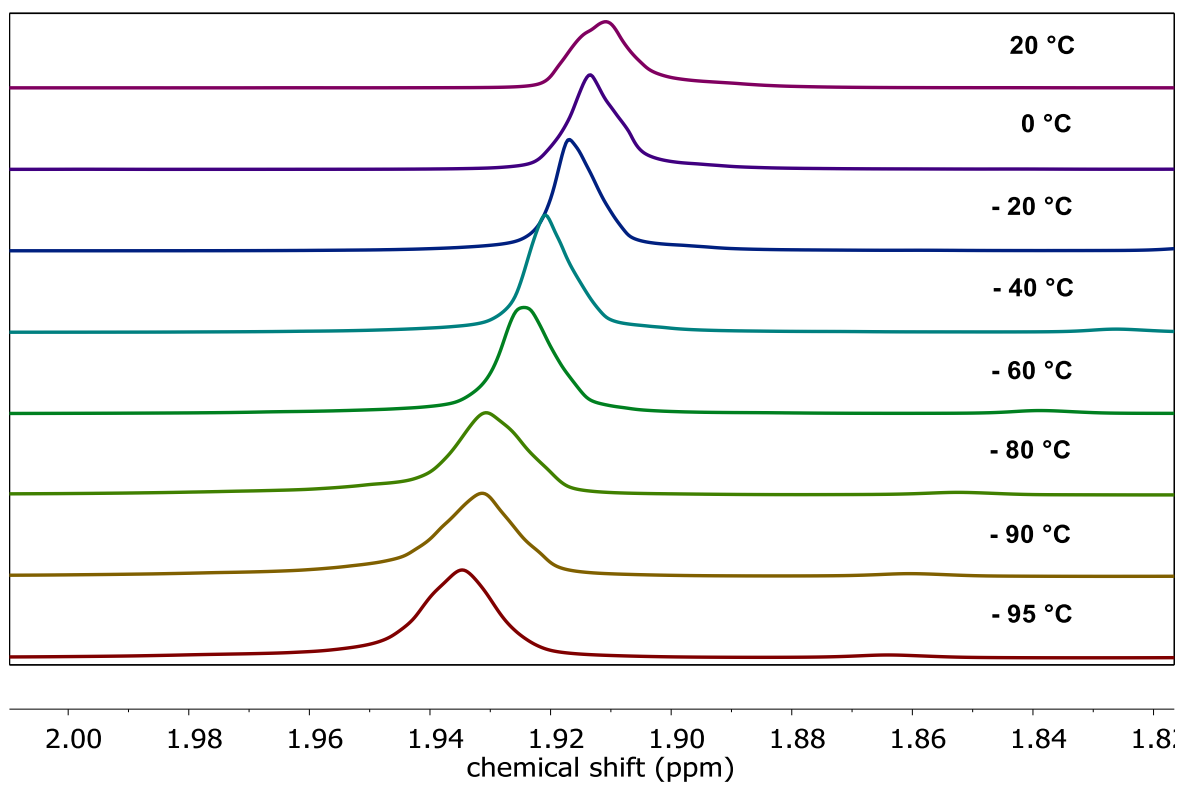


Figure S15: ^1H -VT-NMR of $[\text{Ni}(\text{GaCp}^)(\text{dvds})] (2) + \text{GaCp}^*$ at different temperatures.*

LIFDI-MS spectra

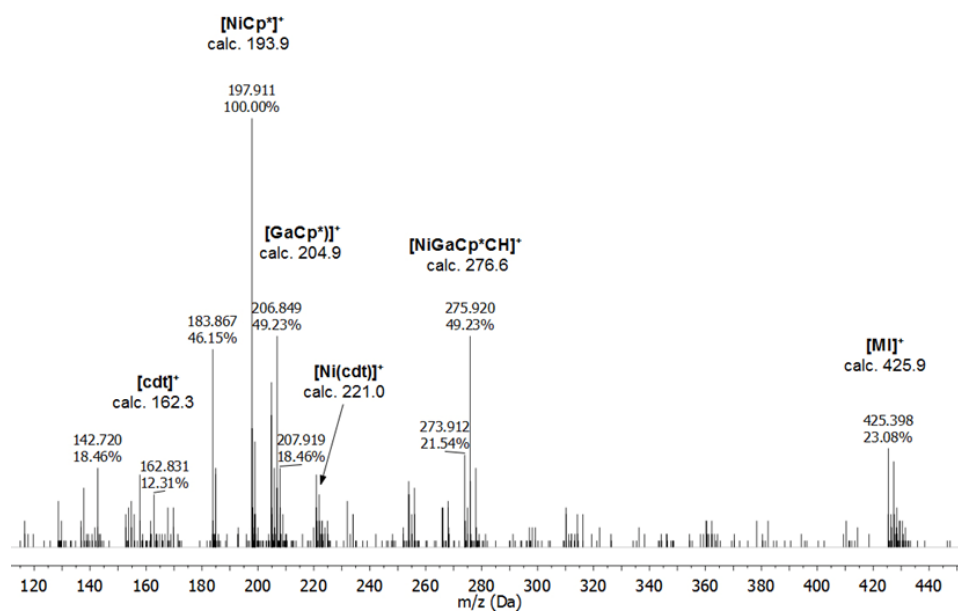


Figure S16: LIFDI-MS spectrum of 1 and related fragments.

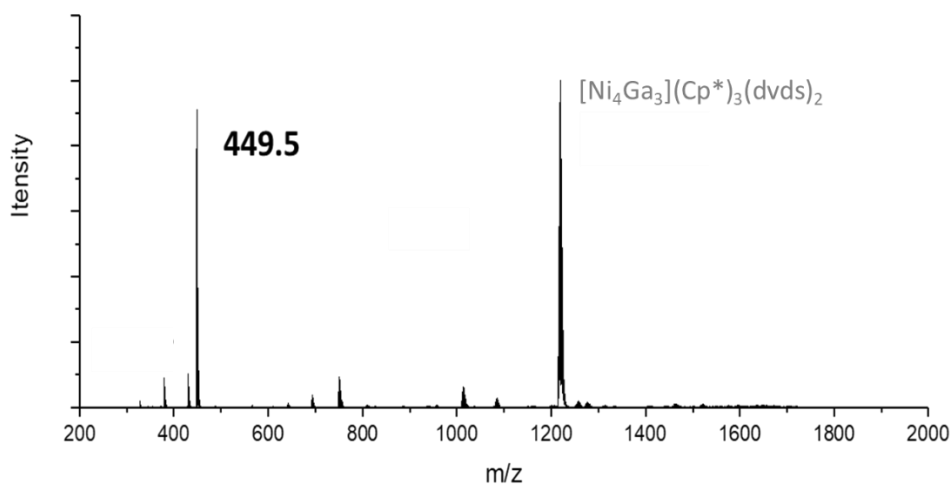


Figure S17: LIFDI-MS spectrum of 2. Thermally induced conversion to 3 observable.

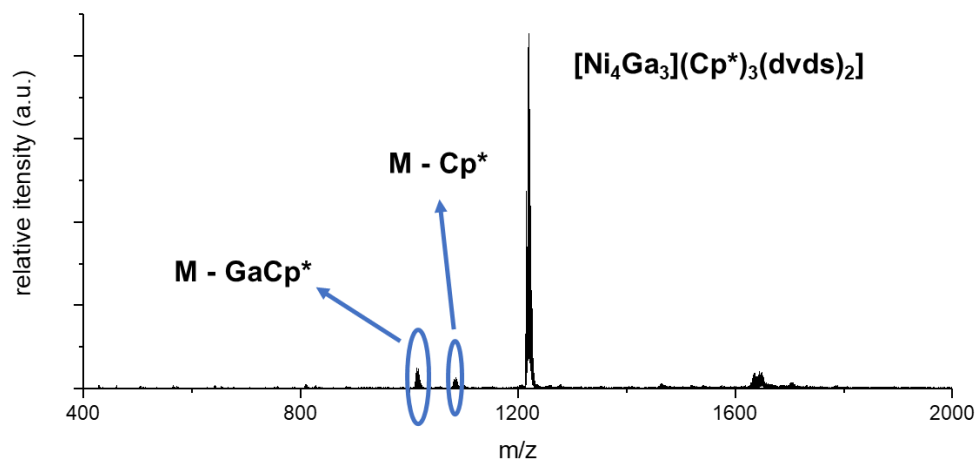


Figure S18: LIFDI-MS spectrum of pure **3**, showing product mass and related fragments.

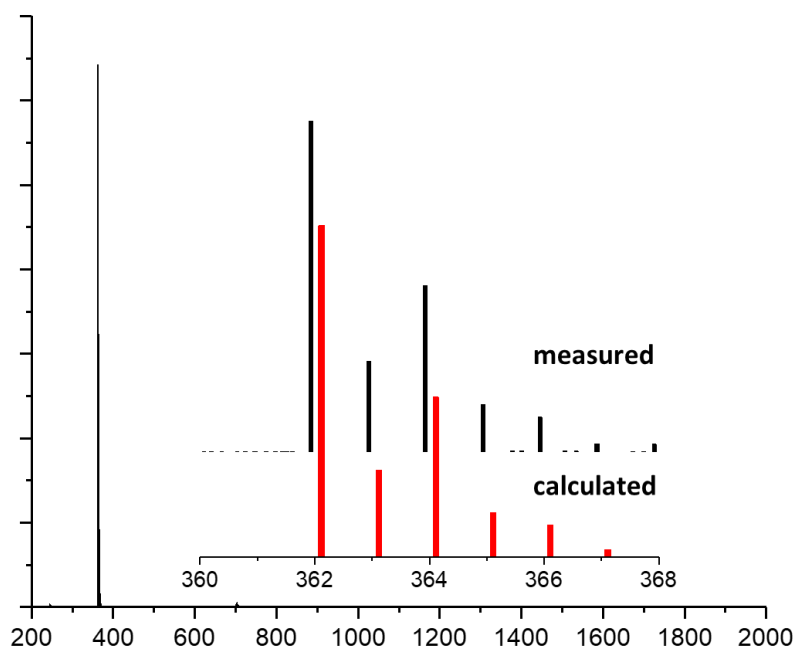


Figure S19: LIFDI-MS spectrum of $\text{Ni}(\text{PEt}_3)(\text{dvds})$, with isotopic pattern.

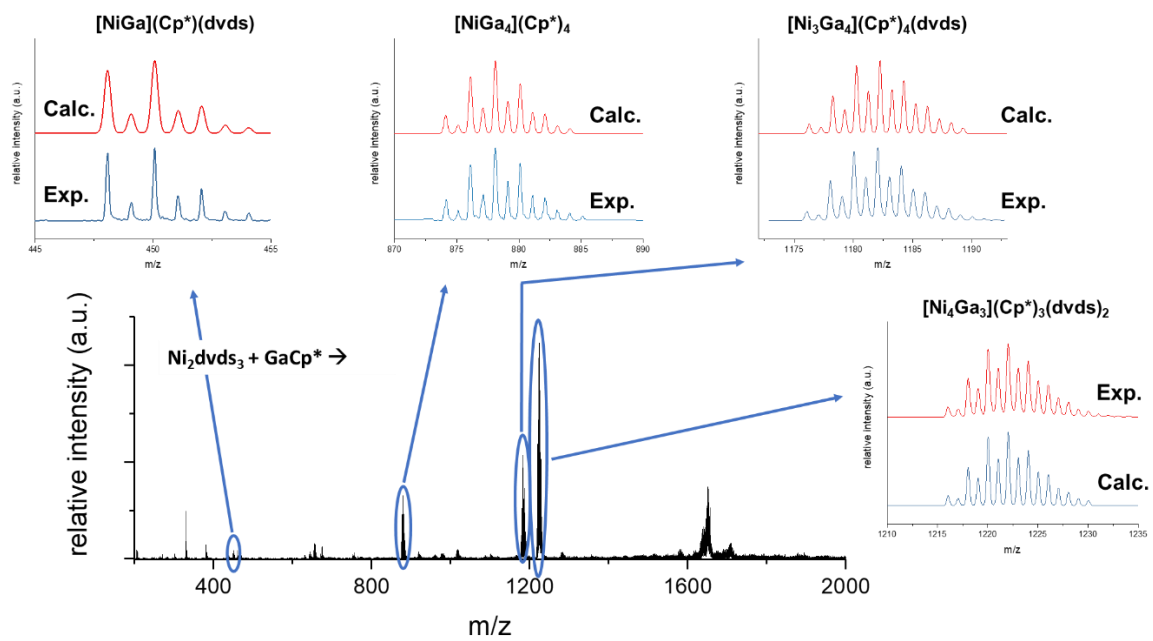


Figure S20: LIFDI-MS spectrum of reaction solution $[\text{Ni}_2\text{dvds}_3] + 2 \text{ eq GaCp}^* 2\text{h}$ at ambient temperature with peak assignment.

IR spectra

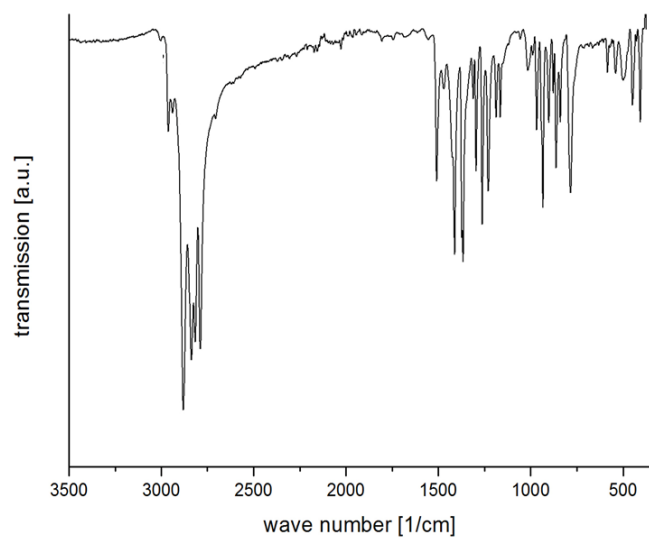


Figure S21: IR spectra of $[\text{Ni}(\text{GaCp}^*)(\text{cdt})]$ (1).

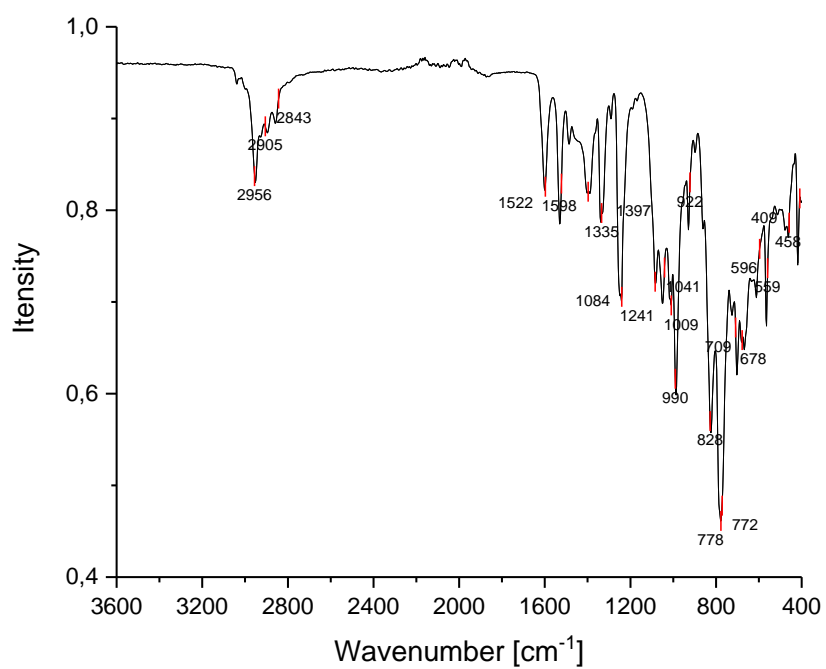


Figure S22: IR spectrum of $[\text{Ni}_2\text{dvds}_3]$.

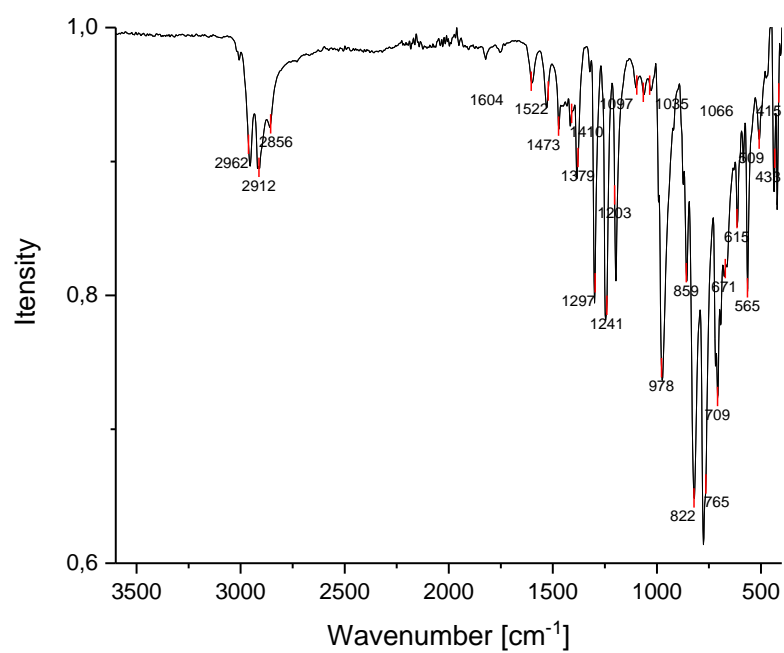


Figure S23: IR spectrum of $[\text{Ni}(\text{GaCp}^*)(\text{dvds})]$ (2).

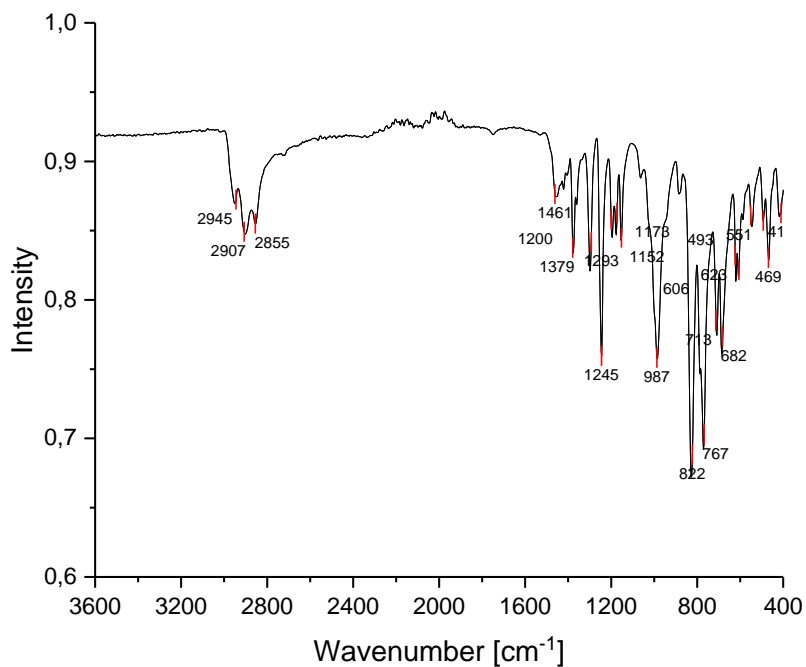


Figure S24: IR spectrum of $[\text{Ni}_2(\text{GaNiCp}^*)_2(\text{GaCp}^*)(\text{dvds})_2]$ (3).

Optimized Structures on BP86-D3/TZVPP level of theory, if not stated otherwise. Existence of local minima tested positive frequencies.

XYZ coordinates of optimized molecules

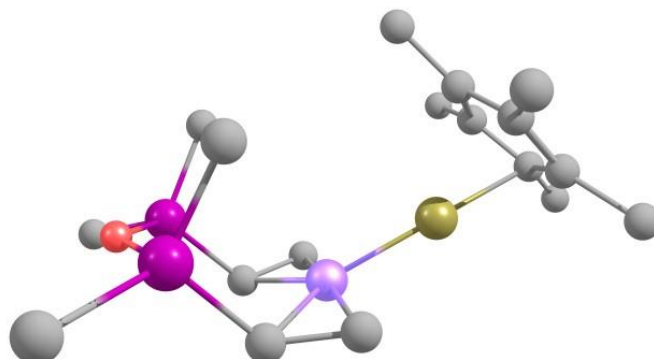


Figure S25: DFT optimized structure of $[Ni(GaCp^*)(dvds)]$ (**1**), hydrogen atoms omitted for clarity.

H	14.920085000000	35.093186000000	-7.224156000000
C	15.570100000000	34.211354000000	-7.296929000000
C	16.424825000000	34.053902000000	-6.076925000000
Ga	17.950333000000	35.707374000000	-5.350744000000
C	17.748047000000	33.506881000000	-6.037057000000
C	18.195040000000	33.528926000000	-4.666703000000
C	19.486577000000	32.968680000000	-4.154159000000
H	19.821141000000	33.484150000000	-3.244584000000
H	20.290084000000	33.050091000000	-4.897673000000
H	19.380806000000	31.901120000000	-3.903878000000
C	17.139747000000	34.089617000000	-3.869510000000
C	17.157504000000	34.267944000000	-2.382049000000
H	18.175923000000	34.424063000000	-2.003364000000
H	16.750859000000	33.381764000000	-1.869672000000
H	16.551729000000	35.129214000000	-2.071217000000
C	18.506591000000	32.939947000000	-7.198145000000
H	19.591443000000	33.043503000000	-7.065767000000
H	18.237855000000	33.436251000000	-8.139616000000
H	18.294339000000	31.866311000000	-7.323065000000
C	16.050563000000	34.412299000000	-4.741451000000
C	14.734123000000	34.991013000000	-4.325244000000
H	14.830495000000	35.624068000000	-3.433934000000
H	14.289737000000	35.603815000000	-5.120246000000
H	14.010574000000	34.196139000000	-4.084452000000
H	16.176831000000	34.320076000000	-8.205235000000
H	14.918141000000	33.335806000000	-7.443234000000
Si	16.248597000000	40.176391000000	-4.169515000000
C	16.267219000000	41.783115000000	-3.198387000000
H	16.661750000000	41.626505000000	-2.184424000000
H	15.255303000000	42.203911000000	-3.111798000000
H	16.900832000000	42.530606000000	-3.696130000000
C	15.156883000000	38.902443000000	-3.316602000000
H	15.473115000000	38.722316000000	-2.279290000000
H	14.111809000000	39.241685000000	-3.298025000000
H	15.192372000000	37.944539000000	-3.853778000000
C	17.967503000000	39.482679000000	-4.366248000000

C	18.389134000000	38.293319000000	-3.730193000000
H	19.449691000000	38.099792000000	-3.544246000000
H	17.715603000000	37.767944000000	-3.048571000000
H	18.750959000000	40.164587000000	-4.720065000000
O	15.601238000000	40.546598000000	-5.659460000000
Si	15.723845000000	39.678977000000	-7.075462000000
C	14.528219000000	38.224407000000	-7.023688000000
H	14.850267000000	37.501024000000	-6.260889000000
H	13.514992000000	38.563260000000	-6.767019000000
H	14.477583000000	37.701370000000	-7.989212000000
C	15.256338000000	40.864829000000	-8.453822000000
H	15.949292000000	41.717312000000	-8.484708000000
H	14.241547000000	41.261184000000	-8.306580000000
H	15.291093000000	40.364916000000	-9.432179000000
H	16.913864000000	37.016171000000	-7.897401000000
C	17.733408000000	37.694931000000	-7.648683000000
H	18.689502000000	37.422692000000	-8.105547000000
C	17.458776000000	39.031757000000	-7.281382000000
H	18.263899000000	39.764448000000	-7.416862000000
Ni	17.950335000000	37.949864000000	-5.663132000000

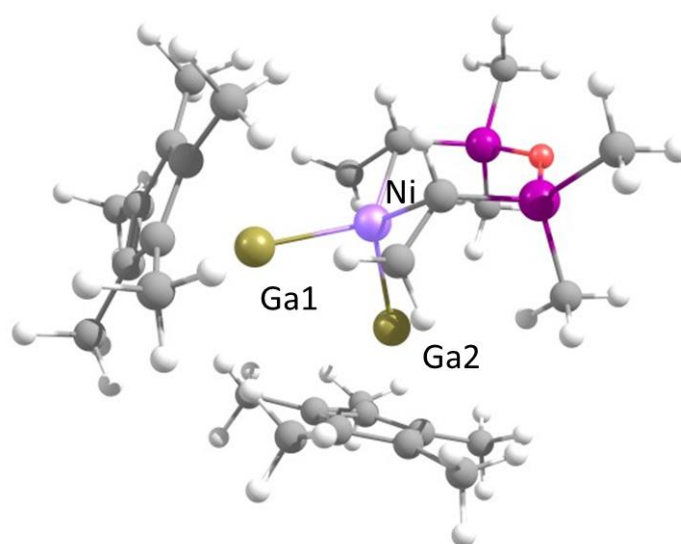


Figure S26: DFT based structure of $[Ni(GaCp^*)(dvs)]_2$, with different Ni-Ga distances.

Ga	8.982731000000	9.449575000000	8.019433000000
Ni	7.788839000000	10.822931000000	9.604885000000
Si	5.682157000000	12.169182000000	7.538205000000
Si	8.277536000000	13.629588000000	8.054148000000
O	6.770440000000	13.417284000000	7.386001000000
C	10.256441000000	7.445350000000	8.547287000000
C	9.986893000000	7.444791000000	7.141380000000
C	10.684356000000	8.554681000000	6.559272000000
C	11.379836000000	9.238969000000	7.607794000000
C	11.116891000000	8.551137000000	8.832777000000
C	9.757363000000	6.457005000000	9.554821000000
H	10.527867000000	5.712797000000	9.812460000000
H	8.880378000000	5.909034000000	9.186734000000
H	9.464186000000	6.953229000000	10.494135000000
C	9.180176000000	6.427397000000	6.392960000000

H	8.687115000000	6.866150000000	5.515067000000
H	8.397385000000	5.984632000000	7.023242000000
H	9.812468000000	5.600814000000	6.030515000000
C	10.732997000000	8.898849000000	5.102002000000
H	10.868655000000	9.977351000000	4.944660000000
H	9.811009000000	8.602936000000	4.583835000000
H	11.568318000000	8.388804000000	4.595232000000
C	12.289901000000	10.416138000000	7.432655000000
H	13.323132000000	10.095799000000	7.222438000000
H	12.324638000000	11.043633000000	8.333716000000
H	11.971792000000	11.055766000000	6.599401000000
C	11.660038000000	8.896908000000	10.182877000000
H	12.515777000000	8.257900000000	10.453870000000
H	10.897546000000	8.764287000000	10.967177000000
H	11.998644000000	9.939599000000	10.231605000000
C	5.910541000000	9.972024000000	9.411114000000
H	5.911963000000	9.289495000000	8.560310000000
H	5.555166000000	9.529038000000	10.343100000000
C	5.859334000000	11.360071000000	9.212289000000
H	5.544436000000	11.963505000000	10.073458000000
C	3.976264000000	12.944458000000	7.403728000000
H	3.859231000000	13.471265000000	6.445931000000
H	3.815067000000	13.673983000000	8.209937000000
H	3.187559000000	12.182066000000	7.473590000000
C	5.935926000000	10.928398000000	6.153383000000
H	5.155736000000	10.154077000000	6.156193000000
H	6.912249000000	10.430099000000	6.239205000000
H	5.900048000000	11.440343000000	5.181451000000
C	8.486798000000	15.479229000000	8.306621000000
H	8.379342000000	16.020413000000	7.355790000000
H	9.476752000000	15.712774000000	8.723461000000
H	7.727295000000	15.865834000000	9.000766000000
C	9.584080000000	12.992636000000	6.866519000000
H	9.484977000000	11.908163000000	6.713722000000
H	10.600173000000	13.195397000000	7.232021000000
H	9.470671000000	13.483248000000	5.889592000000
C	8.385168000000	12.766583000000	9.706823000000
H	7.800913000000	13.210855000000	10.522334000000
C	9.452408000000	11.934600000000	10.086028000000
H	9.731364000000	11.827610000000	11.135943000000
H	10.264482000000	11.724801000000	9.387684000000
Ga	8.248373000000	9.382879000000	11.360430000000
C	8.868476000000	8.388038000000	13.389420000000
C	9.847940000000	7.259520000000	13.487735000000
H	9.986428000000	6.946111000000	14.535029000000
H	9.511819000000	6.377162000000	12.927606000000
H	10.836365000000	7.540854000000	13.100877000000
C	7.439625000000	8.258014000000	13.263978000000
C	6.874708000000	9.570768000000	13.325810000000
C	7.942665000000	10.509186000000	13.486819000000
C	7.781172000000	11.995397000000	13.569258000000
H	7.523361000000	12.319179000000	14.589902000000
H	8.701944000000	12.520477000000	13.284003000000
H	6.981505000000	12.348067000000	12.903203000000
C	5.421165000000	9.921486000000	13.239768000000
H	4.990787000000	10.099706000000	14.237846000000

H	5.259645000000	10.835319000000	12.650642000000
H	4.836030000000	9.118285000000	12.773622000000
C	6.686104000000	6.966492000000	13.167166000000
H	6.459140000000	6.560699000000	14.165943000000
H	7.259974000000	6.200519000000	12.628674000000
H	5.729789000000	7.092033000000	12.642771000000
C	9.172596000000	9.784052000000	13.531285000000
C	10.538941000000	10.362341000000	13.738921000000
H	10.808090000000	10.378870000000	14.807021000000
H	11.311387000000	9.780359000000	13.218966000000
H	10.603136000000	11.396026000000	13.374152000000

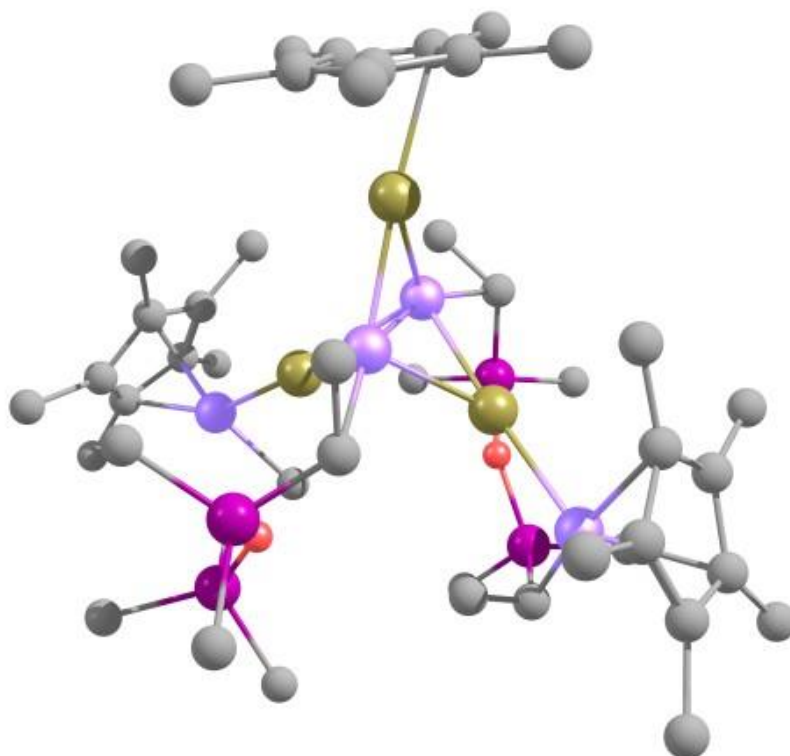


Figure S27: Optimized structure of **3** (BP86-D3/SVP), hydrogen atoms omitted for clarity.

Ga	-7.692660000000	16.606720000000	35.446846000000
Ga	-9.067487000000	14.263919000000	33.690673000000
Ni	-9.707891000000	16.470517000000	34.270123000000
Ni	-9.237655000000	14.878033000000	35.907831000000
Ni	-5.727758000000	17.377966000000	36.320816000000
Ni	-9.007787000000	13.510293000000	31.541542000000
Si	-5.052942000000	17.688561000000	33.153625000000
Si	-6.323462000000	12.406698000000	32.866647000000
O	-6.741590000000	17.489940000000	33.130874000000
O	-7.188069000000	12.920434000000	34.256716000000
Si	-8.021438000000	18.359403000000	32.418253000000
C	-9.547697000000	17.307030000000	32.479453000000
H	-9.602675000000	16.495633000000	31.728469000000
H	-7.360310000000	17.752614000000	30.087313000000
C	-10.759340000000	17.711159000000	33.100838000000
H	-11.726143000000	17.287740000000	32.775222000000
H	-10.847757000000	18.706030000000	33.574069000000
C	-8.264572000000	19.955743000000	33.390094000000

H	-9.072025000000	20.579744000000	32.955411000000
H	-7.334154000000	20.556989000000	33.406211000000
H	-8.537123000000	19.713148000000	34.436811000000
C	-7.542160000000	18.706926000000	30.623212000000
H	-6.626522000000	19.327039000000	30.538456000000
H	-8.364263000000	19.238245000000	30.100268000000
C	-4.572626000000	19.498942000000	32.928565000000
H	-4.879988000000	19.896050000000	31.940132000000
H	-3.470012000000	19.606657000000	33.003870000000
H	-5.026924000000	20.128765000000	33.716924000000
C	-4.373519000000	16.657749000000	31.724094000000
H	-4.717719000000	17.052556000000	30.745826000000
H	-4.721897000000	15.608545000000	31.804589000000
H	-3.263711000000	16.654913000000	31.725058000000
C	-4.468099000000	17.081426000000	34.809259000000
H	-3.482242000000	17.467970000000	35.133679000000
C	-4.886524000000	15.841873000000	35.391432000000
H	-4.212956000000	15.300218000000	36.078798000000
H	-5.559545000000	15.161020000000	34.835528000000
Si	-7.339111000000	12.404017000000	35.896006000000
C	-9.020511000000	13.926757000000	37.652776000000
C	-8.969926000000	13.015718000000	36.554574000000
H	-9.870336000000	12.404159000000	36.348320000000
C	-5.921572000000	13.102110000000	36.913606000000
H	-4.941086000000	12.906406000000	36.436171000000
H	-5.917551000000	12.629920000000	37.917745000000
H	-6.028538000000	14.197377000000	37.042507000000
C	-7.285389000000	10.516354000000	35.912988000000
H	-8.066078000000	10.084212000000	35.254879000000
H	-7.478282000000	10.161562000000	36.947055000000
H	-6.302713000000	10.113626000000	35.594575000000
C	-4.503617000000	12.793404000000	33.186914000000
H	-3.890995000000	12.563519000000	32.290515000000
H	-4.106525000000	12.194823000000	34.033286000000
H	-4.363946000000	13.865247000000	33.432363000000
C	-6.548928000000	10.555467000000	32.590699000000
H	-6.210309000000	10.287369000000	31.568436000000
H	-7.618398000000	10.279941000000	32.674082000000
H	-5.972289000000	9.943636000000	33.311239000000
C	-7.042874000000	13.319893000000	31.412540000000
H	-6.826572000000	12.850304000000	30.431299000000
C	-7.432307000000	14.700401000000	31.392388000000
H	-7.456258000000	15.246287000000	30.430952000000
H	-7.210445000000	15.368528000000	32.245804000000
H	-12.181513000000	19.536043000000	35.622589000000
C	-12.291417000000	19.237840000000	36.684025000000
H	-13.072589000000	19.890554000000	37.130867000000
H	-11.336054000000	19.475372000000	37.191611000000
C	-12.639205000000	17.783439000000	36.816477000000
C	-12.242424000000	16.914212000000	37.893301000000
C	-12.773109000000	15.600606000000	37.620811000000
C	-12.667648000000	14.391181000000	38.502452000000
H	-13.614793000000	14.215228000000	39.057639000000
H	-12.454200000000	13.470566000000	37.922027000000
H	-11.864141000000	14.504378000000	39.255303000000
C	-13.497771000000	15.663581000000	36.374664000000

C	-14.232368000000	14.521709000000	35.735132000000
H	-15.254692000000	14.406110000000	36.157723000000
H	-14.344432000000	14.667987000000	34.642981000000
H	-13.705989000000	13.558045000000	35.888842000000
C	-11.416231000000	17.301852000000	39.085212000000
H	-12.049360000000	17.657570000000	39.926986000000
H	-10.814296000000	16.450038000000	39.458082000000
H	-10.706554000000	18.116195000000	38.840040000000
C	-13.421621000000	17.012172000000	35.883947000000
C	-14.052136000000	17.521863000000	34.621804000000
H	-15.113272000000	17.811214000000	34.785296000000
H	-13.525537000000	18.414428000000	34.232627000000
H	-14.043235000000	16.755080000000	33.821065000000
Ga	-11.227604000000	16.095130000000	35.958335000000
H	-11.995130000000	13.489639000000	33.593840000000
C	-12.084890000000	13.974446000000	32.602012000000
H	-11.931166000000	15.057809000000	32.777232000000
H	-13.128203000000	13.824704000000	32.247158000000
C	-11.099829000000	13.415321000000	31.617015000000
C	-10.729223000000	14.025850000000	30.356351000000
C	-9.943169000000	13.079790000000	29.618738000000
C	-9.344189000000	13.287905000000	28.260542000000
H	-9.261522000000	14.365167000000	28.014671000000
H	-8.325622000000	12.852227000000	28.189979000000
H	-9.952077000000	12.813919000000	27.458329000000
C	-9.811058000000	11.882636000000	30.418833000000
C	-9.118572000000	10.628310000000	29.976857000000
H	-8.906555000000	9.953744000000	30.827514000000
H	-9.742819000000	10.061291000000	29.251750000000
H	-8.153509000000	10.842618000000	29.473672000000
C	-11.185388000000	15.369763000000	29.871105000000
H	-10.390751000000	15.899487000000	29.308080000000
H	-12.063581000000	15.279369000000	29.193976000000
H	-11.483951000000	16.025672000000	30.710612000000
C	-10.529095000000	12.075473000000	31.652636000000
C	-10.750058000000	11.058920000000	32.734995000000
H	-9.887653000000	10.369417000000	32.828156000000
H	-10.884626000000	11.544181000000	33.722750000000
H	-11.652198000000	10.436247000000	32.542876000000
H	-7.115990000000	15.781978000000	39.412035000000
C	-7.537206000000	16.729773000000	39.025005000000
H	-7.943754000000	17.292473000000	39.894418000000
H	-8.391827000000	16.468515000000	38.365484000000
C	-6.506512000000	17.537789000000	38.301071000000
C	-6.811652000000	18.717190000000	37.503527000000
C	-5.561117000000	19.324611000000	37.123070000000
C	-5.406880000000	20.630373000000	36.403226000000
H	-5.414595000000	21.489052000000	37.111447000000
H	-4.453032000000	20.679757000000	35.842572000000
H	-6.228781000000	20.793534000000	35.678756000000
C	-4.492006000000	18.536391000000	37.704166000000
C	-3.026155000000	18.817960000000	37.569660000000
H	-2.636357000000	19.404554000000	38.430562000000
H	-2.431728000000	17.882240000000	37.521343000000
H	-2.805042000000	19.400351000000	36.652939000000
C	-8.188707000000	19.290793000000	37.332309000000

H	-8.517977000000	19.818605000000	38.255173000000
H	-8.229108000000	20.019918000000	36.500416000000
H	-8.941268000000	18.502077000000	37.115344000000
C	-5.074653000000	17.438092000000	38.419436000000
C	-4.326808000000	16.365887000000	39.154273000000
H	-4.124348000000	16.646721000000	40.211440000000
H	-4.893691000000	15.413798000000	39.166963000000
H	-3.345733000000	16.156795000000	38.681220000000
H	-8.088868000000	14.230542000000	38.154616000000
H	-9.910469000000	13.965816000000	38.303224000000

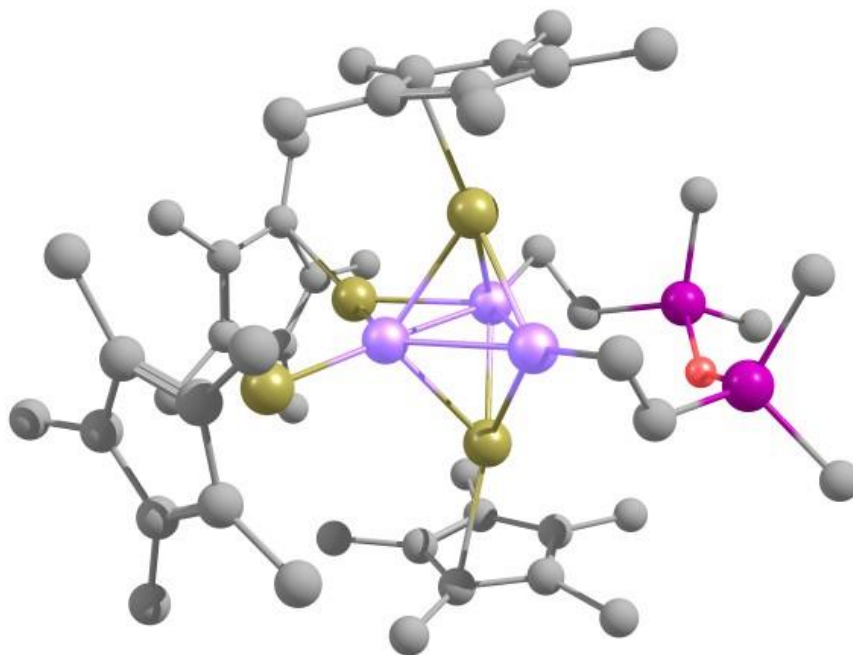


Figure S28: Optimized structure of of $[Ni_3(GaCp^*)_4(dvds)]$ (BP86-D3/SVP), hydrogen atoms omitted for clarity.

Ni	7.314132000000	1.454366000000	5.899296000000
Ni	8.144742000000	3.196231000000	4.461574000000
Ni	10.247913000000	2.362219000000	4.849787000000
Ga	6.029723000000	3.882107000000	4.186225000000
C	4.225462000000	5.248309000000	4.882159000000
C	4.349104000000	6.509435000000	5.687149000000
H	3.491679000000	7.187370000000	5.485958000000
H	4.363322000000	6.305399000000	6.773322000000
H	5.271763000000	7.076511000000	5.445940000000
C	3.973163000000	3.916970000000	5.364192000000
C	3.799246000000	3.054252000000	4.225113000000
C	3.951290000000	3.846864000000	3.033068000000
C	3.772587000000	3.390343000000	1.613812000000
H	2.757061000000	3.639161000000	1.235599000000
H	4.500514000000	3.873832000000	0.931098000000
H	3.902609000000	2.296350000000	1.512825000000
C	3.463863000000	1.594264000000	4.332021000000
H	2.561800000000	1.444030000000	4.962744000000
H	3.255324000000	1.143189000000	3.344551000000
H	4.289473000000	1.017333000000	4.800126000000
C	3.906871000000	3.438408000000	6.785774000000
H	2.993828000000	2.832779000000	6.964091000000
H	3.894655000000	4.277473000000	7.506853000000

H	4.78032000000	2.79161100000	7.02875000000
C	4.22547300000	5.20270900000	3.44032900000
C	4.35556300000	6.39752100000	2.54129200000
H	3.40058500000	6.96622400000	2.49056500000
H	5.13368300000	7.10220700000	2.89751500000
H	4.61709100000	6.10726900000	1.50555800000
Ga	8.89776100000	3.01205200000	6.73562500000
C	7.99828000000	3.59717800000	9.09751900000
C	6.73820400000	3.02348900000	9.67511100000
H	6.40367000000	3.57538400000	10.58178800000
H	5.90516500000	3.05785600000	8.94566500000
H	6.87210100000	1.96351500000	9.97124200000
C	8.07243300000	4.67576100000	8.14610800000
C	9.46325100000	4.91358700000	7.85433700000
C	10.24361900000	3.98176300000	8.63246400000
C	11.74075400000	3.97438900000	8.71226300000
H	12.11095600000	4.73231700000	9.43862400000
H	12.13520800000	2.99238700000	9.03609900000
H	12.20272100000	4.21599900000	7.73330200000
C	10.00982400000	5.97906300000	6.95769700000
H	10.21888600000	6.92538900000	7.50452500000
H	10.95554000000	5.65093800000	6.48538400000
H	9.30419500000	6.21233100000	6.13663600000
C	6.92839700000	5.45605400000	7.57928200000
H	6.71817100000	6.37868900000	8.16419800000
H	6.00469500000	4.85133000000	7.56317800000
H	7.12952800000	5.76257800000	6.53241300000
C	9.33683400000	3.18750400000	9.41261500000
C	9.73580400000	2.21819700000	10.48717300000
H	10.02527500000	2.75745900000	11.41699700000
H	8.90982300000	1.53202100000	10.75622100000
H	10.60391000000	1.59456100000	10.19499600000
Ga	8.57722600000	0.89647500000	3.90507900000
C	9.47046800000	0.53485200000	1.64954200000
C	10.68143200000	1.27888300000	1.17741200000
H	10.64868100000	1.46407500000	0.08370300000
H	10.75771000000	2.26995900000	1.67773300000
H	11.61500500000	0.72549100000	1.39628300000
C	8.11610200000	0.98831500000	1.50655600000
C	7.25266500000	0.03428000000	2.13633400000
C	8.07487800000	-1.01017100000	2.69493700000
C	7.61729500000	-2.30342900000	3.29786700000
H	7.68111000000	-3.13257100000	2.55915800000
H	8.24280400000	-2.59161400000	4.16513600000
H	6.56516600000	-2.25479700000	3.63964700000
C	5.76293700000	0.13540100000	2.22849000000
H	5.26519400000	-0.10807000000	1.26464900000
H	5.35478900000	-0.54814300000	2.99745300000
H	5.46107200000	1.16194500000	2.51370500000
C	7.69240100000	2.28004500000	0.87706200000
H	7.83733300000	2.27483300000	-0.22568200000
H	8.27121300000	3.12819000000	1.29506300000
H	6.62489300000	2.49453700000	1.07339400000
C	9.45153900000	-0.69693500000	2.38744800000
C	10.59705200000	-1.61620100000	2.68131500000
H	10.61322600000	-2.47455200000	1.97398100000

H	11.576181000000	-1.106425000000	2.600164000000
H	10.517613000000	-2.033575000000	3.703927000000
Ga	9.881086000000	4.350475000000	3.540318000000
C	11.317180000000	5.584145000000	2.238299000000
C	12.764328000000	5.202269000000	2.108475000000
H	13.324575000000	5.928417000000	1.478680000000
H	13.266822000000	5.170593000000	3.095342000000
H	12.885913000000	4.203232000000	1.643815000000
C	10.767936000000	6.468419000000	3.250700000000
C	9.377774000000	6.672037000000	2.941306000000
C	9.076288000000	5.953017000000	1.734876000000
C	7.719047000000	5.892487000000	1.099956000000
H	7.311886000000	6.908564000000	0.911903000000
H	7.739724000000	5.354675000000	0.133277000000
H	6.991108000000	5.368321000000	1.758251000000
C	8.370151000000	7.459880000000	3.727270000000
H	7.882018000000	8.235350000000	3.099150000000
H	7.562073000000	6.801340000000	4.118253000000
H	8.828370000000	7.973333000000	4.593935000000
C	11.590990000000	7.189398000000	4.278534000000
H	12.224199000000	7.964148000000	3.793286000000
H	12.274978000000	6.510928000000	4.827300000000
H	10.960694000000	7.701883000000	5.028207000000
C	10.269367000000	5.299805000000	1.286495000000
C	10.457056000000	4.579160000000	-0.016100000000
H	10.597220000000	5.306979000000	-0.845435000000
H	11.353368000000	3.930996000000	-0.001125000000
H	9.590224000000	3.944549000000	-0.280306000000
Si	11.364025000000	-0.310766000000	6.140541000000
C	12.504872000000	-1.801164000000	5.908344000000
H	13.564675000000	-1.490759000000	6.021822000000
H	12.292342000000	-2.578582000000	6.671774000000
H	12.393632000000	-2.266483000000	4.909382000000
C	11.692490000000	0.424150000000	7.840366000000
H	11.610864000000	-0.334321000000	8.642488000000
H	12.719646000000	0.841540000000	7.870271000000
H	10.977363000000	1.243334000000	8.049655000000
C	11.696737000000	0.994910000000	4.839961000000
H	11.844045000000	0.642004000000	3.802627000000
C	12.209749000000	2.285006000000	5.148547000000
H	12.790890000000	2.848414000000	4.396466000000
H	12.427319000000	2.572213000000	6.191958000000
O	9.769877000000	-0.884200000000	6.022660000000
Si	8.504022000000	-1.361440000000	7.040214000000
C	8.527423000000	-3.250318000000	7.077459000000
H	9.496546000000	-3.618249000000	7.474421000000
H	7.717060000000	-3.641625000000	7.727020000000
H	8.391473000000	-3.683962000000	6.066107000000
C	8.704091000000	-0.676152000000	8.779457000000
H	7.833638000000	-0.970993000000	9.401355000000
H	9.618841000000	-1.043817000000	9.281968000000
H	8.743276000000	0.430249000000	8.739822000000
C	6.848152000000	-0.743418000000	6.390278000000
H	6.449748000000	-1.173538000000	5.453798000000
C	5.964687000000	0.044062000000	7.146371000000
H	4.912178000000	0.176674000000	6.840603000000

H 6.200631000000 0.349529000000 8.179164000000

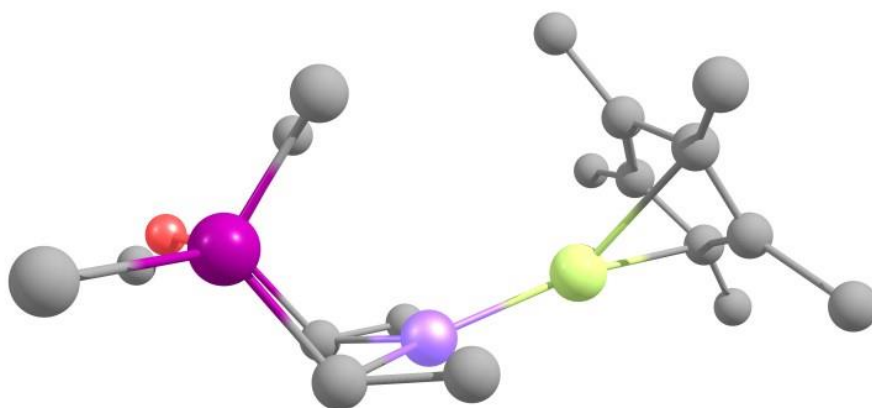


Figure S29: Optimized structure of $[Ni(AlCp^*)(dvds)]$, hydrogens omitted for clarity.

H	14.882938000000	35.048303000000	-7.232925000000
C	15.551568000000	34.180158000000	-7.299599000000
C	16.415601000000	34.054578000000	-6.081552000000
Al	17.784569000000	35.692091000000	-5.367569000000
C	17.757517000000	33.551888000000	-6.041168000000
C	18.207987000000	33.600563000000	-4.676494000000
C	19.537692000000	33.128873000000	-4.170816000000
H	19.849073000000	33.679740000000	-3.274043000000
H	20.325716000000	33.248762000000	-4.925407000000
H	19.499623000000	32.061525000000	-3.903190000000
C	17.141854000000	34.133867000000	-3.878210000000
C	17.169699000000	34.347589000000	-2.395014000000
H	18.183670000000	34.563073000000	-2.034522000000
H	16.813831000000	33.453572000000	-1.860100000000
H	16.526071000000	35.184986000000	-2.096397000000
C	18.540530000000	33.029410000000	-7.207616000000
H	19.618751000000	33.188352000000	-7.077243000000
H	18.244029000000	33.516604000000	-8.145237000000
H	18.381612000000	31.947473000000	-7.335308000000
C	16.035680000000	34.413956000000	-4.746133000000
C	14.705100000000	34.961483000000	-4.329428000000
H	14.789668000000	35.612020000000	-3.449853000000
H	14.239370000000	35.548940000000	-5.130988000000
H	14.009392000000	34.148011000000	-4.071640000000
H	16.151604000000	34.292684000000	-8.211461000000
H	14.920430000000	33.287641000000	-7.429966000000
Si	16.276232000000	40.135260000000	-4.161247000000
C	16.340502000000	41.744427000000	-3.193859000000
H	16.709903000000	41.577202000000	-2.172099000000
H	15.345602000000	42.207630000000	-3.128404000000
H	17.013739000000	42.462734000000	-3.682846000000
C	15.119329000000	38.909076000000	-3.319202000000
H	15.417657000000	38.710773000000	-2.279802000000
H	14.090082000000	39.294089000000	-3.309356000000
H	15.117014000000	37.952804000000	-3.860941000000
C	17.962315000000	39.368796000000	-4.328589000000
C	18.313299000000	38.133721000000	-3.715928000000
H	19.358400000000	37.904489000000	-3.487943000000
H	17.605144000000	37.644579000000	-3.041806000000

H	18.787814000000	40.023282000000	-4.635500000000
O	15.650495000000	40.530836000000	-5.654828000000
Si	15.753031000000	39.662344000000	-7.072676000000
C	14.504912000000	38.248721000000	-7.024175000000
H	14.799984000000	37.516590000000	-6.258251000000
H	13.503152000000	38.622410000000	-6.770617000000
H	14.439034000000	37.725406000000	-7.988826000000
C	15.316183000000	40.870673000000	-8.443264000000
H	16.039553000000	41.697719000000	-8.474110000000
H	14.317572000000	41.303373000000	-8.287487000000
H	15.327302000000	40.375628000000	-9.424711000000
H	16.834279000000	36.955180000000	-7.900666000000
C	17.682249000000	37.589735000000	-7.629537000000
H	18.619091000000	37.287141000000	-8.106932000000
C	17.457449000000	38.951713000000	-7.283990000000
H	18.287931000000	39.650628000000	-7.442087000000
Ni	17.915640000000	37.877970000000	-5.660749000000

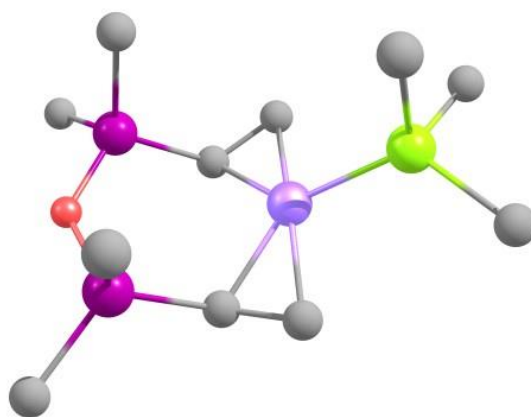


Figure S30: Calculated structure of $[Ni(PMe_3)(dvds)]$ - hydrogens omitted for clarity.

P	16.939148000000	35.818577000000	-5.130772000000
Si	16.821931000000	40.668814000000	-4.189542000000
C	17.621408000000	42.212249000000	-3.479292000000
H	18.200779000000	41.975247000000	-2.575623000000
H	16.864315000000	42.963946000000	-3.214404000000
H	18.305584000000	42.666246000000	-4.209868000000
C	15.652210000000	39.905148000000	-2.927323000000
H	16.177345000000	39.602357000000	-2.010282000000
H	14.872831000000	40.627314000000	-2.646125000000
H	15.150238000000	39.019830000000	-3.342012000000
C	18.108949000000	39.424531000000	-4.703188000000
C	18.323570000000	38.206917000000	-4.018817000000
H	19.301506000000	37.717598000000	-4.046017000000
H	17.735800000000	37.971070000000	-3.126194000000
H	18.937460000000	39.800083000000	-5.316636000000
O	15.943308000000	41.165330000000	-5.514224000000
Si	15.445644000000	40.230786000000	-6.800694000000
C	13.902314000000	39.267325000000	-6.313397000000
H	14.135926000000	38.518307000000	-5.543234000000
H	13.140239000000	39.945983000000	-5.905404000000
H	13.460972000000	38.741996000000	-7.172385000000
C	15.053927000000	41.427543000000	-8.193457000000

H	15.949190000000	41.998140000000	-8.477758000000
H	14.278334000000	42.145929000000	-7.891996000000
H	14.697526000000	40.891269000000	-9.084384000000
H	15.516633000000	37.297037000000	-7.506067000000
C	16.542128000000	37.676566000000	-7.542385000000
H	17.211419000000	37.089492000000	-8.179065000000
C	16.794799000000	39.040592000000	-7.279721000000
H	17.720916000000	39.466499000000	-7.684359000000
Ni	17.313299000000	37.871792000000	-5.714466000000
C	18.336513000000	34.984917000000	-4.228574000000
C	15.506448000000	35.852913000000	-3.943569000000
C	16.455221000000	34.591655000000	-6.441899000000
H	15.592145000000	36.825438000000	-3.438833000000
C	15.357325000000	34.744664000000	-2.897805000000
H	14.606523000000	35.927497000000	-4.573799000000
H	18.388023000000	35.477550000000	-3.246404000000
H	19.238385000000	35.314505000000	-4.765663000000
C	18.356589000000	33.462353000000	-4.076429000000
H	17.402109000000	34.258278000000	-6.895655000000
H	15.953094000000	35.185239000000	-7.216913000000
C	15.573809000000	33.395063000000	-6.072549000000
H	15.357772000000	32.794675000000	-6.967975000000
H	14.609735000000	33.723332000000	-5.662490000000
H	16.044433000000	32.734133000000	-5.336269000000
H	15.212872000000	33.757436000000	-3.351085000000
H	14.488989000000	34.947173000000	-2.254757000000
H	16.239286000000	34.691534000000	-2.246206000000
H	18.354196000000	32.959746000000	-5.052312000000
H	17.500912000000	33.088326000000	-3.502749000000
H	19.270436000000	33.148380000000	-3.551789000000

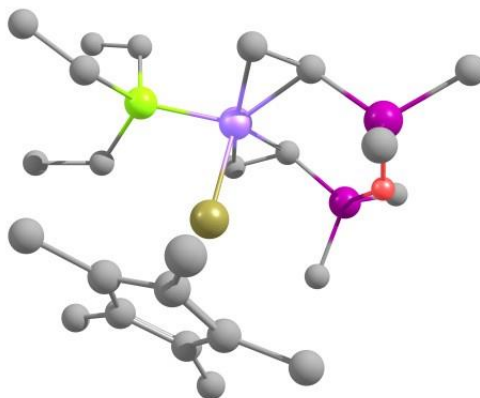


Figure S31: Optimized structure of $[\text{Ni}(\text{GaCp}^*)(\text{PEt}_3)(\text{dvds})]$, hydrogens omitted for clarity.

Ga	8.789639000000	9.982084000000	8.848844000000
Ni	7.328495000000	11.562018000000	10.012298000000
Si	5.923912000000	11.778506000000	7.083038000000
Si	8.333915000000	13.556979000000	7.646637000000
O	7.415621000000	12.485632000000	6.714325000000
C	9.551222000000	7.559312000000	8.760792000000
C	9.312749000000	7.993949000000	7.411058000000
C	10.259751000000	9.030542000000	7.099088000000
C	11.084014000000	9.238249000000	8.260244000000
C	10.645344000000	8.325097000000	9.285173000000
C	8.842853000000	6.427696000000	9.449191000000

H	9.259910000000	5.440310000000	9.148656000000
H	7.760956000000	6.404244000000	9.204403000000
H	8.933882000000	6.490811000000	10.551713000000
C	8.350601000000	7.361718000000	6.446509000000
H	8.093415000000	8.042864000000	5.613187000000
H	7.401256000000	7.059210000000	6.933793000000
H	8.786078000000	6.442092000000	5.994448000000
C	10.363146000000	9.739649000000	5.776767000000
H	11.108194000000	10.557479000000	5.813834000000
H	9.398103000000	10.195981000000	5.471544000000
H	10.675088000000	9.047387000000	4.964939000000
C	12.274836000000	10.148382000000	8.374169000000
H	13.228035000000	9.581449000000	8.283129000000
H	12.306533000000	10.675576000000	9.350353000000
H	12.280988000000	10.923597000000	7.583856000000
C	11.326650000000	8.111037000000	10.606087000000
H	12.168666000000	7.388091000000	10.516546000000
H	10.636360000000	7.697923000000	11.369681000000
H	11.756677000000	9.049070000000	11.011703000000
C	5.555551000000	10.601724000000	9.736457000000
H	5.698258000000	9.604283000000	9.285937000000
H	4.924423000000	10.591044000000	10.644589000000
C	5.611753000000	11.767608000000	8.935280000000
H	5.087792000000	12.657997000000	9.335297000000
C	4.588288000000	12.815631000000	6.241204000000
H	4.778174000000	12.896773000000	5.151038000000
H	4.569133000000	13.844482000000	6.657301000000
H	3.581360000000	12.371631000000	6.386400000000
C	5.945760000000	10.029506000000	6.397931000000
H	4.951280000000	9.545933000000	6.482580000000
H	6.683367000000	9.412124000000	6.948702000000
H	6.243704000000	10.034154000000	5.329893000000
C	7.985181000000	15.298761000000	7.004398000000
H	8.206291000000	15.372439000000	5.919562000000
H	8.599330000000	16.055183000000	7.536143000000
H	6.917406000000	15.564696000000	7.149396000000
C	10.146672000000	13.117023000000	7.411627000000
H	10.370813000000	12.131362000000	7.866813000000
H	10.809680000000	13.875123000000	7.876184000000
H	10.390041000000	13.050855000000	6.332172000000
C	7.841673000000	13.456434000000	9.455686000000
H	7.008935000000	14.120091000000	9.760937000000
C	8.682055000000	12.993582000000	10.495499000000
H	8.547220000000	13.374980000000	11.524637000000
H	9.712138000000	12.662530000000	10.274568000000
P	7.618140000000	10.511284000000	11.905541000000
C	6.561708000000	11.331272000000	13.216568000000
H	7.112957000000	12.256526000000	13.492318000000
C	6.134651000000	10.544456000000	14.460085000000
H	6.996456000000	10.206892000000	15.066350000000
H	5.493871000000	11.172377000000	15.113891000000
H	5.541257000000	9.648572000000	14.188003000000
H	5.663837000000	11.681807000000	12.665556000000
C	9.349843000000	10.500660000000	12.599036000000
H	9.800800000000	11.446812000000	12.239847000000
C	9.581571000000	10.359276000000	14.106174000000

H	10.668752000000	10.383201000000	14.329315000000
H	9.117457000000	11.192953000000	14.670733000000
H	9.182628000000	9.411636000000	14.514891000000
H	9.871403000000	9.701180000000	12.034598000000
C	7.097989000000	8.717089000000	11.895784000000
C	7.638206000000	7.751619000000	12.952501000000
H	8.745213000000	7.698897000000	12.926599000000
H	7.337839000000	8.029000000000	13.981209000000
H	7.261161000000	6.725333000000	12.761706000000
H	5.987757000000	8.726754000000	11.890295000000
H	7.395610000000	8.366931000000	10.884401000000

EDA-NOCV data

Intermetalloid clusters are known to exhibit complex electronic structures.^{3 4} To better understand these fascinating compounds, calculations on the DFT level of theory were applied to analyze their bonding situations by EDA-NOCV (Energy Decomposition Analysis with extension for Natural Orbitals for Chemical Valance).

Table S1: EDA-NOCV data of $[Ni(GaCp^*)(dvds)]$ (2).

Energy in [kcal/mol]	(Cp*Ga)Ni-(dvds)	(dvds)Ni-(GaCp*)
ΔE_{int}	-122.22	-36.46
ΔE_{Pauli}	406.03	101.24
ΔE_{Elec}	-285.13	-79.77
ΔE_{Orb}	-226.53	-44.65
ΔE_{π}	-	-5.89
ΔE_{σ}	-	-28.30

Table S2: EDA-NOCV data of $[Ni(AlCp^*)(dvds)]$.

Energy in [kcal/mol]	(Et₃P)Ni-(dvds)	(Et₃P)-Ni(dvds)
ΔE_{int}	-115.91	-53.92
ΔE_{Pauli}	440.15	136.38
ΔE_{Elec}	-298.77	-120.46
ΔE_{Orb}	-241.65	-55.60
ΔE_{π}	-	-7.64
ΔE_{σ}	-	-31.40

Table S3: EDA-NOCV data of $[Ni(PEt_3)(dvds)]$.

Energy in [kcal/mol]	(Cp*Al)Ni-dvds	(Cp*Al)-Ni(dvds)
ΔE_{int}	-120.69	-48.63
ΔE_{Pauli}	473.88	148.34
ΔE_{Elec}	-301.08	-118.67
ΔE_{Orb}	-240.59	-64.31
ΔE_{π}	-	-
ΔE_{σ}	-	-42.66

QTAIM analysis

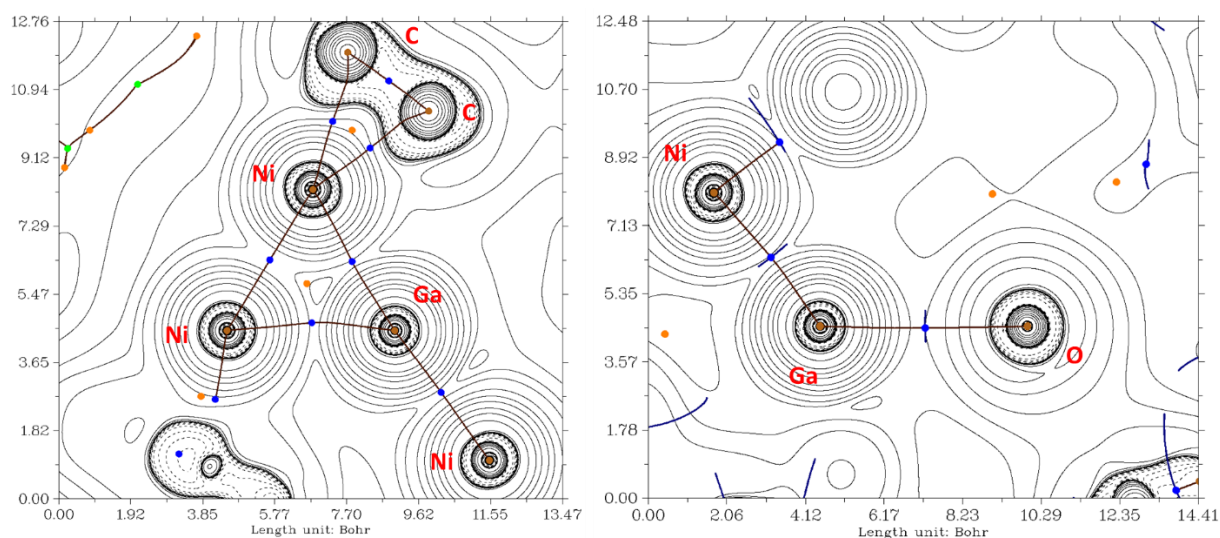


Figure S32: QTAIM schemes for **3**. Bond critical points indicate Ni-Ni interactions in the Ni₂-unit and Ni-Ga interactions in GaNiCp (left). Further the bond critical between Ga (GaNiCp) and O (dvds) suggests strong Ga-O interactions (right). Bond critical point = blue, ring critical point = orange.

Energy Decomposition Analyses with the natural orbital for chemical valence extension (EDA-NOCV)⁵⁻⁷ were carried out using the ADF (2017.113) program package⁸ at the BP86/TZ2P+ level of theory with the previously optimized uncontracted Slater-type orbitals (STOs) were employed as basis functions in self-consistent field (SCF) calculations.⁹ Triple-zeta quality basis sets were used which were augmented by two sets of polarization functions (p and d functions for H, d and f for other atoms). An auxiliary set of s, p, d, f and g STOs was used to fit the molecular densities and to represent the Coulomb and exchange potentials accurately in each SCF cycle. Scalar relativistic effects were considered using the zero-order regular approximation (ZORA).^{10, 11, 12-14} The bond formation between the interacting fragments is divided into three steps within the EDA calculations. In the first step, these fragments (in the frozen geometry of the whole molecule) are superimposed without electronic relaxation yielding the quasi classical electrostatic attraction ΔE_{elstat} . The second step involves anti-symmetrization and normalization of the product wave function which gives the repulsive term ΔE_{Pauli} . In the final step, the molecular orbitals are allowed to relax which gives the stabilizing orbital interaction ΔE_{orb} . This orbital term can be further divided into contributions of different symmetry, representing different bonding situations (σ , π , etc.). Dispersion forces are accounted for using Grimme's D3 dispersion corrections. These contributions sum up to the total interaction energy ΔE_{int} :

$$\Delta E_{int} = \Delta E_{elstat} + \Delta E_{Pauli} + \Delta E_{orb} + \Delta E_{disp}$$

Calculations within the formalism of the quantum theory of atom in molecules (QTAIM)¹⁵ were performed using the MULTIWFN package.¹⁶

References for additional data

1. Maciejewski, H.; Marciniak, B.; Kownacki, I., Catalysis of hydrosilylation: Part XXXIV. High catalytic efficiency of the nickel equivalent of Karstedt catalyst $[\{\text{Ni}(\eta\text{-CH}_2\text{CHSiMe}_2)_2\text{O}\}_2\{\mu\text{-}(\eta\text{-CH}_2\text{CHSiMe}_2)_2\text{O}\}]$. *J. Organomet. Chem.* **2000**, 597 (1), 175-181.
2. Hitchcock, P. B.; Lappert, M. F.; Warhurst, N. J. W., Synthesis and Structure of a *rac*-Tris(divinylsiloxane)diplatinum(0) Complex and its Reaction with Maleic Anhydride. *Angew. Chem. Int. Ed.* **1991**, 30 (4), 438-440.
3. Buchin, B.; Gemel, C.; Cadenbach, T.; Fischer, R. A., Coordination Chemistry of $\text{Ga}(\text{C}_5\text{Me}_4\text{Ph})$: Novel Homoleptic d¹⁰ Cluster Complexes of Palladium. *Inorg. Chem.* **2006**, 45 (4), 1789-1794.
4. Weßing, J.; Ganesamoorthy, C.; Kahlal, S.; Marchal, R.; Gemel, C.; Cador, O.; Da Silva, A. C. H.; Da Silva, J. L. F.; Saillard, J.-Y.; Fischer, R. A., The Mackay-Type Cluster $[\text{Cu}_{43}\text{Al}_{12}](\text{Cp}^*)_{12}$: Open-Shell 67-Electron Superatom with Emerging Metal-Like Electronic Structure. *Angew. Chem. Int. Ed.* **2018**, 57 (44), 14630-14634.
45. Banh, H.; Hornung, J.; Kratz, T.; Gemel, C.; Pöthig, A.; Gam, F.; Kahlal, S.; Saillard, J.-Y.; Fischer, R. A., Embryonic brass: pseudo two electron Cu/Zn clusters. *Chem. Sci.* **2018**, 9 (48), 8906-8913.
6. Parafiniuk, M.; Mitoraj, M. P., On the origin of internal rotation in ammonia borane. *J. Mol. Model* **2014**, 20 (6), 2272.
7. Michalak, A.; Mitoraj, M.; Ziegler, T., Bond Orbitals from Chemical Valence Theory. *J. Phys. Chem. A.* **2008**, 112 (9), 1933-1939.
8. Mitoraj, M. P.; Michalak, A.; Ziegler, T., A Combined Charge and Energy Decomposition Scheme for Bond Analysis. *J. Chem. Theory Comput.* **2009**, 5 (4), 962-975.
9. te Velde, G.; Bickelhaupt, F. M.; Baerends, E. J.; Fonseca Guerra, C.; van Gisbergen, S. J. A.; Snijders, J. G.; Ziegler, T., Chemistry with ADF. *J. Comput. Chem.* **2001**, 22 (9), 931-967.
10. Snijders, J. G.; Vernooijs, P.; Baerends, E. J., Roothaan-Hartree-Fock-Slater atomic wave functions: Single-zeta, double-zeta, and extended Slater-type basis sets for 87Fr-103Lr. *Atomic Data and Nuclear Data Tables* **1981**, 26 (6), 483-509.
11. Chang, C.; Pelissier, M.; Durand, P., Regular Two-Component Pauli-Like Effective Hamiltonians in Dirac Theory. *Phys. Scr.* **1986**, 34 (5), 394.
12. Heully, J. L.; Lindgren, I.; Lindroth, E.; Lundqvist, S.; Martensson-Pendrill, A. M., Diagonalisation of the Dirac Hamiltonian as a basis for a relativistic many-body procedure. *J. Phys. B.: At. Mol. Phys.* **1986**, 19 (18), 2799.
13. Snijders, J. G.; Sadlej, A. J., Perturbation versus variation treatment of regular relativistic Hamiltonians. *Chem. Phys. Lett.* **1996**, 252 (1), 51-61.
14. Lenthe, E. v.; Baerends, E. J.; Snijders, J. G., Relativistic regular two-component Hamiltonians. *J. Chem. Phys.* **1993**, 99 (6), 4597-4610.
15. van Lenthe, E.; van Leeuwen, R.; Baerends, E. J.; Snijders, J. G., Relativistic regular two-component Hamiltonians. *Int. J. Quantum Chem.* **1996**, 57 (3), 281-293.

16. Bader, R. F. W., *Atoms in Molecules*. Oxford University Press Inc.: New York, 1994.
17. Lu, T.; Chen, F., Multiwfn: a multifunctional wavefunction analyzer. *J. Comput. Chem.* **2012**, 33 (5), 580-92.

2.2 Investigating Inseparable Cluster Ensembles: A Ni/Ga Case Study.

Maximilian Muhr,^{+,a} Lena Staiger,^{+,a} Johannes Stephan,^a Karina Hemmer,^a Max Schütz,^a Patricia Heiß,^a Christian Jandl,^a Mirza Cokoja,^a Tim Kratky,^a Sebastian Günther,^a Dominik Huber,^a Samia Kahlal,^b Jean-Yves Saillard,^{*,b} Olivier Cador,^b Augusto C. H. Da Silva,^c Juarez L. F. Da Silva,^{*,c} Janos Mink,^d Christian Gemel,^a and Roland A. Fischer^{*,a}

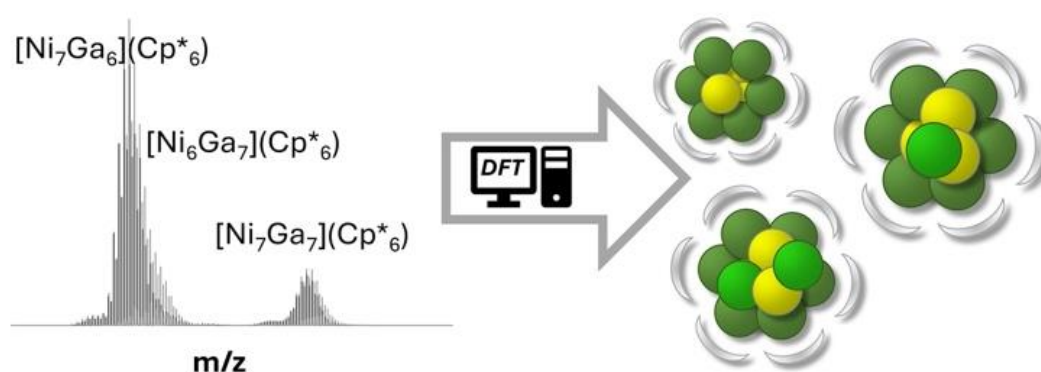
[a] Department of Chemistry and Catalysis Research Center, Technical University of Munich, Lichtenbergstrasse 4, D-85748 Garching, Germany

[b] Univ Rennes, CNRS, ISCR-UMR 6226, F-35000 Rennes, France.

[c] São Carlos Institute of Chemistry, University of São Paulo, P. O. Box 780, 13560-970, São Carlos, SP, Brazil

[d] Hungarian Academy of Sciences, Institute of Material and Environmental Chemistry, Research Centre for Natural Sciences, Magyar tudósok körútja 2, H-1117 Budapest

[+] M.M. and L.S. contributed equally to this work.



The following content was already evaluated through a peer-review process, is however unpublished yet. It is planned to submit the work to the Journal *Nature Communications*.

Author contributions:

Experiments and manuscript writing was done by the two authors. Experimental support by J.S., K.H., M.S., P.H.; C.J. supported with SCXRD, T.K. and S.G. with XPS, J.M. with vibrational and O.C with magnetic measurements. D.H. and M.C. data evaluation and writing support. A.d.S. and J.d.S. screening approach. S.K. and J.Y.S. bonding analysis. C.G. and R.A.F. supervised the research.

2.2.1 Abstract

Do not discard reaction solutions of mixed-metal cluster syntheses! The composition of each cluster in a mixture can be identified by high-resolution mass spectrometry. The structure assignment can be achieved by advanced computational screening and consideration of the complete structural space in combination with a set of spectroscopic techniques. The powerful methodology overcomes the limitation of the typically unselective syntheses of clusters. Exemplary, we demonstrate the application of the methodology on an inseparable ensemble of Ni/Ga clusters, containing Cp*-ligated Ni/Ga cores of similar nuclearities M_{12} , M_{13} and M_{14} . The structure rationalization and bonding analysis is built upon the superatomic complex $[\text{Ni}_6\text{Ga}_6](\text{Cp}^*)_6 = [\text{Ga}_6](\text{NiCp}^*)_6$ (**1**). The obtained structure assignments are validated by reactivity tests using carbon monoxide, which selectively binds to Ni sites, whereas triisopropylsilyl-acetylene selectively binds to Ga sites.

2.2.2 Main Text

The understanding of physical and chemical properties of metal clusters depends on the elucidation of chemical structures, which, however, relies on directed bottom-up wet chemical synthesis. In contrast to organic compounds, metal clusters cannot be accessed in a plannable retrosynthetic fashion. Transient species in cluster growth reactions are usually highly reactive and therefore can follow multiple parallel pathways. This situation further complicates when more than one metal element is involved. For the synthesis of a pure bimetallic cluster, a high trial-and-error effort has therefore to be invested in the optimization of reaction parameters (precise control of reactants stoichiometry, temperature, time, solvent). Typically, the mixed-metal cluster generating reaction solutions contain several, if not many species of very similar composition and structure (including intermediates and isomers). The targeted isolation of individual (stable)

clusters from these solutions may be extremely difficult if not practically impossible.^[3]

A well-studied example for intermetallic compounds is the Ni/Ga case. Solid state Hume-Rothery bulk phases, colloids and nanoparticles as well as small molecular complexes have been thoroughly investigated in the recent past. Atom-precise clusters, however, are unknown to date. This is certainly a consequence of the highly complex synthetic access to pure compounds. But progress in the area of intermetallic clusters wet chemistry may not depend on the isolation of pure clusters. Is it possible to generate structural information on individual species from complex cluster mixtures? We now wish to report on a prime example how to deal with the richness of mixed-metal cluster synthesis. A unique methodology (Figure 1) synergistically combining experiment and theory bypasses the intrinsic limitations of isolating pure

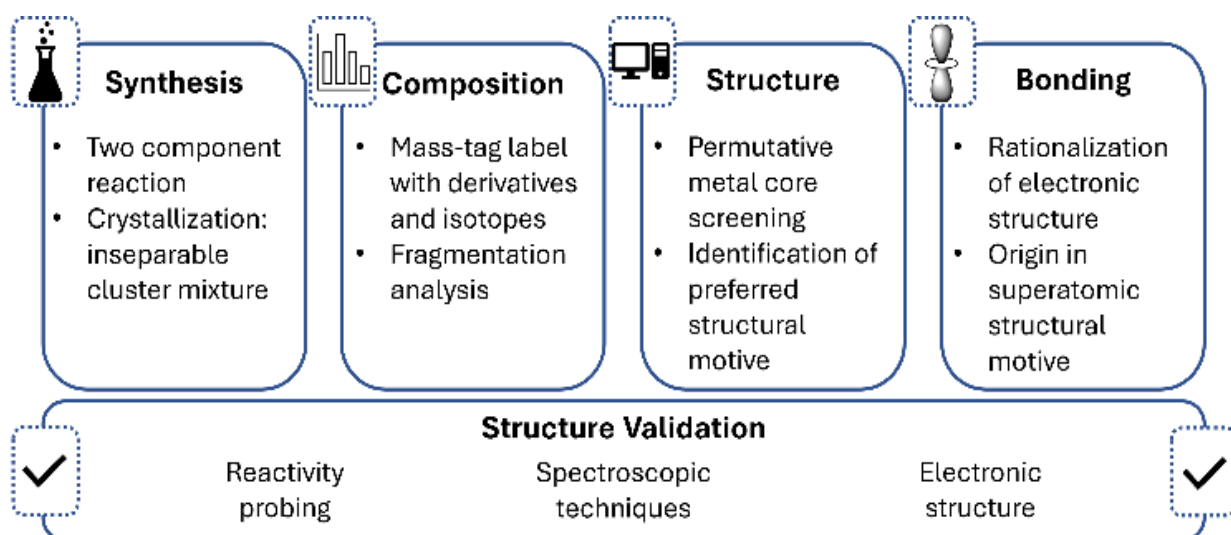


Figure 1: Schematic outline of the developed methodology: After synthesis the compositions of each cluster in the ensemble are unequivocally assigned by high resolution mass spectrometry (mass-tag labels and fragmentation experiments) and their respective structures are assessed by a computational permutative screening approach, taking all possible structures into account. The bonding situation of the species can then be explained through DFT calculations and the individual structure is further validated by spectroscopic characterizations and their chemical reactivity towards probe substrates.

compounds. The key element of this methodology is the assignment of chemical structures to each species in the cluster ensemble by employing a computational permutative approach considering all possible isomers. As input for these calculations serve the elemental compositions which are unequivocally identified by high-resolution mass spectrometry, including mass-tag (e.g. isotope) labeling as well as collision-induced fragmentation experiments. The result of this individual structural assignment is cross-validated by experimental spectroscopic data as well reactivity studies of the whole ensemble. This powerful methodology is demonstrated on an inseparable ensemble of strongly related superatomic Ni/Ga clusters stabilized in a C_5Me_5 ligand shell.

Synthesis

The clusters are generated from the reaction of Ni(0)-olefin complexes with GaCp* in toluene or mesitylene at moderately elevated temperatures (70-110°C). The reaction leads to the parent and inseparable cluster ensemble $[Ni_{6/7/8}Ga_{6/7}](Cp^*)_6$, containing clusters of different metal atomicities (nuclearities): M_{12} , M_{13} and M_{14} respectively (Figure 2). All products are very moisture sensitive and decompose immediately upon exposure to air. Crystalline material is obtained from saturated solutions at ambient temperature. Classical analytical techniques completely failed in characterizing this material: Despite numerous SC-XRD measurements using different batches and crystallization conditions, the results of the refinement remain inconclusive (Figure S22), however, an octahedral $(MCp^*)_6$ shell around an inner metal core is conclusively obtained in all

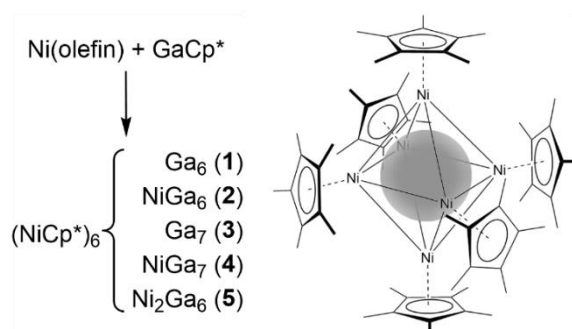


Figure 2: left) Generation of the cluster ensemble, mainly consisting of $[Ni_6Ga_6](Cp^*)_6$ (1), $[Ni_7Ga_6](Cp^*)_6$ (2), $[Ni_6Ga_7](Cp^*)_6$ (3), $[Ni_7Ga_7](Cp^*)_6$ (4) and traces of $[Ni_8Ga_6](Cp^*)_6$ (5). Compositions were established by from LIFDI-MS. right) Structural assignment derived from a DFT screening approach of the full configuration space in combination with analytical and spectroscopic techniques.

structural refinements. However, the exact Ni/Ga distribution could not be obtained. The elemental composition of solid bulk samples of the ensemble obtained by crystallization have been assessed by classic elemental analysis (C, H) as well as atomic absorption spectrometry (Ni, Ga) (Table S22). These results were substantiated by XPS analysis (Figure S25). In all samples the Ni/Ga ratio is close to 1:1 with a slight bias to Ni. However, due the fact that all samples represent practically inseparable mixtures of several clusters, which are isolated as co-crystallites, a detailed interpretation and assignment of the analytical data is not reasonable without independent quantification of the molar ratio of the clusters in the mixtures. Unfortunately, the clusters do not feature species specific spectroscopic features to be useful for deriving the molar ratios.

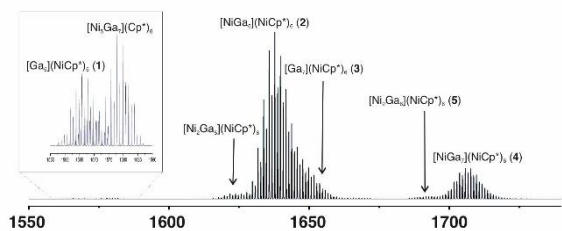


Figure 3: LIFDI mass spectrum of the complex cluster ensemble. All sum formulas (verified by mass-tag labeling) are assigned to the peaks. Box on the left shows patterns between 1560 and 1590 enlarged.

Mass Spectrometric Characterisation

The way out in the identification of the reaction products lies in the accurate analysis of *in-situ* mass spectra, which reveals the elemental compositions of the individual clusters. Sum formulas are accessible by high-resolution m/z data of their molecular ions detected by LIFDI mass spectra (LIFDI = liquid injection field desorption ionization) as well as by careful analysis of their isotopic patterns (Figure S11-13). From the high-resolution mass spectra (Figure 3), it can be deduced, that all clusters present in solution contain exactly six Cp* ligands with different numbers of metal atoms: Ni₆Ga₆ (**1**), Ni₇Ga₆ (**2**), Ni₆Ga₇ (**3**), Ni₇Ga₇ (**4**) and Ni₈Ga₆ (**5**). The unambiguous assignment of sum-formulas is achieved by labeling the clusters with ⁷¹Ga and Cp*^{Et} (C₅Me₄Et), respectively, and relating the observed mass shifts to the number of Ga atoms or Cp* groups in the clusters (Figure S16-18).

Notably, all patterns are very broad and some overlap. The observed m/z values point to the fact that during ionization the clusters lose hydrogen atoms: [Ni₆Ga₆Cp*₆-2H]⁺ (**1**), [Ni₇Ga₆Cp*₆-2H]⁺ (**2**), [Ni₆Ga₇Cp*₆-H]⁺ (**3**), [Ni₇Ga₇Cp*₆-3H]⁺ (**4**) and [Ni₈Ga₆Cp*₆-4H]⁺ (**5**). Such phenomena have been observed in field desorption mass spectra of organic^[6] as well as cluster compounds^[3a, 4] before.

Notably, there is no spectroscopic evidence for C-H activation or dehydrogenation in solution (*vide infra*). Collision experiments in a higher-energy collisional dissociation (HCD) cell allowed the distinction of the molecular ions from their fragment ions formed upon ionization during the mass spectrometric experiment (Figure S19-21). Species containing less than six Cp* ligands were identified as fragment ions, with fragmentation patterns showing the cleavage of Cp* as well as the splitting of NiCp*₂. The latter species is also detected as a molecular ion in the mass spectra. It should also be noted that clusters with other metal cores, in particular the species [Ni₇Ga₅](Cp*)₆ and [Ni₈Ga₅](Cp*)₆ were observed in traces, yet their small quantities did not allow for unambiguous assignment. By varying the Ni(0) olefin precursor (olefin: cod = 1,5-cyclooctadiene, dvds = 1,1,3,3-tetramethyl-1,3-divinyl-disiloxane), the qualitative composition remains always the same, while the quantitative composition varies – Ni(cod)₂ leads to mixtures with Ni₆Ga₇ (**3**), while Ni₂(dvds)₃ gives mixtures with Ni₇Ga₆ (**2**) as the major component (Figure S13). Notably no significant differences between mass spectra from crystalline material or from reaction solution are observed (Figure S14-15).

We want to emphasize that determination of the absolute quantities of the clusters is not feasible based on mass spectrometric peak intensities only, since identical ionizability of different clusters cannot be presupposed and a precise calibration would need pure isolated clusters as references, which are, however, not accessible. Nevertheless, evaluation of the LIFDI-MS data including the labelling experiments unambiguously delivers the elemental composition of each

component present in the ensemble. As an important first result we conclude that the clusters present in solution are all-Cp* ligand-protected and share the formula $[\text{Ni}_{6+x}\text{Ga}_{6+y}](\text{Cp}^*)_6$ ($x+y \leq 2$).

Structure Assignment by Computational screening

For the assignment of chemical structures to the mass spectrometrically-determined compositions of the clusters, a computational permutative approach has been developed using an *ab initio* methodology for total energy calculations. Due to the large number of possible structural isomers, we established a systematic method for screening the complete structural space of M_{13} (**2** and **3**) and M_{14} (**4**) clusters (Figure S28). Our design principle essentially relies on the combination of two independent strategies: First, a set of monometallic clusters is obtained from gas-phase *ab initio* FHI-aims calculations (Figure 4). The metal positions in these monometallic clusters are then randomly substituted by the second metal, resulting in a large set of bimetallic core structures. This scheme was applied with and without the presence of Cp* ligands placed on designed sites above the Ni/Ga clusters. The second strategy uses the

atom positions as input. By exchange of atom positions between four distinct chemical environments of the M_{13} and M_{14} cluster (Figure S34), while keeping the ligand positions unchanged, a second large set of cluster geometries is created. The cluster structures obtained by these two strategies were combined and evaluated.

As a first step of the evaluation process, the whole set of optimized structures was screened for structural similarities with the target of reducing the number of clusters for further analysis. For this purpose a Hungarian algorithm as well as an in-house modified Euclidian similarity distance algorithm were employed.^[7] With the resulting set of unique cluster structures, we performed spin polarized geometrical optimizations using FHI-aims with the PBE functional on the light-tier-2 basis set on each obtained structure and compared all structures in terms of relative energy (Figures S29-32). The most stable isomers of both the M_{13} as well as M_{14} naked clusters (i.e. without the Cp* protecting shell) show the Ni atoms on the structure's inner sites (Figure 4; Figures S35, S37 and S39), following the radius order between the Ni and Ga atoms. The values for excess energy for nanoalloy formation is negative in all cases, i.e., their formation from

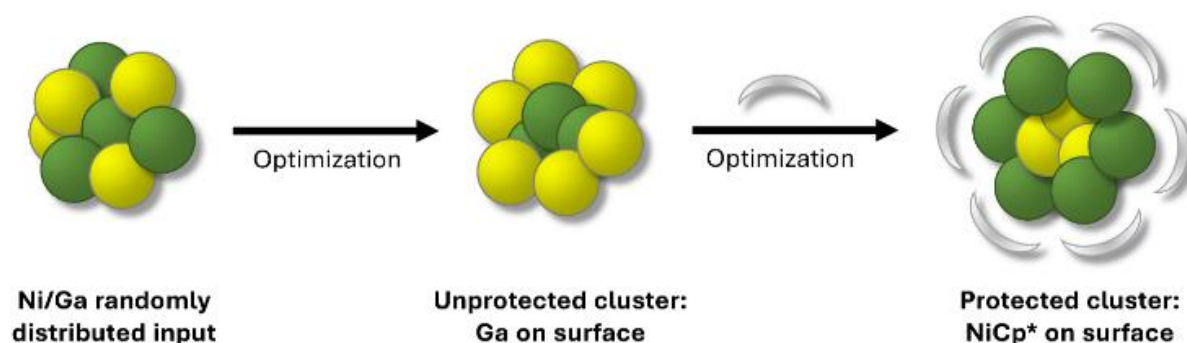


Figure 4: Schematic representation of the DFT screening approach. Optimization of a large set of randomly distributed unprotected bimetallic (Ni: green, Ga: yellow) clusters followed by Cp* (grey) addition to the unprotected clusters, identifies Ni atoms to be located on the surface, attached to the Cp* ligands, in the clusters of the ensemble.

crystallographically estimated core metal the elements is thermodynamically

favorable. Structural parameters as effective coordination number (ECN), average distances (d_{av}), magnetic moments and chemical order (σ) were obtained (ESI, Figures S36, S38 and S40), however there is not an apparent trend in these indicators if compared to the relative energy of the isomers. As the Cp* ligands are added to the calculations, we observe key changes on the favored Ni and Ga positions. Now, the most stable isomers show the Ni atoms on the outermost sites of the clusters (scheme 1b). The Cp* ligands coordinate to these Ni sites (Figure 4; Figures S41, S43-45, S48). Notably, their overall topology is fully consistent with the SC-XRD data (*vide supra*). Especially the M-Cp* distances in the experimental structure point to M being rather Ni than Ga.^[2d, 8] Once the metal atoms at the Cp* binding are exchanged to Ga atoms, an energy increase up to 5 eV (M_{14}) or 4 eV (M_{13}) is observed. The magnetic moments are 1 for the metal-cores Ni₇Ga₇ and Ni₆Ga₇ but are 0 for Ni₇Ga₆. Notably, this is well consistent with the diamagnetic nature of Ni₇Ga₆ concluded from SQUID measurements (*vide infra*). Charge analysis shows a slight charge transfer from the metal core to the Cp* ligands with a correlation of the relative energies and average distance from Cp* to the metal core.

In summary: Our computational *ab-initio* approach, screening the complete structural space of [Ni_{6/7}Ga_{6/7}](Cp*)₆, reveals that the most stable cluster isomers are all built upon the same structural prototype: a pure Ga₆ or NiGa_{6/7} inner core, surrounded by a monometallic (NiCp*)₆ shell. This is well consistent with the interpretation of SC-XRD data, but we can further support this assumption by spectroscopic data, in

particular ¹³C MAS NMR, vibrational spectroscopy and SQUID (*vide supra*).

The reaction obviously includes complete Cp* transfer from Ga to Ni. This is a common transmetalation pattern in the reaction of ECp* (E = Al, Ga, Zn) with transition metal complexes and has also been observed in reactions of GaCp* with organometallic complexes of nickel,^[11] palladium or platinum,^[12] iron,^[13] and rhodium.^[14] The driving force of this Cp* transfer step is related to the formation of thermodynamically stable half-sandwich transition metal fragments with strong TM-Cp* interactions. As discussed in the computational section, this reasoning also applies to this case.

Structure Validation by Spectroscopy

In contrast to mass spectrometric analysis, spectroscopic information does not address individual species directly but concerns the whole cluster ensembles. Dependent on the synthetic conditions ensembles enriched with either **2** or **3** can be produced (*vide supra*). By SQUID/EPR as well as RAMAN studies information on the architecture of the metal core of the clusters is available: SQUID of samples enriched with the intrinsically paramagnetic Ni₆Ga₇ (**3**) indeed show stronger paramagnetism, whereas the corrected SQUID data of samples enriched with diamagnetic Ni₇Ga₆ (**2**) exhibit a “cusp” at 220K, which is indicative for samples with a large diamagnetic component (Figure S26). EPR measurements confirm this interpretation: In all samples a signal centered at $g = 2.13$ is observed, which is considerably more intense in samples enriched in the paramagnetic cluster **3**

(Figure S27). Raman spectra point to significantly different metal core connectivities in **2** and **3** (skeletal Ni-Ga and Ga-Ga stretching modes below 250 cm^{-1})

FT-IR and Raman spectroscopic data of the cluster mixtures (ATR, solid state; Figures S6-S10) confirm the very symmetric and uniform shielding of the metal core by intact Cp* units (Figure 2). No evidence is present for any intramolecular bond activation of the Cp* ligands. A detailed assignment of all IR and Raman signals is given in the supporting information (Table S1) and has also been recently reported and discussed in detail.^[10]

The most valuable information on the ligand shell of the clusters is derived from ^{13}C NMR spectra of cluster ensembles: The (Cp*)₆ ligand shell gives rise to a single set of signals at 98.10 and 12.77 ppm which correspond to the ring carbon atoms and the methyl groups of Cp*, respectively (Figure S2). This strongly indicates the presence of only one metal type coordinated to the Cp*, therefore a ‘homometallic’ (MCp*)₆ shell. The observed chemical shift at 98.1 ppm is typical for NiCp* groups measured in solution^[8a, 8c, 9] while

validating the structure assignment strategy via a DFT screening approach.

Bonding Analysis

To further investigate and rationalize the cluster structures from a bonding point of view and to analyze common features as well as subtle differences in their electronic situations, we optimized the structures of the model series $[\text{Ni}_{6/7/8}\text{Ga}_{6/7}](\text{Cp}^*)_6$ by means of DFT calculations at the BP86/TZ2P level of theory (see Computational Details, ESI). The use of simple C₅H₅ (Cp) in place of the real C₅Me₅ (Cp*) ones allowed a straightforward analysis of their electronic structures. In a second step, the $[\text{Ni}_{6/7/8}\text{Ga}_{6/7}](\text{Cp}^*)_6$ series was also optimized and compared to its Cp counterpart. All the structures discussed below are true energy minima confirmed by frequency calculations and all even-electron species show a significant, although not very large, HOMO-LUMO gap. Selected computed data are given in ESI Table S23. Over the course of our calculations, we identified $[\text{Ni}_6\text{Ga}_6](\text{Cp})_6$ (**1**^{Cp}) as a base frame, as it is part

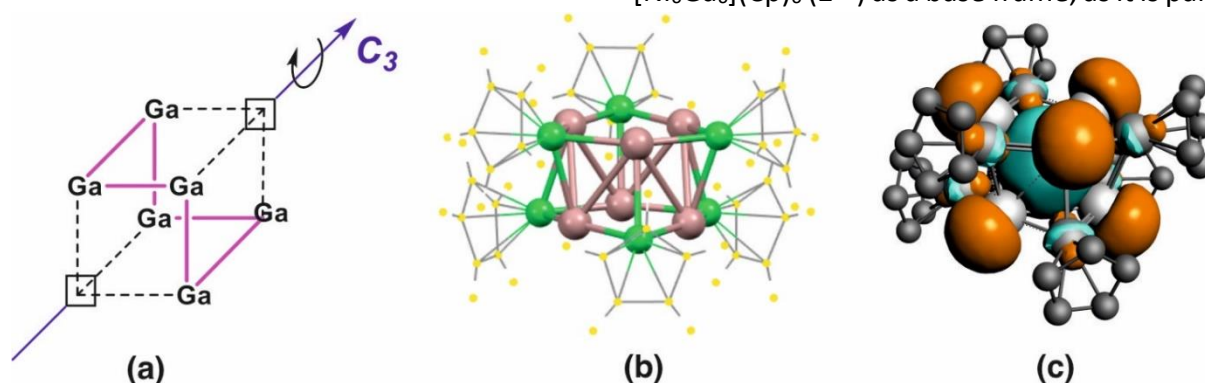


Figure 5: Bonding analysis of $[\text{Ga}_6](\text{NiCp})_6 = [\text{Ni}_6\text{Ga}_6](\text{Cp})_6$ (Cp = C₅H₅): (a) The cubic parentage of the Ga₆ framework. (b) The DFT-optimized geometry and (c) electron density mapping of the LUMO.

GaCp* signals are typically found at 110-115 ppm.^[2d, 8b, 8d] In summary, all spectroscopic data are well consistent with the computationally derived structures, thus

of all other structures. Although **1** appears as a minor component of the cluster ensembles, at least based on LIFDI-MS data, **1**^{Cp} will be our “reference” species in the following bonding analysis.

The lowest energy structure of $\mathbf{1}^{\text{Cp}}$ can be described as an octahedral $(\text{NiCp})_6$ outer shell encapsulating an inner Ga_6 “cube” having two missing vertices that are situated along one of its solid diagonals (Figure 5a?). In such a “cubic” configuration, every “square” face of the “cube” is made of three Ga and one vacant vertex. Each of the six faces of the “cube” are capped by one (NiCp) unit (Figure 5b). Interestingly such cubic core arrangements were often found as structural motives in the screening approach (*vide supra*). The bonding within this Ga_6Ni_6 core is ensured by 36 electrons, three provided by each Ga atom and three by each $\text{Ni}(\eta^5\text{-C}_5\text{R}_5)$ fragment. Neglecting the long $\text{Ga}\dots\text{Ga}$ contacts (~ 3.0 Å), the 36 electrons can be assigned to the 18 Ni-Ga bonds. Within this localized 2-center/2-electron bonding description, the Ni centers obey the 18-electron rule, while the Ga atoms feature a sextet electronic environment, a reasonably stable situation for group 13 elements, although somehow electron-deficient. This electron deficiency is associated with the presence of a rather low-lying vacant sp hybrid orbital on each individual Ga center. The six vacant Ga sp hybrids combine and their lowest (thus bonding) combinations mix somewhat with the occupied Ni-Ga orbitals, thus conferring some $\text{Ga}\dots\text{Ga}$ through-bond attractive interaction, as exemplified by the $\text{Ga}\dots\text{Ga}$ “non-bonding” contacts (Table S23). The LUMO of $\mathbf{1}^{\text{Cp}}$ is the in-phase combination of the six Ga sp hybrids (Figure 5c). With substantial $\text{Ga}\dots\text{Ga}$ overlap inside the Ga_6 cage, it resembles the 2S orbital of a superatom.^[15] The computed HOMO-LUMO gap of $\mathbf{1}^{\text{Cp}}$ (0.65 eV) is indicative of reasonable chemical stability. Thus, $[\text{Ni}_6\text{Ga}_6](\text{Cp})_6$ can be described as an intermetallic superatom complex.

The electronic structure of the superatom base cluster $[\text{Ni}_6\text{Ga}_6](\text{Cp})_6$ ($\mathbf{1}^{\text{Cp}}$) allows for the integration of one or two additional metal atoms resulting in the extended derivative clusters $[\text{Ni}_7\text{Ga}_6](\text{Cp})_6$ ($\mathbf{2}^{\text{Cp}}$), $[\text{Ni}_6\text{Ga}_7](\text{Cp})_6$ ($\mathbf{3}^{\text{Cp}}$), $[\text{Ni}_7\text{Ga}_7](\text{Cp})_6$ ($\mathbf{4}^{\text{Cp}}$) and $[\text{Ni}_8\text{Ga}_6](\text{Cp})_6$ ($\mathbf{5}^{\text{Cp}}$). The optimized structure of $[\text{Ni}_7\text{Ga}_6](\text{Cp})_6$ ($\mathbf{2}^{\text{Cp}}$) (Figure S50a) can be described as resulting from the occupation of one of the “missing” cube vertices in $\mathbf{1}^{\text{Cp}}$ by one additional (“exposed”) Ni atom (Table S23 and Figure S50c). Its bonding to the $\mathbf{1}^{\text{Cp}}$ fragment results from two components. One is associated with a $3d(\text{Ni}_{\text{exp}})$ donation into the accepting orbitals of $\mathbf{1}^{\text{Cp}}$ discussed above (1.05 electron). As a result, the superatomic 2S-type LUMO of $\mathbf{1}^{\text{Cp}}$ is now completed by a $d_{z^2}(\text{Ni}_{\text{exp}})$ contribution in $\mathbf{2}^{\text{Cp}}$ (ESI Figure S50b). The other bonding component results from a similar (1.05 electron), but backward, electron transfer into the $4s/4p$ AOs of the “exposed” Ni from its three Ni neighbors. Adding a Ga atom to the base cluster $\mathbf{1}^{\text{Cp}}$ results in $[\text{Ni}_6\text{Ga}_7](\text{Cp})_6$ ($\mathbf{3}^{\text{Cp}}$). $\mathbf{3}^{\text{Cp}}$ is an odd-electron species, for the sake of simplicity we investigate first its closed-shell cation $[\mathbf{3}^{\text{Cp}}]^+$. It is obvious that the single Ga atom in $\mathbf{3}^{\text{Cp}}$ is substantially weaker bonded to $\mathbf{1}^{\text{Cp}}$ than a the single Ni atom $\mathbf{2}^{\text{Cp}}$, as exemplified by long $\text{Ga}_{\text{exp}}\text{-Ga}$ (3.131 Å) and $\text{Ga}_{\text{exp}}\text{-Ni}$ (3.298 Å) distances (Figure S50c and Table S23). This is consistent with the fact that now there is negligible electron transfer from Ga to the $\mathbf{1}^{\text{Cp}}$ fragment. The major electron transfer occurs between the $3d(\text{Ni})$ and the vacant $4p$ orbitals of the “exposed” Ga^+ (0.83 electron). Therefore, this “exposed” atom does not participate to the 2S-type LUMO of $[\text{Ni}_6\text{Ga}_7](\text{C}_5\text{R}_5)_6^+$ ($\text{R} = \text{H}, \text{Me}$), which resembles that of the uncapped $\mathbf{1}^{\text{Cp}}$. Going now to the ‘real’ neutral, odd-electron, $\mathbf{3}^{\text{Cp}}$, barely changes the cluster structure, which nicely

underlines the electronic flexibility of the base cluster **1^{Cp}**. Occupying the 2S-type LUMO of the cation cluster by a single electron results only in some shortening of the Ga-Ga distances within the **1^{Cp}** cage, in line with the Ga...Ga bonding character of this orbital (Table S23). Calculations show that it is possible to cap the **1^{Cp}** cage on both sides of the C_3 axis by two atoms of Ni and/or Ga nature, thus completing the cube of Figure 5a. The data obtained for **4^{Cp}** and **5^{Cp}** (Table S23) show similar characteristics as their monocapped relatives.

The computed Cp* series of clusters **1-3** provided quite similar results as that of their Cp homologues (Figure S23). They exhibit slightly lower HOMO-LUMO gaps. This is in line with their slightly shorter Ga...Ga contacts. This is also consistent with the fact that their potential energy surfaces were found quite flat and their equilibrium structure less symmetrical than that of their Cp counterparts. In particular, concerning **3** the “exposed” Ga atom is connected to one, rather than three, Ni atoms as in **3^{Cp}**.

To conclude, the electronic structures of clusters **1-3** are strongly related to each other. Thus, clusters **2** and **3** are formed by addition of Ga or Ni atoms to the inner Ga₆ core of the superatomic base cluster **1**, without remarkable structural deviations of the metal core. In some way this may metaphorically be linked to the fact that these clusters occur experimentally only in ensembles, preventing targeted synthesis of single cluster species by the organometallic route.

Structure-Reactivity Relationship

Despite their strong electronic and structural similarities, the clusters should be markedly

different in their chemical reactivity. Thus clusters **2**, **4** and **5** contain naked Ni atoms in the inner core, whereas clusters **1** and **3** contain Ga atoms only. In order to investigate whether this structural difference is reflected in the reactivity of the singular species of the ensemble, we exposed the cluster mixtures to CO as a probe molecule for naked Ni atoms. Pressurizing respective samples in toluene-*d*₈ with CO 2.5 atm at ambient temperatures results in dark red solutions after 120 min. Careful analysis of the LIFDI-MS spectra point to a significant reactivity difference of the four major cluster species **1-5**, (ESI, Figures S56-S59): While the patterns of [Ni₆Ga₆](Cp*)₆ (**1**) and [Ni₆Ga₇](Cp*)₆ (**2**) are virtually unaffected by the presence of CO, the intensity of pattern assignable to the M₁₃ cluster [Ni₇Ga₆](Cp*)₆ (**2**) decreases considerably, indicating a high affinity of this species towards CO (ESI, Figure S58-S59). The pattern of the M₁₄ cluster [Ni₇Ga₇](Cp*)₆ (**4**) is still detectable in the presence of CO, however, in addition its CO adduct [(CO)NiNi₆Ga₇](Cp*)₆ is observed at $m/z = 1734.4$. This striking reactivity difference of the four species nicely correlates with the presence of active nickel atoms in the cluster core. A more detailed analysis of all identified species and cluster degradation products induced by CO can be found in the ESI.

By DFT calculations stable adducts for the interaction of carbon monoxide with [Ni₇Ga₆](Cp*)₆ (**2**) and [Ni₇Ga₇](Cp*)₆ (**4**) were found. The CO binds to the “exposed” Ni atom of the inner core, with rather short Ni-CO distances of 1.774 and 1.770 Å, respectively. The CO lone pair interacts *inter alia* with the superatomic 2S-type LUMO, which has Ni_{exp} character. The whole cluster structures are little affected by the CO coordination.

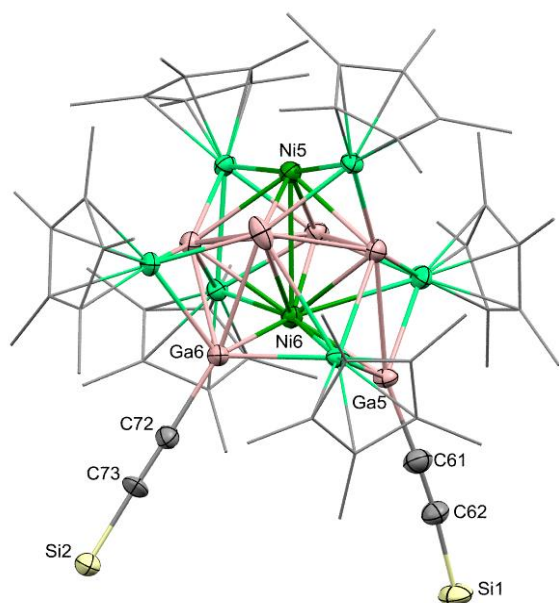


Figure 6: Molecular of $[Ni_8Ga_6](Cp^*)_6(TIPSA)_2$ in the crystalline state. All atom positions unambiguously assigned. All Cp^* attached to Ni, TIPSA attached to Ga. Ni (green), Ga (pink), Cp^* in wireframe, isopropyl groups and H atoms are omitted for clarity. More details see ESI.

As a second probe molecule for screening cluster reactivity, triisopropylsilyl-acetylene (TIPSA) was used. Alkynyl ligands are widely employed as stabilizing ligands for metal clusters.^[16]

In fact, the reaction turned out to be highly selective, allowing separation of a singular species: The cluster ensemble is treated with an excess of triisopropylsilyl-acetylene (TIPSA) under irradiation (350 nm) and the cluster $[Ni_8Ga_6](NCP^*)_6(TIPSA)_2$ was isolated in pure single crystalline form. Here, an unambiguous assignment of the structure, including all metal atom positions, is possible (Figure 6). Indeed, in agreement with all results presented above, the Cp^* ligands are attached to Ni atoms only, while the two alkynyl ligands are attached to Ga atoms and not to Ni (as the CO would). A discussion of the structural details of this derivative, together with insights into its formation mechanism are subjects of ongoing research.

Conclusions and Perspective

Our case study on the novel, superatomic cluster ensembles $[Ni_{6+x}Ga_{6+y}](Cp^*)_6$ ($x + y \leq 2$) demonstrates how to gain valuable structure-property relationship data without isolating analytically pure clusters. Our methodology uses mass spectrometry for determination of cluster compositions from raw synthetic mixtures and relies on advanced computational methods for the elucidation of chemical structures. Uncontrollable cluster synthesis creates a chemical complexity of parallelly formed clusters, each with an individual composition, structure and reactivity. A second level of complexity is related to the analysis of each individual in an (almost) unlimited space of possible isomers (shape, connectivity, element distribution). An advanced computer assisted approach allows us to find a solution for the latter (analytic complexity), which in turn enables us to fully embrace the first (synthetic complexity). In other word the exact chemical structures of a variety of co-existing products is accessible by a new combination of experiment and theory. Based on the present methodology structures can be unambiguous assigned. Structural rationalization then gives insight into the bonding situation and enables the design of experiments to selectively obtain and isolate derivatives in pure form. The introduced “ensemble approach” suggests an avenue for exploiting the rich synthetic complexity. Cluster science is progressed by developing integrated combinatorial methods for synthesis, structural characterization and reactivity studies. We anticipate the discovery of interesting, potentially novel reactivities of so

far unknown, and larger intermetalloid clusters and reactive superatom complexes.

Acknowledgements

We thank Dardan Ukaj for the RAMAN measurements and Dr. Alexander Pöthig and Dr. Wilhelm Klein for their help in the interpretation of the SC-XRD data. We would like to express our thanks to Fabian Schmidt and Dr. Gabriele Raudaschl-Sieber for recording the solution and solid-state NMR spectra, respectively. Finally, we want to acknowledge the contribution of Tobias Steinke, Jana Weßing and Julius Hornung who have laid the scientific foundations on which the discoveries in this work are based. This work was funded by the German Research Foundation (DFG) within a Reinhard Koselleck Project (FI-502/44-1) and the TUM Graduate School. TUM Global Incentive Fund is acknowledged for a travel fund for M.M.; S.K. and J.-Y.S. are grateful to GENCI (Grand Equipment National de Calcul Intensif) for HPC resources (Project A0050807367). The authors gratefully acknowledge support from FAPESP (São Paulo Research Foundation, Grant Numbers 2017/11631-2 and 2018/21401-7), Shell and the strategic importance of the support given by ANP (Brazil's National Oil, Natural Gas and Biofuels Agency) through the R&D levy regulation.

2.2.3 References

[1] a) T. Tsukamoto, T. Kambe, A. Nakao, T. Imaoka, K. Yamamoto, *Nat. Commun.* **2018**, *9*, 3873; b) H. Yang, Y. Wang, J. Yan, X. Chen, X. Zhang, H. Häkkinen, N. Zheng, *J. Am. Chem. Soc.*

2014, *136*, 7197-7200; c) H. Yang, Y. Wang, J. Lei, L. Shi, X. Wu, V. Mäkinen, S. Lin, Z. Tang, J. He, H. Häkkinen, L. Zheng, N. Zheng, *J. Am. Chem. Soc.* **2013**, *135*, 9568-9571; d) W. Kurashige, K. Munakata, K. Nobusada, Y. Negishi, *Chem. Commun.* **2013**, *49*, 5447-5449; e) H. Qian, D.-e. Jiang, G. Li, C. Gayathri, A. Das, R. R. Gil, R. Jin, *J. Am. Chem. Soc.* **2012**, *134*, 16159-16162; f) S. Gonzalez-Gallardo, T. Bollermann, R. A. Fischer, R. Murugavel, *Chem. Rev.* **2012**, *112*, 3136-3170; g) Y. Negishi, T. Iwai, M. Ide, *Chem. Commun.* **2010**, *46*, 4713-4715; h) E. G. Mednikov, M. C. Jewell, L. F. Dahl, *J. Am. Chem. Soc.* **2007**, *129*, 11619-11630.

[2] a) K. Mayer, J. Weßing, T. F. Fässler, R. A. Fischer, *Angew. Chem. Int. Ed.* **2018**, *57*, 14372-14393; b) W.-T. Chang, P.-Y. Lee, J.-H. Liao, K. K. Chakrahari, S. Kahlal, Y.-C. Liu, M.-H. Chiang, J.-Y. Saillard, C. W. Liu, *Angew. Chem. Int. Ed.* **2017**, *56*, 10178-10182; c) T. Steinke, C. Gemel, M. Cokoja, M. Winter, R. A. Fischer, *Angew. Chem. Int. Ed.* **2004**, *43*, 2299-2302; d) P. Jutzi, B. Neumann, L. O. Schebaum, A. Stammler, H.-G. Stammler, *Organometallics* **1999**, *18*, 4462-4464.

[3] a) P. Heiß, J. Hornung, C. Gemel, R. A. Fischer, *Chem. Commun.* **2022**; b) F. Pan, S. Wei, L. Guggolz, A. R. Eulenstein, F. Tambornino, S. Dehnen, *J. Am. Chem. Soc.* **2021**, *143*, 7176-7188; c) F. Pan, M. Lukanowski, F. Weigend, S. Dehnen, *Angew. Chem. Int. Ed.* **2021**, *60*, 25042-25047; d) S. Mitzinger, L. Broeckert, W. Massa, F. Weigend, S. Dehnen, *Nat. Commun.* **2016**, *7*, 10480.

- [4] M. Schütz, C. Gemel, M. Muhr, C. Jandl, S. Kahlal, J.-Y. Saillard, R. A. Fischer, *Chem. Sci.* **2021**, *12*, 6588-6599.
- [5] M. Muhr, P. Heiß, M. Schütz, R. Bühler, C. Gemel, M. H. Linden, H. B. Linden, R. A. Fischer, *Dalton Trans.* **2021**, *50*, 9031-9036.
- [6] a) T. M. Schaub, C. L. Hendrickson, J. P. Quinn, R. P. Rodgers, A. G. Marshall, *Anal. Chem.* **2005**, *77*, 1317-1324; b) C. E. Heine, M. M. Geddes, *Org. Mass Spectrom.* **1994**, *29*, 277-282.
- [7] a) L. Zibordi-Besse, P. Tereshchuk, A. S. Chaves, J. L. F. Da Silva, *J. Phys. Chem. A* **2016**, *120*, 4231-4240; b) A. S. Chaves, M. J. Piotrowski, J. L. F. Da Silva, *Phys. Chem. Chem. Phys.* **2017**, *19*, 15484-15502.
- [8] a) M. Muhr, J. Hornung, J. Weßing, C. Jandl, C. Gemel, R. A. Fischer, *Inorg. Chem.* **2020**, *59*, 5086-5092; b) T. Cadenbach, C. Gemel, R. Schmid, M. Halbherr, K. Yusenko, M. Cokoja, R. A. Fischer, *Angew. Chem. Int. Ed.* **2009**, *48*, 3872-3876; c) V. Ritleng, C. Barth, E. Brenner, S. Milosevic, M. J. Chetcuti, *Organometallics* **2008**, *27*, 4223-4228; d) P. Jutzi, L. O. Schebaum, *J. Organomet. Chem.* **2002**, *654*, 176-179.
- [9] E. E. Bunel, L. Valle, N. L. Jones, P. J. Carroll, C. Barra, M. Gonzalez, N. Munoz, G. Visconti, A. Aizman, J. M. Manriquez, *J. Am. Chem. Soc.* **1988**, *110*, 6596-6598.
- [10] J. Mink, L. Staiger, M. Muhr, C. Gemel, M. Drees, L. Hajba, J. Mihály, C. Németh, B. V. Lokshin, K. Hemmer, M. Schütz, M. Cokoja, R. A. Fischer, *J. Raman Spectrosc.* **2021**, *52*, 2317-2337.
- [11] M. Molon, C. Gemel, P. Jerabek, L. Trombach, G. Frenking, R. A. Fischer, *Inorg. Chem.* **2014**, *53*, 10403-10411.
- [12] T. Bollermann, K. Freitag, C. Gemel, M. Molon, R. W. Seidel, M. von Hopffgarten, P. Jerabek, G. Frenking, R. A. Fischer, *Inorg. Chem.* **2011**, *50*, 10486-10492.
- [13] B. Buchin, C. Gemel, A. Kempter, T. Cadenbach, R. A. Fischer, *Inorg. Chim. Acta* **2006**, *359*, 4833 - 4839.
- [14] a) T. Cadenbach, C. Gemel, R. Schmid, S. Block, R. A. Fischer, *Dalton Trans.* **2004**, 3171-3172; b) T. Cadenbach, C. Gemel, R. Schmid, R. A. Fischer, *J. Am. Chem. Soc.* **2005**, *127*, 17068-17078.
- [15] E. Roduner, *Phys. Chem. Chem. Phys.* **2018**, *20*, 23812-23826.
- [16] a) S.-D. Bian, H.-B. Wu, Q.-M. Wang, *Angew. Chem. Int. Ed.* **2009**, *48*, 5363-5365; b) X.-K. Wan, X.-L. Cheng, Q. Tang, Y.-Z. Han, G. Hu, D.-e. Jiang, Q.-M. Wang, *J. Am. Chem. Soc.* **2017**, *139*, 9451-9454; c) M.-M. Zhang, X.-Y. Dong, Z.-Y. Wang, H.-Y. Li, S.-J. Li, X. Zhao, S.-Q. Zang, *Angew. Chem. Int. Ed.* **2020**, *59*, 10052-1005.

2.2.4 Additional Data and Information

Synthesis procedures

Synthesis of **1A** – major component (**3**). $[\text{Ni}(\text{cod})_2]$ (500 mg, 1.181 mmol) was suspended in toluene (5 ml) and $\text{Ga}(\text{C}_5\text{Me}_5)$ (435 mg, 2.122 mmol) was added at room temperature. The dark solution was heated to 65 °C for 2 days. Upon slow cooling to room temperature, a black solid (200 mg) was obtained, which was extracted with 16 ml of hot (100 °C) mesitylene. The hot mesitylene solution was concentrated under reduced pressure and analytically pure single crystals of **1A** were obtained upon slow cooling to room-temperature, isolated by means of canula filtration and dried under reduced pressure to yield **1A** as black crystalline solid (155 mg).

Synthesis of **1B** – major component (**2**). * $\text{Ga}(\text{C}_5\text{Me}_5)$ (482 mg, 1.07 mmol) was added to a solution of $[\text{Ni}(\text{GaC}_5\text{Me}_5)(\text{dvds})]$ (290 mg, 1.42 mmol) in toluene (2 mL). After heating the dark red reaction solution to 110 °C for 3 h, the hot solution was filtered via a canula. The solution was allowed to cool to ambient temperature overnight and a black precipitate was formed. This was separated from the reaction solution by means of canula filtration. The residue was washed with small amounts of cold *n*-hexane and dried under reduced pressure, to yield **1B** as black crystalline solid (60.8 mg). **The synthesis can be performed also with $[\text{Ni}_2(\text{dvds})_3]$ instead of $[\text{Ni}(\text{GaC}_5\text{Me}_5)(\text{dvds})]$, while the Ni/Ga ratio is kept constant. Work up, yield, and spectroscopic results are identical.*

General Procedure for Reactions with CO. 10 mg of **1A** or **1B** were dissolved in 0.4 mL toluene- d_8 in a high-pressure J-Young NMR tube. The reaction mixture was pressurized with 1.0 bar CO at 25°C for 2 h. LIFDI-MS analysis, 0.1 ml of the reaction mixture was diluted with 0.2 mL toluene. For IR measurements, the reaction mixture dropped on the IR instrument and the solvent was evaporated.

Detail on Density Functional Theory Calculations

Part I (Screening): Our total energy calculations were based on spin-polarized density functional theory (DFT) within the semilocal exchange-correlation energy functional proposed by Perdew–Burke–Ernzerhof (PBE).^[S1] The Kohn–Sham (KS) orbitals, which are required to solve the KS equations, were described by numeric atom-centered orbitals (NAO), as implemented in the all-electron Fritz–Haber Institute ab initio molecular simulations (FHI-aims) package.^[S2] As provided within the FHI-aims package, we employed a minimal NAO basis set with a set of additional NAO added hierarchically up to the second basis set improvement, called light-tier2 in FHI-aims notation. For the relativistic corrections, we employed the scalar-relativistic framework with zero-order regular approximation (ZORA).^[S3] Thus, the present framework, provides great flexibility to screen large number of complex trial configurations (geometric optimizations), which is required in the present study. For the self-consistency solution of the KS equations, we employed a total energy criterion of 10⁻⁵ eV, while the equilibrium geometries were obtained once the atomic forces were smaller than 10⁻² eV Å⁻¹.

For the vibrational frequency calculations, we decreased the forces criteria for 10^{-4} eV \AA^{-1} to calculate the Hessian matrix elements using atomic displacements of 2.5×10^{-3} \AA . To avoid fractional occupation of the highest occupied molecular orbitals (HOMO) and lowest unoccupied molecular orbitals (LUMO), we employed a Gaussian broadening of 1 meV.

Part II (Bonding analysis): Density Functional Theory (DFT) calculations^[S8] were carried out with the use of the Amsterdam Density Functional code (ADF2017)[S9] with the addition of Grimme's D3 empirical corrections^[S10] in order to consider dispersion effects. The triple- ξ Slater basis set plus two polarization functions (STO-TZP),^[S11] was used, together with the Becke-Perdew (BP86)^[S12-13] exchange-correlation functional. All the optimized structures were confirmed as true minima on their potential energy surface by analytical vibration frequency calculations. The NMR chemical shifts were computed according to the gauge-independent atomic orbitals (GIAO) method,^[S14] assuming the Zero Order Regular Approximation (ZORA) for clusters with $S = 1/2$.^[S15]

NMR MAS Spectroscopy

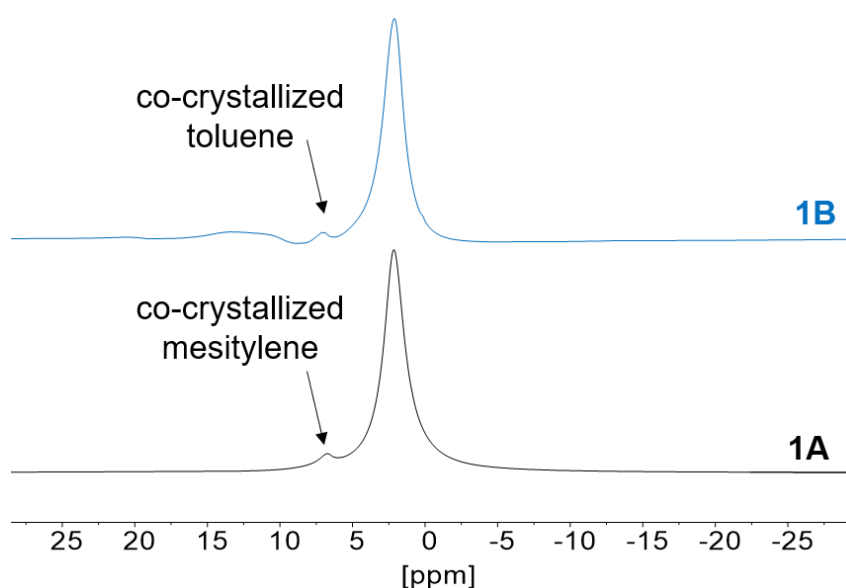


Figure S1: ^1H MAS NMR spectra of **1A** (3 major component) and **1B** (2 major component) showing a broad signal at 2.15 ppm assigned to the Cp^* shell. δ [ppm] = 6.71 (mesitylene, CH), 2.04 (s, Cp^*).

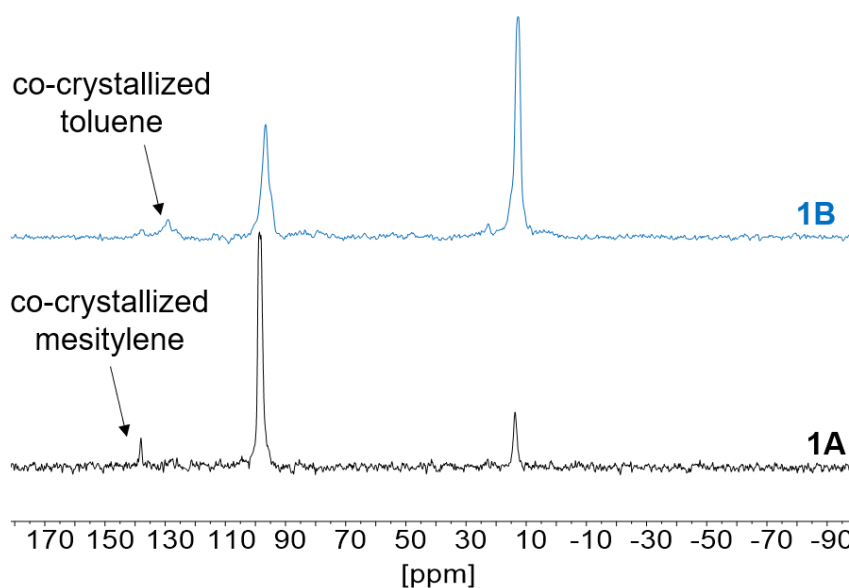


Figure S2: ^{13}C MAS NMR spectra of **1A** (3 major component) and **1B** (2 major component). Top, blue ^{13}C NMR: δ = 129.0 (toluene, ArC), 96.9 (Cp^* , ring), 12.3 (Cp^* , CH_3) ppm. Bottom, black ^{13}C NMR: δ = 138.1 (mesitylene, ArC), 98.7 (Cp^* , ring), 13.7 (Cp^* , CH_3) ppm. The ^{13}C Cp^* ring shifts fit well to shifts of the NiCp^* signals of $[(\mu_2\text{-Ga}(\text{C}_5\text{Me}_5))(\text{Ni}_2)(\mu_2\text{-GaNi}(\text{C}_5\text{Me}_5))_2(\text{dvds})_2]$ (Figure S3). Despite the paramagnetism of **3** (**1A** major component) shifts of **2** and **3** are very similar and in a common range. This phenomena has been observed before for bigger metal clusters, like for the polyradical cluster $[\text{Cu}_{43}\text{Al}_{12}](\text{Cp}^*)_{12}$.

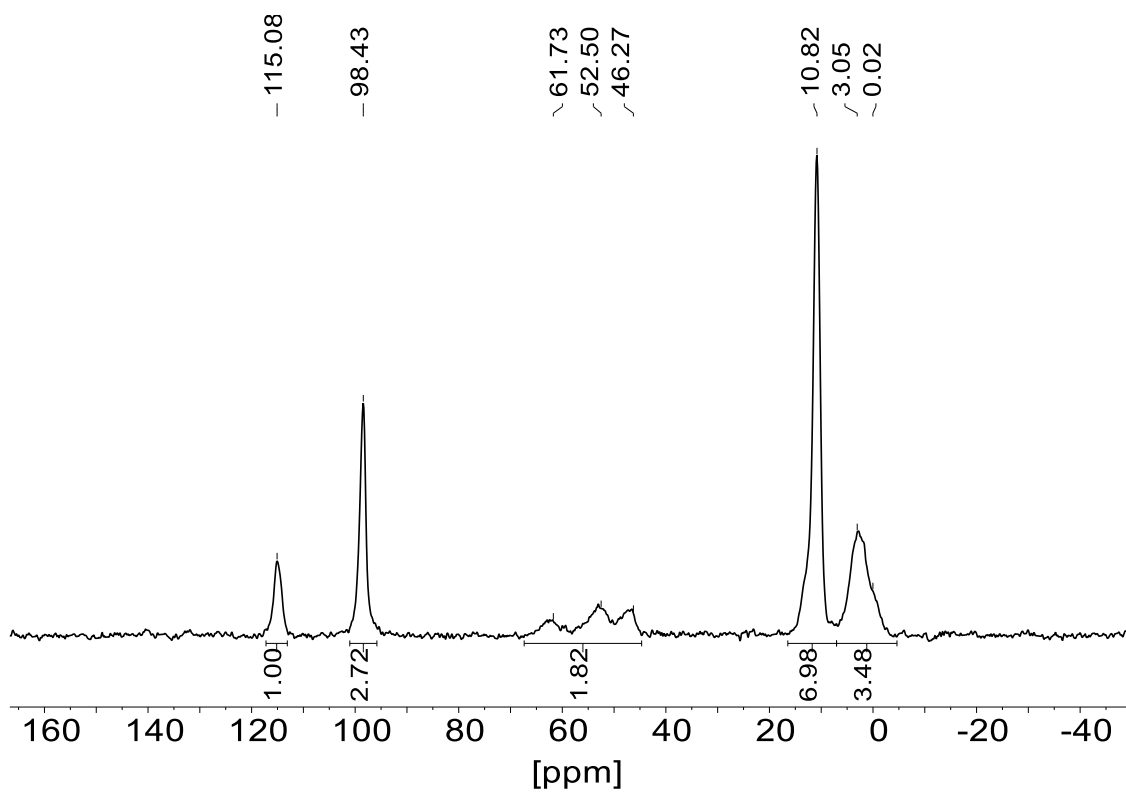


Figure S3: ^{13}C MAS NMR spectra of $[(\mu_2\text{-Ga}(\text{C}_5\text{Me}_5))(\text{Ni}_2)(\mu_2\text{-GaNi}(\text{C}_5\text{Me}_5)_2(\text{dvds})_2)]$. ^{13}C NMR: $\delta = 115.08$ (GaCp*, ring), 98.43 (NiCp*, ring), 61.73 – 46.27 (dvds, HC=CH₂), 10.82 (Cp*, CH₃), 3.05 – 0.02 (dvds, CH₃) ppm.

NMR Spectroscopy in Solution

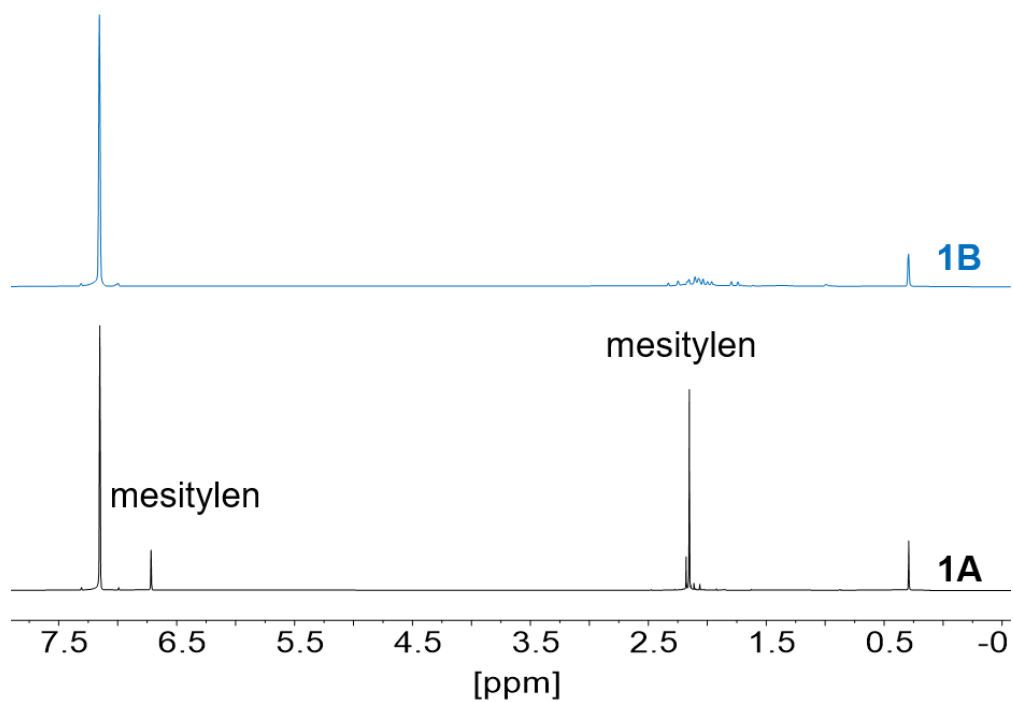


Figure S4: ^1H NMR in toluene- d_8 for **1A** (3 major component) and **1B** (2 major component). For **1B**, residual signals of DVDs are apparent. For both mixtures, no cluster signals are detected due to its bad solubility.

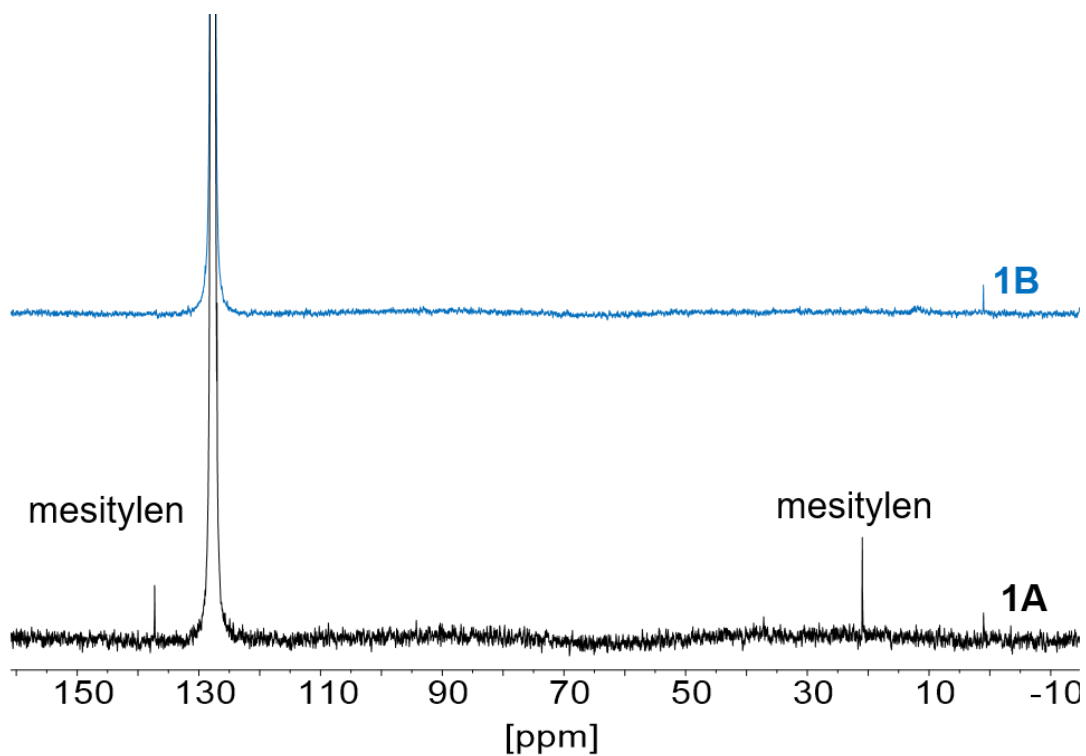


Figure S5: ^{13}C NMR in toluene- d_8 for **1A** (3 major component) and **1B** (2 major component). For both mixtures, no cluster signals are detected due to its bad solubility.

Infrared Spectroscopy

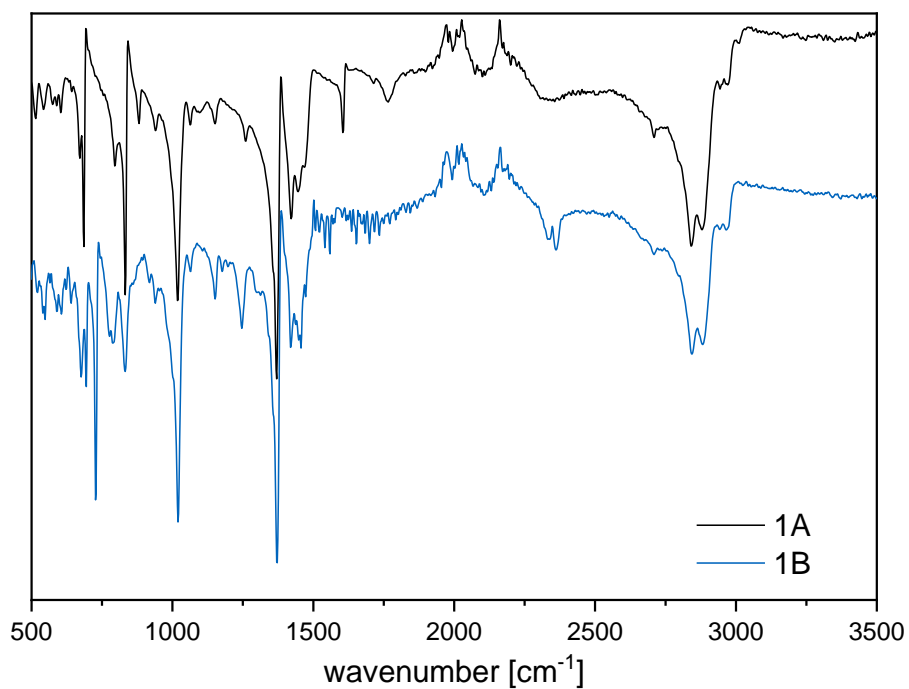


Figure S6: FT-ATR-IR spectra of **1A** (3 major component) and **1B** (2 major component). IR (ATR, neat, cm^{-1}): 2968, 2881, 2843, 2705, 1460, 1422, 1372, 1022, 728, 1153, 1072, 947, 797, 696, 671, 596, 546, 465.

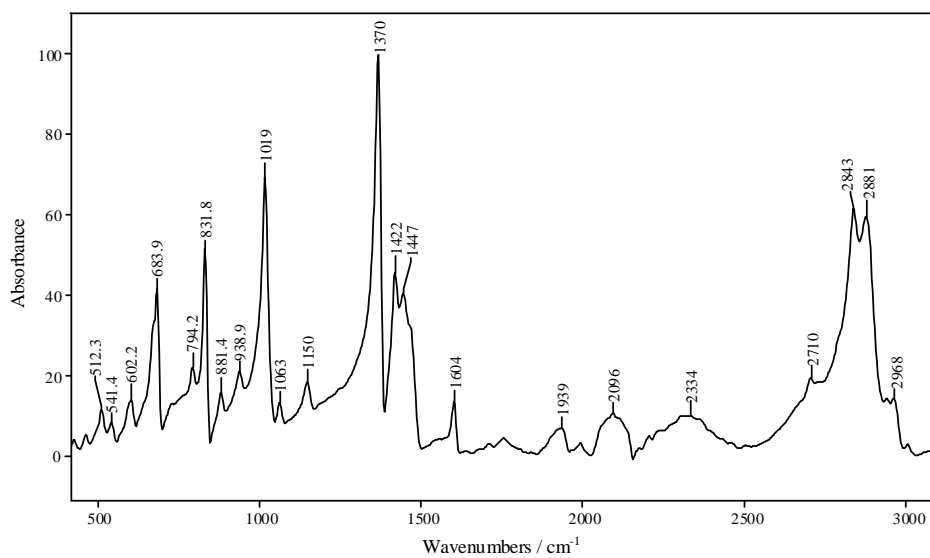


Figure S7: Mid-infrared ATR spectrum of solid **1A** (3 major component) sample without ATR correction. The band intensities are normalized to the strongest band at 1370 cm^{-1} , taken as 100 arbitrary intensity units. (The experimentally recorded intensity of this band was 0.14 absorbance units).

Raman Spectroscopy

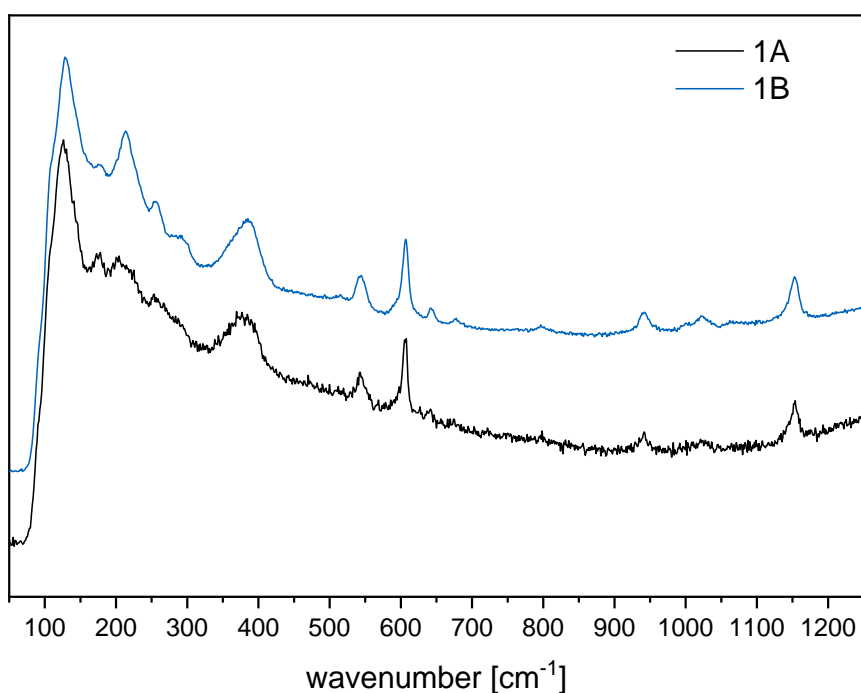


Figure S8: Raman spectra of **1A** (3 major component) and **1B** (2 major component).

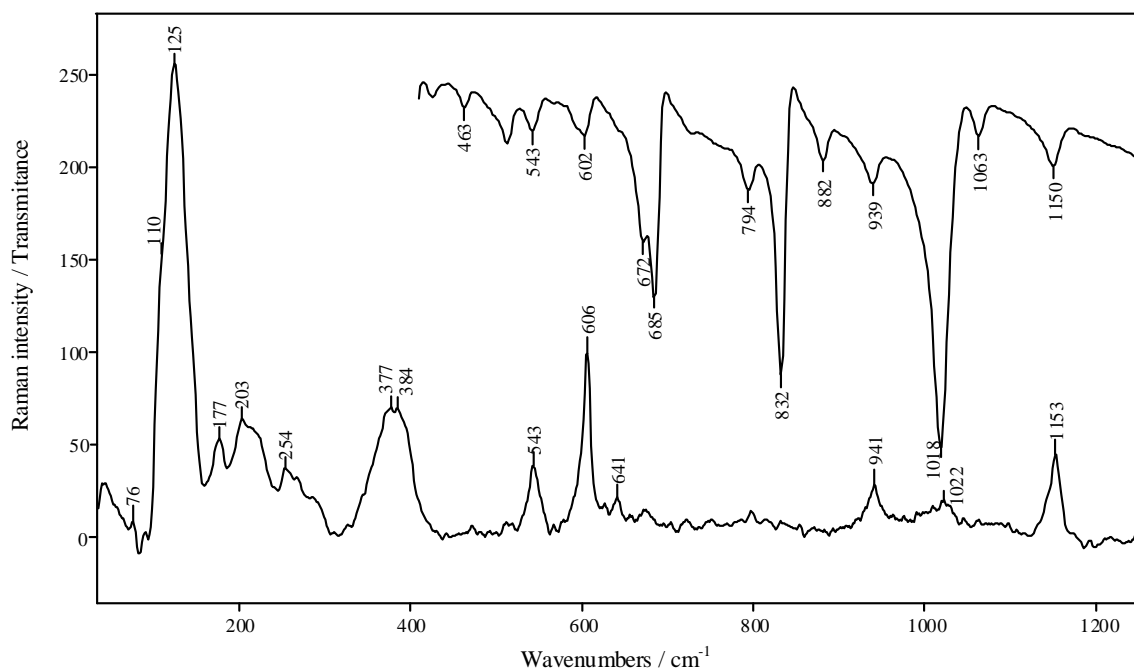


Figure S9: Mid-infrared ATR spectrum (upper trace) of solid **1A** (3 major component) without ATR correction and Raman spectrum (lower trace). The IR band intensities are normalized to the strongest band at 1370 cm⁻¹, taken as 100 arbitrary intensity units. Raman band intensities are normalized to the strong band at 606 cm⁻¹, taken as 100 intensity units.

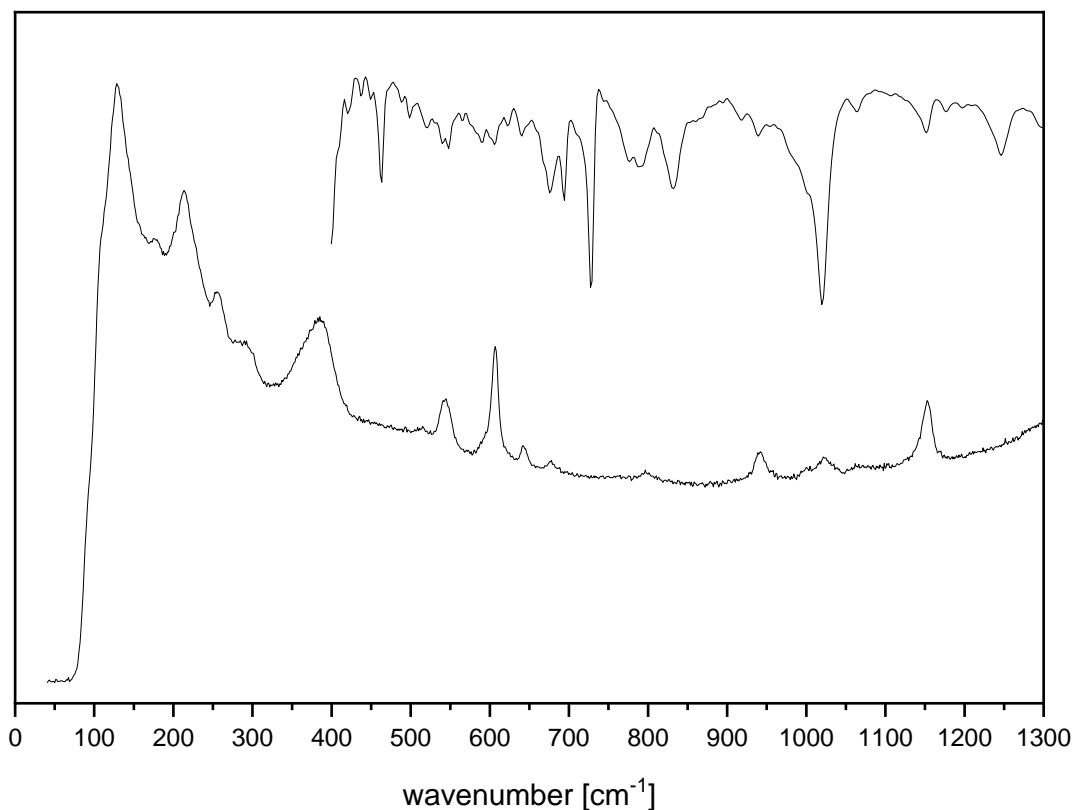


Figure S10: Mid-infrared ATR spectrum (upper trace) of solid **1B** (2 major component) without ATR correction and Raman spectrum (lower trace).

Table S1: Experimental infrared and Raman frequencies (cm^{-1}) and their tentative assignments for **1A**. Relative band intensities are in brackets; Selected bands for 100 intensity units; Abbreviation of weak bands and band shapes; w, weak; vw, very weak; b, broad; sh, shoulder.

Infrared	Raman	Suggested assignments and their notations
3011(3) ^a		
2968(15) 2945(15)		CH ₃ asym stretch ($n_a\text{CH}_3$)
2881(60) 2843(63)		CH ₃ sym stretch ($n_s\text{CH}_3$)
2797(33)sh 2736(24)sh 2709(26) 2365(4) 1759(6)		Combination bands and overtones 2 x 1370 (2 x $d_s\text{CH}_3$)
1605(15)		
1468(30) 1447(39)		CH ₃ asym deform ($d_a\text{CH}_3$)
1422(49)		$n_1(A_1)$ ^b ring sym CC stretch and C-Me stretch ($n_s\text{CC}$) $n_6(E_1)$ $n_a\text{CC}$ ring
1370(100) ^c		CH ₃ sym deform umbrella ($d_a\text{CH}_3$); $n_{11}(E_2)$ ring CC asym stretch + C-Me asym stretch
1247vw ^d		

1150(16)	1153(44) 1134w,sh	$n_{12}(E_2)$ (?)
1063(10)	1061(4) 1046(5)	$n_{12}(E_2)$ ring CC stretch + C-Me stretch + CH_3 rocking (rCH_3)
1019(63) 990 w,sh 939(19)	1022(20) 991(5) 941(38)	CH_3 rocking (rCH_3)
882(15) 860w,sh	871(5), b 854(7)	$n_7(E_1)$ (?)
832(53)	832(5) 815(5)	$n_7(E_1)$ ring CC asym stretch (n_aCC)
794(30) 758w,b 726w,sh	798(14) 750(4) 723(9) 704(5)	
685(40) 672(30)	674(15)	$n_{16}(E_2)$ ring in plane deform (dCCC)
626w,sh 603(11)	627(15) 606(100) ^c	$n_2(A_1)$ ring CC sym stretch (n_sCC)
593w,sh 567vw	590(30)sh 567(8)	
543(10) 513(12)	543(38) 515(7)	$n_5(A_2)$ C-Me in plane deform (bCMe)
497w,sh	492(3)	
463(4)	472(6) 462w,sh 442(3) 430(4)	$n_{14}(E_2)$ ring CCC in plane deform (dCCC)
	384(70)	$n_4(A_1)$ Ni-Cp* sym stretch (n_s Ni-Cp*)
	286(31) 267(30) 253(37)	$n_{10}(E_1)$ Ni-Cp* asym stretch (tilt mode) (n_a Ni-Cp*)
	217(53)sh 203(64)	$n_3(A_1)$ C-Me out of plane deform (gCMe) $n_8(E_1)$ C-Me in plane deform (bCMe)
	177(53)	$n_{13}(E_2)$ C-Me in plane deform (bCMe)
	126(250)	$n_9(E_1)$ C-Me out of plane deform (gCMe)
	110(150)sh	$n_{15}(E_2)$ C-Me oop deform (gCMe)
	177(53) 177 (250) 110(150)sh	Ni-Ga, Ga-Ga stretching modes
	90(3) 76(7) 43(3)	Cluster skeletal deformations and lattice modes

LIFDI Mass Spectra

Isolated clusters

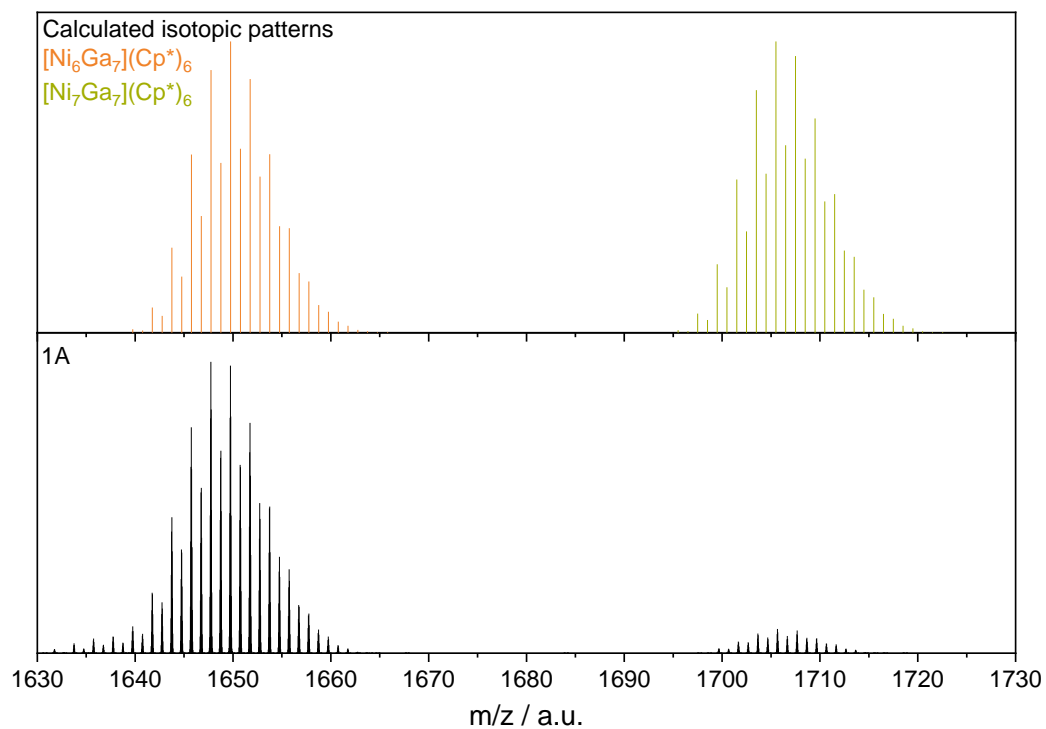


Figure S11: Relevant cut out of LIFDI mass spectra of cluster mixtures **1A** (3 major component) exhibiting molecular ion signals of $[\text{Ni}_6\text{Ga}_7](\text{Cp}^*)_6$ (orange) and $[\text{Ni}_7\text{Ga}_7](\text{Cp}^*)_6$ (green).

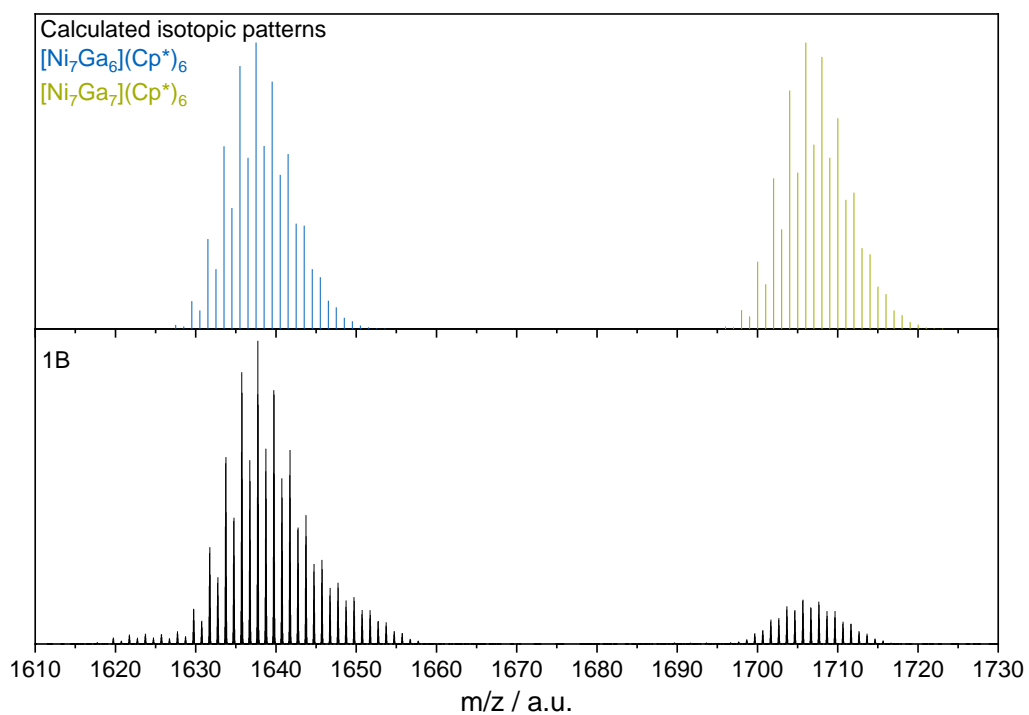


Figure S12: Relevant cut out of LIFDI mass spectra of cluster mixtures **1B** (2 major component) exhibiting molecular ion signals of $[\text{Ni}_7\text{Ga}_6](\text{Cp}^*)_6$ (blue) and $[\text{Ni}_7\text{Ga}_7](\text{Cp}^*)_6$ (green).

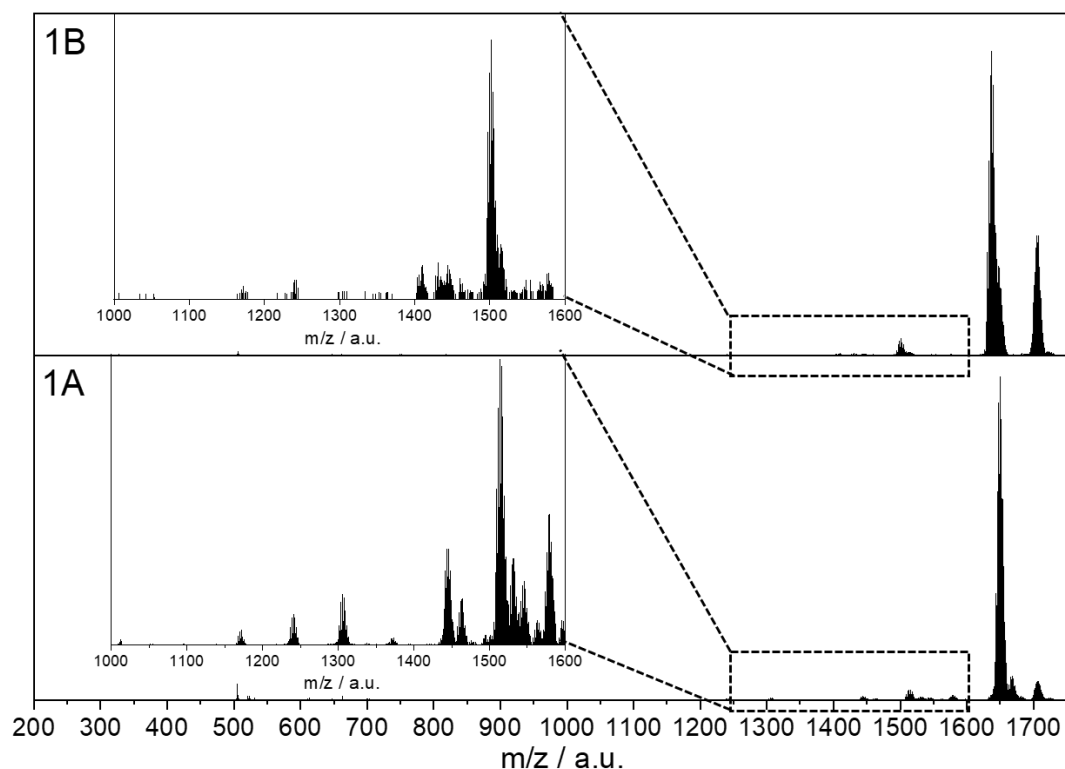


Figure S13: Full LIFDI mass spectra of cluster mixtures **1A** (major component **3**, bottom) and **1B** (major component **2**, top). $m/z = 1639.5$ ($[\text{Ni}_7\text{Ga}_6\text{Cp}^*_6]^+$, calc. 1638.6), 1649.3 ($[\text{Ni}_6\text{Ga}_7\text{Cp}^*_6]^+$, calc. 1650.3), 1706.7 ($[\text{Ni}_7\text{Ga}_7\text{Cp}^*_6]^+$, calc. 1706.7) with zoom-in for a better depiction of signals < 1400 m/z .

Table S2: Measured clusters and related mass shifts by H-atom and C_5Me_5 fragmentation including reactivity tests.

Measured m/z	Measured cluster	Attributed cluster
328.1694	$[\text{Ni}(\text{C}_5\text{Me}_5)_2]^+$	$[\text{Ni}(\text{C}_5\text{Me}_5)_2]$
750.2112	$[(\text{Ni}_7\text{Ga}_6)(\text{C}_5\text{Me}_5)_5]^{2+} - 3\text{H}$	$[(\text{Ni}_7\text{Ga}_6)(\text{C}_5\text{Me}_5)_6]$
819.3131	$[(\text{Ni}_7\text{Ga}_6)(\text{C}_5\text{Me}_5)_6]^{2+} - 2\text{H}$	$[(\text{Ni}_7\text{Ga}_6)(\text{C}_5\text{Me}_5)_6]$
877.3982	$[\text{Ni}_4\text{Ga}_3(\text{C}_5\text{Me}_5)_3(\text{CO})]^+$	$[\text{Ni}_4\text{Ga}_3(\text{C}_5\text{Me}_5)_3(\text{CO})]$
933.4577	$[\text{Ni}_3\text{Ga}_4(\text{C}_5\text{Me}_5)_3(\text{CO})_3]^+$	$[\text{Ni}_3\text{Ga}_4(\text{C}_5\text{Me}_5)_3(\text{CO})_3]$
989.2956	$[\text{Ni}_4\text{Ga}_3(\text{C}_5\text{Me}_5)_3(\text{CO})_5]^+$	$[\text{Ni}_4\text{Ga}_3(\text{C}_5\text{Me}_5)_3(\text{CO})_5]$
1166.6057	$[\text{Ni}_4\text{Ga}_4(\text{C}_5\text{Me}_5)_4(\text{CO})_4]^+$	$[\text{Ni}_4\text{Ga}_4(\text{C}_5\text{Me}_5)_4(\text{CO})_4]$
1194.5725	$[\text{Ni}_4\text{Ga}_4(\text{C}_5\text{Me}_5)_4(\text{CO})_5]^+$	$[\text{Ni}_4\text{Ga}_4(\text{C}_5\text{Me}_5)_4(\text{CO})_5]$
1237.3485	$[\text{Ni}_6\text{Ga}_5(\text{C}_5\text{Me}_5)_4]^+ - 3\text{H}$	$[\text{Ni}_6\text{Ga}_5(\text{C}_5\text{Me}_5)_6]$
1306.3661	$[\text{Ni}_6\text{Ga}_6(\text{C}_5\text{Me}_5)_4]^+ - 4\text{H}$	$[\text{Ni}_6\text{Ga}_6(\text{C}_5\text{Me}_5)_6]$
1444.0381	$[\text{Ni}_6\text{Ga}_6(\text{C}_5\text{Me}_5)_5]^+ - \text{H}$	$[\text{Ni}_6\text{Ga}_6(\text{C}_5\text{Me}_5)_6]$
1503.0914	$[\text{Ni}_7\text{Ga}_6(\text{C}_5\text{Me}_5)_5]^+ - 3\text{H}$	$[\text{Ni}_7\text{Ga}_6(\text{C}_5\text{Me}_5)_6]$
1513.9057	$[\text{Ni}_6\text{Ga}_7(\text{C}_5\text{Me}_5)_5]^+ - 2\text{H}$	$[\text{Ni}_6\text{Ga}_7(\text{C}_5\text{Me}_5)_6]$
1568.9456	$[(\text{NiGa}_5)(\text{NiC}_5\text{Me}_5)_6]^+ - 3\text{H}$	$[(\text{NiGa}_5)(\text{NiC}_5\text{Me}_5)_6]$
1579.3361	$[(\text{Ga}_6)(\text{NiC}_5\text{Me}_5)_6]^+ - 2\text{H}$	$[(\text{Ga}_6)(\text{NiC}_5\text{Me}_5)_6]$
1639.5566	$[(\text{NiGa}_6)(\text{NiC}_5\text{Me}_5)_6]^+ - 2\text{H}$	$[(\text{NiGa}_6)(\text{NiC}_5\text{Me}_5)_6]$
1649.3240	$[(\text{Ga}_7)(\text{NiC}_5\text{Me}_5)_6]^+ - \text{H}$	$[(\text{Ga}_7)(\text{NiC}_5\text{Me}_5)_6]$
1706.7280	$[(\text{NiGa}_7)(\text{NiC}_5\text{Me}_5)_6]^+ - 3\text{H}$	$[(\text{NiGa}_7)(\text{NiC}_5\text{Me}_5)_6]$
1707-1720	$[(\text{NiGa}_7)(\text{NiC}_5\text{Me}_5)_6\text{H}_x]^+$	$[(\text{NiGa}_7)(\text{NiC}_5\text{Me}_5)_6\text{H}_x]$
1736.3855	$[(\text{OC})(\text{NiGa}_7)(\text{NiC}_5\text{Me}_5)_6]^+ - \text{H}$	$[(\text{OC})(\text{NiGa}_7)(\text{NiC}_5\text{Me}_5)_6]$

Table S3: Tabular pattern of $[\text{Ni}(\text{C}_5\text{Me}_5)_2]$.

m/z	relative intensity
327,15701	37.93278
328,16404	100
329,16723	19.61349
330,15796	36.38609
331,1646	7.58823

Table S4: Tabular pattern of $[(\text{Ni}_7\text{Ga}_6)(\text{C}_5\text{Me}_5)_5]^{2+}$.

m/z	relative intensity
745,80136	17.28214
746,30392	7.71162
746,80698	37.57649
747,31055	20.74337
747,81464	58.15704
748,31923	29.88889
748,81461	79.66233
749,32022	49.39291
749,82633	95.72439
750,32322	55.73508
750,82059	100
751,31846	54.4833
751,8266	78.69696
752,32548	41.59237
752,82484	47.76618
753,32471	20.88495
753,82507	25.83276
754,32594	7.04958
754,81746	6.00376

Table S5: Tabular pattern of $[(\text{Ni}_7\text{Ga}_6)(\text{C}_5\text{Me}_5)_6]^{2+}$.

m/z	relative intensity
816,89204	50.69447
817,39056	23.0507
817,88954	77.38423
818,38898	37.35102
818,88887	100
819,38922	52.53035
819,89003	81.15509
820,3913	48.33168
820,89303	54.86947
821,38405	24.85441

821,88669	20.98484
822,3898	6.66308
822,88216	10.80773

Table S6: Tabular pattern of $[Ni_4Ga_3(C_5Me_5)_3(CO)]^+$.

m/z	relative intensity
873,85517	58.76044
874,86066	16.6387
875,85558	100
876,86452	32.12259
877,85052	92.31414
878,86291	30.05687
879,85229	63.71766
880,85575	17.21035
881,8485	26.51345
873,85517	58.76044
874,86066	16.6387
875,85558	100
876,86452	32.12259
877,85052	92.31414
878,86291	30.05687
879,85229	63.71766
880,85575	17.21035
881,8485	26.51345

Table S7: Tabular pattern of $[Ni_4Ga_3(C_5Me_5)_3(CO)]^+$.

m/z	relative intensity
927,85029	16.66429
928,85642	5.04295
929,85075	64.47679
930,86014	22.27274
931,8442	100
932,85684	37.42308
933,84407	97.40764
934,84642	36.92606
935,85038	58.68291
936,84236	23.04152
937,83592	28.04804
938,84471	10.69985
939,84145	10.1901
940,83979	5.1593

Table S8: Tabular pattern of $[Ni_4Ga_3(C_5Me_5)_3(CO)_5]^+$.

m/z	relative intensity
985,84822	60.61613
986,84725	17.13547
987,83308	100
988,83514	34.33648
989,83871	97.8972
990,84382	35.30131
991,83565	59.49191
992,82896	15.3932
993,83863	21.93666

Table S9: Tabular pattern of $[Ni_4Ga_4(C_5Me_5)_4(CO)_4]^+$.

m/z	relative intensity
1161,88361	45.36654
1162,89857	21.68904
1163,89602	86.79557
1164,89476	43.87516
1165,89479	100
1166,89611	49.3013
1167,87978	83.13031
1168,88366	39.98315
1169,88883	46.22334
1170,87629	21.47925
1171,88403	20.9447
1172,87402	9.101
1173,88435	7.35934

Table S10: Tabular pattern of $[Ni_4Ga_4(C_5Me_5)_4(CO)_5]^+$.

m/z	relative intensity
1189,87819	41.57827
1190,89107	19.46198
1191,88574	85.48513
1192,88165	41.27225
1193,87881	100
1194,87722	47.8827
1195,87688	79.99068
1196,8778	38.12319
1197,87998	46.5697
1198,88341	19.94846
1199,86839	18.99554

1200,87433	7.61123
1201,88153	5.51062

Table S11: Tabular pattern of $[(Ni_6Ga_5)(C_5Me_5)_4]^+$.

m/z	relative intensity
1231,64151	42.66806
1232,64663	13.85806
1233,65298	69.96209
1234,63998	34.84223
1235,64877	92.64551
1236,6588	50.97934
1237,64942	100
1238,6619	46.77776
1239,65492	82.11756
1240,64914	35.3182
1241,66531	46.75654
1242,66194	22.06385
1243,65978	21.8133
1577,56791	10.56862
1578,54904	5.18729

Table S12: Tabular pattern of $[(Ni_6Ga_5)(C_5Me_5)_4]$.

m/z	relative intensity
1299,55839	30.94977
1300,55881	15.95074
1301,56039	60.02883
1302,56313	32.42021
1303,56703	93.05909
1304,57209	50.80303
1305,57832	100
1306,5633	54.87798
1307,57183	91.3854
1308,55908	47.4851
1309,56992	70.09436
1310,55943	30.98551
1311,57259	38.86939
1312,56437	18.86574
1313,55727	17.742
1314,57391	6.85318
1315,5691	6.81482

Table S13: Tabular pattern of $[(Ni_6Ga_6)(C_5Me_5)_5]^+$.

m/z	relative intensity
1437,70467	18.6758
1438,71352	29.19795
1439,69753	55.74515
1440,70847	60.86807
1441,69452	85.80158
1442,70758	80.38935
1443,69568	100
1444,71084	80.60071
1445,70100	82.86013
1446,71828	63.09803
1447,71051	68.1918
1448,70376	36.56838
1449,69803	28.72266
1450,69332	8.96359
1451,68965	7.35914

Table S14: Tabular pattern of $[(Ni_7Ga_6)(C_5Me_5)_5]^+$.

m/z	relative intensity
1497,60857	29.69234
1498,59859	8.12387
1499,61714	36.13902
1500,63672	8.7817
1501,62974	41.27537
1502,62375	8.8802
1503,61875	39.21342
1504,64242	22.27703
1505,63942	100
1506,63741	28.44248

Table S15: Tabular pattern of $[(Ni_6Ga_7)(C_5Me_5)_5]^+$.

m/z	relative intensity
1507,6364	33.57786
1508,63638	22.04713
1509,63736	67.2132
1510,63933	40.5724
1511,6423	88.86922
1512,61837	53.44879
1513,62331	100
1514,62926	60.84805
1515,63621	83.02229

1516,61615	45.44515
1517,62508	59.89516
1518,63501	28.86777
1519,61786	31.09466
1520,62979	15.53685
1521,61458	11.94242

Table S16: Tabular pattern of [(NiGa₅)(NiC₅Me₅)₆].

m/z	relative intensity
1560,55985	9.20692
1561,55442	20.34585
1562,54993	36.94623
1563,5464	43.7215
1564,54382	66.67271
1565,5422	69.97564
1566,54153	86.48722
1567,54182	88.79004
1568,54307	100
1569,54528	91.27486
1570,54844	91.6635
1571,55257	78.68838
1572,55767	67.81736
1573,56373	49.88777
1574,54112	41.67222
1575,54908	27.38829
1576,55801	18.49319
1577,56791	10.56862
1578,54904	5.18729

Table S17: Tabular pattern of [(Ga₆)(NiC₅Me₅)₆].

m/z	relative intensity
1571,84759	31.24904
1572,85297	14.12468
1573,8297	43.56054
1574,86662	17.28074
1575,84523	80.36374
1576,85444	39.45797
1577,83491	100
1578,84603	56.47025
1579,85814	97.14968
1580,8414	56.72672
1581,82558	68.13657
1582,84055	37.02157
1583,8266	37.88993
1584,8435	9.67171

1585,83142	8.97115
------------	---------

Table S18: Tabular pattern of **1B**.

m/z	relative intensity
1629,73434	11.58002
1630,76454	7.67025
1631,76446	31.93859
1632,76529	21.99933
1633,76705	61.64393
1634,76972	41.65335
1635,74195	89.66781
1636,74644	60.61426
1637,75187	100
1638,75822	64.44706
1639,734	83.70823
1640,74218	54.66276
1641,75128	64.00252
1642,76132	38.40984
1643,74068	42.48728

Table S19: Tabular pattern of **1A**.

m/z	relative intensity
1639,74946	9.22273
1640,75765	6.6503
1641,73523	20.7523
1642,74526	17.4663
1643,75622	46.64255
1644,73648	35.59128
1645,74928	77.53418
1646,76301	56.74664
1647,74596	100
1648,76154	69.47934
1649,74628	98.72563
1650,7319	64.63276
1651,75025	79.04945
1652,73767	51.51337
1653,75787	50.32614
1654,74709	33.08134
1655,73719	28.79991
1656,72819	16.50902
1657,75209	13.61196
1658,74489	8.10834
1659,73859	5.67744

Table S20: Tabular pattern of [(NiGa₇)(NiC₅Me₅)₆].

m/z	relative intensity
1697,65659	5.28835
1698,65226	10.12338
1699,68203	23.98616
1700,67948	30.90347
1701,6778	55.1649
1702,67701	58.46905
1703,6771	85.18713
1704,67806	76.55479
1705,67991	100
1706,64921	82.74693
1707,65279	95.6326
1708,65727	74.27194
1709,66263	74.1018
1710,66887	50.20393
1711,67601	45.4295
1712,65042	29,08788
1713,65931	23.24051
1714,66909	12.0013
1715,64605	7.66613

Table S21: Tabular pattern of [(OC)(NiGa₇)(NiC₅Me₅)₆].

m/z	relative intensity
1729,71408	32.62559
1730,70393	18.98724
1731,69464	64.33649
1732,7204	37.52542
1733,71284	90.225
1734,70614	57.06226
1735,70028	100
1736,69528	58.90946
1737,69114	86.8921
1738,68785	49,3679
1739,68542	61.50577
1740,68385	31.82106
1741,68314	37.1474
1742,68329	16.39531
1743,68431	18.84153
1744,68618	7.55527
1745,65433	9.1702

Cluster mixtures

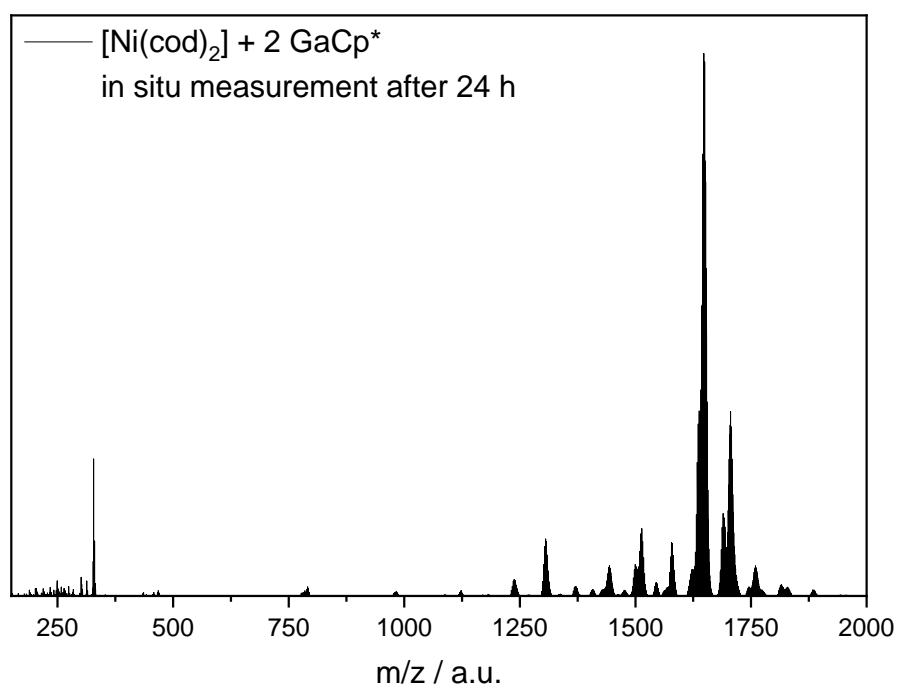


Figure S14: Full LIFDI mass spectra of the reaction mixture of 1.0 equiv. [Ni(cod)₂] and 2.0 equiv. GaCp* in toluene at 60 °C after 24 h (analog to the synthesis of **1A**) showing the similar signals compared to isolated crystals of **1A** (major component **3**) and some additional signals with lower and higher masses.

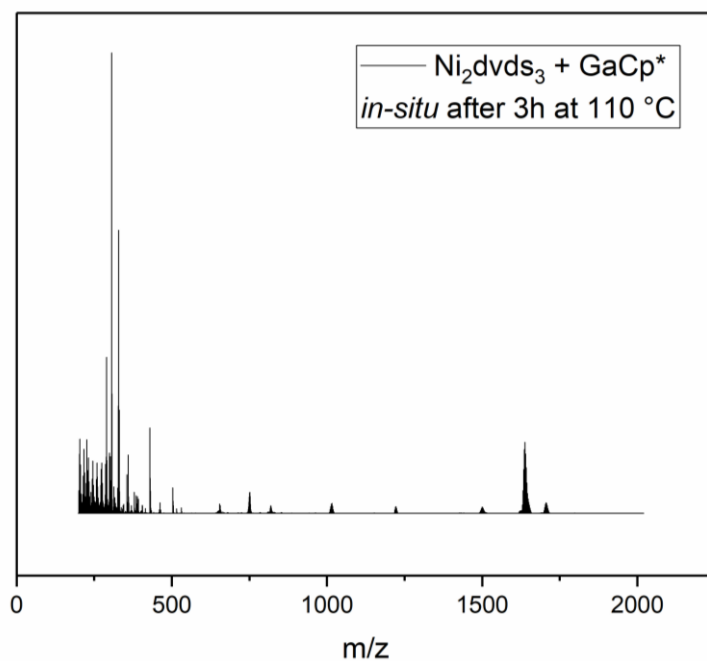


Figure S15: In-situ LIFDI-MS spectrum of the reaction of Ni₂dvds₃ and 2 eq GaCp* in toluene at 110 °C after 3 h. Similar signals compared to isolated crystals of **1B** (major component **2**) and some additional signals with lower masses are observed.

Labeling and Fragmentation Experiments

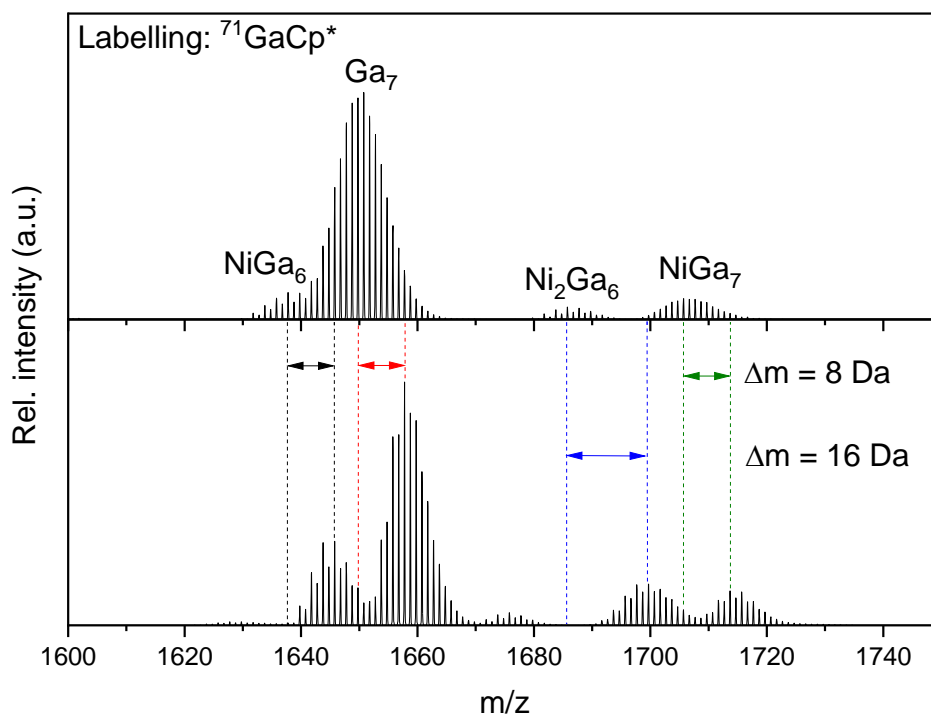


Figure S16: Cutout of the LIFDI MS spectrum of the labelling experiment - $\text{Ni}(\text{cod})_2$ (1.0 eq.) and $^{71}\text{GaCp}^*$ (1.0 eq.) in toluene at 60 °C for 24 h - showing a mass shift of $m/z = 8$ (top: LIFDI MS spectrum of GaCp^* supported cluster ensemble with natural abundance, bottom: LIFDI MS spectrum of ^{71}Ga -labelled ensemble). REMARK: The Ni_2Ga_6 cluster shows a higher shift of 16 Da due to its low concentration and enhanced fragmentation of the molecular ion; nevertheless, the observed and calculated pattern of the ^{71}Ga labelled species fits well.

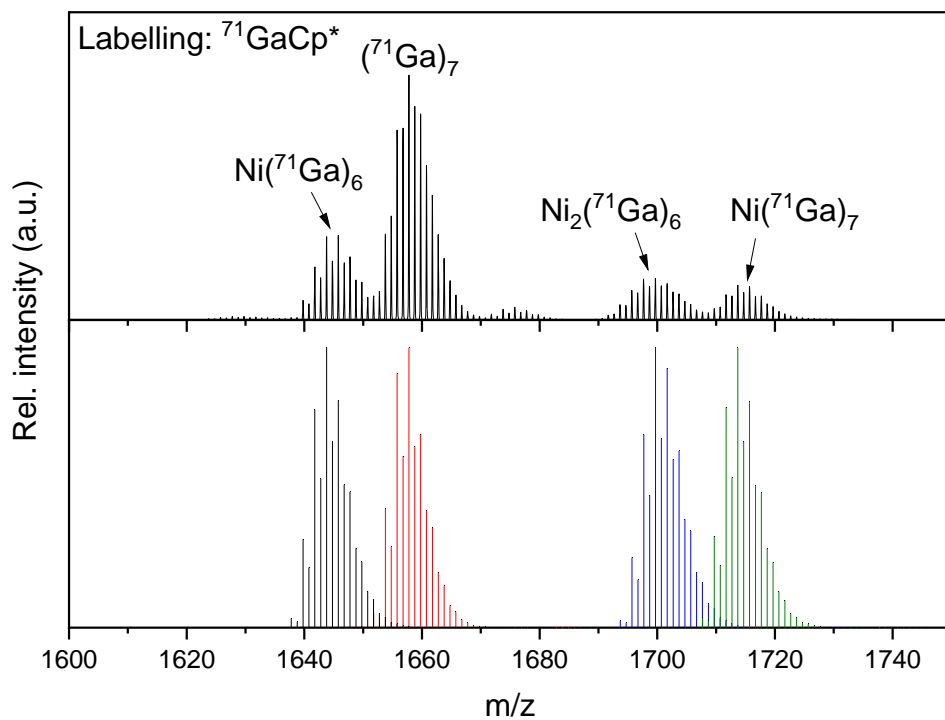


Figure S17: Comparison of measured (top) and calculated (bottom) isotopic patterns of $^{71}\text{GaCp}^*$ labelled cluster species obtained from $\text{Ni}(\text{cod})_2$ (1.0 eq.) and $^{71}\text{GaCp}^*$ (1.0 eq.) in toluene at 60 °C after 24 h.

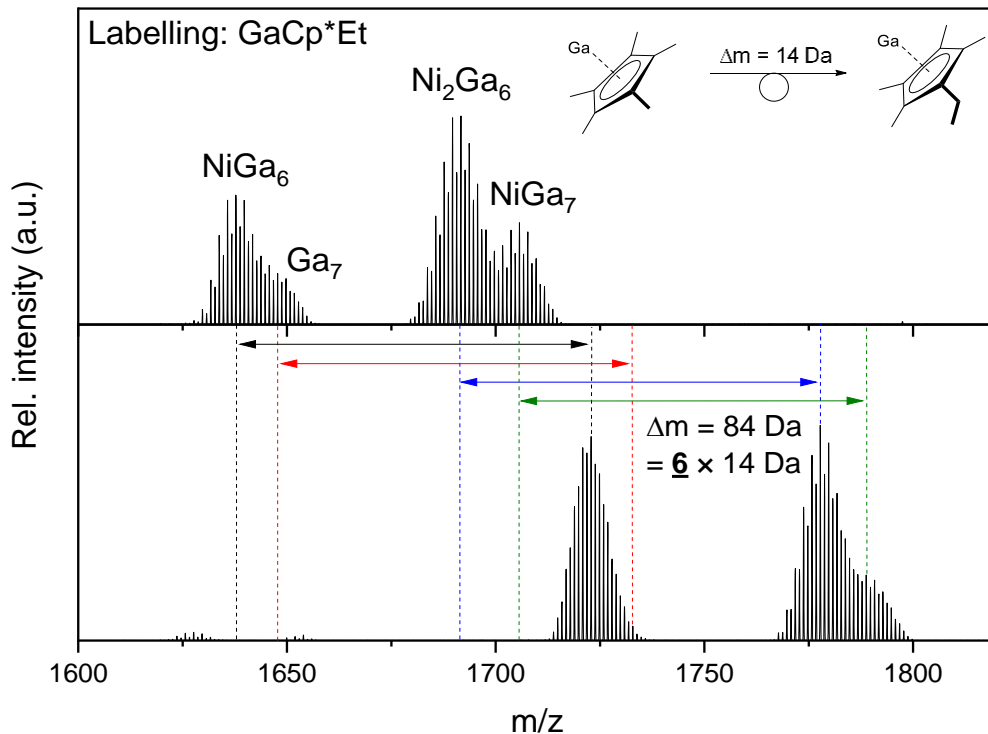


Figure S18: Comparison of Cp^* (top) and Cp^*Et supported cluster ensembles (bottom) generated from $\text{Ni}(\text{cdt})$ (1.0 eq.) and GaCp^* (1.0 eq.) in toluene at 110 °C (4 h); all Cp^*Et labelled cluster species show a mass shift of 84 Da indicating six Cp^* units per cluster.

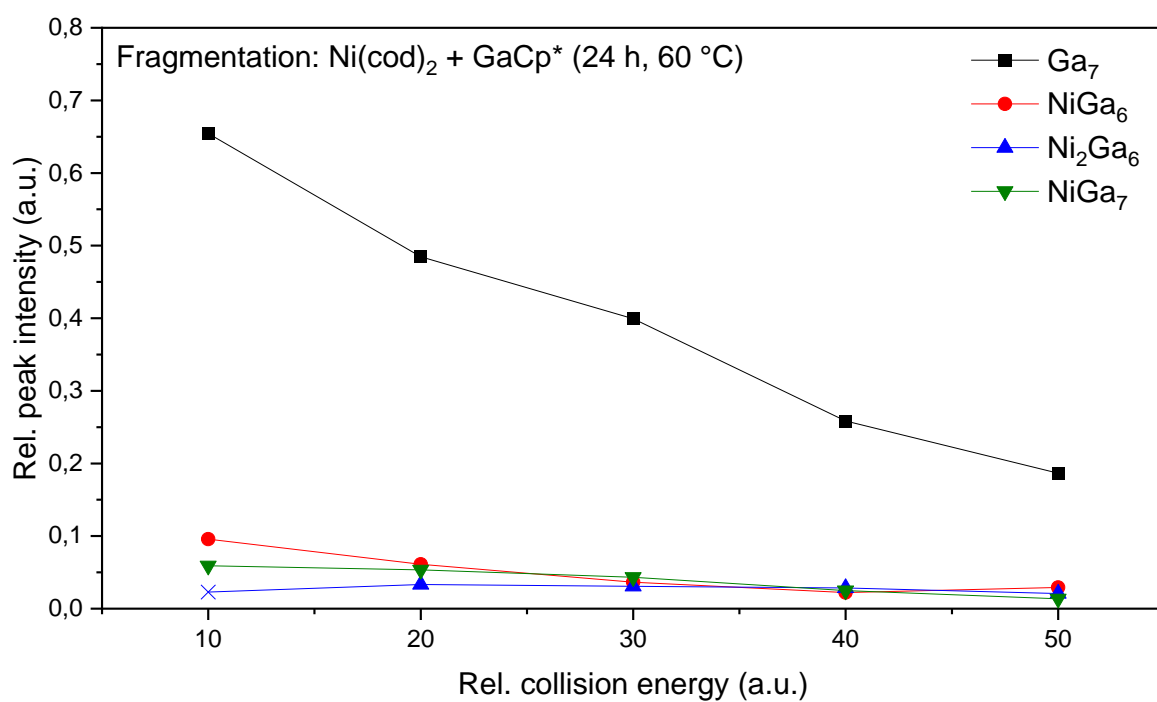


Figure S19: *I* vs. CE plots for molecular ions of the reaction mixture generated from $\text{Ni}(\text{cod})_2$ (1.0 eq.) and GaCp^* (1.0 eq.) in toluene at 60 °C after 24 h; outliers are highlighted with a cross.

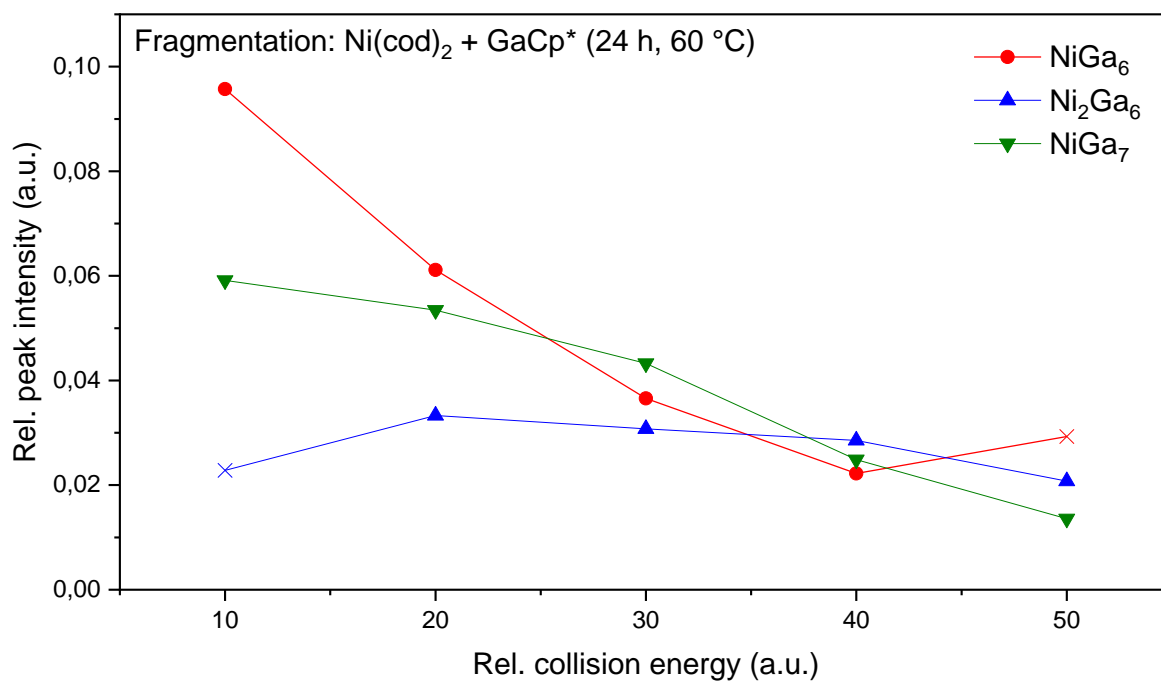


Figure S20: Cutout of the *I* vs. CE plots for the cluster species NiGa_6 , Ni_2Ga_6 and NiGa_7 ; outliers are highlighted with a cross.

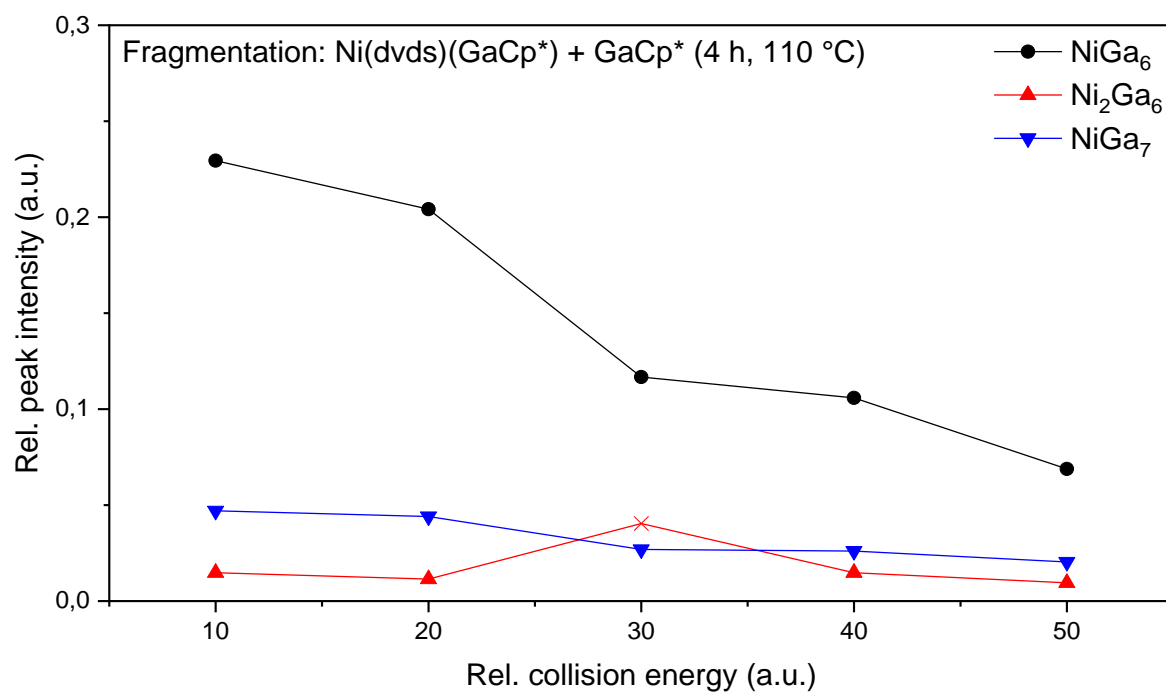


Figure S21: *I vs. CE* plots for molecular ions of the reaction mixture generated from [Ni(dvds)(GaCp*)] (1.0 eq.) and GaCp* (1.0 eq.) in toluene at 110 °C after 4 h; outliers are highlighted with a cross.

SCXRD analysis

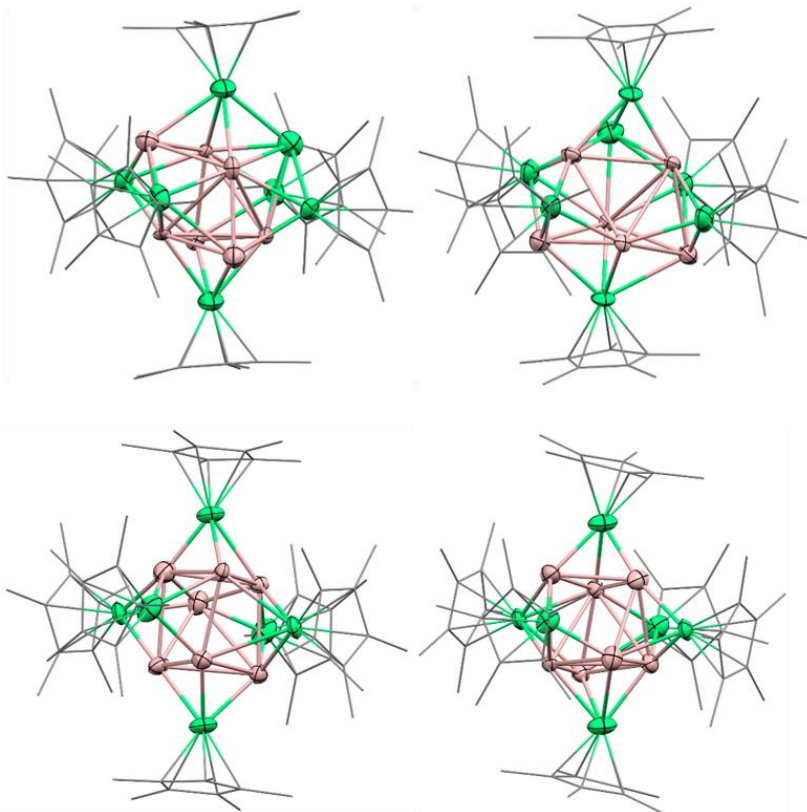


Figure S22: Optimized structures obtained by SC-XRD measurements.

Crystal data

$(\text{C}_{60}\text{H}_{90}\text{Ga}_{6.66}\text{Ni}_{6.61}) \cdot 2(\text{C}_9\text{H}_{12})$	$F(000) = 973$
$M_r = 1904.01$	
Triclinic, P	$D_x = 1.655 \text{ Mg m}^{-3}$
Hall symbol: $-P\ 1$	Melting point: $?$ K
$a = 12.6698 (7) \text{ \AA}$	Mo $K\alpha$ radiation, $\lambda = 0.71073 \text{ \AA}$
$b = 12.7434 (7) \text{ \AA}$	Cell parameters from 9932 reflections
$c = 13.9656 (8) \text{ \AA}$	$\theta = 2.2\text{--}25.7^\circ$
$\alpha = 88.476 (2)^\circ$	$\mu = 3.93 \text{ mm}^{-1}$
$\beta = 69.582 (2)^\circ$	$T = 100 \text{ K}$
$\gamma = 65.805 (2)^\circ$	Fragment, black
$V = 1909.59 (19) \text{ \AA}^3$	$0.45 \times 0.30 \times 0.27 \text{ mm}$
$Z = 1$	

Data collection

<u>Bruker Photon CMOS</u> diffractometer	<u>6995</u> independent reflections
Radiation source: <u>IMS microsource</u>	<u>6070</u> reflections with $I > 2\sigma(I)$
<u>Helios optic</u> monochromator	$R_{\text{int}} = \underline{0.028}$
Detector resolution: <u>16</u> pixels mm^{-1}	$\theta_{\text{max}} = \underline{25.4}^\circ$, $\theta_{\text{min}} = \underline{2.2}^\circ$
<u>phi- and omega-rotation scans</u>	$h = \underline{-15}$ <u>15</u>
Absorption correction: <u>multi-scan SADABS 2016/2, Bruker</u>	$k = \underline{-15}$ <u>15</u>
$T_{\text{min}} = \underline{0.503}$, $T_{\text{max}} = \underline{0.745}$	$l = \underline{-16}$ <u>16</u>
<u>50781</u> measured reflections	

Refinement

Refinement on F^2	Secondary atom site location: <u>difference Fourier map</u>
Least-squares matrix: <u>full</u>	Hydrogen site location: <u>inferred from neighbouring sites</u>
$R[F^2 > 2\sigma(F^2)] = \underline{0.039}$	<u>H-atom parameters constrained</u>
$wR(F^2) = \underline{0.097}$	$W = 1/[\sigma^2(FO^2) + (0.040P)^2 + 3.3861P]$ WHERE $P = (FO^2 + 2FC^2)/3$
$S = \underline{1.04}$	$(\Delta/\sigma)_{\text{max}} = \underline{0.004}$
<u>6995</u> reflections	$\Delta\rho_{\text{max}} = \underline{0.55}$ e \AA^{-3}
<u>914</u> parameters	$\Delta\rho_{\text{min}} = \underline{-0.65}$ e \AA^{-3}
<u>1633</u> restraints	Extinction correction: <u>none</u>
<u>0</u> constraints	Extinction coefficient: <u>-</u>
Primary atom site location: <u>iterative</u>	

PXRD analysis

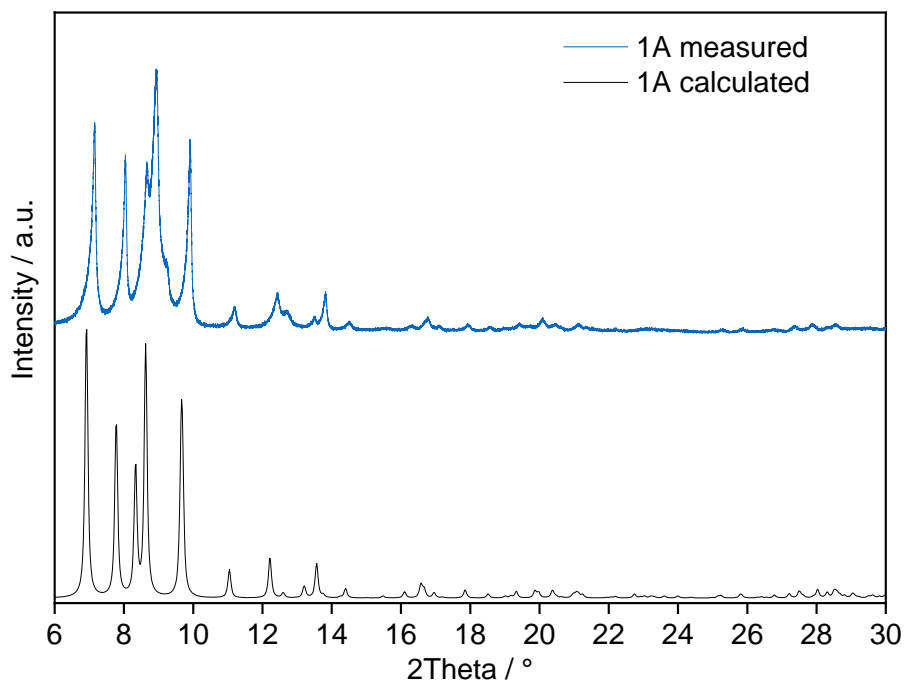


Figure S23: PXRD measurement of **1A** (major component **3**) and comparison with calculated pattern out of SCXRD measurements.

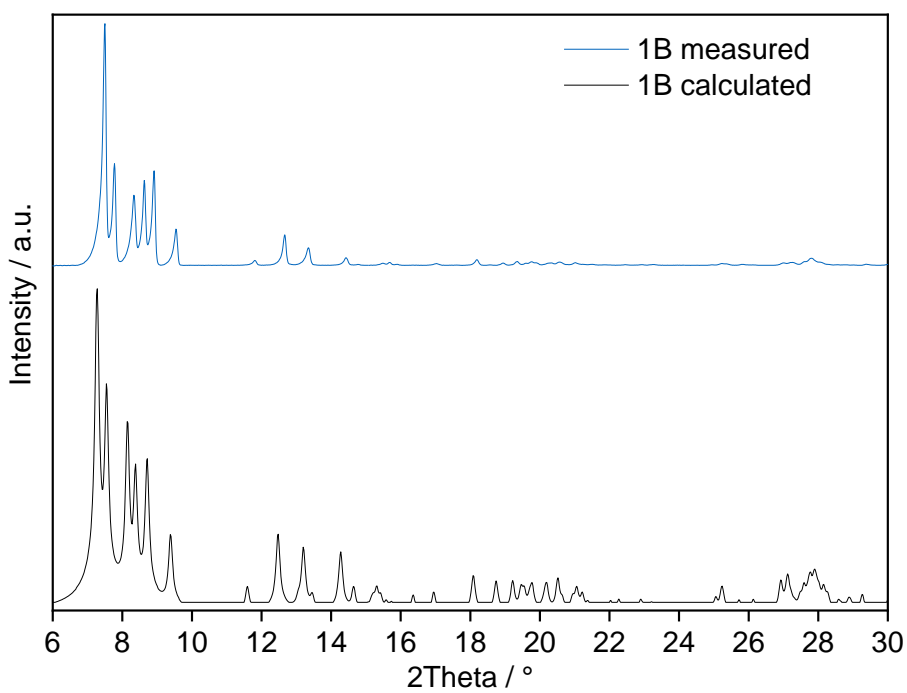


Figure S24: PXRD measurement of **1B** (major component **2**) and comparison with calculated pattern out of SXRD measurements.

XPS measurements

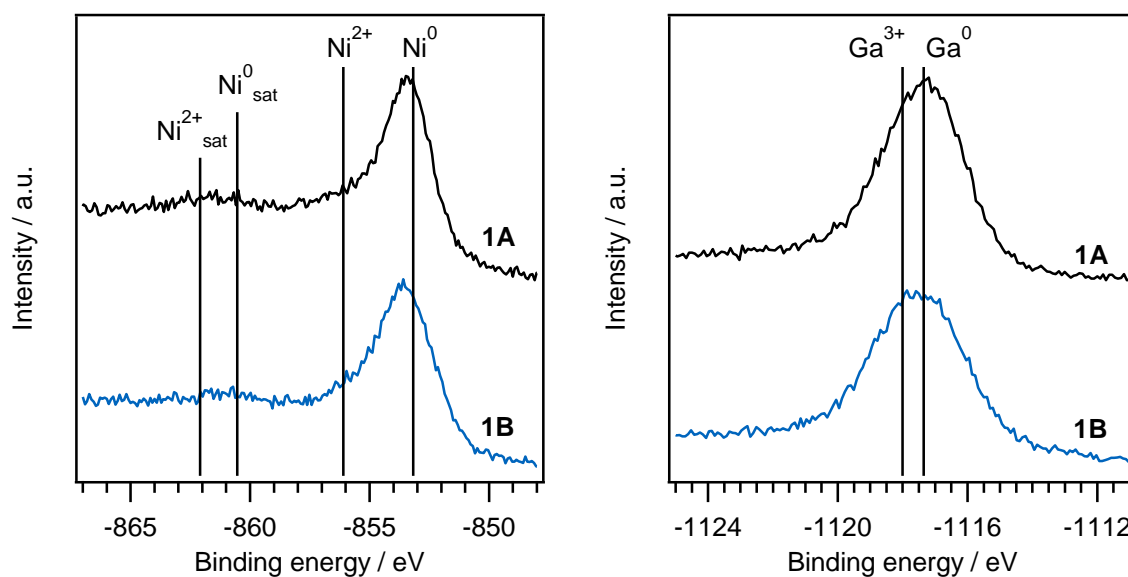


Figure S25: Ni $2p_{3/2}$ (left) and Ga $2p_{3/2}$ (right) photoemission spectra of **1A** (major component **3**) and **1B** (major component **2**) evidence the presence of both metals predominately in their metallic state. For comparison, lines pinpoint the Ni $2p_{3/2}$ binding energy of Ni^0 and Ni^{2+} species (main line and satellite) as well as the Ga $2p_{3/2}$ binding energy of Ga^0 and Ga^{3+} species, respectively. As the binding energy of metallic and oxidic species in the cluster components **1A** and **1B** might vary from the one obtained for bulk materials we determined the binding energy for the oxidized species after oxidizing the clusters in air.

The metallic reference was obtained by electron-induced reduction upon Ar^+ ion sputtering. The oxidation states were confirmed considering the peak position and shape of the Ni LMM and Ga LMM Auger spectra, respectively. Quantitative analysis of the Ni $2p_{3/2}$ and Ga $2p_{3/2}$ spectra reveals a molar Ni/Ga ratio of 1.1 (**1A**) and 1.0 (**1B**).

Elemental Analysis

Table S22: AAS analysis of **1A** (major component **3**) and **1B** (major component **2**) and theoretical values of various cluster compounds.

	%C	%H	%Ni	%Ga	Ni/Ga ratio
1A	42.6	5.5	27.4	24.3	1.12
1B	45.0	5.6	25.1	24.2	1.04
$[\text{Ni}_8\text{Ga}_6](\text{Cp}^*)_6$	42.3	5.7	27.5	24.5	1.12
$[\text{Ni}_7\text{Ga}_6](\text{Cp}^*)_6$	43.7	5.8	24.9	25.4	0.98
$[\text{Ni}_7\text{Ga}_7](\text{Cp}^*)_6$	42.0	5.6	23.9	28.4	0.84
$[\text{Ni}_6\text{Ga}_7](\text{Cp}^*)_6$	43.5	5.8	21.2	29.4	0.72
$[\text{Ni}_9\text{Ga}_5](\text{Cp}^*)_6$	42.7	5.4	31.3	20.7	1.51

SQUID and EPR measurements

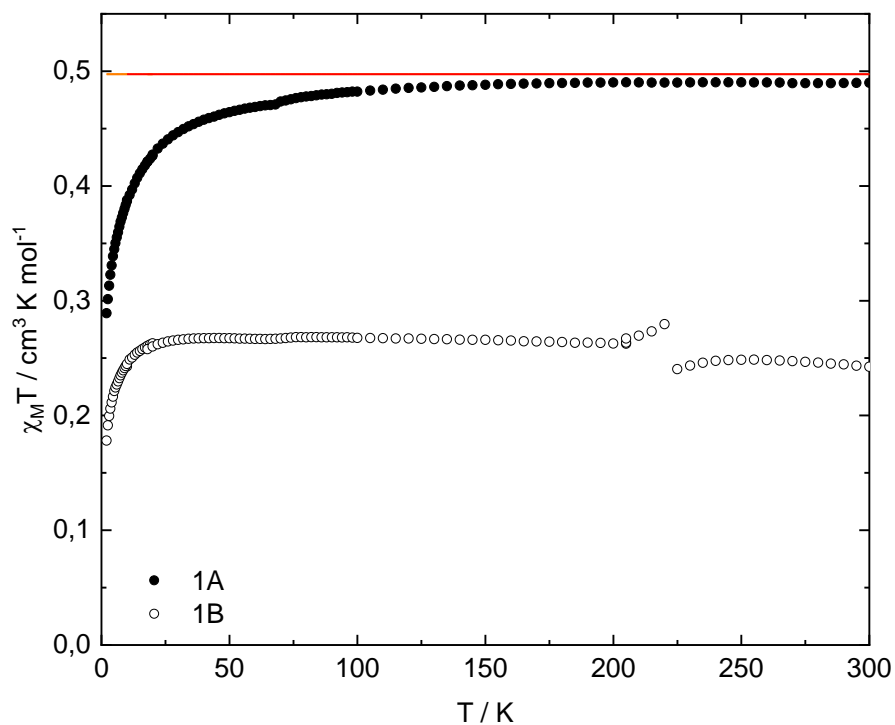


Figure S26: $\chi_M T$ of **1A** (major component **3**; closed circles) and **1B** (major component **2**; open squares) detected by SQUID measurements plotted against the temperature T . The red line indicates an isolated spin $\frac{1}{2}$ with $g = 2.30$.

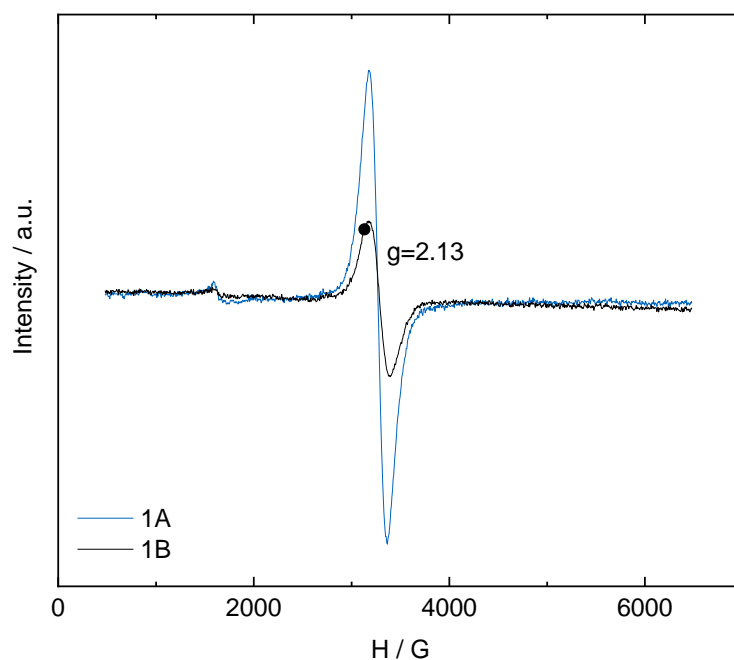


Figure S27: EPR spectra of **1A** (major component **3**; blue) and **1B** (major component **2**; black) measured at room temperature.

Procedures and Strategies for the Atomic Structure Generation

Here, we propose a systematic approach to study of the M₁₃ and M₁₄ clusters protected by (C₅Me₅)₆ ligands. Figure summarizes the strategy and procedures employed to generate the atomic structure configurations. As we show in the Figure, initially the study is divided on two pathways. The right side of the scheme was tentatively performed for the naked clusters based on the XRD data. Furthermore, on the left of the scheme, a pure theoretical approach based on a previous work from our group, in which the transition metal (TM) clusters with 215 atoms were studied. These paper shows a rich conformational set for unary clusters that was used to enrich our structural set.

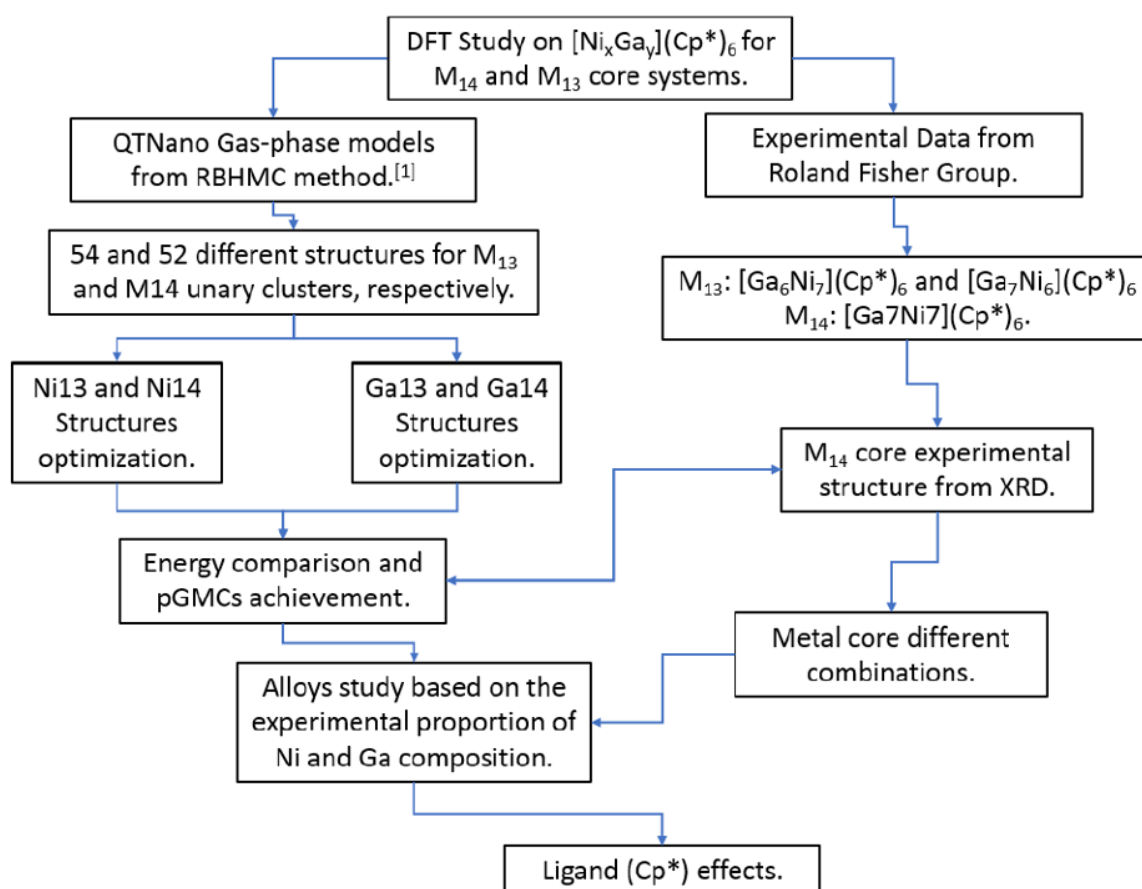


Figure S28: Systematic approach to generate atomic structure configurations for the M₁₃ and M₁₄ clusters.

Structural Analyses of the Unary and Binary Clusters

To characterize the most important structural parameters of the unary and binary clusters, namely, coordination number and bond lengths, we employed the effective coordination concept (ECC), which yields the following parameters: (i) weighted bond lengths, d_{av}^i , and effective coordination number, ECN^i , in number of nearest neighbor (NNN), for each atom, i , within the cluster. Those values are obtained using a self-consistent approach based on exponential decay functions. The ECC considers that every atom i is surrounded by atoms j at different distances, and using an exponential decay function, a weight is calculated for each i j distance. As expected, the closest atoms have a larger weight and the more distant ones have a smaller weight. Thus, ECN^i is obtained by the following equation:

$$ECN^i = \sum_j \exp \left[1 - \left(\frac{d_{ij}}{d_{av}^i} \right)^6 \right]$$

where d_{ij} is the distance between atom i and j , while d_{av}^i is obtained by the following equation:

$$d_{av}^{i,new} = \frac{\sum_j d_{ij} \exp \left[1 - \left(\frac{d_{ij}}{d_{av}^{i,old}} \right)^6 \right]}{\sum_j \exp \left[1 - \left(\frac{d_{ij}}{d_{av}^{i,old}} \right)^6 \right]}$$

d_{av}^i is obtained self-consistently, i.e., $|d_{av}^{i,new} - d_{av}^{i,old}| < 0.00010$. The smallest bond length between the atom i and all j atoms, $d_{i \min}$, is used as the initial value for d_{av}^i . The final values of d_{av}^i are obtained within 3-4 iterations, which are then used to calculate ECN_i as indicated above, which is obtained by the sum of all weights and does not have to be an integer value. The average results, ECN_{av} and d_{av} , are obtained by the following equations:

$$ECN_{av} = \frac{1}{N} \sum_{i=1}^N ECN^i$$
$$d_{av} = \frac{1}{N} \sum_{i=1}^N d_{av}^i$$

where N is the total number of atoms in the cluster. This approach is suitable for systems with lower symmetry, which is the case of systems addressed in this study.

Atomic Structure of the Unprotected Unary M_{13} and M_{14} Clusters

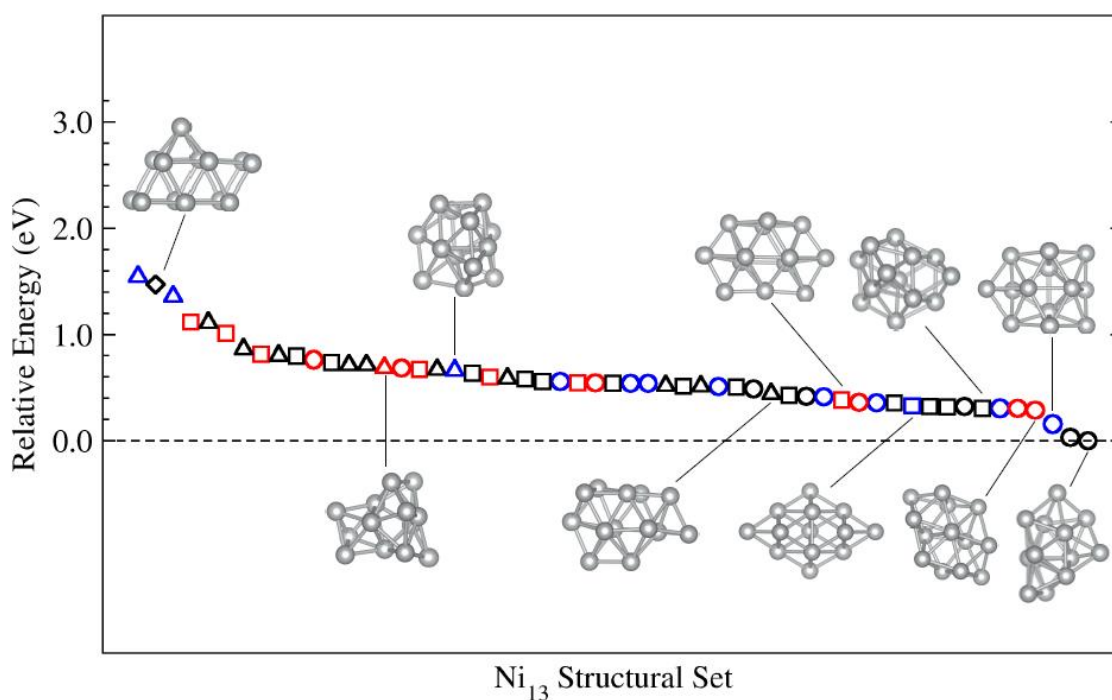


Figure S29: Atomic structure configurations optimized for the Ni_{13} clusters. Using clustering algorithms all optimized structures were separated into 10 groups, and the lowest energy configuration of each group are indicated within the figure.

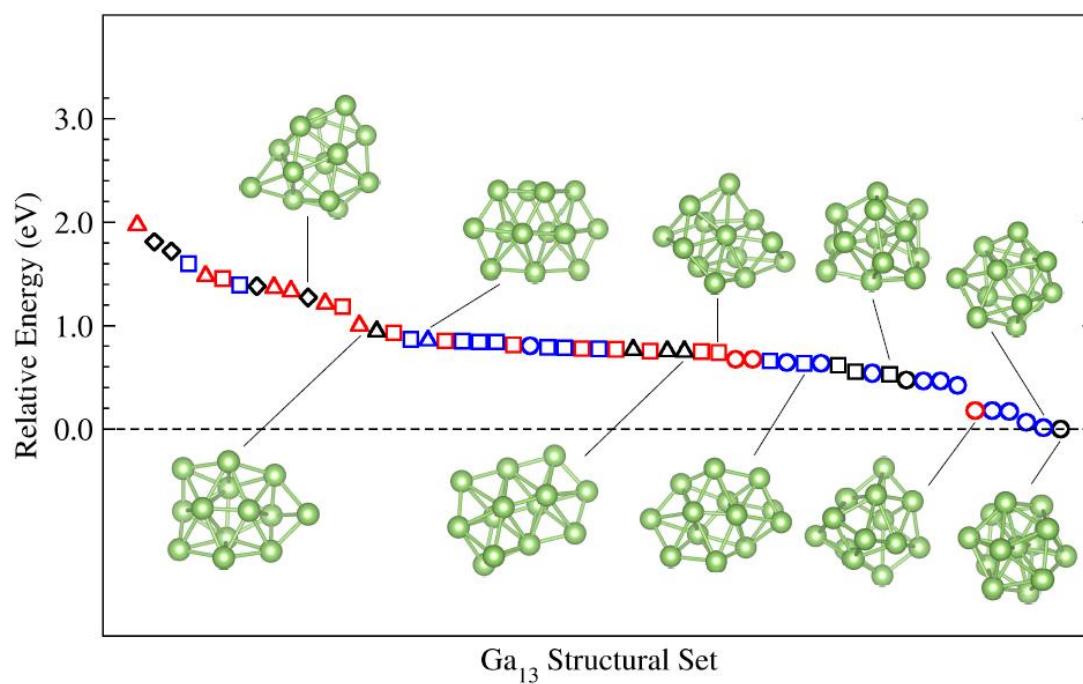


Figure S30: Atomic structure configurations optimized for the Ga_{13} clusters. Using clustering algorithms all optimized structures were separated into 10 groups, and the lowest energy configuration of each group are indicated within the figure.

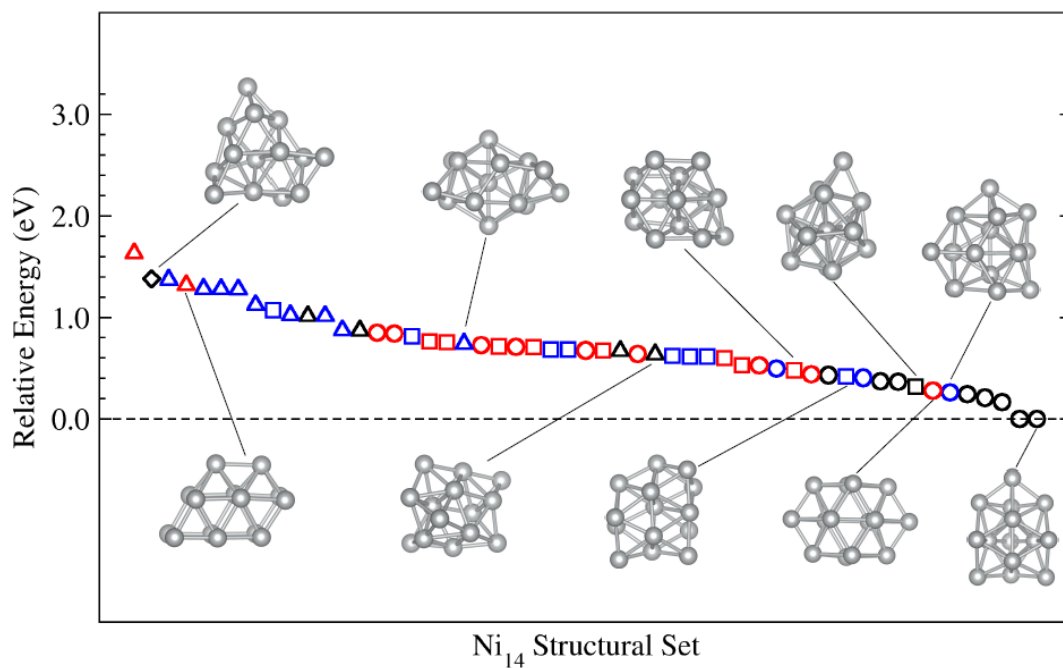


Figure S31: Atomic structure configurations optimized for the Ni₁₄ clusters. Using clustering algorithms all optimized structures were separated into 10 groups, and the lowest energy configuration of each group are indicated within the figure.

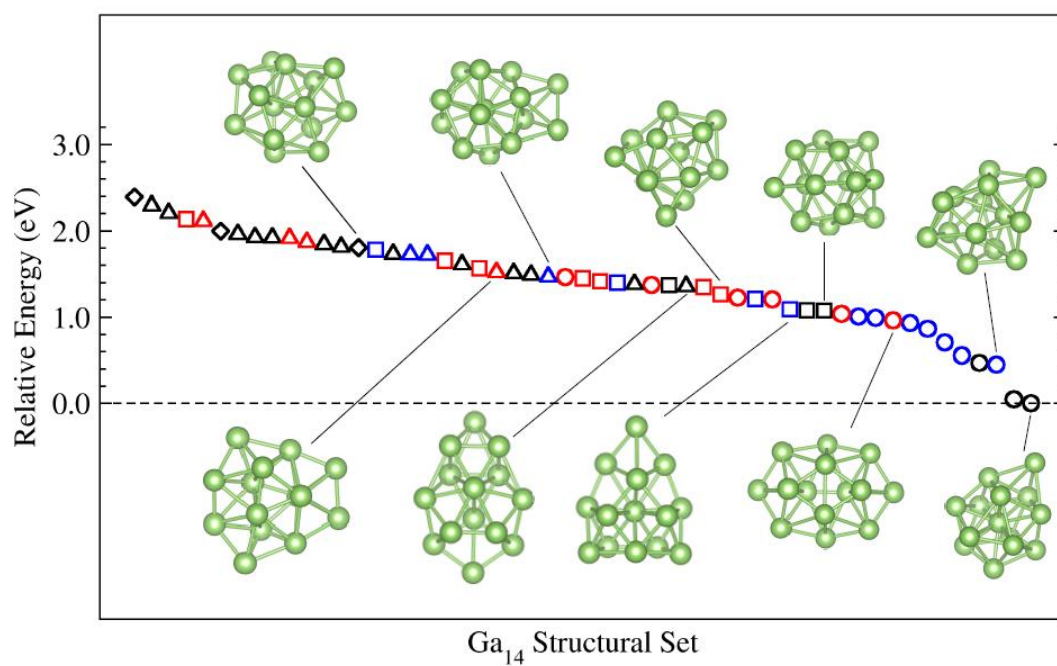


Figure S32: Atomic structure configurations optimized for the Ni₁₃ clusters. Using clustering algorithms all optimized structures were separated into 10 groups, and the lowest energy configuration of each group are indicated within the figure.

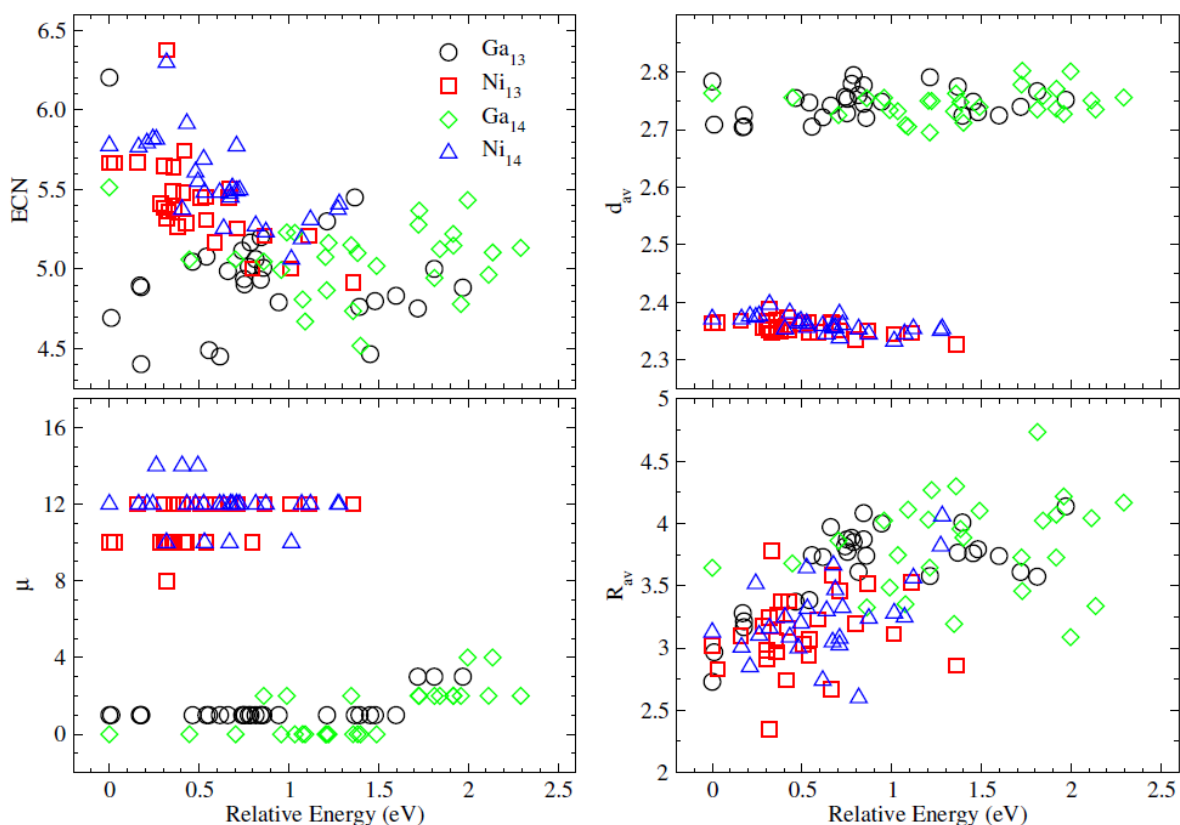


Figure S33: Structural parameters for the Ni_{13} , Ga_{13} , Ni_{14} , and Ga_{14} clusters: average effective coordination number, ECN, in number of nearest neighbor (NNN), average weighted bond length, d_{wv} , in Å, average cluster radius, R_{ov} , in Å, and dipole moment, μ , in Debye.

Unprotected Binary M_{13} and M_{14} Clusters

Structure Frame from XRD Results

Figure S indicates the structure for the M_{14} cluster obtained from the experimental XRD results without the indication of the ligands. Thus, based on the geometric analysis of the structure, we can provide the following observations: (i) the atoms indicated in light blue are near to the geometric center, and are called first shell, while the atoms in light pink belong to the second shell of atoms. (ii) the atoms indicated by green indicates the atoms in the equatorial vertices, while the remaining the dark brown atoms defined the axial vertices. Although the present structure framework is provided, the correct positions of the Ni and Ga was confirmed by density functional theory calculations by assuming all possible sites as occupied by the Ni or Ga atoms for a given composition. Thus, using an enumeration process, and analysis of the similarity among the configurations to remove similar structures (modified Euclidean metrics analysis), we could obtain and identify the lowest energy configurations for the protected clusters. Similar procedure was employed for M_{13} clusters.

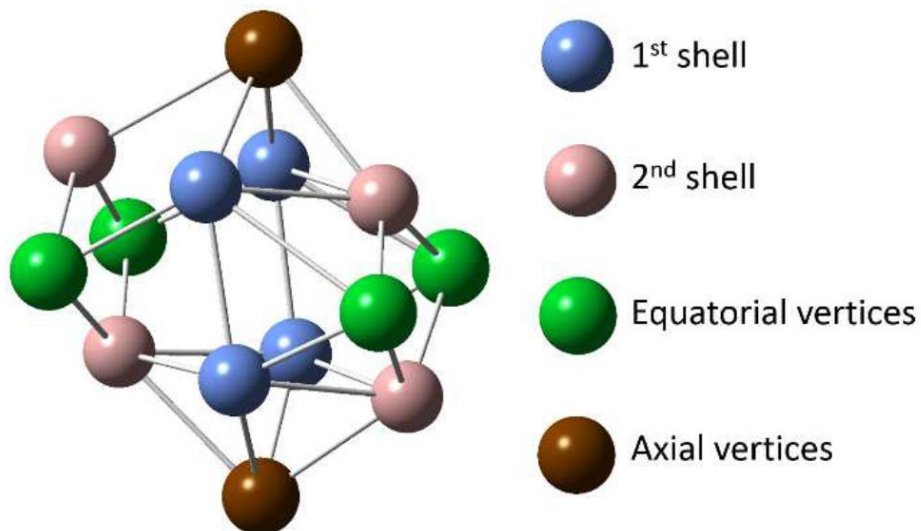


Figure S34: Atomic structure of the M_{14} cluster based on the SCXRD results.

Ni_7Ga_7

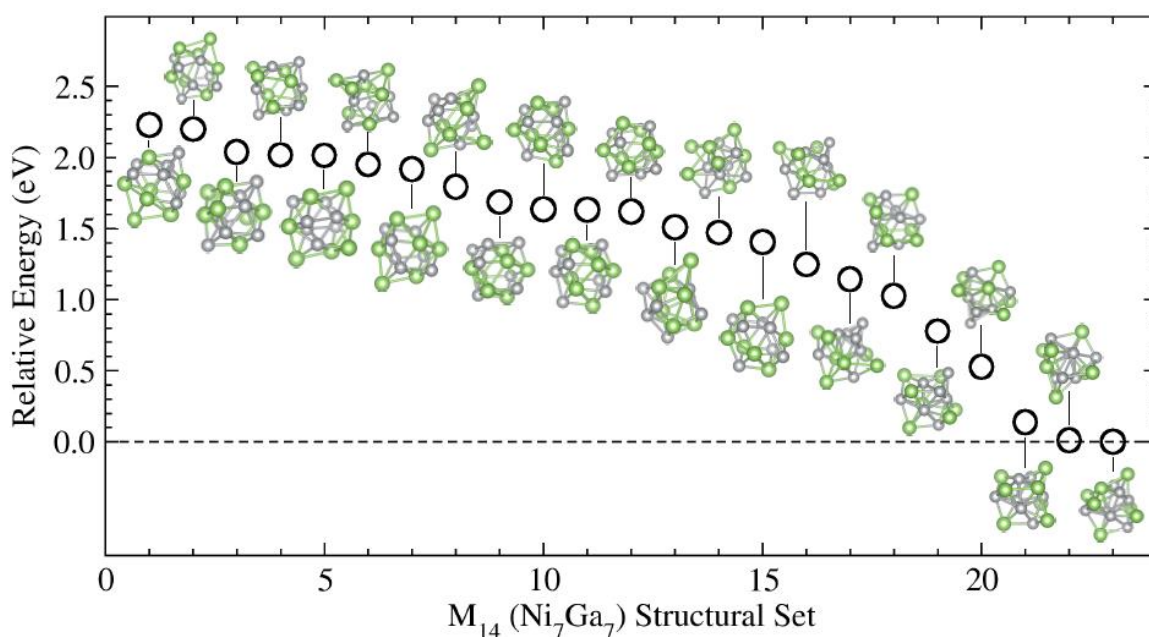


Figure S35: Structural set for the unprotected Ni_7Ga_7 clusters. The magnetic moment is equal to 1 for the major part of the structures, except for the structure 21, that is 1.25 eV above lowest energy configuration for these systems. In the lowest energy configuration, the Ni atoms preferential sites are in the inner sites of the clusters, and these trends is observed on the systems 18, 14, 23 and 2, that shows relative total energies smaller than 1 eV from the lowest energy configuration. The excess energy was further calculated, resulting to negative values for all the systems, that represents a stabilization of the alloy clusters in comparison to the unary Ni_{14} and Ga_{14} clusters.

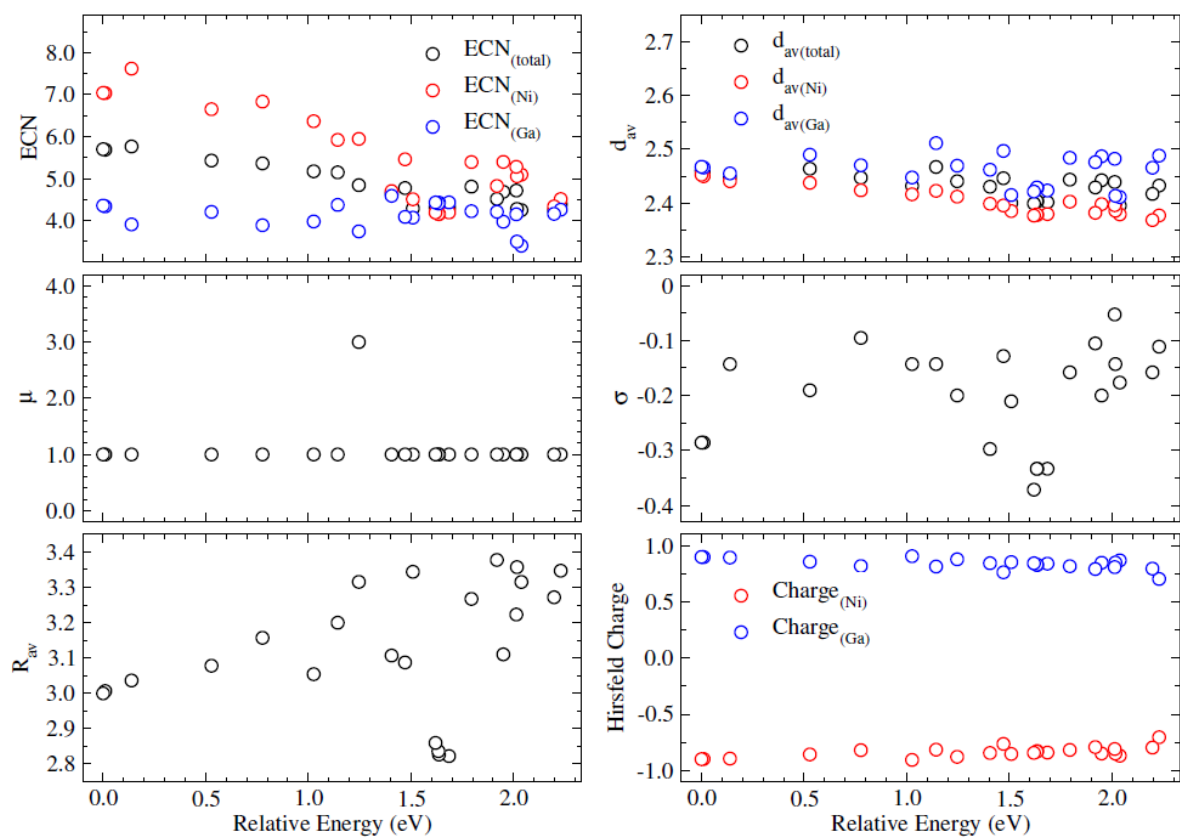


Figure S36: Geometrical and electronic analyses for the unprotected Ni_7Ga_7 clusters: average effective coordination number, ECN, in number of nearest neighbor (NNN), average weighted bond length, d_{av} , in \AA , average cluster radius, R_{av} , in \AA , and dipole moment, μ , in Debye, chemical ordering parameter, σ , and effective Hirshfeld charge, e .

Ni_6Ga_7

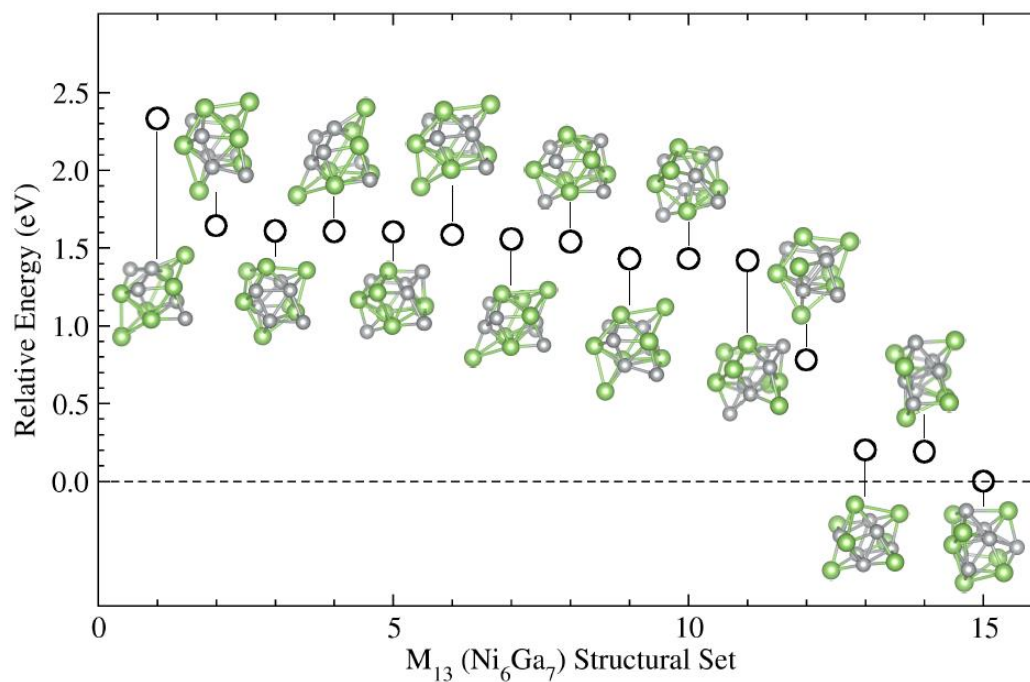


Figure S37: Structural set for Ni_6Ga_7 naked clusters.

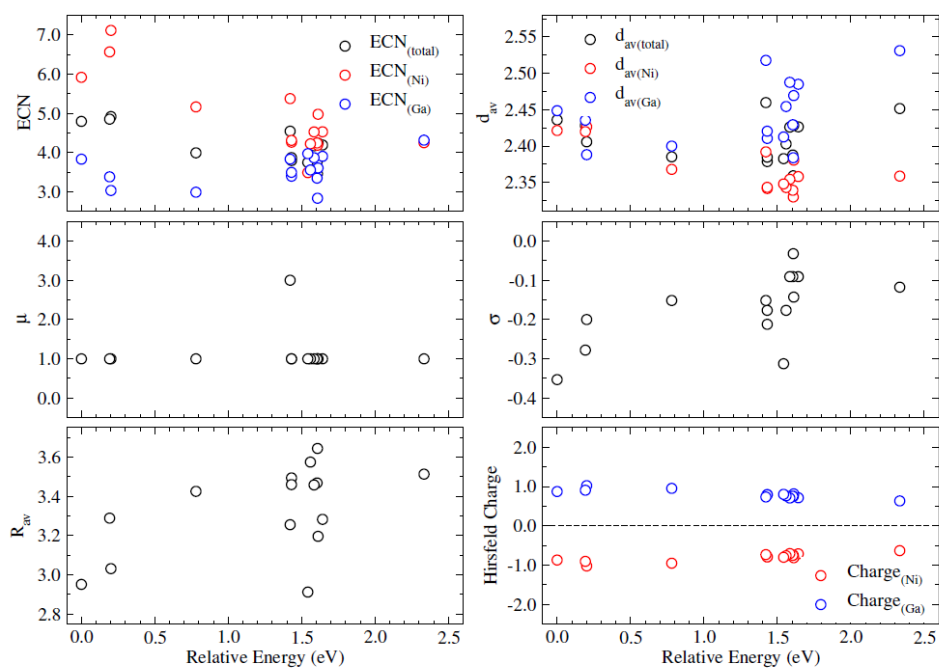


Figure S38: Geometrical and electronic analyses for the unprotected Ni_6Ga_7 clusters: average effective coordination number, ECN, in number of nearest neighbor (NNN), average weighted bond length, d_{av} , in \AA , average cluster radius, R_{av} , in \AA , and dipole moment, μ , in Debye, chemical ordering parameter, σ , and effective Hirshfeld charge, e .

Ni_7Ga_6

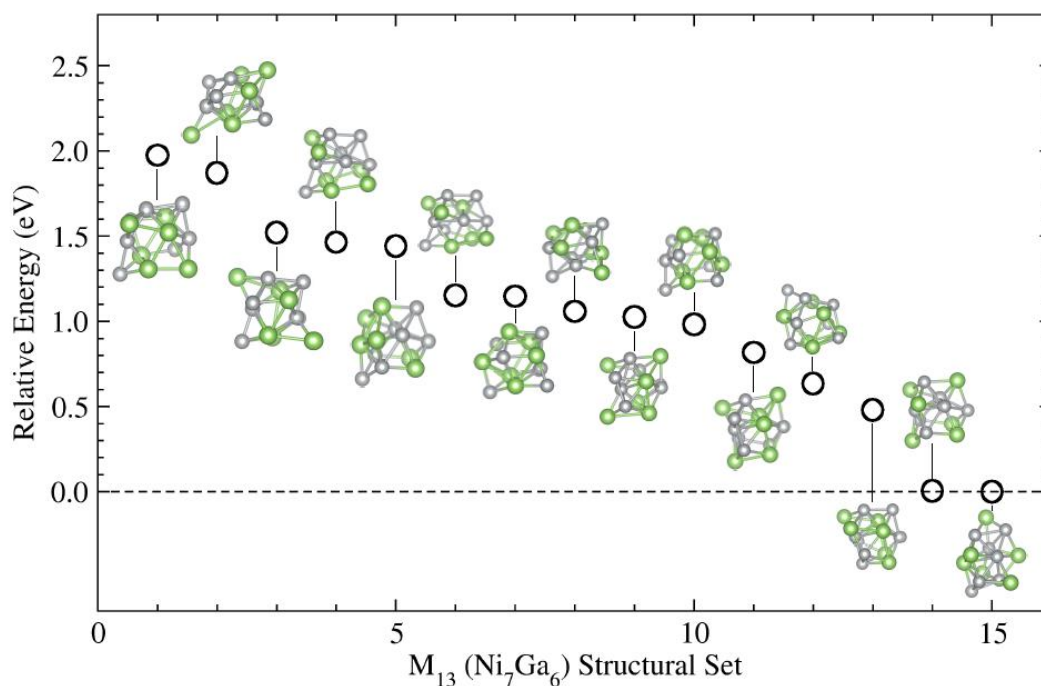


Figure S39: Structural set for Ni_7Ga_6 naked clusters.

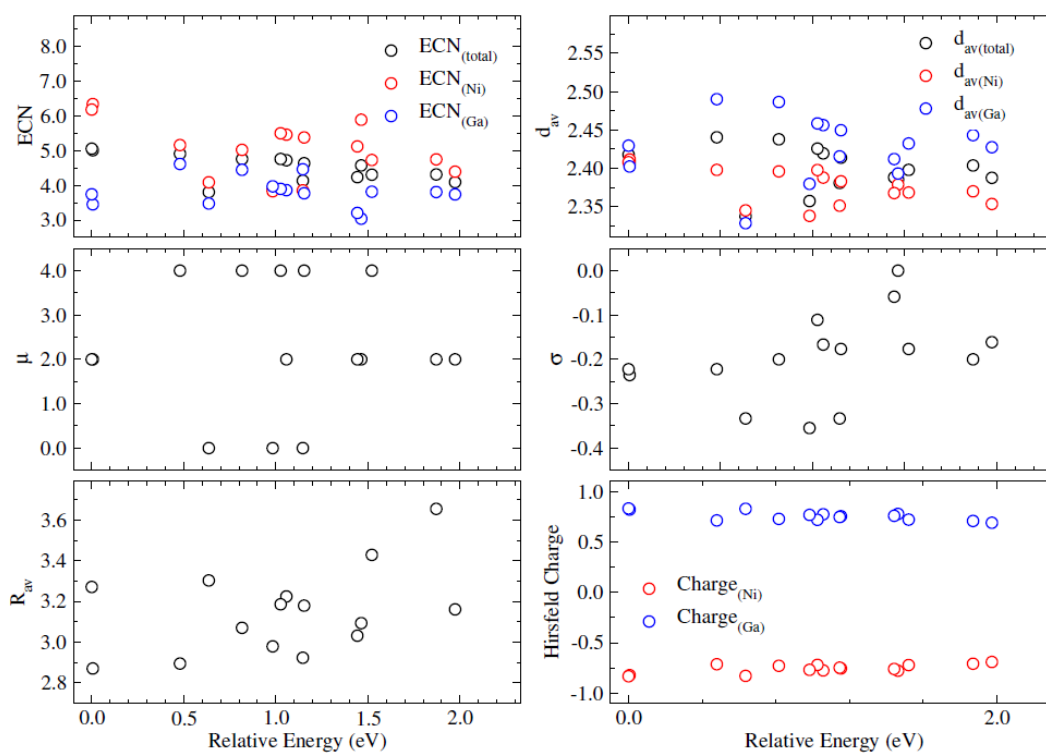


Figure S40: Geometrical and electronic analyses for the unprotected Ni_7Ga_6 clusters: average effective coordination number, ECN, in number of nearest neighbor (NNN), average weighted bond length, d_{av} , in \AA , average cluster radius, R_{av} , in \AA , and dipole moment, μ , in Debye, chemical ordering parameter, σ , and effective Hirschfeld charge, e .

Protected Binary M_{13} and M_{14} Clusters

Ni_7Ga_7

Using the previous core structure separated in 4 different regions, as shown in Figure S, were selected 10 different systems for the Cp* coordination study. We have inserted the Cp* ligands on the 6 vertices of the molecule, as showed on Figure S. The relative energies were calculated considering the lowest energy's isomer as the referential (zero energy). If we compare to the previous results, on the naked clusters, the preferential sites for the Ni atoms migrate from the inner to the surfaces sites on the Cp* coordinated systems. The magnetic moment for the more stable isomer is 1, varying to 3 in an interval of few eV. The coordination of the Cp* ligand contributes to the stabilization of the Ni atoms on the surface and the unpaired electrons stabilization, as see on the quadruplet isomers on the interval smaller than 1 eV from the lowest energy isomers.

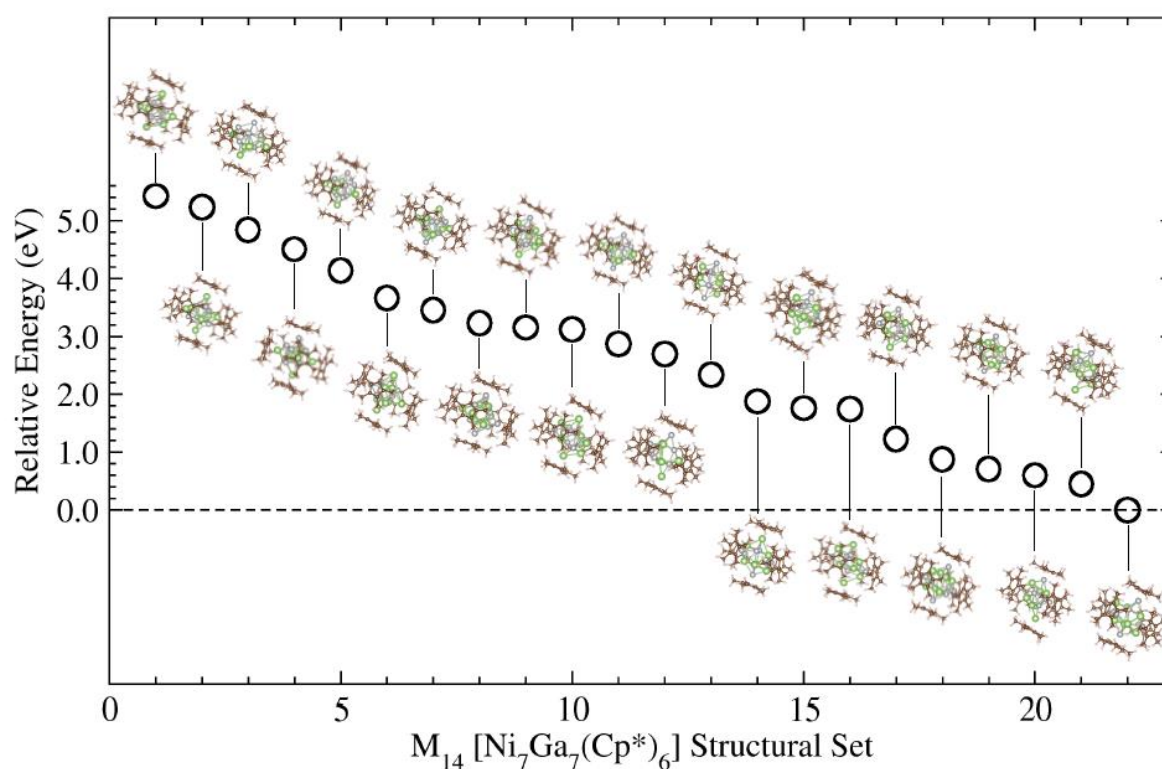


Figure S41: All calculated configurations for the $[Ni_7Ga_7(Cp^*)_6]$ systems.

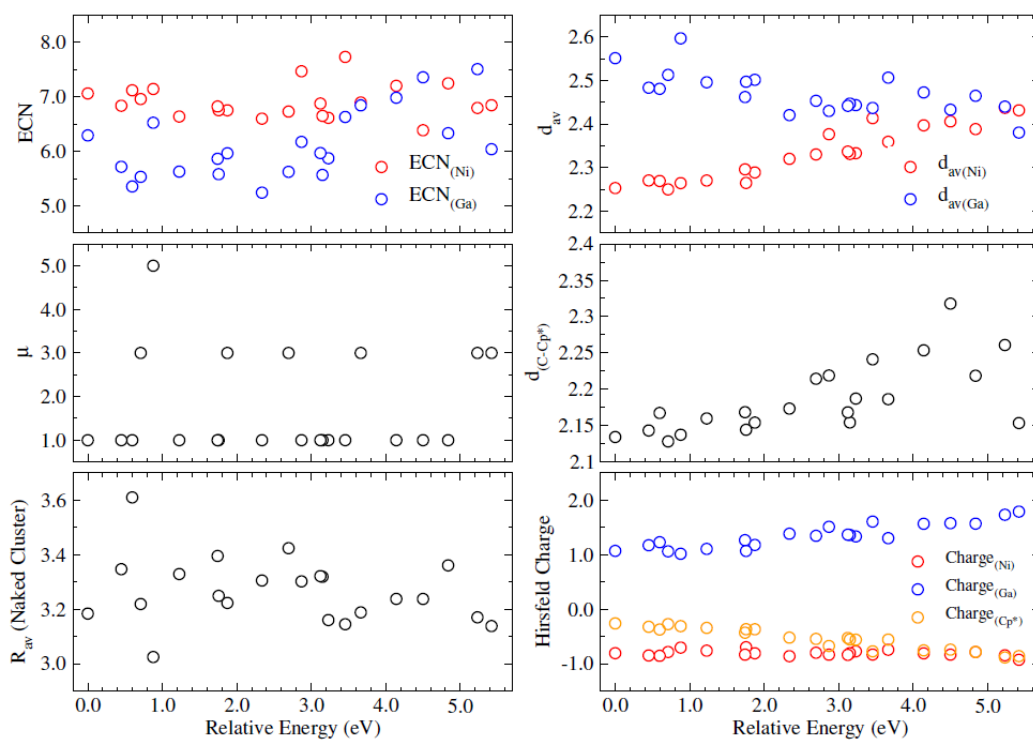


Figure S42: Geometrical and electronic analyses for the protected $[\text{Ni}_7\text{Ga}_7(\text{Cp}^*)_6]$ clusters (only metal atoms): average effective coordination number, ECN, in number of nearest neighbor (NNN), average weighted bond length, d_{av} , in Å, average cluster radius, R_{av} , in Å, and dipole moment, μ , in Debye, chemical ordering parameter, σ , and effective Hirshfeld charge, e .

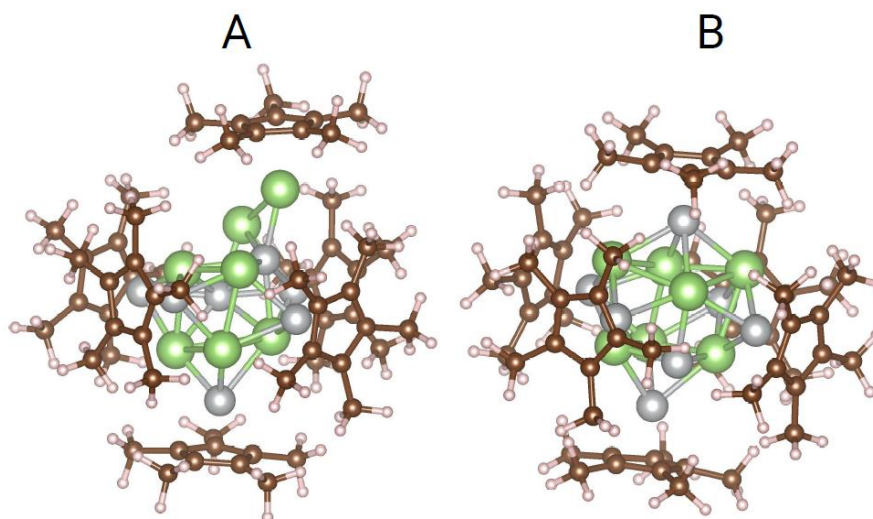


Figure S43: Lowest energy configurations obtained for the protected $[\text{Ni}_7\text{Ga}_7(\text{Cp}^*)_6]$ systems obtained from the structures based on the unary systems (A) and on the experimental XRD structure (B).

Ni_7Ga_6 and Ni_6Ga_7

Figure S shows all configurations optimized by the FHI-aims package for the protected Ni_7Ga_6 clusters, i.e., 14 different configurations. From the results, the energy different between the highest and lowest energy configurations is about 4.0 eV, which can be explained by the location of the Ni atoms, i.e., those atoms bind to the ligands, as indicated in Figure S. Furthermore, in Figure S of the most important geometric parameters for all calculated configurations, which can be seen clearly by the preference of the Ni atoms for high-coordination sites (supported by the effective coordination number). Similar results are also observed for the protected Ni_6Ga_7 clusters.

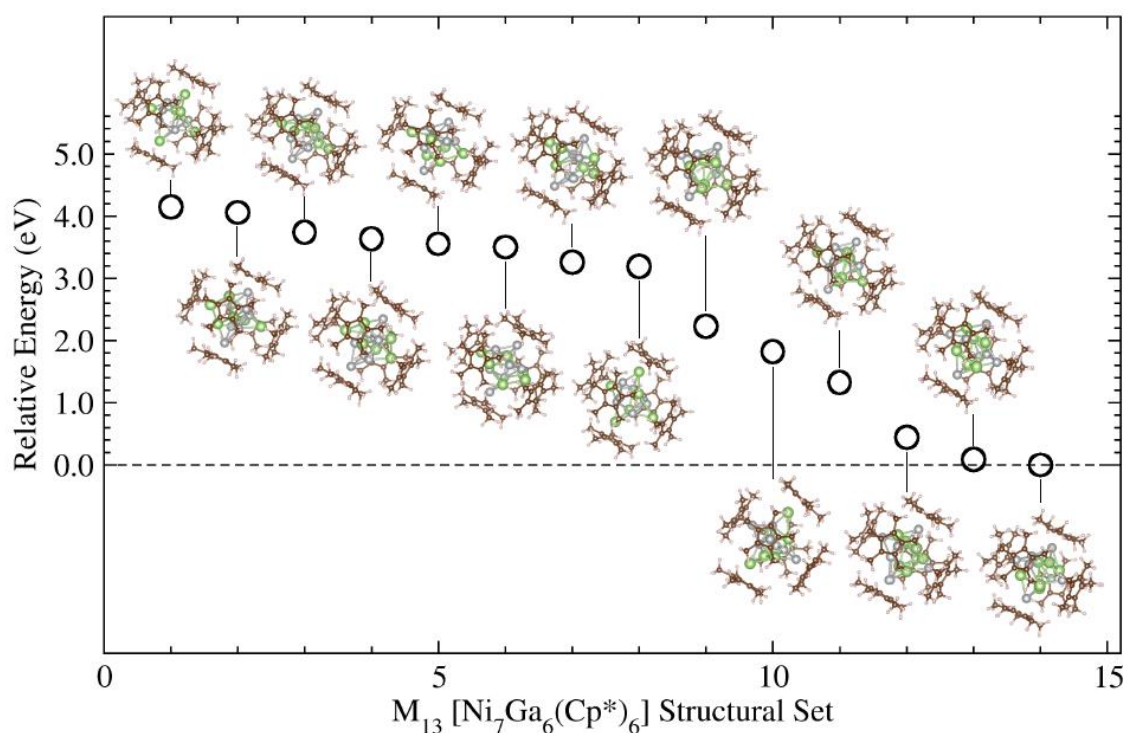


Figure S44: Structural configurations optimized for the protected $[Ni_7Ga_6(Cp^*)_6]$ clusters.

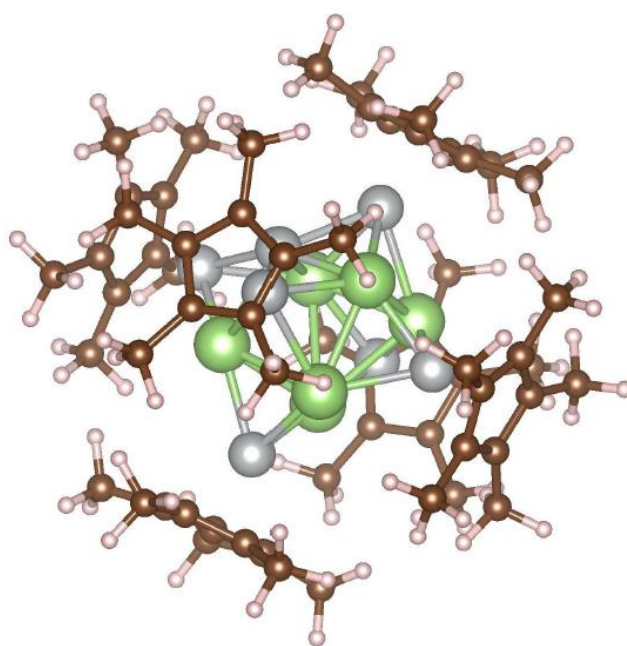


Figure S45: Lowest energy configuration for the protected $[\text{Ni}_7\text{Ga}_6(\text{Cp}^*)_6]$ systems.

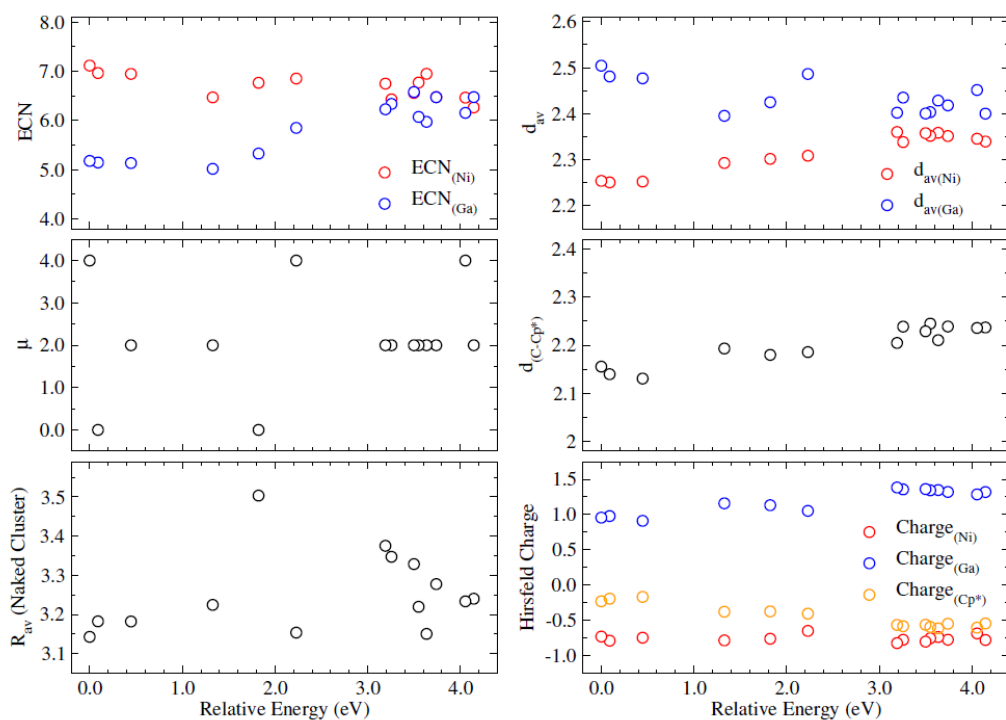


Figure S46: Geometrical and electronic analyses for the protected $[\text{Ni}_7\text{Ga}_6(\text{Cp}^*)_6]$ clusters (only metal atoms): average effective coordination number, ECN, in number of nearest neighbor (NNN), average weighted bond length, d_{av} , in Å, average cluster radius, R_{av} , in Å, and dipole moment, μ , in Debye, chemical ordering parameter, σ , and effective Hirshfeld charge, e .

Ni_6Ga_7

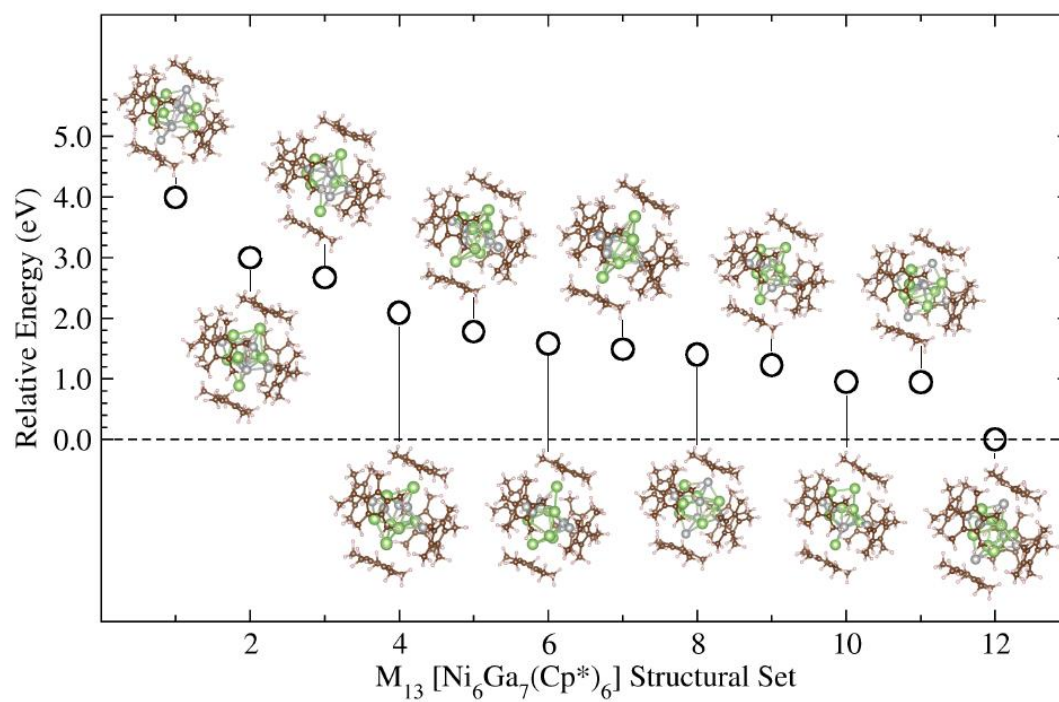


Figure S47: Structural configurations optimized for the protected $[Ni_6Ga_7(Cp^)_6]$ clusters.*

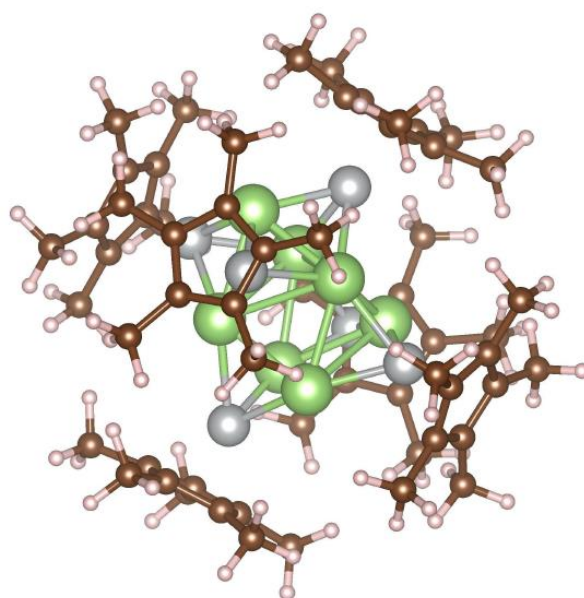


Figure S48: Lowest energy configuration for the protected $[Ni_6Ga_7(Cp^)_6]$ cluster.*

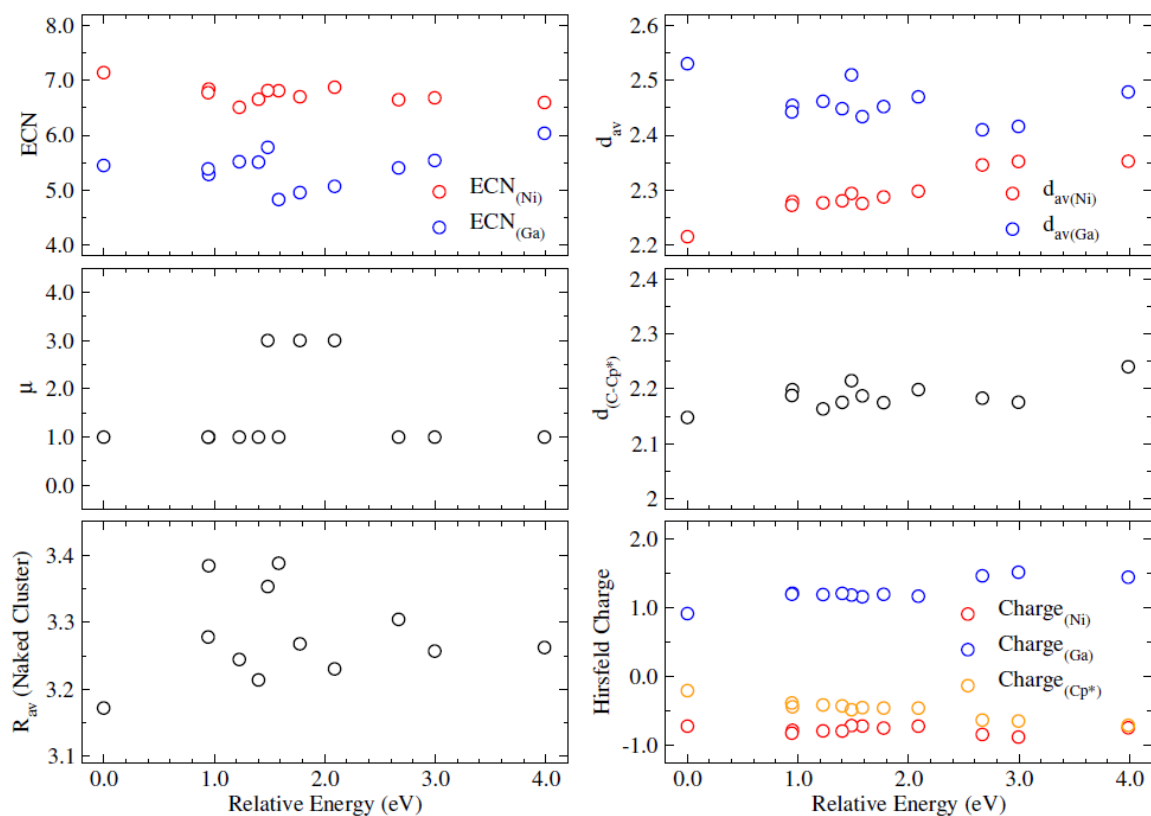


Figure S49: Geometrical and electronic analyses for the protected $[Ni_6Ga_7(Cp^*)_6]$ clusters (only metal atoms): average effective coordination number, ECN, in number of nearest neighbor (NNN), average weighted bond length, d_{av} , in Å, average cluster radius, R_{av} , in Å, and dipole moment, μ , in Debye, chemical ordering parameter, σ , and effective Hirshfeld charge, e .

DFT calculations – Part 2

Bonding Analysis - Computational Details

Density Functional Theory (DFT) calculations^[S8] were carried out with the use of the Amsterdam Density Functional code (ADF2017)^[S9] with the addition of Grimme's D3 empirical corrections^[S10] in order to consider dispersion effects. The triple- ξ Slater basis set plus two polarization functions (STO-TZP),^[S11] was used, together with the Becke-Perdew (BP86)^[S12-13] exchange-correlation functional. All the optimized structures were confirmed as true minima on their potential energy surface by analytical vibration frequency calculations. The NMR chemical shifts were computed according to the gauge-independent atomic orbitals (GIAO) method,^[S14] assuming the Zero Order Regular Approximation (ZORA) for clusters with $S = 1/2$.^[S15]

Table S23: HOMO-LUMO gaps (Δ_{H-L}) and selected averaged interatomic distances (in Å) of the computed clusters. Ni_{exp} and Ga_{exp} designate "exposed" atoms.

	Δ_{H-L} (eV)	Ni-Ga	Ga-Ga	Ni_{exp} -Ga	Ni_{exp} -Ni	Ga_{exp} -Ga	Ga_{exp} -Ni
$[Ga_6](NiC_p)_6$	0.65	2.457	3.009	-	-	-	-
$[NiGa_6](NiC_p)_6$	0.69	2.452	2.907	2.349	2.771	-	-
$\{[Ga_7](NiC_p)_6\}^+$	0.72	2.451	2.923	-	-	3.131	3.298
$[Ga_7](NiC_p)_6$	-	2.471	2.873	-	-	3.124	3.289
$[NiGa_7](NiC_p)_6$	-	2.471	2.823	2.373	2.756	3.161	3.224
$[Ni_2Ga_6](NiC_p)_6$	0.71	2.471	2.844	2.359	2.762	-	-
$[Ga_6](NiC_p^*)_6$	0.51	2.492	2.878	-	-	-	-
$[NiGa_6](NiC_p^*)_6$	0.55	2.482	2.798	2.412	2.761	-	-
$\{[Ga_7](NiC_p^*)_6\}^+$	0.55	2.500	2.851	-	-	3.117	3.079
$[Ga_7](NiC_p^*)_6$	-	2.523	2.817	-	-	3.123	3.076
$[NiGa_7](NiC_p^*)_6$	-	2.491	2.780	2.414	2.761	3.231	3.164
$[Ni_2Ga_6](NiC_p^*)_6$	0.55	2.499	2.802	2.395	2.756	-	-

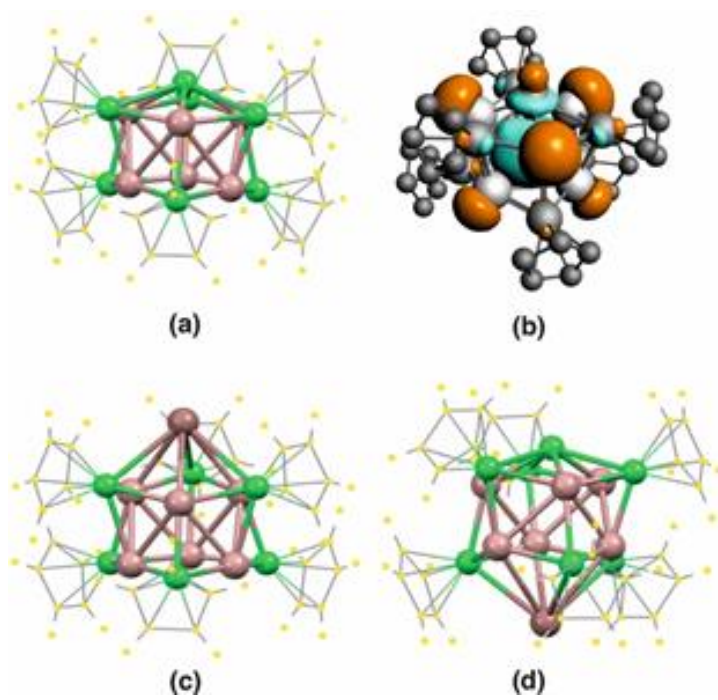


Figure S50. The optimized geometries of: (a) $[\text{NiGa}_6](\text{NiCp})_6$, (b) LUMO of $[\text{NiGa}_6](\text{NiCp})_6$ (c) $\{[\text{Ga}_7](\text{NiCp})_6\}^+$ and (d) $[\text{NiGa}_7](\text{NiCp})_6$.

Reactivity Tests: CO

While in $[\text{Ga}_6](\text{NiCp}^*)_6$ and $[\text{Ga}_7](\text{NiCp}^*)_6$ all nickel atoms are protected by a Cp^* ligand, the M_{13} cluster $[\text{NiGa}_6](\text{NiCp}^*)_6$ and the M_{14} cluster $[\text{NiGa}_7](\text{NiCp}^*)_6$ exhibit an additional and exposed "active" nickel atom, without Cp^* capping as part of the inner Ni/Ga core which is available for the Ni-CO coordination. For the M_{13} cluster $[\text{NiGa}_6](\text{NiCp}^*)_6$, however, the intermediate adduct complex $[(\text{CO})\text{NiGa}_6](\text{NiCp}^*)_6$ is apparently not stable, leading to cluster degradation. We also assume that all clusters degrade over time in the presence of CO. Degradation products can be observed in ^1H , ^{13}C and ^{71}Ga NMR, IR spectroscopy and LIFDI-MS. The presence of free GaCp^* (^1H NMR: 1.92 ppm; ^{13}C NMR: 113 and 9.4 ppm; ^{71}Ga NMR: -650 ppm), $\text{Ni}(\text{CO})_x$ (^{13}C : 192 ppm; IR) and one dominating pseudo- C_3 symmetric molecule probably assignable to $\text{Ni}(\text{CO})_3(\text{GaCp}^*)$ or related species (^{13}C : 184 and 100 ppm, IR: 1950 and 1987 and 2066 cm^{-1} ; ESI Figures S51-55). This is also reflected in the LIFDI-MS spectrum: several smaller species are observed and the main products of this reaction are the species $[(\text{CO})_x\text{Ni}_4\text{Ga}_4](\text{Cp}^*)_4$ ($x = 4, 5$) and $[(\text{CO})_y\text{Ni}_4\text{Ga}_3](\text{Cp}^*)_3$ ($y = 1, 3, 5$) (ESI, Figure S55-59).

NMR spectroscopy

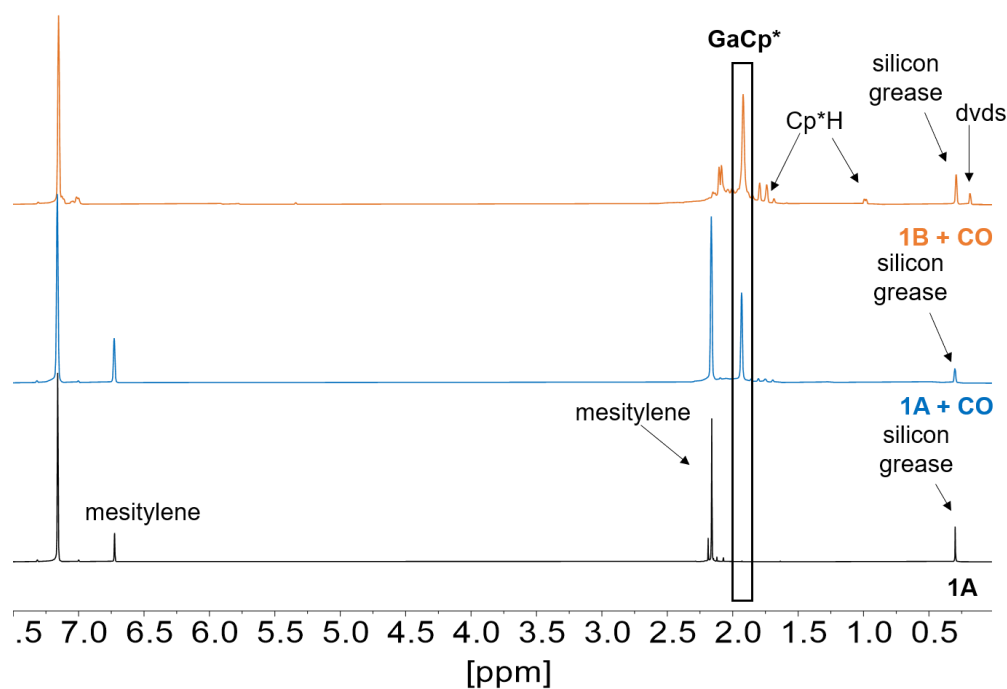


Figure S51: ^1H NMR spectra (toluene- d_8) of **1A** (major component **3**) and **1B** (major component **2**) upon exposure to CO showing a signal of free GaCp^* . ^1H NMR (400 MHz, toluene- d_8 , r.t.): δ_{H} [ppm] = 6.17 (s, mesitylene-CH), 2.17 (s, mesitylene- CH_3), 1.93 (GaCp^*). The residues of dvds in **1B** originate from co-crystallized dvds.

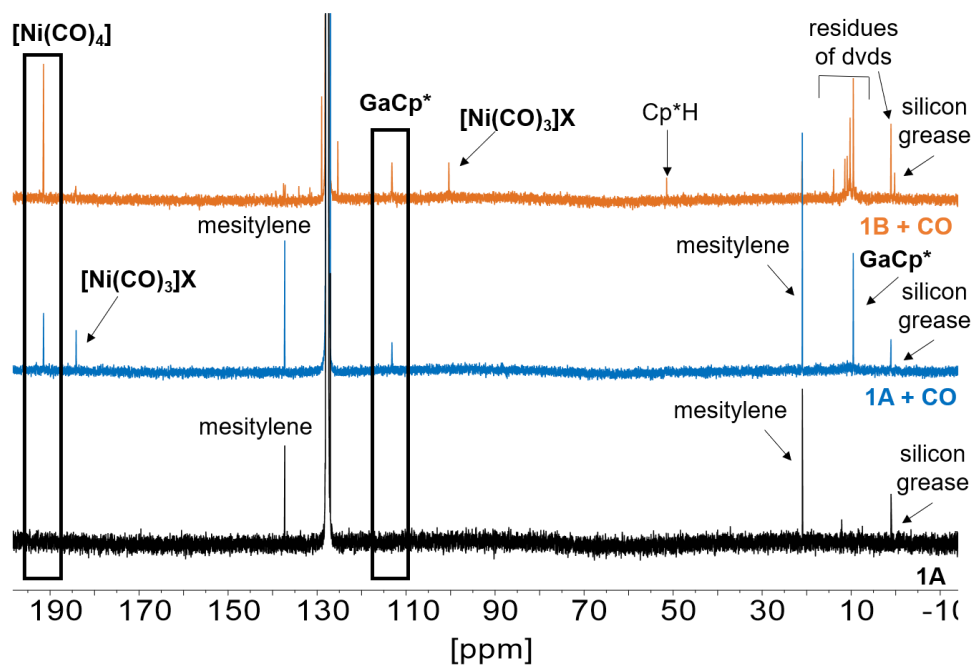


Figure S52: ^{13}C NMR spectra (toluene- d_8) of **1A** (major component **3**) and **1B** (major component **2**) upon exposure to CO showing a signal of $[\text{Ni}(\text{CO})_4]$, free GaCp^* and $[\text{Ni}(\text{CO})_3]\text{X}$. ^{13}C NMR (400 MHz, toluene- d_8 , r.t.): δ_{C} [ppm] = 192 (s, $\text{Ni}(\text{CO})_4$), 137 (s, mesitylene- C_{arom}), 113 (s, GaCp^* , C_{arom}), 20.9 (s, mesitylene- CH_3), 9.44 (s, GaCp^* , CH_3). The residues of dvds in **1B** originate from co-crystallized dvds.

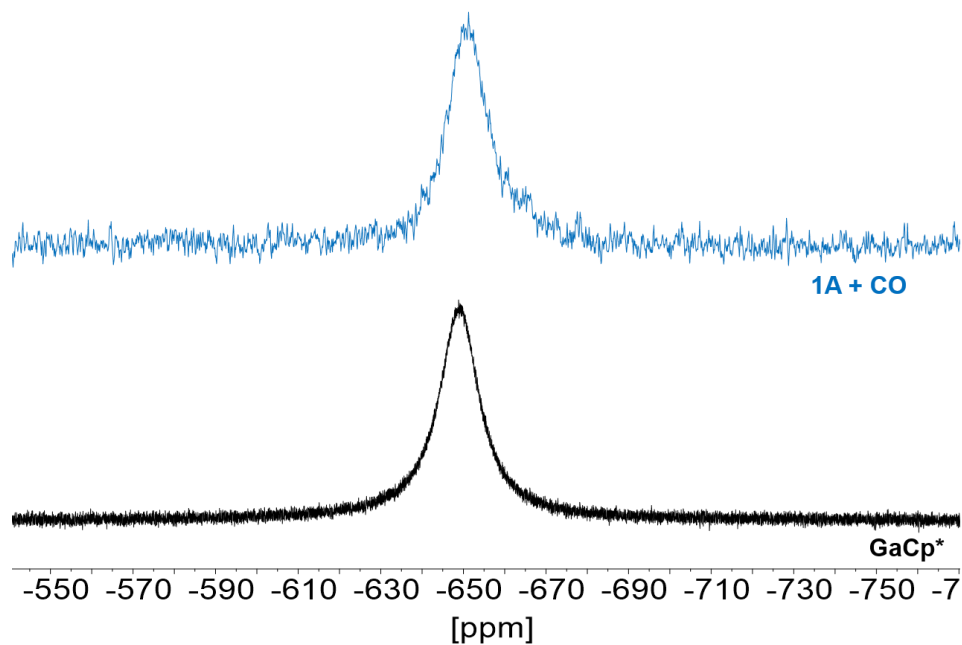


Figure S53: ^{71}Ga NMR spectra (toluene- d_8) of **1A** (major component **3**) and **1B** (major component **2**) upon exposure to CO (blue, top) showing a signal of free GaCp^* (see reference, black, bottom). ^{71}Ga NMR (400 MHz, toluene- d_8 , r.t.): δ_{Ga} [ppm] = -650 (GaCp^*).

IR spectroscopy

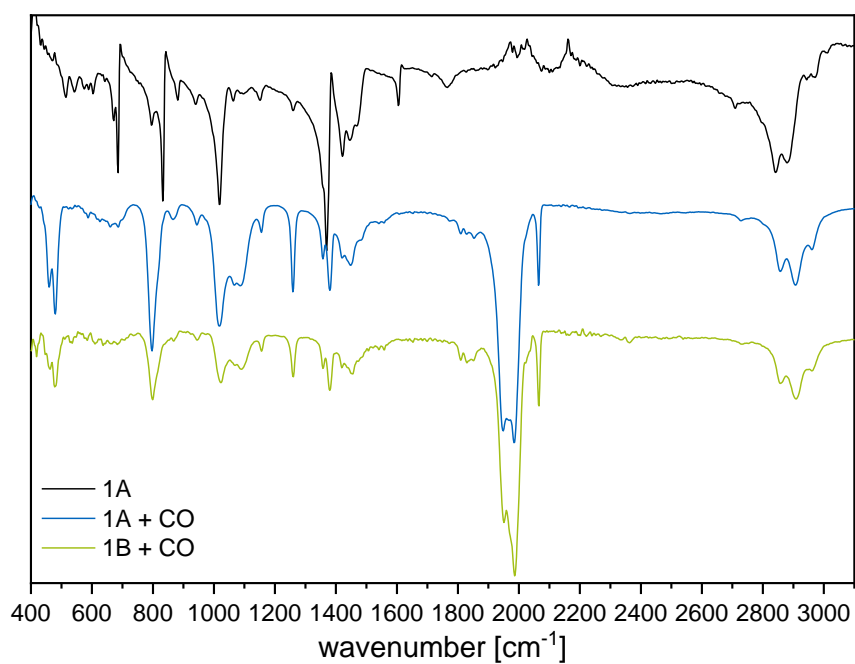


Figure S54: FT-IR measurements of **1A** (major component **3**) and **1B** (major component **2**) with CO. IR (ATR, neat, cm⁻¹): 2960 (w), 2900 (m), 2857 (m), 2066 (s), 1987 (s), 1950 (s), 1851 (w), 1829 (w), 1808 (w), 1483 (w), 1448 (w), 1380 (w), 1357 (m), 1258 (s), 1155 (w), 1089 (m), 1067 (m), 1021 (s), 945 (s), 863 (w), 799 (w), 685 (w), 659 (w), 626 (w), 587 (w), 480 (m), 459 (s).

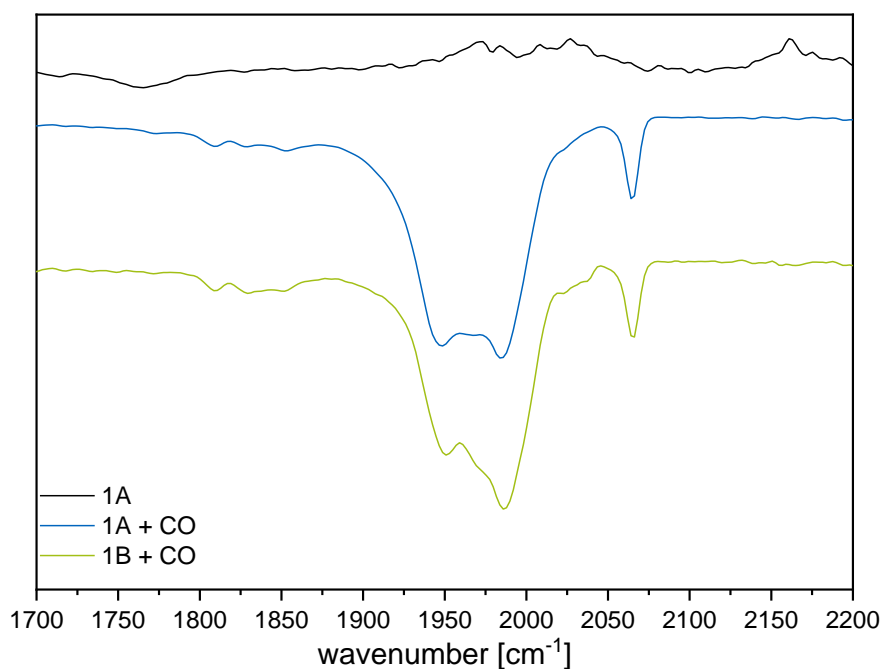


Figure S55: Representative cutout of FT-IR measurements of **1A** (major component **3**) and **1B** (major component **2**) upon exposure to CO showing new signals which can be assigned to species with a X-Ni(CO)₃ structure.

LIFDI-MS measurements

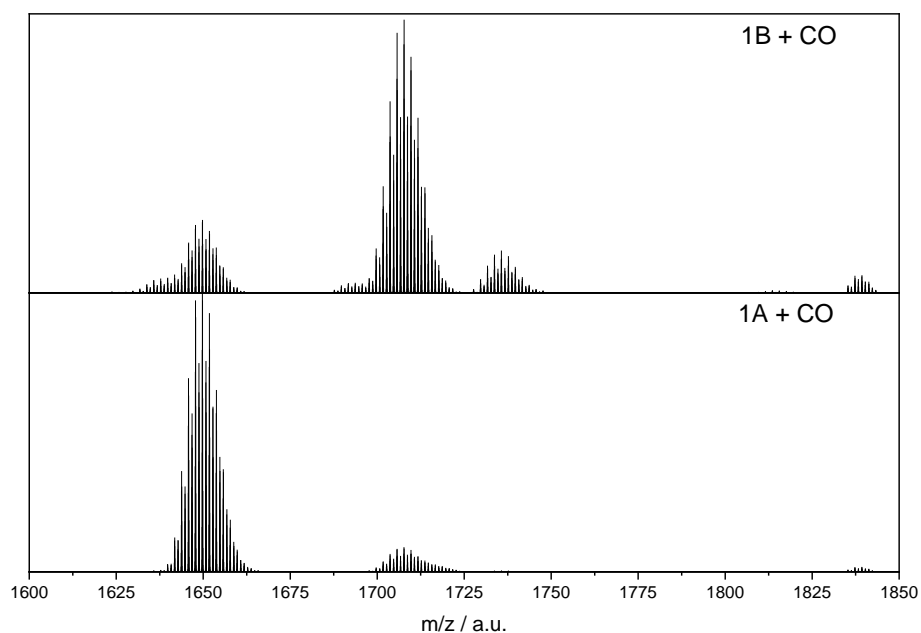


Figure S56: Representative cut-out of LIFDI-MS measurements of **1A** (major component **3**, bottom) and **1B** (major component **2**, top) upon exposure to CO showing the new signals $[\text{Ni}_7\text{Ga}_7](\text{Cp}^*)_6\text{CO}$ ($m/z = 1736.9$) and $[\text{Ni}_8\text{Ga}_8](\text{Cp}^*)_6$ ($m/z = 1837.3$). MS (LIFDI-TOF, toluene): $m/z = 1165.9$ ($[\text{Ni}_6\text{Ga}_2\text{Cp}^*_5]^+$, calc. 1167.1), 1193.8 ($[\text{Ni}_6\text{Ga}_2\text{Cp}^*_5\text{CO}]^+$, calc. 1195.1), 1637.8 ($[\text{Ni}_7\text{Ga}_6\text{Cp}^*_6]^+$, calc. 1638.6), 1649.8 ($[\text{Ni}_6\text{Ga}_7\text{Cp}^*_6]^+$, calc. 1650.3), 1706.7 ($[\text{Ni}_7\text{Ga}_7\text{Cp}^*_6]^+$, calc. 1706.2), 1734.4 ($[\text{Ni}_6\text{Ga}_7\text{Cp}^*_6\text{CO}]^+$, calc. 1734.2), 1835.9 ($[\text{Ni}_6\text{Ga}_9\text{Cp}^*_6]^+$, calc. 1836.7).

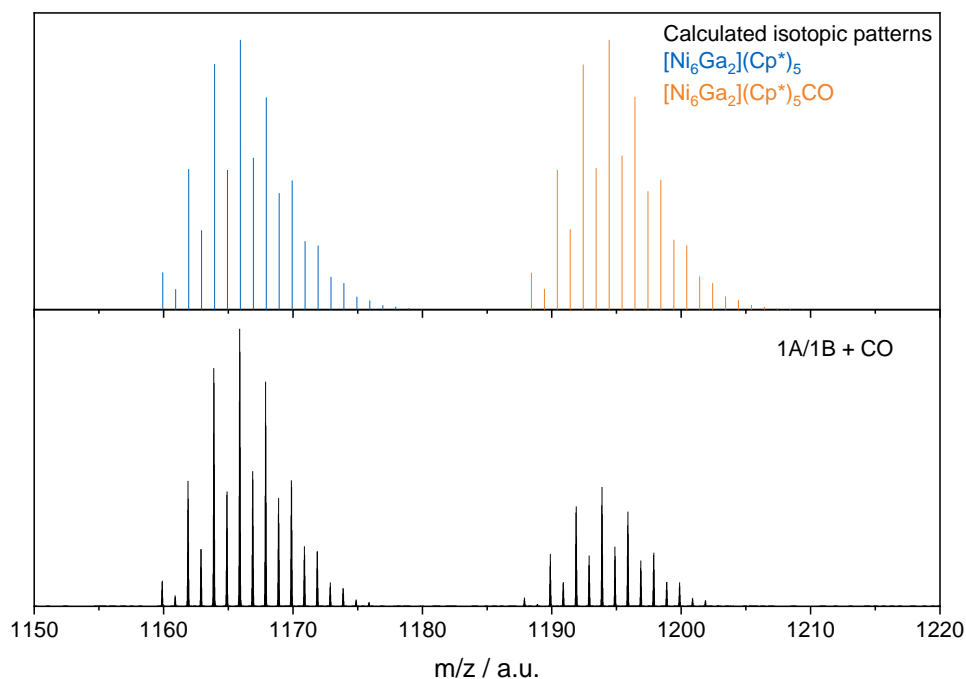


Figure S57: Representative cut-out and zoom-in of LIFDI-MS spectra of **1** upon exposure to CO showing the new signals $[\text{Ni}_6\text{Ga}_2](\text{Cp}^*)_5$ ($m/z = 1167.1$) and the corresponding CO adduct $[\text{Ni}_6\text{Ga}_2](\text{Cp}^*)_5\text{CO}$ ($m/z = 1195.1$). Both **1A** (major component **3**) and **1B** (major component **2**) show identical signals in this region.

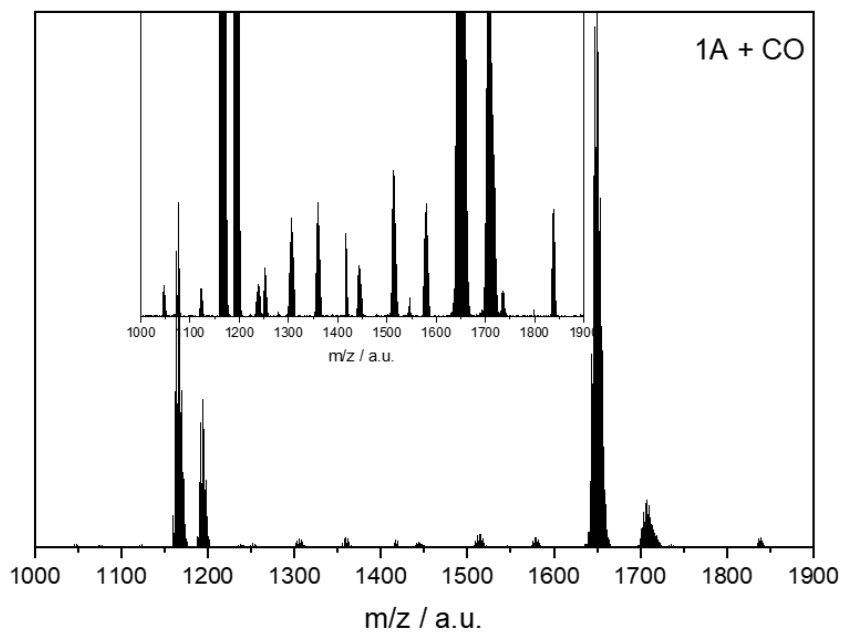


Figure S58: Full LIFDI mass spectra of cluster mixture 1A (major component 3) after treatment with CO zoom-in for a better identification of small cluster signals.

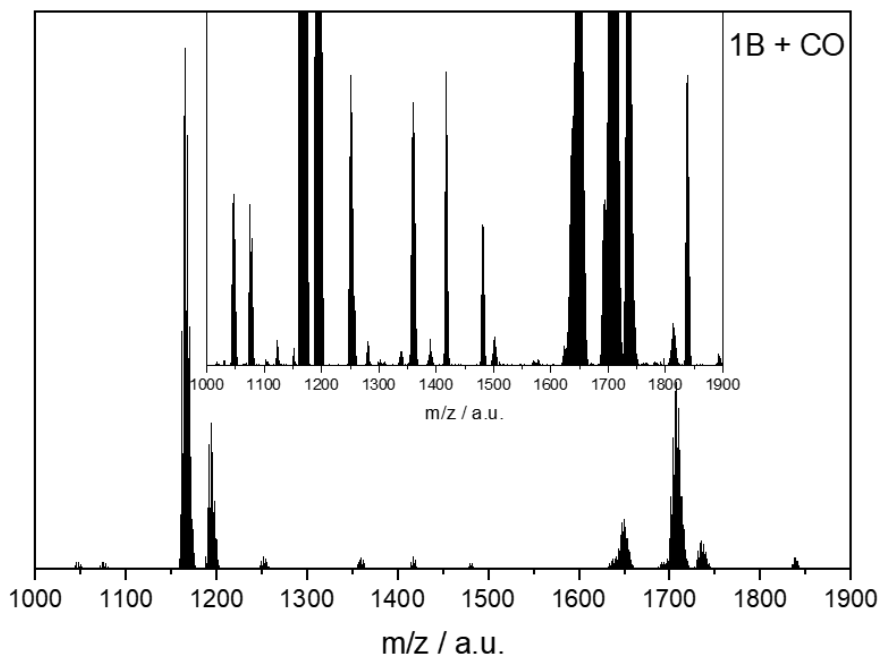


Figure S59: Full LIFDI mass spectra of cluster mixture 1B (major component 2) after treatment with CO with zoom-in for a better identification of small cluster signals.

References for Additional Data

- [S1] Bruker AXS Inc., *APEX suite of crystallographic software, APEX 3 Version 2015-5.2*, Madison, Wisconsin, USA, **2015**.
- [S2] Bruker AXS Inc., *SAINT, Version 8.34A and SADABS, Version 2014/5*, Madison, Wisconsin, USA, **2014**.
- [S3] G. Sheldrick, *Acta Crystallogr., Sect. A* **2008**, *64*, 112-122.
- [S4] C. B. Hubschle, G. M. Sheldrick, B. Dittrich, *J. Appl. Crystallogr.* **2011**, *44*, 1281-1284.
- [S5] a) G. Sheldrick, *Acta Crystallogr., Sect. A* **2015**, *71*, 3-8. b) G. Sheldrick, *Acta Crystallogr., Sect. C* **2015**, *71*, 3-8.
- [S6] *International Tables for Crystallography, Vol. C* (Ed.: A. J. Wilson), Kluwer Academic Publishers, Dordrecht, The Netherlands, **1992**, Tables 6.1.1.4 (pp. 500–502), 4.2.6.8 (pp. 219–222), and 4.2.4.2 (pp. 193–199).
- [S7] C. F. Macrae, I. J. Bruno, J. A. Chisholm, P. R. Edgington, P. McCabe, E. Pidcock, L. Rodriguez-Monge, R. Taylor, J. van de Streek, P. A. Wood, *J. Appl. Cryst.* **2008**, *41*, 466–470.
- [S6] Parr, R. G.; Yang, W. *Density-Functional Theory of Atoms and Molecules*. **1994**, Oxford University Press, UK.
- [S7] a) G. te Velde, F. M. Bickelhaupt, S. J. A. van Gisbergen, C. F. Guerra, E. J. Baerends, J. G. Snijders, T. Ziegler, *J. Comput. Chem.* **2001**, *22*, 931-967; b) ADF2016, SCM, *Theoretical Chemistry*, Vrije Universiteit: Amsterdam, The Netherlands; <http://www.scm.com>.
- [S8] S. Grimme, *J. Comput. Chem.* **2006**, *27*, 1787–1799.
- [S9] E. V. Lenthe, E. J. Baerends, *J. Comput. Chem.* **2003**, *24*, 1142–1156.
- [S10] A. D. Becke, *Phys. Rev. A* **1988**, *38*, 3098–3100.
- [S11] J. P. Perdew, *Phys. Rev. B* **1986**, *33*, 8822–8824.
- [S12] G. Schreckenbach, T. Ziegler, *J. Phys. Chem.* **1995**, *99*, 606-611.
- [S13] G. J. Snijders, E. J. A. Baerends, *Mol. Phys.* **1978**, *36*, 1789-1804.

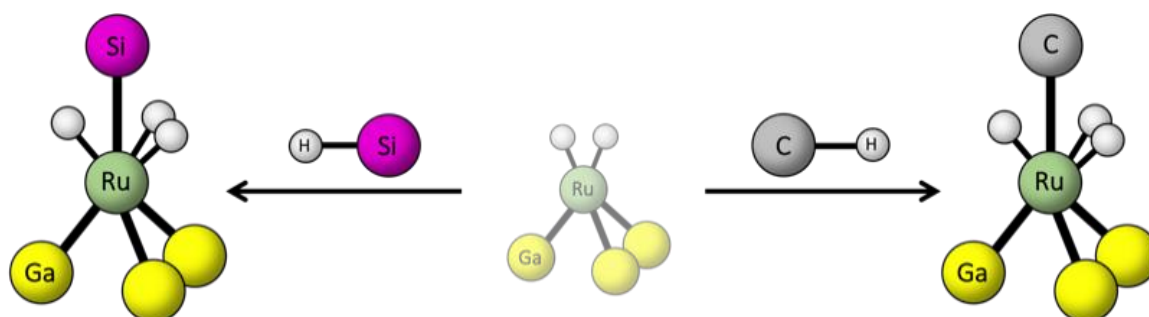
2.3 C-H and Si-H Activation Reactions at Ru/Ga Complexes: a Combined Experimental and Theoretical Case Study on the Ru-Ga Bond.

Maximilian Muhr^{+a}, Raphael Bühler^{+a}, Hao Liang^b, Jonas Gilch^a, Christian Jandl^a, Samia, Kahlal^b, Jean-Yves Saillard^{*b}, Christian Gemel^a, Roland A. Fischer^{*a}

[a] Chair of Inorganic and Metalorganic Chemistry, Department of Chemistry, Catalysis Research Center, Technical University Munich, Lichtenbergstraße 4, D-85748 Garching, Germany

[b] UMR-CNRS, 6226 "Institut des Sciences Chimiques de Rennes, Univ Rennes, CNRS, ISCR-UMR 6226, 35000 Rennes (France).

[+] M.M. and R.B. contributed equally to this work.



The following content has been published: *Chem. Eur. J.*, **2022**, 28, 54.

Reprinted with permission from Chemistry – A European Journal. Copyright the authors, Chemistry – A European Journal published by Wiley-VCH GmbH.

Author contributions:

The manuscript was written by the two authors. Most experiments were planned by M.M. and mainly performed R.B.; Initial DFT calculations by M.M.; J.G. supported experiments and C.J. supported with SCXRD measurements and evaluation. H.L. and S.K. DFT calculations; J.Y.S. writing of theoretical part. C.G. and R.A.F. supervised the research.

2.3.1 Abstract

Treatment of [Ru(COD)(MeAllyl)₂] and [Ru(COD)(COT)] with GaCp* under hydrogenolytic conditions leads to reactive intermediates which activate Si-H or C-H bonds, respectively. The product complexes [Ru(GaCp*)₃(SiEt₃)H₃] (**1**) and [Ru(GaCp*)₃(C₇H₇)H₃] (**2**) are formed with HSiEt₃ or with toluene as the solvent, respectively. While **1** was isolated and fully characterized by NMR, MS, IR and SC-XRD, **2** was too labile to be isolated and was observed and characterized *in-situ* by using mass spectrometry, including labelling experiments for the unambiguous assignment of the elemental composition. The structural assignment was confirmed by DFT computations. The relative energies of the four isomers possible upon toluene activation at the *ortho*-, *meta*-, *para*- and CH₃-positions have been determined and point to aromatic C-H activation. The Ru-Ga bond was analyzed by EDA and QTAIM and compared to the Ru-P bond in the analogue phosphine compound. Bonding analyses indicate that the Ru-GaCp* bond is weaker than the Ru-PR₃ bond.

2.3.2 Main Text

Cooperative effects between transition metals TM and electropositive metals E (e.g. group 12 and 13 elements) play an important role in bond activation reactions of small molecules¹⁻⁹, both in molecular compounds as well as intermetallic solid-state materials¹⁰⁻¹². The cooperative effects are mostly attributed to the electronic properties of intermetallic bonds, featuring electrophilic centers E(d⁺) in direct vicinity to an electron rich TM(d⁻) with pronounced reductive character.¹³⁻¹⁶ Key examples are the Ni/Al complex $[(\text{Cp}^*\text{Al})_3\text{Ni}(\text{m-H})\text{Al}(\text{C}_6\text{H}_5)(\text{h}^1\text{-Cp}^*)]$, which is formed by C-H activation of C₆H₆ (benzene) at the coordinatively unsaturated 16 VE intermediate $[\text{Ni}(\text{AlCp}^*)_3]$,¹⁷ and the Rh/Ga complex $[\text{Cp}^*\text{Rh}\{\text{h}^5\text{-C}_5\text{Me}_4\text{Ga}(\text{CH}_3)_3\}]$, which is formed by C-C activation of Cp*.¹⁸ DFT calculations revealed that the electrophilic character of the gallium center favors the crucial C-C activation reaction step, allowing the reaction to proceed under extremely mild conditions.

Unsaturated Ruthenium phosphine complexes $[\text{Ru}(\text{PR}_3)_n]$ (n = 3, 4) are well-established and are known to activate H-H¹⁹⁻²¹, C-H²² and C-C²³ bonds. Berry and co-workers reported on an oxidative-addition/reductive-elimination equilibrium of different substituted silanes in $[\text{Ru}(\text{PMe}_3)_4(\text{SiR}_3)\text{H}]$.²⁴ The same complex is also capable of activating the C-H bond of benzene in a sequence of similar reactions. They also report the formation of the polyhydride $[\text{Ru}((\text{PMe}_3)_3(\text{SiEt}_3)\text{H}_3)]$ from $[\text{Ru}(\text{PMe}_3)_4\text{H}_2]$.²⁴

$[\text{Ru}(\text{GaCp}^*)_3\text{H}_2]$, which is formed by H-H activation, has been identified as an intermediate in the formation of the cluster $[(\text{GaCp}^*)_4\text{HRu}(\mu\text{-Ga})\text{RuH}_2(\text{GaCp}^*)_3]$.²⁵

In the light of these results and the fact, that experimental as well as theoretical studies support the isolobal relation between GaCp* and phosphines²⁶⁻³² we were interested to investigate the reactivity of the unsaturated $[\text{Ru}(\text{GaCp}^*)_3\text{H}_2]$ in C-H and Si-H bond activation in the context of cluster growth.

The complex $[(\text{Ru}(\text{GaCp}^*)_3(\text{SiEt}_3)\text{H}_3)]$ (**1**) is obtained from $[\text{Ru}(\text{COD})(\text{MeAllyl})_2]$ (COD = 1,5-cyclooctadiene; MeAllyl = 2-methylallyl) and GaCp* in HSiEt₃ under hydrogenolytic conditions, whereas in less reactive solvents (*n*-hexane, cyclohexane), uncontrolled cluster growth is observed. Complex **1** is a structural analogue to $[\text{Ru}(\text{PMe}_3)_3(\text{SiEt}_3)\text{H}_3]$. It was characterized *via* SC-XRD, NMR, MS, IR, Raman, UV/Vis and elemental analysis. The analogous complex $[\text{Ru}(\text{GaCp}^*)_3(\text{C}_7\text{H}_7)\text{H}_3]$ (**2**) is formed upon C-H activation of toluene and was identified by high-resolution mass spectrometry, with DFT calculations allowing the assignment of a plausible structure. Finally, we performed a detailed comparison of the Ru-Ga and Ru-P bondings, including energy decomposition analysis (EDA) and quantum theory of atoms in molecules (QTAIM) analysis.

Synthesis and Characterization $[\text{Ru}(\text{GaCp}^*)_3(\text{SiEt}_3)\text{H}_3]$ (**1**)

The stoichiometric reaction (based on the Ru/Ga ratio) of $[\text{Ru}(\text{COD})(\text{MeAllyl})_2]$ (COD = 1,5-cyclooctadiene; MeAllyl = 2-methylallyl) with three equivalents of GaCp* in triethylsilane under 3 bar H₂ pressure leads to a dark orange solution after 6 h at 60 °C (fig. 1a). After removing all volatiles *in vacuo*, yellow crystals suitable for single crystal x-ray diffraction (SC-XRD) of **1** can be obtained by recrystallization from *n*-hexane at -30 °C. SC-XRD reveals a ruthenium centered complex,

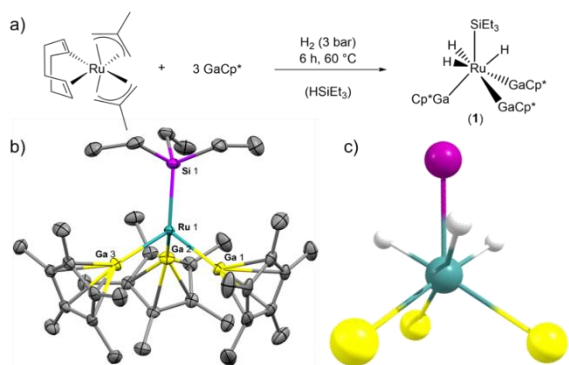


Figure 1: a) Reaction scheme for the synthesis of **1**. b) Molecular structure of $[\text{Ru}(\text{GaCp}^*)_3(\text{SiEt}_3)\text{H}_3]$ (**1**). Ellipsoids at the 50% probability level. H atoms are omitted for clarity. Selected bond lengths (\AA) and angles ($^\circ$): $\text{Ru1-Ga1} = 2.376(3)$, $\text{Ru1-Ga2} = 2.376(4)$, $\text{Ru1-Ga3} = 2.385(6)$, $\text{Ru1-Si1} = 2.373(2)$, $\text{Ga-Cp}^*_{\text{cent}} = 1.970\text{--}1.982$; $\text{Ga1-Ru1-Ga2} = 96.43(2)$, $\text{Ga1-Ru1-Ga3} = 99.36(2)$, $\text{Ga2-Ru1-Ga3} = 97.29(2)$, $\text{Ga1-Ru1-Si1} = 120.98(2)$, $\text{Ga2-Ru1-Si1} = 119.73(2)$, $\text{Ga3-Ru1-Si1} = 118.10(3)$. Space group: $P\ 1\ 21/c\ 1$. c) DFT-optimized structure (BP86/TZ2P) showing the hydrides' positions. $\text{Ru-H} = 1.626\text{--}1.631\ \text{\AA}$; $\text{Si-H} = 2.067\text{--}2.155\ \text{\AA}$. Other C and H atoms omitted for clarity.

tetrahedrally surrounded by three GaCp* ligands and one SiEt₃ unit (fig. 1b). The compound's architecture is isostructural to Berry's complex $[\text{Ru}(\text{PMe}_3)_3(\text{SiEt}_3)\text{H}_3]$. It should be noted that the hydride ligands could not be located with final certainty in the structure refinement. The Ru-Ga bond lengths, which vary only slightly from 2.376(3) \AA to 2.385(6) \AA , as well as the Ga-Cp*_{centroid} distances (1.970 – 1.982 \AA), are in good agreement with distances reported in the literature.^{25, 33-35} The Ru-Si bond length (2.373(2) \AA) also matches Ru-Si bond lengths reported in the literature.^{36,37} Notably, it only differs 0.003 \AA from the isostructural $[\text{Ru}(\text{PMe}_3)_3(\text{SiEt}_3)\text{H}_3]$.²⁴ The tetrahedral structure is distorted, due to the three sterically demanding GaCp*, resulting in Ga-Ru-Si angles ranging from 118.1 ° to 121.0 °. The ¹H NMR gives the expected set of signals for the three GaCp* ($\delta = 1.88$ ppm, s, 45 H) and the three ethyl groups of the silyl ($\delta = 1.26$ ppm, t, 9 H; $\delta = 0.92$ ppm, q, 6 H).

This is in good agreement with the ¹³C signals: The Cp* ligand (ring carbon at $\delta = 113.5$ ppm and methyl groups at $\delta = 10.0$ ppm), as well as the silyl-ethyl signals for CH₃ ($\delta = 10.5$ ppm) and CH₂ groups ($\delta = 20.2$ ppm). Moreover, the ¹H NMR shows one broad singlet at $\delta = -13.31$ ppm with a relative intensity equivalent to 2.7, strongly indicating the presence of three hydrides similar to $[\text{Ru}(\text{PMe}_3)_3(\text{SiEt}_3)\text{H}_3]$. The presence of hydrides is further supported by vibrational spectroscopy: In the infrared spectrum an intensive broad band at 1898 cm^{-1} , along with a small shoulder at 1771 cm^{-1} is present in the typical Ru-H region. The expected band in the Raman spectrum, is observed at 1913 cm^{-1} (fig. S24). High resolution liquid injection field desorption ionization mass spectrometry (LIFDI-MS) gives rise to a signal for $[\text{M-2H}]^{+*}$ ($m/z = 832.131$; calc = 832.134), we attribute the loss of two H atoms to fragmentation. Based on the SC-XRD structural data of **1**, its geometry was fully optimized by DFT calculations at the BP86/TZ2P level (see Computational Details). In analogy to the molecular structure of $[\text{Ru}(\text{PMe}_3)_3(\text{SiEt}_3)\text{H}_3]$ ²⁴, the structure of lowest energy found for **1** (confirmed as a minimum by frequency calculations) corresponds to a configuration in which the three hydrides are located in an umbrella-like arrangement (fig. 1c). The DFT-simulated spectrum (fig. S22) is in reasonable agreement with the experimental data, showing Ru-H bands at 1985 cm^{-1} (symmetric stretch), 1961 cm^{-1} and 1942 cm^{-1} (both asymmetric stretches). This optimized structure is in very good agreement with the crystal structure. Ru-Ga and Ru-Si bonds only differ by less than 0.005 \AA , and bond angles of the 'metal core' (Ru/Ga/Si) only by less than 4°. The computed Si...H distances (2.067

Å – 2.155 Å) are indicative of no bonding interaction. All calculated Ru-H distance are almost equivalent, ranging from 1.626 to 1.631 Å. The computed H-H distances (2.404 Å – 2.493 Å) indicate classical hydride ligands rather than dihydrogen-bonding. This is confirmed in a T_1 relaxation NMR experiment (fig. S5), with $T_1(\text{min}) = 546 - 1231$ ms (193 K – 293 K). The computed ^1H hydride chemical shifts (-10.3 ppm) are 3 ppm lower than their experimental counterparts, whereas the other computed ^1H signals differ by less than 1 ppm than their observed homologues. The same situation is found for the hydride signal in the related complex $[\text{Ru}(\text{PMe}_3)_3(\text{SiEt}_3)\text{H}_3]$ (computed: -7.7 ppm; recorded -10.53 ppm²⁴), whereas the average deviation of all other proton signals is also less than 1 ppm. All these results strongly support the trihydride nature of **1**.

C-H activation of toluene: $[\text{Ru}(\text{GaCp}^)_3(\text{C}_7\text{H}_7)\text{H}_3]$ (**2**)*

After observing that Si-H bonds can be activated, we wanted to investigate whether C-H bonds can also be activated in a similar manner. Thus $[\text{Ru}(\text{COD})(\text{MeAllyl})_2]$ and $[\text{Ru}(\text{COD})(\text{COT})]$ (COT = 1,3,5-cyclooctatriene) were reacted with GaCp^* under analogous reaction conditions to **1** in toluene. Both reactions lead to dark brown solutions even after a short time of 20 minutes. Notably, the formation of **1** seems to be slower as judged by the color change to orange after six hours. LIFDI-MS suggests the formation of a series of toluene containing compounds. As shown by experiments with different Ru precursors, the nature of the Ru source is important for the product distribution, however, differences become prominent only after prolonged reaction times. After one hour the

reaction solutions of $[\text{Ru}(\text{COD})(\text{MeAllyl})_2]/\text{GaCp}^*$ as well as $[\text{Ru}(\text{COD})(\text{COT})]/\text{GaCp}^*$ in toluene contain products producing the same series of ions, which can be assigned to different toluene containing species: $[\text{Ru}_2(\text{GaCp}^*)_4(\text{C}_7\text{H}_8)\text{H}_2]^+$ ($m/z = 1116.056$; $\text{calc} = 1116.058$), $[\text{Ru}_2(\text{Ga})(\text{GaCp}^*)_3(\text{C}_7\text{H}_8)\text{H}]^+$ ($m/z = 980.933$; $\text{calc} = 980.933$), $[\text{Ru}_2(\text{GaCp}^*)_3(\text{C}_7\text{H}_8)\text{H}_2]^+$ ($m/z = 912.015$; $\text{calc} = 912.014$), $[\text{Ru}(\text{GaCp}^*)_3(\text{C}_7\text{H}_8)\text{H}_2]^+$ ($m/z = 810.109$; $\text{calc} = 810.110$), $[\text{Ru}(\text{GaCp}^*)_2(\text{C}_7\text{H}_8)]^+$ ($m/z = 604.051$; $\text{calc} = 604.051$). While the mass spectrum of the reaction solution of $[\text{Ru}(\text{COD})(\text{COT})]/\text{GaCp}^*$ remains largely unchanged over time, the mass spectrum of the reaction solution of $[\text{Ru}(\text{COD})(\text{MeAllyl})_2]/\text{GaCp}^*$ reveals almost exclusively the ion $[\text{Ru}(\text{GaCp}^*)_3(\text{C}_7\text{H}_7)\text{H}_3]^+$ (**2**⁺) after 48 hours. We conclude from the measured sum formula that this signal does not represent a fragment but rather the molecular ion **2**⁺, since the corresponding neutral complex **2** satisfies the 18 valence electron (VE) rule and is isoelectronic to **1**. A

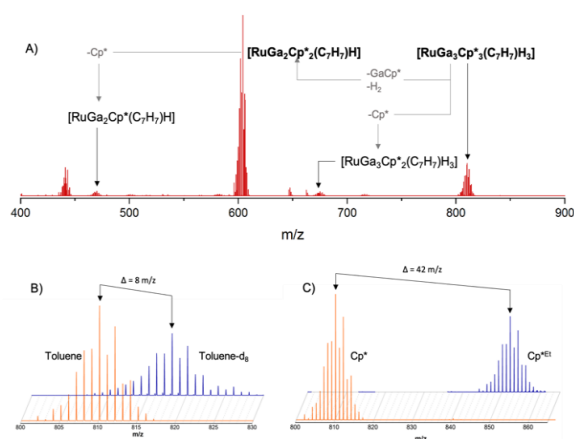


Figure 2: a) size focused LIFDI-MS spectrum of **2** with the composition of the molecular ion and the main fragments given. b) LIFDI-MS patterns of **2** for the reaction in toluene and the labeling experiment using toluene- d_8 and c) the LIFDI-MS patterns of **2** with Cp^* and Cp^{Et} . The m/z difference of 8 and 42 respectively shows the incorporation of one toluene and three Cp^* into the compound.

pattern at $m/z = 604.051$

[[Ru(GaCp*)₂(C₇H₈)]⁺⁺) is assigned to the fragment [M-GaCp*-2H]⁺⁺ of **2** (fig. 2a). These assignments and the composition of **2** could be confirmed by double labelling experiments with toluene-d₈ (fig. 2b) and with the mono ethyl-substituted derivative GaCp*^{Et} (Cp*^{Et} = 1-ethyl-2,3,4,5-tetramethylcyclopentadienyl) (fig. 2c), revealing the expected *m/z* differences of respectively 8 and 42 (three additional CH₂ groups).

In contrast to **1**, compound **2** could not be isolated. It is formed in solution after long reaction times and can be enriched, although some thermal degradation in solution is also observed then, becoming obvious from the formation of metallic precipitate and mirror. We also noticed a stark influence of the concentration, i.e. **2** can be enriched only when working at low concentrations (C_{total} < 5 mg/mL). Combined with the unstable nature of **2** under reduced pressure, it was thus impossible to crystallize the compound or to characterize enriched/pure samples with solution spectroscopic techniques (NMR, IR). Nevertheless ¹H NMR of reaction solutions shows hydride signals (-14.15, -15.63, -16.03 and -16.22 ppm, fig. S6), as does the IR spectrum with bands at 1807 and 1861 cm⁻¹

(fig. S23). Inspired by the thermal induced reductive elimination of HSiEt₃ from [(Cp*Al)₃NiH(SiEt₃)] yielding [(Cp*Al)₃Ni(m-H)Al(C₆H₅)(h¹-Cp*)] by subsequent C-H activation of benzene¹⁷, we attempted the preparation of a pure sample of **2** from thermal treatment of **1** in toluene. Even under harsh conditions, no reaction was observed. A similar behaviour was observed for the treatment of a solution of **2** with an excess of HSiEt₃.

As no experimental access to structural data was possible, reasonable structures representing energy minima for the postulated trihydride complex **2** were calculated on the DFT level of theory. The energetically most favorable structures correspond to activated toluene in *ortho*, *meta*, *para* and benzylic position, respectively (fig. 3). Their computed relative energies indicate that the products upon C-H activation at an aromatic position are almost equal in energy and are favored with respect to the activation at the benzylic position. The energy difference between the *ortho* and *meta* isomers is insignificant and that of the *para* relative is barely larger. Thus, even if not considering the possibility of topological isomerism for each individual *ortho*, *meta* and *para* system, the possibility of having several isomers in solution should not be excluded. These calculations only reflect thermodynamic stability. In order to investigate differences in regioselectivity between each site's activation, we performed analogous experiments in benzene (all-aromatic) as well as in *tert*-butylbenzene (no benzylic C-H). Indeed, in both cases the respective signals (*m/z*) of the expected activation products were observed by LIFDI-MS (fig. S12 and S13; benzene: *m/z* = 796.094; calc = 796.094; *tert*-

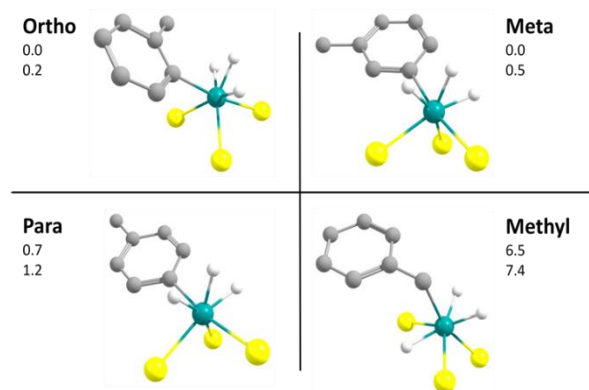


Figure 3: Calculated isomers of **2** with their relative total (ΔE) and free (ΔG) energy differences in kcal/mol (top: ΔE ; bottom: ΔG). Cp* and hydrogen atoms of toluene omitted for clarity.

butylbenzene: $m/z = 852.155$; calc = 852.157). The presence of the respective benzene- d_6 activation is further supported by the corresponding hydride signal (-16.56 ppm; fig. S7).

Taken together our experimental and computational data it is reasonable to assume that the formation of **2** proceeds *via* C-H activation of toluene on the electron-deficient intermediate $[(\text{Cp}^*\text{Ga})_3\text{RuH}_2]$.²⁵ To validate this hypothesis, the hydrogenolysis of ruthenium complexes with GaCp^* was performed in *n*-hexane to prevent C-H or Si-H activation. This may lead to the activation of a second H_2 equivalent.³⁸ While there is no experimental evidence for a potential $[(\text{Cp}^*\text{Ga})_3\text{RuH}_4]$, cluster growth reactions are observed by LIFDI-MS (fig. S14). This points to reactive intermediates and related competing reactions between bond activation (in aromatic solvents or silane) and cluster growth.

Starting from $[(\text{Cp}^*\text{Ga})_3\text{RuH}_2]$, DFT calculations allow the rationalization of the observed reactivity from a thermodynamic point of view. C-H activation of toluene at

$[(\text{Cp}^*\text{Ga})_3\text{RuH}_2]$ is thermodynamically favorable according to free energy calculations ($\Delta G = -11.8$ kcal/mol). Note that replacing toluene by benzene barely changes the reaction energy ($\Delta G = -11.3$ kcal/mol). Replacing $[(\text{Cp}^*\text{Ga})_3\text{RuH}_2]$ by its hypothetical phosphine-ligated analogue $[(\text{PMe}_3)_3\text{RuH}_2]$ cancels the exergonicity of the toluene C-H activation reaction ($\Delta G = +1.4$ kcal/mol). A similar trend and energetic difference are found for the Si-H addition of HSiEt_3 on the same electron-deficient species. In the case of $[(\text{Cp}^*\text{Ga})_3\text{RuH}_2]$, $\Delta G = -43.1$ kcal/mol, whereas in the case of $[(\text{PMe}_3)_3\text{RuH}_2]$, $\Delta G = -28.8$ kcal/mol.

Theoretical Investigations on the Ru-Ga and Ru-P Bonding

Both **1** and $[\text{Ru}(\text{PMe}_3)_3(\text{SiEt}_3)\text{H}_3]$ are hepta-coordinated Ru(IV) 18 VE complexes that can be described as made of a pseudo-octahedral $[\text{RuL}_3\text{H}_3]$ ($L = \text{GaCp}^*, \text{PMe}_3$) unit to which an SiEt_3 ligand is added along the C_3 axis. The four Ru(IV) electrons are expected to occupy non-bonding 4d orbitals, i.e., those which do not point towards ligands, namely MOs of dominant xy and x^2-y^2 character (considering the z axis colinear with the Ru-Si bond). As shown by the Kohn-Sham orbital diagrams of **1** and $[\text{Ru}(\text{PMe}_3)_3(\text{SiEt}_3)\text{H}_3]$ (fig. 4), these two orbitals are the HOMO and HOMO-1 of the complexes. Despite their qualitatively related electronic structures, both complexes have some differences, as exemplified by their HOMO-LUMO gaps, that of **1** being much lower than that of its phosphine analogue. The lowest metal-ligand antibonding orbital of **1** is its LUMO, whereas it is the LUMO+1 in the phosphine complex. Selected computed data for both complexes are gathered in Table S1. They show roughly similar bond distances around Ru in both complexes, with similar Wiberg indices, which however

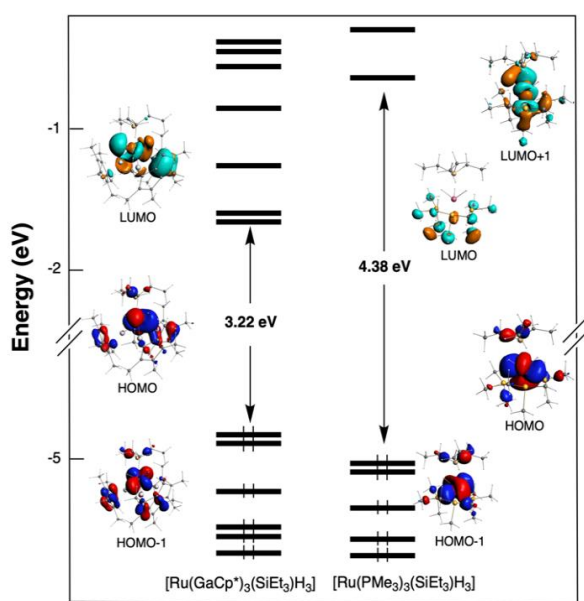


Figure 4: Kohn-Sham MO diagrams of **1** and $[\text{Ru}(\text{PMe}_3)_3(\text{SiEt}_3)\text{H}_3]$.

indicate that the Ru-Ga bonding is somewhat weaker than the Ru-P one. To gain deeper insights into the Ru-L (L = GaCp*, PMe₃) bonding in **1** and [Ru(PMe₃)₃(SiEt₃)H₃], we performed an energy decomposition analysis (EDA) of the interaction between two frozen molecular fragments, according to the Morokuma-Ziegler procedure.³⁹⁻⁴¹ The decomposition of the total bonding energy (TBE) between the [RuH₃(SiEt₃)] fragment and its L₃ shell is provided in Table 1. TBE is expressed as the sum of four components: the Pauli repulsion (E_{Pauli}), the electrostatic interaction energy (E_{elstat}), the orbital interaction energy (E_{orb}) and the component associated with the dispersion forces (E_{disp}). From comparing these TBE values, it is clear that the Ru-L bonding is stronger in the case where L = PMe₃ than for L = GaCp*. Whereas the E_{Pauli} and E_{elstat} components of the two compounds differ significantly, their sum, which is often approximated to the steric part of the interaction energy are about the same (E_{Steric} = 2.37 and 2.48 eV for L = GaCp* and PMe₃, respectively). Since the E_{disp} contributions are also similar, the TBE main difference originates from the E_{orb} components, which reflect difference in covalency. This is also consistent with the difference in the HOMO-LUMO gaps. A similar qualitative trend is found for the hypothetical unsaturated species [Ru(GaCp*)₃H₂] [Ru(PMe₃)₃H₂].

Another point of view can be provided by the quantum theory of atoms in molecules (QTAIM) approach.⁴²⁻⁴³ Selected QTAIM data associated with the Ru-Ga/P bond critical points in **1** and [Ru(PMe₃)₃(SiEt₃)H₃] are collated in Table S2.

In both compounds, the positive value of the Laplacian density, the negative values of the energy and potential energy densities and

the larger than 1 $|V|/G$ ratio are not contradicting the typical description of a ligand-to-metal dative bonding in both compounds.⁴⁴⁻⁴⁶ The delocalisation index is indicative of a weaker Ru-Ga covalent interaction, in agreement with the EDA analysis and Wiberg bond indices. The AIM charges indicate a more negatively polarized Ru in the case of Ru-Ga as compared to Ru-P. This points to a bond polarization of the form TM(δ^-)-E(δ^+), which could already be expected from previous reports^{19, 22-23, 31}, As shown in Tables 1, S1 and S2, the Ru-Ga vs. Ru-P bonding features are maintained on the hypothetical 16 VE intermediates [RuL₃H₂] (L = GaCp*, PMe₃).

Conclusion

Ru/Ga complexes have been investigated with respect to their behavior in C-H and Si-H bond activation reactions. [Ru(GaCp*)₃H₂] has been proposed as the crucial intermediate in the bond activation reactions, DFT calculations confirming the increased reactivity with respect to the phosphine analogue [Ru(PMe₃)₃H₂].

[Ru(GaCp*)₃H₂] has also been described in earlier studies as a reactive intermediate on

Table 1: Morokuma-Ziegler energy decomposition analysis of **1**, [Ru(GaCp*)₃H₂], and their trimethylphosphine analogues. All values are in eV.

Compound	[Ru(GaCp*) ₃ (SiEt ₃)H ₃] (1)	[Ru(PMe ₃) ₃ (SiEt ₃)H ₃]	[Ru(GaCp*) ₃ H ₂]	[Ru(PMe ₃) ₃ H ₂]
Fragmentation	[RuH ₃ (SiEt ₃)] + [GaCp*] ₃	[RuH ₃ (SiEt ₃)] + [PMe ₃] ₃	[RuH ₂] + [GaCp*] ₃	[RuH ₂] + [PMe ₃] ₃
E_{Pauli}	11.52	15.19	11.55	16.94
E_{elstat}	-9.15	-12.71	-9.82	-14.35
E_{orb}	-5.99	-8.04	-6.86	-9.67
E_{disp}	-1.45	-1.36	-0.84	-0.94
TBE ^a	-5.08	-6.93	-5.97	-8.02

the way to Ru/Ga clusters. Thus, reductive elimination of Cp*H leads to a ligand stabilized Ru/Ga cluster with a linear Ru-Ga-Ru backbone.²⁵ This underlines the crucial role of transient and/or intermediate species in cluster growth reactions. The "proto" cluster species [Ru(GaCp*)₃H₂] obviously can act as a reactive building block for larger clusters, whereby substrate or solvent molecules actively intervene in the reaction process by stabilizing the intermediate by an equilibrium of oxidative addition and reductive elimination reactions. Controlling the resulting complexity often remains a challenge. One possible approach to control cluster growth, however, which has been recently successfully employed in the synthesis of Ni/Al and Ni/Ga clusters is the use of alkynes as additives.⁴⁷ A propagation of this idea with the aim of investigating larger Ru/Ga clusters is part of an ongoing project and will be presented in future work.

Computational Details

Density Functional Theory (DFT) calculations were carried out with the use of the ADF2020 code^{49,50} with the addition of Grimmes's D3 empirical corrections⁵¹ to take into account dispersion effects. The triple-zeta with two polarization functions (TZ2P) basis set was used, together with the BP86^{52,53} exchange-correlation functional. All the optimized structures were confirmed as true minima on their potential energy surface by analytical vibration frequency calculations. Wiberg bond indices were computed with the NBO 6.0 program⁵⁴ implemented in the ADF2020 package. The QTAIM analysis⁴²⁻⁴³ was performed as implemented in the ADF2019 suite.⁵⁵⁻⁵⁶ The ¹H NMR chemical shifts were computed on the BP86/TZ2P-optimized structures, according to the GIAO method,⁵⁷

with the B3LYP functional⁵⁸ and taking into account solvent (benzene) effect *via* the COSMO model.^{59,60}

Synthetic Protocols

[Ru(GaCp*)₃(SiEt₃)(H)₃] (**1**). A solution of 450 mg (1.0 eq., 1.410 mmol) [Ru(COD)(MeAllyl)₂] and 867 mg (3.0 eq., 4.230 mmol) GaCp* in 6 mL HSiEt₃ is freeze-pump-thawed-degassed and pressurized with 3 bar H₂ in a 150 mL Fisher-Porter bottle. The reaction solution turns from yellow to dark orange over 6 h at 60 °C. Residual HSiEt₃ is removed in vacuo and 830 mg (71 %, 0.995 mmol) of **1** are obtained by recrystallization from *n*-hexane. ¹H NMR (C₆D₆, 400 MHz): δ [ppm] = 1.88 (s, 45 H, GaCp*), 1.26 (t, 9H, SiCH₂-CH₃), 0.92 (q, 6H, Si-H₂C), -13.31 (s, 3H, Ru-H). ¹³C NMR (C₆D₆, 101 MHz): δ [ppm] = 113.5 (s, C₅(CH₃)₅), 20.2 (s, Si-CH₂), 10.5 (s, SiCH₂-CH₃) 10.0 (s, C₅(CH₃)₅). ATR-IR [cm⁻¹]: 1898, 1771 (Ru-H). Raman [cm⁻¹]: 1913 (Ru-H). UV-Vis (cyclohexane) λ_{max} = 226 nm, 281 nm, 344 nm. LIFDI-MS m/z = 832.1313 [M-2H]⁺. (calc = 832.1339). Elemental analysis calc. for RuGa₃C₃₆H₆₃Si: C, 51.83; H, 7.61; Ga, 25.07; Ru, 12.12; Si, 3.37. Found: C, 51.74; H, 7.77; Ga, 24.3; Ru, 12.0; Si, 3.79.

[Ru(GaCp)₃(C₇H₇)H₃] (**2**)

50.0 mg [Ru(cod)(MeAllyl)₂] (1.0 eq., 0.157 mmol) and 65.0 mg GaCp* (2.0, 0.313 mmol) are inserted into a 150 mL Fisher-Porter Bottle, dissolved in 14 mL toluene. The solution is freeze-pump-thawed-degassed and pressurized with 3 bar H₂. The reaction mixture is stirred at 60 °C for 48 hours and then canula filtrated.

LIFDI-MS m/z = 810.1088 [M]⁺ (calc = 810.1100), m/z = 604.0508 [M-GaCp*₂H]⁺ (calc = 604.0514).

Acknowledgements

This work was funded by the German Research Foundation (DFG) within a Reinhard Koselleck Project (FI-502/44-1), the TUM Graduate School and the GENCI French national computer resource center (grant A0030807367). H.L. thanks the China Scholarship Council for a Ph.D. grant. The authors thank Dardan Ukaj for measuring the Raman spectrum of **1**.

2.3.3 References

- [1] R. C. Cammarota, M. V. Vollmer, J. Xie, J. Ye, J. C. Linehan, S. A. Burgess, A. M. Appel, L. Gagliardi, C. C. Lu, *J. Am. Chem. Soc.* **2017**, *139*, 14244-14250.
- [2] J. Fajardo, J. C. Peters, *J. Am. Chem. Soc.* **2017**, *139*, 16105-16108.
- [3] I. Fujii, K. Semba, Q.-Z. Li, S. Sakaki, Y. Nakao, *J. Am. Chem. Soc.* **2020**, *142*, 11647-11652.
- [4] H. Kameo, J. Yamamoto, A. Asada, H. Nakazawa, H. Matsuzaka, D. Bourissou, *Angew. Chem. Int. Ed.* **2019**, *131*, 18959-18963.
- [5] R. Seki, N. Hara, T. Saito, Y. Nakao, *J. Am. Chem. Soc.* **2021**, *143*, 6388-6394.
- [6] W.-C. Shih, O. V. Ozerov, *J. Am. Chem. Soc.* **2017**, *139*, 17297-17300.
- [7] J. Takaya, N. Iwasawa, *J. Am. Chem. Soc.* **2017**, *139*, 6074-6077.
- [8] M. V. Vollmer, J. Ye, J. C. Linehan, B. J. Graziano, A. Preston, E. S. Wiedner, C. C. Lu, *ACS Catal.* **2020**, *10*, 2459-2470.
- [9] R. Yamada, N. Iwasawa, J. Takaya, *Angew. Chem. Int. Ed.* **2019**, *58*, 17251-17254.
- [10] M. Armbrüster, K. Kovnir, M. Friedrich, D. Teschner, G. Wowsnick, M. Hahne, P. Gille, L. Szentmiklósi, M. Feuerbacher, M. Heggen, F. Girgsdies, D. Rosenthal, R. Schlögl, Y. Grin, *Nat. Mater.* **2012**, *11*, 690-693.
- [11] J. Prinz, C. A. Pignedoli, Q. S. Stöckl, M. Armbrüster, H. Brune, O. Gröning, R. Widmer, D. Passerone, *J. Am. Chem. Soc.* **2014**, *136*, 11792-11798.
- [12] F. Studt, F. Abild-Pedersen, T. Bligaard, Z. Sørensen Rasmus, H. Christensen Claus, K. Nørskov Jens, *Science* **2008**, *320*, 1320-1322.
- [13] M. Armbrüster, *Sci. Technol. Adv. Mater* **2020**, *21*, 303-322.
- [14] J. Campos, *Nat. Rev. Chem.* **2020**, *4*, 696-702.
- [15] S. Furukawa, T. Komatsu, *ACS Catal.* **2017**, *7*, 735-765.
- [16] K. Mayer, J. Weßing, T. F. Fässler, R. A. Fischer, *Angew. Chem. Int. Ed.* **2018**, *57*, 14372-14393.
- [17] T. Steinke, C. Gemel, M. Cokoja, M. Winter, R. A. Fischer, *Angew. Chem. Int. Ed.* **2004**, *116*, 2349-2352.
- [18] T. Cadenbach, C. Gemel, R. Schmid, R. A. Fischer, *J. Am. Chem. Soc.* **2005**, *127*, 17068-17078.
- [19] R. H. Crabtree, D. G. Hamilton, *J. Am. Chem. Soc.* **1986**, *108*, 3124-3125.
- [20] R. O. Harris, N. K. Hota, L. Sadavoy, J. M. C. Yuen, *J. Organomet. Chem.* **1973**, *54*, 259-264.
- [21] S. Wesselbaum, T. vom Stein, J. Klankermayer, W. Leitner, *Angew. Chem. Int. Ed.* **2012**, *51*, 7499-7502.
- [22] Z. Ruan, S.-K. Zhang, C. Zhu, P. N. Ruth, D. Stalke, L. Ackermann, *Angew. Chem. Int. Ed.* **2017**, *56*, 2045-2049.
- [23] E. L. Dias, S. T. Nguyen, R. H. Grubbs, *J. Am. Chem. Soc.* **1997**, *119*, 3887-3897.
- [24] V. K. Dioumaev, L. J. Procopio, P. J. Carroll, D. H. Berry, *J. Am. Chem. Soc.* **2003**, *125*, 8043-8058.

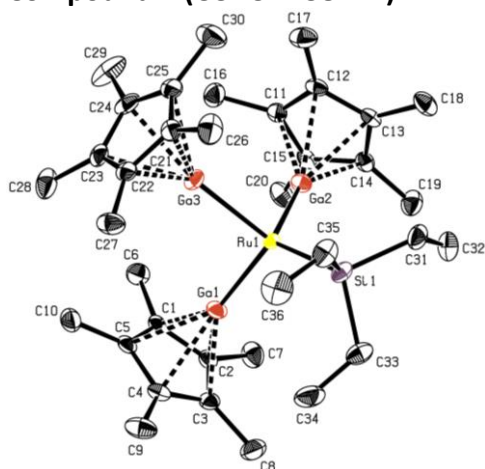
- [25] T. Cadenbach, C. Gemel, R. Schmid, M. Halbherr, K. Yusenko, M. Cokoja, R. A. Fischer, *Angew. Chem. Int. Ed.* **2009**, *48*, 3872-3876.
- [26] R. A. Fischer, J. Weiß, *Angew. Chem. Int. Ed.* **1999**, *38*, 2830-2850.
- [27] J. Hornung, J. Weßing, P. Jerabek, C. Gemel, A. Pöthig, G. Frenking, R. A. Fischer, *Inorg. Chem.* **2018**, *57*, 12657-12664.
- [28] M. Muhr, J. Hornung, J. Weßing, C. Jandl, C. Gemel, R. A. Fischer, *Inorg. Chem.* **2020**, *59*, 5086-5093.
- [29] T. Steinke, C. Gemel, M. Winter, R. A. Fischer, *Chem. Eur. J.* **2005**, *11*, 1636-1646.
- [30] J. Uddin, C. Boehme, G. Frenking, *Organometallics* **2000**, *19*, 571-582.
- [31] J. Uddin, G. Frenking, *J. Am. Chem. Soc.* **2001**, *123*, 1683-1693.
- [32] W. Uhl, M. Benter, S. Melle, W. Saak, G. Frenking, J. Uddin, *Organometallics* **1999**, *18*, 3778-3780.
- [33] B. Buchin, C. Gemel, A. Kempter, T. Cadenbach, R. A. Fischer, *Inorg. Chim. Acta* **2006**, *359*, 4833-4839.
- [34] T. Cadenbach, T. Bollermann, C. Gemel, R. A. Fischer, *Dalton Trans.* **2009**, 322-329.
- [35] T. Cadenbach, C. Gemel, T. Bollermann, I. Fernandez, G. Frenking, R. A. Fischer, *Chem. Eur. J.* **2008**, *14*, 10789-10796.
- [36] B. Chatterjee, C. Gunanathan, *Chem. Commun.* **2014**, *50*, 888-890.
- [37] T. Komuro, H. Tobita, *Chem. Commun.* **2010**, *46*, 1136-1137.
- [38] B. Chaudret, R. Poilblanc, *Organometallics* **1985**, *4*, 1722-1726.
- [39] F. M. Bickelhaupt, E. J. Baerends, in *Rev. Comput. Chem, Vol. 15* (Eds.: K. B. Lipkowitz, D. B. Boyd), Wiley, New-York, **2000**, pp. 1-86.
- [40] K. Morokuma, *J. Chem. Phys.* **1971**, *55*, 1236-1244.
- [41] T. Ziegler, R. Arvi, *Inorg. Chem.* **1979**, *18*, 1558-1565.
- [42] R. F. W. Bader, *Atoms in Molecules - A Quantum Theory*, Oxford University Press, **1990**.
- [43] P. L. A. Popelier, in *The Chemical Bond, Vol. 1*, Wiley-VCH, **2014**, pp. 271-308.
- [44] A. A. Adeniyi, P. A. Ajibade, *J. Biomol. Struct. Dyn.* **2014**, *32*, 1351-1365.
- [45] R. Gericke, J. Wagler, *Inorg. Chem.* **2020**, *59*, 6359-6375.
- [46] C. Lepetit, P. Fau, K. Fajerweg, M. L. Kahn, B. Silvi, *Coord. Chem. Rev.* **2017**, *345*, 150-181.
- [47] P. Heiß, J. Hornung, C. Gemel, R. A. Fischer, *Chem. Commun.* **2022**, Accepted Manuscript.
- [48] M. Muhr, P. Heiß, M. Schütz, R. Bühler, C. Gemel, M. H. Linden, H. B. Linden, R. A. Fischer, *Dalton Trans.* **2021**, *50*, 9031-9036.
- [49] G. te Velde, F. M. Bickelhaupt, E. J. Baerends, C. Fonseca Guerra, S. J. A. van Gisbergen, J. G. Snijders, T. Ziegler, *J. Comput. Chem.* **2001**, *22*, 931-967.
- [50] E. J. Baerends, T. Ziegler, A. J. Atkins, J. Autschbach, D. Bashford, O. Baseggio, A. Bérces, F. M. Bickelhaupt, C. Bo, P. M. Boerritger, L. Cavallo, C. Daul, D. P. Chong, D. V. Chulhai, L. Deng, R. M. Dickson, J. M. Dieterich, D. E. Ellis, M. van Faassen, A. Ghysels, A. Giammona, S. J. A. van Gisbergen, A. Goetz, A. W. Götz, S. Gusarov, F. E. Harris, P. van den Hoek, Z. Hu, C. R. Jacob, H. Jacobsen, e. al., *SCM*, **2020**.
- [51] S. Grimme, *J. Comput. Chem.* **2006**, *27*, 1787-1799.

- [52] A. D. Becke, *Phys. Rev. A* **1988**, *38*, 3098-3100.
- [53] J. P. Perdew, *Phys. Rev. B* **1986**, *33*, 8822-8824.
- [54] E. D. Glendening, C. R. Landis, F. Weinhold, *J. Comput. Chem.* **2013**, *34*, 1429-1437.
- [55] J. I. Rodríguez, *J. Comput. Chem.* **2012**, *34*, 681-686.
- [56] J. I. Rodríguez, R. F. W. Bader, P. W. Ayers, C. Michel, A. W. Götz, C. Bo, *Chem. Phys. Lett.* **2009**, *472*, 149-152.
- [57] G. Schreckenbach, T. Ziegler, *J. Phys. Chem.* **1995**, *99*, 606-611.
- [58] P. J. Stephens, F. J. Devlin, C. F. Chabalowski, M. J. Frisch, *J. Phys. Chem.* **1994**, *98*, 11623-11627.
- [59] A. Klamt, G. Schüürmann, *J. Chem. Soc., Perkin Trans. 2* **1993**, 799-805.
- [60] A. Klamt, *J. Phys. Chem.* **1995**, *99*, 2224-223.

2.3.4 Additional Data and Information

Crystallography

Compound 1 (CCDC 2158227)



Diffractometer operator C. Jandl
scanspeed 1-10 s per frame
dx 70 mm
3051 frames measured in 10 data sets
phi-scans with $\Delta\phi = 0.5$
omega-scans with $\Delta\omega = 0.5$
shutterless mode

Crystal data

$C_{36}H_{60}Ga_3RuSi$

$M_r = 831.16$

Monoclinic, $P2_1/c$

Hall symbol: $-P\ 2ybc$

$a = 19.487(2)\ \text{\AA}$

$b = 11.1759(13)\ \text{\AA}$

$c = 19.650(2)\ \text{\AA}$

$\beta = 112.779(3)^\circ$

$V = 3945.7(7)\ \text{\AA}^3$

$Z = 4$

$F(000) = 1708$

$D_x = 1.399\ \text{Mg m}^{-3}$

Melting point: ? K

Mo $K\alpha$ radiation, $\lambda = 0.71073\ \text{\AA}$

Cell parameters from 9377 reflections

$\theta = 2.5\text{--}25.7^\circ$

$\mu = 2.45\ \text{mm}^{-1}$

$T = 100\ \text{K}$

Fragment, yellow

$0.20 \times 0.14 \times 0.11\ \text{mm}$

Data collection

Bruker D8 Venture
diffractometer 7224 independent reflections

Radiation source: TXS rotating anode 6728 reflections with $I > 2\sigma(I)$

Helios optic monochromator $R_{\text{int}} = \underline{0.048}$

Detector resolution: 16 pixels mm^{-1} $\theta_{\text{max}} = \underline{25.4^\circ}$, $\theta_{\text{min}} = \underline{2.3^\circ}$

phi- and ω -rotation scans $h = \underline{-23}$ 23

Absorption correction: multi-scan
SADABS 2016/2, Bruker $k = \underline{-13}$ 11

$T_{\text{min}} = \underline{0.681}$, $T_{\text{max}} = \underline{0.745}$ $l = \underline{-23}$ 23

82487 measured reflections

Refinement

Refinement on F^2 Secondary atom site location: difference
Fourier map

Least-squares matrix: full Hydrogen site location: inferred from
neighbouring sites

$R[F^2 > 2\sigma(F^2)] = \underline{0.025}$ H-atom parameters constrained

$wR(F^2) = \underline{0.065}$ $W = 1/[\Sigma^2(FO^2) + (0.0237P)^2 + 7.0356P]$
WHERE $P = (FO^2 + 2FC^2)/3$

$S = \underline{1.04}$ $(\Delta/\sigma)_{\text{max}} = \underline{0.022}$

7224 reflections $\Delta\rho_{\text{max}} = \underline{1.12}$ e \AA^{-3}

388 parameters $\Delta\rho_{\text{min}} = \underline{-0.85}$ e \AA^{-3}

0 restraints Extinction correction: none

0 constraints Extinction coefficient: -

Primary atom site location: iterative

NMR spectra

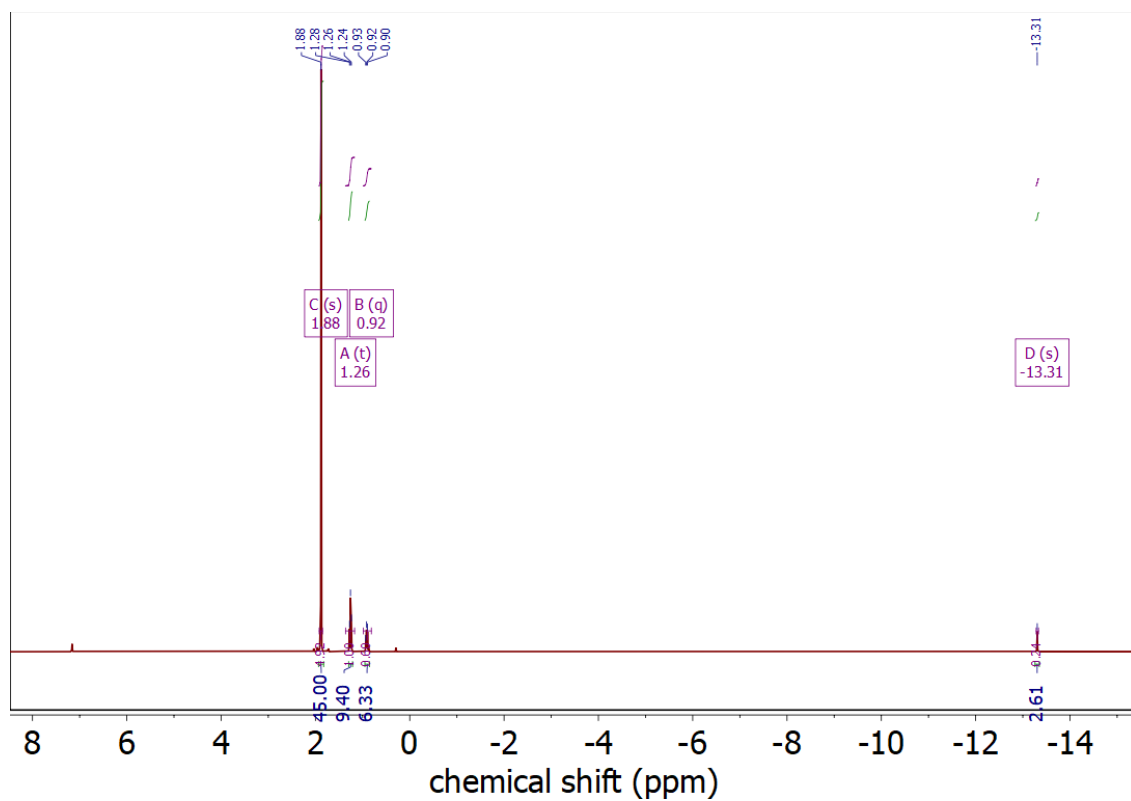


Figure S1: Proton NMR spectrum of 1 in C_6D_6 .

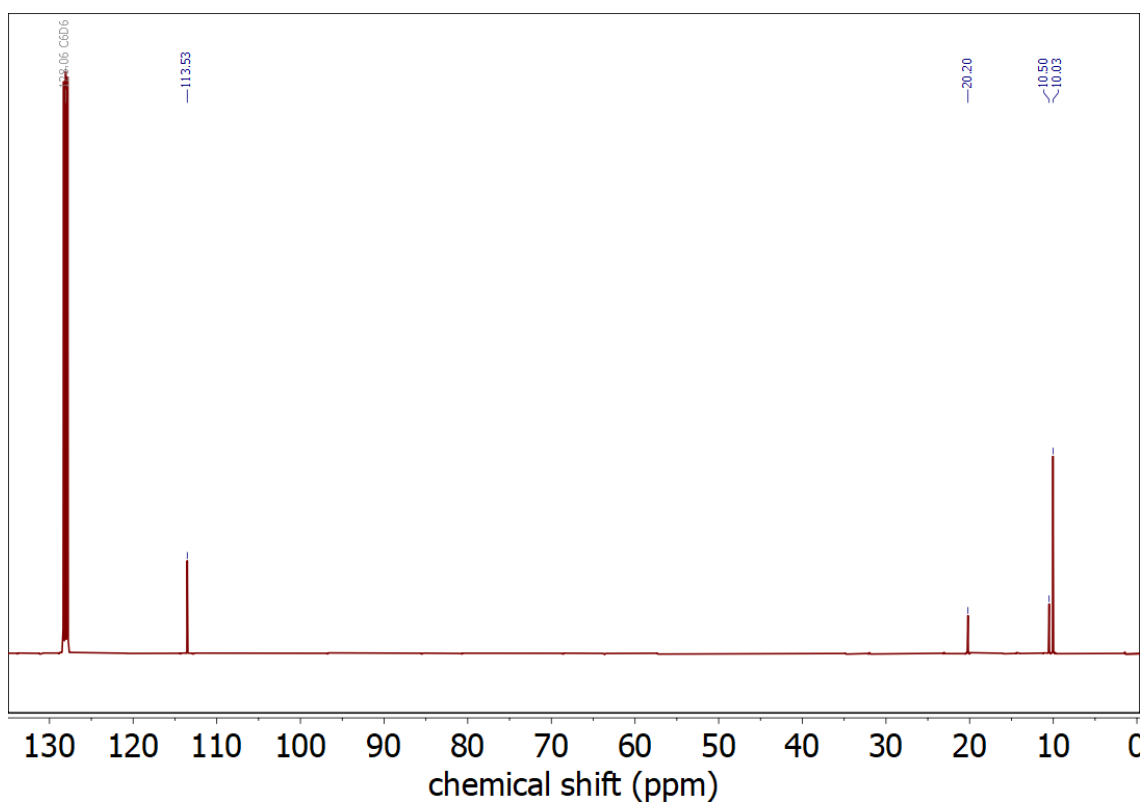


Figure S2: ^{13}C NMR spectrum of 1 in C_6D_6 .

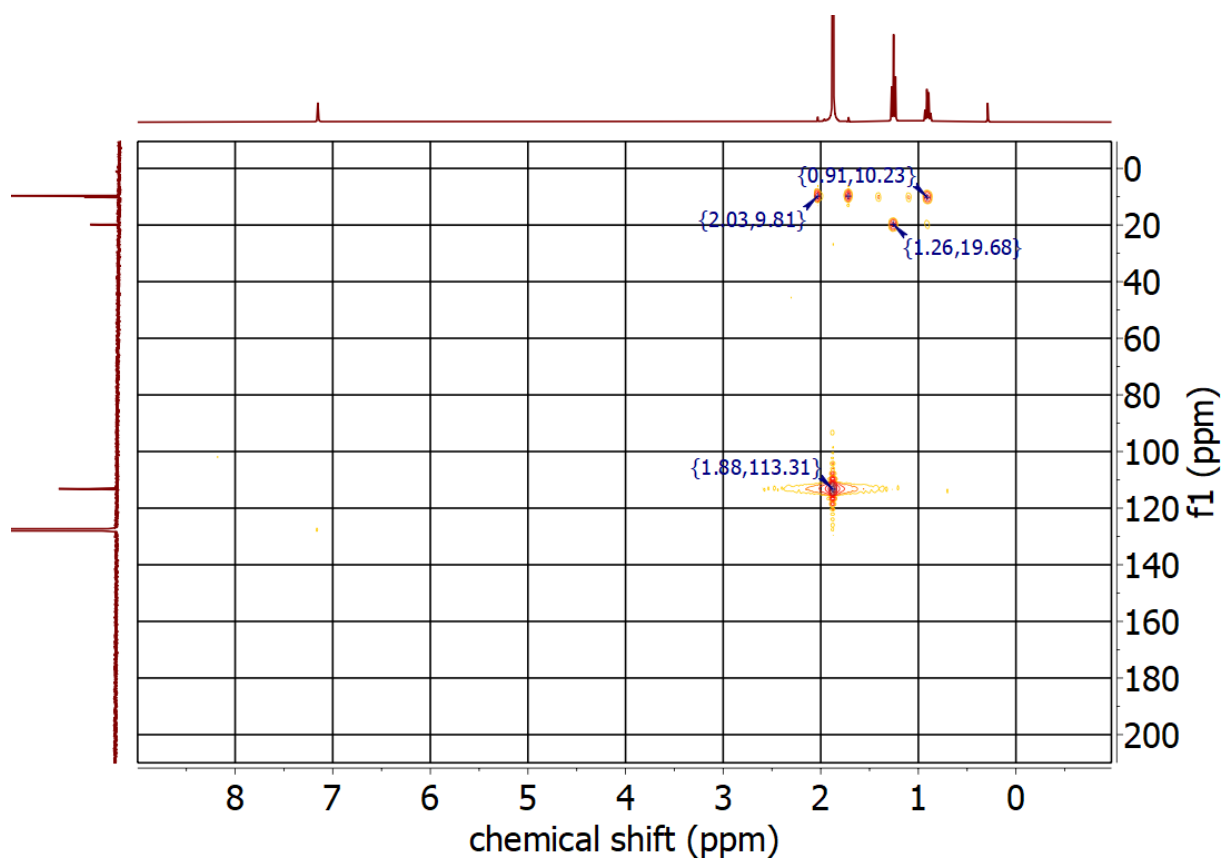


Figure S3: Heteronuclear Multiple Bond Correlation (HMBC) NMR spectrum of 1.

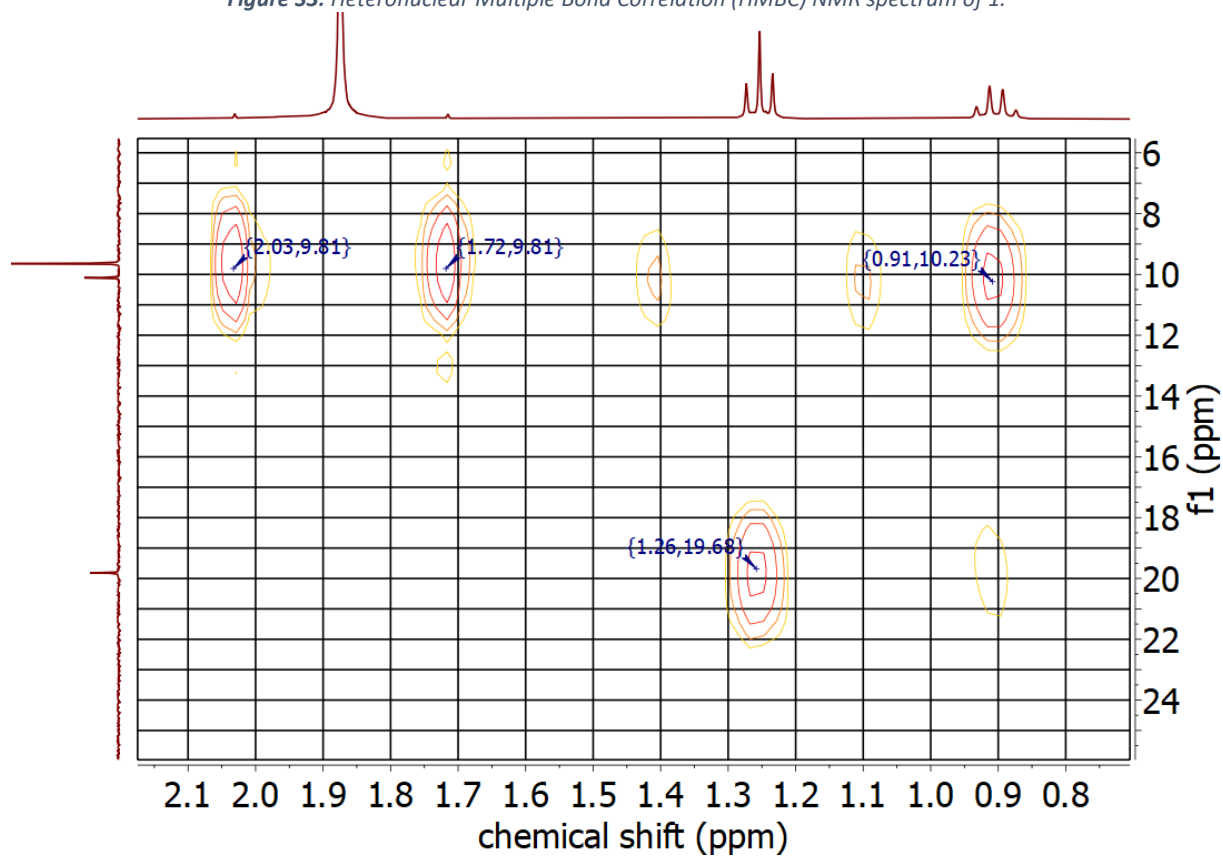


Figure S4: HMBC zoomed-in.

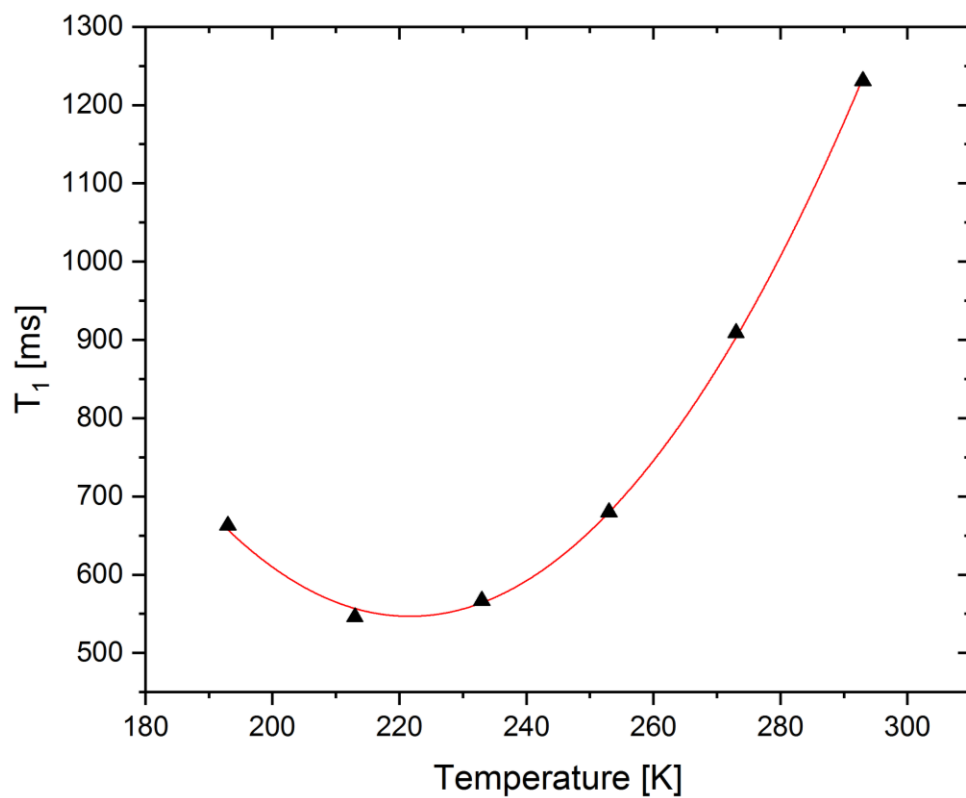


Figure S5: T₁ values of the hydrides of 1 determined via NMR as a function of temperature.

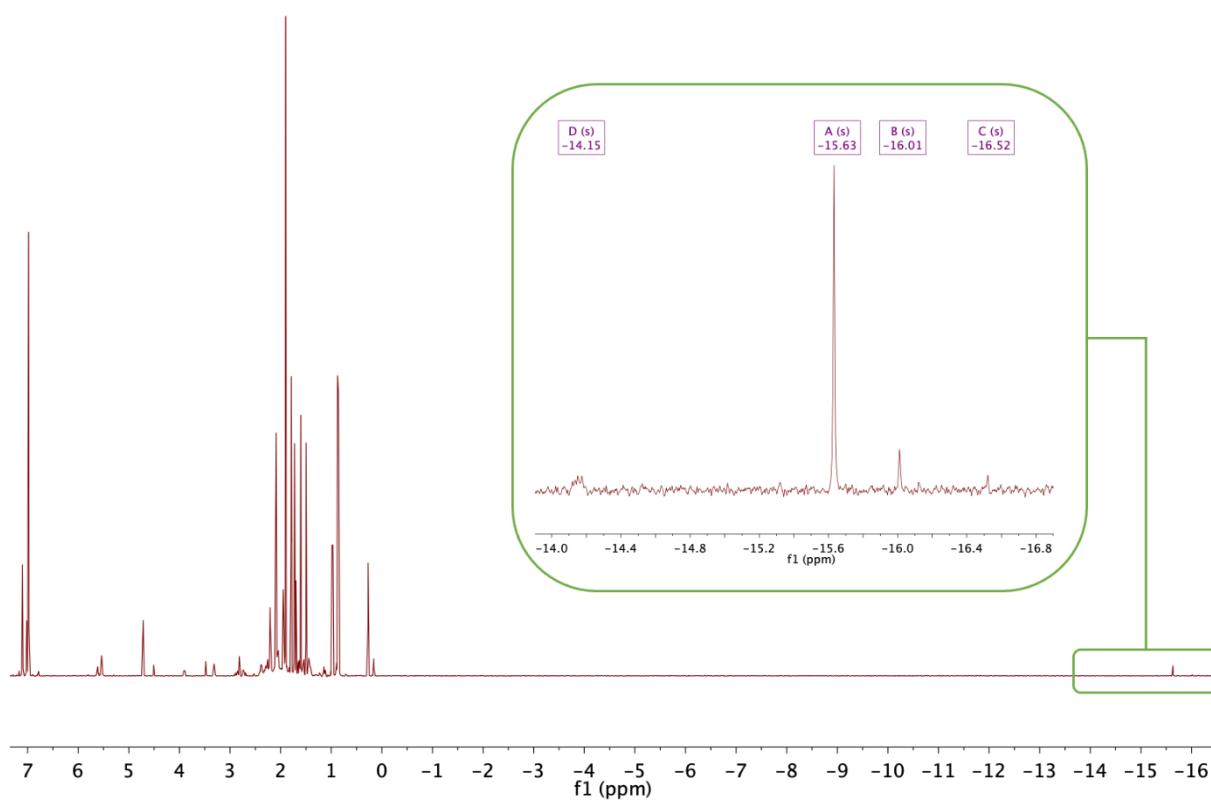


Figure S6: ¹H NMR spectrum of the reaction solution of 2 in toluene-d₈.

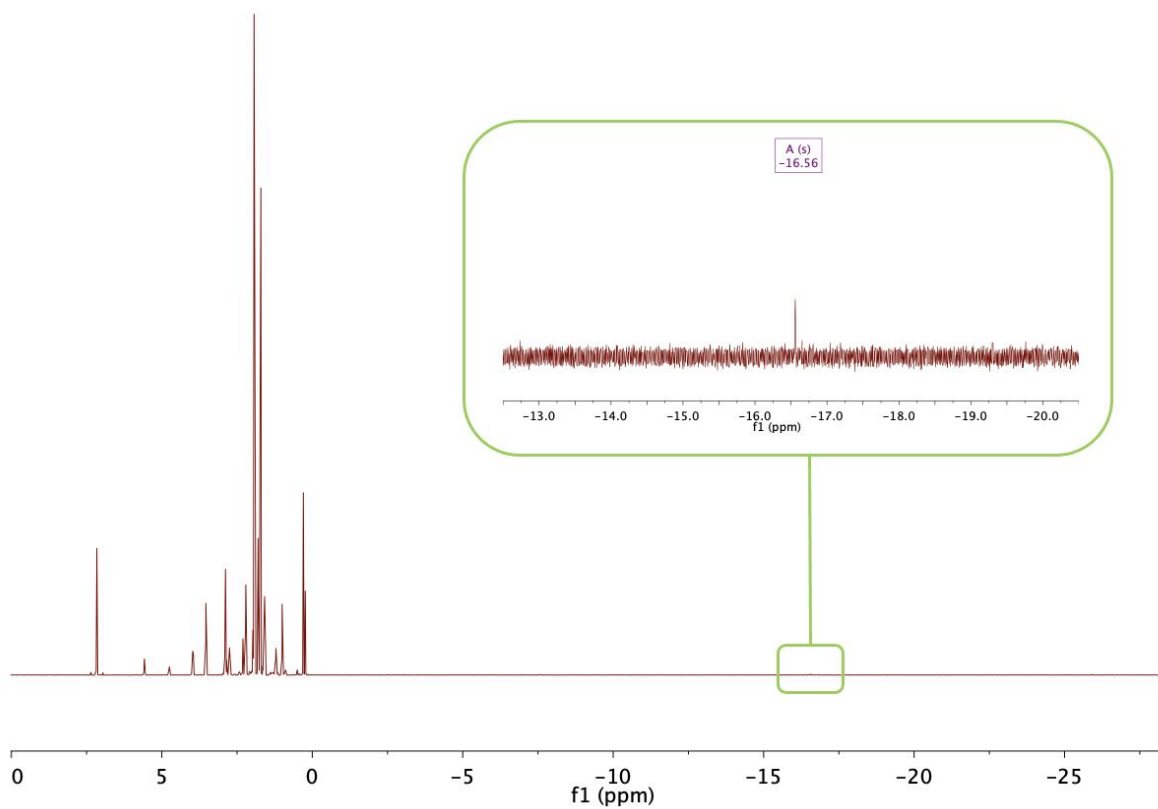


Figure S7: ^1H NMR spectrum of the reaction solution of the benzene analogue of 2 C_6D_6 .

LIFDI-MS spectra

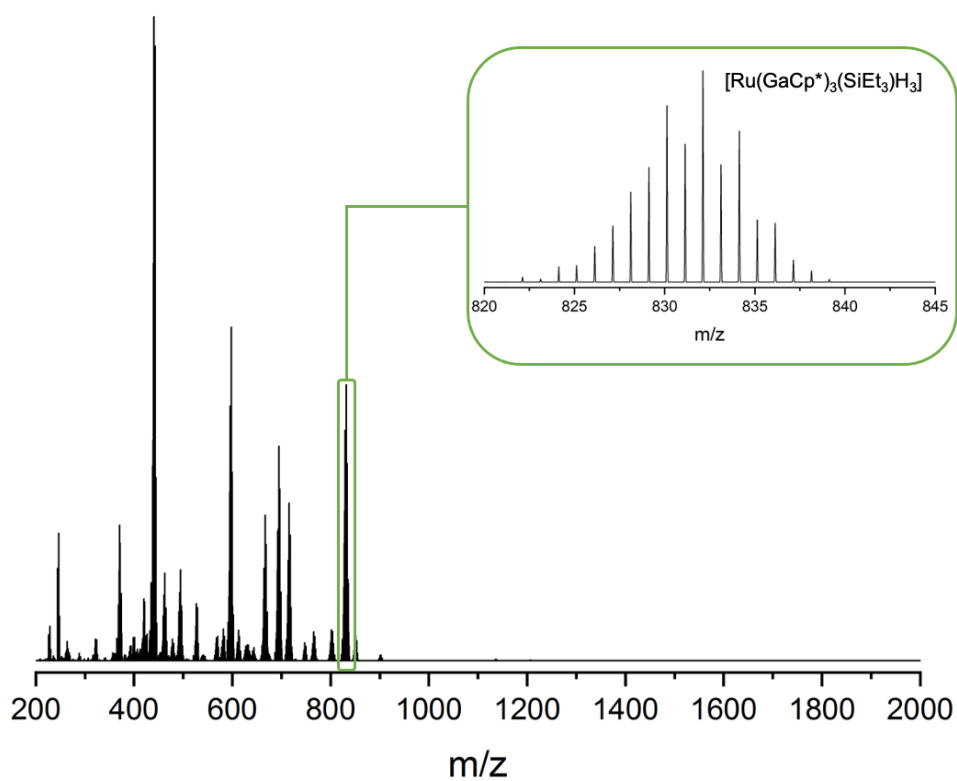


Figure S8: LIFDI-MS of 1.

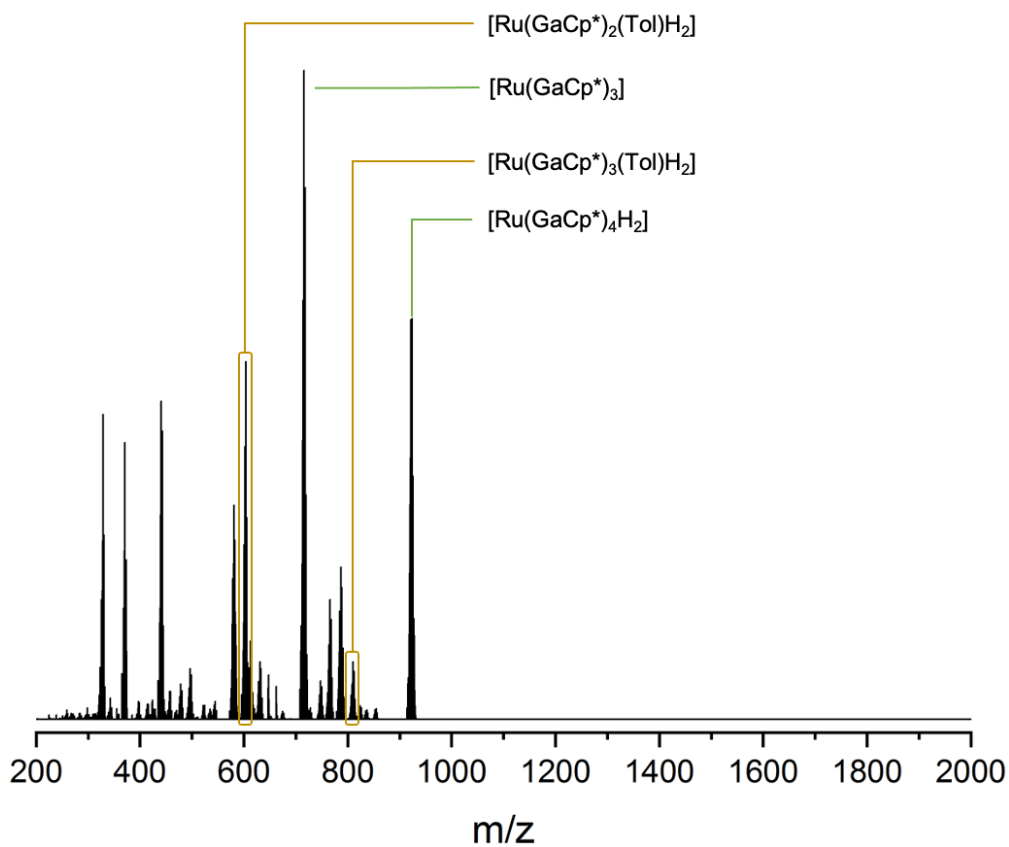


Figure S9: LIFDI-MS of the reaction solution of $[\text{Ru}(\text{COD})(\text{COT})]$ with GaCp^* under H_2 after 1 hour.

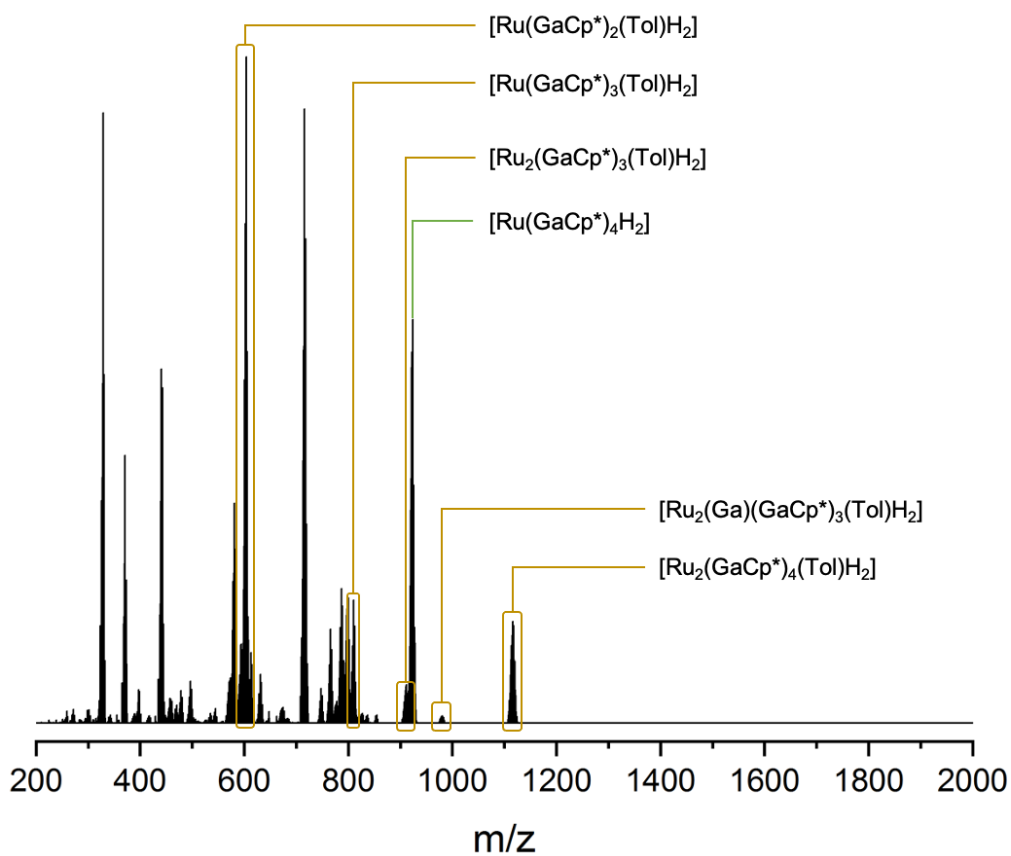


Figure S10: LIFDI-MS of the reaction solution of $[\text{Ru}(\text{COD})(\text{MeAllyl})_2]$ with GaCp^* under H_2 after 1 hour.

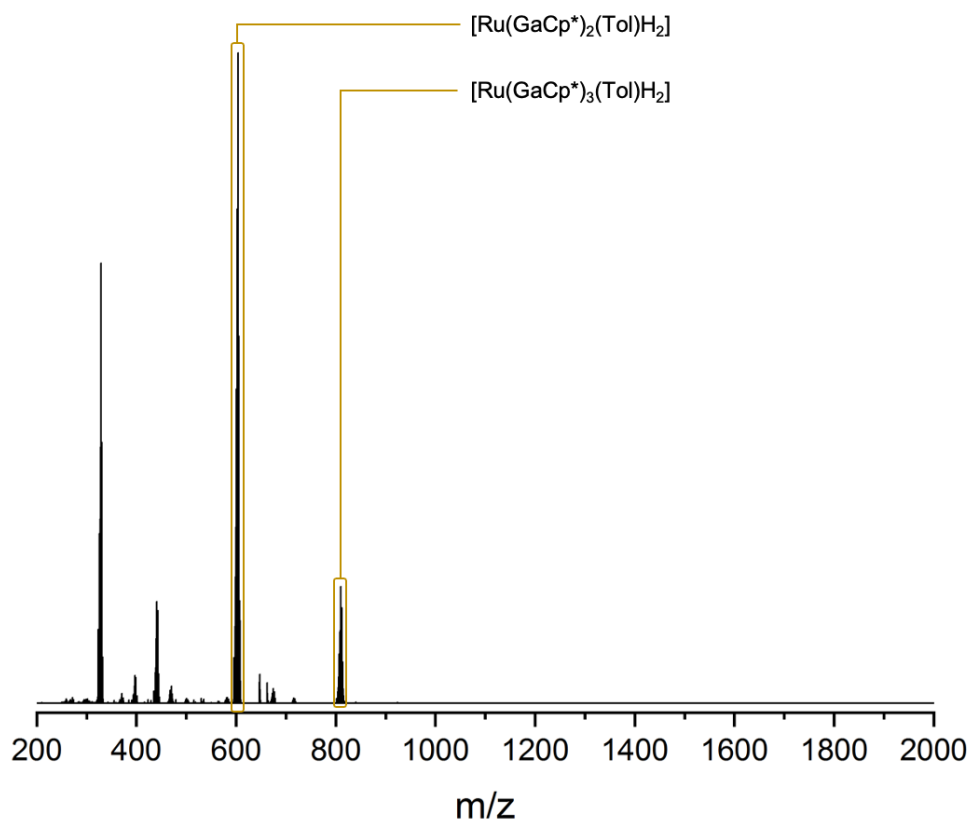


Figure S11: LIFDI-MS of the size-focused reaction solution of 2.

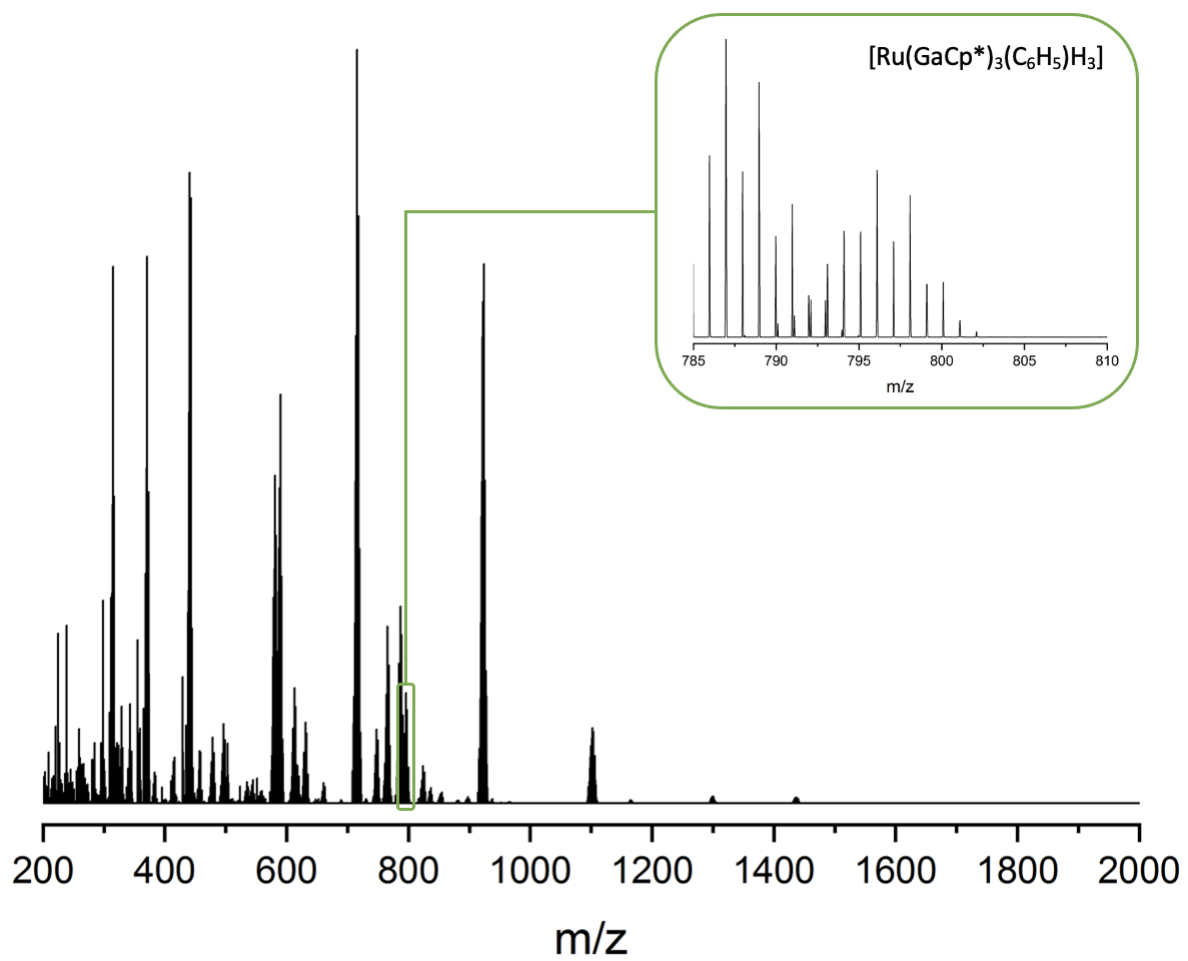


Figure S12: LIFDI-MS of the reaction solution of the analog of 2 in benzene.

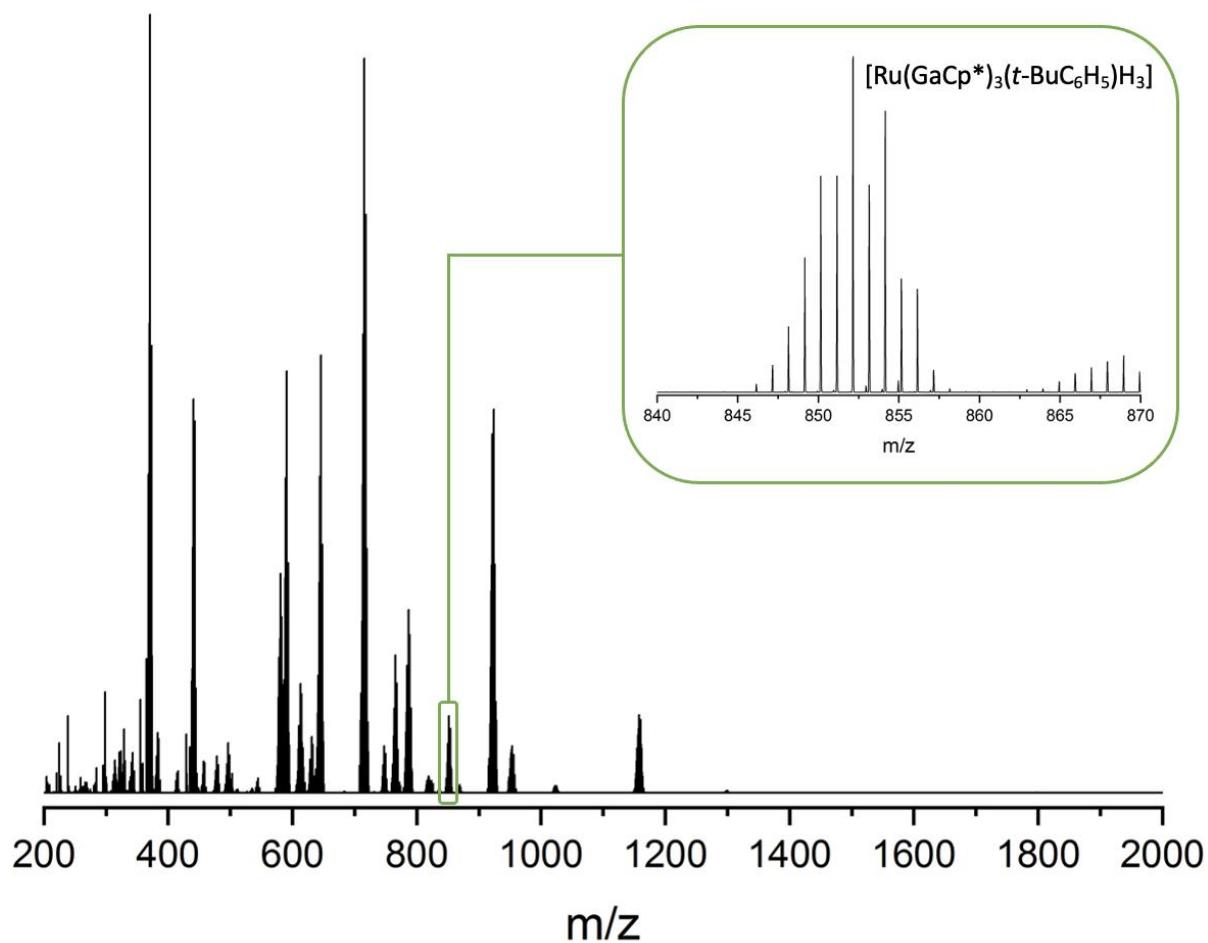


Figure S13: LIFDI-MS of the reaction solution of the analog of 2 in tert-butyl benzene.

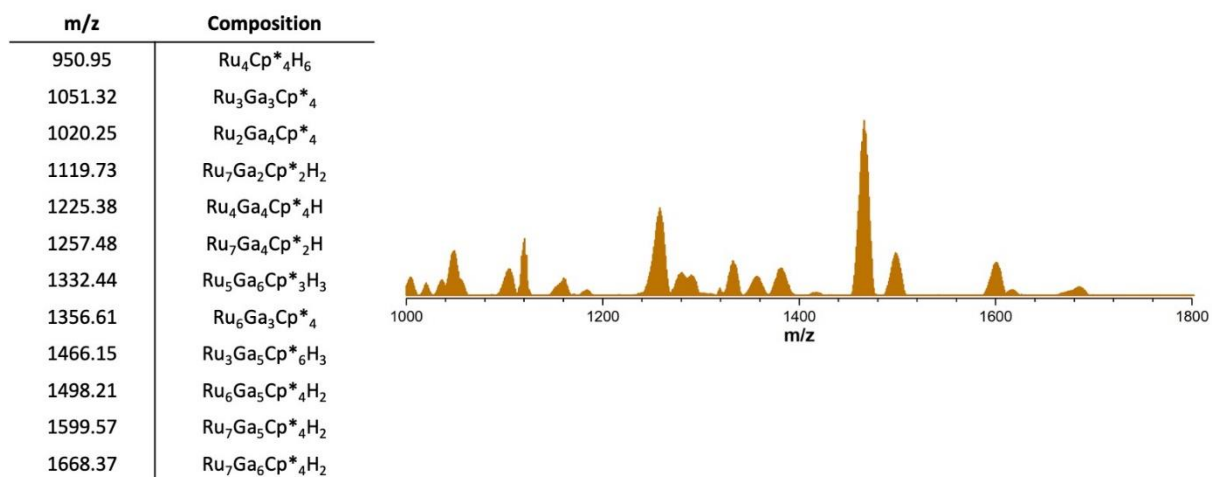


Figure S14: LIFDI-MS of the reaction solution of $[\text{Ru}(\text{COD})(\text{MeAllyl})_2]$ with GaCp^* under dihydrogen in cyclohexane with the sum formula of the RuGa polyhydride clusters obtained via Cp^{Et} labelling experiments.

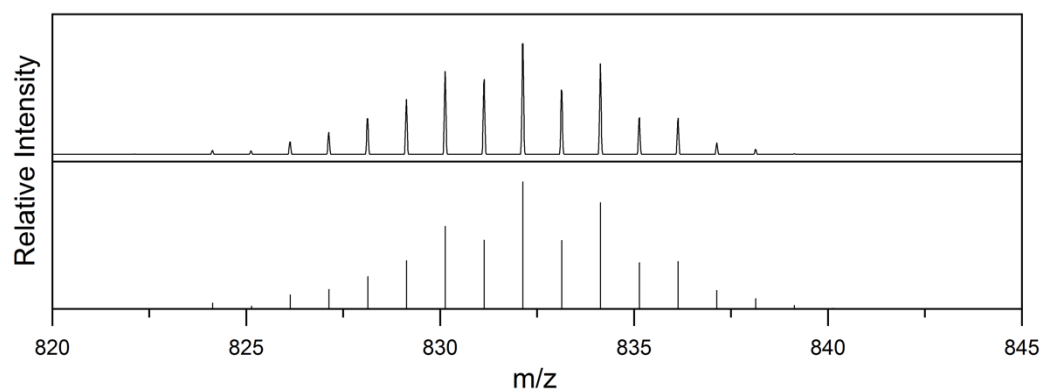


Figure S15: Experimental (top) and theoretical (bottom) pattern of $[M-2H]^+$ fragment of $[Ru(GaCp^*)_3(SiEt_3)H_3]$ (**1**).

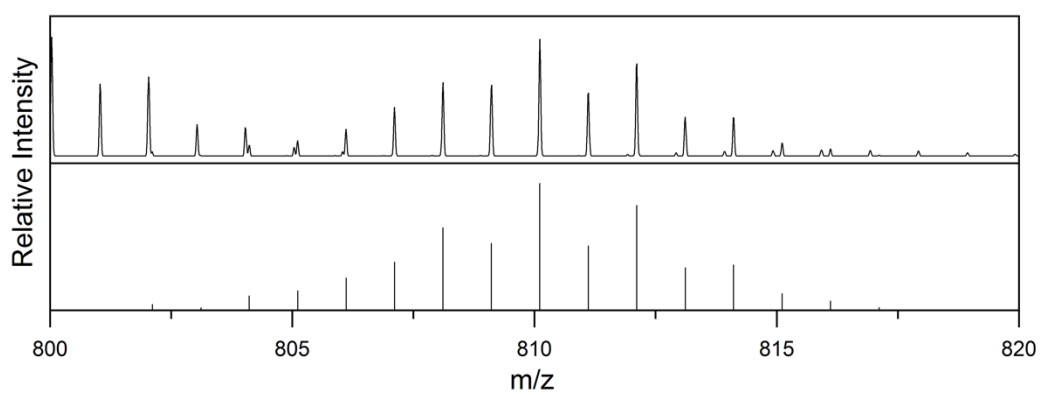


Figure S16: Experimental (top) and theoretical (bottom) pattern of $[Ru(GaCp^*)_3(C_7H_7)H_3]$ (**2**).

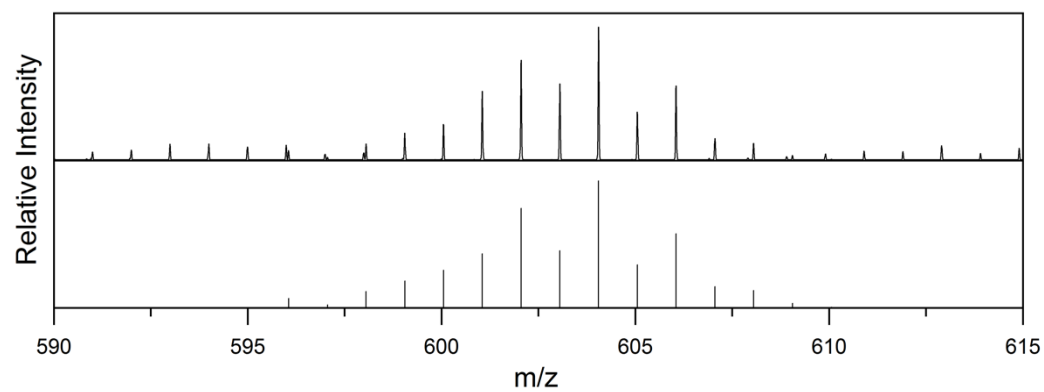


Figure S17: Experimental (top) and theoretical (bottom) pattern of $[M-GaCp^*-2H]^+$ fragment of $[Ru(GaCp^*)_3(C_7H_7)H_3]$ (**2**).

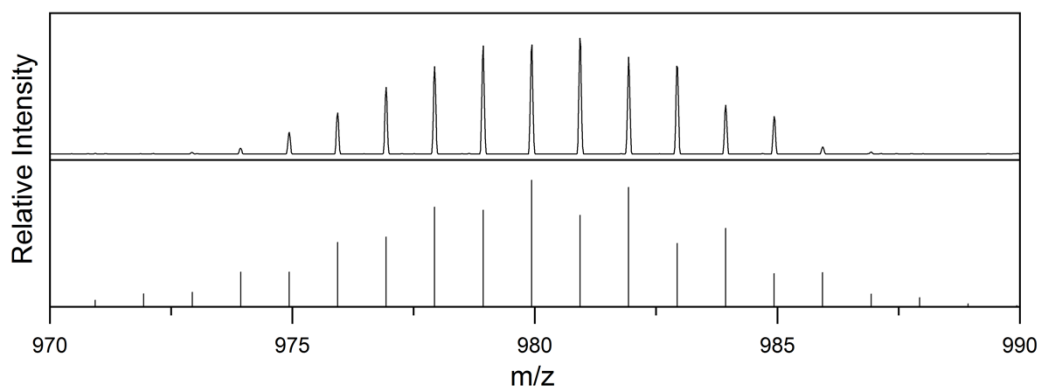


Figure S18: Experimental (top) and theoretical (bottom) pattern of $[Ru_2(GaCp^*)_4(Tol)H_2]^+$.

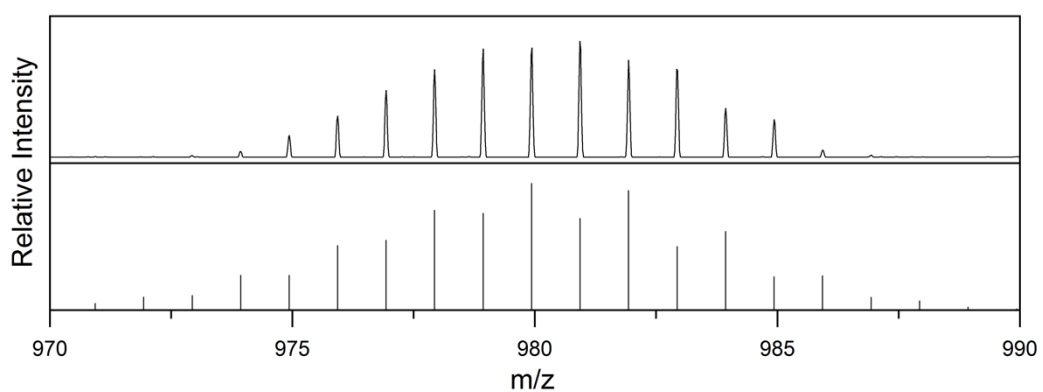


Figure S19: Experimental (top) and theoretical (bottom) pattern of $[Ru_2(Ga)(GaCp^*)_3(Tol)H]^+$.

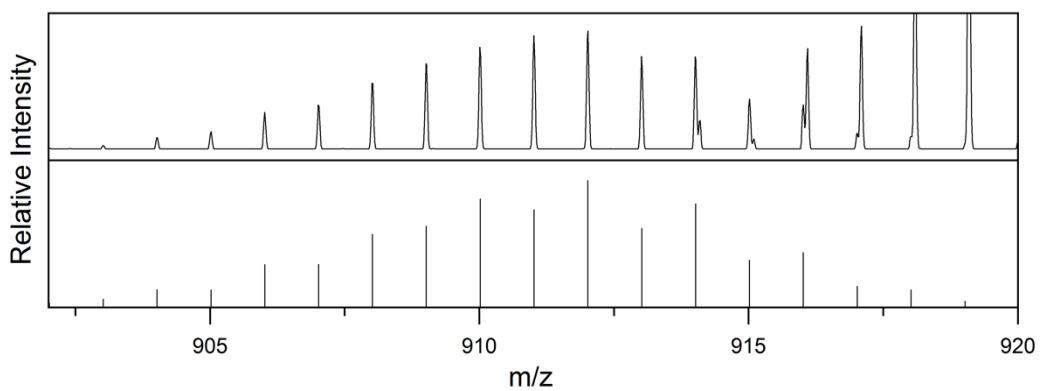


Figure S20: Experimental (top) and theoretical (bottom) pattern of $[Ru_2(GaCp^*)_3(Tol)H_2]^+$.

Vibrational spectra

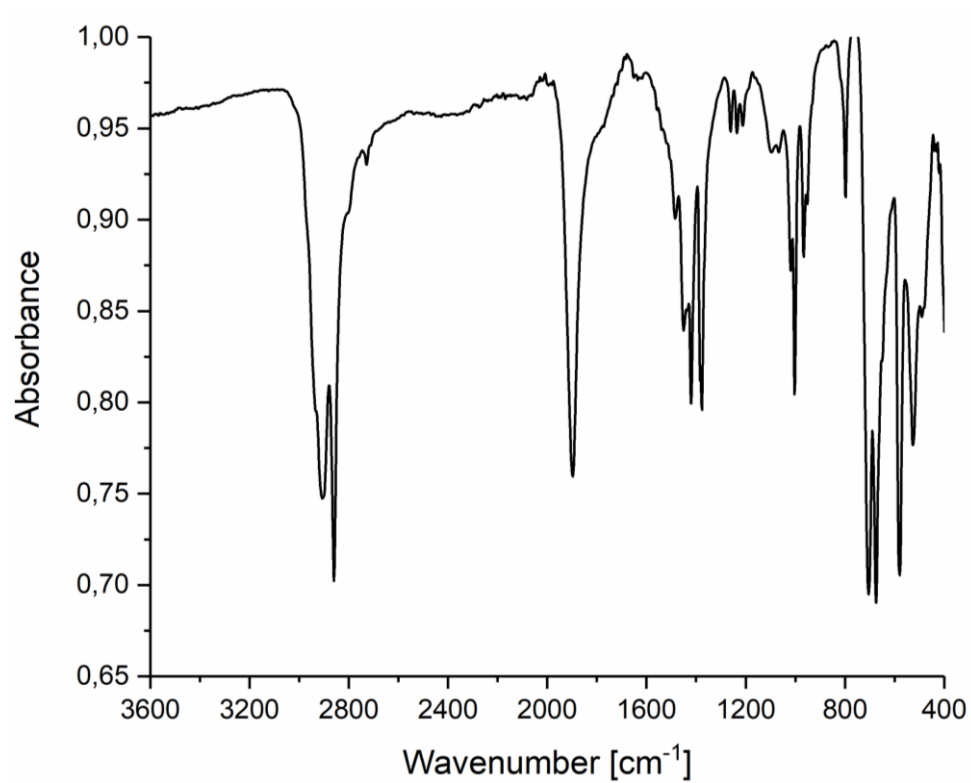


Figure S21: ATR-IR spectrum of 1.



Figure S22: Calculated IR spectra of 1.

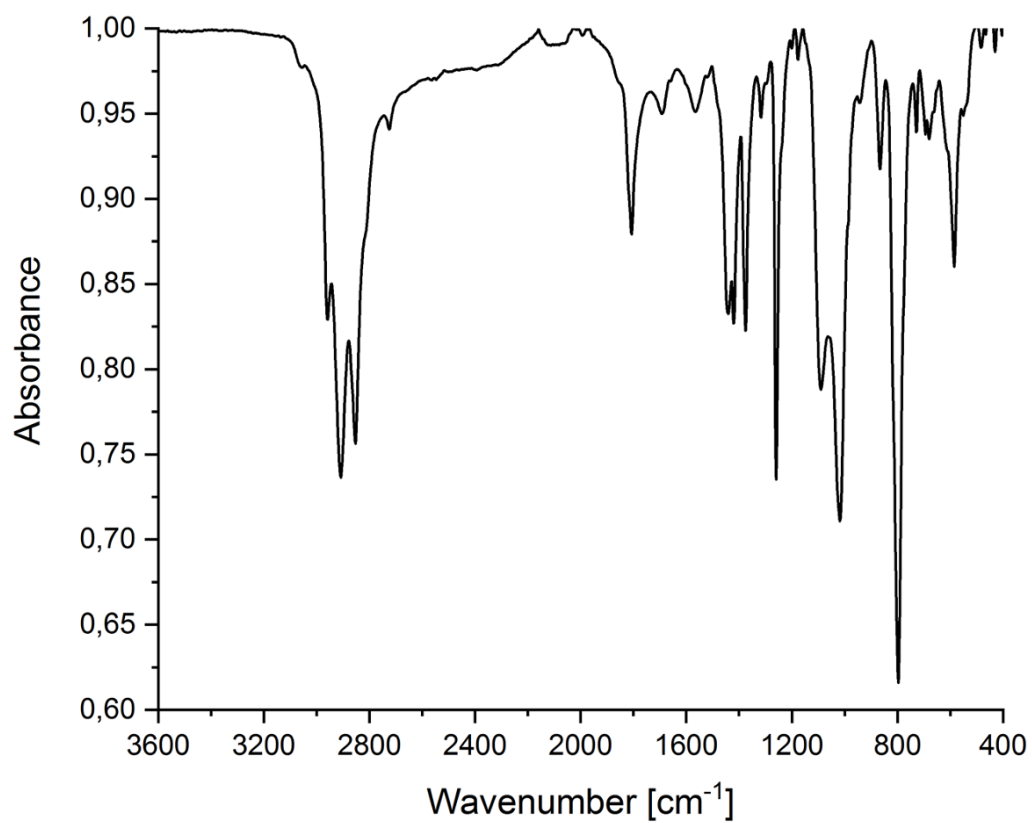


Figure S23: ATR-IR spectrum of the reaction solution of **2** (solvent evaporated of the window).

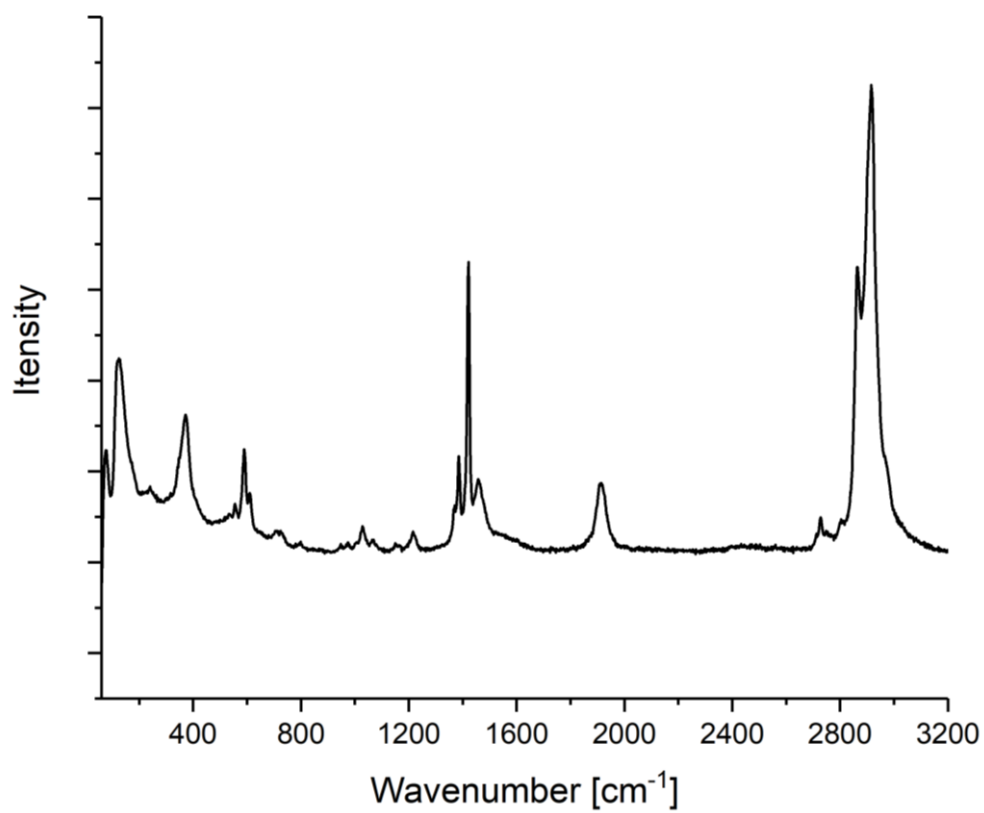


Figure S24: Solid-state Raman spectrum of **1**.

UV-Vis spectra

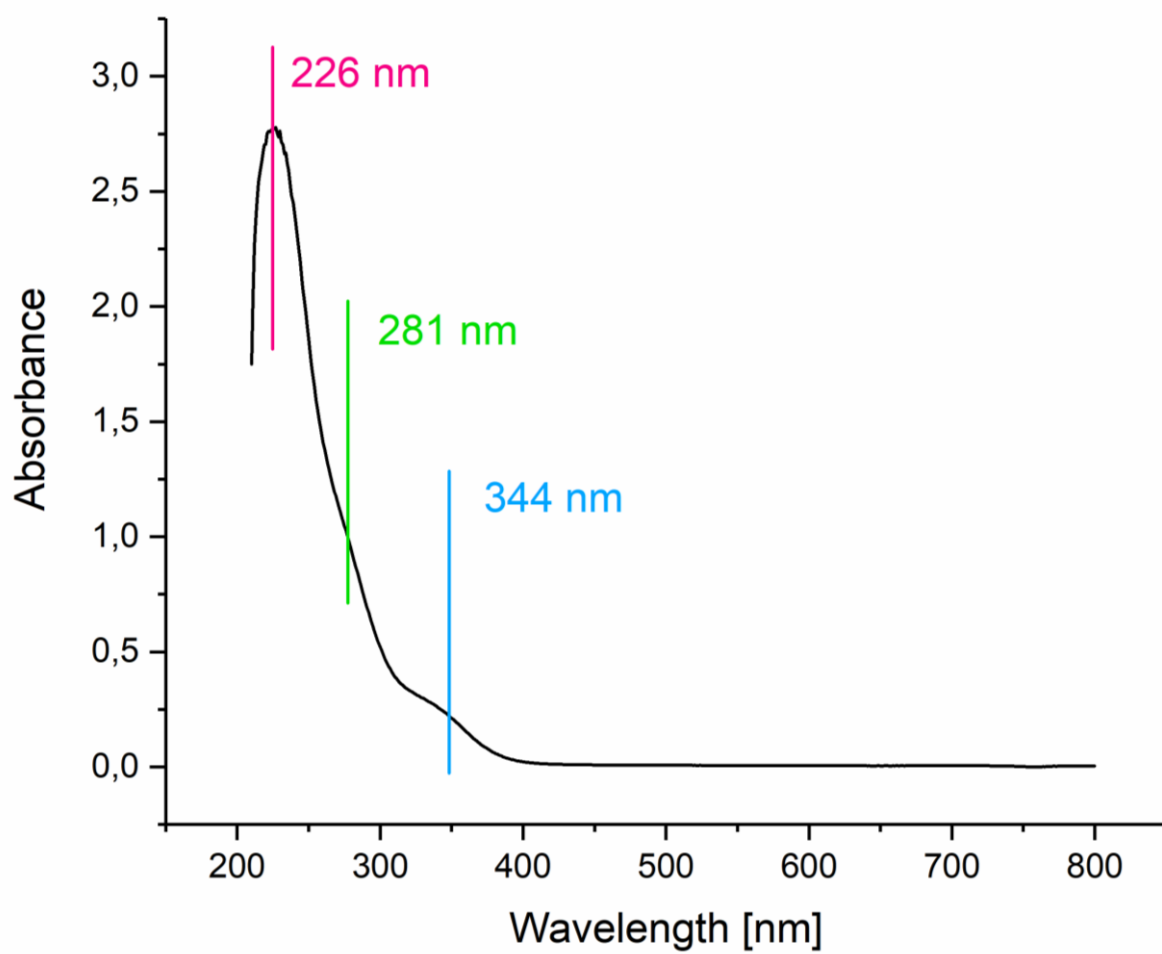


Figure S25: UV-Vis of 1 in cyclohexane.

Computational Results

Bonding details

Table S1. Selected computed data for complexes **1**, [Ru(GaCp*)₃H₂], and their triphenylphosphine analogues.

Compound	Distances (Å) and WBI's into brackets		
	Ru-H (av.)	Ru-Ga/P (av.)	Ru-Si
[Ru(GaCp*) ₃ (SiEt ₃)H ₃] (1)	1.628 [0.343]	2.381 [0.361]	2.370 [0.283]
Ru(PMe ₃) ₃ (SiEt ₃)H ₃	1.656 [0.374]	2.317 [0.419]	2.404 [0.277]
[Ru(GaCp*) ₃ H ₂]	1.624 [0.476]	2.350 [0.517]	-
[Ru(PMe ₃) ₃ H ₂]	1.658	2.256 [0.600]	-

Table S2. QTAIM descriptors of the Ru-E (E = Ga, P) bonds in **1**, [Ru(PMe₃)₃(SiEt₃)H₃], [Ru(GaCp*)₃H₂] and their triphenylphosphine analogues.^{a,b}

Compound		[Ru(GaCp*) ₃ (SiEt ₃)H ₃] (1)	[Ru(PMe ₃) ₃ (SiEt ₃)H ₃]	[Ru(GaCp*) ₃ H ₂]	[Ru(PMe ₃) ₃ H ₂]
Atom charge ^a	Ru	-0.35	0.02	-0.17	0.07
	E	0.63	1.32	0.60	1.27
Delocalisation index ^a	δ	0.87	0.94	1.06	1.00
bcp indicators ^{a,b}	ρ	0.069	0.095	0.075	0.098
	$\nabla^2\rho$	0.122	0.166	0.133	0.179
	H	-0.023	-0.043	-0.028	-0.045
	V	-0.077	-0.127	-0.088	-0.135
	$ V /G$	1.426	1.512	1.467	1.500

^a Averaged values. ^b ρ , $\nabla^2\rho$, H, V and G are the electron density, Laplacian of ρ density, energy density, potential energy density and kinetic energy density values at the bcp, respectively. All values in a.u.

XYZ coordinates

[Ru(GaCp*)₃(SiEt₃)H₃] (**1**)

Ru	2.321870350000	5.410122840000	5.859755510000
Ga	2.629144750000	3.116546080000	5.293111230000
Ga	4.557749780000	6.126541010000	5.463548620000
Ga	1.426793140000	6.074049090000	3.754707190000
Si	1.374689480000	5.944351160000	7.965785720000
C	4.633208230000	1.914042990000	4.793450840000
C	4.643420520000	2.088270300000	6.208557650000
C	3.487225130000	1.453528550000	6.750894540000
C	2.742751270000	0.881599720000	5.667137370000
C	3.462036100000	1.166637560000	4.443401530000
C	5.640118820000	2.489394370000	3.846190270000
C	5.650922340000	2.881496990000	6.979033940000
C	3.101557160000	1.434939440000	8.197274530000
C	1.507818870000	0.040458190000	5.785085300000
C	3.116792570000	0.640349720000	3.084205510000
C	5.815484760000	7.288425420000	3.858171620000
C	4.996127040000	8.269781840000	4.493595180000
C	5.346340450000	8.321830830000	5.877822960000
C	6.385326720000	7.367358510000	6.112039240000
C	6.681218560000	6.721681580000	4.855334580000
C	5.758206790000	6.896823180000	2.413229360000
C	3.891835920000	9.053583950000	3.855728890000
C	4.676068420000	9.185031750000	6.900108730000
C	7.102631260000	7.124504980000	7.405058570000
C	7.792075050000	5.745320430000	4.618493500000
C	-0.203709830000	6.789704560000	2.327111340000
C	-0.707844680000	5.551371790000	2.840068850000
C	0.159667310000	4.505235260000	2.407297520000
C	1.203613090000	5.077064010000	1.620738540000
C	0.988606820000	6.495219950000	1.562941040000
C	-0.843382640000	8.137686340000	2.469097490000
C	-1.908907810000	5.361609810000	3.713634110000
C	0.024920440000	3.065616210000	2.790612740000
C	2.348626120000	4.326969560000	1.011148320000
C	1.770925950000	7.483637240000	0.753430000000
C	2.621969110000	6.675228730000	9.219194640000
C	3.896437630000	5.863255570000	9.466937670000
C	0.622789540000	4.438734600000	8.880748660000
C	-0.264976720000	3.490301810000	8.068313700000
C	0.025153320000	7.300702450000	7.905781640000
C	-1.047616200000	7.180386600000	6.820141140000
H	6.612167350000	1.980312270000	3.925685360000
H	5.813334800000	3.556732250000	4.054497300000
H	5.307076050000	2.407230400000	2.804427140000
H	6.088077500000	3.674725670000	6.356454470000
H	6.478811120000	2.250695730000	7.337996090000
H	5.196721260000	3.366449970000	7.852569390000
H	2.023549660000	1.279817170000	8.326266850000
H	3.356996870000	2.384398770000	8.687029530000
H	3.620685440000	0.632163680000	8.742794250000
H	0.877903290000	0.115251660000	4.889310240000
H	0.895860460000	0.342196260000	6.644640680000
H	1.761752590000	-1.022584950000	5.919600100000
H	3.437117280000	1.322318440000	2.285480690000
H	2.036917630000	0.480842440000	2.971722480000
H	3.608120020000	-0.327985720000	2.900430990000
H	4.725509610000	6.913983410000	2.037572790000
H	6.147304300000	5.883074850000	2.254990670000
H	6.348084670000	7.578971380000	1.782076060000
H	4.186410360000	10.098701820000	3.675753200000
H	2.995599280000	9.066339520000	4.492596470000
H	3.603685970000	8.621944850000	2.889203300000
H	4.981084740000	10.237766180000	6.800882600000
H	4.917698810000	8.863579210000	7.919923740000
H	3.582226910000	9.146434190000	6.793870810000
H	7.417227070000	6.077346480000	7.504232540000
H	6.468295010000	7.358661200000	8.268489740000
H	8.008027230000	7.746714890000	7.480209030000
H	7.596357730000	5.107823190000	3.747018160000
H	7.949544610000	5.086714950000	5.482773230000
H	8.743402420000	6.268116740000	4.432126130000
H	-1.553138830000	8.329337200000	1.649318860000

H	-0.099082810000	8.944280070000	2.451676110000
H	-1.398639890000	8.222980360000	3.411540430000
H	-2.725681450000	4.869102030000	3.164464970000
H	-2.290829050000	6.316703640000	4.090961990000
H	-1.672362760000	4.734869640000	4.585373430000
H	-0.787618790000	2.571983970000	2.235586360000
H	-0.196465090000	2.957192240000	3.862646300000
H	0.948359110000	2.511248670000	2.583384110000
H	2.046251570000	3.794641290000	0.096671710000
H	2.751067760000	3.578901780000	1.709671290000
H	3.172639390000	4.999502080000	0.743045820000
H	2.821483110000	7.183220780000	0.645806950000
H	1.756136470000	8.482961560000	1.206957550000
H	1.356339840000	7.581178060000	-0.262186000000
H	2.886784210000	7.684540320000	8.865801560000
H	2.076894670000	6.818881900000	10.168198740000
H	4.474354630000	5.753843090000	8.538142640000
H	3.664422640000	4.847230530000	9.820611660000
H	4.551244110000	6.327487310000	10.220010980000
H	1.463956370000	3.870156100000	9.310392870000
H	0.059643790000	4.839055590000	9.741230550000
H	-1.138403040000	4.011728470000	7.651308720000
H	-0.639916950000	2.650092290000	8.672586870000
H	0.289785920000	3.075174530000	7.214393770000
H	-0.445619850000	7.328928010000	8.903545940000
H	0.553097690000	8.262633310000	7.793569220000
H	-1.773134050000	8.007188250000	6.856828360000
H	-1.612134060000	6.241569780000	6.909872300000
H	-0.585061280000	7.178711400000	5.823220450000
H	0.728405960000	5.151825760000	6.068907610000
H	2.280857940000	6.966375600000	6.347072370000
H	2.852569750000	4.704057510000	7.225074700000

[Ru(GaCp*)₃H₂] (1)

Ru	2.273820100000	5.094785260000	5.896830670000
Ga	3.257640950000	3.341867600000	4.874110420000
Ga	4.230378280000	6.477211960000	6.048131020000
Ga	1.358428440000	6.073662170000	3.911691940000
C	4.877964190000	1.827223680000	4.599092380000
C	4.969843310000	1.810258420000	6.019716840000
C	3.750902730000	1.290432590000	6.546304160000
C	2.882604430000	0.970871640000	5.475552790000
C	3.547078370000	1.299863870000	4.240776120000
C	5.981113920000	2.073639330000	3.614859890000
C	6.084117110000	2.367394370000	6.849864880000
C	3.399929070000	1.241683990000	7.999614340000
C	1.475181250000	0.474016760000	5.610226970000
C	3.161855070000	0.828252370000	2.870428910000
C	5.496271160000	7.136019220000	4.109671790000
C	4.811517120000	8.315831490000	4.528524440000
C	5.241322270000	8.637875800000	5.849929170000
C	6.209076990000	7.653297120000	6.253069030000
C	6.369996140000	6.727293810000	5.164802070000
C	5.260222180000	6.425730090000	2.812761040000
C	3.766157000000	9.021461910000	3.725296660000
C	4.809531910000	9.818601770000	6.665587730000
C	7.003031060000	7.665732660000	7.523875210000
C	7.329970250000	5.579355930000	5.126909610000
C	-0.185984130000	6.860606840000	2.354424470000
C	-0.750521010000	5.645567550000	2.862742310000
C	0.096274430000	4.566463890000	2.475330020000
C	1.192700760000	5.099436420000	1.735106420000
C	1.024139240000	6.522213440000	1.651293470000
C	-0.784736610000	8.230467260000	2.457508970000
C	-1.998642780000	5.509414140000	3.680375930000
C	-0.092137910000	3.135149160000	2.871594620000
C	2.326970420000	4.303864760000	1.164443370000
C	1.863510210000	7.474482890000	0.855537680000
H	6.447548520000	1.125111990000	3.304647150000
H	6.770886420000	2.700199450000	4.045446030000
H	5.622116200000	2.571659050000	2.704314560000
H	6.959771030000	2.619245390000	6.240660980000

H	6.405328550000	1.647720680000	7.616431420000
H	5.764782740000	3.280999220000	7.375965850000
H	2.545663410000	0.579418360000	8.184334910000
H	3.129398750000	2.244695750000	8.366150240000
H	4.244882400000	0.884699590000	8.604647730000
H	0.981107160000	0.397989690000	4.634551690000
H	0.873127840000	1.149585040000	6.234895340000
H	1.445194400000	-0.522300510000	6.075498980000
H	3.566103420000	1.474705720000	2.081618730000
H	2.073046190000	0.791349720000	2.744541410000
H	3.548462240000	-0.187705200000	2.691912340000
H	4.183544470000	6.285236650000	2.634704490000
H	5.724965060000	5.432016120000	2.806811000000
H	5.667886980000	6.987904520000	1.958406380000
H	4.165573750000	9.372007390000	2.762322820000
H	3.363906470000	9.891312100000	4.257625120000
H	2.918619030000	8.350959950000	3.500065840000
H	5.461244070000	10.688503010000	6.487240230000
H	4.846403330000	9.601795700000	7.741061140000
H	3.782473310000	10.123258460000	6.427279440000
H	7.307708740000	6.653961770000	7.822129810000
H	6.430796860000	8.096740930000	8.355697590000
H	7.921317890000	8.264610360000	7.415311100000
H	6.952995790000	4.766400880000	4.493771220000
H	7.505984070000	5.164027310000	6.127179710000
H	8.306975140000	5.885361020000	4.721126350000
H	-1.438915680000	8.447818470000	1.598382630000
H	-0.012547650000	9.010749800000	2.484033330000
H	-1.393190760000	8.337919690000	3.364816830000
H	-2.848746130000	5.176382720000	3.064376790000
H	-2.285184240000	6.461812470000	4.143740930000
H	-1.867447520000	4.774025150000	4.485748120000
H	-1.087454950000	2.764426860000	2.587449100000
H	0.014459200000	3.006744100000	3.960748880000
H	0.652656810000	2.492616170000	2.386812430000
H	1.991534040000	3.644436760000	0.349976640000
H	2.795861580000	3.663406800000	1.928493480000
H	3.110742120000	4.955317510000	0.760476720000
H	2.917142750000	7.168964480000	0.824585210000
H	1.829677690000	8.488900920000	1.272273450000
H	1.509548450000	7.538585470000	-0.185689620000
H	1.012824070000	4.077004110000	5.758399270000
H	2.635923160000	4.088545800000	7.114583680000

[Ru(PMe₃)₃(SiEt₃)H₃]

Ru	2.519249180000	5.405357850000	5.949096270000
P	3.205674710000	3.198196760000	5.796262780000
P	4.476525670000	6.377271700000	5.174716960000
P	1.248910280000	5.411211100000	4.012612420000
Si	1.414811780000	6.394766910000	7.842003800000
C	0.101125020000	3.993426140000	3.722204370000
C	2.036072050000	5.502450280000	2.340641090000
C	0.064549310000	6.812762040000	3.864419010000
C	5.899306590000	6.417020560000	6.348178610000
C	4.339968990000	8.157447360000	4.712673290000
C	5.393347020000	5.744424410000	3.695002420000
C	1.979490220000	1.911422610000	6.280989240000
C	3.710691670000	2.506057900000	4.155591770000
C	4.658453500000	2.687157030000	6.809045320000
C	2.042596040000	8.106387530000	8.432603290000
C	3.544074610000	8.247401830000	8.686740380000
C	1.495083570000	5.383805760000	9.469925210000
C	1.445500600000	3.859598230000	9.378778060000
C	-0.441774160000	6.778468940000	7.573968950000
C	-1.360510240000	5.583366770000	7.304954820000
H	-0.529900650000	4.157217490000	2.837909860000
H	0.677181610000	3.070824870000	3.580249410000
H	-0.534762450000	3.866058650000	4.606142240000
H	2.719630860000	4.655918820000	2.204790180000
H	1.284700380000	5.490804150000	1.538886730000
H	2.617489310000	6.430048650000	2.267061850000

H	0.625368230000	7.753992300000	3.908522230000
H	-0.511945640000	6.766215180000	2.930105980000
H	-0.619691760000	6.787618670000	4.719514200000
H	6.758575060000	6.956924810000	5.926608130000
H	5.589159660000	6.885918580000	7.286800220000
H	6.194730310000	5.385256380000	6.573539310000
H	3.932209060000	8.712491260000	5.565286410000
H	5.307124620000	8.587144590000	4.416927150000
H	3.629313150000	8.251889820000	3.881994430000
H	5.796677280000	4.749363010000	3.919300660000
H	4.725901050000	5.661060100000	2.831443890000
H	6.231277480000	6.408449200000	3.441606100000
H	1.084269430000	2.022888080000	5.658585340000
H	2.386907650000	0.898089780000	6.160716420000
H	1.684830090000	2.070633270000	7.323011520000
H	2.863813230000	2.560652280000	3.460747930000
H	4.531731860000	3.094921510000	3.733678810000
H	4.026622780000	1.457567110000	4.244360340000
H	4.472930920000	2.960310910000	7.854275570000
H	4.855082570000	1.608755590000	6.734511920000
H	5.543898960000	3.238309440000	6.468854540000
H	1.714696480000	8.862729810000	7.700022690000
H	1.487191570000	8.324994260000	9.361336480000
H	4.103285050000	8.175951320000	7.745599200000
H	3.921566590000	7.451209140000	9.345456010000
H	3.804690540000	9.210741610000	9.150596520000
H	2.423981480000	5.684589600000	9.982392400000
H	0.670649220000	5.755898760000	10.102543840000
H	0.546205040000	3.512471000000	8.850226200000
H	1.458639520000	3.378282680000	10.368451260000
H	2.312878180000	3.490049020000	8.815542430000
H	-0.780202970000	7.306780100000	8.481561250000
H	-0.520741860000	7.514720990000	6.757456130000
H	-2.403660340000	5.883883020000	7.124041130000
H	-1.362719930000	4.885741940000	8.154445600000
H	-1.019457540000	5.011545530000	6.429745180000
H	1.167024660000	4.748719190000	6.644447760000
H	2.003012180000	6.972034390000	6.060654560000
H	3.293714680000	5.449629430000	7.415842920000

[Ru(PMe₃)₃H₂]

Ru	2.514795750000	5.233223630000	5.857647850000
P	3.215257110000	3.193944250000	5.756197160000
P	4.477204660000	6.274066440000	5.233836310000
P	1.291118430000	5.356872000000	3.912731680000
C	-0.011331240000	4.078020880000	3.631943110000
C	2.017972490000	5.438996380000	2.209671590000
C	0.245521470000	6.887216890000	3.873646730000
C	5.808550240000	6.488372430000	6.498797100000
C	4.235804210000	8.047493260000	4.745658400000
C	5.506530050000	5.699468930000	3.805841530000
C	2.117512920000	1.923131890000	6.506949640000
C	3.522229450000	2.453104870000	4.092058610000
C	4.817131600000	2.808514790000	6.582535140000
H	-0.623537780000	4.292499890000	2.744461400000
H	0.458069190000	3.093604110000	3.511128560000
H	-0.644223610000	4.041025510000	4.526242190000
H	2.611065410000	4.534803860000	2.024292420000
H	1.247967870000	5.529286310000	1.430002120000
H	2.690276290000	6.304405250000	2.149265950000
H	0.892925930000	7.773386210000	3.876613310000
H	-0.401193840000	6.919197760000	2.985377840000
H	-0.378278350000	6.912965820000	4.775778690000
H	6.664273350000	7.064671850000	6.118466530000
H	5.374994890000	6.996811870000	7.368521610000
H	6.151772520000	5.502084970000	6.832973540000
H	3.707219530000	8.574667420000	5.550511840000
H	5.190431780000	8.557600400000	4.553494730000
H	3.614800800000	8.092336190000	3.842043580000
H	5.901576300000	4.698979840000	4.024134320000

H	4.880333820000	5.630204320000	2.908696860000
H	6.350691830000	6.376052880000	3.611468960000
H	1.144000750000	1.961495180000	6.005335190000
H	2.544911450000	0.913634700000	6.424888260000
H	1.964855140000	2.185608500000	7.559784690000
H	2.584102380000	2.428831190000	3.525372810000
H	4.239135940000	3.076147730000	3.545433260000
H	3.916055480000	1.430426040000	4.174477180000
H	4.754370850000	3.137744580000	7.625529440000
H	5.043242650000	1.734233320000	6.538039660000
H	5.625324110000	3.364510380000	6.092119680000
H	1.121882640000	4.647124750000	6.540768600000
H	3.051884120000	5.155111390000	7.424417550000

[Ru(GaCp*)₃(C₇H₇)H₃] (2_{Methyl})

Ru	-0.456351570000	-0.032008010000	1.252493710000
Ga	1.853692820000	0.371264400000	1.058871690000
Ga	-2.036083080000	1.256317050000	0.071929690000
Ga	-0.442073370000	-1.567076220000	-0.575634650000
H	0.136754020000	-1.248348050000	2.167821240000
H	-1.711556590000	-0.952321310000	1.735156050000
H	-0.082447900000	1.538590200000	0.891408090000
H	-1.597367910000	1.604598810000	3.122610170000
H	-1.211785330000	0.029074300000	3.862606700000
C	3.965275000000	1.078796370000	1.009675820000
C	3.545834950000	1.201893590000	-0.363075570000
C	3.969602130000	-0.331868120000	1.339608020000
C	3.296079290000	-0.106243300000	-0.867995840000
C	3.547852380000	-1.048716970000	0.174729900000
C	-2.346892560000	3.730519090000	0.204578970000
C	-3.372674590000	2.978043440000	-0.451978470000
C	-1.158039700000	3.637221780000	-0.571784550000
C	-2.790556750000	2.417592620000	-1.670063130000
C	-1.420456080000	2.831044200000	-1.715375470000
C	-0.661868130000	-3.926410180000	-0.806748380000
C	-0.333178740000	-3.321669980000	-2.070115190000
C	-1.956421850000	-3.471400660000	-0.424958050000
C	-1.446056820000	-2.492023160000	-2.460442290000
C	-2.440361380000	-2.589954970000	-1.438528410000
C	4.490822110000	2.181659760000	1.873935480000
H	4.334909080000	1.971308090000	2.937783830000
H	5.570810480000	2.321930780000	1.708645010000
H	3.995642590000	3.136939170000	1.660346590000
C	3.452133910000	2.486369780000	-1.127753190000
H	2.642680040000	2.462991310000	-1.868058710000
C	3.263557360000	3.336372340000	-0.460941060000
H	4.389147030000	2.695687350000	-1.667071770000
C	2.771782390000	-0.452831280000	-2.225514870000
H	1.765440350000	-0.901990820000	-2.163875700000
H	2.698586910000	0.432463260000	-2.867835450000
H	3.419434420000	-1.182861850000	-2.731604050000
C	3.331054660000	-2.525154840000	0.063059890000
H	3.342326500000	-3.011182920000	1.045405570000
H	2.358919810000	-2.745442920000	-0.401807260000
H	4.107442130000	-3.001599840000	-0.555058140000
C	4.407589700000	-0.914816820000	2.648000570000
H	5.491364500000	-1.108322430000	2.651612320000
H	4.185656470000	-0.235324420000	3.480072510000
H	3.900793030000	-1.865614480000	2.856207630000
C	-2.505140430000	4.475984170000	1.495001930000
H	-1.576702050000	4.478006050000	2.079013640000
H	-2.786408110000	5.526178960000	1.319533560000
H	-3.285686640000	4.031154020000	2.124710680000
C	-4.827994830000	2.955010600000	-0.093901930000
H	-5.318027710000	2.031742530000	-0.428769980000
H	-4.978323920000	3.035628100000	0.990161480000
H	-5.361615040000	3.797345660000	-0.562028230000
C	-3.566443670000	1.760465640000	-2.770191860000
H	-3.987873370000	2.514745110000	-3.453113070000
H	-2.934078380000	1.094128720000	-3.369868790000

H	-4.404653680000	1.167096730000	-2.384153140000
C	-0.393388950000	2.396244560000	-2.716536470000
H	0.350716120000	1.728503100000	-2.253142580000
H	-0.847384200000	1.853426530000	-3.554073950000
H	0.149919240000	3.256942140000	-3.132351850000
C	0.183656680000	4.186410990000	-0.201756310000
H	0.097669260000	5.021472250000	0.503622270000
H	0.814542620000	3.415874490000	0.272151760000
H	0.723261800000	4.547117960000	-1.087757780000
C	0.188982820000	-4.897416060000	-0.046118640000
H	0.157331700000	-4.703922980000	1.034176290000
H	-0.147905380000	-5.933278660000	-0.206626320000
H	1.238915800000	-4.845283030000	-0.359358010000
C	0.854742390000	-3.642055510000	-2.924648220000
H	1.119757880000	-2.806066730000	-3.584240510000
H	1.741346670000	-3.882924530000	-2.324427920000
H	0.651552660000	-4.512767930000	-3.568317830000
C	-1.549107930000	-1.732499510000	-3.747243940000
H	-1.885606050000	-2.380386760000	-4.571692530000
H	-2.268743480000	-0.908173440000	-3.668368340000
H	-0.584227990000	-1.300230340000	-4.045111610000
C	-3.747088900000	-1.862783720000	-1.375739080000
H	-3.869094330000	-1.347830790000	-0.410097900000
H	-3.830263130000	-1.112936750000	-2.171157880000
H	-4.597926890000	-2.552735210000	-1.482837100000
C	-2.677067930000	-3.787055390000	0.847858890000
H	-3.635430850000	-4.290280180000	0.650504780000
H	-2.081958000000	-4.443666700000	1.493126130000
H	-2.890840870000	-2.870349560000	1.418960660000
C	-0.823961060000	0.837107480000	3.236205780000
C	0.404195540000	1.418559330000	3.814219290000
C	0.759924660000	2.763940940000	3.584843080000
C	1.271770730000	0.654344450000	4.621431720000
C	1.907773540000	3.321298730000	4.141644420000
H	0.110466570000	3.373435390000	2.954362570000
C	2.420572740000	1.208949140000	5.181847160000
H	1.026379460000	-0.393138210000	4.803862280000
C	2.748138790000	2.549210130000	4.950469690000
H	2.147480380000	4.368918450000	3.952765110000
H	3.060934280000	0.595432860000	5.818223770000
H	3.640098120000	2.986848360000	5.398812940000

[Ru(GaCp*)₃(C₇H₇)H₃] (2_{Ortho})

Ru	0.865243500000	-0.889493620000	-0.553467950000
Ga	-0.200252800000	-0.675663020000	1.597585130000
Ga	-1.177952890000	-1.738218790000	-1.466958570000
Ga	0.540036970000	1.449790380000	-0.976844010000
H	1.245457050000	-2.194488680000	0.321242820000
H	1.201651860000	-0.791807570000	-2.123445800000
H	1.662489560000	-2.091066190000	-1.224686710000
C	0.093897050000	-1.066115990000	3.905254810000
C	0.043377550000	-2.349242800000	3.281802830000
C	-1.158337770000	-0.403222540000	3.657939950000
C	-1.236536050000	-2.496128780000	2.658073420000
C	-1.984255530000	-1.297819270000	2.883087000000
C	-2.185836590000	-0.703309540000	-3.405506980000
C	-3.164155250000	-0.757126060000	-2.367062620000
C	-1.804502120000	-2.038249450000	-3.735756400000
C	-3.397606460000	-2.132651720000	-2.047968900000
C	-2.545168500000	-2.931040940000	-2.894198050000
C	0.863611140000	3.106410410000	0.714115760000
C	-0.470722740000	3.235746650000	0.214753720000
C	1.773550810000	3.327846410000	-0.362035160000
C	-0.399424220000	3.537739100000	-1.180796990000
C	0.999118240000	3.576251440000	-1.549372940000
C	1.226731480000	-0.504378230000	4.708480970000
H	1.332634000000	0.578369720000	4.560374490000
H	1.072762090000	-0.674177410000	5.785444950000
H	2.182426100000	-0.968792620000	4.436884090000
C	1.150376960000	-3.353493600000	3.210794940000
H	1.259983880000	-3.748519810000	2.190877540000
H	2.113561330000	-2.912537670000	3.492732270000

H	0.963314800000	-4.206768210000	3.879881490000
C	-1.669007870000	-3.676753540000	1.846162990000
H	-2.535627880000	-3.433833090000	1.218747000000
H	-0.863787040000	-4.016238690000	1.179747290000
H	-1.951365940000	-4.525990060000	2.486643630000
C	-3.390007880000	-1.030646100000	2.441548800000
H	-3.564905990000	0.039423580000	2.269872630000
H	-3.619384020000	-1.556682030000	1.506542620000
H	-4.119058300000	-1.366769040000	3.195008950000
C	-1.592758590000	0.897205660000	4.259161740000
H	-1.990759880000	0.741401150000	5.274346300000
H	-0.762145100000	1.609397410000	4.342541870000
H	-2.384906000000	1.375805420000	3.670387010000
C	-1.613091090000	0.550289790000	-3.986187070000
H	-0.659219940000	0.358623860000	-4.492317540000
H	-2.294883850000	1.009984620000	-4.718417370000
H	-1.423972630000	1.298347960000	-3.202562160000
C	-3.773370390000	0.437063170000	-1.698363900000
H	-4.309323270000	0.158498140000	-0.782813080000
H	-2.999770090000	1.167318450000	-1.416472570000
H	-4.487397120000	0.954523920000	-2.356902690000
C	-4.432229580000	-2.672667580000	-1.109372100000
H	-5.352426490000	-2.944764610000	-1.650074360000
H	-4.086337250000	-3.576855700000	-0.590501790000
H	-4.713675020000	-1.936256740000	-0.346282830000
C	-2.531664450000	-4.428533130000	-2.953174130000
H	-1.555125900000	-4.813280830000	-3.273886120000
H	-2.756878290000	-4.874815510000	-1.975767360000
H	-3.282197610000	-4.806568870000	-3.665307090000
C	-0.787035620000	-2.430388580000	-4.763134420000
H	-1.216493230000	-2.428760400000	-5.776790120000
H	0.068122670000	-1.741144160000	-4.765497530000
H	-0.394455920000	-3.437247660000	-4.575100310000
C	1.224539640000	2.745577570000	2.119810220000
H	2.275052700000	2.445214020000	2.196826970000
H	1.051657400000	3.585459990000	2.809821400000
H	0.617676790000	1.898307000000	2.476567360000
C	-1.711222550000	3.026865300000	1.026706240000
H	-2.609708850000	3.012395360000	0.398249420000
H	-1.671155680000	2.070520040000	1.571322750000
H	-1.841566720000	3.820257890000	1.777795500000
C	-1.544520210000	3.884147360000	-2.081327780000
H	-1.757234300000	4.963943770000	-2.041913610000
H	-1.330771640000	3.634905420000	-3.127953630000
H	-2.466360180000	3.360354520000	-1.798390890000
C	1.542798410000	3.950158900000	-2.894910100000
H	2.526975250000	3.497505740000	-3.068722600000
H	0.879457410000	3.625259160000	-3.706714530000
H	1.662791980000	5.041164750000	-2.985016440000
C	3.266820500000	3.328902930000	-0.270142550000
H	3.639132650000	4.328470830000	0.003182490000
H	3.629902000000	2.614884200000	0.478198240000
H	3.731014810000	3.053498970000	-1.223953140000
C	2.823950500000	-0.272460320000	-0.030404660000
C	3.166844100000	-0.163947480000	1.335802100000
C	3.864572320000	0.008690390000	-0.957175610000
C	4.437660500000	0.198345490000	1.784738930000
H	2.405992200000	-0.372685050000	2.087856910000
C	5.145196940000	0.358926600000	-0.497039410000
C	5.447383210000	0.460037050000	0.859416380000
H	4.635331530000	0.267132040000	2.856298660000
H	5.924983070000	0.566525940000	-1.233762010000
H	6.450539550000	0.737239570000	1.184457550000
C	3.656498880000	-0.023846700000	-2.450376790000
H	3.308395330000	-1.008911180000	-2.788563150000
H	2.881461300000	0.694930640000	-2.761076380000
H	4.585938490000	0.221866290000	-2.980799540000

[Ru(GaCp*)₃(C₇H₇)H₃] (2_{Meta})

Ru	0.877602650000	-0.891767850000	-0.534097020000
Ga	-0.192029180000	-0.685573070000	1.610473820000

Ga	-1.157451700000	-1.721588610000	-1.493773490000
Ga	0.566017010000	1.454588550000	-0.955052220000
H	1.245290480000	-2.201866450000	0.336814050000
H	1.338084270000	-0.769020830000	-2.079900520000
H	1.669480740000	-2.103946270000	-1.192560120000
C	0.067545710000	-1.048847590000	3.917119750000
C	0.050789020000	-2.338927060000	3.306603650000
C	-1.194871820000	-0.412952150000	3.645761440000
C	-1.218153670000	-2.517262390000	2.668157020000
C	-1.992429330000	-1.332732600000	2.872173370000
C	-2.175357940000	-0.664128330000	-3.411023060000
C	-3.150051050000	-0.731464430000	-2.369547650000
C	-1.797705410000	-1.994859770000	-3.762043440000
C	-3.384329110000	-2.110888740000	-2.069783830000
C	-2.536012470000	-2.898093210000	-2.929558590000
C	0.873047490000	3.119447950000	0.735070700000
C	-0.462784780000	3.247969900000	0.240182840000
C	1.779648790000	3.335935960000	-0.345327640000
C	-0.397063790000	3.547553780000	-1.154689540000
C	0.999253120000	3.583015820000	-1.530247790000
C	1.171827980000	-0.462269230000	4.741147450000
H	1.252468110000	0.623536770000	4.599117540000
H	1.002417120000	-0.639169830000	5.814668290000
H	2.143362980000	-0.901698210000	4.485680750000
C	1.180263630000	-3.319344950000	3.260251780000
H	1.306114010000	-3.728792260000	2.248004670000
H	2.130977690000	-2.851389620000	3.541172670000
H	1.007810360000	-4.165370770000	3.942325810000
C	-1.615989190000	-3.711377310000	1.858087870000
H	-2.475456410000	-3.487879850000	1.213783220000
H	-0.793844830000	-4.041253300000	1.207860370000
H	-1.894873870000	-4.560631020000	2.500008340000
C	-3.394380190000	-1.095593500000	2.403064950000
H	-3.586641840000	-0.030053650000	2.222401010000
H	-3.595340830000	-1.630340290000	1.466573140000
H	-4.131016920000	-1.442439230000	3.144172460000
C	-1.662258100000	0.883731620000	4.230415950000
H	-2.052520270000	0.731368260000	5.249113810000
H	-0.851310230000	1.619839600000	4.300550330000
H	-2.469042390000	1.331844190000	3.637772730000
C	-1.604894250000	0.597115810000	-3.977239960000
H	-0.655894370000	0.411357430000	-4.494604800000
H	-2.292074960000	1.069483730000	-4.696278330000
H	-1.407394670000	1.332412280000	-3.183788930000
C	-3.753787660000	0.454607680000	-1.681237840000
H	-4.306404320000	0.161278660000	-0.780410250000
H	-2.975461290000	1.168220570000	-1.370737820000
H	-4.451640540000	0.996319810000	-2.337508240000
C	-4.415465470000	-2.664732160000	-1.135434030000
H	-5.327370980000	-2.954345470000	-1.681076160000
H	-4.058288550000	-3.561182200000	-0.610422260000
H	-4.714070800000	-1.930051990000	-0.377433200000
C	-2.525601190000	-4.394637830000	-3.009744030000
H	-1.551438530000	-4.776678610000	-3.340725800000
H	-2.747086710000	-4.854176020000	-2.037635270000
H	-3.280366170000	-4.761228200000	-3.723486390000
C	-0.789673860000	-2.375273400000	-4.802953730000
H	-1.229916500000	-2.366343090000	-5.811975870000
H	0.063642740000	-1.683898640000	-4.808535250000
H	-0.392499500000	-3.382658450000	-4.627642680000
C	1.236216020000	2.773049970000	2.144044860000
H	2.297342360000	2.516143780000	2.229247990000
H	1.024992170000	3.606696540000	2.830909730000
H	0.660496580000	1.902960760000	2.498307400000
C	-1.699841670000	3.040490780000	1.057572150000
H	-2.601632230000	3.033831260000	0.433714080000
H	-1.661537800000	2.081241900000	1.596825530000
H	-1.822932220000	3.830306250000	1.813783470000
C	-1.546107580000	3.894032930000	-2.050144200000
H	-1.762232720000	4.972978430000	-2.004935330000
H	-1.334677390000	3.650799690000	-3.098560990000
H	-2.465441180000	3.365888020000	-1.767142180000

C	1.536762970000	3.957954020000	-2.878132460000
H	2.518311400000	3.502545820000	-3.058614830000
H	0.867585170000	3.636905850000	-3.686656580000
H	1.659253800000	5.048882570000	-2.966341060000
C	3.273811580000	3.331274800000	-0.262078780000
H	3.652537490000	4.325819240000	0.020402880000
H	3.638037700000	2.605871660000	0.474922120000
C	3.730440250000	3.063109930000	-1.221495550000
H	2.818906240000	-0.289074810000	0.006059690000
C	3.193997250000	-0.057542880000	1.345185540000
C	3.840313450000	-0.120859260000	-0.953856040000
C	4.485183110000	0.330092340000	1.731318380000
H	2.449167490000	-0.175544760000	2.134986960000
C	5.133504290000	0.261750220000	-0.593078220000
H	3.618726970000	-0.290996150000	-2.007446710000
C	5.463014650000	0.494900350000	0.742987110000
H	5.893691150000	0.386659470000	-1.367134330000
H	6.473369600000	0.802323240000	1.018760550000
C	4.812906730000	0.541115610000	3.189515970000
H	3.935962970000	0.892430060000	3.750051670000
H	5.146959260000	-0.396230300000	3.661230870000
H	5.619092990000	1.275604950000	3.318303880000

[Ru(GaCp*)₃(C₇H₇)H₃] (2_{Para})

Ru	0.881385400000	-0.893700020000	-0.536419880000
Ga	-0.200305740000	-0.689209150000	1.601588210000
Ga	-1.138492440000	-1.738915570000	-1.511145450000
Ga	0.560301610000	1.451354800000	-0.963929510000
H	1.248157870000	-2.201475230000	0.337312390000
H	1.361145660000	-0.768334870000	-2.076374800000
H	1.691306480000	-2.099001480000	-1.184912150000
C	0.090722260000	-1.056133800000	3.907128620000
C	0.050695890000	-2.345714420000	3.296728280000
C	-1.167446260000	-0.405637490000	3.652553330000
C	-1.227977960000	-2.509047150000	2.674009900000
C	-1.985838280000	-1.315370370000	2.888096800000
C	-2.170963910000	-0.671609300000	-3.417908780000
C	-3.136406730000	-0.740792500000	-2.367998570000
C	-1.797993150000	-2.001575480000	-3.775947270000
C	-3.369977460000	-2.120437980000	-2.070111160000
C	-2.530091870000	-2.906490520000	-2.939356820000
C	0.849004400000	3.122361910000	0.721125840000
C	-0.485077180000	3.243719900000	0.219755500000
C	1.759556530000	3.341338250000	-0.355392980000
C	-0.414327390000	3.541660980000	-1.175150120000
C	0.983320840000	3.582863510000	-1.544360940000
C	1.215301550000	-0.480847270000	4.712202710000
H	1.307478570000	0.603412860000	4.565983760000
H	1.061159490000	-0.653743710000	5.788683080000
H	2.177218380000	-0.933214240000	4.442076580000
C	1.167223690000	-3.339963510000	3.235258900000
H	1.274950610000	-3.750260510000	2.221271440000
H	2.127399560000	-2.884521730000	3.504159060000
H	0.992708630000	-4.184288240000	3.918954670000
C	-1.648857100000	-3.698920120000	1.869289970000
H	-2.520287780000	-3.469446260000	1.243603090000
H	-0.841815000000	-4.031572750000	1.201597670000
H	-1.918480120000	-4.548471090000	2.514736790000
C	-3.392482200000	-1.062215860000	2.441510030000
H	-3.573201260000	0.004413210000	2.255140680000
H	-3.617741840000	-1.602083270000	1.513544700000
H	-4.120414040000	-1.392258180000	3.198724820000
C	-1.614148710000	0.895236140000	4.243849600000
H	-2.007123610000	0.743645490000	5.261635550000
H	-0.791462050000	1.617532870000	4.318072250000
H	-2.413447340000	1.359609570000	3.653476340000
C	-1.603598510000	0.591210250000	-3.983683760000
H	-0.667438410000	0.404290420000	-4.523469740000
H	-2.302912460000	1.076034980000	-4.682429080000
H	-1.383404140000	1.316769040000	-3.187037270000

C	-3.727263580000	0.444500000000	-1.667341540000
H	-4.286301510000	0.147505110000	-0.771727450000
H	-2.940593960000	1.144098970000	-1.345894900000
H	-4.416120570000	1.002779830000	-2.319158540000
C	-4.390945830000	-2.675326690000	-1.125367990000
H	-5.314454150000	-2.950823220000	-1.658648310000
H	-4.032741710000	-3.580431260000	-0.616345530000
H	-4.670078340000	-1.946531730000	-0.354306810000
C	-2.523289210000	-4.402715360000	-3.026134820000
H	-1.552275410000	-4.785121870000	-3.365883360000
H	-2.738651410000	-4.866201800000	-2.054539600000
H	-3.283811990000	-4.764686010000	-3.736103520000
C	-0.802934570000	-2.381566790000	-4.829409840000
H	-1.257854560000	-2.379757950000	-5.831963680000
H	0.046537600000	-1.685913760000	-4.850814900000
H	-0.397987490000	-3.386129010000	-4.655372600000
C	1.206747050000	2.780787780000	2.132484940000
H	2.268448470000	2.529084040000	2.224942480000
H	0.986725810000	3.614812470000	2.816217850000
H	0.633248450000	1.908729440000	2.485061090000
C	-1.724751540000	3.032247320000	1.032316870000
H	-2.624666990000	3.029485010000	0.405800790000
H	-1.688619810000	2.069923670000	1.566589440000
H	-1.849445130000	3.817994330000	1.792438670000
C	-1.561087660000	3.881498700000	-2.076175860000
H	-1.784298010000	4.959009040000	-2.031064740000
H	-1.342751090000	3.640543610000	-3.123669230000
H	-2.478345450000	3.347059680000	-1.798526600000
C	1.524872870000	3.959565520000	-2.890103910000
H	2.510225350000	3.510401570000	-3.065519830000
H	0.861632810000	3.633299520000	-3.701438720000
H	1.640642360000	5.051185820000	-2.979138100000
C	3.253526880000	3.344984690000	-0.264176210000
H	3.624913270000	4.342382020000	0.018285960000
H	3.617590910000	2.623356750000	0.476717320000
H	3.716560580000	3.077830760000	-1.220812630000
C	2.812680090000	-0.279189660000	0.029868870000
C	3.182798650000	-0.062791970000	1.372587310000
C	3.845175190000	-0.089785920000	-0.914201760000
C	4.472374570000	0.327314070000	1.745993840000
H	2.442191990000	-0.195201610000	2.162118360000
C	5.135431280000	0.295184150000	-0.546366210000
H	3.634024490000	-0.245417900000	-1.972691330000
C	5.479743740000	0.517088450000	0.793528140000
H	4.697962720000	0.487721350000	2.803963680000
H	5.893177270000	0.432159760000	-1.322627950000
C	6.878971050000	0.915869950000	1.189951500000
H	6.901118270000	1.339148950000	2.202877450000
H	7.560750720000	0.051217860000	1.179029490000
H	7.295026690000	1.663476110000	0.499938810000

Toluene

C	-3.699168640000	-1.009217670000	0.002314500000
C	-2.302695830000	-1.016361190000	0.011386790000
C	-1.610338070000	0.196210760000	0.002744050000
C	-2.310373200000	1.403787740000	-0.012453310000
C	-3.712042990000	1.425785040000	-0.017721920000
C	-4.394174150000	0.201057620000	-0.013177290000
H	-4.250428760000	-1.950106960000	0.003562270000
H	-1.757887180000	-1.960420540000	0.020131200000
H	-0.519897640000	0.202652820000	0.003867880000
H	-1.760910830000	2.346936760000	-0.023147420000
H	-5.485683940000	0.197311300000	-0.024564990000
C	-4.466478350000	2.730875980000	-0.001334890000
H	-5.432882360000	2.640879310000	-0.513888730000
H	-4.671355630000	3.051984770000	1.031536070000
H	-3.892399050000	3.531286740000	-0.485511400000

Triethylsilane

Si	1.331017540000	6.048971600000	8.129909160000
----	----------------	----------------	----------------

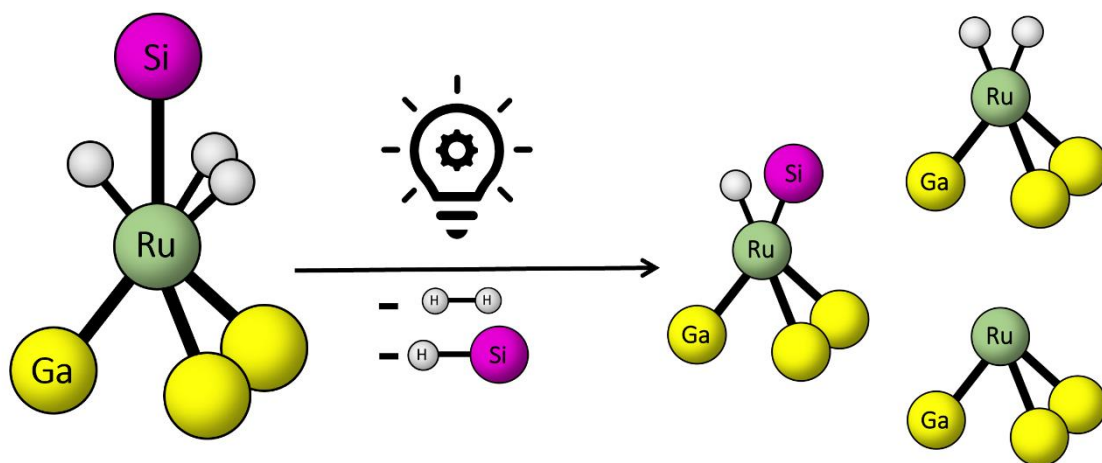
C	2.696326690000	6.713854030000	9.258007040000
C	3.891104520000	5.761459700000	9.430151630000
C	0.569509990000	4.478998160000	8.866259460000
C	-0.127947780000	3.552922540000	7.855397420000
C	0.044478430000	7.403382140000	7.833843560000
C	-1.128765800000	7.017283480000	6.918719120000
H	3.038162900000	7.676885430000	8.845540530000
H	2.253350810000	6.949513220000	10.239740150000
H	4.356703180000	5.528963140000	8.462079080000
H	3.584455920000	4.807367920000	9.881388240000
H	4.668046070000	6.193276210000	10.076630380000
H	1.374087430000	3.925043250000	9.376229580000
H	-0.134140840000	4.777589600000	9.661040860000
H	-0.966982960000	4.054411910000	7.355016690000
H	-0.525264360000	2.649270400000	8.339159140000
H	0.569704080000	3.230817500000	7.070034860000
H	-0.334954090000	7.734005510000	8.815087880000
H	0.578378030000	8.271916960000	7.414413810000
H	-1.795238450000	7.870825610000	6.730352260000
H	-1.738335340000	6.219649320000	7.364398780000
H	-0.774253810000	6.652695000000	5.944214210000
H	1.946789140000	5.681201990000	6.808759460000

2.4 Photochemically Generated Reactive Sites at Ruthenium/Gallium Clusters: Catalysis vs. Cluster Growth.

Maximilian Muhr^{+a}, Raphael Bühler^{+a}, Johannes Stephan^a, Robert Wolf^a, Max Schütz^a, Christian Gemel^a, Roland A. Fischer^{*a}

[a] Chair of Inorganic and Metalorganic Chemistry, Department of Chemistry, Catalysis Research Center, Technical University Munich, Lichtenbergstraße 4, D-85748 Garching, Germany

[+] M.M. and R.B. contributed equally to this work.



Catalysis • Cluster Growth • Intermediate Trapping

The following content has not been evaluated through a peer-review process and is unpublished yet. It is however currently submitted to the Journal *Chemical Communications*.

Author contributions:

Experiments and manuscript writing by the two authors. J.S. and M.S. performed SCXRD. Experimental support by R.W.; C.G. and R.A.F. supervised the research.

2.4.1 Abstract

Irradiation of $[\text{Ru}(\text{GaCp}^*)_3(\text{SiEt}_3)\text{H}_3]$ (**1**) at 350 nm induces the reductive elimination of dihydrogen and triethylsilane and generates unsaturated Ru/Ga species. The reactive intermediate $[\text{Ru}(\text{GaCp}^*)_3]$ was trapped by diphosphine coordination to yield the stable complex $[(\text{dppe})\text{Ru}(\text{GaCp}^*)_3]$ (**4**). The photochemically generated RuGa_3 species perform either catalytic hydrogenation of alkynes or Ru/Ga cluster growth.

2.4.2 Main Text

The study of naked metal clusters in the gas phase shows an extensive spectrum of unique species and structure-dependent reactivities towards small molecules.^[1] The wet chemical approach, however, offers a larger variety of analytical methods to study clusters and cluster-substrate interactions.^[2] The inevitable protective ligand shell prevents clusters agglomeration in solution, it however intrinsically inhibits cluster-substrate interaction to a certain extent. The intrinsic polyradicalic reactivity of the superatom $[\text{Cu}_{43}\text{Al}_{12}](\text{Cp}^*)_{12}$, for example, is suppressed by the protective Cp^* shell.^[2b] Partial removal of the ligand sphere in order to generate the required reactive sites, often causes undesired cluster growth reactions up to the formation of nanoparticles out of the non-scalable regime.^[3] Exemplary, this can be avoided when the ligand removal is performed in a rigid confined environment: decarbonylation of a $[\text{NBu}_4]_2[\{\text{Pt}_3(\text{CO})_6\}_4]$ cluster encapsulated in a ZIF-8 metal-organic framework yields naked $\text{Pt}_{12\pm x}$ atomically defined nanoclusters, which are active in hydrogenation catalysis.^[4] However, ligand do not necessarily have to be removed to achieve cluster reactivity. By clever choice of the ligand, it can take a dual role as stabilizer and substrate, as in the catalytic hydrogenation of COD performed by the Zintl-cluster $[\eta^4\text{-Ge}_9(\text{Si}(\text{SiMe}_3)_3)\text{Rh}(\text{COD})]$.^[5] Other ligands, such as hydrides, combine the advantage of acting both as protecting ligands hindering agglomeration while maintaining reactivities towards

substrates.^[6] Exemplary, $[\text{Cu}_6(\text{AlCp}^*)_6\text{H}_4]$ was shown to react stoichiometrically with nitriles by hydride migration into the $\text{C}\equiv\text{N}$ bond.^[7]

The ruthenium-gallium polyhydride complex $[\text{Ru}(\text{GaCp}^*)_3(\text{SiEt}_3)\text{H}_3]$ (**1**) has recently been investigated in the context of C-H and Si-H bond activations mediated by Ru/Ga complexes.^[8] It can be conveniently prepared from $[\text{Ru}(\text{cod})(2\text{-Methylallyl})_2]$ in the presence of GaCp^* in HSiEt_3 as the solvent under hydrogenolytic conditions. **1** is thermally surprisingly unreactive in contrast to the related Ni/Al complex $[\text{Ni}(\text{AlCp}^*)_3(\text{SiEt}_3)\text{H}]$: a reductive elimination of HSiEt_3 can be achieved thermally yielding the 16 VE intermediated $[\text{Ni}(\text{AlCp}^*)_3]$ which is capable of aromatic C-H bond activation.^[9] Nonetheless, photochemical reductive elimination of hydrogen from Ruthenium-phosphine-complexes has been shown to give transient reactive species with active sites.^[10]

Irradiating complex **1** for 30 minutes at 350 nm, leads to the formation of free triethyl silane and dihydrogen as indicated by in-situ ^1H NMR spectroscopy. The reductive elimination process is not quantitative, also at prolonged irradiation times, indicating a reversible reductive elimination/oxidative addition equilibrium and the establishment of a photostationary state. Analysis *via* inert atmosphere liquid injection field desorption ionization mass spectrometry (LIFDI-MS)^[11] shows only negligible cluster growth after eight hours of irradiation (Fig. S27-28). Possible reaction products of reductive elimination include the two

16 VE (valence electron) Ru(II) species $[\text{Ru}(\text{GaCp}^*)_3(\text{SiEt}_3)\text{H}]$ (**2_{Hsi}**), $[\text{Ru}(\text{GaCp}^*)_3\text{H}_2]$ (**2_{H2}**) as well as the 14 VE Ru(0) complex $[\text{Ru}(\text{GaCp}^*)_3]$ (**3**). In situ ^1H NMR spectroscopy of the reaction solution reveals the presence of two new hydride signals at -11.46 and -14.58 ppm (Fig. S3-6). This equilibrium can be overcome by irradiating **1** in the presence of H_2 . This leads to gradual degradation of **1** and the formation of a mixture of larger Ru/Ga cluster species. Free, uncoordinated HSiEt_3 can be identified in large amounts after complete conversion of **1** together with considerable amounts of Cp^*H (Fig. S19-20). It can be postulated that these conditions lead to the formation of a transient $[\text{Ru}(\text{GaCp}^*)_3\text{H}_4]$ species, in analogy to the $[\text{Ru}(\text{PR}_3)_3\text{H}_4]$ ^[12], and undercoordinated species resulting from Cp^*H elimination inducing cluster growth reactions. This is well in line with the observed cluster growth reactions. *In situ* LIFDI-MS reveals that the major

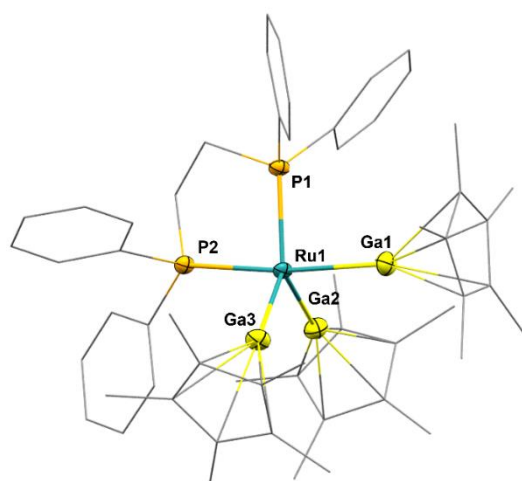


Figure 1: Molecular structure of the trigonal bipyramidal Ru(0) complex $[(\text{dppe})\text{Ru}(\text{GaCp}^*)_3]$ (**4**). Thermal ellipsoids are given at 50% probability level. C atoms in wireframes, H atoms and co-crystallized *n*-hexane unit omitted for clarity. Selected bond lengths (Å) and angles (°): Ru1-Ga1: 2.393; Ru1-Ga2: 2.353; Ru1-Ga3: 2.371; Ru1-P1: 2.239; Ru1-P2: 2.257; Ga-Cp*_{centroid}: 2.049-2.060; Ga1-Ru-P2: 173.16; Ga2-Ru-P1: 117.82; P1-Ru-Ga3: 133.51; Ga2-Ru-Ga3: 108.65.

patterns can be attributed to species in this mixture with the sum formulas $\text{Ru}_2\text{Ga}_4\text{Cp}^*_4\text{H}_5$, $\text{Ru}_3\text{Ga}_9\text{Cp}^*_5\text{H}_5$, $\text{Ru}_2\text{Ga}_8\text{Cp}^*_7\text{H}_3$ and $\text{Ru}_3\text{Ga}_9\text{Cp}^*_6\text{H}_5$ - with a notable high amount of hydride ligands (Fig. S41-42).

To stabilize one of the reductive elimination products (**2_{H2}**, **2_{Hsi}** and **3**), the photolysis of **1** was performed in the presence phosphines. The use of the chelating phosphine ligand 1,2-bis(diphenylphosphino)ethane (dppe) under similar conditions (r.t., 48 h, 350 nm) afforded the isolation of $[(\text{dppe})\text{Ru}(\text{GaCp}^*)_3]$ (**4**) in the form of red-orange needles. The composition is supported by a peak at $m/z = 1114.1656$ (calc. 1114.1671) in the LIFDI mass spectrum (Fig 29-30). **4** is formed by double reductive elimination of H_2 and HSiEt_3 from **1**, indicating that complete reduction of **1** to Ru(0) is possible under photolytic conditions.

The compound crystallizes in the space group $P2_1/n$ as a trigonal bipyramidal structure with one co-crystallized *n*-hexane molecule (Figure 1). The Ru-Ga bond lengths (2.353 – 2.393 Å) are in a common range^[3c, 8, 13], whereas the Ru-P bond lengths (2.239 – 2.257) are slightly shorter than in $[(\text{Cp}^*\text{Ga})_3\text{Ru}(\text{PPh}_3)_2]$ ^[13a] as well as $[(\text{dmpe})_2\text{Ru}(\text{L})]$ (L = CO, PMe_3 ; dmpe = 1,2-bis(dimethylphosphino)ethane)^[14] and about 0.1 Å shorter than Ru-P bonds in comparable Ru(0) compounds.^[15] The ^1H NMR in C_6D_{12} (Fig. S7-9) matches the crystal structure: one singlet for the three Cp^* groups ($\delta = 1.65$ ppm, 45 H) of the GaCp^* ligands and a multiplet of the ethylene bridge ($\delta = 1.80$ ppm, 4 H) of the dppe ligand as well as the respective two

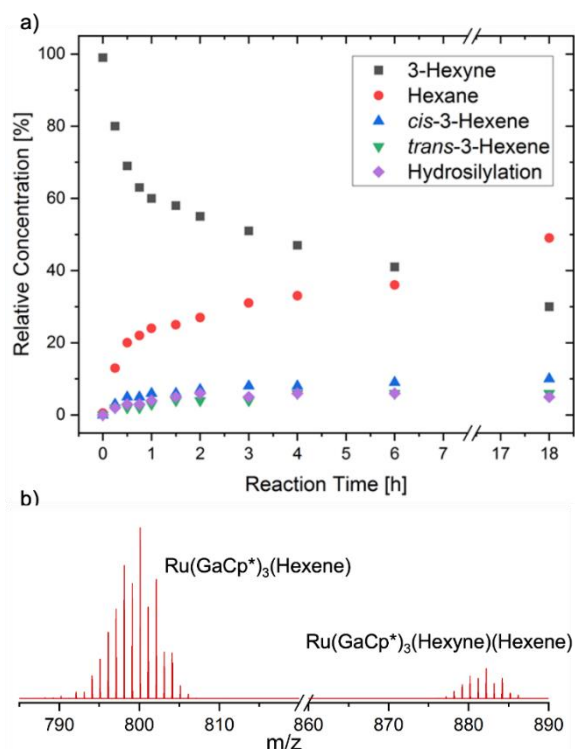


Figure 2: a) Relative concentration of the catalysis of 3-hexyne (5 mol% cat.) and the reaction products *n*-hexane, *cis*- and *trans*-hexene and hydrosilylation products. b) excerpt of in-situ LIFDI mass spectrum during catalysis, showing peaks attributed to catalytic intermediates.

multiplets of the phenyl groups ($\delta = 7.11$ ppm, 12 H; $\delta = 7.73$ ppm, 8 H). The co-crystallised *n*-hexane is also observed ($\delta = 0.89$ ppm, 6 H; $\delta = 1.29$ ppm, 8 H). The expected ^{13}C peaks are observed as well and match the 2D NMR data (Fig. S10-17). The ^{31}P spectrum shows one singlet at 94.6 ppm along with a very small signal of free dppe at -12.9 ppm (Fig. S18). Neither the ^1H , nor the IR spectrum (Fig. S45) of **4** shows any peaks that can be attributed to ruthenium hydrides.

Analogues of **4** could be observed via LIFDI-MS using 1,2-bis(diphenylphosphino)benzene and the monodentate phosphines triethyl phosphine or trimethyl phosphine, respectively (Fig. S31-36). In both cases the reaction products were observed *via* LIFDI mass spectrometry but could not be isolated as pure compounds. A single

crystal of $[(\text{PEt}_3)_2\text{Ru}(\text{GaCp}^*)_3]$, however, could be obtained (Fig. S2), though no further analytics could be performed. Both clusters are not stable in solution, however, no decomposition products could be identified so far.

The unsaturated nature of the photolytically generated reactive intermediates suggests the activity of **1** as hydrogenation catalyst under photolytic conditions. Indeed, photolysis of a solution of **1** in C_6D_{12} in the presence of 3-hexyne (20.0 eq.) under dihydrogen pressure (2 bar) leads to the formation of *n*-hexane as the main product together with *cis*- and *trans*-3-hexene in minor amounts (Figure 2a; Fig. S21-22). Stoichiometric amounts (based on **1**, 5%) of hydrosilylation products are also detected (Fig. S21). A steep onset of the catalytic conversion of 3-hexyne is observed (1 h, 40%). The conversion rate, however, declines notably: after 6 h only a total of 59% is hydrogenated and only 70% after 18 h. A full conversion is never reached. This observation can be reasoned by competing catalysis vs. cluster growth at lower alkyne concentrations. LIFDI mass spectra (Fig. S43-44) after the catalysis confirm the formation of numerous larger Ru/Ga polyhydride clusters. We attribute the

cluster growth to the stabilizing effect of alkyne and alkene ligands over the course of the catalysis preventing the catalytically active complexes from agglomeration and undergoing cluster growth reactions. A plausible catalysis intermediate, stabilized by such ligand is observed by LIFDI-MS at $m/z = 882.1997$ (calc. 882.2039), corresponding to the 18 VE species $[\text{Ru}(\text{GaCp}^*)_3(\text{hexyne})(\text{hexene})]$ (Figure 2b; Fig. S37-40).

Performing a catalytic hydrosilylation in analogous conditions to the 3-hexyne catalysis (r.t., 350 nm, 20.0 eq. 3-hexyne, 100 eq. HSiEt_3) fails, as only stoichiometric quantities of hydrosilylation products are observed (Fig. S23-24). Through the multiple observations, we propose a catalytic mechanism (Figure 3). The activation of precatalyst **1** is achieved through the alkyne hydrosilylation and subsequent dihydrogen activation forming the 16 VE species $[\text{Ru}(\text{GaCp}^*)_3\text{H}_2]$ (**2_{H2}**). This then activates 3-hexyne forming the 18 VE species $[\text{Ru}(\text{GaCp}^*)_3(\text{hexyne})\text{H}_2]$ (**A₁**) and subsequently, through hydride insertion the 16 VE species $[\text{Ru}(\text{GaCp}^*)_3(\text{hexene})]$ (**A₂**). These species are observed *via* LIFDI-MS ($m/z = 800.1251$; calc. 800.1257; Fig. S37-40). Even though they cannot be distinguished from one another by MS, they are consecutive reaction products. Through activation of a further equivalent of H_2 and subsequent insertion, *n*-hexane is formed and **2_{H2}** is regenerated. However, a competing cycle occurs where **A₂** is coordinated by a further 3-hexyne yielding the 18 VE species **B**, which is also observed in LIFDI-MS. The observation of 3-hexene can be explained

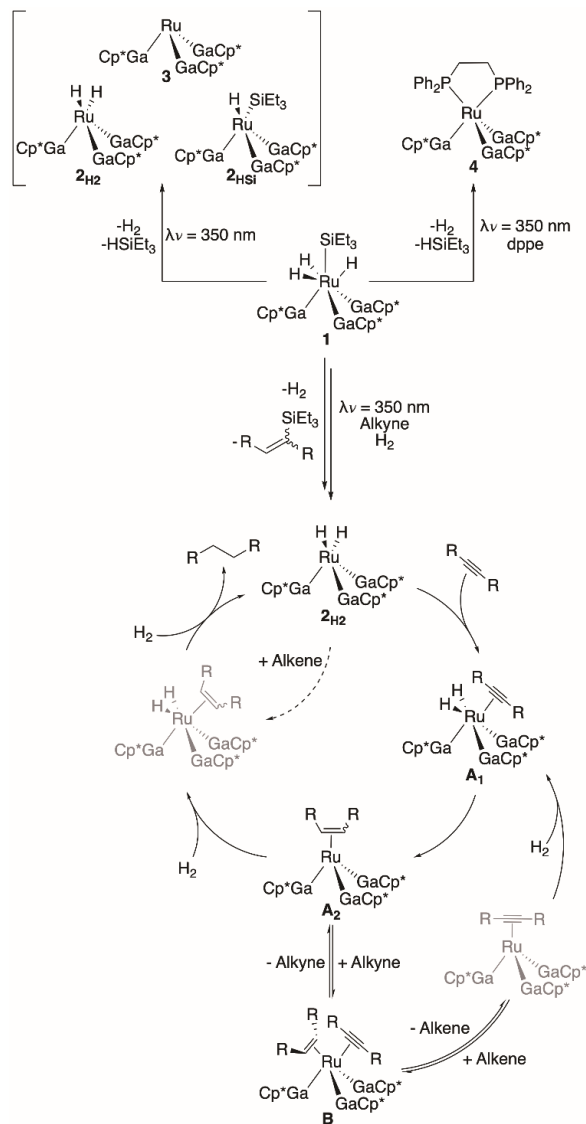


Figure 3: Overview of the reactions possible from **1** with the presumed photochemically generated species **2_{H2}**, **2_{HSi}** and **3** as well as the reaction to **4**. Additionally, a proposed catalytic cycle for the hydrogenation of 3-hexyne with **1** as catalyst under photochemical conditions is given. Intermediates **2_{H2}**, **A₁**, **A₂** and **B** (depicted in black) are supported by experimental evidence (^1H NMR, LIFDI-MS). Intermediates depicted in grey are logical necessary intermediates for which no experimental evidence could be obtained.

through dissociation of the alkene from **B**. The competing nature of both cycles is supported by LIFDI-MS analysis of the catalysis in the presence of 100 eq. 3-hexyne where only **B** is observed (Fig. S37-40). This results in a much slower alkyne conversion. As such, the competing reactions possible from **A₂** are the limiting factor of the catalysis.

In summary, we have presented a novel approach towards the controlled generation of reactive free coordination sites at bimetallic species utilizing photochemistry. In this example, we could specifically induce the reductive elimination of dihydrogen and/or triethyl silane under mild conditions without affecting other bonds. The silyl and hydrides can thus be interpreted as selectively removable protecting groups for the active metal centre. The generated reactive species could be trapped by phosphines and was shown to be photochemically reduced from Ru(IV) to Ru(0). The species themselves are active in hydrogenation catalysis and mass spectrometric investigations bring evidence for a catalytic intermediate. It could further be shown to act as seeds for cluster growth under certain conditions. Building on this work, we aim to achieve better control over the competing catalysis and cluster growth reactions. Doing so will help us identify either catalytically active clusters or clusters as deactivation products of the catalytically active species. We are therefore currently studying the role of different substrates and additives in similar reactions.

The authors are grateful to Daniel P. Schwinger (Prof. Thorsten Bach) for the experimental introduction to the photochemical setup. In addition, we would like to thank Thomas Pickl for initial refinement of the crystallographic data of **4**. This work was funded by the German Research Foundation (DFG) within a Reinhard Koselleck Project (FI 502/44-1). Support by the TUM Graduate School is acknowledged.

2.4.3 References

- [1] a) Y. Ren, Y. Yang, Y.-X. Zhao, S.-G. He, *JACS Au* **2022**, *2*, 197-203; b) J. F. Eckhard, T. Masubuchi, M. Tschurl, R. N. Barnett, U. Landman, U. Heiz, *J. Phys. Chem. A* **2021**, *125*, 5289-5302; c) E. C. Tyo, S. Vajda, *Nat. Nanotechnol.* **2015**, *10*, 577-588.
- [2] a) M. Schütz, C. Gemel, W. Klein, R. A. Fischer, T. F. Fässler, *Chem. Soc. Rev.* **2021**, *50*, 8496-8510; b) J. Weßing, C. Ganesamoorthy, S. Kahlal, R. Marchal, C. Gemel, O. Cador, A. C. H. Da Silva, J. L. F. Da Silva, J.-Y. Saillard, R. A. Fischer, *Angew. Chem. Int. Ed.* **2018**, *57*, 14630-14634; c) B. E. Petel, W. W. Brennessel, E. M. Matson, *J. Am. Chem. Soc.* **2018**, *140*, 8424-8428.
- [3] a) L. Staiger, T. Kratky, S. Günther, A. Urstoeger, M. Schuster, O. Tomanek, R. Zbořil, R. W. Fischer, R. A. Fischer, M. Cokoja, *Nanoscale* **2021**, *13*, 15038-15047; b) L. Staiger, T. Kratky, S. Günther, O. Tomanek, R. Zbořil, R. W. Fischer, R. A. Fischer, M. Cokoja, *ChemCatChem* **2021**, *13*, 227-234; c) T. Cadenbach, C. Gemel, R. Schmid, M. Halbherr, K. Yussenko, M. Cokoja, R. A. Fischer, *Angew. Chem. Int. Ed.* **2009**, *48*, 3872-3876; d) M. Cokoja, H. Parala, M.-K. Schröter, A. Birkner, M. W. E. van den Berg, W. Grünert, R. A. Fischer, *Chem. Mater.* **2006**, *18*, 1634-1642.
- [4] K. Kratzl, T. Kratky, S. Günther, O. Tomanec, R. Zbořil, J. Michalička, J. M. Macak, M. Cokoja, R. A. Fischer, *J. Am. Chem. Soc.* **2019**, *141*, 13962-13969.
- [5] a) O. P. E. Townrow, S. B. Duckett, A. S. Weller, J. M. Goicoechea, *Chem. Sci.* **2022**, *13*, 7626-7633; b) O. P. E.

- Townrow, C. Chung, S. A. Macgregor, A. S. Weller, J. M. Goicoechea, *J. Am. Chem. Soc.* **2020**, *142*, 18330-18335.
- [6] a) J. Takaya, *Chem. Sci.* **2021**, *12*, 1964-1981; b) N. A. Eberhardt, H. Guan, *Chem. Rev.* **2016**, *116*, 8373-8426; c) S. E. Clapham, A. Hadzovic, R. H. Morris, *Coord. Chem. Rev.* **2004**, *248*, 2201-2237.
- [7] C. Ganesamoorthy, J. Wessing, C. Kroll, R. W. Seidel, C. Gemel, R. A. Fischer, *Angew. Chem. Int. Ed.* **2014**, *53*, 7943-7947.
- [8] M. Muhr, R. Bühler, H. Liang, J. Gilch, C. Jandl, S. Kahlal, J.-Y. Saillard, C. Gemel, R. A. Fischer, *Chem. Eur. J.* **2022**, *28*, e202200887.
- [9] T. Steinke, C. Gemel, M. Cokoja, M. Winter, R. A. Fischer, *Angew. Chem. Int. Ed.* **2004**, *43*, 2299-2302.
- [10] a) R. N. Perutz, B. Procacci, *Chem. Rev.* **2016**, *116*, 8506-8544; b) P. L. Callaghan, R. Fernández-Pacheco, N. Jasim, S. Lachaize, T. B. Marder, R. N. Perutz, E. Rivalta, S. Sabo-Etienne, *Chem. Commun.* **2004**, 242-243; c) C. Hall, W. D. Jones, R. J. Mawby, R. Osman, R. N. Perutz, M. K. Whittlesey, *J. Am. Chem. Soc.* **1992**, *114*, 7425-7435; d) P. Bergamini, S. Sostero, O. Traverso, *J. Organomet. Chem.* **1986**, *299*, C11-C14.
- [11] M. Muhr, P. Heiß, M. Schütz, R. Bühler, C. Gemel, M. H. Linden, H. B. Linden, R. A. Fischer, *Dalton Trans.* **2021**, *50*, 9031-9036.
- [12] B. Chaudret, R. Poilblanc, *Organometallics* **1985**, *4*, 1722-1726.
- [13] a) T. Cadenbach, C. Gemel, T. Bollermann, R. A. Fischer, *Inorg. Chem.* **2009**, *48*, 5021-5026; b) T. Cadenbach, T. Bollermann, C. Gemel, R. A. Fischer, *Dalton Trans.* **2009**, 322-329; c) T. Cadenbach, C. Gemel, T. Bollermann, I. Fernandez, G. Frenking, R. A. Fischer, *Chem. Eur. J.* **2008**, *14*, 10789-10796.
- [14] W. D. Jones, M. Libertini, *Inorg. Chem.* **1986**, *25*, 1794-1800.
- [15] a) D. J. Tindall, M. Menche, M. Schelwies, R. A. Paciello, A. Schäfer, P. Comba, F. Rominger, A. S. K. Hashmi, T. Schaub, *Inorg. Chem.* **2020**, *59*, 5099-5115; b) H. Braunschweig, C. Brunecker, R. D. Dewhurst, C. Schneider, B. Wennemann, *Chem. Eur. J.* **2015**, *21*, 19195-19201; c) M. Grellier, L. Vendier, S. Sabo-Etienne, *Angew. Chem. Int. Ed.* **2007**, *46*, 2613-2615; d) S. Sentets, M. d. C. Rodriguez Martinez, L. Vendier, B. Donnadiou, V. Huc, N. Lugan, G. Lavigne, *J. Am. Chem. Soc.* **2005**, *127*, 14554-14555.

2.4.4 Additional Data and Information

Synthetic Protocol

[(dppe)Ru(GaCp*)₃] (**4**): A cyclohexane (7 ml) solution of 75 mg **1** (1.0 eq.; 0.090 mmol) and 40 mg dppe (1.1 eq.; 0.010 mmol) are irradiated in a photoreactor (350 nm) for 24 h. The reddish solution is filtered through a syringe filter and the solvent is removed *in vacuo*. The residue is dissolved in 3 ml *n*-hexane. The solution is cannula filtered and concentrated to about 1.5 ml. After storing the solution over night at -30 °C, 26 mg (0.023 mmol; 26 %) of **4** is obtained in the form of orange-red needles. ¹H NMR (C₆D₁₂, 400 MHz): δ [ppm] = 7.33 (m, 8 H, Ph-P), 7.11 (m, 12 H, Ph-P), 1.80 (m, 4 H, H₂C-CH₂), 1.65 (s, 45 H, GaCp*), 1.29 (m, 8 H, CH₂ in *n*-hexane), 0.89 (t, 6 H, CH₃ in *n*-hexane). ¹³C NMR (C₆D₁₂, 101 MHz): δ [ppm] = 128.4 (s, phenyl), 127.4 (m, phenyl), 114.5 (s, Cp* ring), 32.5 (s, *n*-hexane), 23.5 (s, *n*-hexane), 14.4 (s, *n*-hexane), 10.7 (s, Cp* methyl). ³¹P NMR (C₆D₁₂, 101 MHz): δ [ppm] = 94.6 (s, dppe). LIFDI-MS [M]⁺: m/z = 1114.1656 (calc. 1114.1671). **Elemental analysis** calc. for RuGa₃P₂C₅₆H₆₉: C, 60.36; H, 6.24; Ga, 18.77; Ru, 9.07; P, 5.56. Found: C, 59.43; H, 6.37.

General Procedure for Catalytic Reactions.

5 mg of **1** were dissolved in 0.4 mL cyclohexane-*d*₁₂ in a J-Young NMR tube and 20 – 100 eq. 3-hexyne were added. The reaction solution was degassed by freeze-pump-thaw and was pressurized with 2.0 bar at 25°C. The NMR tube was irradiated for 24 h in a photoreactor at 350 nm. Conversion and selectivity was determined by ¹H NMR spectroscopy.

General Procedure Photochemistry

Photochemical reactions (λ = 350 nm) were carried out in Duran phototubes (1 cm diameter, 10 mL) or J-Young NMR tube under argon atmosphere in a photoreactor with a cylindrical array of 16 light tubes of the type Luzchem LZC-UVA with 8 W nominal power. Supplier states a spectral range from 300 to 400 nm.

Crystallographic Data

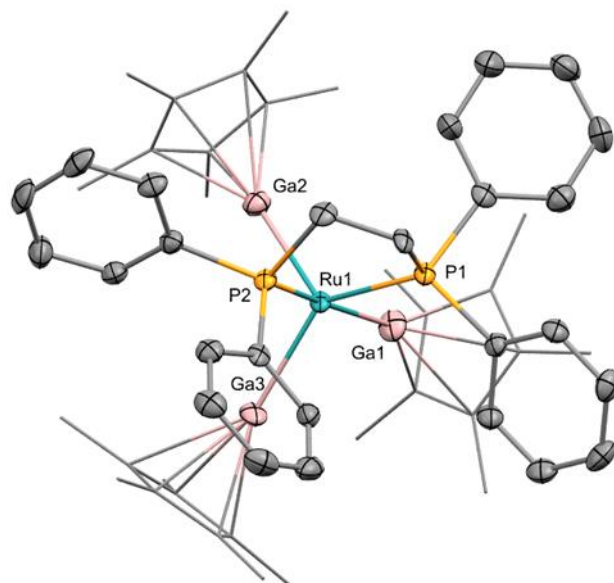


Figure S1: Crystal structure of $[(dppe)Ru(GaCp^*)_3]$. Co-crystallized molecule *n*-hexane and hydrogen atoms omitted for clarity. Ellipsoids drawn at 50% probability. Cp^* in wireframes.

Table S1: Crystallographic data table for compound 4.

Chemical formula	$C_{62}H_{83}Ga_3P_2Ru$	
Formula weight	1200.45	
Temperature	100(2) K	
Wavelength	0.71073 Å	
Crystal size	0.059 x 0.066 x 0.225 mm	
Crystal habit	red-orange fragment	
Crystal system	monoclinic	
Space group	P 1 21/n 1	
Unit cell dimensions	$a = 19.841(3)$ Å	$\alpha = 90^\circ$
	$b = 12.724(2)$ Å	$\beta = 99.625(7)^\circ$
	$c = 22.940(4)$ Å	$\gamma = 90^\circ$
Volume	$5709.8(16)$ Å ³	
Z	4	
Density (calculated)	1.397 g/cm ³	
Absorption coefficient	1.753 mm ⁻¹	
F(000)	2488	
Diffractionmeter	Bruker D8 Venture	
Radiation source	TXS rotating anode, Mo	

Theta range for data collection	2.41 to 25.68°	
Index ranges	-24<=h<=24, -15<=k<=15, -27<=l<=27	
Reflections collected	226471	
Independent reflections	10838 [R(int) = 0.1954]	
Coverage of independent reflections	99.9%	
Absorption correction	Multi-Scan	
Structure solution technique	direct methods	
Structure solution program	SHELXT 2014/5 (Sheldrick, 2014)	
Refinement method	Full-matrix least-squares on F ²	
Refinement program	SHELXL-2018/3 (Sheldrick, 2018)	
Function minimized	$\sum w(F_o^2 - F_c^2)^2$	
Data / restraints / parameters	10838 / 0 / 630	
Goodness-of-fit on F ²	1.021	
Δ/σ_{\max}	0.001	
Final R indices	6979 data; I>2 σ (I)	R1 = 0.0496,
	all data	wR2 = 0.0861
		R1 = 0.1073,
		wR2 = 0.1037
Weighting scheme	$w=1/[\sigma^2(F_o^2)+(0.0318P)^2+16.8706P]$ where $P=(F_o^2+2F_c^2)/3$	
Largest diff. peak and hole	0.982 and -0.774 eÅ ⁻³	
R.M.S. deviation from mean	0.114 eÅ ⁻³	

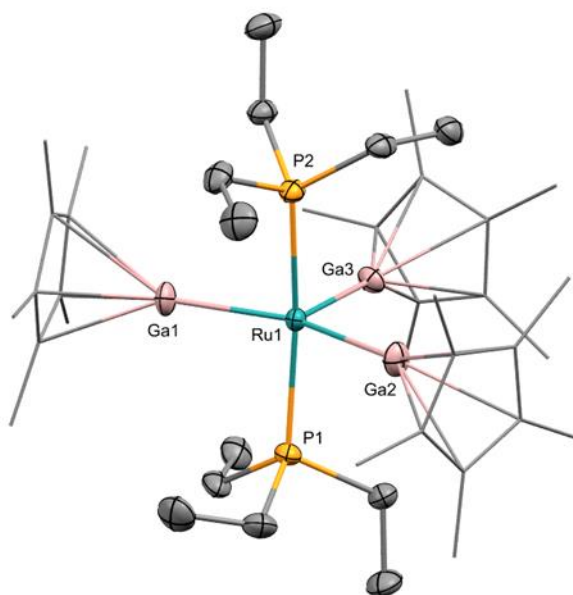


Figure S2: Crystal structure of $[(Et_3P)_2Ru(GaCp^*)_3]$. Co-crystallized molecule *n*-hexane and hydrogen atoms omitted for clarity. Ellipsoids drawn at 50% probability. Cp^* in wireframes.

Table S2: Crystallographic data table for compound $[Ru(GaCp^*)_3(PEt_3)_2]$.

Chemical formula	$C_{48}H_{89}Ga_3P_2Ru$	
Formula weight	1038.36	
Temperature	123(2) K	
Wavelength	0.71073 Å	
Crystal size	0.238 x 0.321 x 0.374 mm	
Crystal habit	orange fragment	
Crystal system	orthorhombic	
Space group	P 21 21 21	
Unit cell dimensions	$a = 12.268(4)$ Å	$\alpha = 90^\circ$
	$b = 19.291(7)$ Å	$\beta = 90^\circ$
	$c = 21.580(6)$ Å	$\gamma = 90^\circ$
Volume	5107.(3) Å ³	
Z	4	
Density (calculated)	1.350 g/cm ³	
Absorption coefficient	1.948 mm ⁻¹	
F(000)	2176	
Diffractometer	Bruker D8 Venture	
Radiation source	TXS rotating anode, Mo	

Theta range for data collection	2.18 to 25.90°	
Index ranges	-14<=h<=15, -23<=k<=23, -26<=l<=26	
Reflections collected	137597	
Independent reflections	9858 [R(int) = 0.0279]	
Coverage of independent reflections	99.3%	
Absorption correction	Multi-Scan	
Structure solution technique	direct methods	
Structure solution program	SHELXT 2014/5 (Sheldrick, 2014)	
Refinement method	Full-matrix least-squares on F ²	
Refinement program	SHELXL-2018/3 (Sheldrick, 2018)	
Function minimized	$\Sigma w(F_o^2 - F_c^2)^2$	
Data / restraints / parameters	9858 / 12 / 510	
Goodness-of-fit on F ²	1.059	
Δ/σ_{\max}	0.004	
Final R indices	9566 data; I>2 σ (I)	R1 = 0.0190,
	all data	wR2 = 0.0509
		R1 = 0.0200,
		wR2 = 0.0513
Weighting scheme	$w=1/[\sigma^2(F_o^2)+(0.0287P)^2+2.3981P]$ where $P=(F_o^2+2F_c^2)/3$	
Largest diff. peak and hole	0.747 and -0.438 eÅ ⁻³	
R.M.S. deviation from mean	0.067 eÅ ⁻³	

NMR Spectra

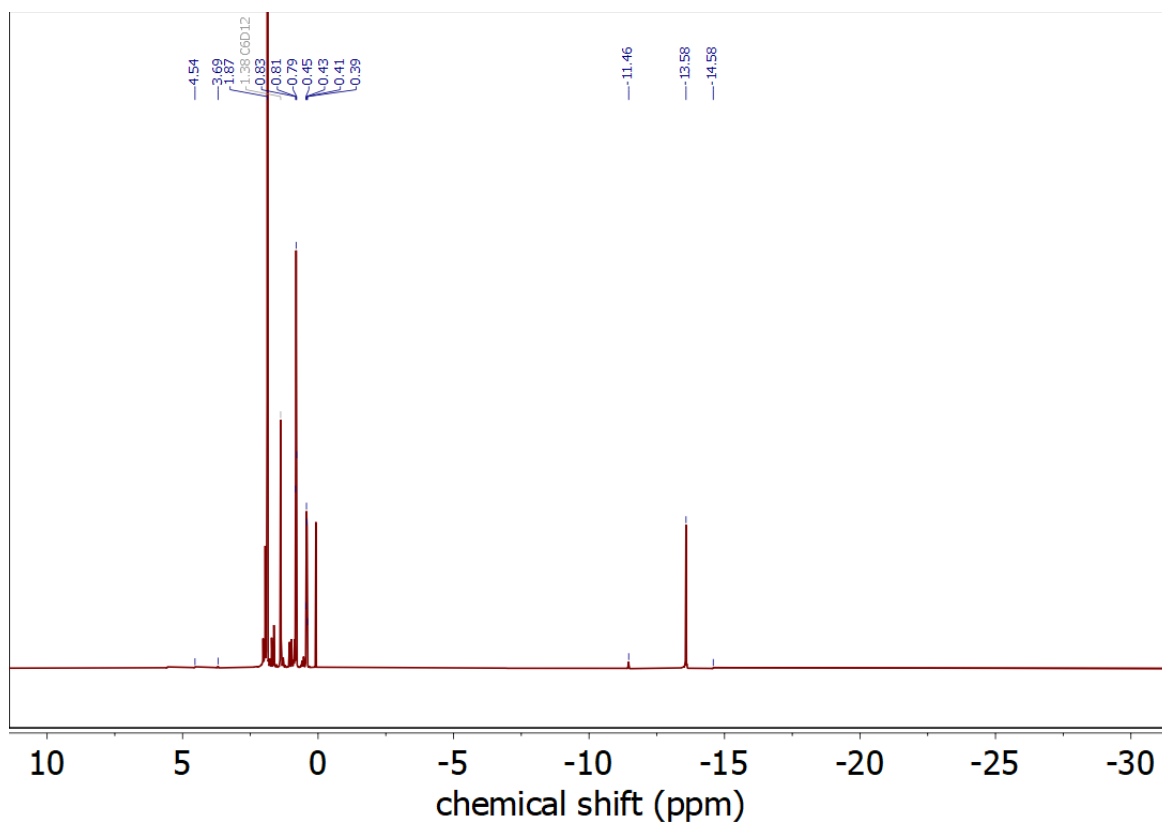


Figure S3: ^1H NMR spectrum of **1** after 30 min irradiation at 350 nm in C_6D_{12} .

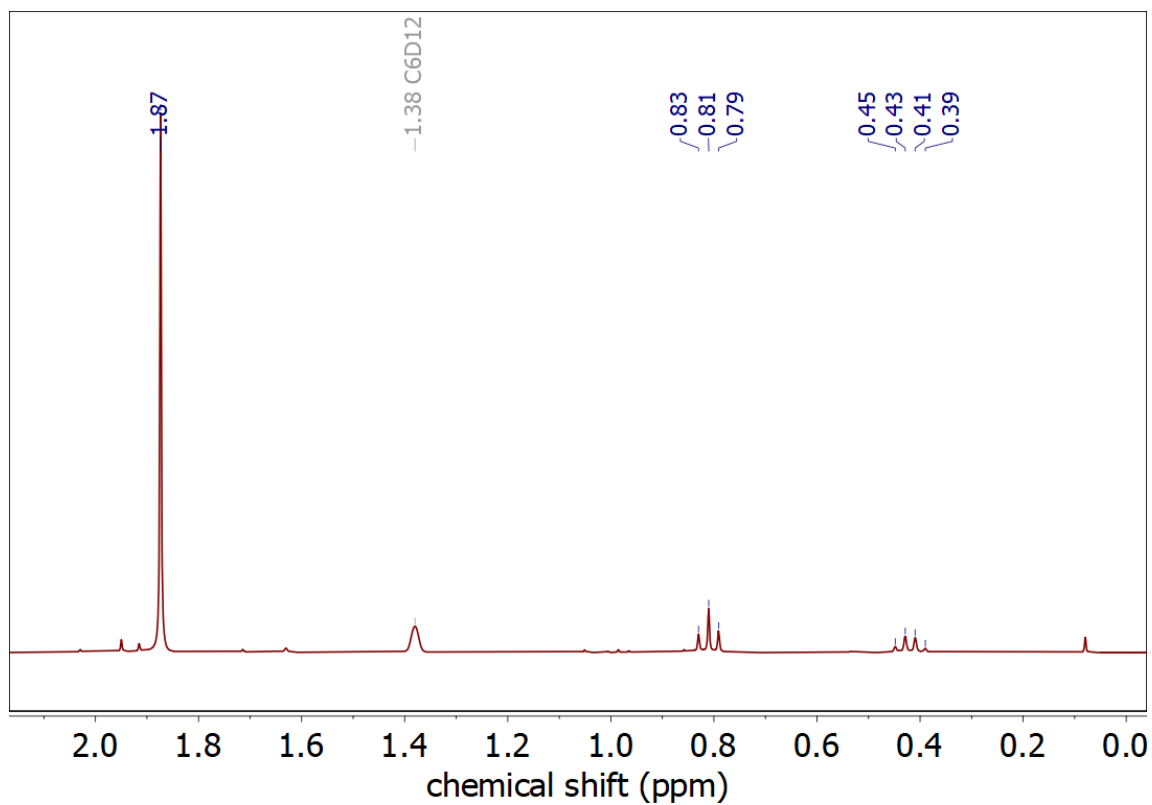


Figure S4: ^1H NMR spectrum of **1** after 30 min irradiation at 350 nm in C_6D_{12} . Excerpt of the aliphatic range.

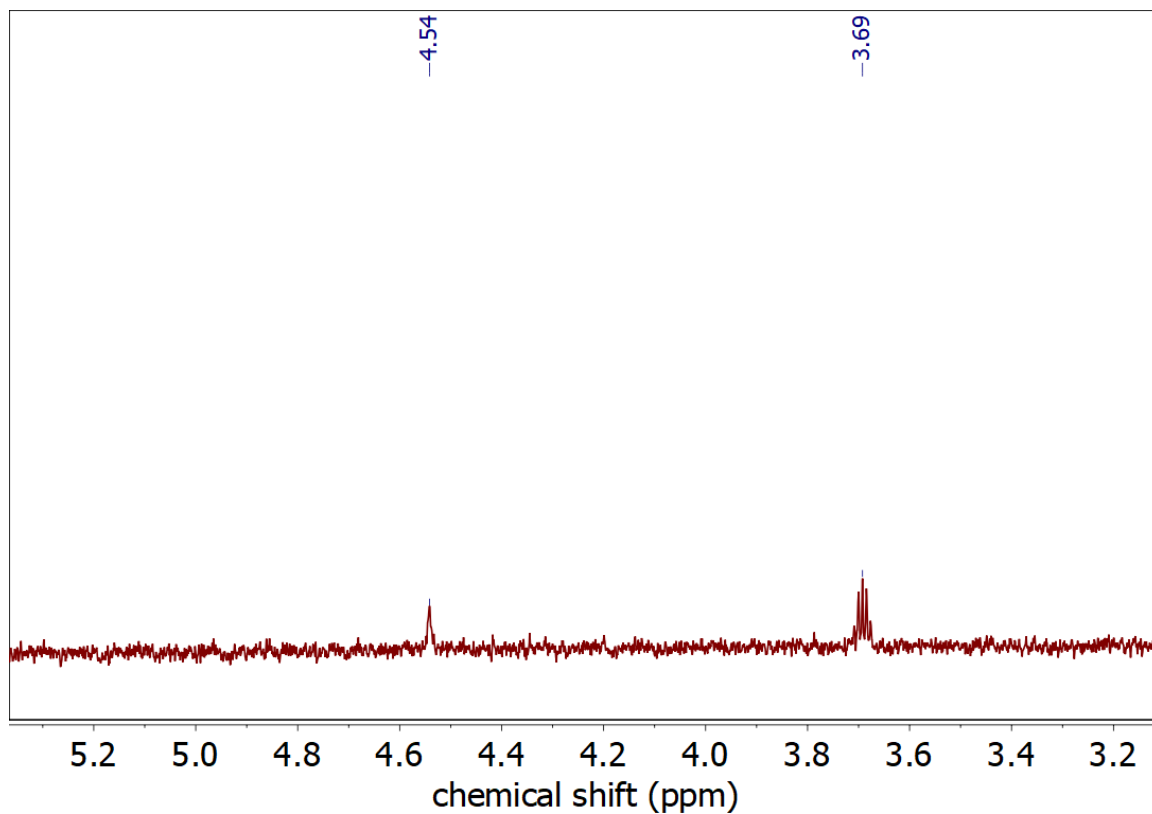


Figure S5: ^1H NMR spectrum of **1** after 30 min irradiation at 350 nm in C_6D_{12} . Excerpt showing free hydrogen (4.54 ppm) and free triethylsilane (3.69 ppm, H-Si).

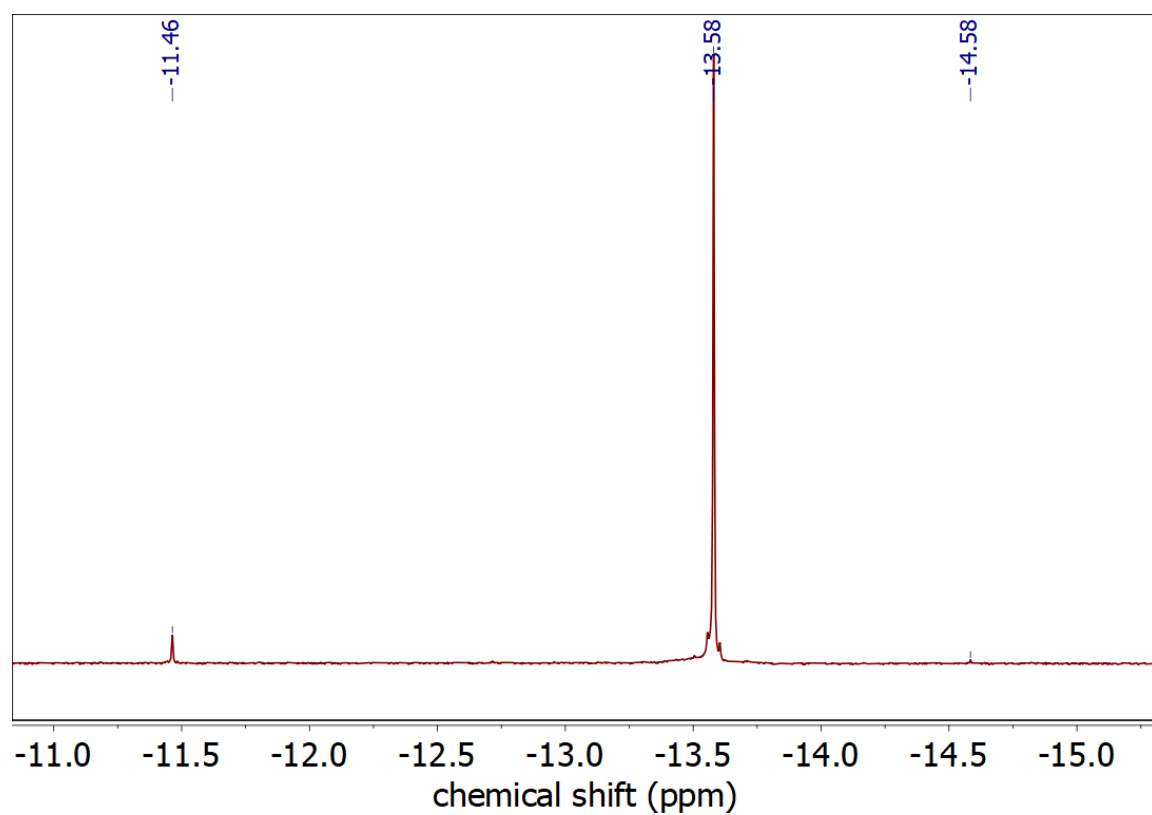


Figure S6: ^1H NMR spectrum of **1** after 30 min irradiation at 350 nm in C_6D_{12} . Excerpt of the hydridic range, showing two new signals at -11.46 and -14.58 ppm.

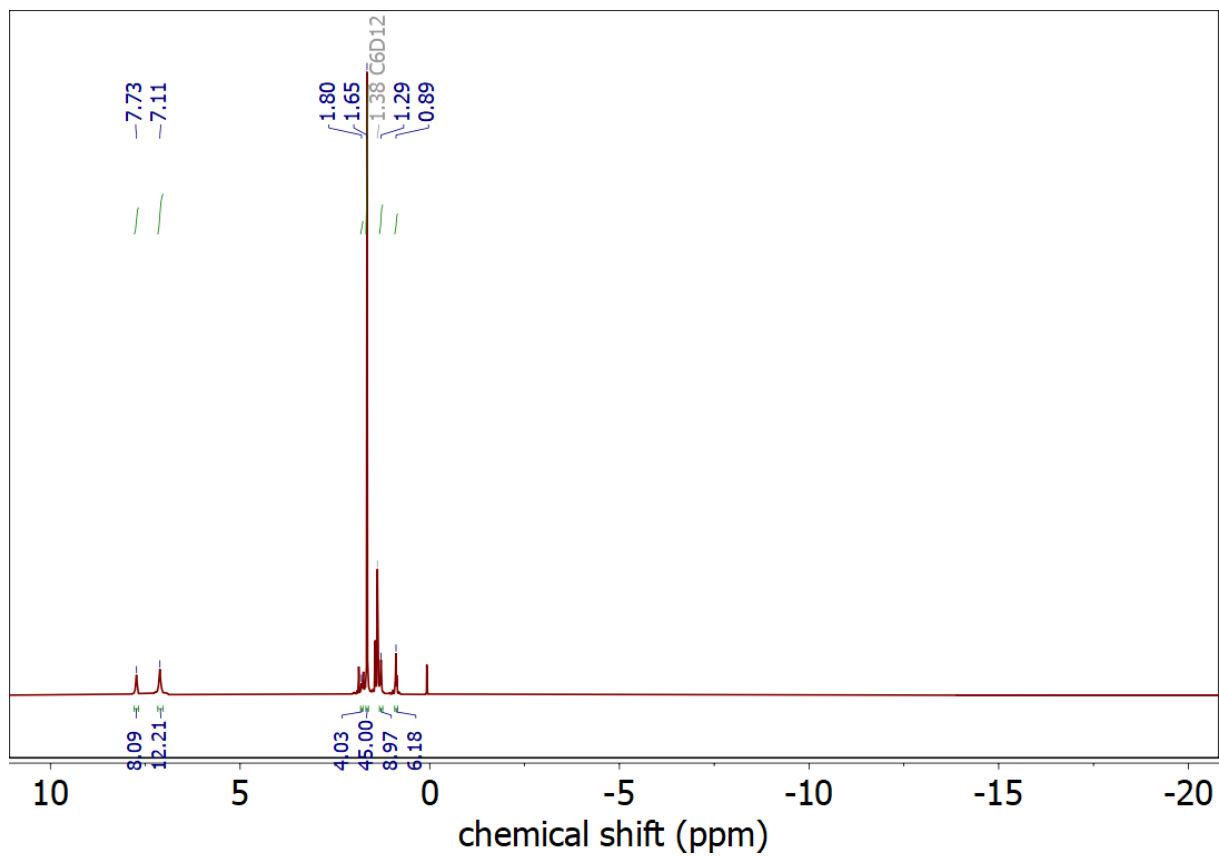


Figure S7: Full range ^1H NMR of **4** in C_6D_{12} . No new hydride signals.

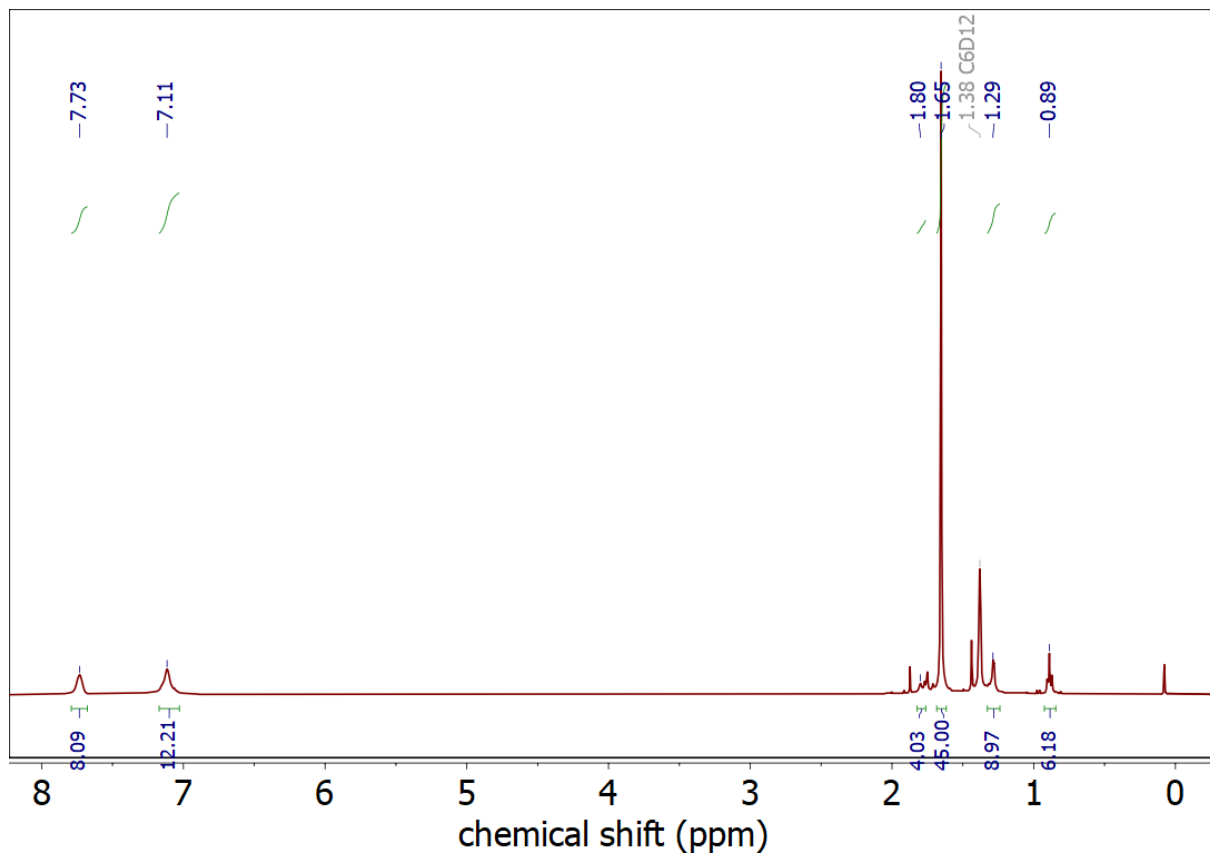


Figure S8: Zoomed into ^1H NMR of **4** in C_6D_{12} .

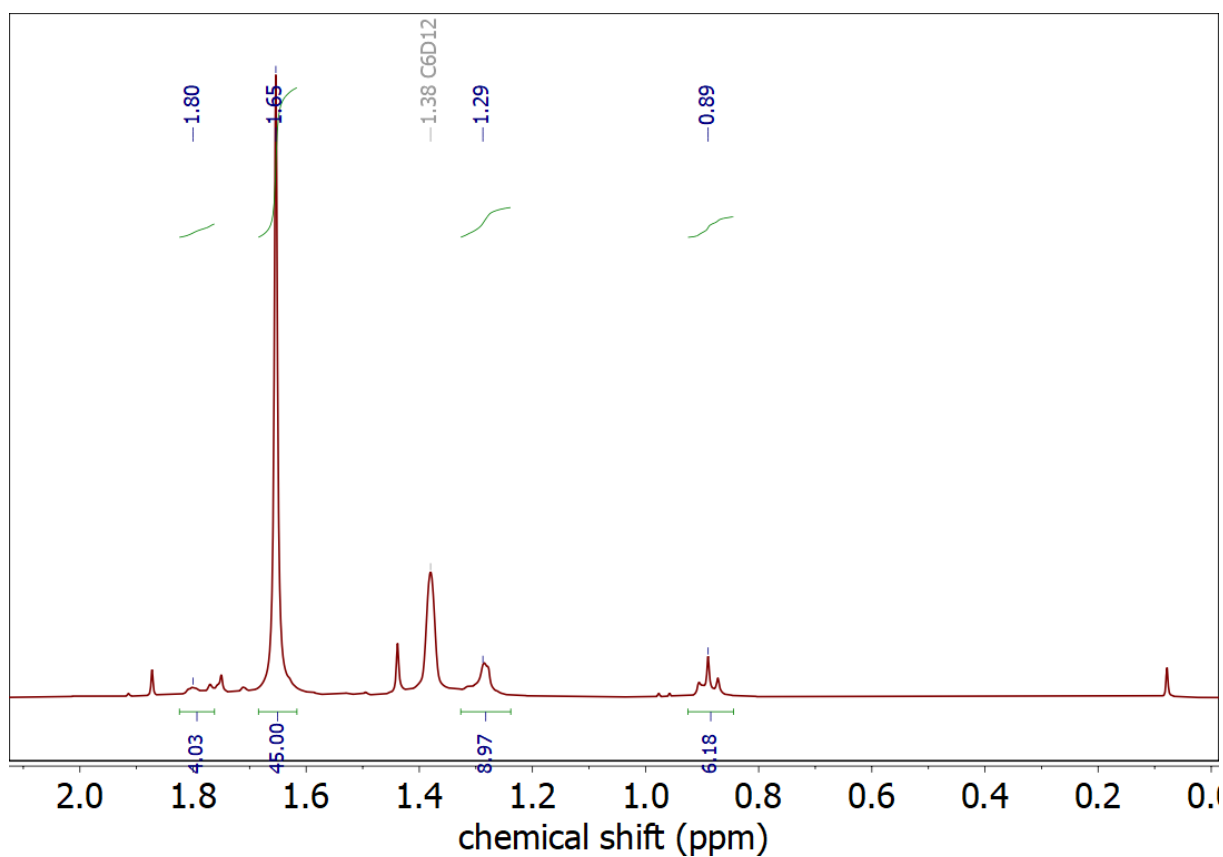


Figure S9: Zoomed into ^1H NMR of **4** in C_6D_{12} – aliphatic range.

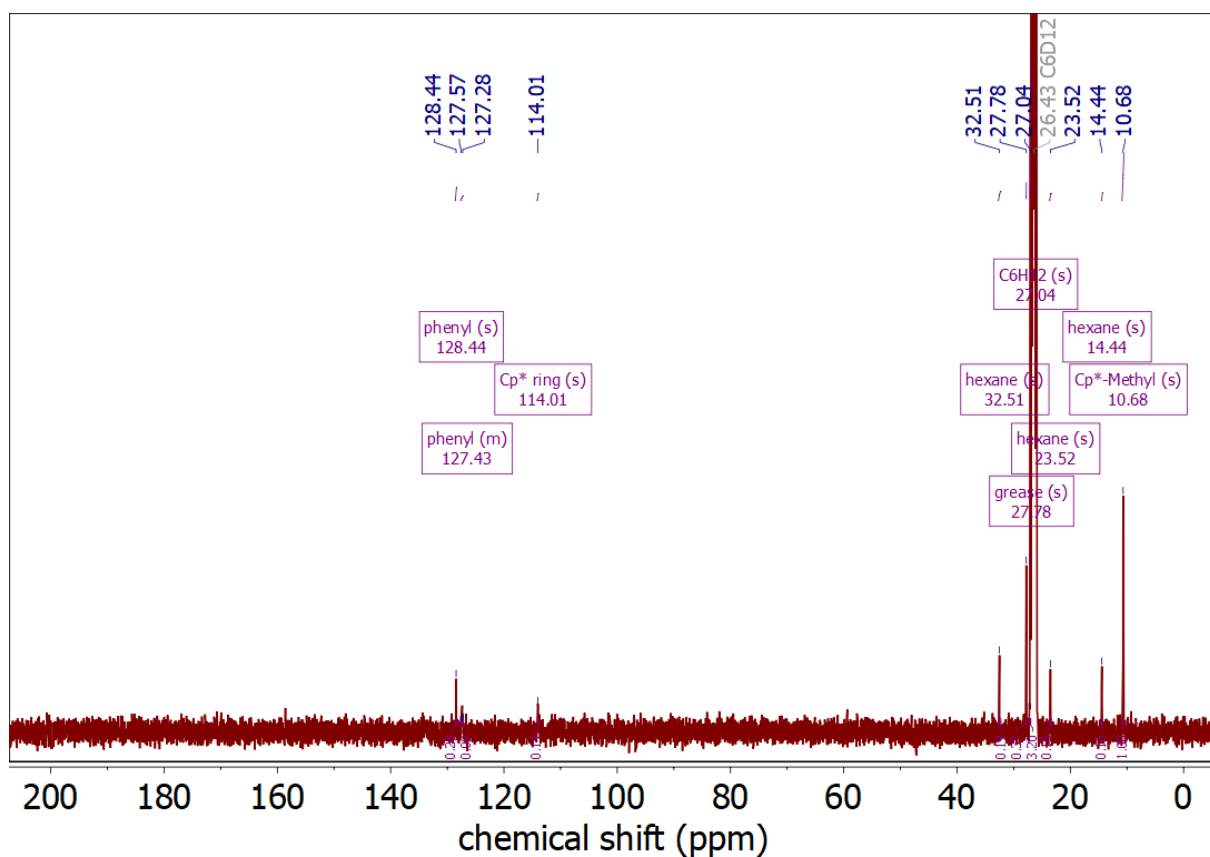


Figure S10: Full range ^{13}C NMR of **4** in C_6D_{12} .

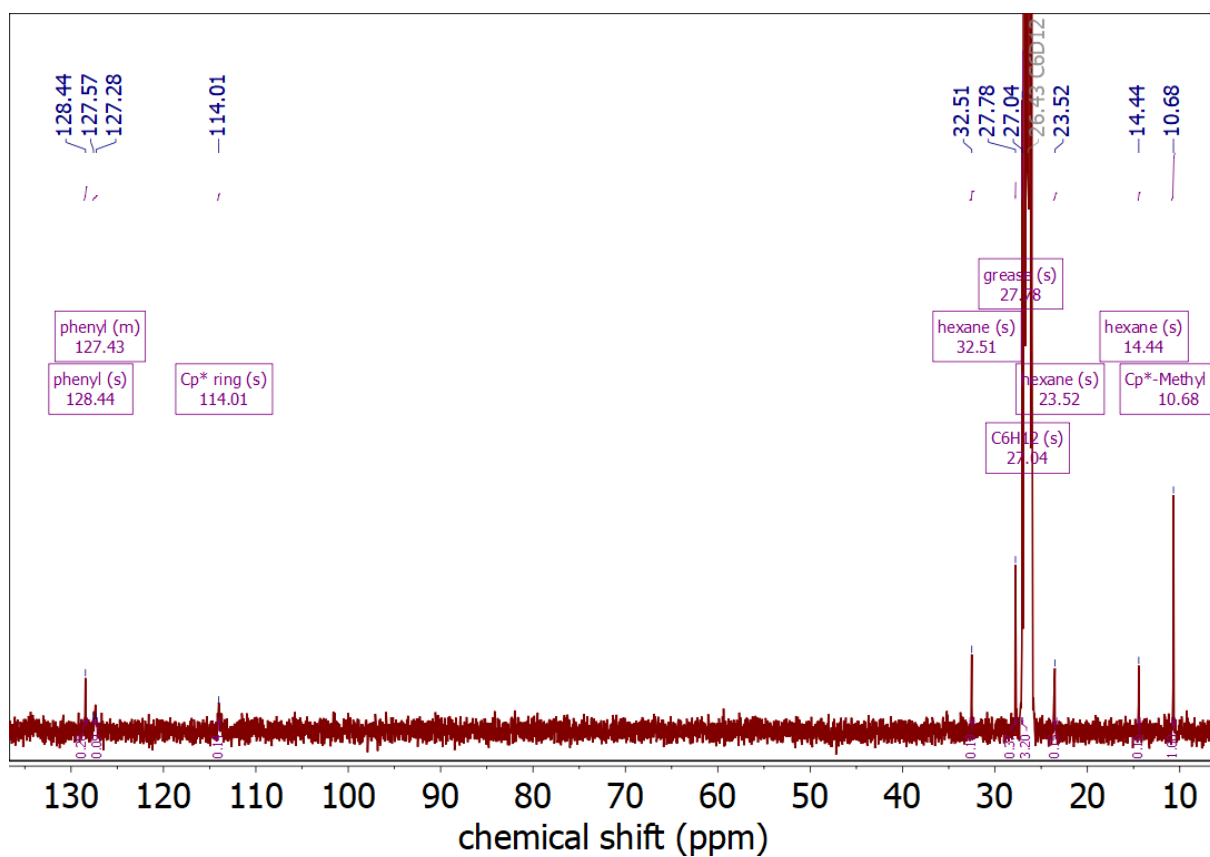


Figure S11: Zoomed into ^{13}C NMR of **4** in C_6D_{12} .

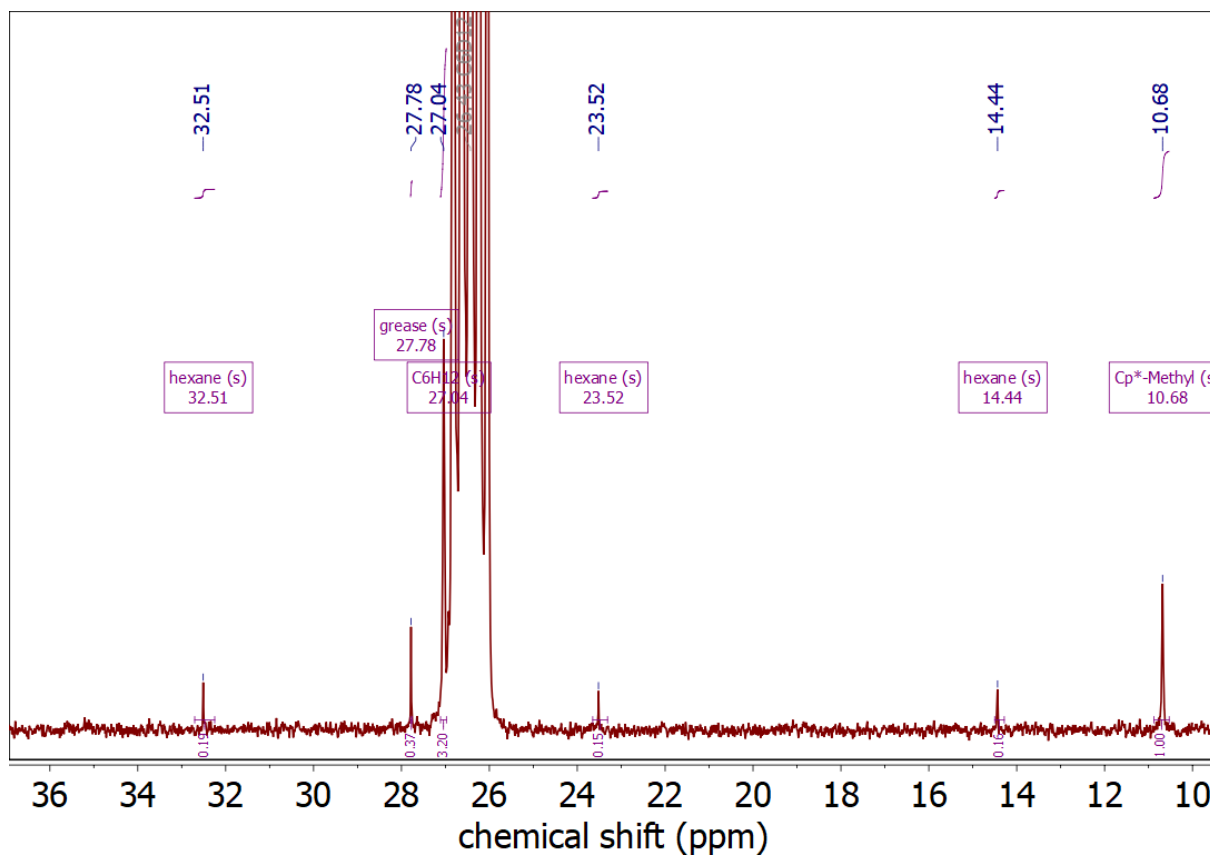


Figure S12: ^{13}C NMR of **4** in C_6D_{12} – aliphatic range.

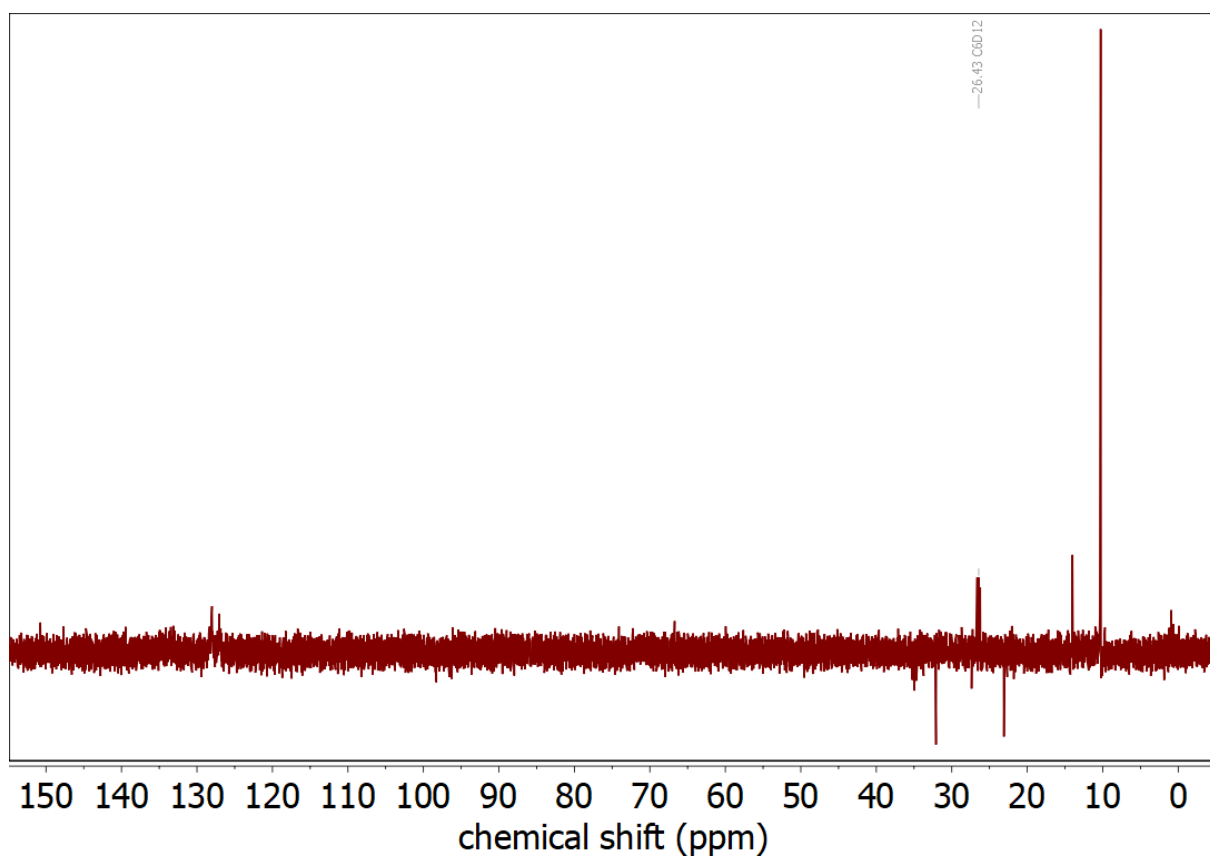


Figure S13: Full range DEPT 135 of **4** in C_6D_{12} .

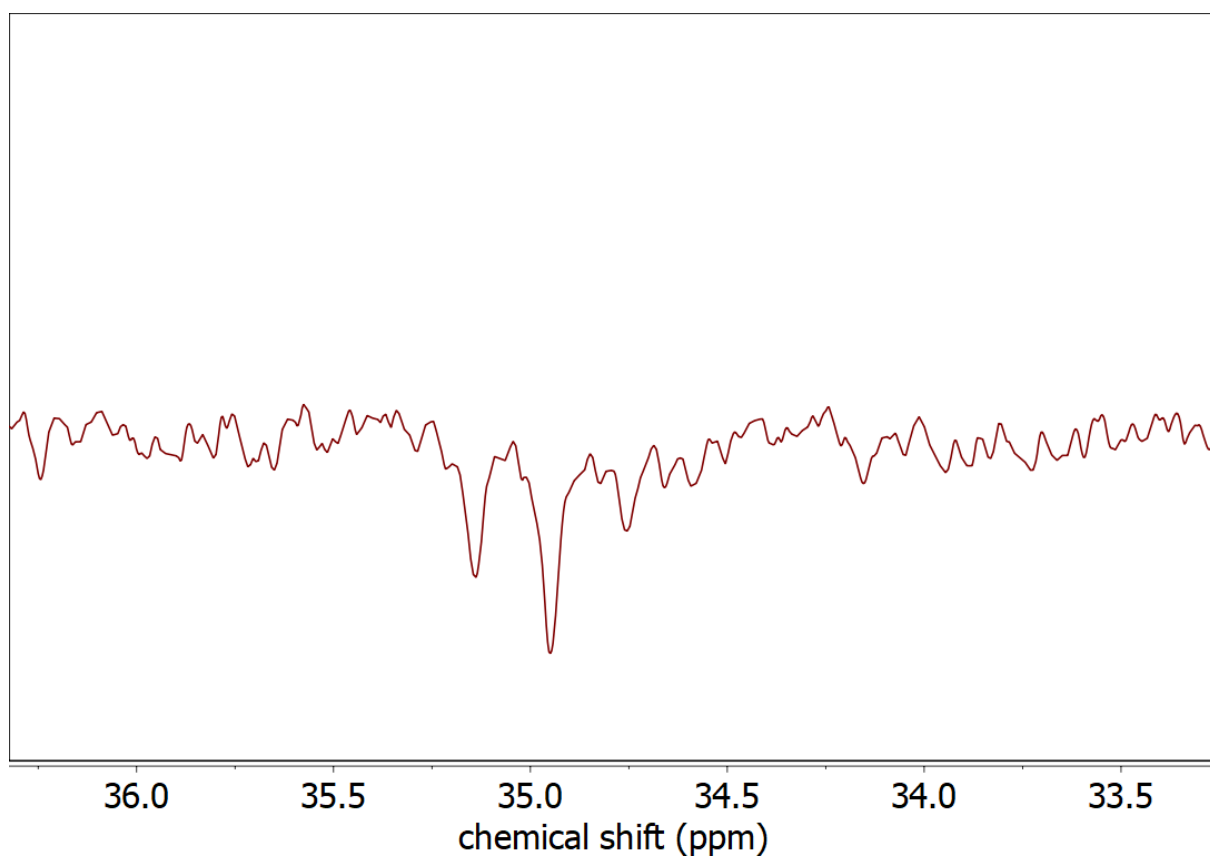
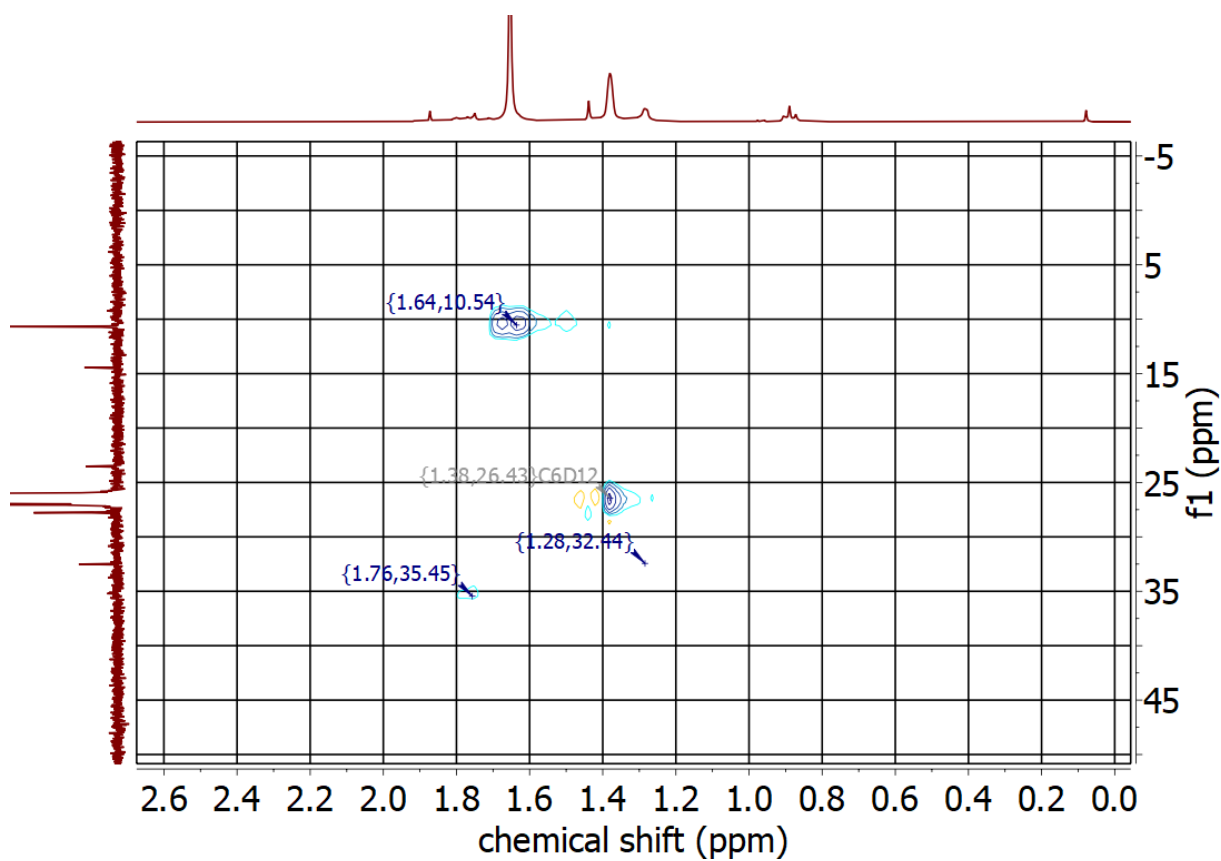
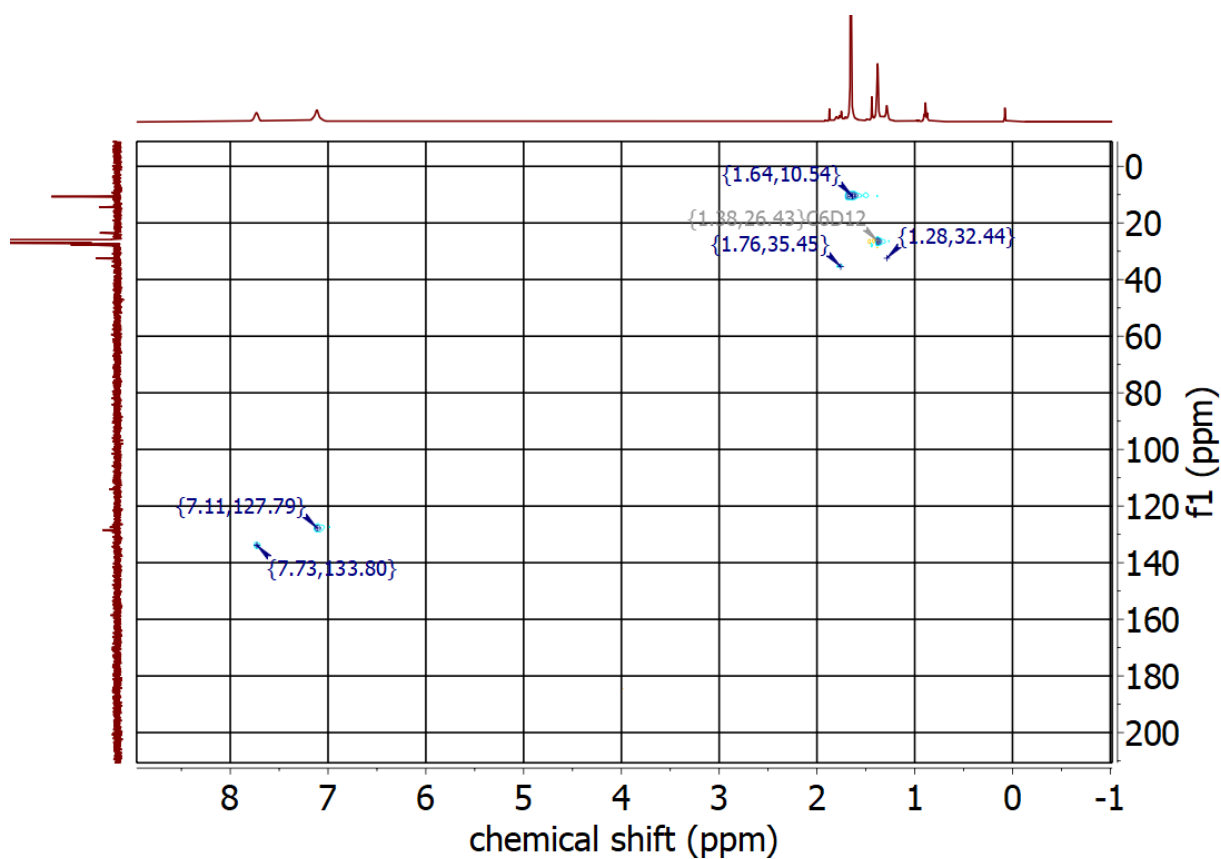


Figure S14: Zoomed into DEPT 135 of **4** in C_6D_{12} . Negative ^{13}C triplet (due to ^{31}P coupling) of dppe H_2C-CH_2 bridge.



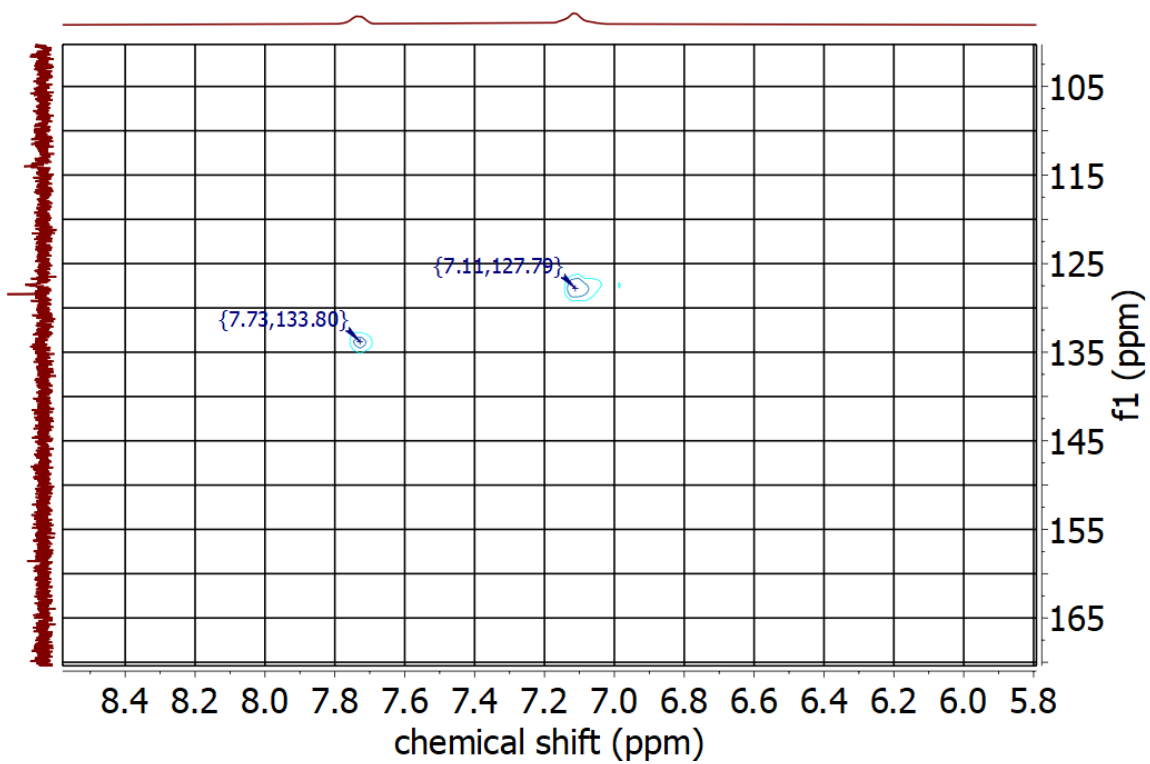


Figure S17: HSQC spectrum of 4 in C_6D_{12} – aromatic range.

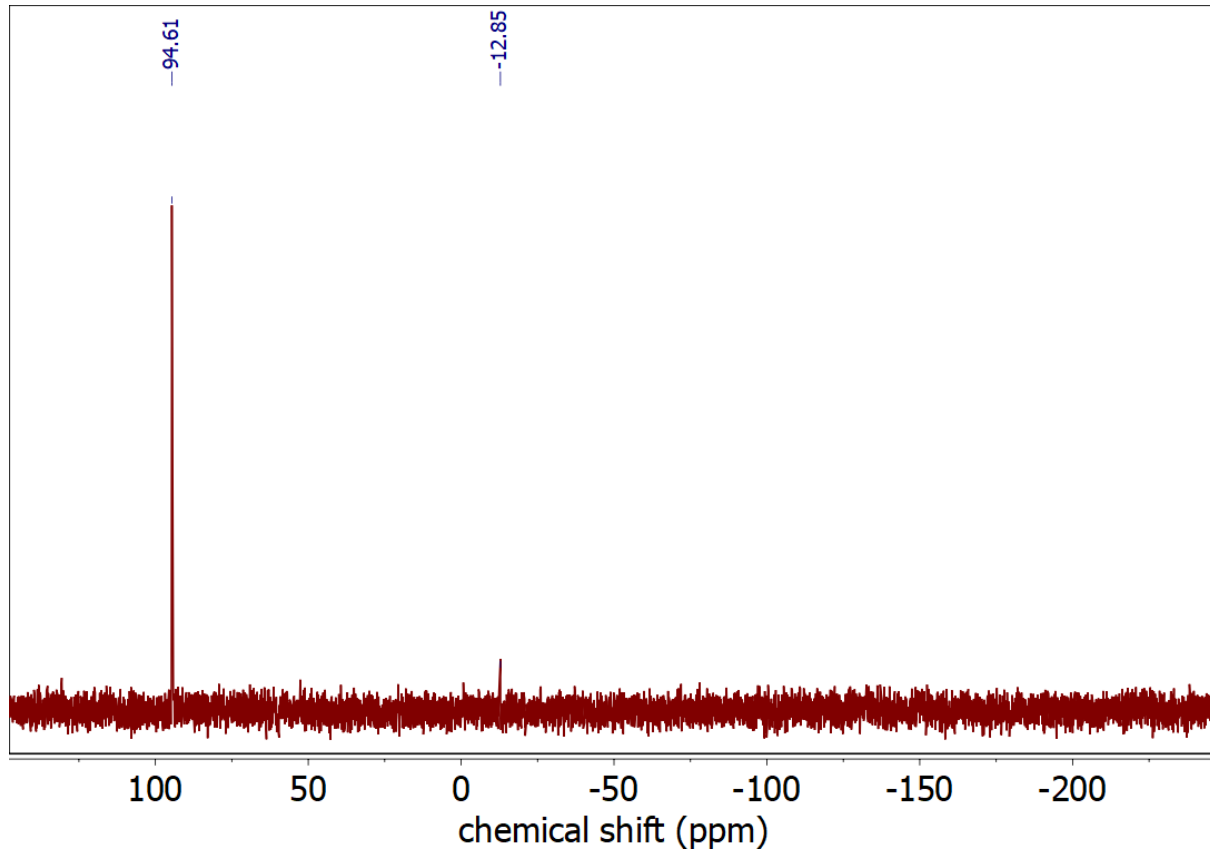


Figure S18: Full range ^{31}P spectrum of 4 in C_6D_{12} .

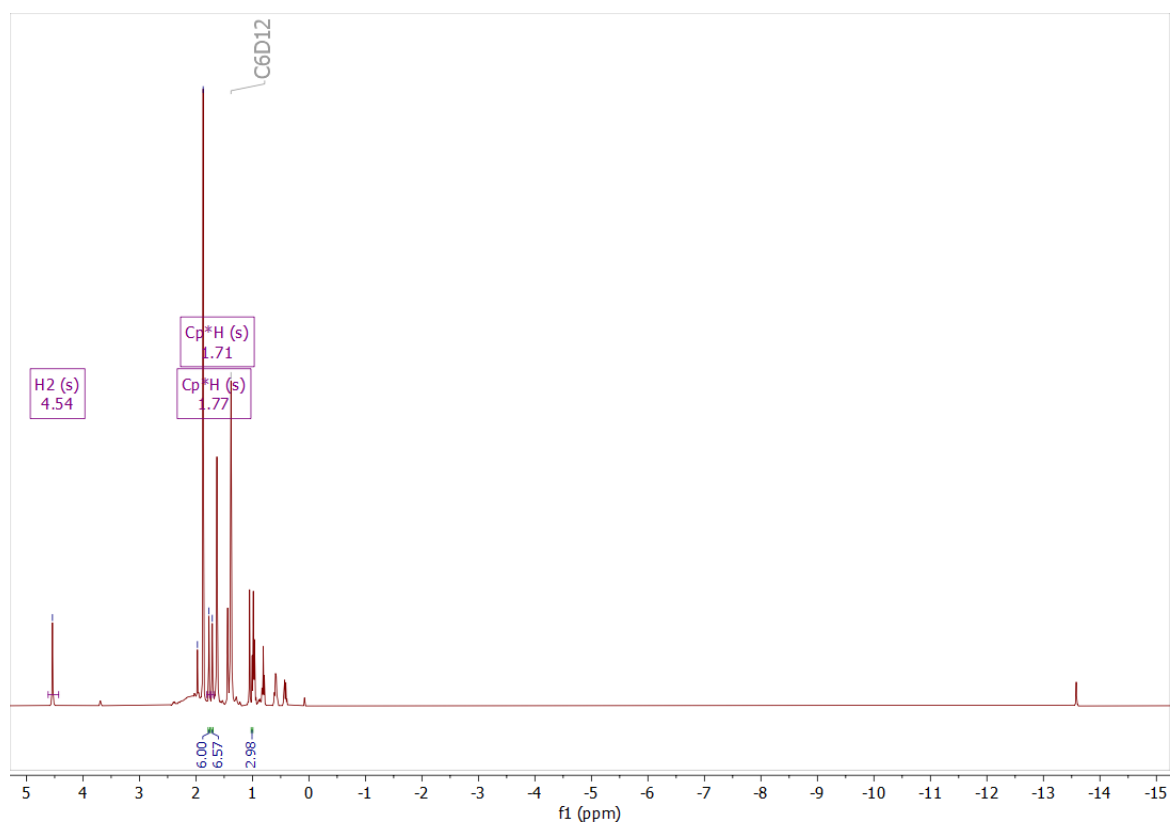


Figure S19: ^1H NMR spectrum of the reaction of **1** with H_2 under 1 h irradiation (350 nm).

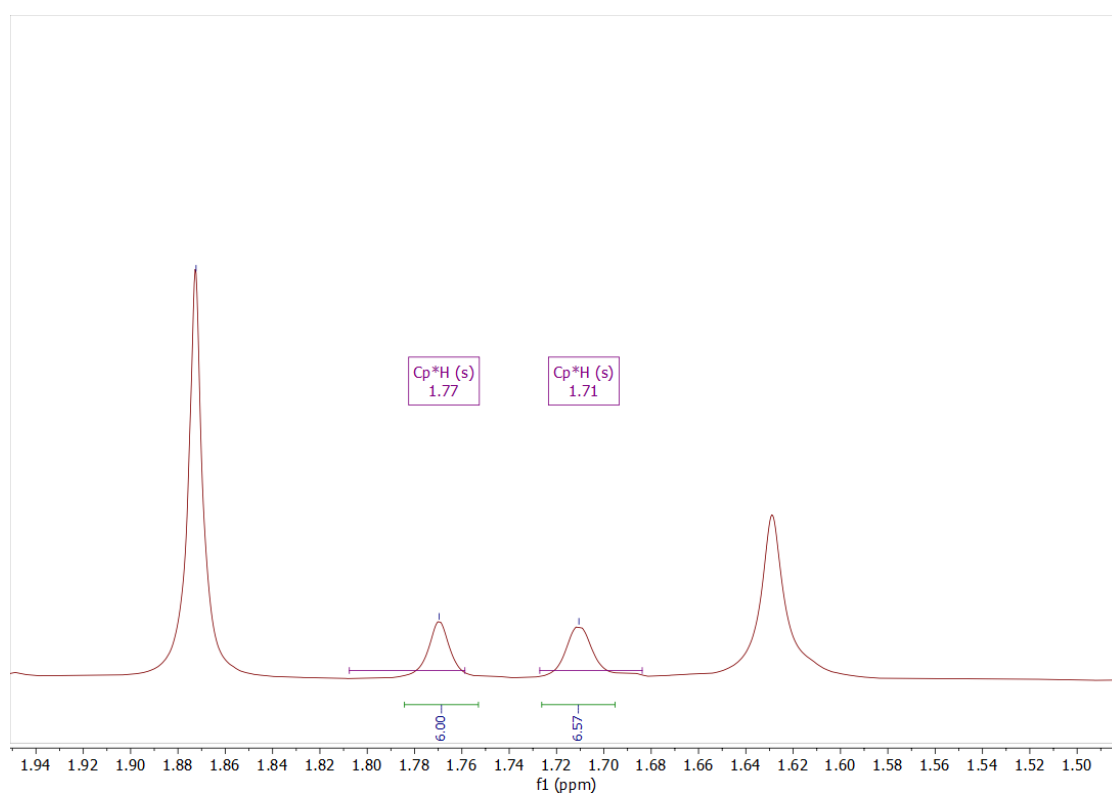


Figure S20: Excerpt of ^1H NMR spectrum of the reaction of **1** with H_2 under 1 h irradiation (350 nm). Showing peaks of free Cp^*H at 1.71 and 1.77 ppm.

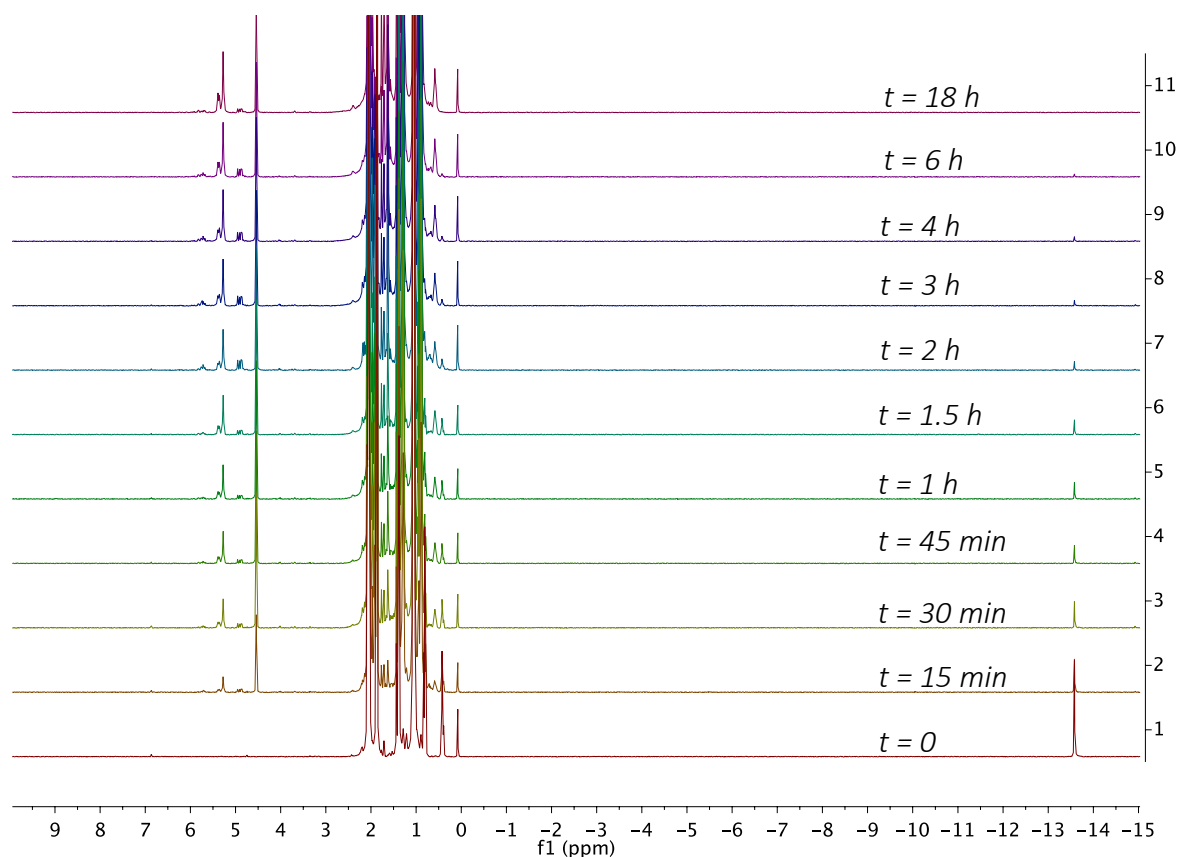


Figure S21: Full range stacked ^1H NMR spectra of the conversion of 3-hexyne with **1** (5 mol%) under a dihydrogen atmosphere (2 bar) at 350 nm. Hydride shift of **1** at -13.6 ppm ; alkenes and hydrosilylation products between 4.75 and 6.0 ppm .

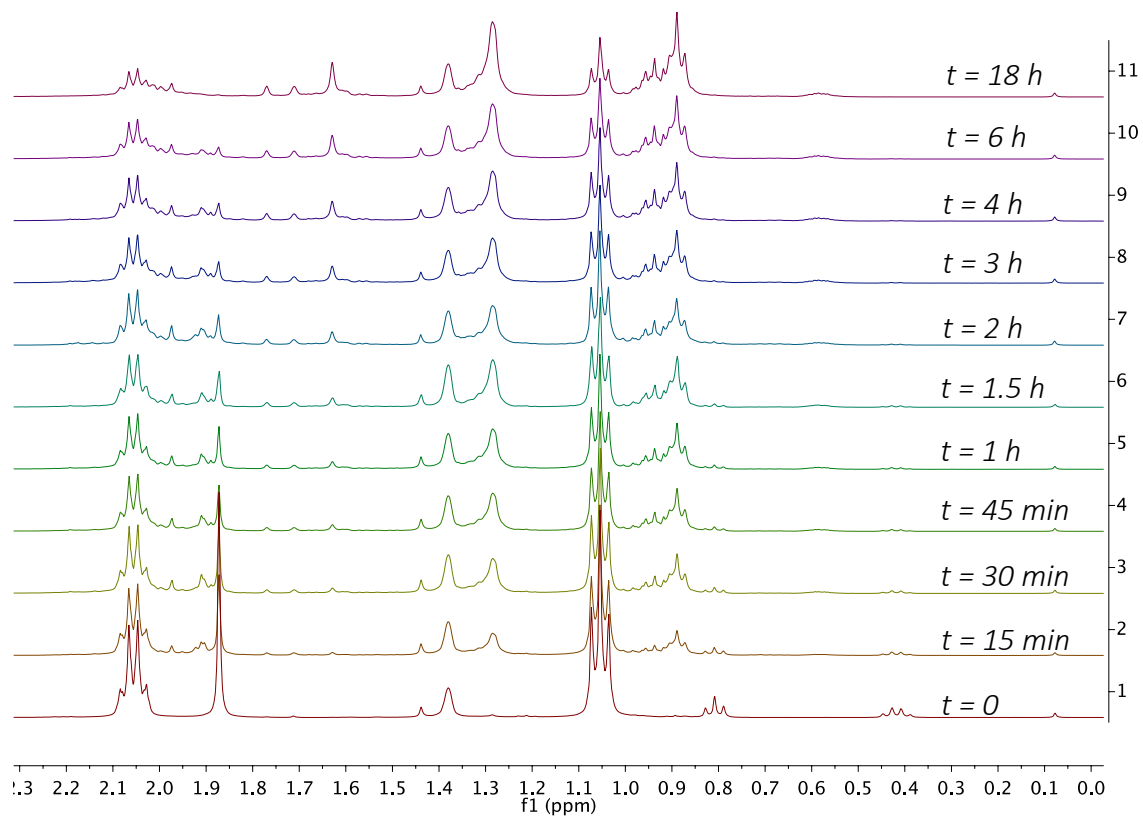


Figure S22: Zoomed in stacked ^1H NMR spectra of the conversion of 3-hexyne with **1** (5 mol%) under a dihydrogen atmosphere (2 bar) at 350 nm. 3-Hexyne at 2.06 and 1.05 ppm ; n-hexane (CH_2) between 1.20 and 1.36 ppm ; CH_3 of n-hexane and hexenes between 0.85 and 1.01 ppm .

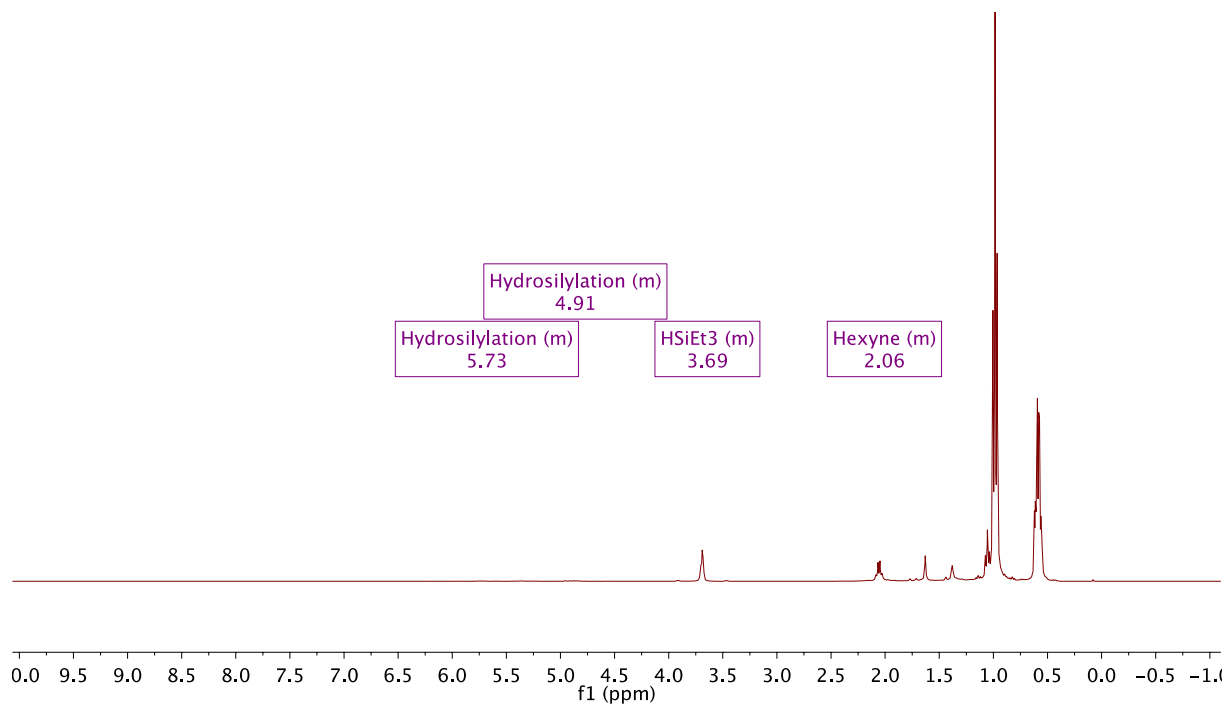


Figure S23: Full range ^1H NMR spectrum of the conversion of 3-hexyne (1.0 eq.) and HSiEt₃ (5.0 eq.) with **1** (5 mol% against 3-hexyne) at 350 nm.

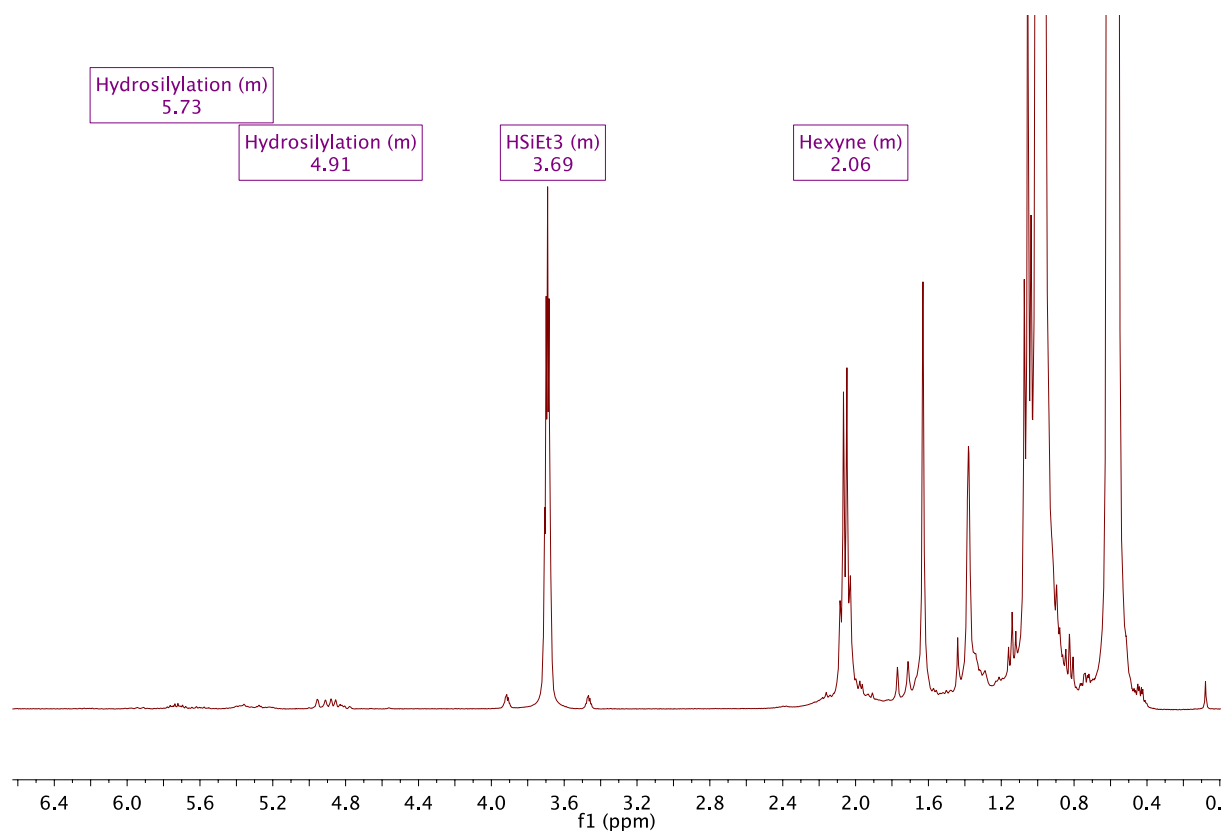


Figure S24: Zoomed in ^1H NMR spectrum of the conversion of 3-hexyne (1.0 eq.) and HSiEt₃ (5.0 eq.) with **1** (5 mol% against 3-hexyne) at 350 nm.

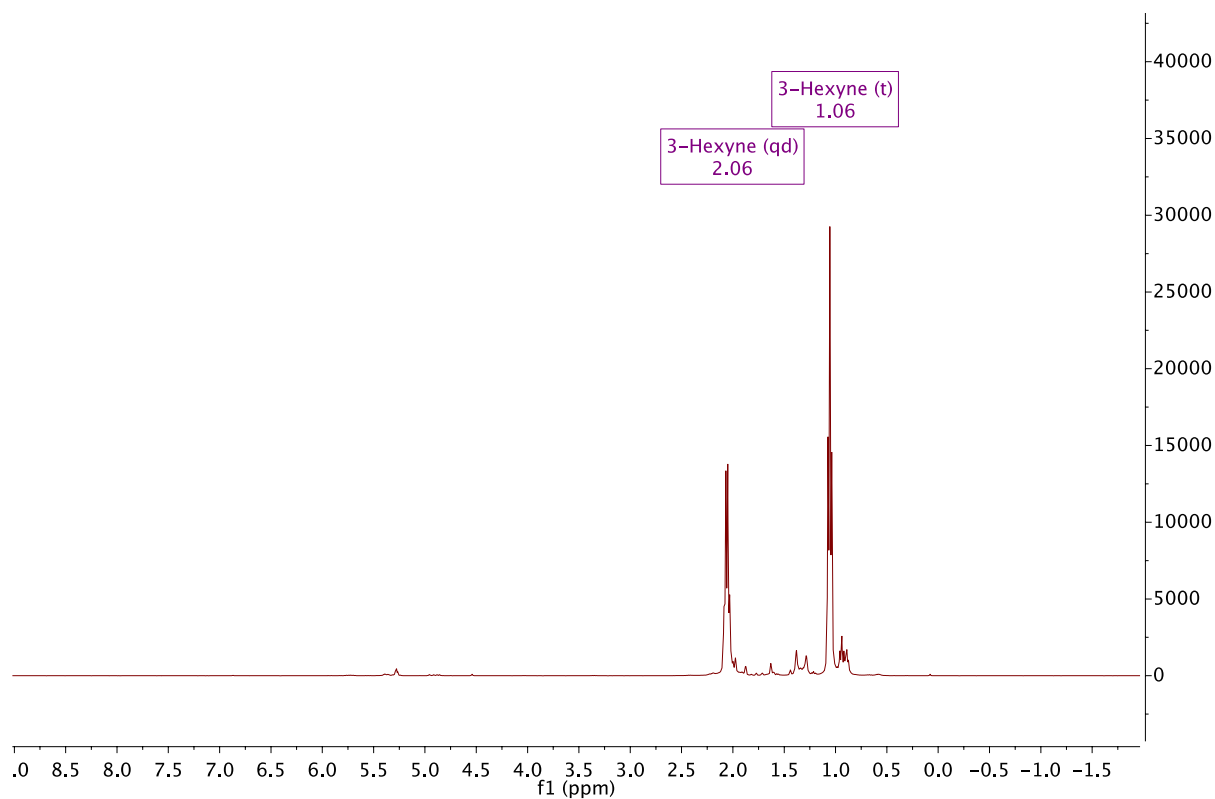


Figure S25: Full range ^1H NMR spectra of the conversion of 3-hexyne with **1** (1 mol%) under a dihydrogen atmosphere (2 bar) after 24h at 350 nm.

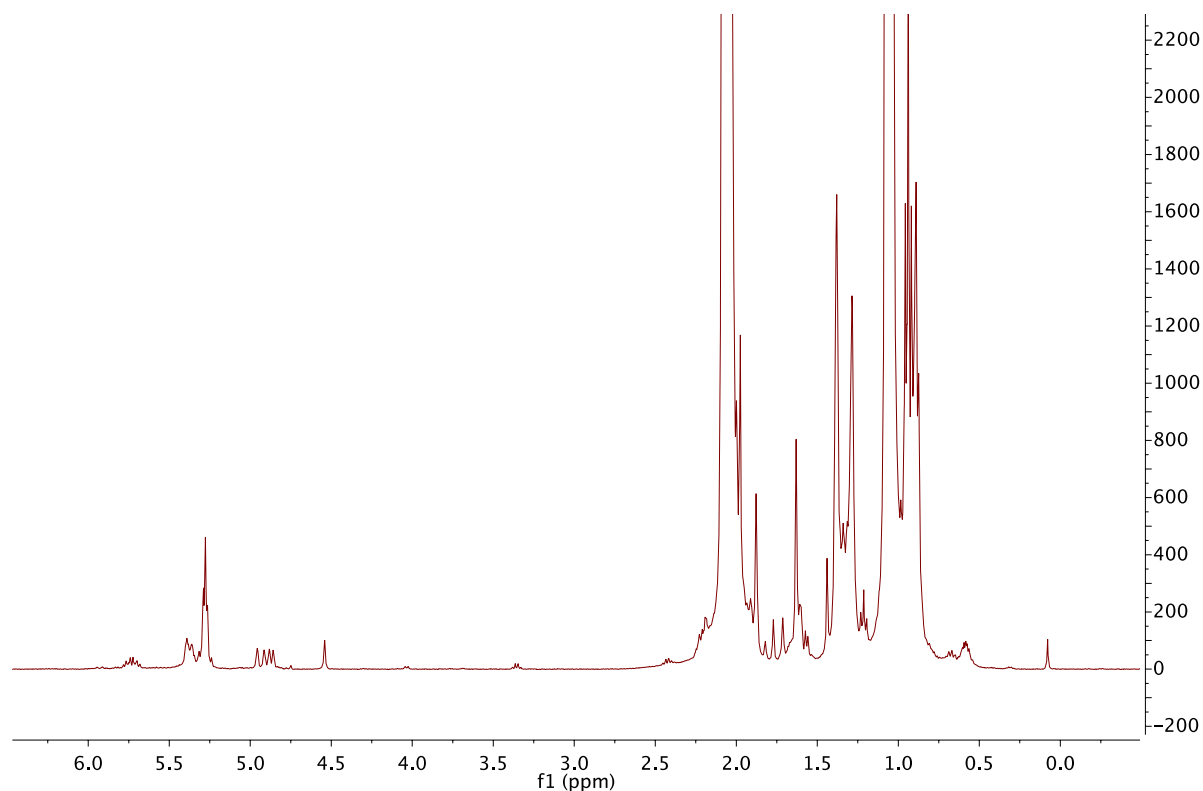


Figure S26: Zoomed in ^1H NMR spectra of the conversion of 3-hexyne with **1** (1 mol%) under a dihydrogen atmosphere (2 bar) after 24h at 350 nm. Hexenes and hydrosilylation products between 4.75 and 6.0 ppm; n-hexane (CH_2) between 1.20 and 1.36 ppm; CH_3 of n-hexane and hexenes between 0.85 and 1.01 ppm.

LIFDI-MS Spectra

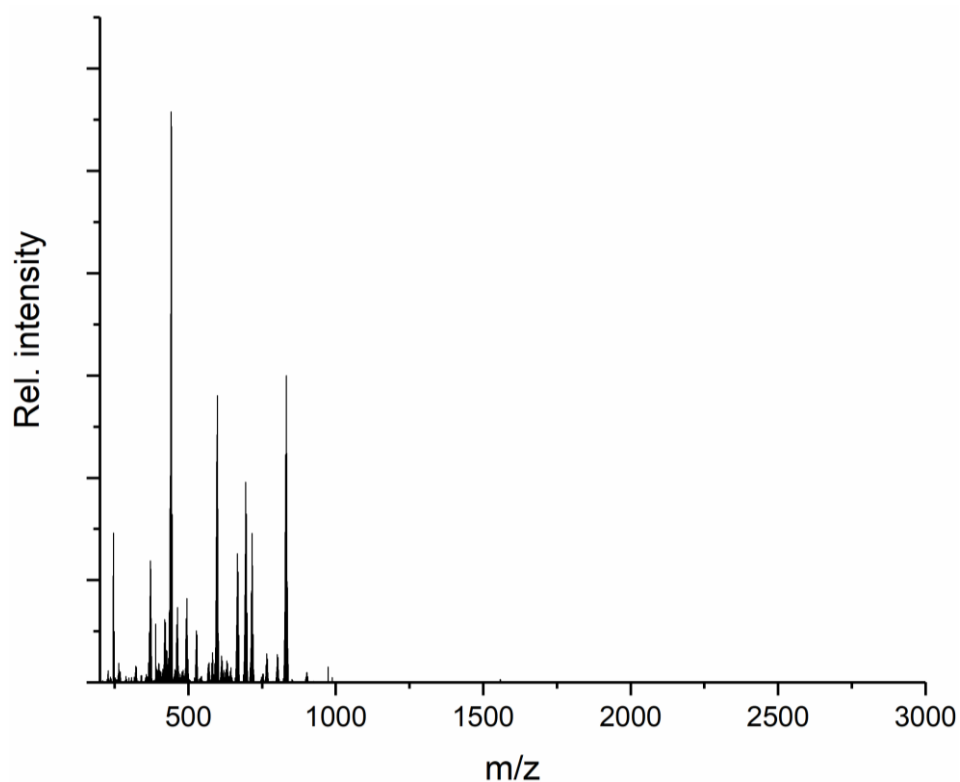


Figure S27: LIFDI mass spectrum of **1** after 8 h irradiation in cyclohexane. Main pattern corresponds to **1** ($m/z = 832.13$) $[M-2H]^+$.

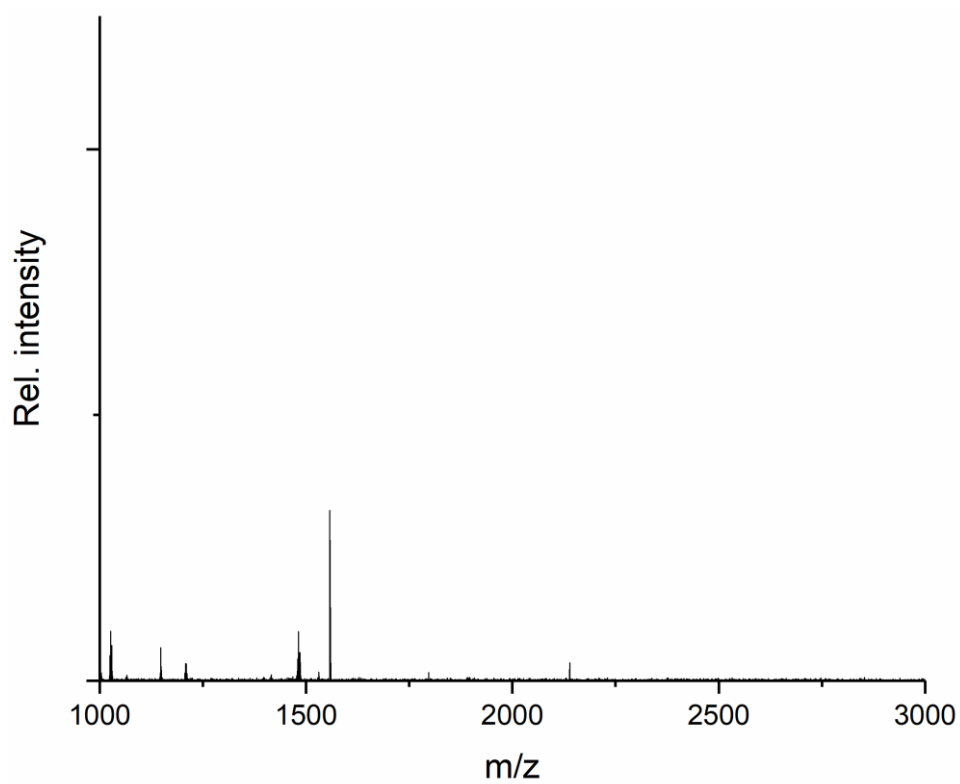


Figure S28: Excerpt of LIFDI mass spectrum of **1** after 8 h irradiation in cyclohexane. No peaks at higher masses – barely any cluster growth visible.

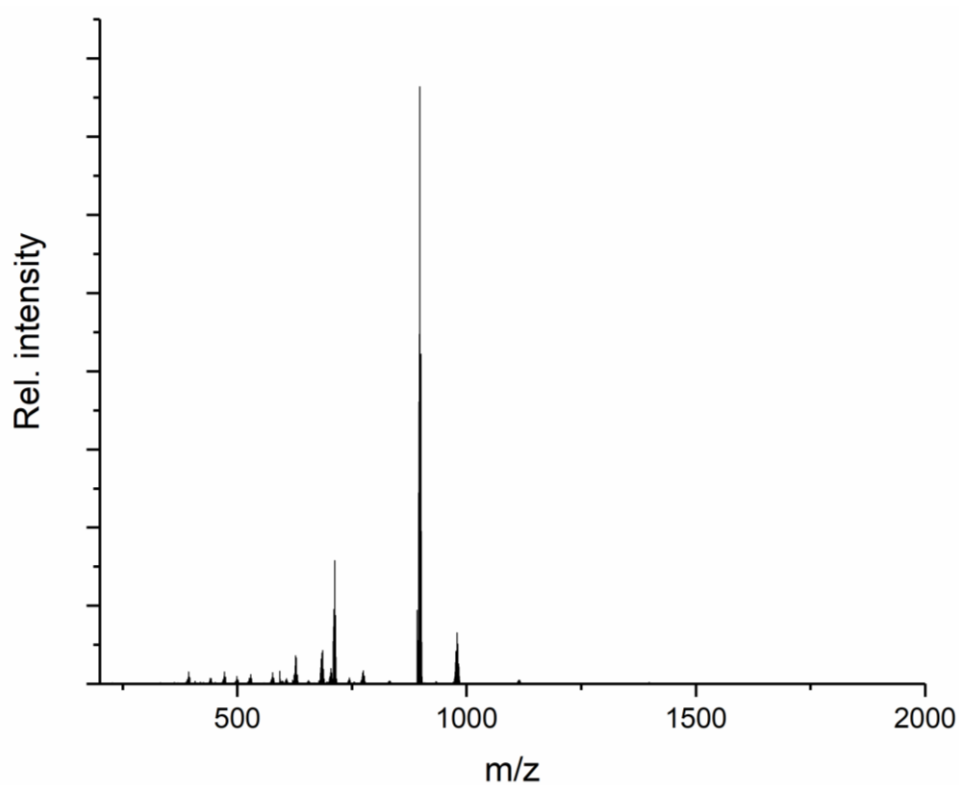


Figure S29: LIFDI mass spectrum of $[(dppe)Ru(GaCp^*)_3]$ **4**. $[M]^+$ ($m/z = 1114.1656$; calc. 1114.1671); $[M-Cp^*]^+$ ($m/z = 979.0478$; calc. 979.0497); $[M-2Cp^*-Ga]^+$ ($m/z = 775.0068$; calc. 775.0080). Main peak at $m/z = 898.1727$ attributed to $[Ru(dppe)_2]$ (calc. 775.0080), formation assumed upon ionization.

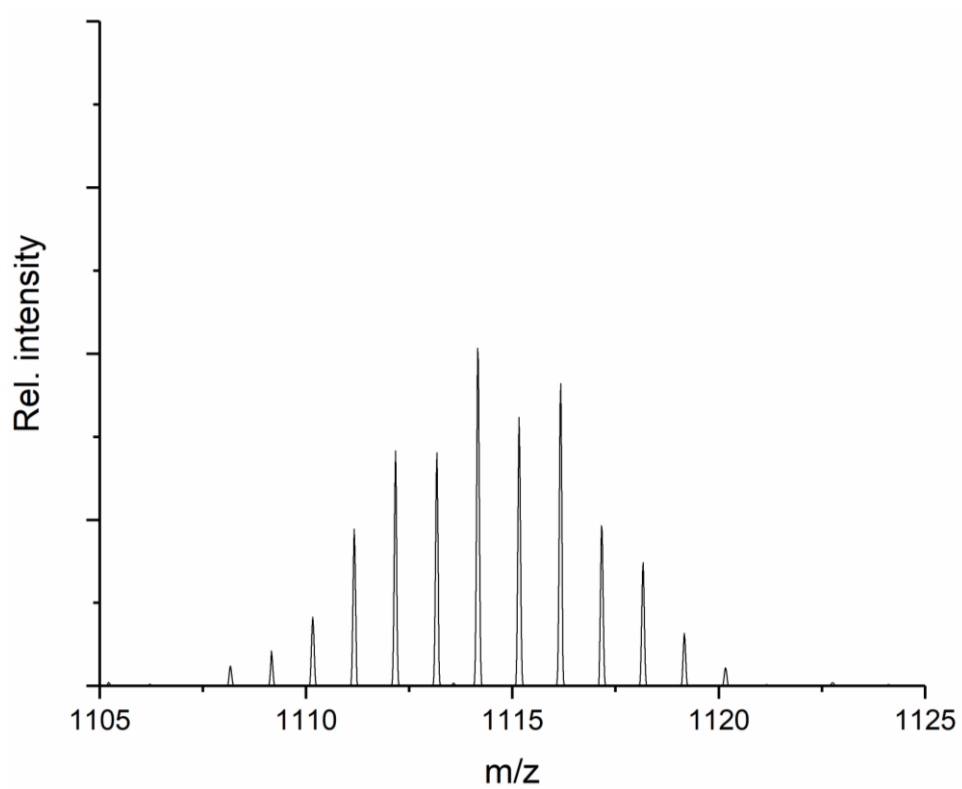


Figure S30: LIFDI mass spectrum of **4**. Excerpt of isotopic pattern of **4**. $[M]^+$ ($m/z = 1114.1656$; calc. 1114.1671).

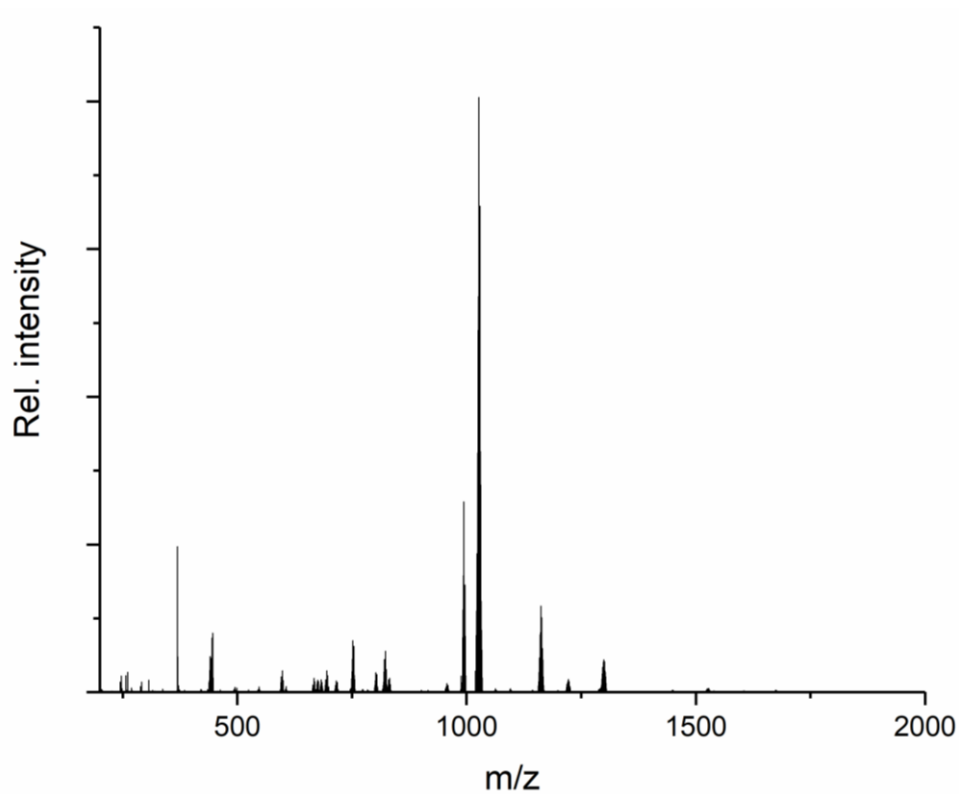


Figure S31: In situ LIFDI mass spectrum of the reaction **1** with 1 eq 1,2-bis(diphenylphosphino)benzene after 24 h irradiation (350 nm).

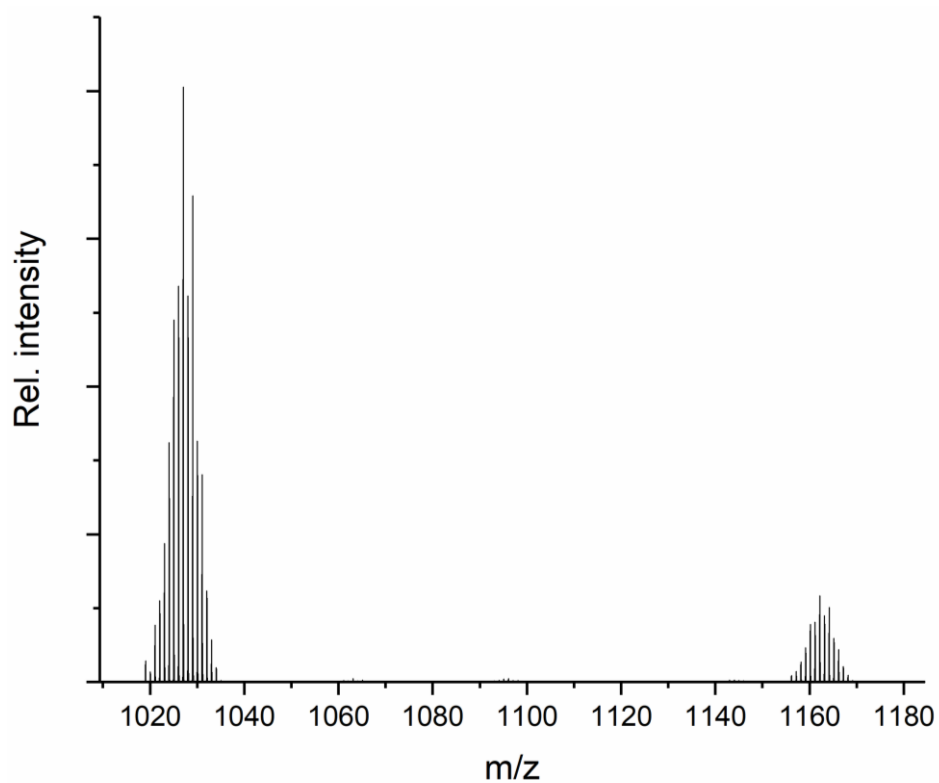


Figure S32: Excerpt of LIFDI mass spectrum of the reaction **1** with 1 eq 1,2-bis(diphenylphosphino)benzene (dppbz) after 24 h irradiation (350 nm). Peaks assigned to: $m/z = 1162.18$ $[(dppbz)Ru(GaCp^*)_3]^+$ (calc. 1162.17); $m/z = 1027.05$ $[M-Cp^*]^+$ (calc. 1027.05).

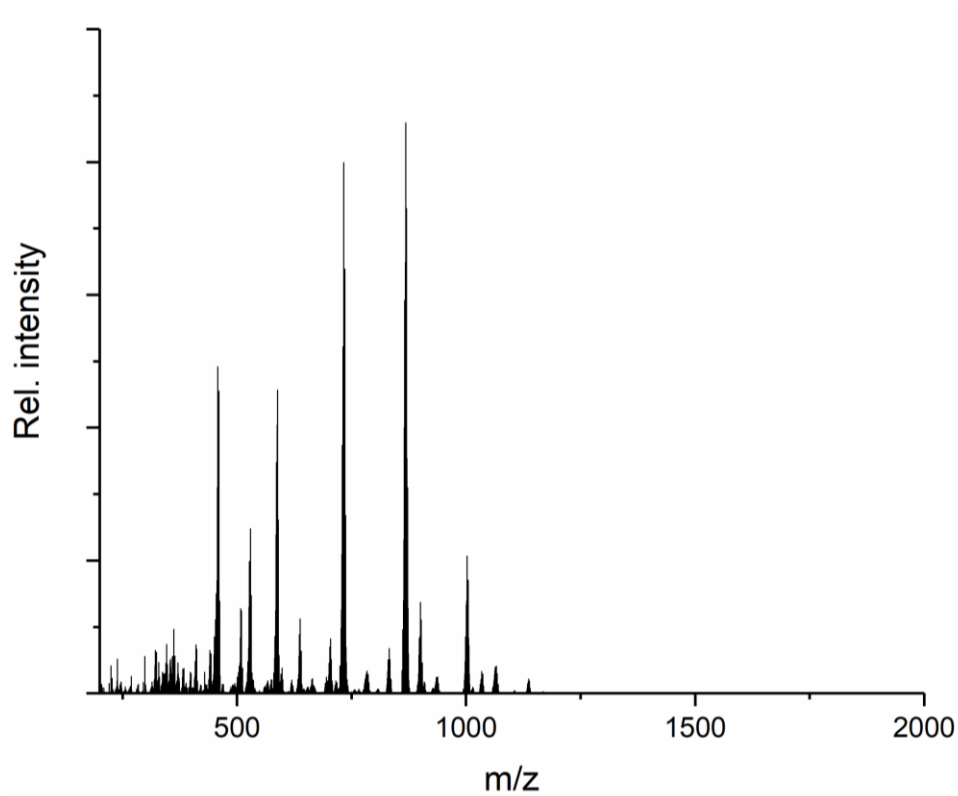


Figure S33: In situ LIFDI mass spectrum of the reaction 1 with 2 eq trimethyl phosphine after 24 h irradiation (350 nm).

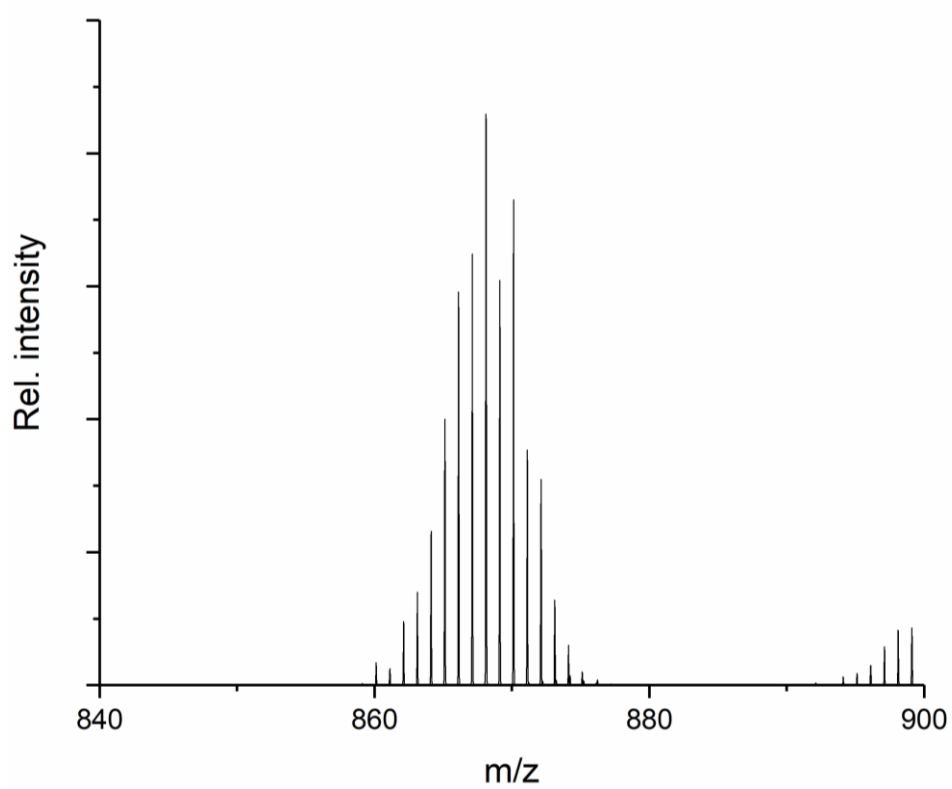


Figure S34: Excerpt of LIFDI mass spectrum of the reaction 1 with 2 eq trimethyl phosphine (PMe_3) after 24 h irradiation (350 nm). Peak assigned to: $m/z = 868.1195$ $[(\text{Me}_3\text{P})_2\text{Ru}(\text{GaCp}^*)_3]^+$ (calc. 868.1202).

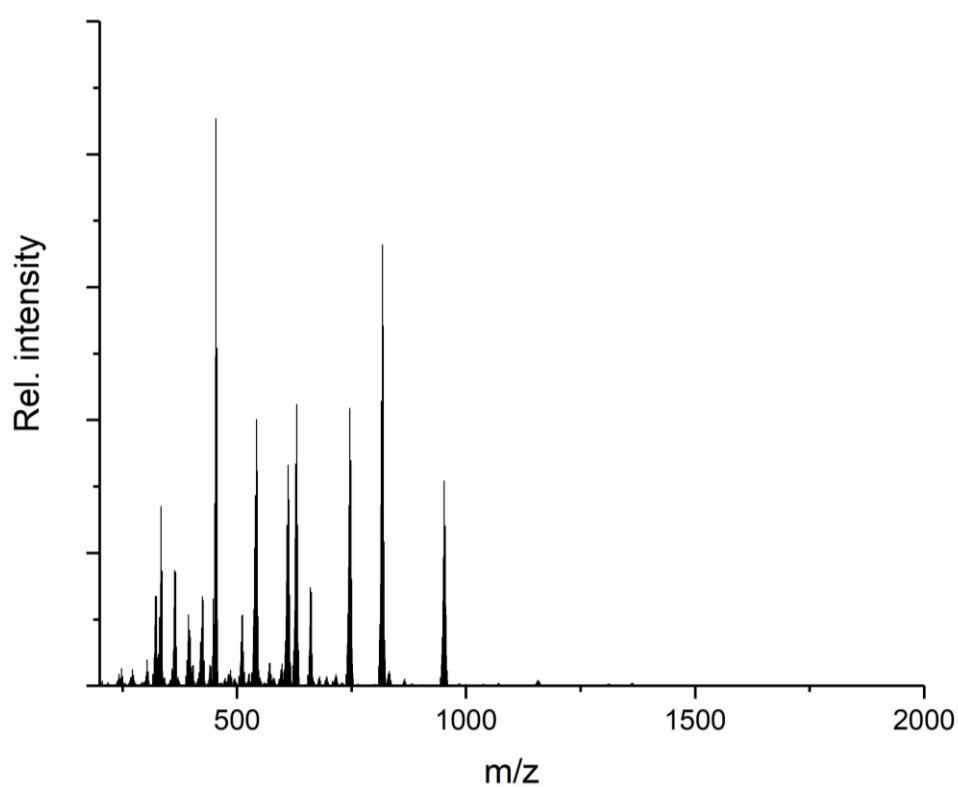


Figure S35: In situ LIFDI mass spectrum of the reaction **1** with 2 eq triethyl phosphine after 24 h irradiation (350 nm).

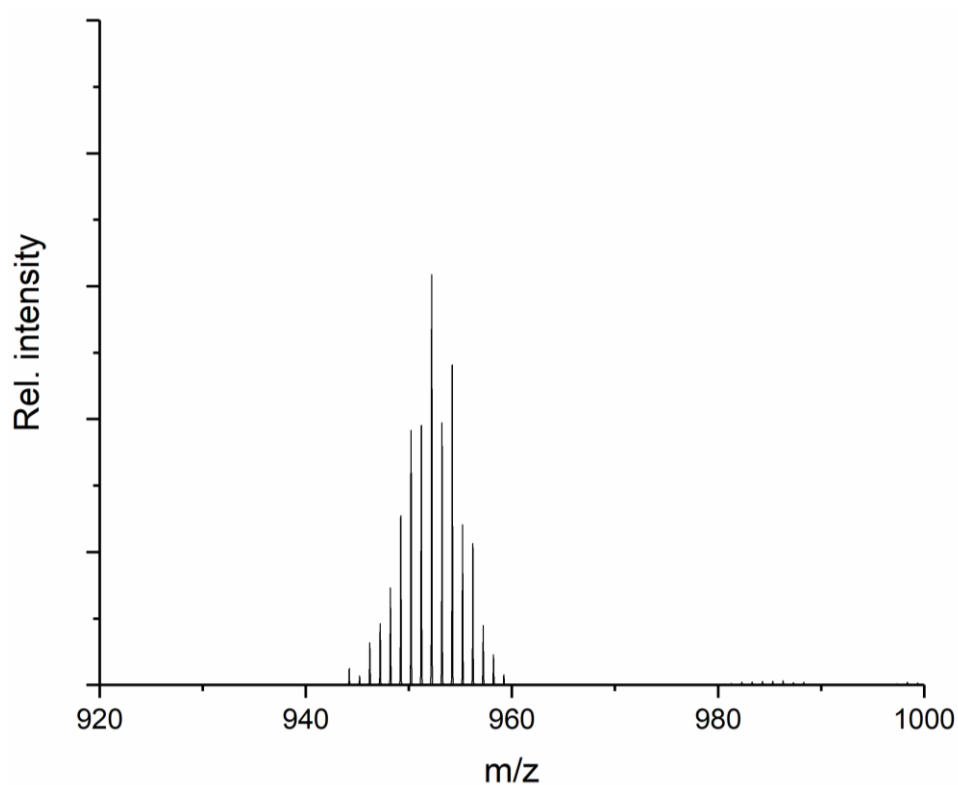


Figure S36: Excerpt of LIFDI mass spectrum of the reaction **1** with 2 eq triethyl phosphine (PEt_3) after 24 h irradiation (350 nm). Peak assigned to: $m/z = 952.2143$ [$(\text{Et}_3\text{P})_2\text{Ru}(\text{GaCp}^*)_3$] $^+$ (calc. 952.2141).

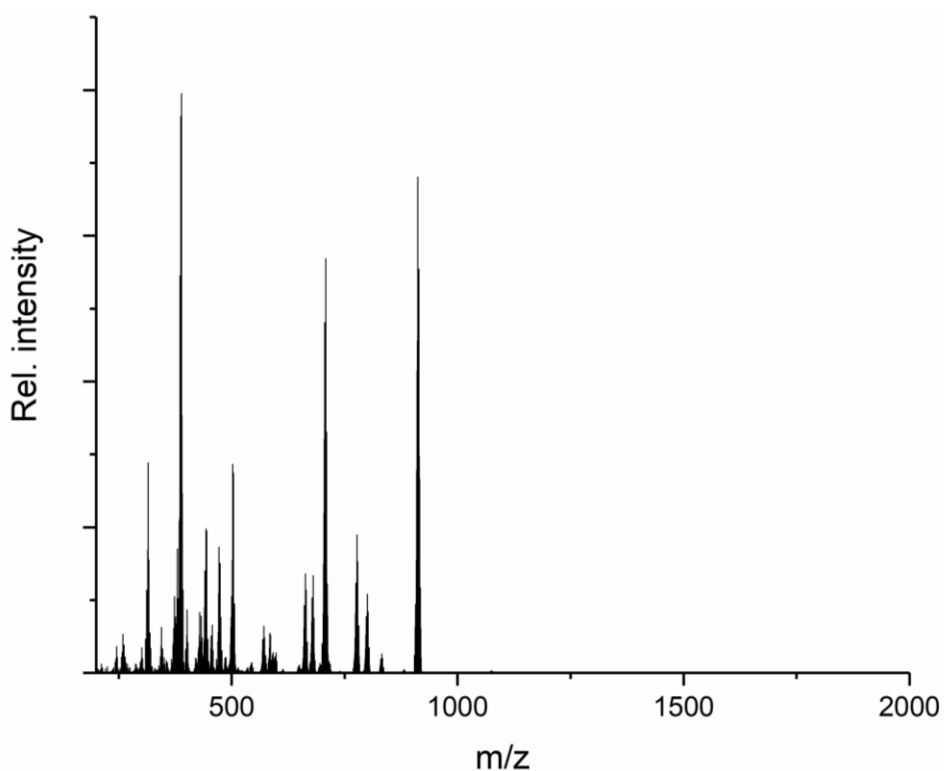


Figure S37: In-situ LIFDI mass spectrum of catalytic hydrogenation of 20 eq 3-hexyne under irradiation.

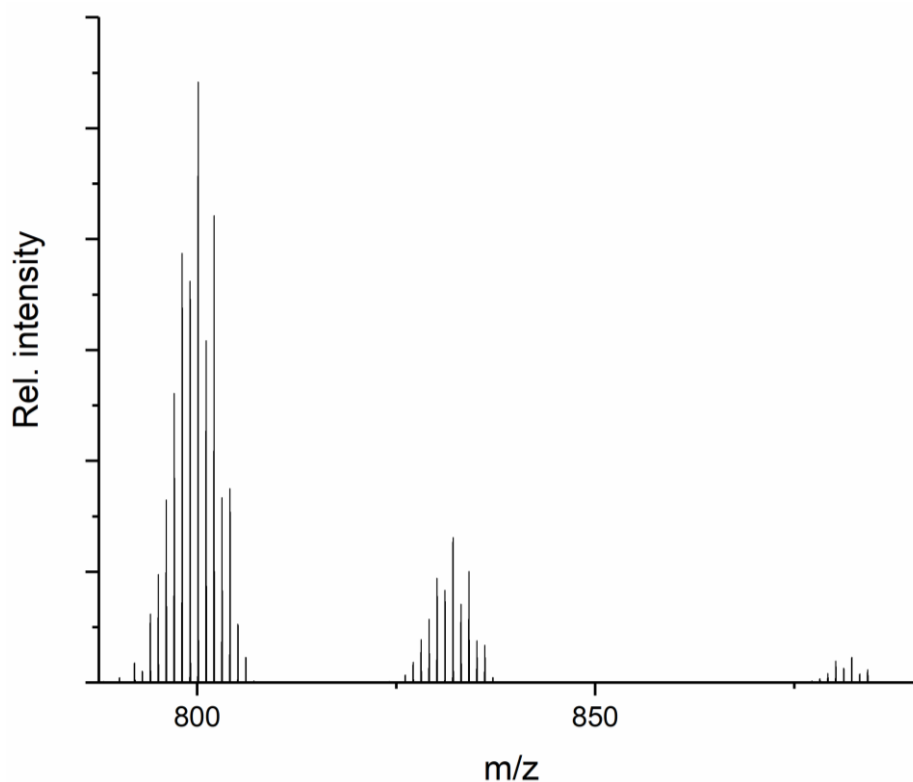


Figure S38: Excerpt of in-situ LIFDI mass spectrum of catalytic hydrogenation of 20 eq 3-hexyne under irradiation. Peak attributed to $[\text{Ru}(\text{GaCp}^*)_3(\text{hexene})]$ (A; $m/z = 800.1251$; calc. 800.1257) significantly more intense than peak attributed to $[\text{Ru}(\text{GaCp}^*)_3(\text{hexyne})(\text{hexene})]$ (B; $m/z = 882.2044$; calc. 882.2039). Inverse to reaction with higher 3-hexyne concentration. Peak at $m/z = 832$ results from unconverted **1**.

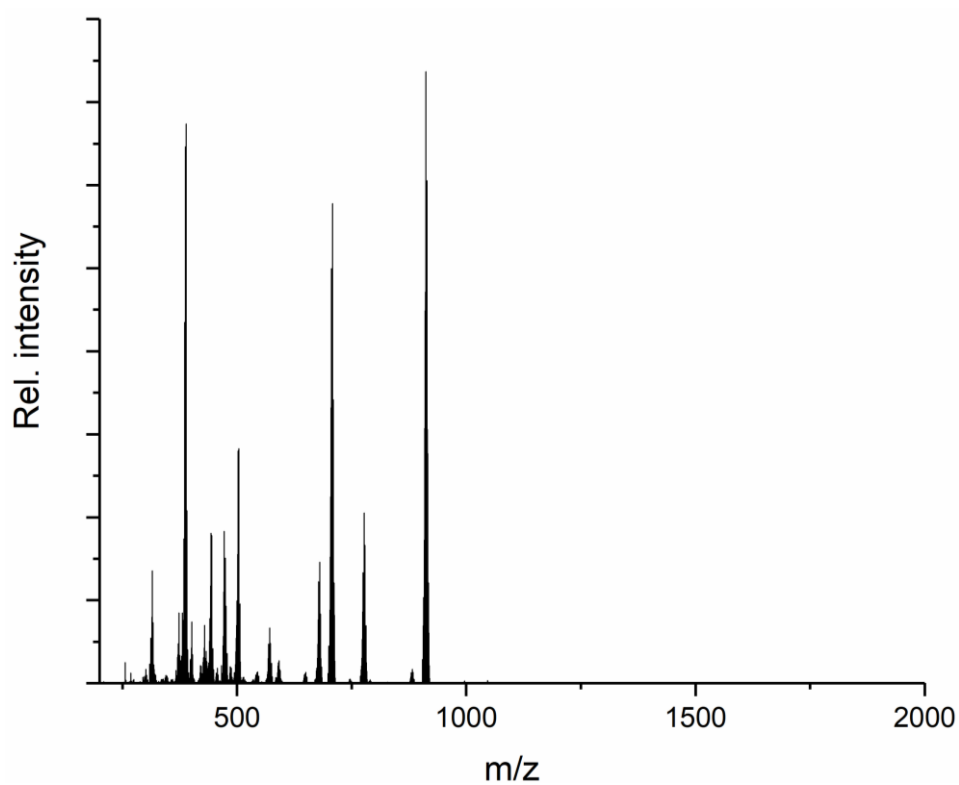


Figure S39: In-situ LIFDI mass spectrum of catalytic hydrogenation of 100 eq 3-hexyne under irradiation.

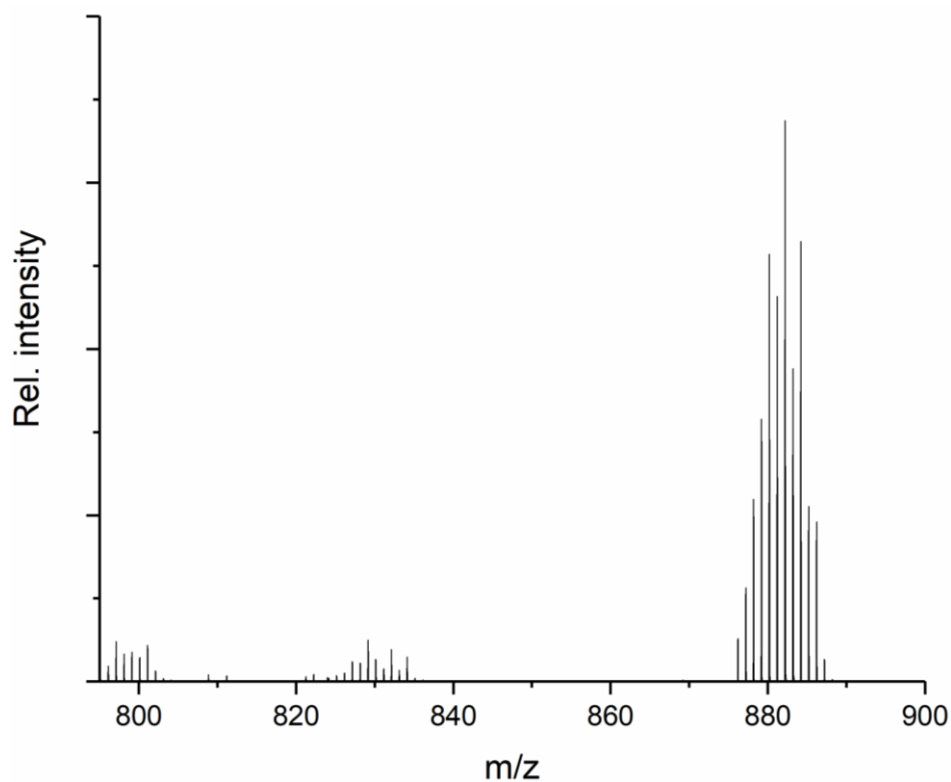


Figure S40: Excerpt of in-situ LIFDI mass spectrum of catalytic hydrogenation of 100 eq 3-hexyne under irradiation. Peak attributed to $[\text{Ru}(\text{GaCp}^*)_3(\text{hexyne})(\text{hexene})]$ (B; $m/z = 882.1997$; calc. 882.2039) significantly more intense than peak attributed to $[\text{Ru}(\text{GaCp}^*)_3(\text{hexene})]$ (A_2 ; $m/z = 800.1180$; calc. 800.1257). Inverse to reaction with lower 3-hexyne concentration. Peak at $m/z = 832$ results from unconverted **1**.

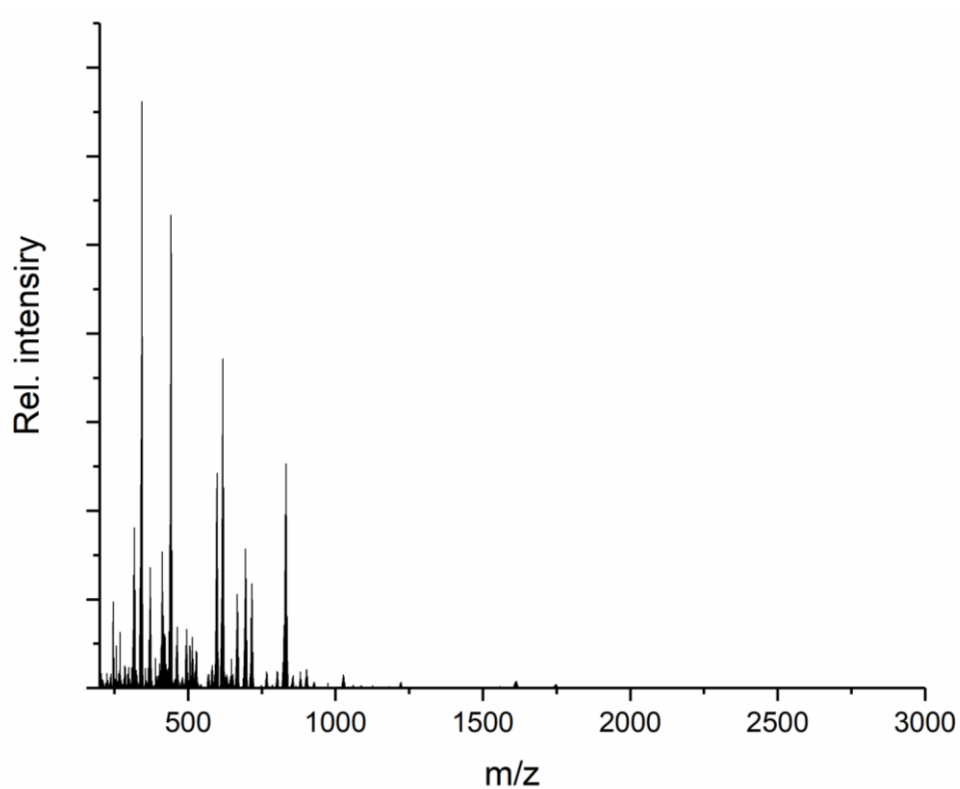


Figure S41: LIFDI mass spectrum of the reaction of **1** with H_2 under 3 h irradiation (350 nm).

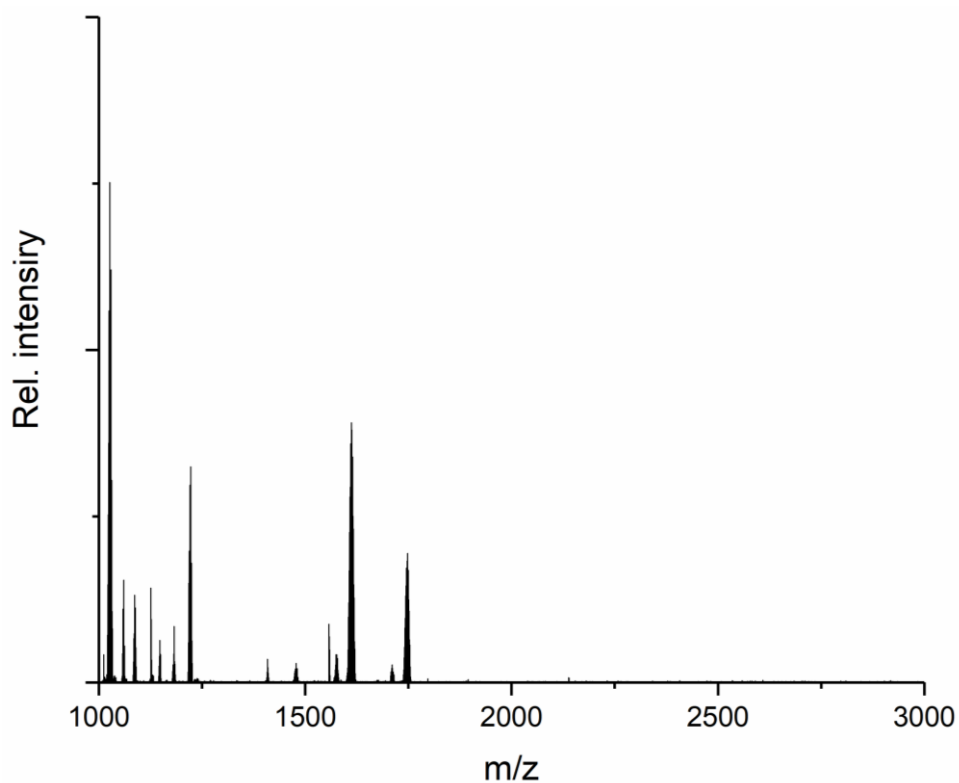


Figure S42: Excerpt of LIFDI mass spectrum of the reaction of **1** with H_2 under 3 h irradiation (350 nm). Peaks assigned to composition as following: $m/z = 1026.96$ ($Ru_2Ga_4Cp^*_4H_5$), $m/z = 1612.60$ ($Ru_3Ga_9Cp^*_5H_5$), $m/z = 1710.07$ ($Ru_2Ga_8Cp^*_7H_3$) and $m/z = 1747.73$ ($Ru_3Ga_9Cp^*_6H_5$).

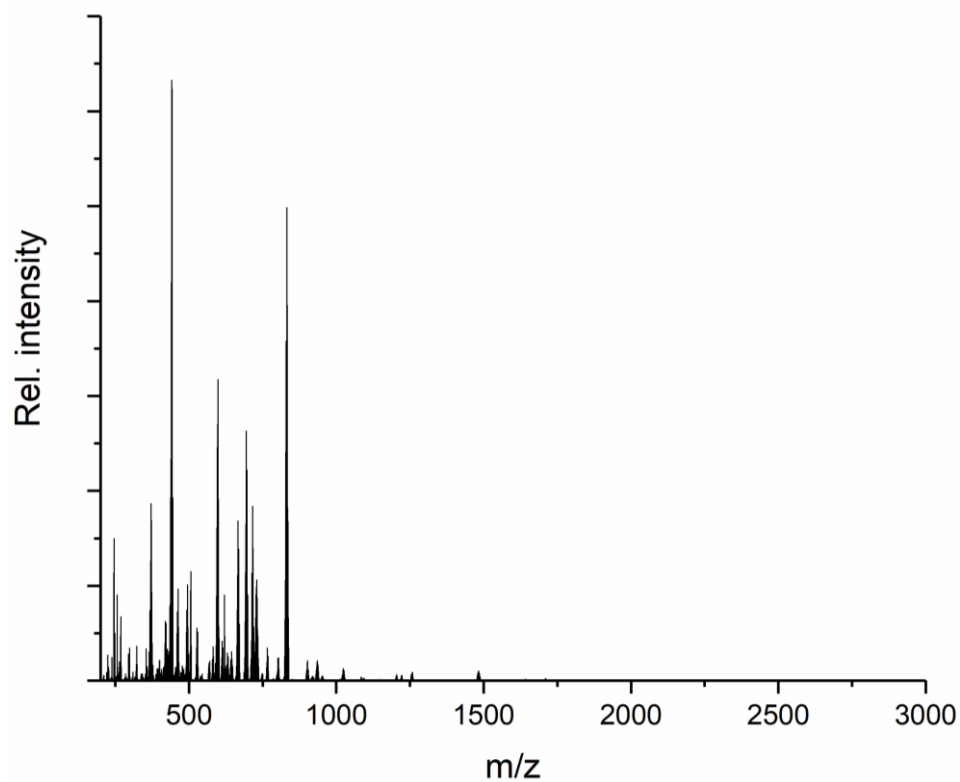


Figure S43: LIFDI mass spectrum after the catalytic conversion 3-hexyne with **1** and H₂ (2 bar) under 24 h irradiation (350 nm) in cyclohexane-d₁₂.

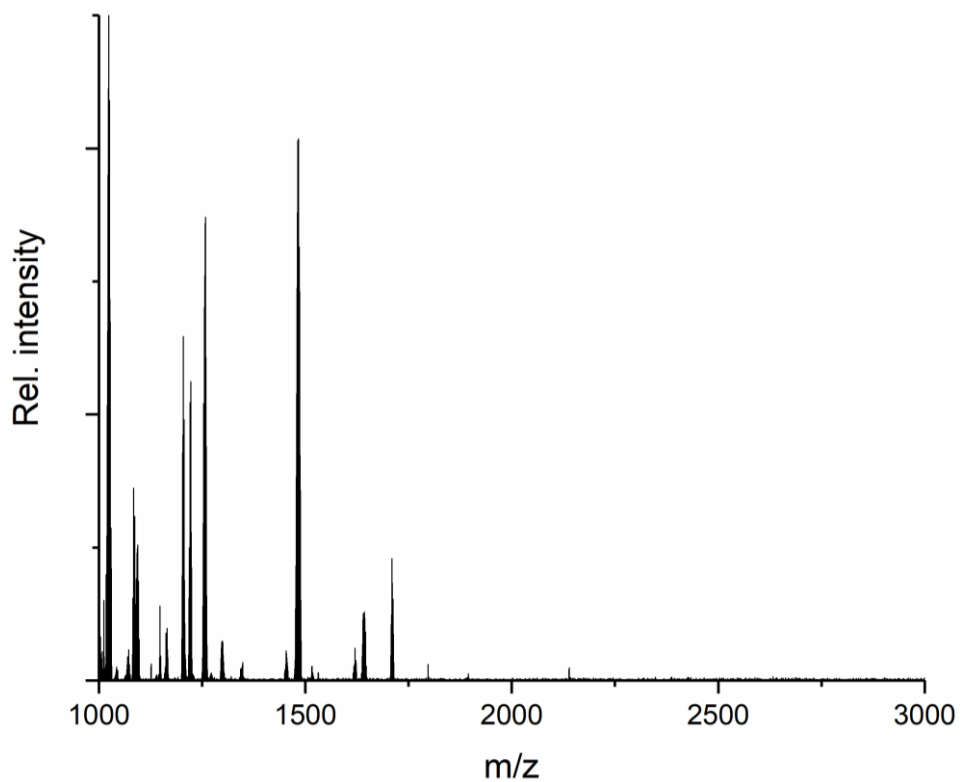


Figure S44: Excerpt of LIFDI mass spectrum after the catalysis. Several new clusters are formed: $m/z = 1024.00$ ($Ru_2Ga_4Cp^*_4H_2$); $m/z = 1093.92$ ($Ru_2Ga_5Cp^*_4H$); 1481.96 ($Ru_2Ga_7Cp^*_5SiEt_3H$); $m/z = 1710.07$ ($Ru_2Ga_8Cp^*_7H_3$).

Infrared Spectra

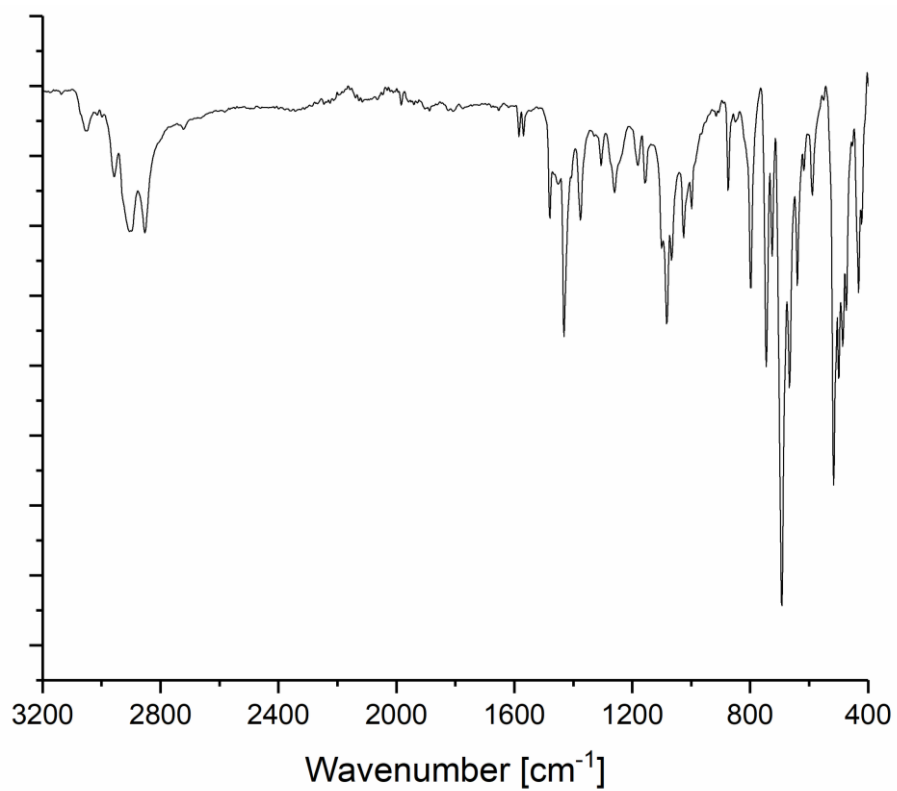


Figure S45: ATR-IR spectrum of $[\text{Ru}(\text{GaCp}^*)(\text{dppe})]$ (**4**). No typical Ru-H bands (range between 1600 and 2000 cm^{-1}).

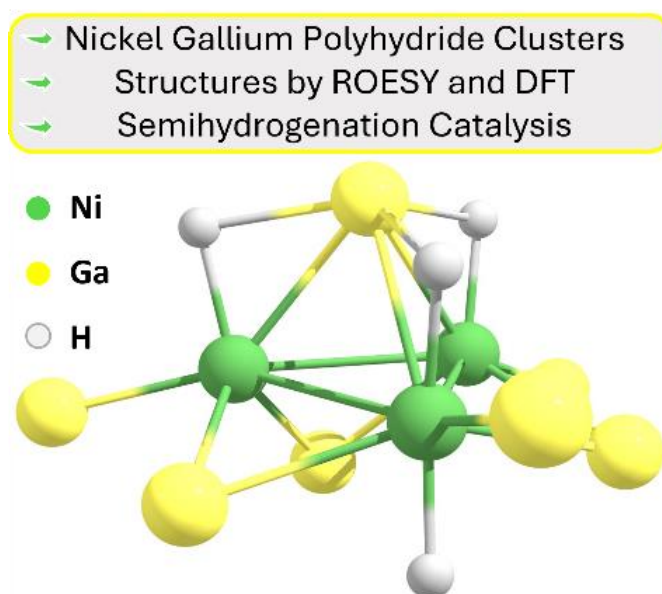
2.5 Alkyne Semihydrogenation with Polyhydride Ni/Ga Clusters.

Maximilian Muhr,^{a,b} Hao Liang,^c Lars Allmendinger,^d Raphael Bühler,^{a,b} Fabrizio Napoli,^{a,b} Dardan Ukaj,^{a,b} Christian Jandl,^{a,b} Samia Kahlal,^c Jean-Yves Saillard,^c Christian Gemel,^{a,b} and Roland A. Fischer*^{a,b}

[a, b] Technical University of Munich, TUM School of Natural Sciences, Department of Chemistry and Catalysis Research Centre, Chair of Inorganic and Metal-Organic Chemistry, Lichtenbergstraße 4, D-85748 Garching, Germany

[c] Univ Rennes, CNRS, ISCR-UMR 6226, F-35000 Rennes, France.

[d] Department of Pharmacy, Ludwig-Maximilians-University Munich, Butenandtstrasse 7, D-81377 Munich, Germany.



The following content was already evaluated through a peer-review process, is however unpublished yet. It is planned to submit the work to the Journal *Angewandte Chemie*.

Author contributions:

Experiments and manuscript writing by M.M.; Experimental support by R.B., F.N., D.U.; C.J. performed SCXRD. 2D NMR by L.A.; DFT calculations by H.L., S.K. and J.Y.S.; C.G. and R.A.F. supervised the research.

2.5.1 Abstract

The bimetallic, deca-nuclear Ni_3Ga_7 -cluster of the formula $[\text{Ni}_3(\text{GaTMP})_3(\mu^2\text{-GaTMP})_3(\mu^3\text{-GaTMP})]$ (**1**, TMP = 2,2,6,6-tetramethylpiperidiny) reacts reversibly with hydrogen under the formation of a series of (poly-)hydride clusters **2**. Low-temperature 2D NMR experiments at $-80\text{ }^\circ\text{C}$ show that **2** consist of a mixture of a di- (**2_{Di}**), tetra- (**2_{Tetra}**) and hexahydride species (**2_{Hexa}**). The structures of **2_{Di}** and **2_{Tetra}** are assessed by a combination of 2D NMR spectroscopy and DFT calculations. The cooperation of both metals is essential for the high hydrogen uptake of the cluster. Polyhydrides **2** are catalytically active in the semihydrogenation of 4-octyne to 4-octene with good selectivity. The example is the first of its kind and conceptually relates properties of molecular, atom-precise transition metal / main group metal clusters to the respective solid-state phase in catalysis.

2.5.2 Main Text

Molecular compounds with direct bonds between transition metals (TM) and group 11-13 metals (E) exhibit characteristically modified reactivity with respect to their monometallic components.^[1] Especially complexes of late TMs coordinated by E(I) (E = Al, Ga, In) ligands have been investigated in the context of bond activation reactions. The complex $[\text{Cp}^*\text{Rh}(\text{CH}_3)_2(\text{GaCp}^*)]$, for example, shows a facile intermolecular C-C bond activation of a Cp^* ligand ($\text{Cp}^* = \text{C}_5\text{Me}_5$).^[2] Intramolecular C-H bond activations are observed for $[\text{M}(\text{AlCp}^*)_5]$ (M = Fe, Al).^[3] The intermolecular C-H and Si-H activation of C_6H_6 and HSiEt_3 are mediated by unsaturated intermediates such as $[\text{Ni}(\text{AlCp}^*)_3]$ ^[4] and $[\text{Ru}(\text{GaCp}^*)_3(\text{H})_2]$ ^[5]. These reactivities can often be attributed to cooperative effects of the two metals and are a consequence of the high donor capacity of the ECp^* ligand, resulting in strongly polarized $\text{TM}^{\ominus}-\text{E}^{\oplus}$ bonds. The thermodynamic driving force results from the irreversible oxidation of E(I) to E(III) and the formation of strong E-C bonds. Thus, no catalytic reactions have been identified so far.^[6] Herein we report a first example that put the above introduced properties of TM complexes or clusters stabilized by E(I) ligands with direct TM-E bonds into value for catalytic reactions: The Ni/Ga cluster $[\text{Ni}_3(\text{GaTMP})_7]$ (**1**, TMP = 2,2,6,6-tetramethylpiperidiny) reversibly reacts with hydrogen, enabling the catalytic alkyne to alkene semihydrogenation with moderately good selectivity (Figure 1). The use of the cluster protecting amide ligand is of crucial importance here. Related Ni/Ga clusters protected by Cp^* are known, however, these undergo Cp^* -transfer reactions from Ga to Ni, leading to deactivation of the Ni centres.^[7] In contrast, the σ^1 -amide preferably

coordinates to Ga and the Ga-amide bond is stable even under hydrogenolytic conditions.^[8] We identified a series of (poly-)hydride clusters $[\text{Ni}_3(\text{GaTMP})_7(\text{H})_x]$ (**2**, $x = 2,4,6$) as the key species for driving the catalytic alkyne semihydrogenation and succeeded in accurately determining their structures by 2D NMR methods in conjunction with DFT calculations. The structural assignment allows for identification of the non-innocent role of the Ga ligands.

We like to put our work into the context of conceptually linking the molecular cluster and the solid-state chemistry of intermetallics.^[1] Intermetallic solid-state materials represent an important class of industrially relevant catalysts. A Pd/Ag alloy is typically used in the purification of ethylene feedstocks from trace acetylene impurities.^[9] Generally, the dilution of the catalytically more active TM in a matrix of catalytically much less active E leads to improved selectivity due to the formation of isolated TM atoms or small TM clusters at the catalysts surface.^[10] Intermetallic NiGa phases have been investigated as catalysts for the alkyne semihydrogenation, especially the Ni_5Ga_3 phase exhibits excellent balance of activity and selectivity.^[11] This motivated us

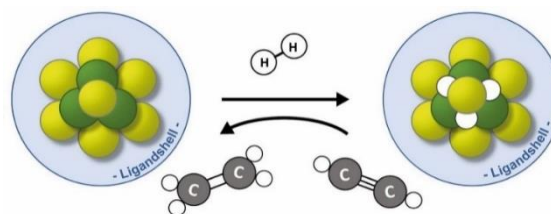


Figure 1: Conceptual scheme depicting the reaction of the alkylamide ligand protected cluster $[\text{Ni}_3(\text{GaTMP})_7]$ (**1**, left) with H_2 to yield the (poly-)hydride clusters $[\text{Ni}_3(\text{GaTMP})_7(\text{H})_x]$ (**2**, right; $x = 2,4,6$). Color code: yellow, Ga; green Ni; white, H; blue, TMP ligand shell (TMP = 2,2,6,6-tetramethylpiperidiny). The (poly-)hydride clusters **2** (right) enable catalytic semihydrogenation of alkynes to alkenes. The structures of **1** and **2** may serve as a molecular model for the catalytically active sites at the surface of the Ni_5Ga_3 solid-state phase.

to explore the chemistry of ligated, atom-precise clusters with well-defined active centres and to discover catalytic reactivity patterns and intermediates structurally related to solid-state materials.

The stoichiometric reaction of $\text{Ni}(\text{cod})_2$ with $[\text{GaTMP}]_4$ ^[12] at 60 °C in toluene gives the new, dark purple Ni_3 -cluster $[\text{Ni}_3(\text{GaTMP})_7]$ (**1**, Figure 2). The already reported, related Ni_2 -cluster $[\text{Ni}_2(\text{GaTMP})_7]$ is observed by LIFDI-MS (Figures S33-S34) as an intermediate in this reaction.^[13] Accordingly, the reaction of pure $[\text{Ni}_2(\text{GaTMP})_7]$ with $\text{Ni}(\text{cod})_2$ leads to **1**. Cooling reaction solutions of **1** to -30 °C overnight, yields dark purple single crystals of space group $P2_1/n$. Single crystal X-ray diffraction (SC-XRD) reveals the molecular structure of **1** in the solid state: A central Ni_3 -triangle is coordinated by three terminal GaTMP , three Ni_2 -edge bridging μ^2 - GaTMP as well as one capping μ^3 - GaTMP ligand over one side of the Ni_3 -triangle (Figure 2). The overall structure of **1**, written as $[\text{Ni}_3(\text{GaTMP})_3(\mu^2\text{-GaTMP})_3(\mu^3\text{-GaTMP})]$ is very similar to that of $[\text{Ni}_3(i\text{Pr}_2\text{Im})_3(\mu^2\text{-CO})_3(\mu^3\text{-CO})]$ ($i\text{Pr}_2\text{Im} = 1,3$ -di(isopropyl)-imidazol-2-ylidene).^[14] This similarity further underlines the comparable coordination properties of the formally two electron donating GaTMP with CO and N -heterocyclic carbene (NHC) ligands.^[13a] The Ni_3 triangle is almost perfectly unilateral (Ni-Ni distances: 2.383 - 2.396 Å, Ni_3 angles; 59.7° - 60.3°) and in good agreement with other Ni clusters known in literature.^[7b, 14, 15] The terminal and bridging μ^2 - GaTMP ligands are almost in plane with the Ni_3 -triangle. The terminal Ni-Ga (2.175 - 2.184 Å) bonds are distinctly shorter than the $\text{Ni-}\mu^2\text{-Ga}$ (2.214 - 2.227 Å) and the $\text{Ni-}\mu^3\text{-Ga}$ (2.314 - 2.411 Å) bonds, which is in line with other Ga(I) stabilized transition metal cluster

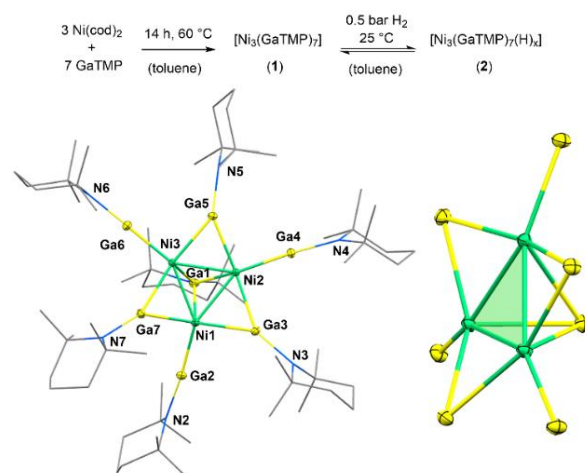


Figure 2: Above: Reaction scheme of the cluster synthesis of **1** and the conversion by H_2 addition to yield the (poly)hydridic species **2**. – Below: The molecular structure of **1** in the solid-state is shown left (thermal ellipsoids are given at the 50% probability level). TMP ligands are given in wireframe depiction and H atoms are omitted for clarity. Selected bond length (Å) and angle (deg) ranges: Ni-Ni 2.383 - 2.396, $\text{Ni-}\mu^1\text{-Ga}$ 2.175 - 2.184, $\text{Ni-}\mu^2\text{-Ga}$ 2.214 - 2.227, $\text{Ni-}\mu^3\text{-Ga}$ 2.314 - 2.411; Ni-Ni-Ni 59.7° - 60.3°. The Ni/Ga metal core structure of **1** is shown at the right side. TMP ligands are omitted. Green plane highlights the well-accessible Ni_3 triangle.

compounds.^[7b, 13a, 16] The ^1H NMR (Figures S1-S2) and ^{13}C NMR spectra (Figures S3-S4) of **1** in toluene- d_8 are consistent with the molecular symmetry in the solid state structure: ^1H signals can be divided into two groups with a ratio of 3:4, indicating a fluxional process exchanging the μ^2 - and μ^3 -bridging GaTMP ligands. All ^1H and ^{13}C chemical shifts are in similar ranges with respect to $[\text{Ni}_2(\text{GaTMP})_7]$.^[13a] A detailed assignment of the NMR data of **1** can be found in the SI.

The coordination environment of the Ni centres in **1** suggests some reactivity towards small molecules. While one face of the Ni_3 triangle is shielded by bulky GaTMP ligands, the other remains open and accessible towards potential substrates. At the same time, the electron donating Ga(I) ligands generate electron-rich nickel centres and introduce $\text{Ni}^{\text{II-}}\text{-Ga}^{\text{I+}}$ bond polarization that should facilitate oxidative addition reactions. Indeed, when a solution of **1** in toluene- d_8 is subjected to 1 bar

H₂, a series of new hydride clusters **2** is formed in equilibrium with **1**, namely [Ni₃(GaTMP)₇(H)_x] (**2**_{Di}, x = 2; **2**_{Tetra}, x = 4; **2**_{Hexa}, x = 6). In the ¹H NMR spectrum of **2** at room temperature, only one broad, coalesced singlet at -8.66 ppm is present (Figures S7-S10). Likewise, the aliphatic region gives rise to one new set of TMP signals, indicating fluxional processes which exchange hydride ligands (intermolecularly) as well as TMP ligands (inter- or intramolecularly).

As indicated by the integral ratios of the TMP ligands, the equilibrium can be shifted from **1** to **2** with increasing H₂ pressure (ratio **1/2**: 3.4/1 at 1 bar, 0.6/1 at 3 bar; NMR at r. t. after 15 min reaction; see Figure S26). The hydride formation is fully reversible: When H₂ is removed from solutions containing **2**, e.g. by purging with inert gas, only signals as those of **1** can be detected (Figure S30-31). The reversible nature of the H₂ activation and hydride coordination, as well as the fact that more than equivalent of hydrogen is activated, is further supported by a H/D-exchange experiment: Pressuring a sample of **1** in toluene-*d*₈ consecutively with D₂ (1.5 bar) and H₂ (3 bar), results in the observation of a significant amount HD (4.51 ppm)^[17] in the ¹H NMR spectrum (Figure S25). Single crystals of **2** suitable for (low-temperature) X-ray diffraction studies could not be obtained and likewise the lability of **2** prohibited characterization by LIFDI-MS. The structural assignment of **2** was thus based on detailed NMR spectroscopic studies. At -80 °C the coalescent hydride signal of **2** [Ni₃(GaTMP)₇(H)_x] splits into five distinct singlets at -6.09, -7.58, -8.15, -9.02 and -9.31 ppm (Figures S11-S14). According to their T₁ relaxation time (500 – 700 ms), all signals are related to classic metal-hydride bonding (Figure S22).^[18] A ¹H,¹H COSY spectrum

at -80 °C reveals coupling between the hydrides represented by the signals at -7.58 and -9.31 ppm (integral ratio 1:1) as well as coupling between the hydrides represented by the signals at -5.97, -8.32 and -9.02 ppm (integral ratio 1:1:2). This points to a dihydride complex **2**_{Di} and as well as to a tetrahydride complex **2**_{Tetra}, respectively (Figure S15-16). The four remaining small peaks at -6.98, -7.13, -7.78 and -9.44 ppm are attributed to the hexahydride complex **2**_{Hexa} under the assumption that further related signal(s) may be covered by the broad peaks of **2**_{Di} and **2**_{Tetra}. Notably no correlated COSY cross peaks are found for **2**_{Hexa}, probably due to its low concentration and resulting small signal intensities. Surprisingly, the H₂ pressure does not influence the quantitative distribution of signals of **2**, at least in the experimentally accessible range of 1-3 bar.

In order to gain insight into the location of the hydride ligands in the three (poly)hydride complexes of **2**, different isomers for each complex were calculated at the DFT level of theory (computational details given in SI). Several local minima could be identified for **2**_{Di} as well as for **2**_{Tetra}. The isomers differ in the exact distribution of the hydride ligands over the Ni₃Ga₇ framework. Hydride ligands were found in terminal Ni-H, μ²-bridging (Ni-H-Ni, Ni-H-Ga) positions as well as μ³-(H-Ni₃)-bridging positions. A figure depicting all computationally identified isomers of **2** as well as their calculated relative energies are given in the SI (Figures S39-S41; Table S2). The Ni-Ni distances in **2** are distinctly longer than those in **1**, whereas the Ni-Ga bond lengths remain almost the same. Notably, the μ²-hydride bridged Ni-Ni bond in **2**_{Di} is about 0.2 Å shorter as the other Ni-Ni bonds. For **2**_{Di}, four energetic minima were located, two of which exhibit a hydride distribution reflecting the

unsymmetric nature of the ^1H NMR spectrum (two signals, integral ratio 1:1). In both structures one Ni-Ni edge is μ^2 -bridged by a hydride, while the second hydride is terminally coordinated to the remaining Ni atom, either on the same (*cis-2_{Di}*) or the opposite side (*trans-2_{Di}*, +3.7 kcal/mol) of the Ni₃ triangle. In the case of **2_{Tetra}** only one isomer was found with a suitable symmetry reflecting the 1:1:2 integral ratio observed in the hydridic region of the ^1H NMR spectrum. For **2_{Hexa}** only one minimum structure has been found, with unsymmetrically hydride distribution, featuring three terminal Ni-H and three μ^2 -bridged Ni-H-Ga moieties (Figure S43).

The calculated structures were spectroscopically confirmed by phase-sensitive NOESY experiments at -80 °C (Nuclear Overhauser Effect Spectroscopy; Figure S17). However, a clear discrimination between the NOE signals of the hydrides in spatial proximity and signals due to chemical exchange (EXSY) was not unambiguously possible. Probably this is due to slow molecular tumbling rates at such low temperatures, leading to fast relaxation rates and consequently yielding negative NOEs, which are showing the same sign as those arising from chemical exchange. Thus, phase-sensitive ROESY (Rotating Frame Overhauser Effect Spectroscopy) experiments were performed (Figures S18-S21). Regardless of the relaxation rate, they give antiphase cross peaks with respect to the diagonals for ROEs and respective cross peaks with the same phase as the diagonals for signals originating from chemical exchange. This in consequence enables to distinguish between signals related to either proximity or to chemical exchange. It is worth mentioning that the results from the ROESY spectrum were in good accordance with the initially performed NOESY spectra. The

ROESY spectrum allows a clear discrimination of different calculated structures according to the hydride distribution, in particular with respect to the relative intramolecular proximity of hydride ligands. While in *trans-2_{Di}* the H-H distance is calculated to be 4.22 Å, this distance is only 3.18 Å in the optimized structure of *cis-2_{Di}* (Figure 3), suggesting that the experimentally observed isomer of **2_{Di}** is *cis-2_{Di}*, which is also the energetically more favorable isomer. The structure of **2_{Tetra}** can be assigned in a similar manner: The energetically most favorable isomer, according to DFT, contains three μ^2 -Ni-H-Ga, bringing each Ni to the μ^3 -Ga, as well as one terminal Ni-H – resulting in an overall C_s symmetric structure (Figure 3). The ROE cross-peaks of **2_{Tetra}** are only observed for hydrides with a H-H distance of 3.01 Å and 3.23 Å, respectively, but not

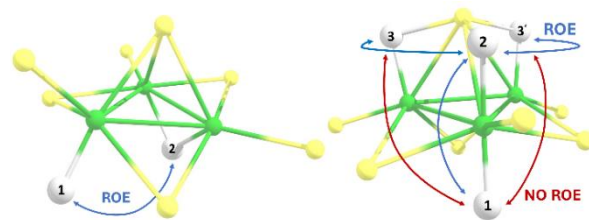


Figure 3: Calculated structures of **2_{Di}** and **2_{Tetra}** with interpretation for respective ROESY signals. Intramolecular hydride-hydride distance is the reason for ROE signals. Blue arrow – ROE signal; red arrow – no ROE signal. TMP ligands omitted for clarity, Ni (green), Ga (yellow) and H (white). Left) Calculated structure of *cis-2_{Di}* with $d_{12} = 3.18$ Å (ROE signal). Right) Calculated structure of **2_{Tetra}** with $d_{12} = 3.01$ Å (ROE signal), $d_{23/3'} = 3.23$ Å (ROE signal) and $d_{13/3'} = 4.43$ Å (no ROE signal).

between the hydrides with a distance of 4.43 Å. The minimum structure of **2_{Tetra}** is in line with the symmetry observed in the ^1H NMR spectrum, as well as the ROESY cross peaks. For **2_{Hexa}** only one local minimum structure could be found (Figure S43). In this structure, the six hydridic ligands are unsymmetrically coordinated which agrees with the four distinct small signals in the ^1H NMR spectrum, considering that the two remaining signals could be covered by the

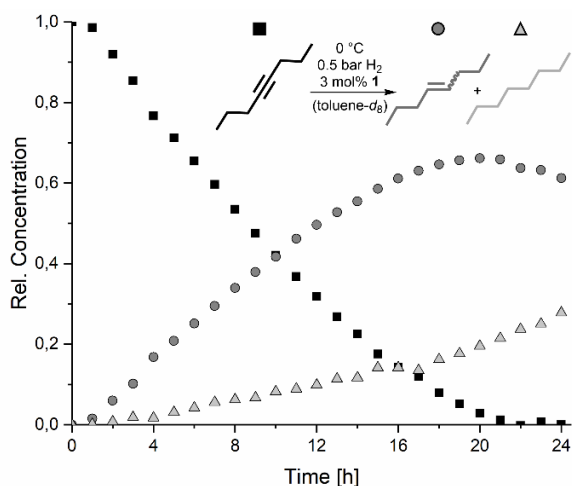


Figure 4: Relative concentrations of the catalytic substrates vs. time. 4-octyne (black, square), 4-octene (dark grey, circle), n-octane (light grey, triangle) under given reaction conditions.

broad signals of **2_{Di}** and **2_{Tetra}**. It should be noted, however, that no hydridic ROE signals were detected for **2_{Hexa}**, presumably due to its low concentration, and therefore a clear deduction of the structure is not possible. Interestingly, EXSY cross peaks are found between the signals of **2_{Tetra}** (-8.3 and -9.0 ppm) and two of the signals assigned to **2_{Hexa}** (-6.9 and -7.1 ppm), respectively, indicating intermolecular hydride exchange between the two species (Figure S21). No EXSY signal between free H₂ and **2_{Tetra}** or **2_{Hexa}** are observed. Notably, all hydride signals of **2** show ROE cross peaks to the TMP methyl signals, including the hydride signals attributed to **2_{Hexa}**. Most interestingly, the high hydrogen load of **2_{Tetra}** does not prevent the cluster from further hydrogen uptake. We attribute this feature to the involvement of the non-innocent Ga ligands, which serve as 'storage sites' for the hydrides (Figure 3) and thus keeping the Ni₃ site accessible for additional hydrogen.

The catalytic activity of **1** in the semihydrogenation of 4-octyne (Figure 4) has been examined by *in-situ* ¹H NMR

spectroscopy. An NMR tube containing a reaction solution of 4-octyne, mesitylene (internal standard) and 3 mol% **1** in toluene-*d*₈ was pressurized at 0 °C with 0.5 bar of H₂. The solution was constantly kept at 0 °C and ¹H NMR spectra were recorded in 30 min intervals. After 8 h, ca. 50 % of the alkyne is converted with high selectivity (90%) for the alkene (5% *n*-octane; turnover number [TON] = 15.0; turnover frequency [TOF] = 2.5 h⁻¹). The alkene concentration reaches a maximum of ca. 67% after 20 h, however, accompanied by increasing alkane formation (ca. 20% alkane; selectivity 71%; TON = 23.3; TOF = 1.2 h⁻¹). Note that, related studies at Ni/Ga nanocolloids or nanocrystals yield similar semihydrogenation selectivity (Table S2).^[11a-c] Determination of the alkene *cis/trans* ratio is not possible by NMR (Figure S37), due to partial overlap of all signals. Nonetheless, a substantial *cis* excess can be concluded from combining NMR and GC-FID (gas chromatography flame ionization detection) data (Figure S40). *In-situ* monitoring (¹H NMR) of the reaction under catalytic conditions shows the presence of **1**, **2** as well as the substrates only. No other species or intermediates can be identified. When treating **1** with 4-octyne in the absence of hydrogen all signals remain unchanged, with respect to the spectra of the pure compounds. We suggest the coordination of the alkyne to **2** over the open face of the Ni₃ triangle in some fashion, however, we cannot determine which species, are the catalytically active one(s). The presence of 4-octyne does not change the quantitative ratio of the three polyhydride species when cooling the reaction solution down to -80 °C, where no further catalytic activity is observed. After full conversion of 4-octyne, **1** and **2** are present in solution along with TMPH, indicating some catalyst

degradation (Figure S38-39). Due to the so far limited experimental information on key intermediates, a rigorous computational modeling of the catalytic cycle exceeds the scope of this work. Nevertheless, we like to suggest that the structure of **2**_{Tetra} (Figure 3) would allow for bimetallic cooperativity and an essential role of the Ga in the catalytic cycle. The μ^3 -Ga would serve as the 'storage site' for the hydrides, vacating the open Ni₃ site for further substrate coordination. This synergetic function of the Ni and Ga sites would not be possible with chemically innocent spectator ligands, such as CO, NHCs or phosphines. Experiments extending the substrate scope are underway. For example, using the terminal alkyne 1-octyne resulted in a (metallic) precipitate, presumably a consequence of the C-H acidity of terminal alkynes. Taking into account that acetylides are good cluster stabilizing ligands,^[19] we assume the cluster growth under these conditions.

In summary, our data support the concept of relating the Ni/Ga clusters **1** and **2** to several intermetallic Ni/Ga solid-state phases that have recently been intensively studied as catalysts for alkyne semihydrogenation. Specifically, the Ni₅Ga₃ phase exhibits triangular Ni₃ structural motifs in proximity to Ga at the catalyst surface, quite in analogy to **1**. It shows improved catalytic properties with respect to bulk Ni or the Ni₁Ga₁ phase with isolated surface nickel atoms.^[11a] Thus, bimetallic clusters may serve as molecular mimics of local properties of the respective intermetallic solid-state surface and allow applying the pool of analytical methods for the determination of molecular structures (SC-XRD, 1D and 2D NMR, mass spectrometry, etc.). The accurate localization of the hydride ligands in **2** by 2D NMR methods and DFT

serves as an example. Our work may stimulate further studies on bimetallic cluster structure/reactivity relationships as a function of the selection and stoichiometry of metals and the coordinative environment of active sites at the atom-precise level. This perspective has been promoted in recent literature by us and others.^[20]

Acknowledgements

This work was funded by the German Research Foundation (DFG) within a Reinhard Koselleck Project (FI 502/44-1). Support by the TUM Graduate School is acknowledged. H.L. thanks the China Scholarship Council for a Ph.D. grant. S.K. and J.-Y.S. are grateful to GENCI (Grand Equipment National de Calcul Intensif) for HPC resources (Project A0050807367). The authors thank Jürgen Kudermann for GC measurements and Dr. Mirza Cokoja for helpful discussions. We are grateful to Brigitte Breitenstein (LMU) and Prof. Konstantin Karaghiosoff (LMU) for recording and support by interpretation of NMR spectra. Yannick Coppel (LCC CRNS Toulouse) is acknowledged for discussion on NOESY and ROESY data interpretation.

2.5.3 Reference

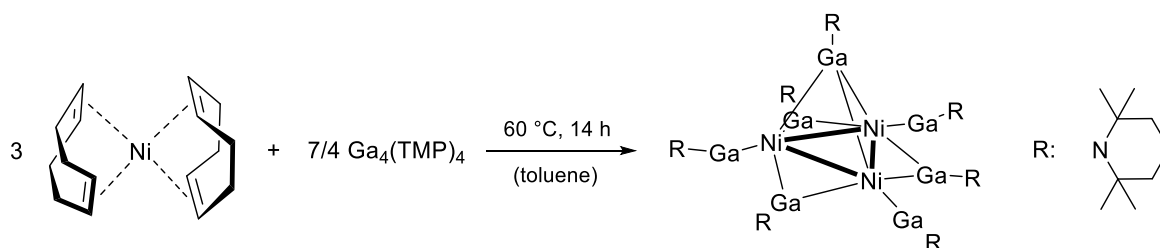
- [1] a) J. Campos, *Nat. Rev. Chem.* **2020**, *4*, 696-702; b) K. Mayer, J. Weßing, T. F. Fässler, R. A. Fischer, *Angew. Chem. Int. Ed.* **2018**, *57*, 14372-14393; c) M. Schütz, C. Gemel, W. Klein, R. A. Fischer, T. F. Fässler, *Chem. Soc. Rev.* **2021**, *50*, 8496-8510.
- [2] T. Cadenbach, C. Gemel, R. Schmid, R. A. Fischer, *J. Am. Chem. Soc.* **2005**, *127*, 17068-17078.

- [3] T. Steinke, M. Cokoja, C. Gemel, A. Kemper, A. Krapp, G. Frenking, U. Zenneck, R. A. Fischer, *Angew. Chem. Int. Ed.* **2005**, *44*, 2943-2946.
- [4] T. Steinke, C. Gemel, M. Cokoja, M. Winter, R. A. Fischer, *Angew. Chem. Int. Ed.* **2004**, *43*, 2299-2302.
- [5] M. Muhr, R. Bühler, H. Liang, J. Gilch, C. Jandl, S. Kahlal, J.-Y. Saillard, C. Gemel, R. A. Fischer, *Chem. Eur. J.* **2022**, e202200887, *accepted article*, DOI:10.1002/chem.202200887.
- [6] In a different approach the catalytic activity of TM centres has been modified by positioning a Lewis-acidic E(III) centre in close proximity. This achieved by the use of sophisticatedly tailored pincer-type ligands. a) R. Seki, N. Hara, T. Saito, Y. Nakao, *J. Am. Chem. Soc.* **2021**, *143*, 6388-6394; b) M. V. Vollmer, J. Ye, J. C. Linehan, B. J. Graziano, A. Preston, E. S. Wiedner, C. C. Lu, *ACS Catal.* **2020**, *10*, 2459-2470; c) I. Fujii, K. Semba, Q.-Z. Li, S. Sakaki, Y. Nakao, *J. Am. Chem. Soc.* **2020**, *142*, 11647-11652; d) R. Yamada, N. Iwasawa, J. Takaya, *Angew. Chem. Int. Ed.* **2019**, *58*, 17251-17254; e) H. Kameo, J. Yamamoto, A. Asada, H. Nakazawa, H. Matsuzaka, D. Bourissou, *Angew. Chem. Int. Ed.* **2019**, *58*, 18783-18787; f) J. Takaya, N. Iwasawa, *J. Am. Chem. Soc.* **2017**, *139*, 6074-6077; g) W.-C. Shih, O. V. Ozerov, *J. Am. Chem. Soc.* **2017**, *139*, 17297-17300; h) J. Fajardo, J. C. Peters, *J. Am. Chem. Soc.* **2017**, *139*, 16105-16108; i) R. C. Cammarota, M. V. Vollmer, J. Xie, J. Ye, J. C. Linehan, S. A. Burgess, A. M. Appel, L. Gagliardi, C. C. Lu, *J. Am. Chem. Soc.* **2017**, *139*, 14244-14250; j) R. C. Cammarota, C. C. Lu, *J. Am. Chem. Soc.* **2015**, *137*, 12486-12489.
- [7] a) P. Heiß, J. Hornung, C. Gemel, R. A. Fischer, *Chem. Commun.* **2022**, *58*, 4332-4335; b) M. Muhr, J. Hornung, J. Weßing, C. Jandl, C. Gemel, R. A. Fischer, *Inorg. Chem.* **2020**, *59*, 5086-5092; c) M. Molon, C. Gemel, P. Jerabek, L. Trombach, G. Frenking, R. A. Fischer, *Inorg. Chem.* **2014**, *53*, 10403-10411.
- [8] J. F. Hartwig, *Organotransition metal chemistry: from bonding to catalysis*, University Science Books, **2010**.
- [9] a) H. Zea, K. Lester, A. K. Datye, E. Rightor, R. Gulotty, W. Waterman, M. Smith, *Appl. Catal. A: Gen.* **2005**, *282*, 237-245; b) C. N. Thanh, B. Didillon, P. Sarrazin, C. Cameron, *U.S. Patent 6054409A* **2000**.
- [10] a) M. A. Rahim, J. Tang, A. J. Christofferson, P. V. Kumar, N. Meftahi, F. Centurion, Z. Cao, J. Tang, M. Baharfar, M. Mayyas, F.-M. Allieux, P. Koshy, T. Daeneke, C. F. McConville, R. B. Kaner, S. P. Russo, K. Kalantar-Zadeh, *Nat. Chem.* **2022**, DOI: 10.1038/s41557-022-00965-6; b) J. Prinz, C. A. Pignedoli, Q. S. Stöckl, M. Armbrüster, H. Brune, O. Gröning, R. Widmer, D. Passerone, *J. Am. Chem. Soc.* **2014**, *136*, 11792-11798; c) K. Kovnir, M. Armbrüster, D. Teschner, T. V. Venkov, F. C. Jentoft, A. Knop-Gericke, Y. Grin, R. Schlögl, *Sci. Technol. Adv. Mater.* **2007**, *8*, 420-427.
- [11] a) Y. Cao, H. Zhang, S. Ji, Z. Sui, Z. Jiang, D. Wang, F. Zaera, X. Zhou, X. Duan, Y. Li, *Angew. Chem. Int. Ed.* **2020**, *59*, 11647-11652; b) K. Schutte, A. Doddi, C. Kroll, H. Meyer, C. Wiktor, C. Gemel, G. van Tendeloo, R. A. Fischer, C. Janiak, *Nanoscale* **2014**, *6*, 5532-5544; c) C. Li, Y. Chen, S. Zhang, J. Zhou, F. Wang, S. He, M. Wei, D. G. Evans, X. Duan, *ChemCatChem* **2014**, *6*, 824-831; d) F. Studt, F. Abild-

- Pedersen, T. Bligaard, R. Z. Sørensen, C. H. Christensen, J. K. Nørskov, *Science* **2008**, *320*, 1320-1322.
- [12] A. Seifert, G. Linti, *Eur. J. Inorg. Chem.* **2007**, *2007*, 5080-5086.
- [13] a) A. Seifert, G. Linti, *Inorg. Chem.* **2008**, *47*, 11398-11404; b) M. Muhr, P. Heiß, M. Schütz, R. Bühler, C. Gemel, M. H. Linden, H. B. Linden, R. A. Fischer, *Dalton Trans.* **2021**, *50*, 9031-9036.
- [14] J. H. J. Berthel, M. W. Kuntze-Fechner, U. Radius, *Eur. J. Inorg. Chem.* **2019**, *2019*, 2618-2623.
- [15] J. C. Calabrese, L. F. Dahl, A. Cavalieri, P. Chini, G. Longoni, S. Martinengo, *J. Am. Chem. Soc.* **1974**, *96*, 2616-2618.
- [16] a) J. Hornung, J. Weßing, P. Jerabek, C. Gemel, A. Pöthig, G. Frenking, R. A. Fischer, *Inorg. Chem.* **2018**, *57*, 12657-12664; b) T. Cadenbach, C. Gemel, R. Schmid, M. Halbherr, K. Yusenkov, M. Cokoja, R. A. Fischer, *Angew. Chem. Int. Ed.* **2009**, *48*, 3872-3876; c) T. Steinke, C. Gemel, M. Winter, R. A. Fischer, *Chem. Eur. J.* **2005**, *11*, 1636-1646; d) P. Jutzi, B. Neumann, L. O. Schebaum, A. Stammler, H.-G. Stammler, *Organometallics* **1999**, *18*, 4462-4464.
- [17] J. Y. C. Chen, A. A. Martí, N. J. Turro, K. Komatsu, Y. Murata, R. G. Lawler, *J. Phys. Chem. B* **2010**, *114*, 14689-14695.
- [18] a) D. G. Hamilton, R. H. Crabtree, *J. Am. Chem. Soc.* **1988**, *110*, 4126-4133; b) J. Campos, L. S. Sharninghausen, R. H. Crabtree, D. Balcells, *Angew. Chem. Int. Ed.* **2014**, *53*, 12808-12811.
- [19] a) M.-M. Zhang, X.-Y. Dong, Z.-Y. Wang, H.-Y. Li, S.-J. Li, X. Zhao, S.-Q. Zang, *Angew. Chem. Int. Ed.* **2020**, *59*, 10052-10058; b) X.-K. Wan, X.-L. Cheng, Q. Tang, Y.-Z. Han, G. Hu, D.-e. Jiang, Q.-M. Wang, *J. Am. Chem. Soc.* **2017**, *139*, 9451-9454; c) S.-D. Bian, H.-B. Wu, Q.-M. Wang, *Angew. Chem. Int. Ed.* **2009**, *48*, 5363-5365.
- [20] a) J. Hornung, M. Muhr, C. Gemel, R. A. Fischer, *Dalton Trans.* **2019**, *48*, 11743-11748. b) C. Ganesamoorthy, J. Weßing, C. Kroll, R. W. Seidel, C. Gemel, R. A. Fischer, *Angew. Chem. Int. Ed.* **2014**, *53*, 7943-7947; c) M. Schütz, C. Gemel, M. Muhr, C. Jandl, S. Kahlal, J.-Y. Saillard, R. A. Fischer, *Chem. Sci.* **2021**, *12*, 6588-6599; d) O. P. E. Townrow, C. Chung, S. A. Macgregor, A. S. Weller, J. M. Goicoechea, *J. Am. Chem. Soc.* **2020**, *142*, 18330-18335; e) O. P. E. Townrow, S. B. Duckett, A. S. Weller, J. M. Goicoechea, *Chem. Sci.* **2022**, *13*, 7626-7633.

2.5.4 Additional Data and Information

Synthesis of **1**



A solution of 84 mg $\text{Ni}(\text{cod})_2$ (3 eq, 0.306 mmol) and 150 mg GaTMP (7 eq, 0.716 mmol) in 10 ml toluene is heated to $60\text{ }^\circ\text{C}$ for 14 hours accompanied by a colour change of the solution from brown-yellow to purple. The solvent is removed under reduced pressure, the residue is extracted with *n*-hexane and cannula filtered. Dark purple crystals are grown from saturated solution at $-30\text{ }^\circ\text{C}$ and 52 mg (0.0316 mmol, 31 %) are isolated after cannula filtration. By subsequent recrystallization from the filtrate, the yield can be increased up to 68 mg (0.0413 mmol, 41 %). **$^1\text{H NMR}$** (400 MHz, 298 K, toluene- d_8): δ [ppm] = 1.77 ppm (36 H, s, methyl, terminal), δ = 1.71 ppm (14 H, m, γ , terminal + bridging), δ = 1.61 ppm (48 H, s, methyl, bridging), δ = 1.54 ppm (12 H, m, β , terminal), δ = 1.44 ppm (16 H, m, β , bridging). **$^{13}\text{C NMR}$** (101 MHz, 298 K, toluene- d_8): δ [ppm] = 56.3 (α , bridging), 55.5 (α , terminal), 41.0 (β , bridging), 40.5 (β , terminal), 36.1 (methyl, bridging), 35.1 (methyl, terminal), 19.4 (γ , bridging + terminal). **LIFDI-MS** m/z [a. u.] = 1645.2854 (calc.: 1645.2848) [M] $^+$; 1505.1409 (calc.: 1505.1409) [M-TMP] $^+$; 1434.2157 (calc.: 1434.2162) [M-GaTMP] $^+$; m/z = 1225.1462 (calc.: 1225.1467) [M-2GaTMP] $^+$, 1014.0781 (calc.: 1014.0786) [M-3GaTMP] $^+$.

Alternative Synthesis of $[\text{Ga}_4(\text{TMP})_4]$ – Transmetalation.

0.79 g LiTMP (5.37 mmol, 1.1 eq.) were added to a solution of 1.00 g GaCp^* (4.88 mmol, 1.0 eq.) in 60 mL THF, resulting in an orange to brown suspension. The reaction mixture was stirred for 5 h at room temperature and the solvent was removed under reduced pressure afterwards. Subsequently, the residue was extracted with 100 mL *n*-hexane and separated by means of cannula filtration. The resulting dark brown solution was concentrated under reduced pressure and stored over night at $-80\text{ }^\circ\text{C}$. The resulting crystals were separated using Whatman filtration and dried *in vacuo*. Afterwards, the crystals were recrystallized in *n*-hexane and again dried *in vacuo*, giving Ga_4TMP_4 as reddish-brown crystals (0.551 g, 54%). **$^1\text{H NMR}$** (400 MHz, benzene- d_6 , 298 K): δ (ppm) = 1.67 (s, 12H), 1.59 – 1.53 (m, 2H), 1.36 – 1.29 (m, 4H).

General Procedure for Reactions with H_2 .

5 mg of **1** were dissolved in 0.4 mL toluene- d_8 in a (high-pressure) J-Young NMR tube. The reaction solution was degassed by freeze-pump-thaw and was pressurized with 0.5 – 3.0 bar at $25\text{ }^\circ\text{C}$. Further handling dependent on the individual experiment.

2D NOESY and ROESY

The two-dimensional experiments were recorded at -80 °C at Avance III NMR spectrometers (Bruker BioSpin GmbH) operating at a spectrometer frequency of 400 MHz equipped with 5 mm direct PABBO/BB/19F-1H/D probe with single axis Z gradient capabilities. Low temperature measurements (-80 °C) were performed using a BCU I cooling unit. Temperature correction was applied using the temperature calibration obtained with an NMR thermometer (4% methanol-*d*₄ in methanol). Spectral processing was performed with MestReNova (v.12.0.0) NMR processing software from Mestrelab Research. A 90° shifted sine-square multiplication and an exponential window of 2.1 Hz in both dimensions prior to FT was applied. Zero filling in F1 has been used to yield a final matrix of 1K x 1K real points in case of NOESY and 2K x 2K in case of ROESY. Automatic phase correction as well as baseline correction was applied in both dimensions.

2D NOESY spectra were recorded with a phase-sensitive pulse sequence (noesygp_{pp}h_{pp}) with varying mixing times (50, 100, 200, 300 ms) from the Bruker pulse program library. Data acquisition was performed with 1024 (F2) x 256 (F1) data points in States-TPPI mode. The recycling delay was 2.0 s and 4 transients per increment were applied at a sweep width of 12 kHz in both dimensions resulting in an acquisition time of 0.1204 s.

2D ROESY spectrum was recorded with a phase-sensitive pulse sequence (roesyph_{pp}.2) from the Bruker pulse program library. The mixing time was set to 50 ms for the spinlock pulse. Data acquisition was performed with 2048 (F2) x 64 (F1) data points in States-TPPI mode. The recycling delay was 2.0 s and 128 transients per increment were applied at a sweep width of 12 kHz in both dimensions resulting in an acquisition time of 0.1204 s.

Crystallography

Deposition Number 2180123 (CCDC)

Diffraction operator C. Jandl
Scan speed 1-2 s per frame
dx 50 mm
2667 frames measured in 11 data sets
phi-scans with delta_phi = 0.5
omega-scans with delta_omega = 0.5
shutterless mode

Crystal data

C₆₃H₁₂₆Ga₇N₇Ni₃·C₇H₈

M_r = 1737.96

D_x = 1.426 Mg m⁻³

Monoclinic, $P2_1/n$

Melting point: ? K

Hall symbol: -P 2yn

Mo $K\alpha$ radiation, $\lambda = \underline{0.71073}$ Å

$a = \underline{16.1809 (15)}$ Å

Cell parameters from 9639 reflections

$b = \underline{20.5515 (18)}$ Å

$\theta = \underline{2.4-26.4}^\circ$

$c = \underline{25.248 (2)}$ Å

$\mu = \underline{3.01}$ mm⁻¹

$\beta = \underline{105.365 (3)}^\circ$

$T = \underline{100}$ K

$V = \underline{8095.9 (12)}$ Å³

Fragment, black

$Z = \underline{4}$

0.30 × 0.25 × 0.17 mm

$F(000) = \underline{3616}$

Data collection

Bruker D8 Venture
diffractometer

15943 independent reflections

Radiation source: TXS rotating anode

14054 reflections with $I > 2\sigma(I)$

Helios optic monochromator

$R_{\text{int}} = \underline{0.035}$

Detector resolution: 16 pixels mm⁻¹

$\theta_{\text{max}} = \underline{26.0}^\circ$, $\theta_{\text{min}} = \underline{2.0}^\circ$

phi- and ω -rotation scans

$h = \underline{-19}$ 19

Absorption correction: multi-scan
SADABS 2016/2, Bruker

$k = \underline{-25}$ 25

$T_{\text{min}} = \underline{0.658}$, $T_{\text{max}} = \underline{0.745}$

$l = \underline{-31}$ 31

258187 measured reflections

Refinement

Refinement on F^2

Secondary atom site location:
difference Fourier map

Least-squares matrix: full

Hydrogen site location: inferred
from neighbouring sites

$R[F^2 > 2\sigma(F^2)] = \underline{0.019}$

H-atom parameters constrained

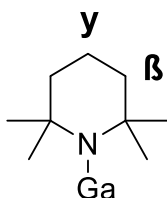
$wR(F^2) = \underline{0.048}$	$W = 1/[\Sigma^2(FO^2) + (0.0207P)^2 + 5.5671P]$ WHERE $P = (FO^2 + 2FC^2)/3$
$S = \underline{1.05}$	$(\Delta/\sigma)_{\max} = \underline{0.003}$
$\underline{15943}$ reflections	$\Delta\rho_{\max} = \underline{0.49} \text{ e } \text{\AA}^{-3}$
$\underline{878}$ parameters	$\Delta\rho_{\min} = \underline{-0.43} \text{ e } \text{\AA}^{-3}$
$\underline{267}$ restraints	Extinction correction: <u>none</u>
$\underline{0}$ constraints	Extinction coefficient: $-$
Primary atom site location: <u>iterative</u>	

Density Functional Theory Calculations

Density Functional Theory (DFT) calculations^[S9] were carried out with the use of the Amsterdam Density Functional code (ADF2017)^[S10] with the addition of Grimme's D3 empirical corrections^[S11] in order to consider dispersion effects. The triple- ξ Slater basis set plus two polarization functions (STO-TZP),^[S12] was used, together with the Becke-Perdew (BP86)^[S13-14] exchange-correlation functional. All the optimized structures were confirmed as true minima on their potential energy surface by analytical vibration frequency calculations.

NMR Spectra

Each TMP gives a set of three signals: four methyl groups (12H, s), two CH₂ groups (4H, m) in β -position and one CH₂ group (2H, m) in γ -position. The three terminal GaTMP ligands of **1** are observed at $\delta = 1.77$ ppm (36 H, s, methyl), $\delta = 1.71$ ppm (6 H, m, γ) and $\delta = 1.54$ ppm (12 H, m, β). The four bridging GaTMP ligands signals arise at $\delta = 1.71$ ppm (8 H, m, γ), $\delta = 1.61$ ppm (48 H, s, methyl) and $\delta = 1.44$ ppm (16 H, m, β).



NMR Spectra of **1**.

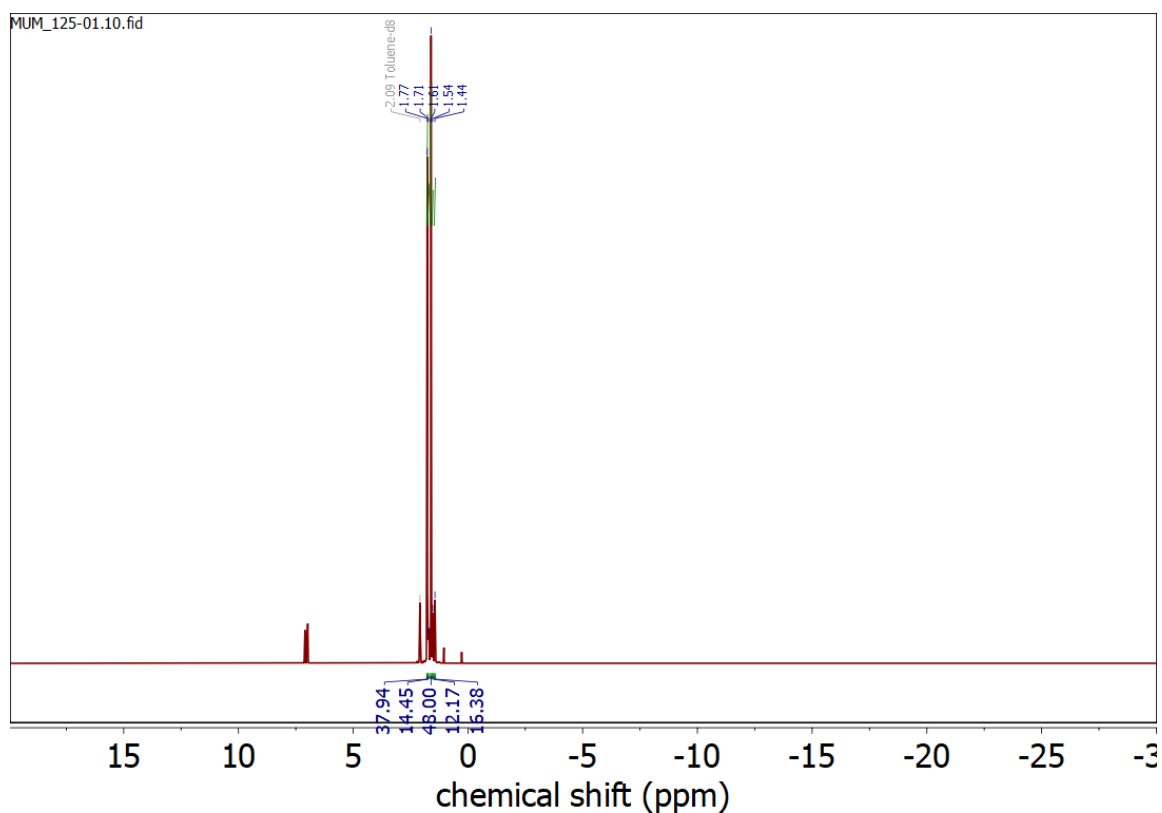


Figure S1: ¹H NMR spectrum of **1** in toluene-d₈.

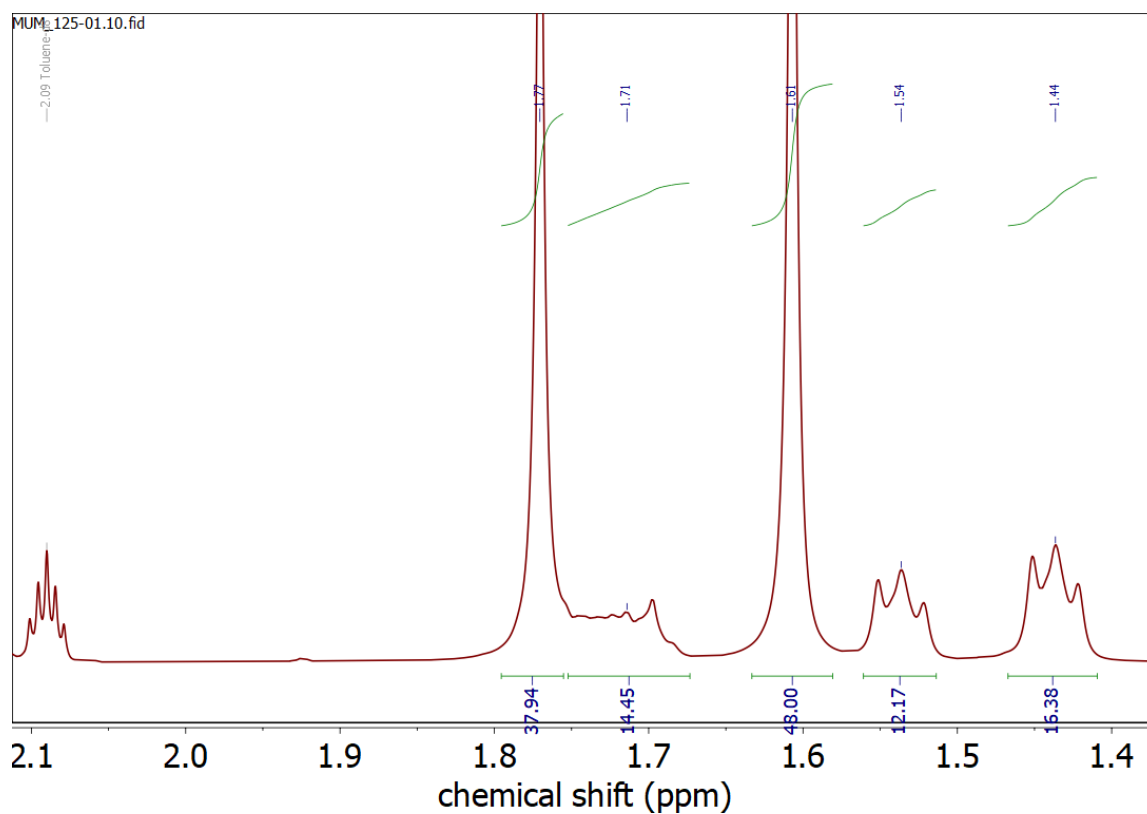


Figure S2: ^1H NMR spectrum of **1** in toluene- d_8 – excerpt of aliphatic region.

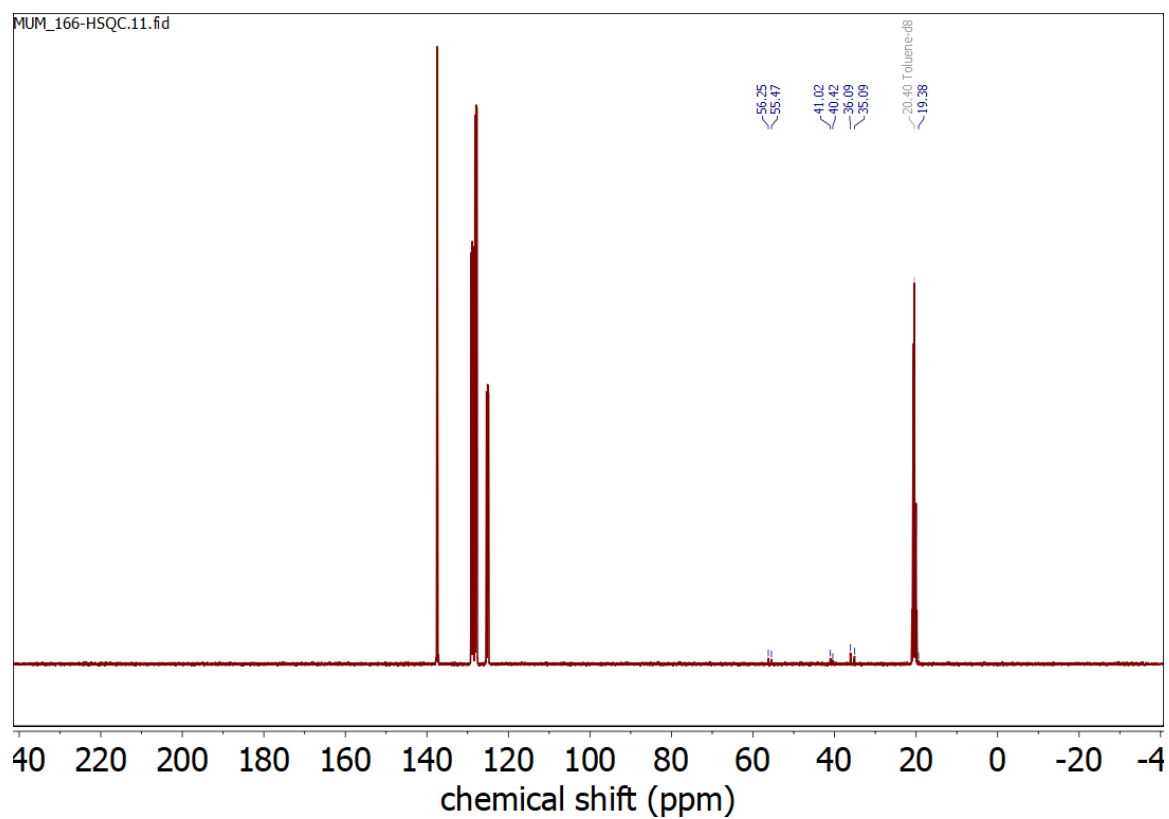


Figure S3: ^{13}C NMR spectrum of **1** in toluene- d_8 .

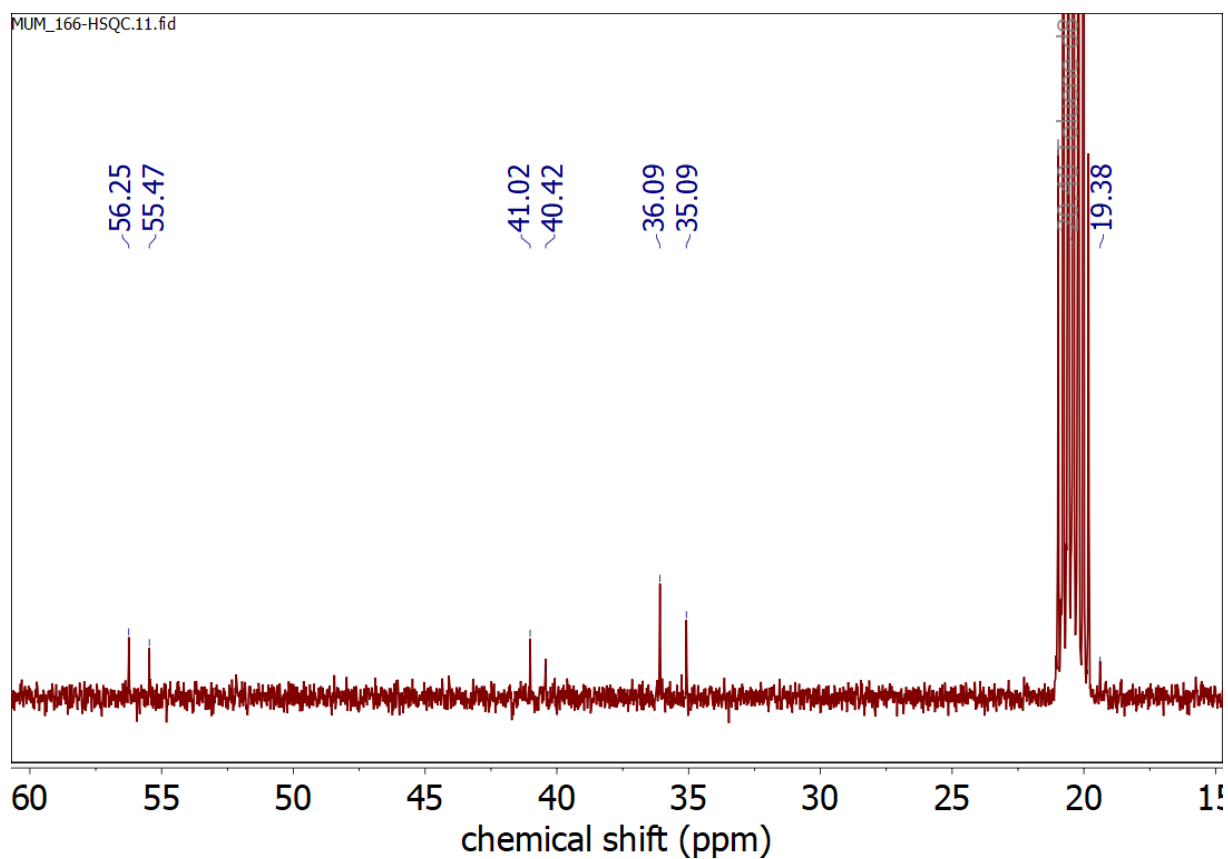


Figure S4: ^{13}C NMR spectrum of **1** in toluene- d_8 . Excerpt from 15 — 60 ppm.

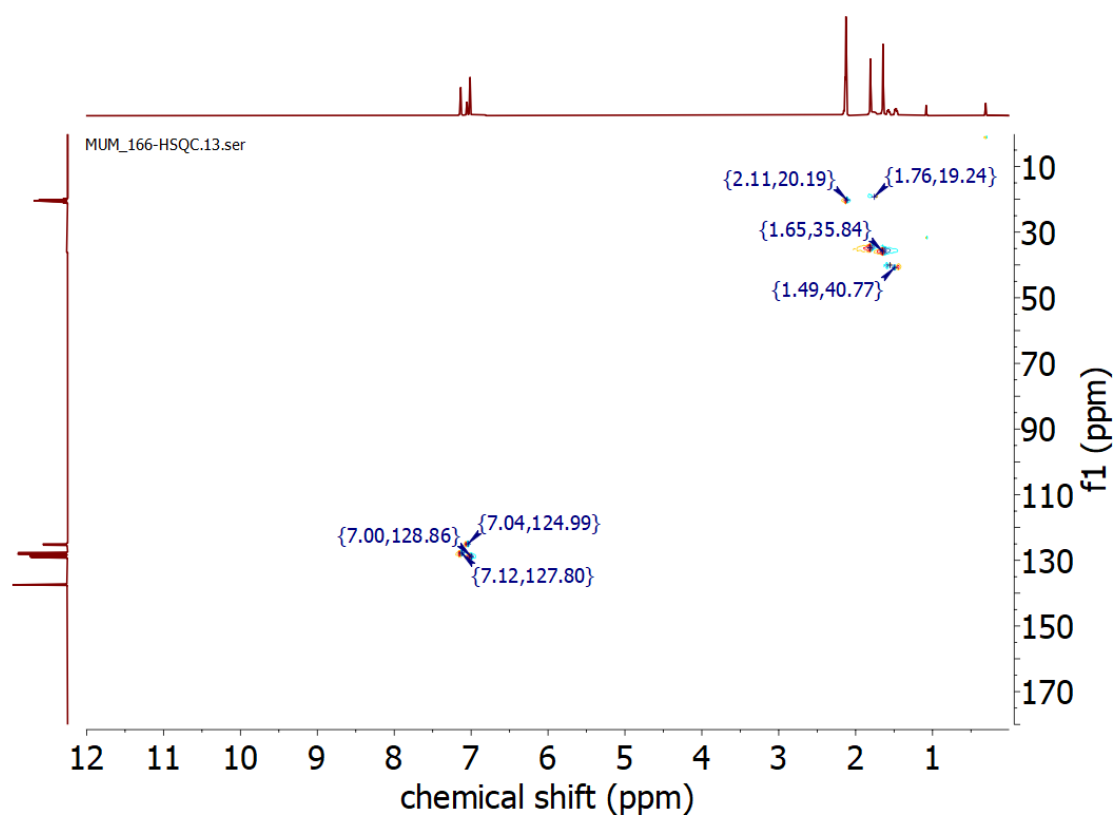


Figure S5: $^1\text{H},^{13}\text{C}$ HSQC NMR spectrum of **1** in toluene- d_8 .

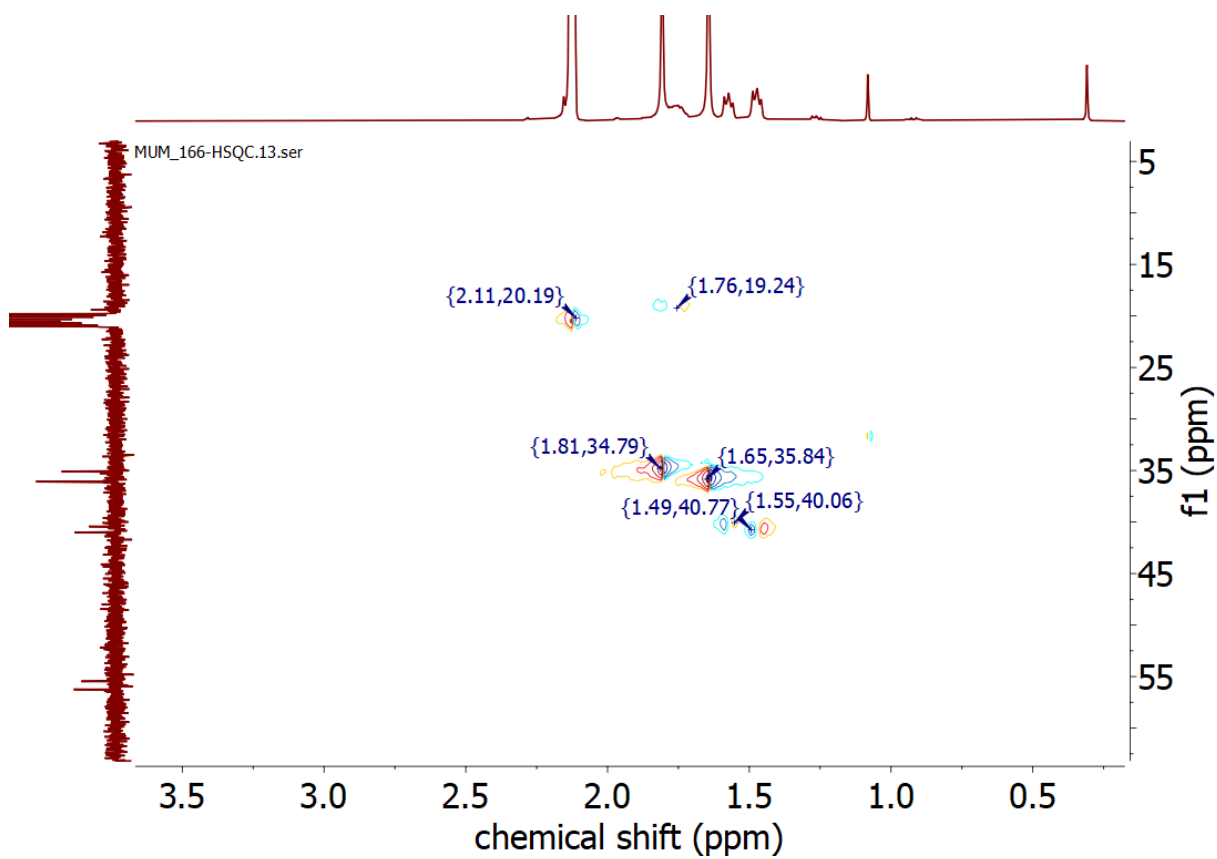


Figure S6: $^1\text{H},^{13}\text{C}$ HSQC of **1** in toluene- d_8 – excerpt.

NMR Spectra of **2**.

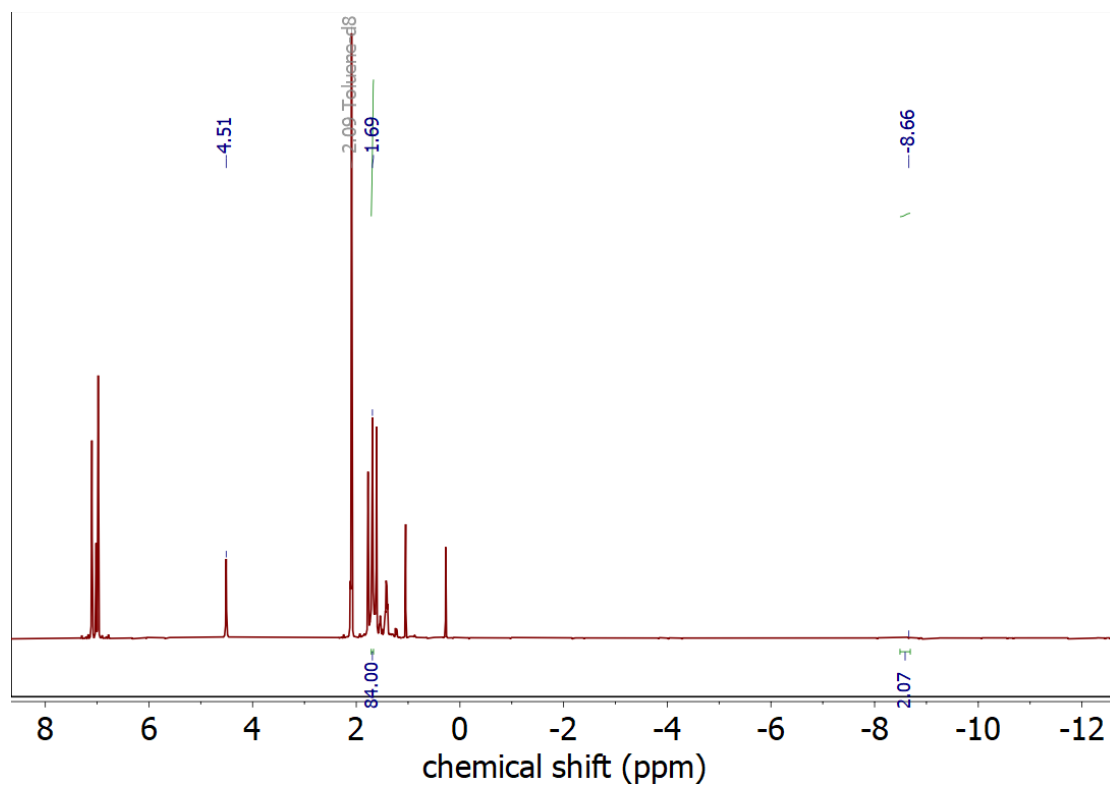


Figure S7: ^1H NMR spectrum of **2** in toluene-d_8 at room temperature.

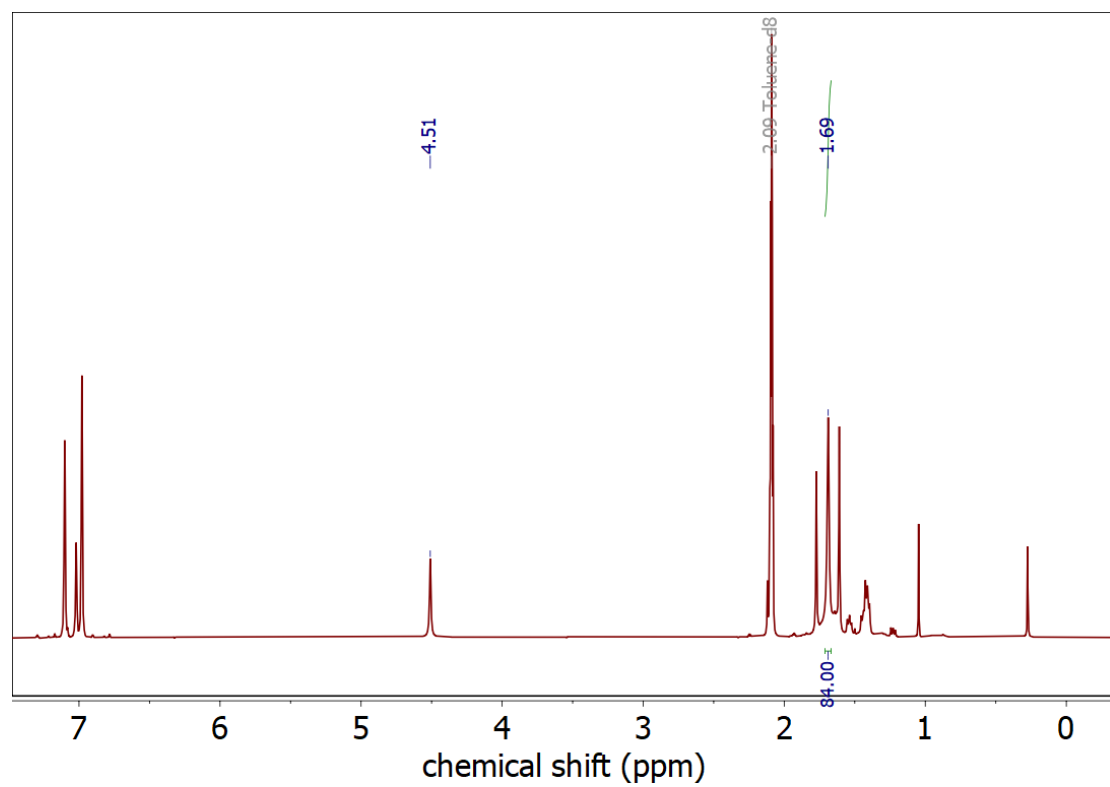


Figure S8: ^1H NMR spectrum of **2** in toluene-d_8 at r.t.

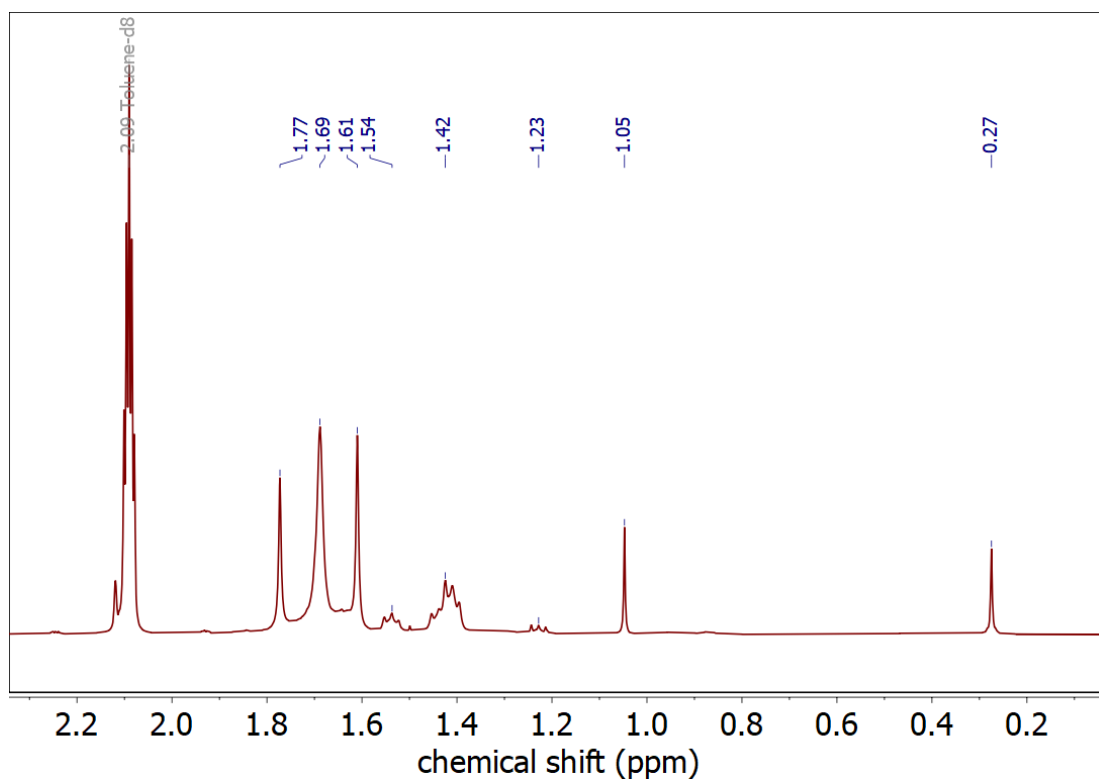


Figure S9: ¹H NMR spectrum of **2** in toluene-d₈ at r.t., aliphatic range. TMP-methyl group signal assigned to **2** at 1.69 ppm.

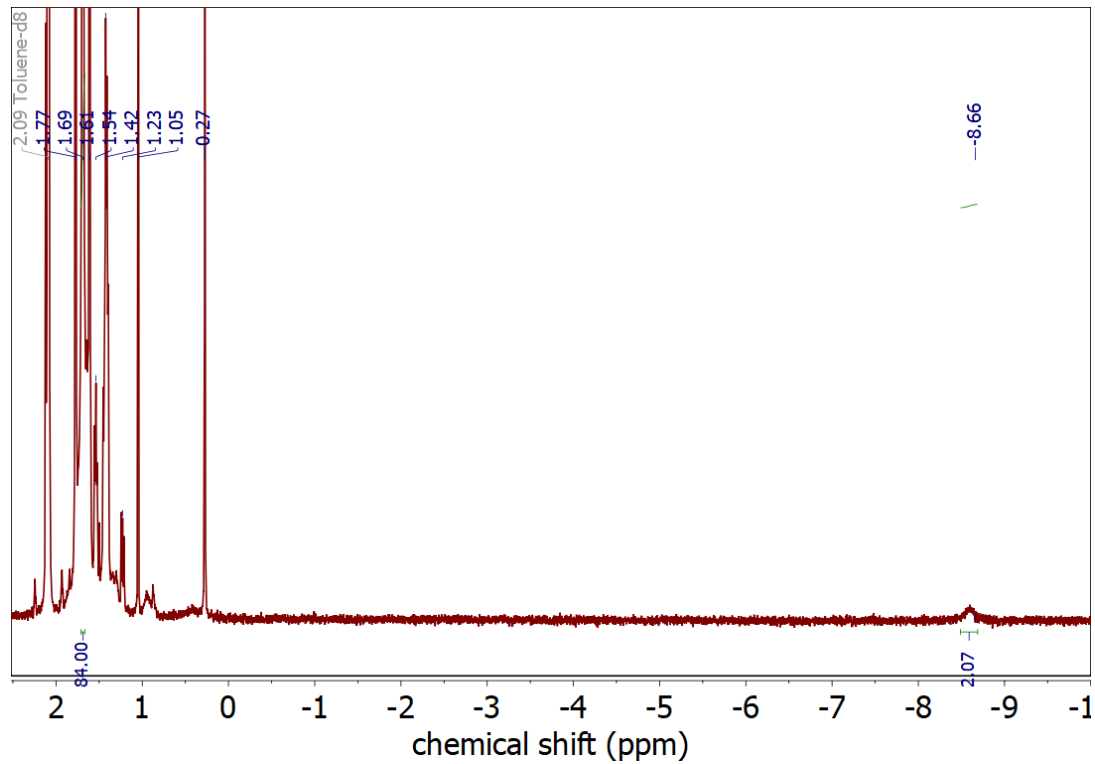


Figure S10: ¹H NMR spectrum of **2** in toluene-d₈ at r.t., showing aliphatic to hydridic region.

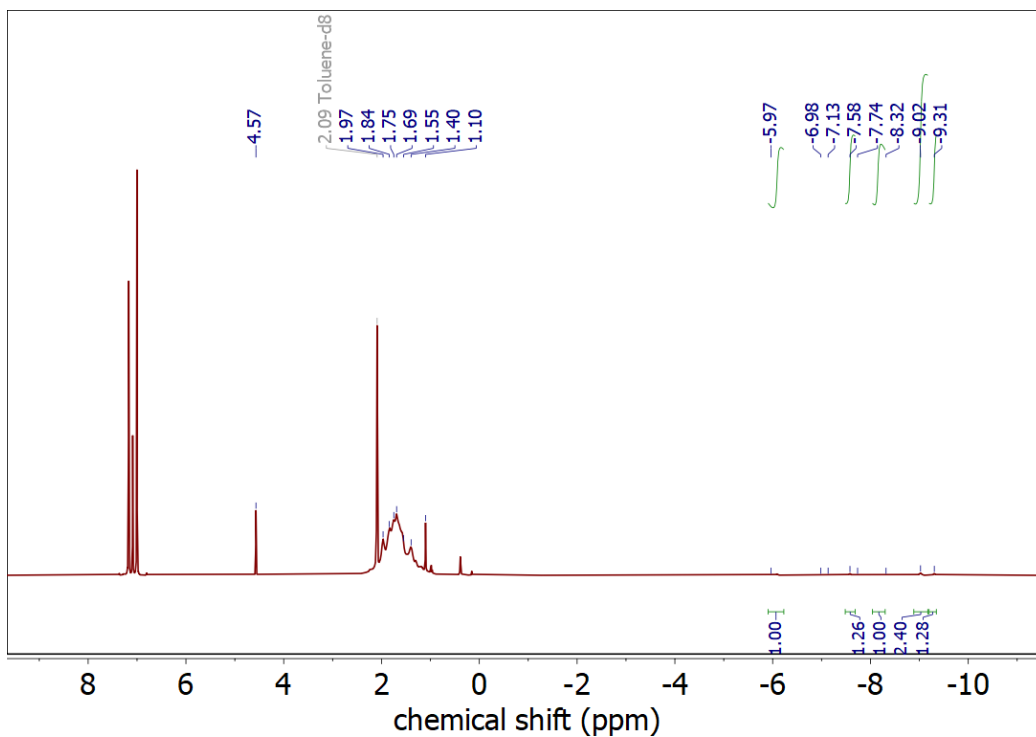


Figure S11: ^1H NMR spectrum of **2** in toluene- d_8 at $-80\text{ }^\circ\text{C}$, full range.

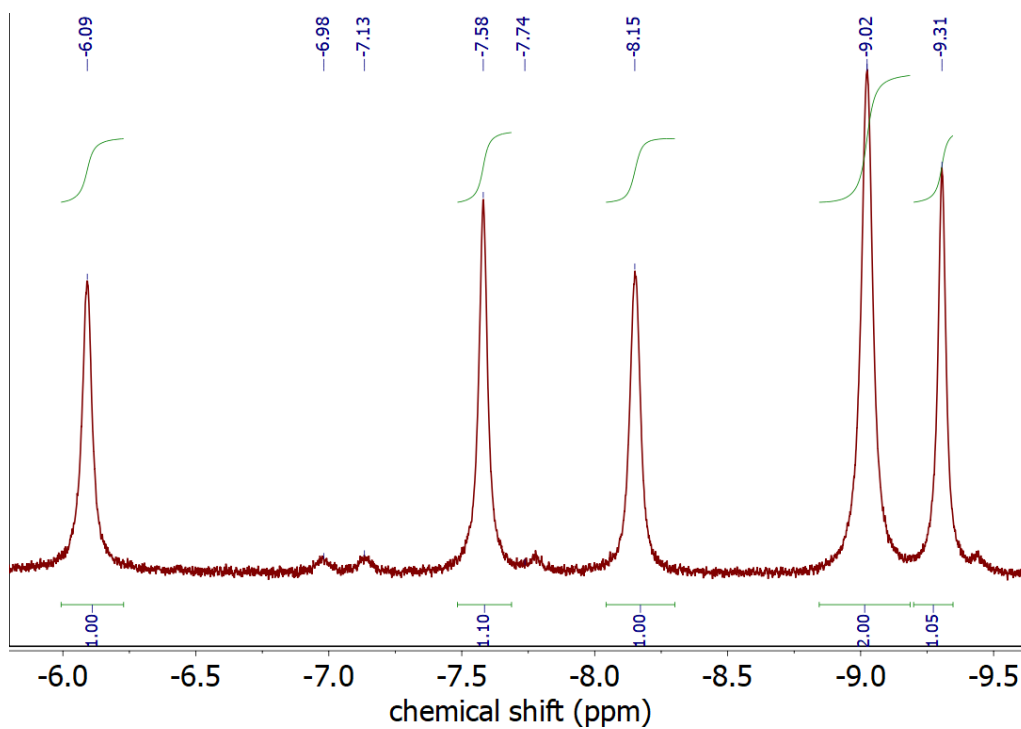


Figure S12: ^1H NMR spectrum of **2** in toluene- d_8 at $-80\text{ }^\circ\text{C}$, excerpt of hydride signal region.

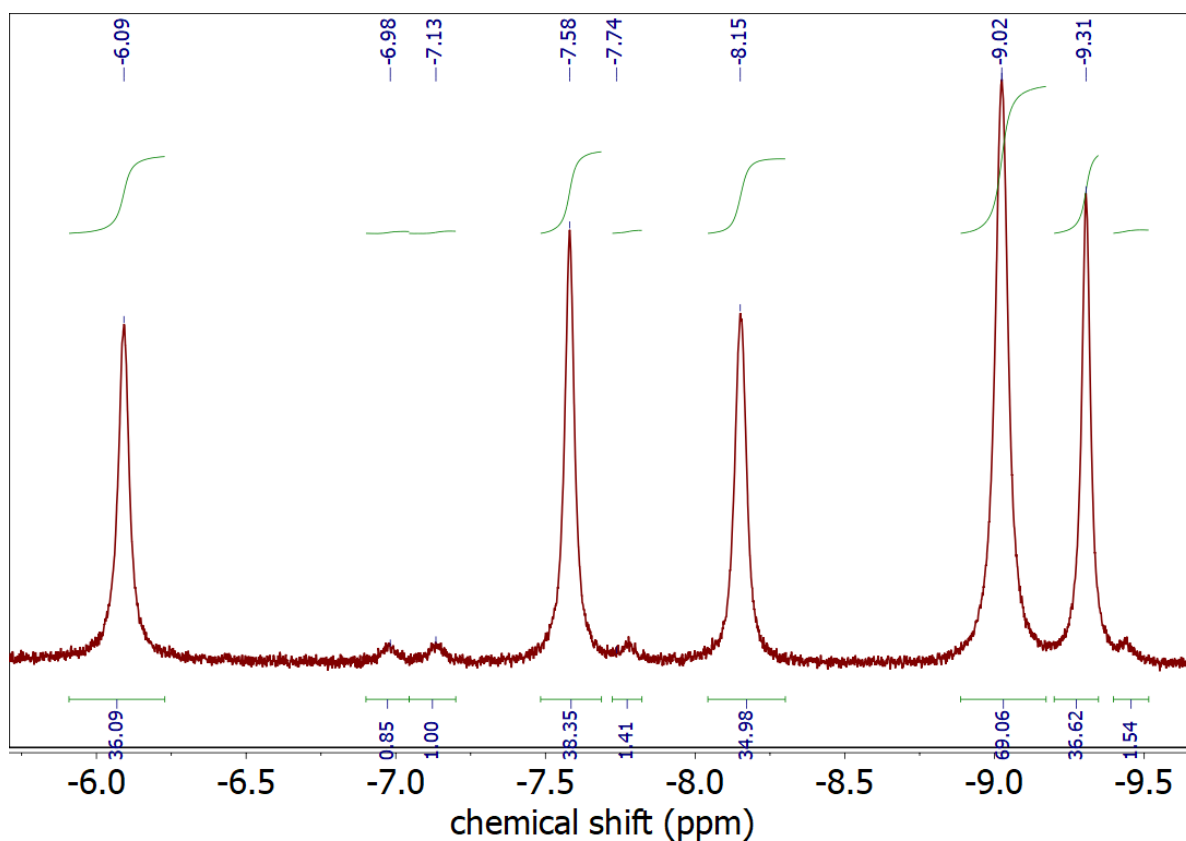


Figure S13: ^1H NMR spectrum of **2** in toluene- d_8 at $-80\text{ }^\circ\text{C}$, with focus on hexahydride integrals.

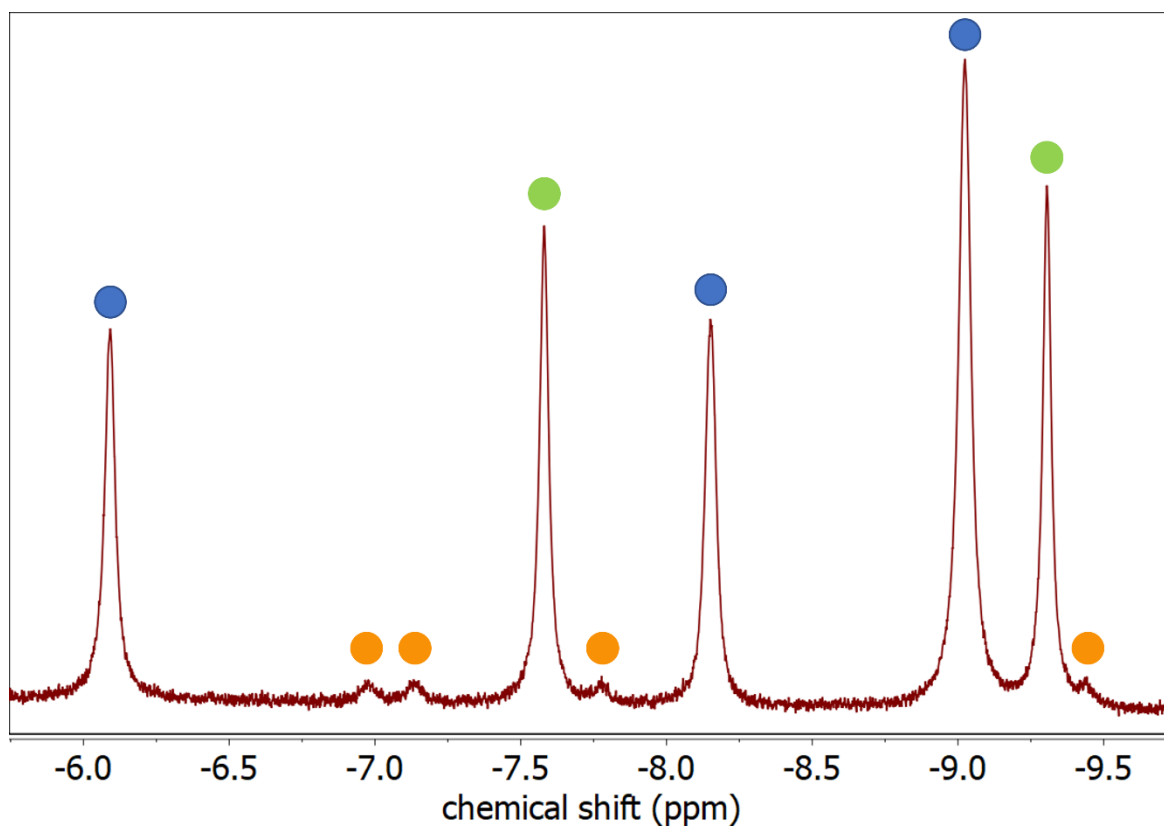


Figure S14: ^1H NMR spectrum at $-80\text{ }^\circ\text{C}$ in toluene- d_8 showing the spitting hydride signals. Assignment of peaks based on $^1\text{H}, ^1\text{H}$ COSY spectrum. Green: $\text{H}_2[\text{Ni}_3\text{Ga}_7\text{TMP}_7]$ (**2_{Di}**), blue: $\text{H}_4[\text{Ni}_3\text{Ga}_7\text{TMP}_7]$ (**2_{Tetra}**) and orange: $\text{H}_6[\text{Ni}_3\text{Ga}_7\text{TMP}_7]$ (**2_{Hexa}**).

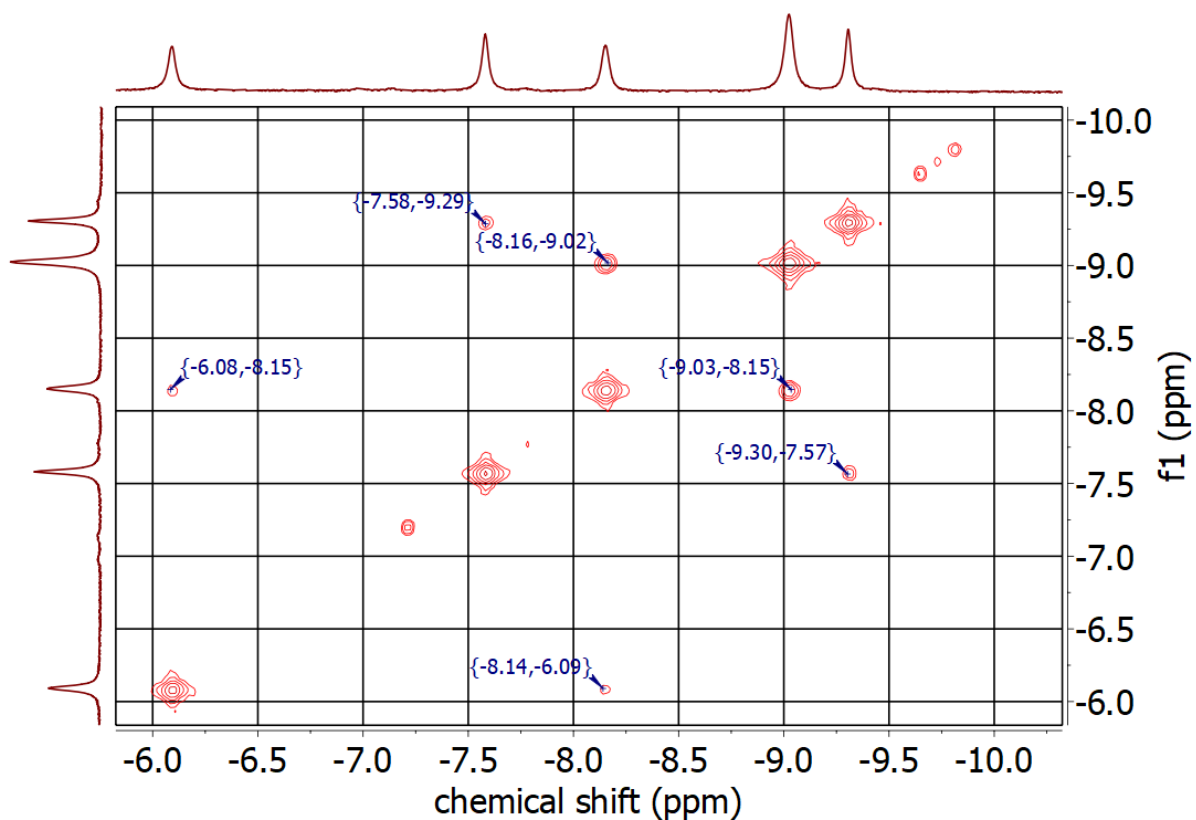


Figure S15: ^1H , ^1H COSY spectrum of **2** in toluene- d_8 at -80°C . Cross peaks marked.

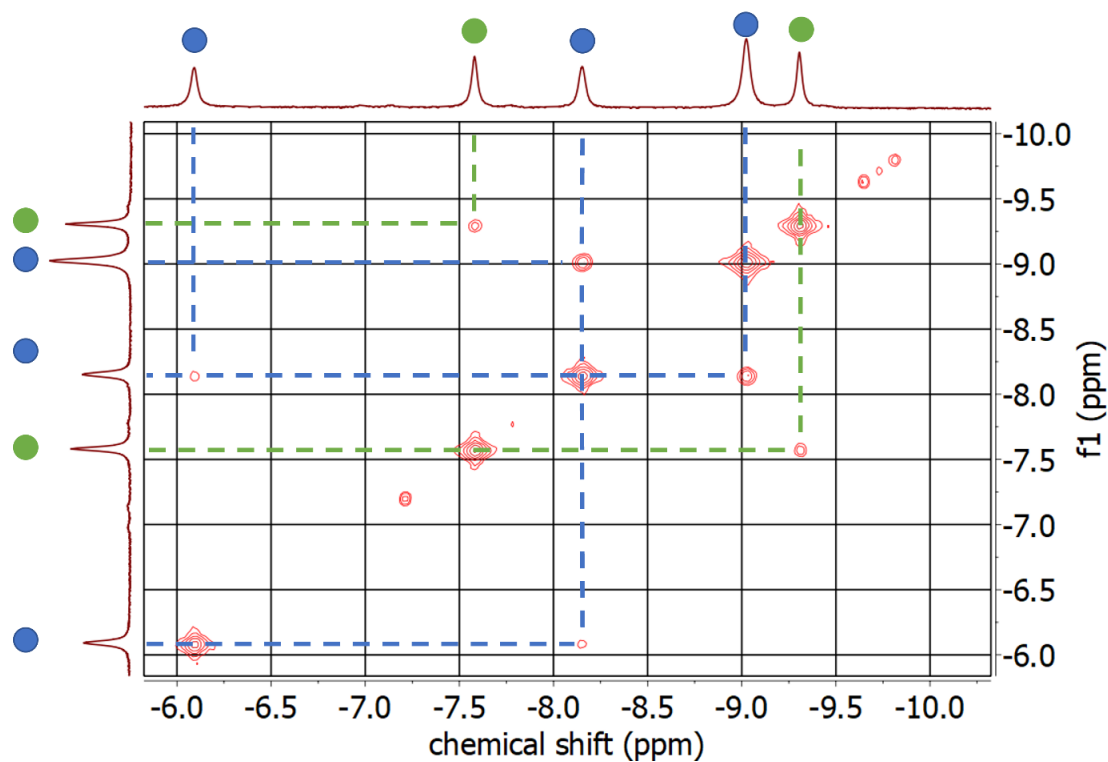


Figure S16: ^1H , ^1H COSY spectrum of **2** in toluene- d_8 at -80°C . Cross peaks assigned to signals in ^1H NMR spectrum and respective species by color. green = dihydride; blue = tetrahydride.

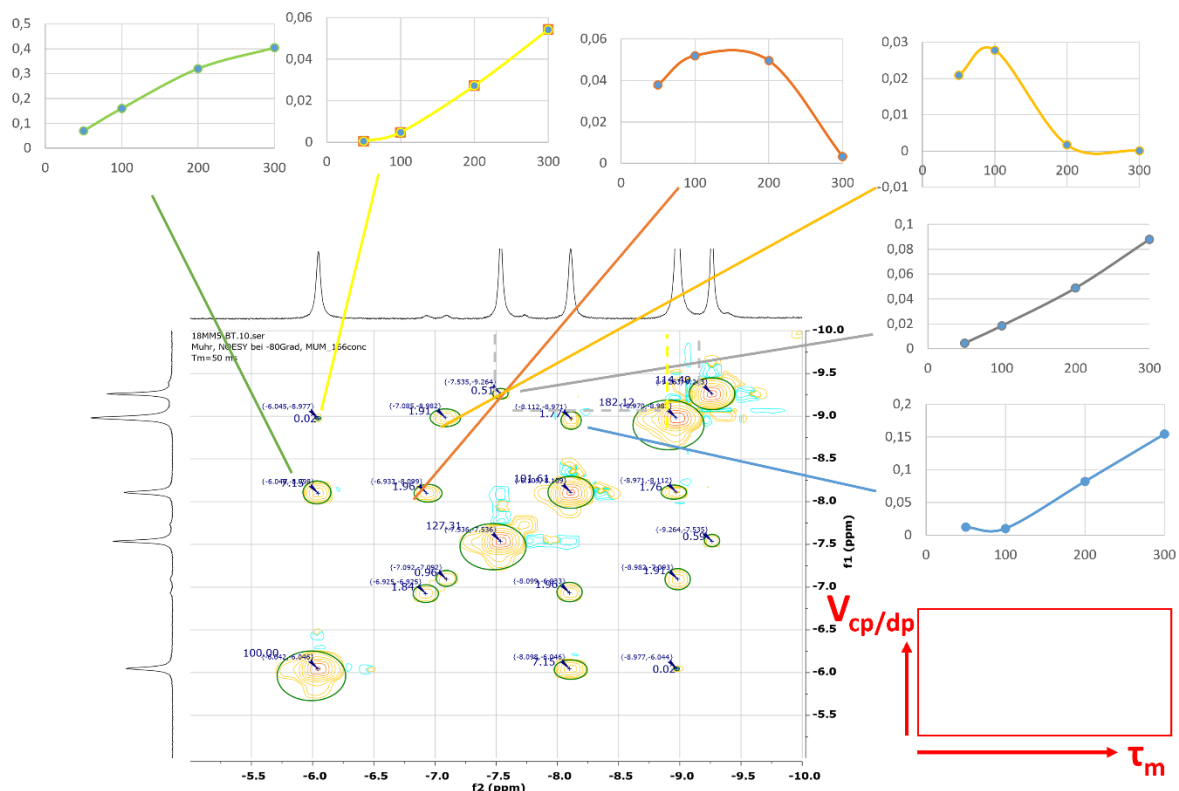


Figure S17: Phase-sensitive 2D NOESY spectrum of **2** in toluene- d_8 at -80° at a mixing time $\tau_m = 50$. Small graphs: NOE/Exchange build-up curves. Peak volume ratios cross peaks (V_{cp}) to diagonal peaks (V_{dp}) on y axis plotted against varying mixing times ($\tau_m=50, 100, 200, 300$ ms) on x axis – exemplified by red box at bottom right.

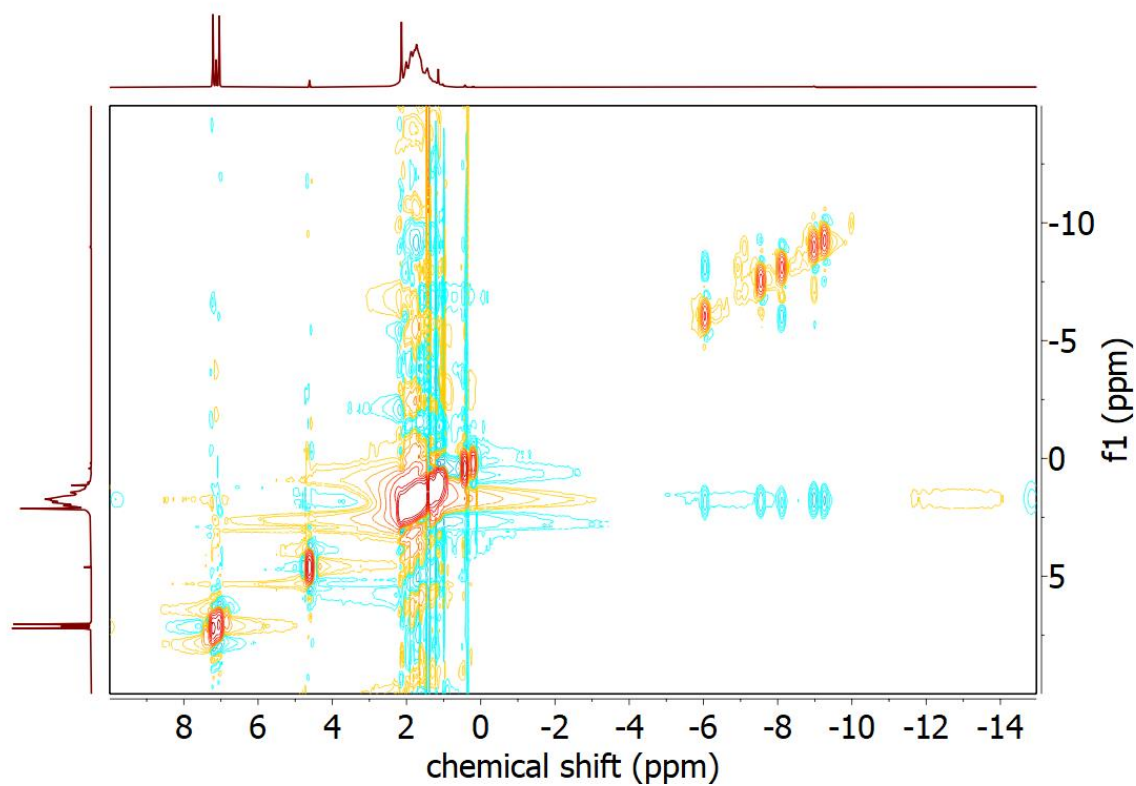


Figure S18: Phase-sensitive 2D ROESY spectrum of **2** in toluene- d_8 at -80°C .

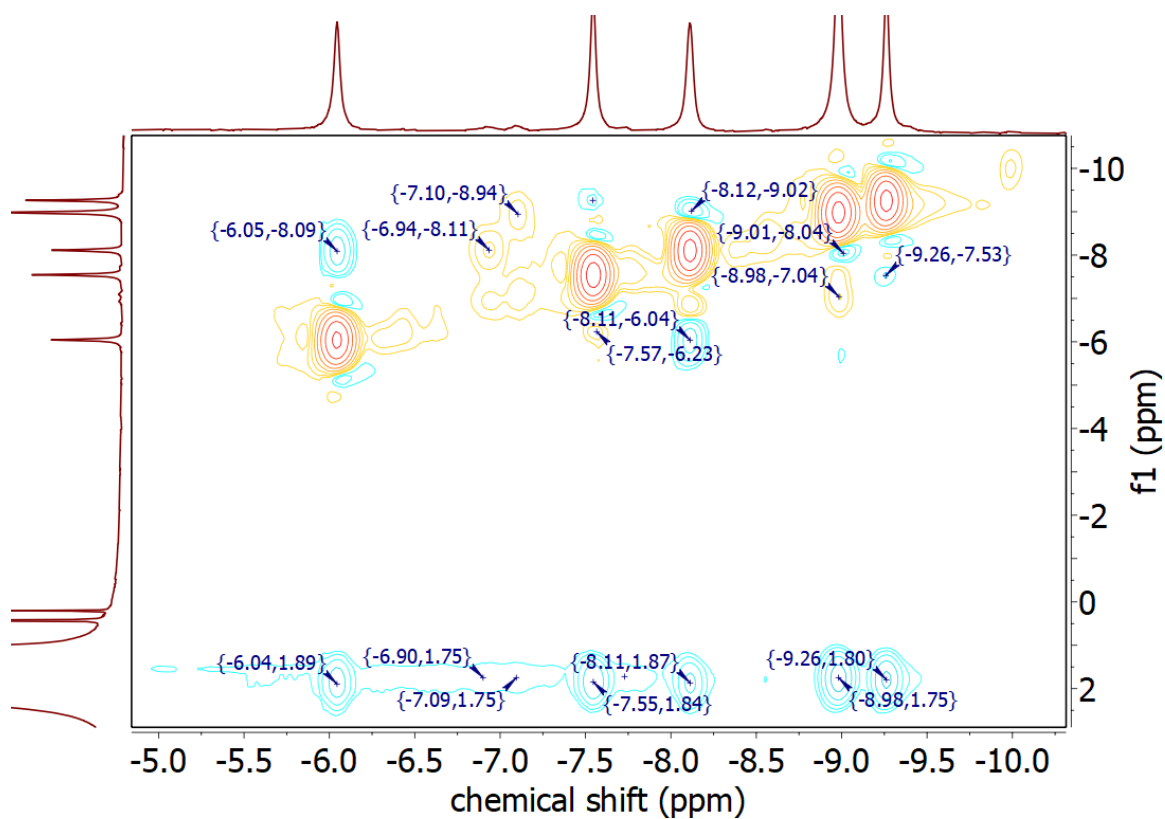


Figure S19: Excerpt of 2D ROESY spectrum of **2** in toluene- d_8 at -80 °C, showing hydride interaction. Blue – ROEs, Yellow – signals due to exchange.

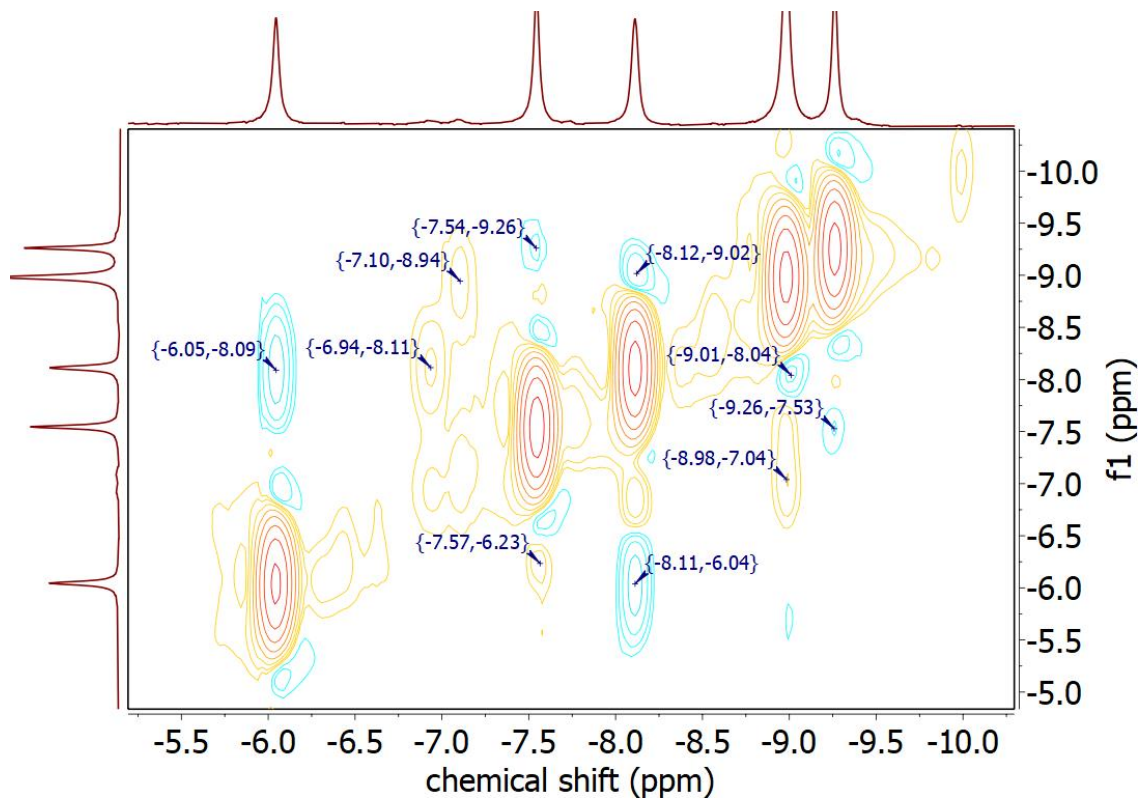


Figure S20: Excerpt of 2D ROESY spectrum of **2** in toluene- d_8 at -80 °C showing hydride interaction. Blue – ROEs, Yellow – signals due to exchange.

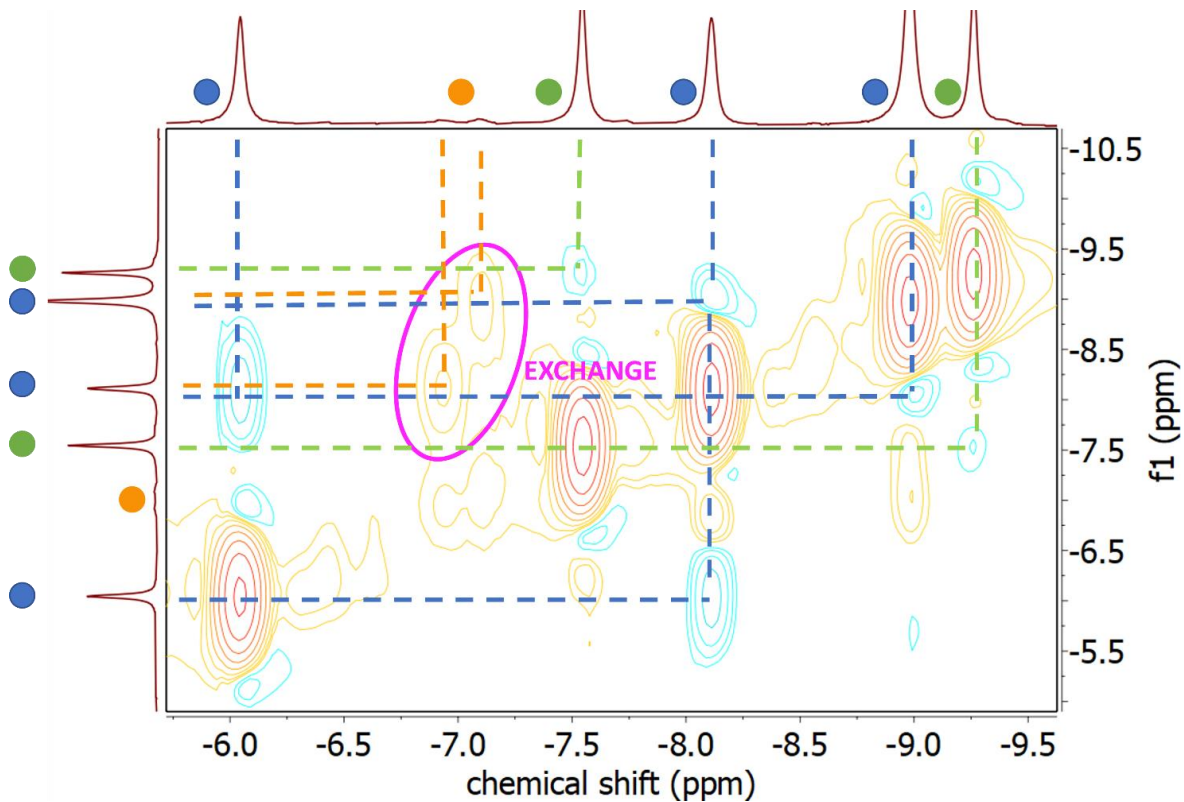


Figure S21: Excerpt of 2D ROESY spectrum of **2** in toluene- d_8 at $-80\text{ }^\circ\text{C}$. Dashed lines depict connections between 2_{Di} (green), 2_{Tetra} (blue) and suggested 2_{Hexa} (orange). Pink ellipse highlights exchange process, presumably between 2_{Tetra} and 2_{Hexa} .

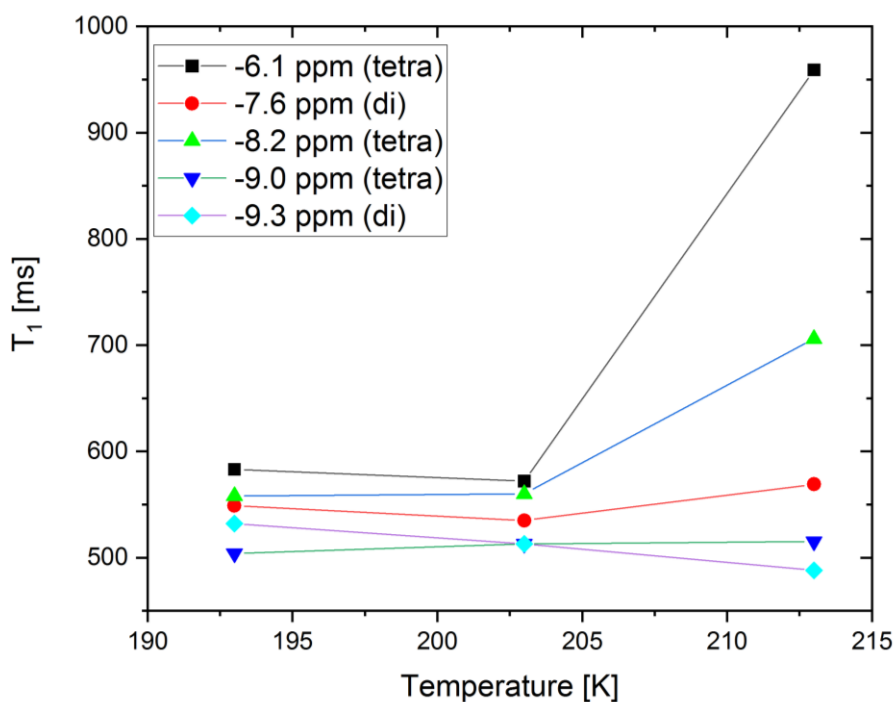


Figure S22: T_1 relaxation times at $-80\text{ }^\circ\text{C}$, $-70\text{ }^\circ\text{C}$ and $-60\text{ }^\circ\text{C}$ for each hydride peak of 2_{Di} and 2_{Tetra} . Pointing to classical hydrides.

NMR Spectra of reaction including 2.

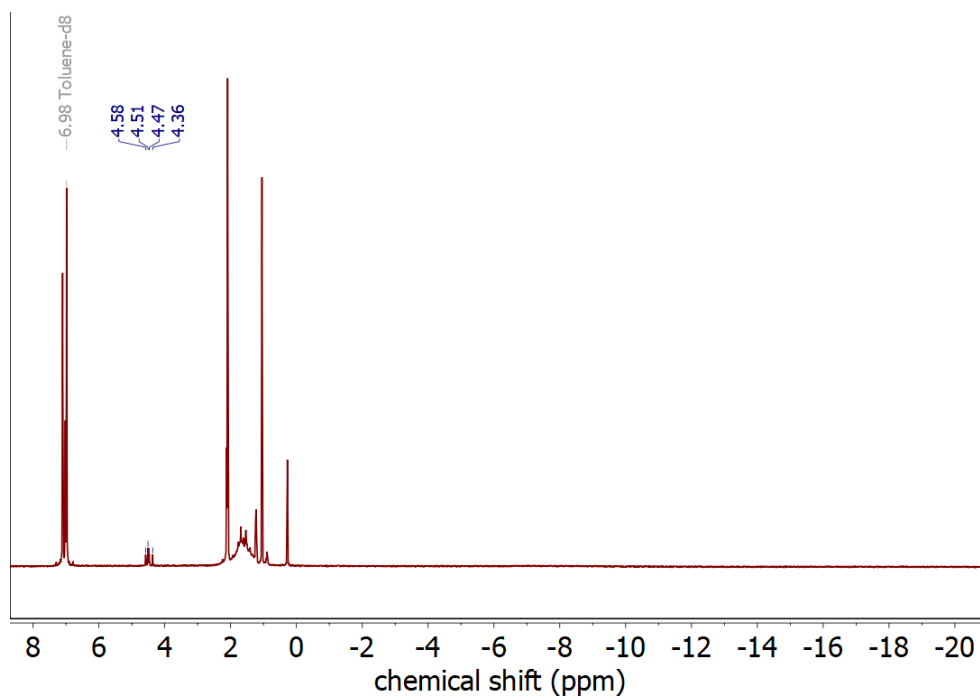


Figure S23: ^1H NMR spectrum of reaction of 1 with D_2 and H_2 in toluene-d_8 at r.t.

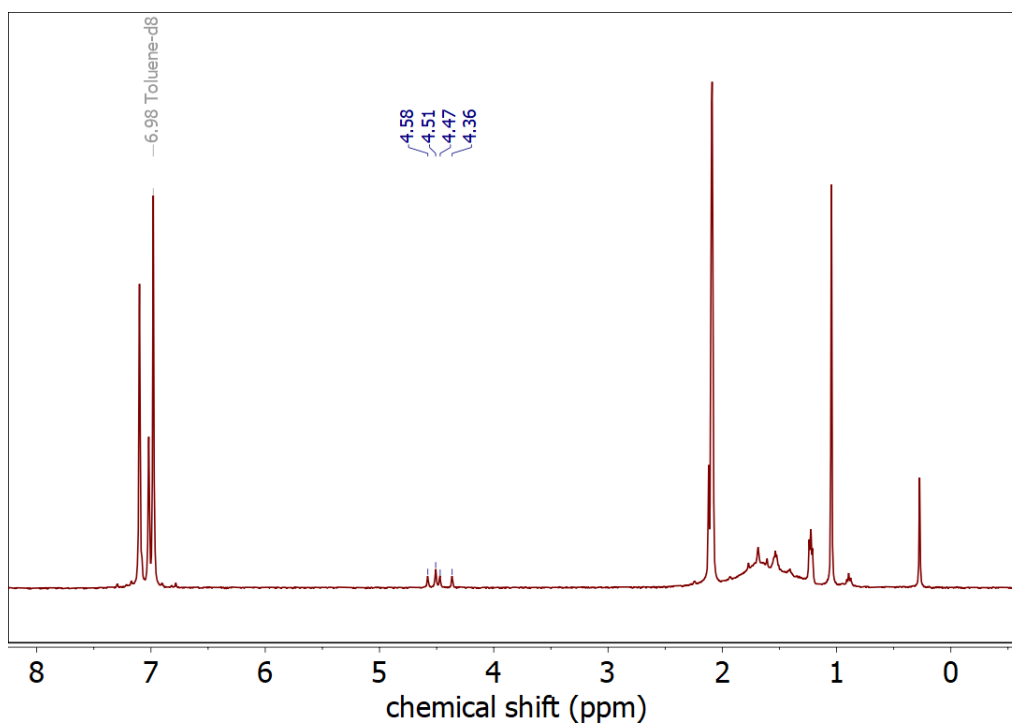


Figure S24: ^1H NMR spectrum of reaction of 1 with D_2 and H_2 in toluene-d_8 at r.t..

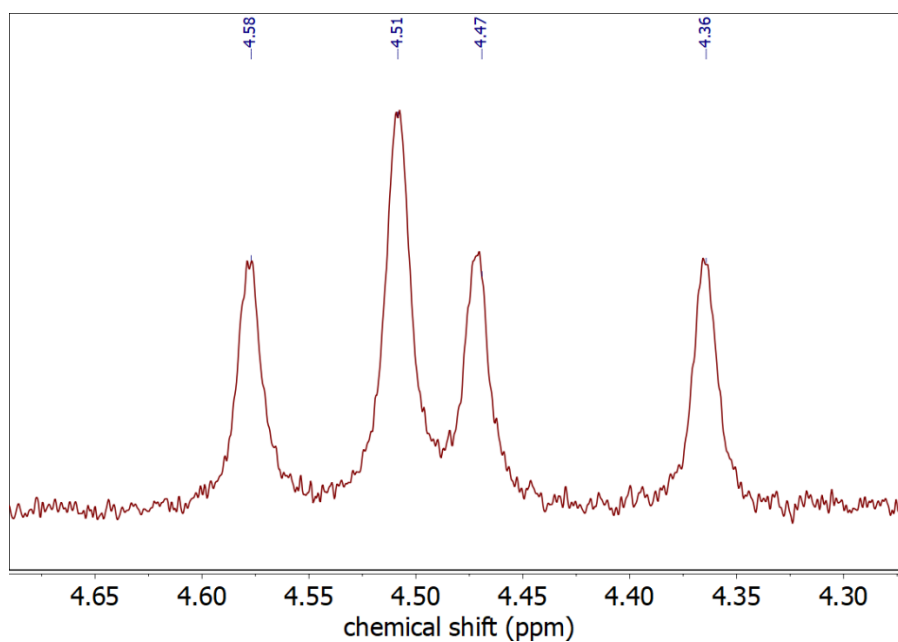


Figure S25: ^1H NMR spectrum of reaction of **1** with D_2 and H_2 in toluene-d_8 at r.t. – zoomed into HD and H_2 peaks.

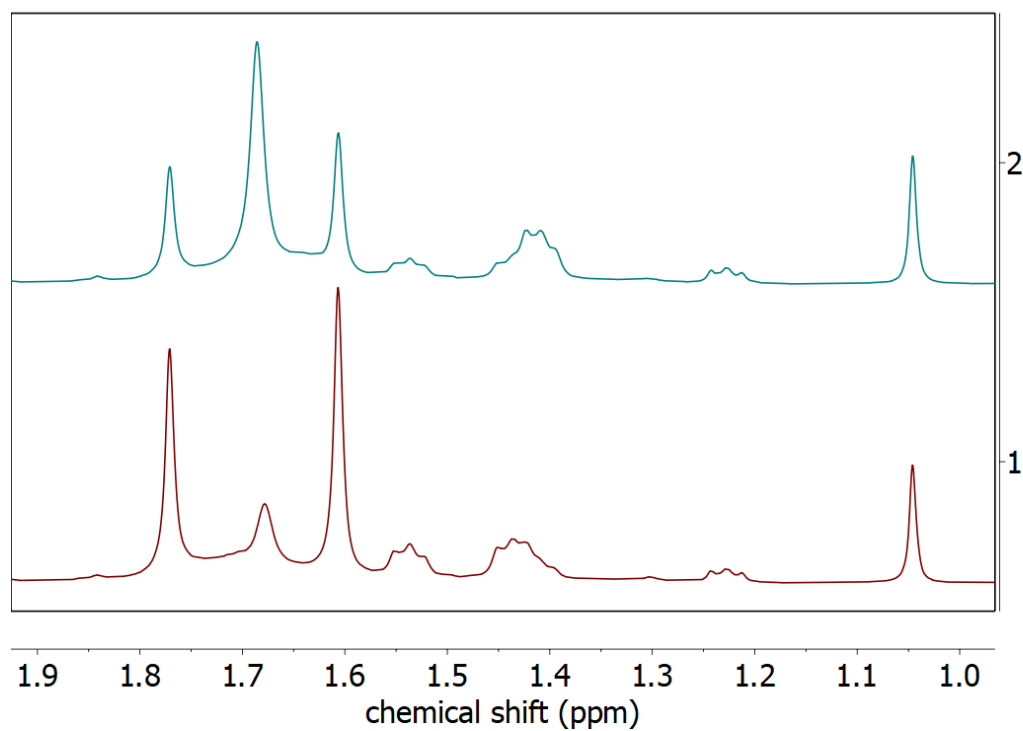


Figure S26: ^1H NMR spectra of reaction of **1** to **2** at 1 bar (bottom, red) and 3 bar (top, green) H_2 pressure in toluene-d_8 at r.t.: at 1 bar the 1/2 ratio (3.4/1) lies on the side of **1**, whereas increased pressure shifts the equilibrium shifts to the side of **2** (1/2 ratio of 0.6/1). Amount of free TMPH remains barely unchanged.

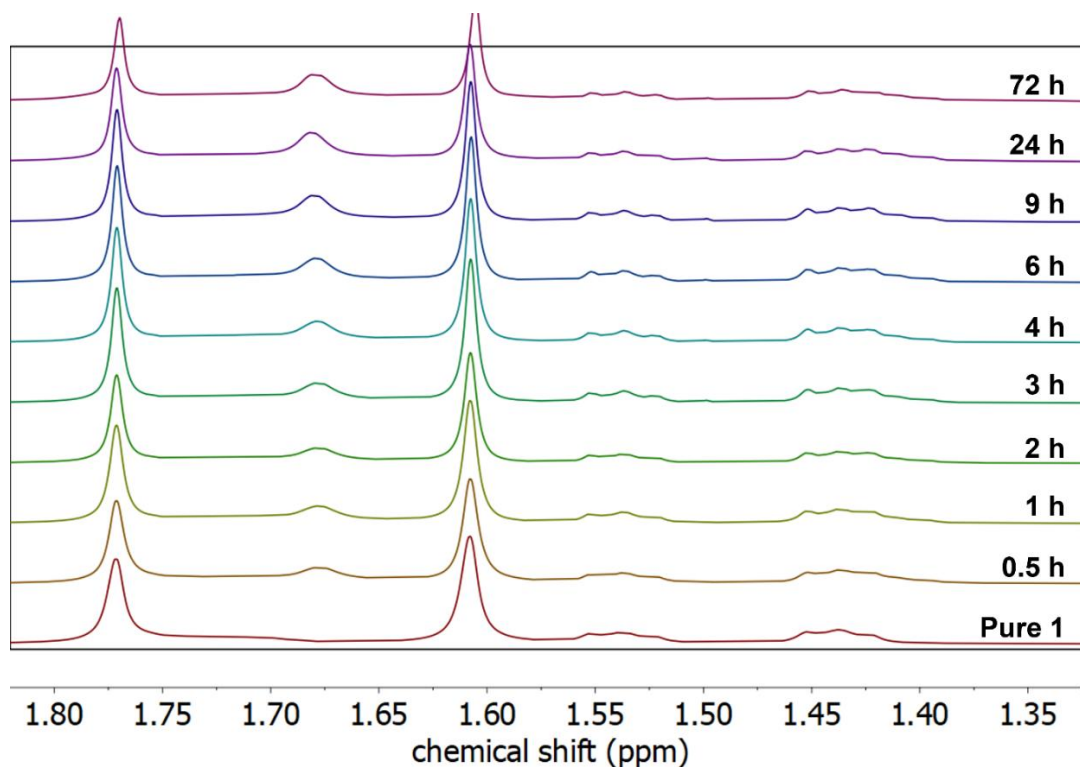


Figure S27: Time dependent ^1H NMR spectra of reaction of **1** to **2** at constant H_2 pressure in toluene- d_8 at r.t. – intensity of **2** increases over time. Ratio **1**/**2**: 1/6 (1 h), 1/4.5 (3 h), 1/3.5 (9 h), 1/3 (24 h) and 1/2.5 (72 h). Notably with increasing reaction progress, but especially after 72 h metallic precipitate is observed. This is in line with the increasing amount of TMPH over time (next figure).

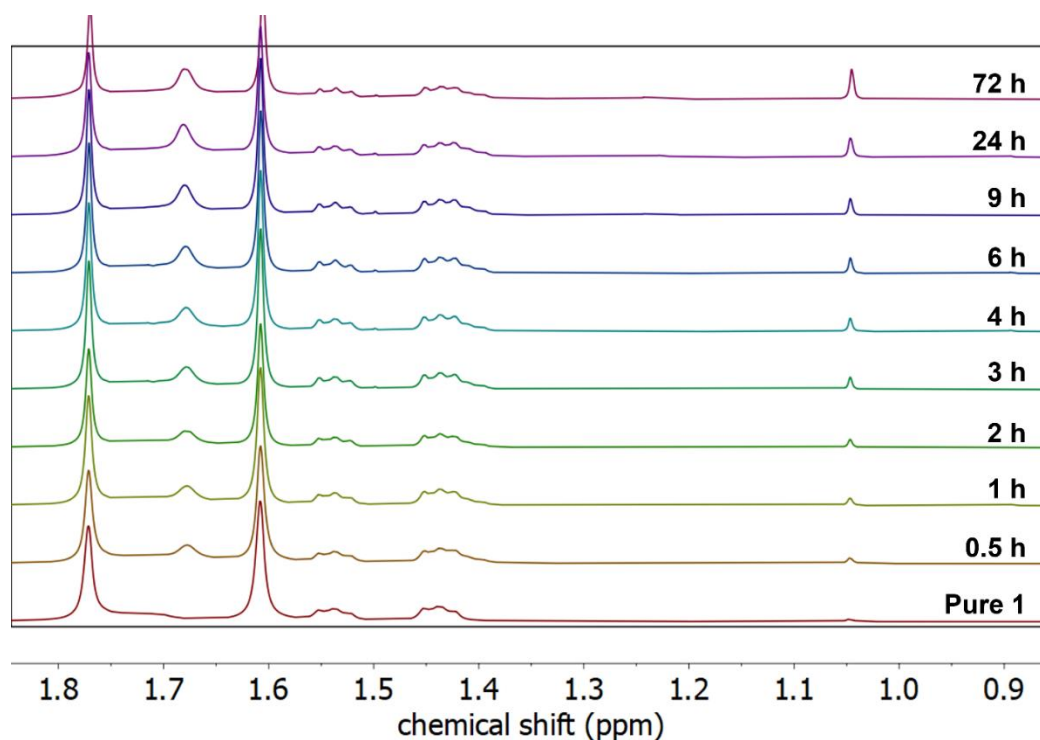


Figure S28: Time dependent ^1H NMR spectra of reaction of **1** to **2** at constant H_2 pressure in toluene- d_8 at r.t. – showing an increasing amount of TMPH over time.

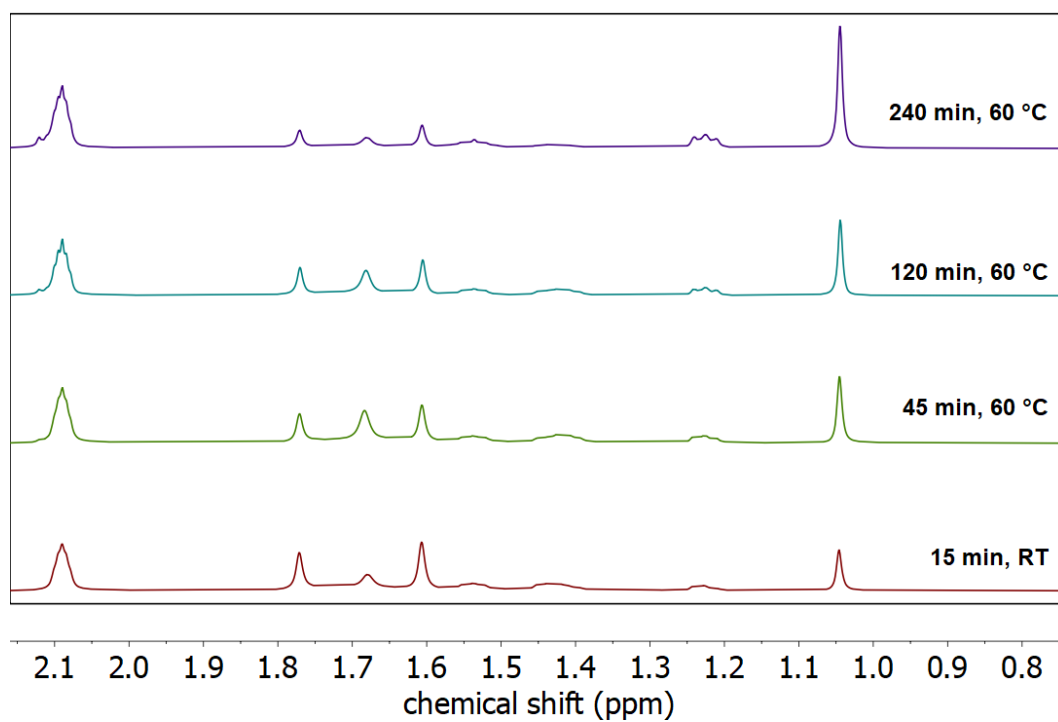


Figure S29: Time dependent ^1H NMR spectra of reaction of **1** to **2** at constant H_2 pressure (1 bar) in toluene- d_8 at $60\text{ }^\circ\text{C}$. The cluster slowly decomposes over time, indicated by metallic precipitate, increasing TMPH signal ($\delta = 1.05\text{ ppm}$) and the relative decrease of the cluster signals compared to the toluene signal.

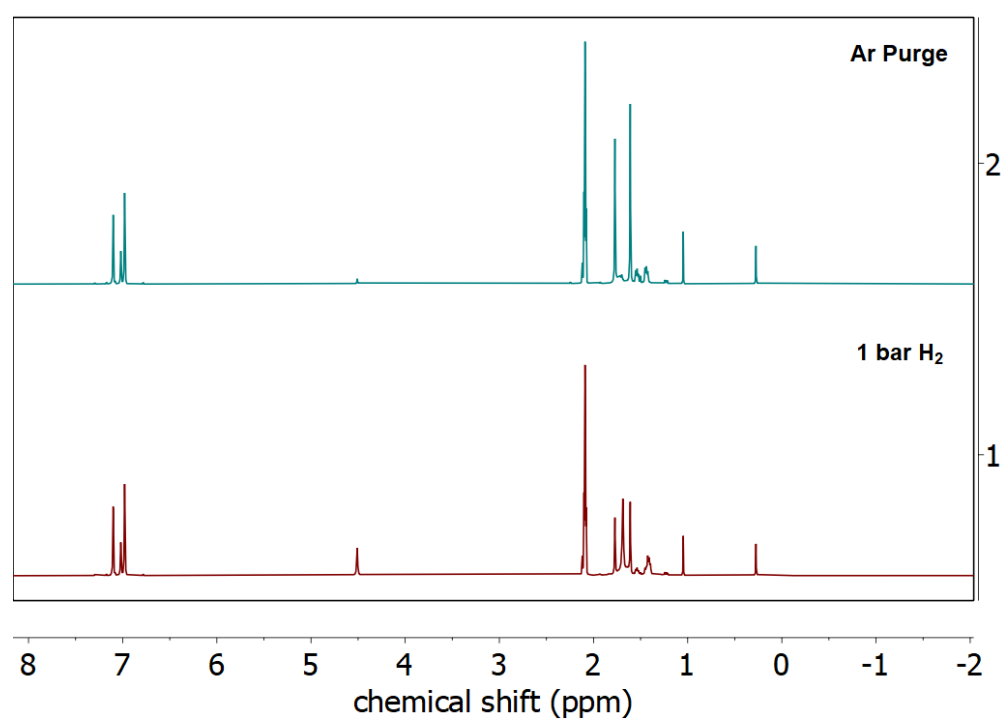


Figure S30: ^1H NMR spectra showing the reversibility of the reaction between **1** + H_2 and **2**. Under 1 bar H_2 pressure (bottom, red) and after quick Ar purge in glovebox (top, blue).

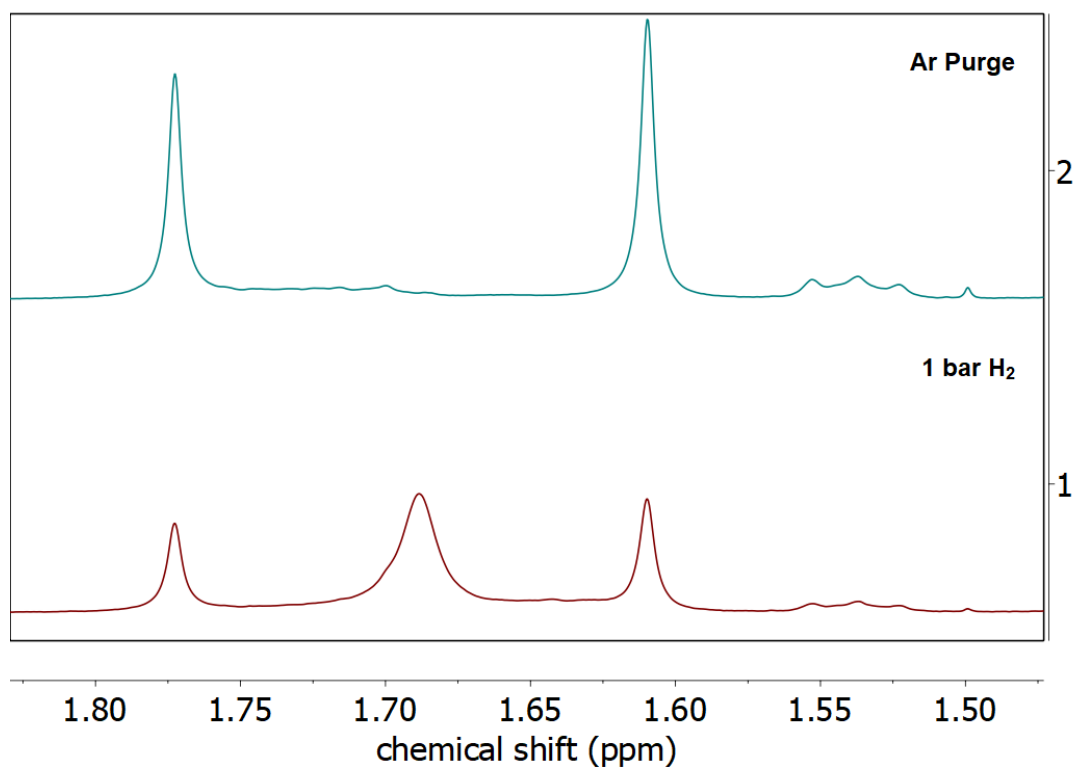


Figure S31: Excerpt of ^1H NMR spectra showing the reversibility of the reaction between **1** + H_2 and **2**. Under 1 bar H_2 pressure (bottom, red) and after quick Ar purge in glovebox (top, blue).

Further Analytics.

LIFDI mass spectrum of **1**.

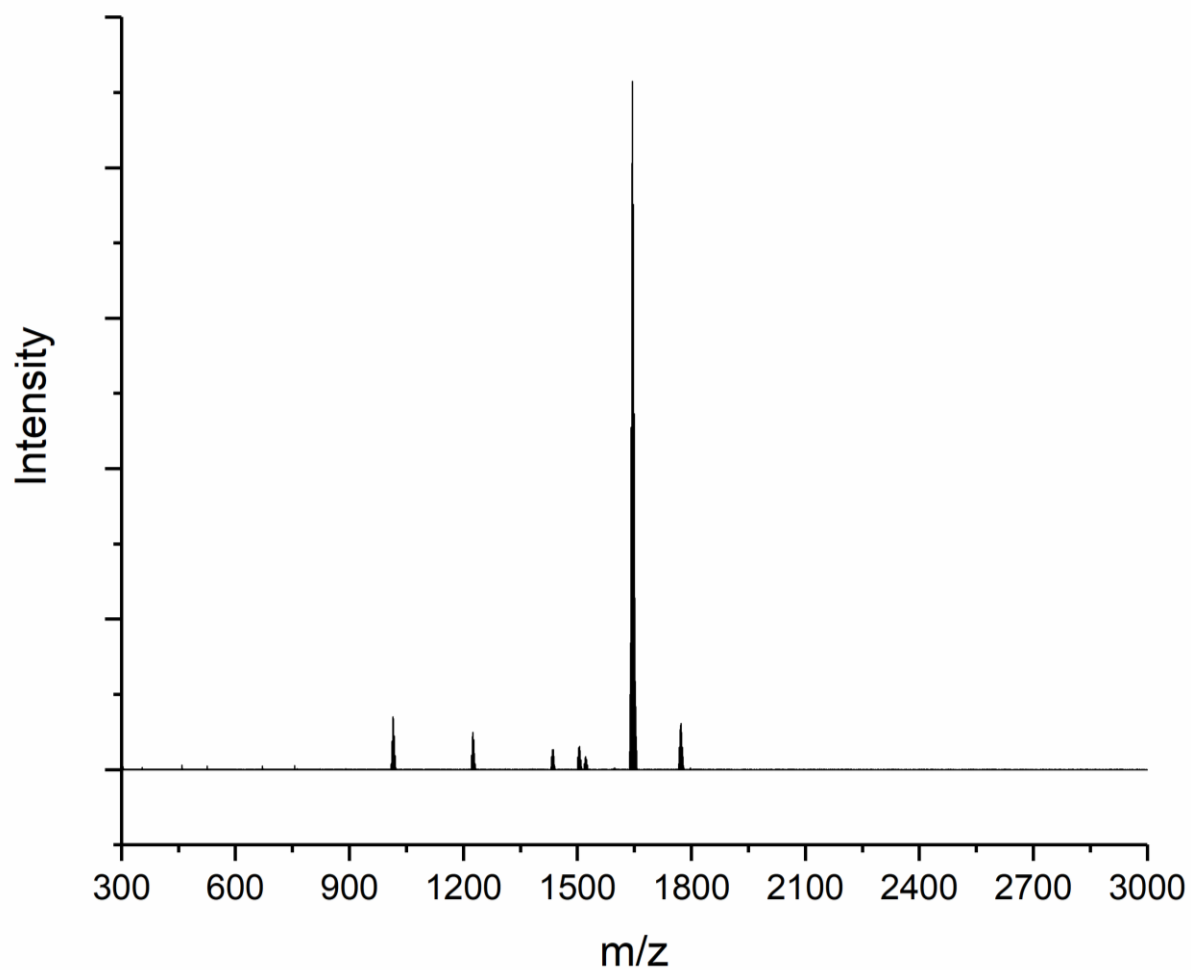


Figure S32: Full range LIFDI-MS spectrum of **1** in toluene.

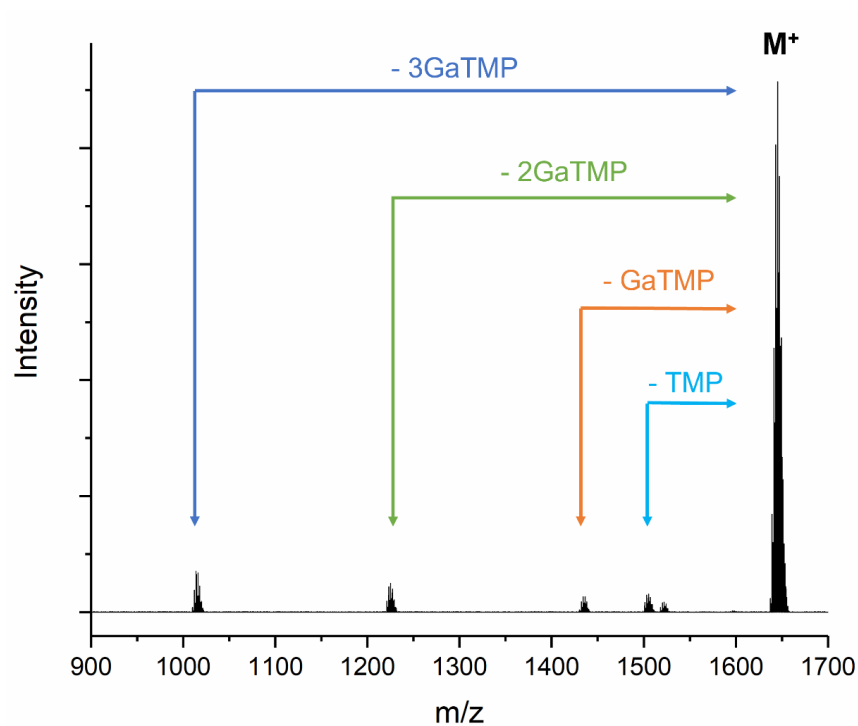


Figure S32: Zoomed LIFDI-MS spectrum of **1**, with assigned fragmentation products: m/z [a. u.] = 1645.2854 (calc.: 1645.2848) $[M]^+$ (black); 1505.1409 (calc.: 1505.1409) $[M-TMP]^+$ (light blue); 1434.2157 (calc.: 1434.2162) $[M-GaTMP]^+$ (orange); 1225.1462 (calc.: 1225.1467) $[M-2GaTMP]^+$ (green); 1014.0781 (calc.: 1014.0786) $[M-3GaTMP]^+$ (dark blue).

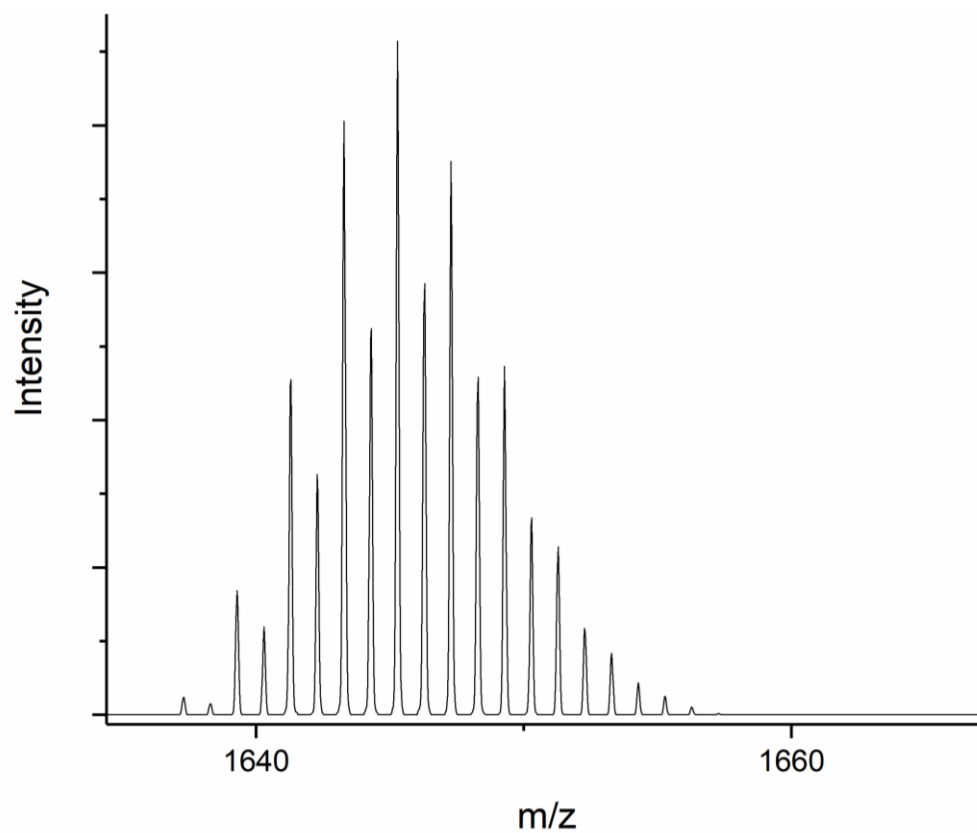


Figure S33: LIFDI-MS spectrum showing isotopic pattern of **1**.

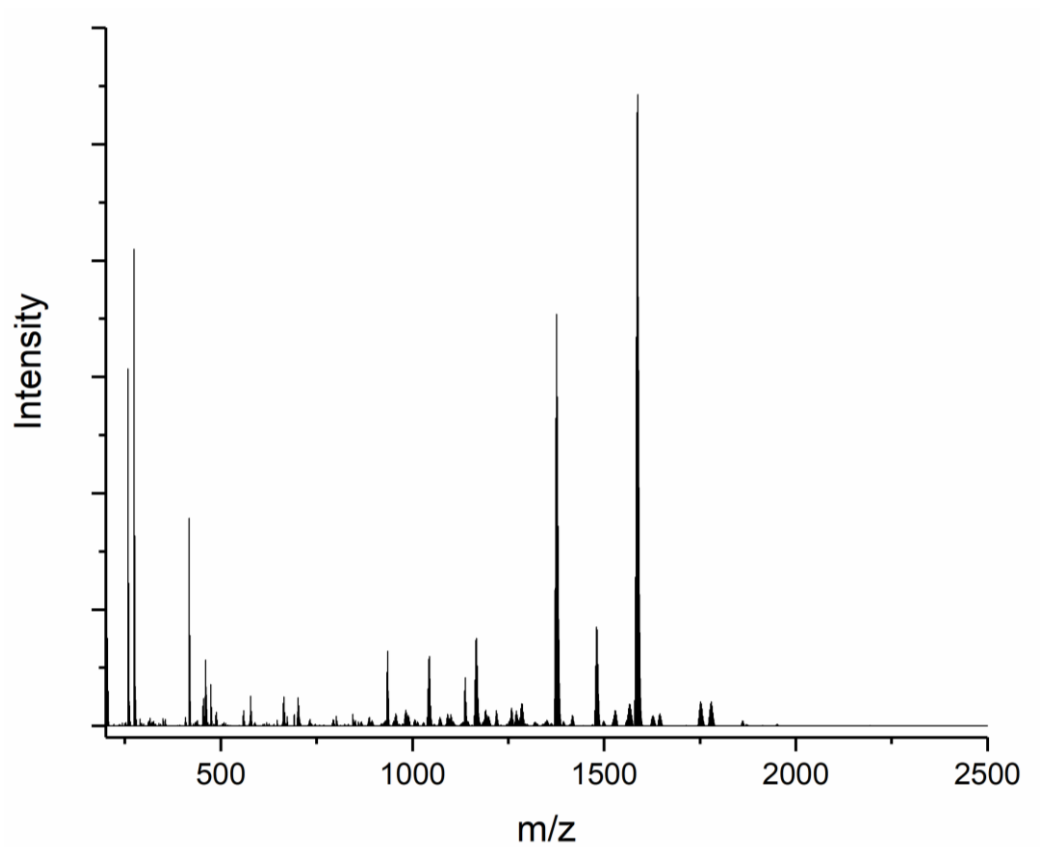


Figure S34: LIFDI mass spectrum of the reaction of 3 eq $\text{Ni}(\text{cod})_2$ with $7/4$ eq $[\text{GaTMP}]_4$ at 60°C after 1 h. Main pattern at $m/z = 1587.3518$ attributed to $[\text{Ni}_2(\text{GaTMP})_7]$.

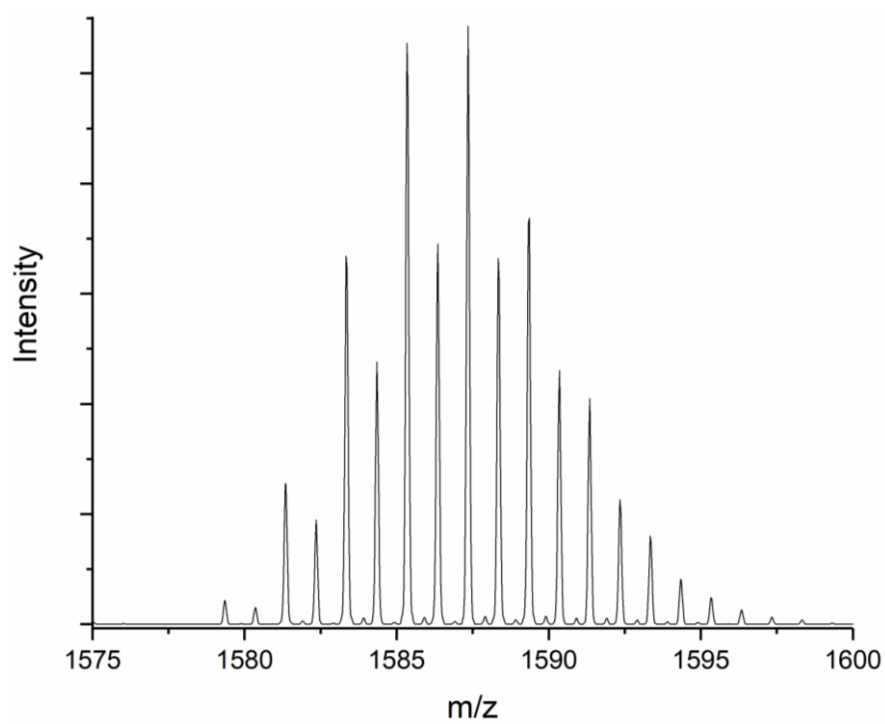
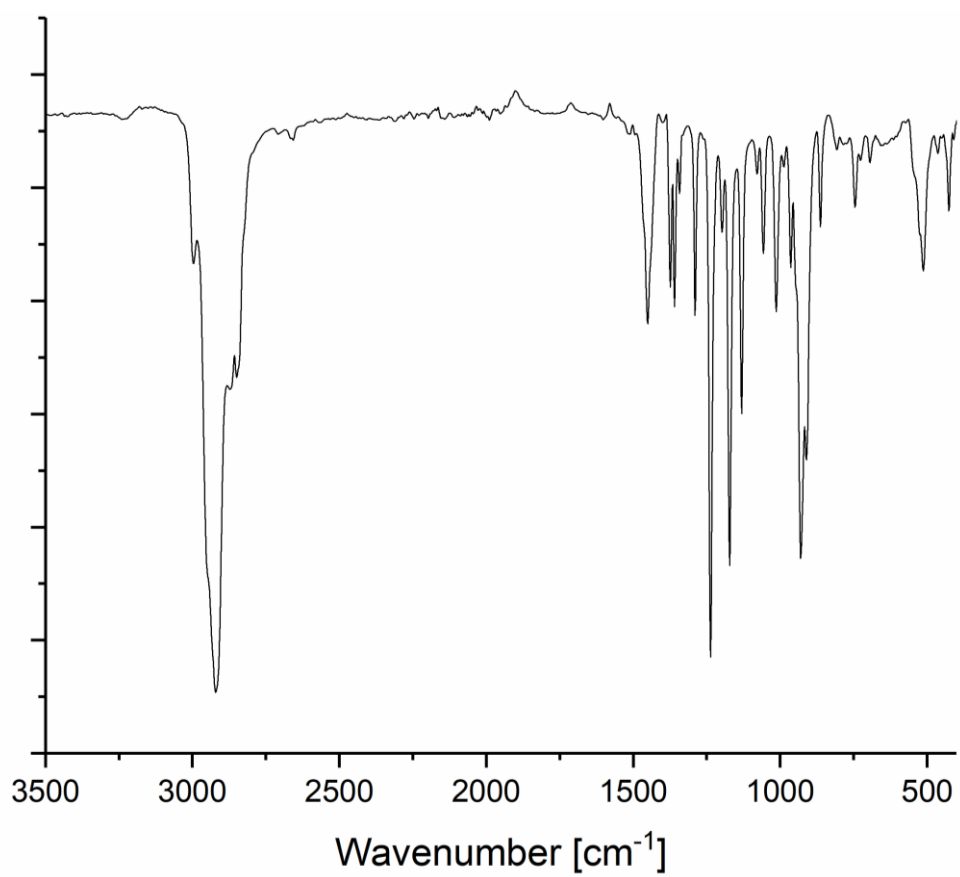


Figure S35: Measured isotopic pattern of $[\text{Ni}_2(\text{GaTMP})_7]$.

IR Spectrum of **1**.



*Figure S36: AT-IR spectrum of **1**.*

UV-Vis spectrum of **1**.

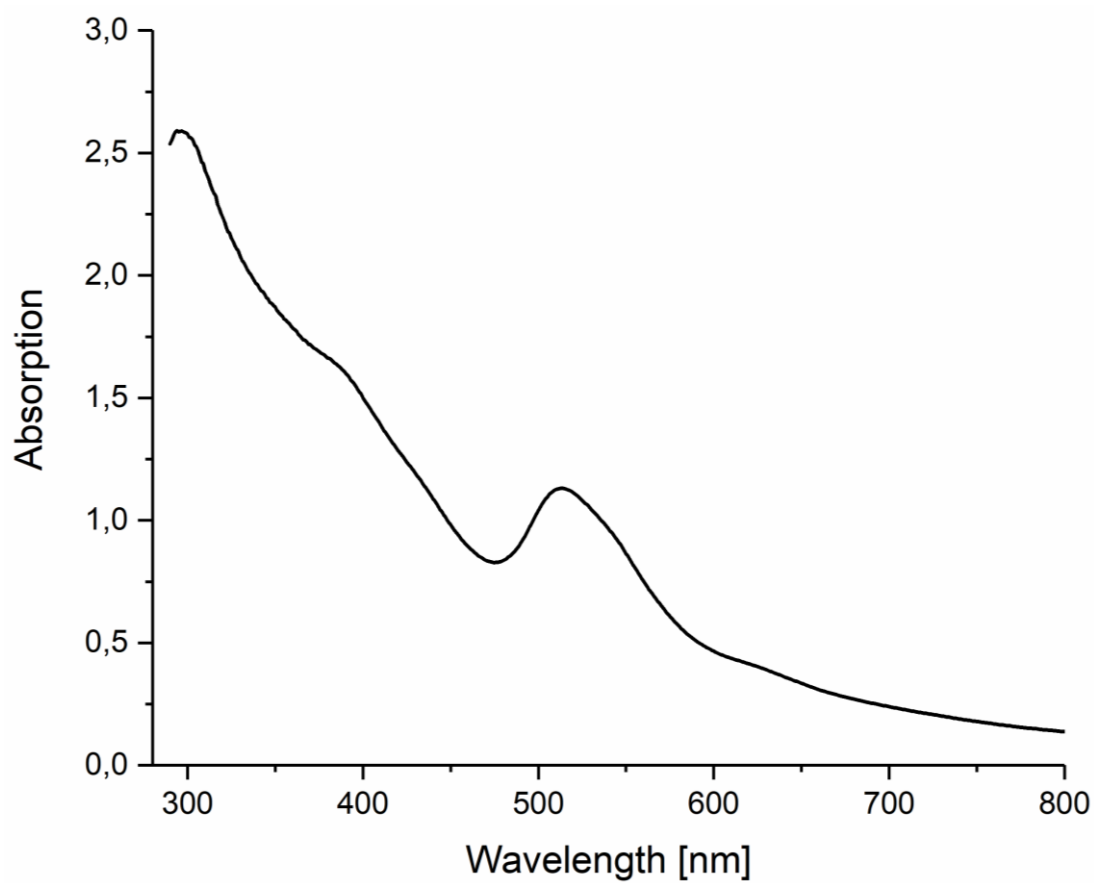


Figure S37: UV-Vis spectrum of 1 in toluene. Absorption maxima at $\lambda = 296$ nm, $\lambda = 389$ nm, $\lambda = 515$ nm and $\lambda = 628$ nm.

Catalysis

General Catalytic Procedure.

A toluene- d_8 (2 mL) solution of 2 mg **1** (0.03 eq), 5.9 μ L 4-octyne (1 eq) and 5.6 μ L mesitylene (1 eq) is prepared and 0.5 mL (25 %) are filled in a baked-out J-Young NMR tube. The reaction solution was degassed by freeze-pump-thaw and was pressurized with 0.5 bar at 0 °C. ^1H NMR spectra were recorded every 30 min at 0 °C.

Table S1: Relative concentration of substrates over course of catalytic reaction. Numbers taken from ^1H NMR integrals (Figure S37). Notably all quantitative values are therefore afflicted with error of around (10 %).

time [h]	4-octyne	4-octene	n-octane
1	1,000	0,000	0,000
2	0,986	0,015	0,001
3	0,920	0,060	0,007
4	0,854	0,102	0,018
5	0,767	0,168	0,017
6	0,712	0,208	0,030
7	0,655	0,251	0,042
8	0,597	0,295	0,056
9	0,535	0,339	0,062
10	0,476	0,379	0,067
11	0,421	0,417	0,082
12	0,368	0,462	0,089
13	0,318	0,496	0,098
14	0,269	0,527	0,114
15	0,225	0,555	0,117
16	0,176	0,586	0,142
17	0,143	0,611	0,142
18	0,120	0,631	0,135
19	0,079	0,646	0,162
20	0,052	0,657	0,177
21	0,028	0,661	0,196
22	0,012	0,659	0,215
23	-	0,637	0,237
24	0,008	0,632	0,250

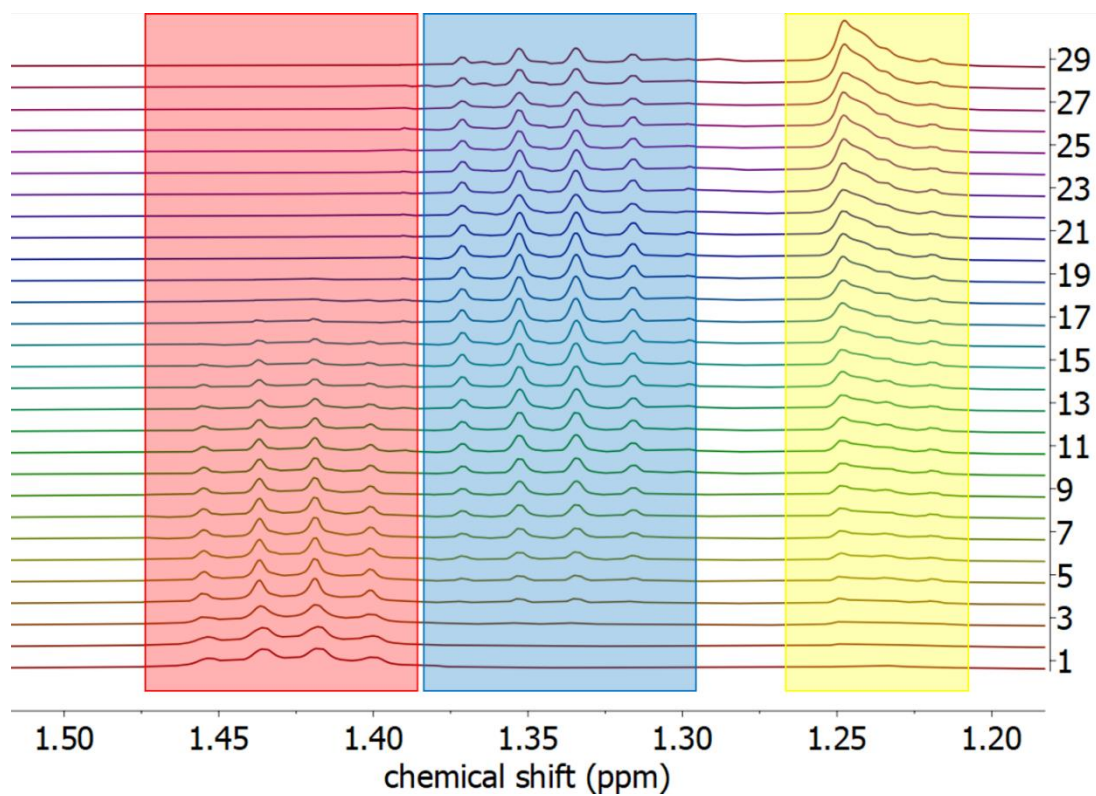


Figure S38: Stacked ¹H NMR spectra in the aliphatic range of the catalytic reaction. Substrate areas marked with colors: 4-octyne (red), 4-octene (blue) and n-octane (yellow). Y-axis marks time in hours.

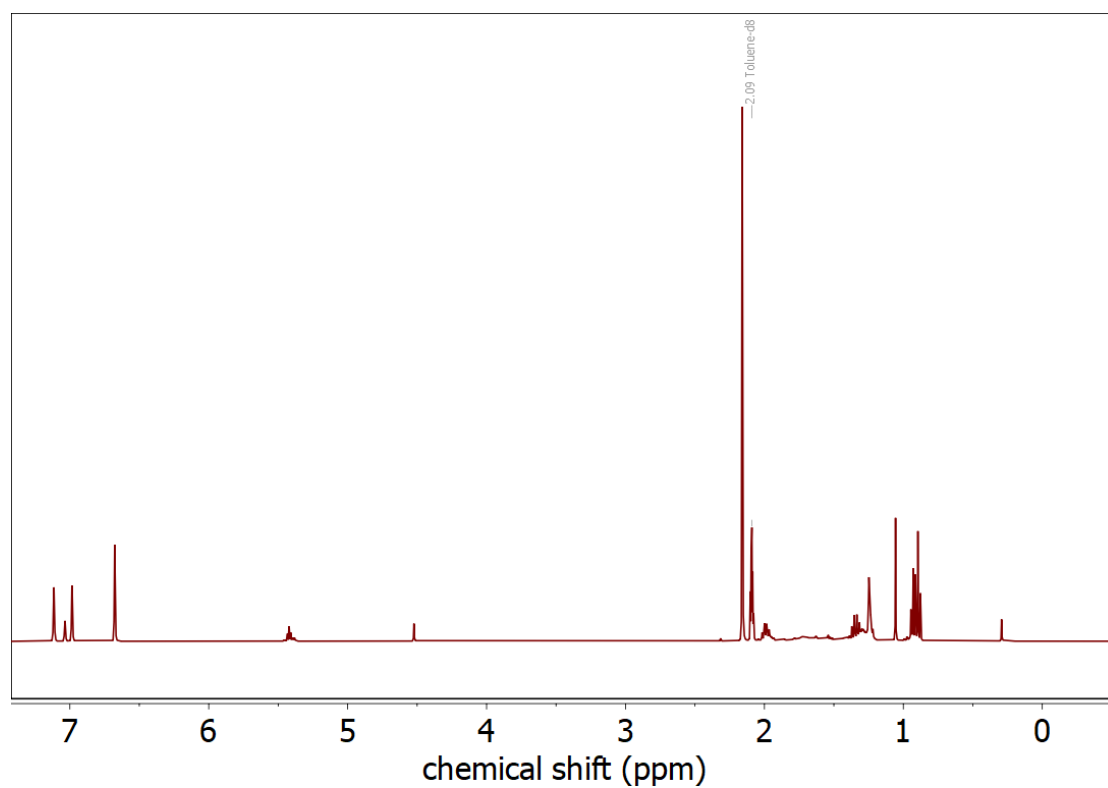


Figure S39: ¹H NMR spectrum after 29 h of the catalytic reaction. Still under catalytic conditions (0 °C, H₂ pressure).

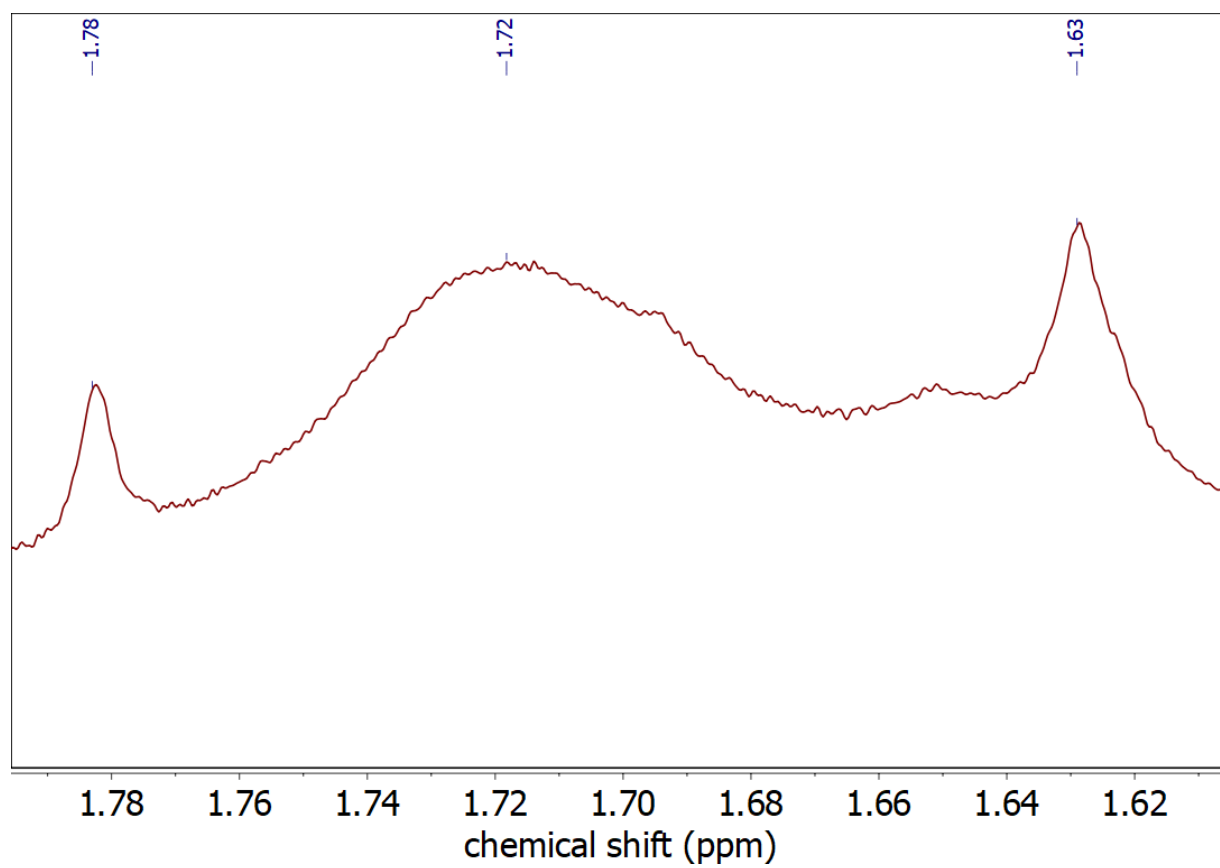


Figure S40: Excerpt of ^1H NMR spectrum after 29 h of the catalytic reaction under catalytic conditions. Peaks of **1** (1.63 and 1.78 ppm) and **2** (1.72 ppm) still visible.

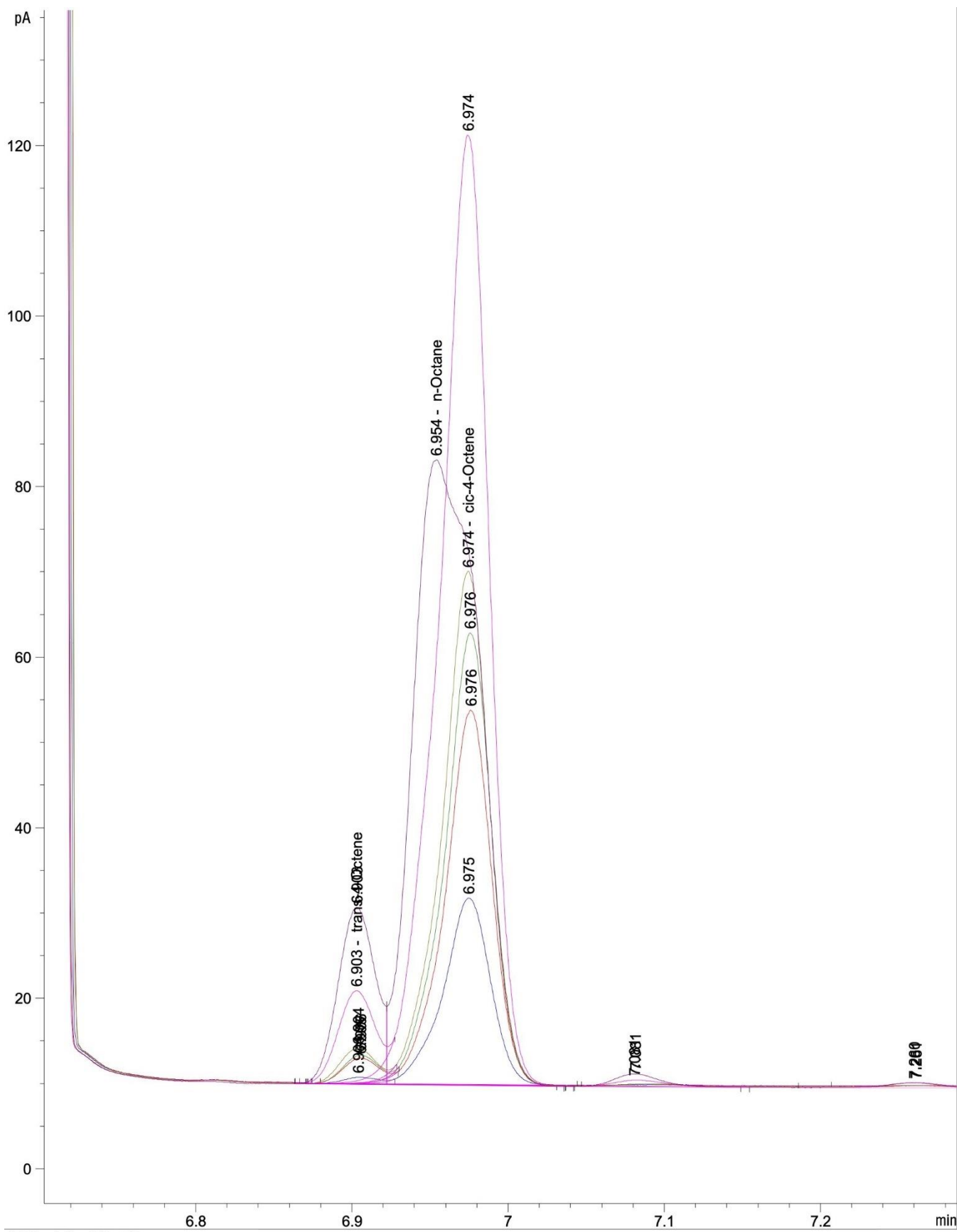


Figure S41: GC-FID overlay of catalytic substrates. Cis-4-octene and n-octane overlap.

Table S2. Selected conversion (*Y*) and semihydrogenation selectivity (*S*) values for 1, nanoparticles^[S15], supported solid-phases^[S16] and pure solid-phases^[S17] with respective substrates. (**S* temperature dependent; values at 140 °C.)

	<i>Y</i>	<i>S</i>	<i>Substrate</i>	<i>Temperature</i>
<i>Cluster (1)</i>	97%	71%	4-Octyne	0 °C
<i>Nanoparticle (Ni₁Ga₁)</i>	82-90%	84-87%	Diphenylacetylene	120 °C
<i>Nanoparticle (Ni₁Ga₁)</i>	86-90%	90-94%	1-Octyne	120 °C
<i>Nanoparticle (Ni)</i>	89%	8%	Diphenylacetylene	120 °C
<i>Nanoparticle (Ni)</i>	96%	3%	1-Octyne	120 °C
<i>Supported solid-phase (Ni₁Ga₁)</i>	~70%	~55%	Diphenylacetylene	50 °C
<i>Supported solid-phase (Ni₅Ga₃)</i>	~90%	~65%	Diphenylacetylene	50 °C
<i>Supported-phase (Ni)</i>	~100%	0	Diphenylacetylene	50 °C
<i>Soild phase (Ni₁Ga₁)*</i>	~50%	~80%	Acetylene	140 °C
<i>Soild phase (Ni₅Ga₃)*</i>	~95%	~50%	Acetylene	140 °C
<i>Soild phase (Ni)*</i>	~100%	~40%	Acetylene	140 °C

DFT Calculations

Energies of calculated compounds.

Table S3: HOMO-LUMO gaps and relative total (ΔE) and room-temperature free (ΔG) energies of the calculated compounds.

	2	2_{Di}				2_{Tetra}				2_{Hexa}
		A	B	C	D	A	B	C	D	
$\Delta E_{HOMO-LUMO}$ (eV)	1.61	1.04	1.33	1.33	1.07	1.37	1.41	1.73	1.41	1.30
ΔE (eV)	-	+0.04	0.00	+0.02	+0.20	+0.09	+0.12	0.00	+1.14	-
ΔG (eV)	-	+0.08	0.00	+0.13	+0.27	+0.07	+1.00	0.00	+1.09	-

Optimized Structures of 2_{Di} .

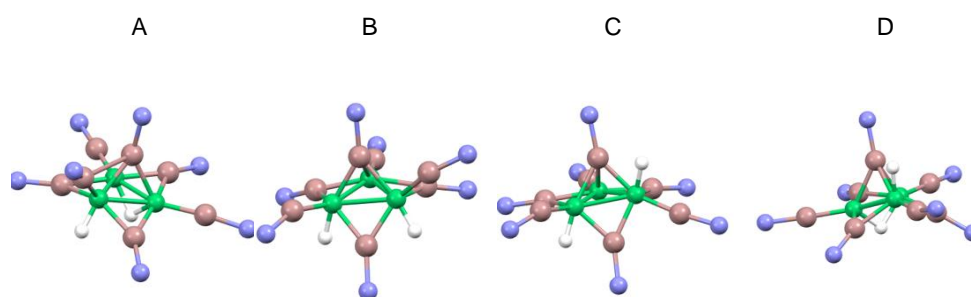


Figure S42: Graphic representation of the computed isomers of 2_{Di} . Color code: Ni = green, Ga = pink, H = white, N = blue. Rest of TMP ligands omitted for clarity. Isomer A = cis- 2_{Di} ; Isomer D = trans- 2_{Di} .

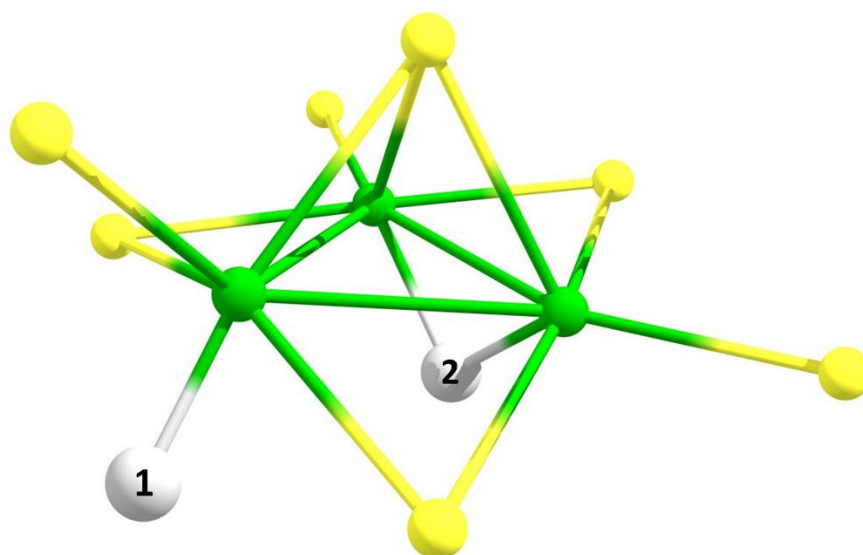


Figure S43: Identified isomer of 2_{Di} (Isomer A). TMP ligands and H atoms are omitted for clarity. Selected bond length (\AA) and angle (deg) ranges: Ni-Ni 2.342 - 2.573, Ni- μ 1-Ga 2.155 - 2.175, Ni- μ 2-Ga 2.231 - 2.325, Ni- μ 3-Ga 2.304 - 2.455, Ni-H1 1.519, Ni- μ 2-H2 1.648 - 1.681; Ni-Ni-Ni 54.4° - 63.3°. Color code: green (Ni), yellow (Ga), white (H).

Optimized Structures of 2_{Tetra} .

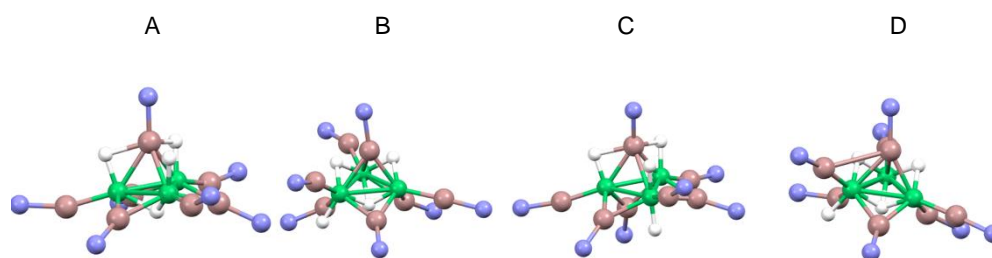


Figure S44: Graphic representation of the computed isomers of 2_{Tetra} . Color code: Ni = green, Ga = pink, H = white, N = blue. Rest of TMP ligands omitted for clarity. Isomer C = 2_{Tetra} .

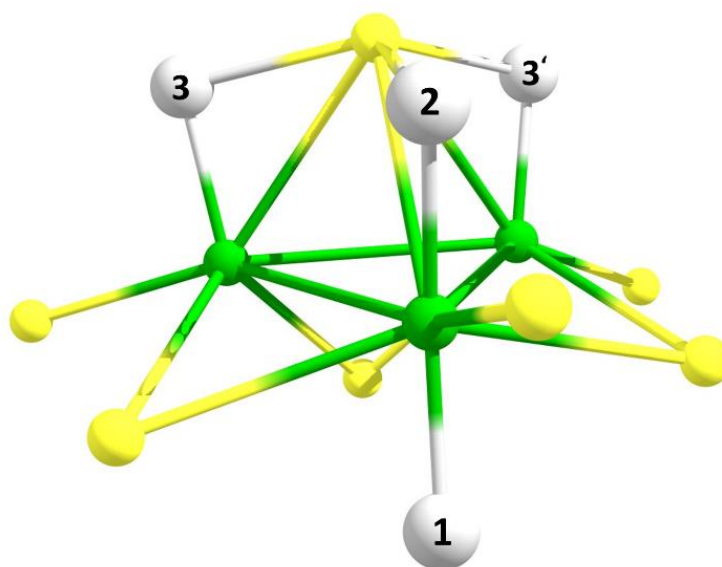


Figure S45: Identified isomer of 2_{Tetra} (Isomer C). TMP ligands and H atoms are omitted for clarity. Selected bond length (\AA) and angle (deg) ranges: Ni-Ni 2.587 - 2.599, Ni- μ 1-Ga 2.144 - 2.151, Ni- μ 2-Ga 2.256 - 2.322, Ni- μ 3-Ga 2.312 - 2.575, Ni-H1 1.496, Ni-H2 1.528, Ni-H3 1.561, Ni-H3' 1.560, μ 3-Ga-H2 1.950, μ 3-Ga-H3 1.837, μ 3-Ga-H3' 1.856, Ni-Ni-Ni 59.7° - 60.2°. Color code: green (Ni), yellow (Ga), white (H).

Optimized Structure of 2_{Hexa} .

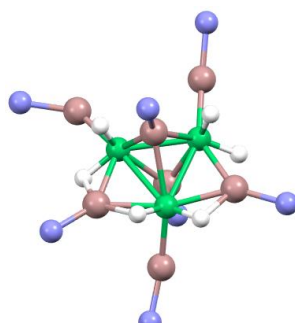


Figure S46: Graphic representation of the optimized structure of 2_{Hexa} . Color code: Ni = green, Ga = pink, H = white, N = blue. Rest of TMP ligands omitted for clarity.

References

- [S1] *APEX suite of crystallographic software*, APEX 3, Version 2019-1.0, Bruker AXS Inc., Madison, Wisconsin, USA, 2019.
- [S2] *SAINT*, Version 8.40A and *SADABS*, Version 2016/2, Bruker AXS Inc., Madison, Wisconsin, USA, 2016/2019.
- [S3] G. M. Sheldrick, *Acta Crystallogr. Sect. A* **2015**, *71*, 3–8.
- [S4] G. M. Sheldrick, *Acta Crystallogr. Sect. C* **2015**, *71*, 3–8.
- [S5] C. B. Hübschle, G. M. Sheldrick, B. Dittrich, *J. Appl. Cryst.* **2011**, *44*, 1281–1284.
- [S6] *International Tables for Crystallography, Vol. C* (Ed.: A. J. Wilson), Kluwer Academic Publishers, Dordrecht, The Netherlands, **1992**, Tables 6.1.1.4 (pp. 500–502), 4.2.6.8 (pp. 219–222), and 4.2.4.2 (pp. 193–199).
- [S7] C. F. Macrae, I. J. Bruno, J. A. Chisholm, P. R. Edgington, P. McCabe, E. Pidcock, L. Rodriguez-Monge, R. Taylor, J. van de Streek, P. A. Wood, *J. Appl. Cryst.* **2008**, *41*, 466–470.
- [S8] A. L. Spek, *Acta Crystallogr. Sect. D* **2009**, *65*, 148–155.
- [S9] Parr, R. G.; Yang, W. *Density-Functional Theory of Atoms and Molecules*. **1994**, Oxford University Press, UK.
- [S10] a) G. te Velde, F. M. Bickelhaupt, S. J. A. van Gisbergen, C. F. Guerra, E. J. Baerends, J. G. Snijders, T. Ziegler, *J. Comput. Chem.* **2001**, *22*, 931–967; b) ADF2016, SCM, *Theoretical Chemistry*, Vrije Universiteit: Amsterdam, The Netherlands; <http://www.scm.com>.
- [S11] S. Grimme, *J. Comput. Chem.* **2006**, *27*, 1787–1799.
- [S12] E. V. Lenthe, E. J. Baerends, *J. Comput. Chem.* **2003**, *24*, 1142–1156.
- [S13] A. D. Becke, *Phys. Rev. A* **1988**, *38*, 3098–3100.
- [S14] J. P. Perdew, *Phys. Rev. B* **1986**, *33*, 8822–8824.
- [S15] K. Schutte, A. Doddi, C. Kroll, H. Meyer, C. Wiktor, C. Gemel, G. van Tendeloo, R. A. Fischer, C. Janiak, *Nanoscale* **2014**, *6*, 5532–5544.
- [S16] C. Li, Y. Chen, S. Zhang, J. Zhou, F. Wang, S. He, M. Wei, D. G. Evans, X. Duan, *ChemCatChem* **2014**, *6*, 824–831.
- [S17] Y. Cao, H. Zhang, S. Ji, Z. Sui, Z. Jiang, D. Wang, F. Zaera, X. Zhou, X. Duan, Y. Li, *Angew. Chem. Int. Ed.* **2020**, *59*, 11647–11652.

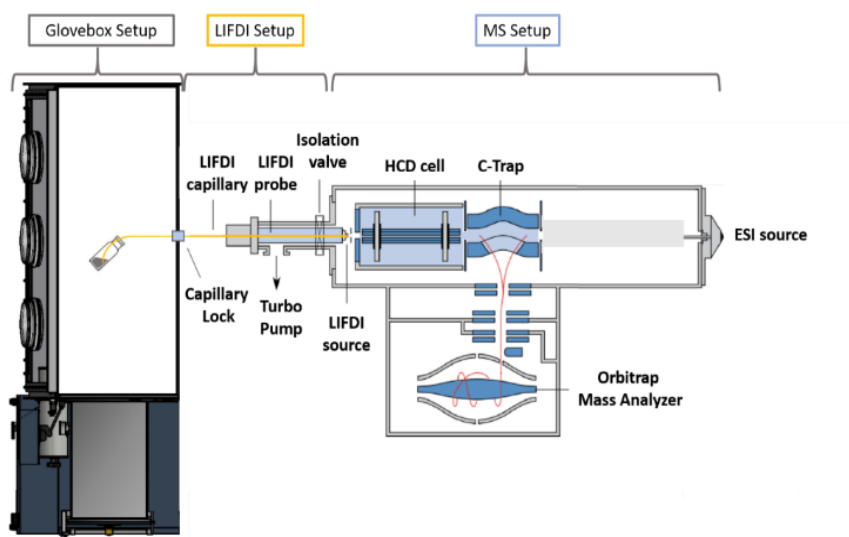
2.6 Enabling LIFDI-MS measurements of highly air sensitive organometallic compounds: A combined MS/glovebox technique.

Maximilian Muhr^{+a,b}, Patricia Hei^{+a,b}, Max Schtz^{a,b}, Raphael Bhler^{a,b}, Christian Gemel^{a,b}, Mathias H. Linden^c, H. Bernhard Linden^c, Roland A. Fischer^{*a,b}

[a, b] Chair of Inorganic and Metalorganic Chemistry, Department of Chemistry and Catalysis Research Center, Technical University Munich, Lichtenbergstrae 4, D-85748 Garching, Germany.

[c] LINDEN CMS GmbH, Auf dem Berge 25, D-28844 Weyhe, Germany.

[+] M.M. and P.H. contributed equally to this work.



The following content has been published: *Dalton Trans.*, **2021**, 50, 9031–9036.

Reprinted with permission from Dalton Transactions. Copyright Royal Society of Chemistry.

Author contributions:

Experiments and manuscript writing by M.M.; Experimental support by M.S. and R.B.; Manufacturing by M.H.L. and H.B.L.; C.G. and R.A.F. supervised the research.

2.6.1 Abstract

A new setup combining a ThermoFisher Exactive Plus Orbitrap Mass Spectrometer with a liquid injection field desorption ionization (LIFDI) source directly connected to an inert atmosphere glovebox is presented. The described setup allows for the analysis of very air- and moisture sensitive samples. Furthermore, the soft nature of LIFDI ionization gives access to the molecular ions of fragile molecules. This new setup is therefore especially useful for sensitive organometallic complexes. The functionality of the new setup is tested against $[(\text{Cp})_2\text{TiCl}]^+$, which is known for its notorious sensitivity to air and moisture. Its drastic colour change from green to orange upon exposure to air further supports the easy detection of traces of oxygen during the experiment. In addition, we applied this setup to the mass spectrometric analysis of the qualitative composition of a Cu/Al cluster mixture, which is not accessible by other analytical methods.

2.6.2 Main Text

Intermetallic materials of catalytically active late transition metals with abundant main group metals such as Cu/Al, Cu/Zn, Fe/Al or Ni/Ga have attracted widespread interest as cost-efficient substitutes for precious metal catalysts.¹⁻³ In nanoparticulate (NP) form they exhibit high activities in various catalytic reactions such as the semi-hydrogenation of alkynes. Christoph Janiak developed synthetic protocols for the preparation of ligand-free NPs from organometallic precursors in ionic liquids with remarkable catalytic activities and selectivities, *e.g.* Ni/Ga NPs with up to 100% selectivity for the semi-hydrogenation of alkynes to alkenes.⁴⁻⁶

Much effort has been devoted to studying catalytic processes on intermetallic material surfaces.^{7, 8} In the course of a long lasting cooperation with Christoph Janiak we became interested in the employment of atom-precise intermetallic clusters as molecular surface models in the investigation of catalytic reaction mechanisms.⁹⁻¹² In this regard, liquid injection field desorption ionization mass spectrometry (LIFDI-MS) was used as a key method giving direct *in-situ* access to the composition of highly reactive and complex reaction solutions. Nevertheless, since a majority of intermetallic clusters are extremely sensitive to air and moisture, a new mass spectrometric setup is required.

Although mass spectrometry (MS) is a very important and well-established method for the structural elucidation of organic and biochemical molecules,¹³⁻¹⁵ it has not yet reached the same level of importance in the analysis of organometallic compounds. Elemental analysis data are frequently cited rather than MS data. Multiple parameters may

be made accountable for this. The analysis of fragmentation patterns of organometallic compounds for example does not have the same degree of importance for structural elucidation as for organic molecules,¹⁶ while the observation of molecular ion signals is more essential. On the other hand, organometallic compounds are very often sensitive to air and moisture, which severely limits instrumental opportunities. *McIndoe* and coworkers have developed an electrospray ionization MS setup coupled to a glovebox for measurements under inert conditions.^{17, 18} However, ionization in nonpolar solvents remains challenging.

One of the softest ionization methods established in mass spectrometry is field desorption (FD) also being nearly solvent independent. Due to a high electric field, the weakest bound electron is removed and the formed ions are detectable. This does not transfer excess energy to the formed ions leading to mass spectra with almost no fragmentation signals.¹⁹⁻²¹ An excellent primer on the method including practical considerations was recently given by *Gross*.²² One limitation of this method is rooted in the demanding sample application. For each experiment, the mechanically fragile emitter is coated with a solution of the sample, before the system is evacuated to 10^{-7} mbar. This procedure is time consuming and causes a high consumption of emitters. In addition, reproducibility of sample loading is difficult to control. Another technique was constructed by *McEwen* where the front area of the MS instrument was wrapped with a plastic bag filled with nitrogen.²³ Evacuating and flushing the bag with inert gas several times lead to almost inert conditions. By this construction $[\text{FeH}(\eta^6\text{-toluene})(\text{P}(\text{OMe})_2)_2]^+\bullet$ was detected as main peak of the spectra. However, due to its

highly demanding and time-consuming procedure, this construction did not become a standard technique for measuring highly air and moisture sensitive metalorganic compounds.

LIFDI-MS overcomes these issues by using a thin fused silica transfer capillary highly facilitating the sample load.²⁴⁻²⁸ The sample is dissolved in an organic solvent with a melting point lower than $-80\text{ }^{\circ}\text{C}$ preventing the solution from solidifying upon contact with vacuum conditions. The solution is applied to the emitter inside of the ion source in a facile and controlled manner ($40\text{ }\mu\text{L}$; 1 mg/mL). After complete evaporation of the solvent under vacuum conditions, the sample remains on the emitter, covering its large surface area.

This capillary setup allows measurements of air and moisture sensitive compounds to be made more easily.²⁶ In a typical procedure, sample preparation is performed under inert conditions (e. g. glovebox) and the sample solutions made available in septum capped vials. At the instrument, the septa of these vials may be penetrated by the LIFDI capillary and the sample is transported to the emitter by the pressure difference. This setup works well for many organometallic compounds.²⁴⁻²⁶

However, when working with very sensitive molecules, as subvalent compounds, metal alkyl compounds or metals in easily oxidizable oxidation states (e.g. M^0), this method reaches its limitations. Through the capillary, the sample vial is connected to the vacuum system of the MS instrument which leads to a constant decrease of the pressure inside the vial, which in consequence results in slow exposure of the sample solution to air and moisture through the vial septum. This not only leads to the failure of the experiment, but can also provoke the irreversible blocking of the capillary due to decomposition of metal containing compounds under formation of solids.

To overcome the described problems, we present in this paper a glovebox-based instrumental setup, which has been developed in cooperation with LINDEN CMS GmbH and GS GLOVEBOX Systemtechnik GmbH (Figure 1). By inserting the LIFDI capillary through a teflon-sealed small hole in the back-wall of the glovebox, a sensitive sample may be injected directly from inside the glovebox preventing the contact with air and moisture. The capillary transports the sample solution to the LIFDI probe which is evacuated by an external turbo pump. An isolation valve prevents exposure of the mass analyzer until 10^{-4} mbar is reached in the probe. When this pressure is reached, the LIFDI probe is automatically moved into the mass spectrometer by an electric motor and the ionization process is triggered by applying voltage to the emitter. After the measurement, the probe is retracted from the instrument, the isolation valve is closed and the LIFDI setup is

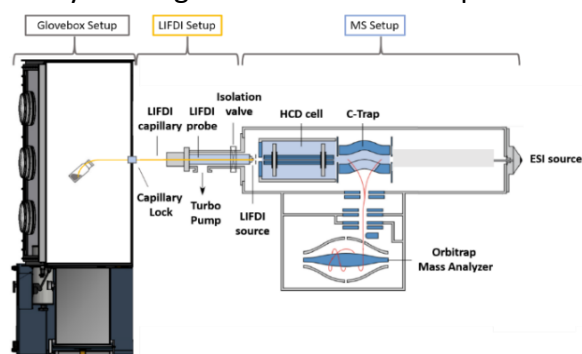
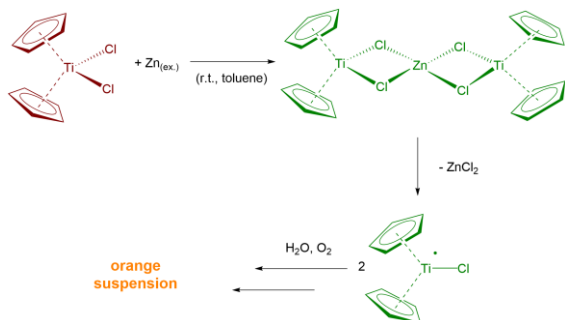


Figure 1: Schematic representation of the combination of a glovebox (modified with permission from GS Glovebox Systemtechnik GmbH), a LIFDI system (designed by LINDEN CMS GmbH) and the mass spectrometer (modified with permission from Thermo Fisher GmbH, Bremen). The devices in the mass spectrometer which are not necessary for LIFDI-MS measurements are omitted for clarity. Copyrights by GS Glovebox Systemtechnik GmbH and Thermo Fisher GmbH.



Scheme 2: Reaction of red $[(Cp)_2TiCl_2]$ with excess of zinc to green trimetallic $[(Cp)_2TiCl_2ZnCl_2Ti(Cp)_2]$. After contact with air an orange solution containing different Ti/O species is formed.

again only evacuated by the external turbo pump. It should be noted that to prevent accidental misuse and irreversible damage to the sensitive *Exactive Plus* mass spectrometer, a plexiglass safety box is installed inside the glovebox, which disables injection when the probe is inserted into the mass analyzer. An additional plexiglass safety box equipped with an electric shutter-type mechanism is installed around the LIFDI apparatus, preventing the probe to be touched while moving.

It should be noted changing the capillary is not further complicated with respect to the common LIFDI setup (without glovebox connection). The capillary, solely, has to be passed through a tiny hole in the back of the glovebox, which is then seal with a rubber plug and a screw joint similar to the one of the LIFDI probe.

In order to evaluate the functionality of this instrumental setup, we used $[(Cp)_2TiCl_2]^+$ (**1**) as a test substance. **1** is notoriously known for its air sensitivity and its oxidation related intense color change, which has also been widely used as cheap and powerful method for the indication of oxygen in glovebox atmospheres (Figure 2). An emerald-green solution of **1** is obtained by reduction of red $[(Cp)_2TiCl_2]$ with zinc powder in toluene after 5 min (Scheme

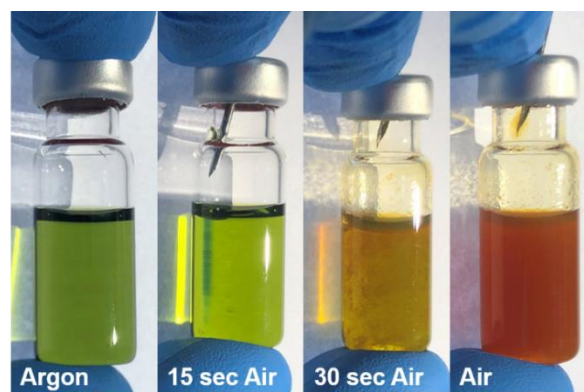


Figure 2: Color change of the reaction solution upon performing the sample vial with the LIFDI capillary.

1).²⁹ Subsequent filtration gives a clear, green solution which does not lead to change color even when stored in the glovebox for several hours.

The LIFDI mass spectrum of this solution indicates the presence of several species which can be traced to the complex $[(Cp)_2TiCl_2ZnCl_2]$, reported as the major reaction product of this reduction.^{29, 30} Thus, the weakly detected molecular ion is observed at m/z 561.8522 (calc. 561.8549) (s. Figure 3, Figure S2). In addition, the fragment ions $[(Cp)_4Ti_2Cl_2]^+$ (m/z 425.9890, calc. 425.9896), $[(Cp)_4Ti_2Cl]^+$ (m/z 391.0205, calc. 391.0207), $[(Cp)_2TiCl]^+$ (m/z 212.9936, calc. 212.9945) or the toluene adduct $[(Cp)TiCl(Tol)]^+$ (m/z 240.0175, calc. 240.0180) are assigned. Very small patterns in this spectrum can be also attributed to oxygen containing products, e.g. $[(Cp)_2TiCl(OH_2)]^+$ (m/z 231.0050, calc. 231.0051), $[(Cp)TiCl_2(OH_2)]^+$ (m/z 200.9349, 200.9348) or $[(Cp)TiCl(OH)(OH_2)]^+$ (m/z 182.9686, calc. 182.9687). Surface-oxidation of the zinc used in the reaction is most probably the oxygen source for the formation of these species. However, the spectra recorded after keeping this solution in the glovebox for 5 min and for 45 min are identical

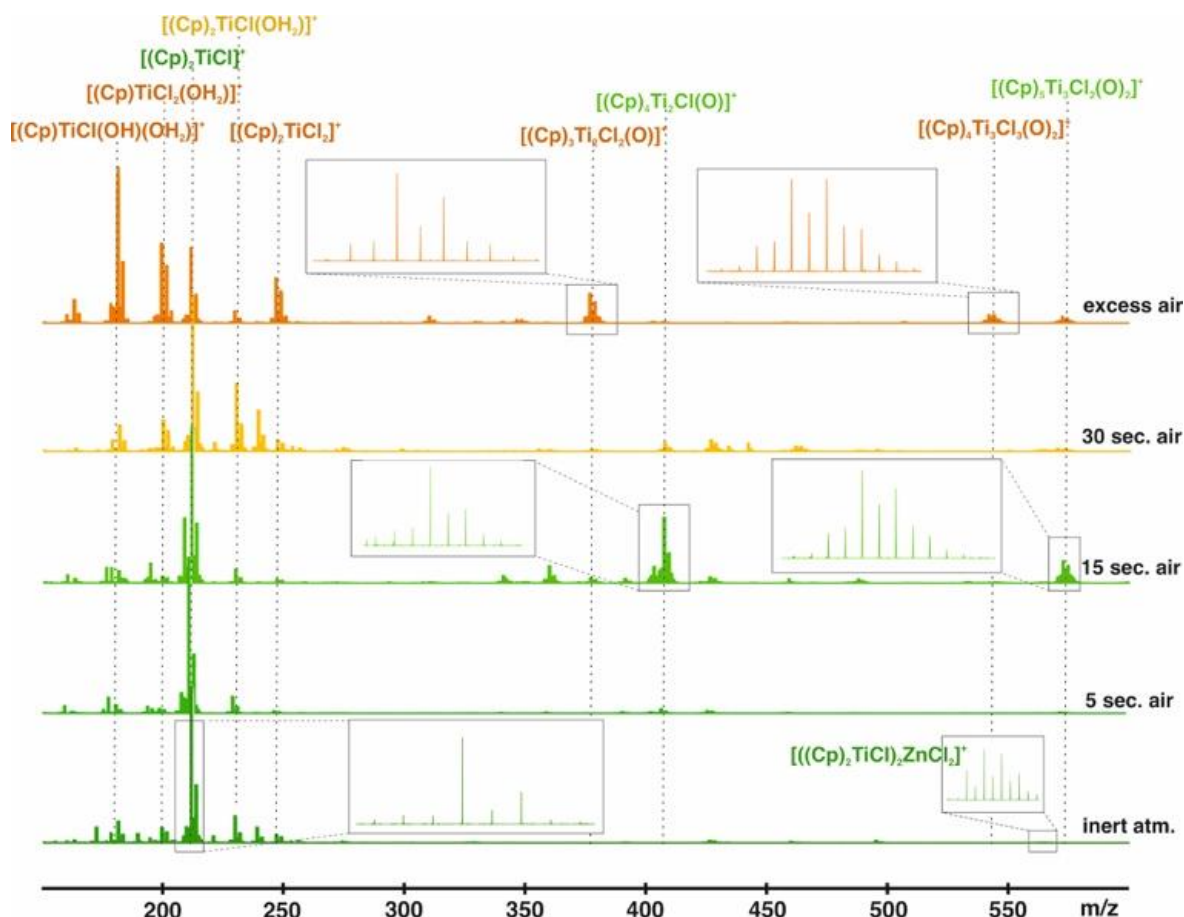


Figure 3: LIFDI mass spectra of $[(Cp)_2TiCl]$ measured by a classic LIFDI-MS setup without a glovebox. After perforating the vial septum with the LIFDI capillary the solution gradually turns from green to orange after only a few seconds. By using the LIFDI-MS/glovebox setup described in this paper, the color of the solution stays green and the spectrum remains unchanged for at least 45min. Most relevant peaks are as follows and ordered by increasing m/z : 182.9680 $[(Cp)TiCl(OH)(OH_2)]^+$, 200.9354 $[(Cp)TiCl_2(OH_2)]^+$, 212.9936 $[(Cp)_2TiCl]^+$, 231.0054 $[(Cp)_2TiCl(OH_2)]^+$, 247.9632 $[(Cp)_2TiCl_2]^+$, 376.9465 $[(Cp)_3Ti_2Cl_2O]^+$, 407.0148 $[(Cp)_4Ti_2ClO]^+$, 542.8914 $[(Cp)_4Ti_3ClO_2]^+$, 561.8522 $[(Cp)_2TiCl)_2ZnCl_2]^+$, 570.9646 $[(Cp)_5Ti_3Cl_2O_2]^+$.

based on the distribution as well as quantity of the patterns (see SI). In contrast, when this measurement is repeated with the traditional LIFDI setup without glovebox connection, a color change of the solution becomes apparent after a few seconds. Already 15 sec after puncturing the septum of the sample vial with the LIFDI capillary and a needle, the solution becomes slightly yellow and patterns attributable to Ti-O species become more prominent in the mass spectrum, i.e. $[(Cp)_4Ti_2ClO]^+$ (m/z 407.0148, calc. 407.0156, Ti/O ratio: 2/1) and $[(Cp)_5Ti_3Cl_2O_2]^+$ (m/z 570.9646, calc. 570.9665, Ti/O ratio: 3/2). These rather Ti-rich compounds disappear after prolonged measurement time and new species with higher oxygen content become

very prominent. Among these oxygen rich species are $[(Cp)TiCl(OH)(OH_2)]^+$ (m/z 182.9680, calc. 182.9687, Ti/O ratio 1/2), or $[(Cp)_2TiCl(OH_2)]^+$ (m/z 231.0054, calc. 231.0051). After allowing an excess of air to get in contact with the sample solutions, the color changes to dark orange, along with precipitation of an orange solid. The spectra now consists of $[(Cp)TiCl(OH)(OH_2)]^+$ (m/z 182.9689, Ti/O ratio 1:2) as the main signal in addition to $[(Cp)_4Ti_3ClO_2]^+$ (m/z 542.8914, calc. 542.8967, Ti/O ratio 3:2), $[(Cp)TiCl_2(OH_2)]^+$ (m/z 200.9354, calc. 200.9348, Ti/O ratio 1:1), and $[(Cp)_3Ti_2Cl_2O]^+$ (m/z 376.9465, calc. 376.9453, Ti/O ratio 2:1). In summary, the more the reaction solution was exposed to air, the larger the amount of oxygen containing

species emerged (Figure). These experiments clearly outline the usefulness of a LIFDI/glovebox connection for the analysis of very air- and moisture sensitive organometallic compounds. The major advantage of submitting samples inside a glovebox to the capillary as well as the probe is under constant inert atmosphere. However, the benefits of working with gloveboxes with respect to handling sample vials capped with septa outside of gloveboxes is not only the increased duration of sample stability, but also the practical simplification of many work steps inside gloveboxes, e.g. sample preparation and dilution or application of the sample solutions to the LIFDI emitter, guaranteeing high experimental reproducibility. This becomes especially important for automation of experiments by e.g. synthesis robots, which is an essential future perspective for our research on intermetallic cluster compounds (*vide infra*).

While the classical LIFDI setup was able to detect the molecular ion peak, it however led to a very fast decay of the green Ti(III) compound $[(\text{Cp})_2\text{TiCl}]_2\text{ZnCl}_2$. Our new setup prevents any contact between sample and air.

There are species even more reactive or prone to oxidation than **1**, such as catalytic intermediates or low-valent metal complexes or clusters. Connecting LIFDI to the protective atmosphere of a glovebox is an important step towards *in-situ* identification of such highly reactive species.

Analysis of Cu/Al cluster libraries

With this instrumental advance we enable reproducible access to complex reaction solutions of mixed-metal clusters. This chemistry offers compounds of unique structures, properties and reactivities. It is, however, affected by challenging product separation and isolation, respectively. This is in line with compounds that simply cannot be isolated in a pure form leading to a loss of information when not characterized *in-situ*. High resolution mass spectrometry is a way to tackle this problem and follow minor reaction products (former known as by-products). To illustrate our new way of thinking we would like to draw attention to a recently submitted work, the reaction of $[\text{CuMes}]$ (abbreviated for $[\text{Cu}_5](\text{Mes})_5$; Mes = mesitylene) with 3.6 eq. of

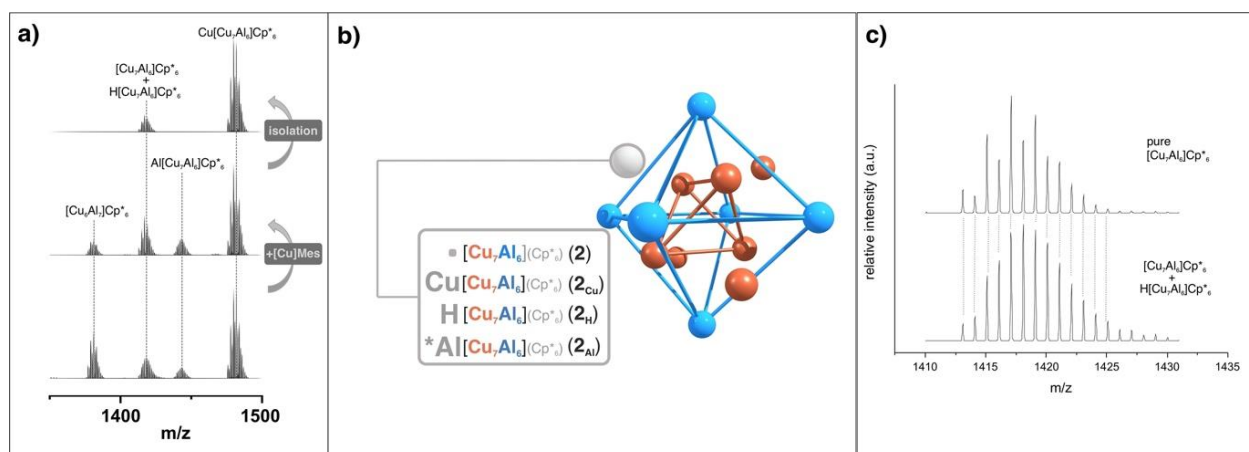


Figure 4: (a) Observing cluster growth reactions by mass spectrometry after addition of $[\text{Cu}_5](\text{Mes})_5$ to solutions of Cu/Al clusters. (b) schematic representation of clusters based on the core cluster $[\text{Cu}_7\text{Al}_6](\text{Cp}^*)_6$ with additional optional atoms (H, Cu, Al) expanding the core. All four species are observed by *in-situ* mass spectrometry. *Note, that with the exception of $\text{Al}[\text{Cu}_7\text{Al}_6](\text{Cp}^*)_6$ all cluster structures are confirmed by DFT calculations. (c) Identification of $\text{H}[\text{Cu}_7\text{Al}_6](\text{Cp}^*)_6$ in a mixture with $[\text{Cu}_7\text{Al}_6](\text{Cp}^*)_6$ by analysis of the isotopic pattern. The pattern shown on the top is pure $[\text{Cu}_7\text{Al}_6](\text{Cp}^*)_6$, the pattern in the bottom contains a mixture of both species.

AlCp* (Cp* = pentamethylcyclopentadienyl).³¹ The reaction results in a complex mixture of intermetalloid $[\text{Cu}_x\text{Al}_y](\text{Cp}^*)_z$ cluster species. Besides the 18 valence electron cation $[\text{CuAl}_4](\text{Cp}^*)_4^+$, the species $[\text{Cu}_8\text{Al}_6](\text{Cp}^*)_6$ (**2_{Cu}**), $[\text{Cu}_6\text{Al}_7](\text{Cp}^*)_6$, $\{[\text{Cu}_7\text{Al}_7](\text{Cp}^*)_6 - 2\text{H}\}$ (**2_{Al}**) and an overlapping peak corresponding to a mixture of $[\text{HCu}_7\text{Al}_6](\text{Cp}^*)_6$ (**2_H**) and $[\text{Cu}_7\text{Al}_6](\text{Cp}^*)_6$ (**2**) are detected (see Figure 4). Addition of precise amounts of CuMes (overall final Cu:Al stoichiometry 1:1.2) to this mixture, followed by prolonged heating induces subtle spectral changes (see Figure 4 a), middle). Analysis of the peak at $m/z = 1417$ reveals now pure **2** instead of **2_H/2**. From these reaction solutions, isolation of the composite **2/2_{Cu}** was possible after crystallization and a short work-up procedure (see Figure 4a, top). Obviously, all the other cluster species, especially those with unligated Al atoms, $[\text{Cu}_6\text{Al}_7](\text{Cp}^*)_6$ and $\{[\text{Cu}_7\text{Al}_7](\text{Cp}^*)_6 - 2\text{H}\}$, are removed or decomposed during the work-up procedure, however, we were able to determine these highly reactive and sensitive compounds by mass spectrometry in combination with a glovebox. The results nicely illustrate two keypoints: without detailed analysis of reaction solutions by LIFDI-MS, feedback on the reaction design and access to pure **2**, as well as its subsequent reactivity assessment would not have been possible. Further, LIFDI-MS analysis of the reaction solution prior to crystallization sheds light on cluster species, which cannot be captured by common crystallization procedures. Due to their naked Al atoms, these species might exhibit unique reactivities, which again can only be detected by MS. Detection likewise reactivity investigation of highly reactive/sensitive molecules require the introduction of a reliable

MS setup to exclude any undesired external influence, mainly moisture and air.

Conclusions

In this contribution, we introduced a new coupled glovebox/MS setup for the mass spectrometric detection of molecular ion signals of very air- and moisture sensitive compounds. The setup was tested on the organometallic complex $[\text{((Cp)}_2\text{TiCl)}_2\text{ZnCl}_2]$, known for its extreme air-sensitivity. By a colour-change from green to orange the oxidation of this complex can also visually be detected. Only by using this new setup, the molecular ion signal of $[\text{((Cp)}_2\text{TiCl)}_2\text{ZnCl}_2]$ is detectable over time. Without the use of a glovebox, oxidation reactions are observed only within a few seconds. The new setup has been further applied to the *in-situ* analysis of Cu/Al clusters allowing the detection of the highly sensitive open shell cluster $[\text{Cu}_7\text{Al}_6](\text{Cp}^*)_6$ together with its closed shell coordination adducts $\text{H}[\text{Cu}_7\text{Al}_6](\text{Cp}^*)_6$, $\text{Cu}[\text{Cu}_7\text{Al}_6](\text{Cp}^*)_6$ and $\text{Al}[\text{Cu}_7\text{Al}_6](\text{Cp}^*)_6$. We expect this new technique to considerably support our future efforts to employ intermetallic clusters of this type as surface model compounds in mechanistic investigation of catalytic processes.

Acknowledgements

This work was funded by the German Research Foundation (DFG) within the projects FI-502/23-2 and FI-502/44-1.

2.6.3 References

1. M. Armbrüster, K. Kovnir, M. Friedrich, D. Teschner, G. Wowsnick, M. Hahne, P. Gille,

- L. Szentmiklósi, M. Feuerbacher, M. Heggen, F. Girgsdies, D. Rosenthal, R. Schlögl and Y. Grin, *Nat. Mater.*, 2012, **11**, 690.
2. F. Studt, F. Abild-Pedersen, T. Bligaard, R. Z. Sørgensen, C. H. Christensen and J. K. Nørskov, *Science*, 2008, **320**, 1320-1322.
 3. K. Schütte, H. Meyer, C. Gemel, J. Barthel, R. A. Fischer and C. Janiak, *Nanoscale*, 2014, **6**, 3116-3126.
 4. C. Janiak, in *Catalysis in Ionic Liquids: From Catalyst Synthesis to Application*, The Royal Society of Chemistry, 2014, DOI: 10.1039/9781849737210-00537, pp. 537-577.
 5. K. Schutte, A. Doddi, C. Kroll, H. Meyer, C. Wiktor, C. Gemel, G. van Tendeloo, R. A. Fischer and C. Janiak, *Nanoscale*, 2014, **6**, 5532-5544.
 6. I. Simon, J. Hornung, J. Barthel, J. Thomas, M. Finze, R. A. Fischer and C. Janiak, *Beilstein J. Nanotech.*, 2019, **10**, 1754-1767.
 7. Z.-P. Wu, S. Shan, S.-Q. Zang and C.-J. Zhong, *Acc. Chem. Res.*, 2020, **53**, 2913-2924.
 8. Z. Li, S. Ji, Y. Liu, X. Cao, S. Tian, Y. Chen, Z. Niu and Y. Li, *Chem. Rev.*, 2020, **120**, 623-682.
 9. K. Freitag, H. Banh, C. Gemel, R. W. Seidel, S. Kahlal, J.-Y. Saillard and R. A. Fischer, *Chem. Commun.*, 2014, **50**, 8681-8684.
 10. H. Banh, J. Hornung, T. Kratz, C. Gemel, A. Pöthig, F. Gam, S. Kahlal, J.-Y. Saillard and R. A. Fischer, *Chem. Sci.*, 2018, **9**, 8906-8913.
 11. J. Hornung, M. Muhr, C. Gemel and R. A. Fischer, *Dalton Trans.*, 2019, **48**, 11743-11748.
 12. C. Ganesamoorthy, J. Weßing, C. Kroll, R. W. Seidel, C. Gemel and R. A. Fischer, *Angew. Chem. Int. Ed.*, 2014, **53**, 7943-7947.
 13. S. Komatsu, C. Tsumori, K. Ohnishi and K. Kai, *ACS Chem. Biol.*, 2020, **15**, 2860-2865.
 14. C.-C. Hsu, M. W. Baker, T. Gaasterland, M. J. Meehan, E. R. Macagno and P. C. Dorrestein, *Anal. Chem.*, 2017, **89**, 8251-8258.
 15. H. Schlüter, J. Rykl, J. Thiemann, S. Kurzawski, J. Gobom, M. Tepel, W. Zidek and M. Linscheid, *Anal. Chem.*, 2007, **79**, 1251-1255.
 16. F. Hufsky and S. Böcker, *Mass Spectrom. Rev.*, 2017, **36**, 624-633.
 17. A. T. Lubben, J. S. McIndoe and A. S. Weller, *Organometallics*, 2008, **27**, 3303-3306.
 18. L. P. Yunker, R. L. Stoddard and J. S. McIndoe, *J Mass Spectrom*, 2014, **49**, 1-8.
 19. H. D. Beckey, *Int. J. Mass Spectrom. Ion Phys.*, 1969, **2**, 500-502.
 20. H.-D. Beckey, *Principles of Field Ionization and Field Desorption Mass Spectrometry*, Pergamon Press, 1977.
 21. H. D. Beckey and H.-R. Schulten, *Angew. Chem. Int. Ed. Eng.*, 1975, **14**, 403-415.
 22. J. H. Gross, *Eur. J. Mass Spectrom.*, 2020, **26**, 241-273.
 23. C. N. McEwen and S. D. Ittel, *Org. Mass Spectrom.*, 1980, **15**, 35-37.
 24. H. B. Linden, *Eur. J. Mass Spectrom.*, 2004, **10**, 459-468.
 25. H. B. Linden and J. H. Gross, *J. Am. Soc. Mass Spectrom.*, 2011, **22**, 2137-2144.
 26. J. H. Gross, N. Nieth, H. B. Linden, U. Blumbach, F. J. Richter, M. E. Tauchert, R. Tompers and P. Hofmann, *Anal. Bioanal. Chem.*, 2006, **386**, 52-58.
 27. L. A. Stanford, S. Kim, G. C. Klein, D. F. Smith, R. P. Rodgers and A. G. Marshall,

- Environ. Sci. Technol.*, 2007, **41**, 2696-2702.
28. A. G. Marshall and R. P. Rodgers, *Proc. Natl. Acad. Sci. U.S.A.*, 2008, **105**, 18090-18095.
29. M. L. H. Green and C. R. Lucas, *J. Chem. Soc. Dalton Trans.*, 1972, 1000-1003.
30. R. J. Enemærke, G. H. Hjøllund, K. Daasbjerg and T. Skrydstrup, *C. R. Acad. Sci., Ser. IIc*, 2001, **4**, 435-438.
31. M. Schütz, C. Gemel, M. Muhr, C. Jandl, S. Kahlal, J.-Y. Saillard and R. A. Fischer, *Chem. Sci.*, **2021**, 12, 6588-6599.

2.6.4 Additional Data and Information

LIFDI spectra details of the reaction: $[(Cp)_2TiCl_2] + Zn$

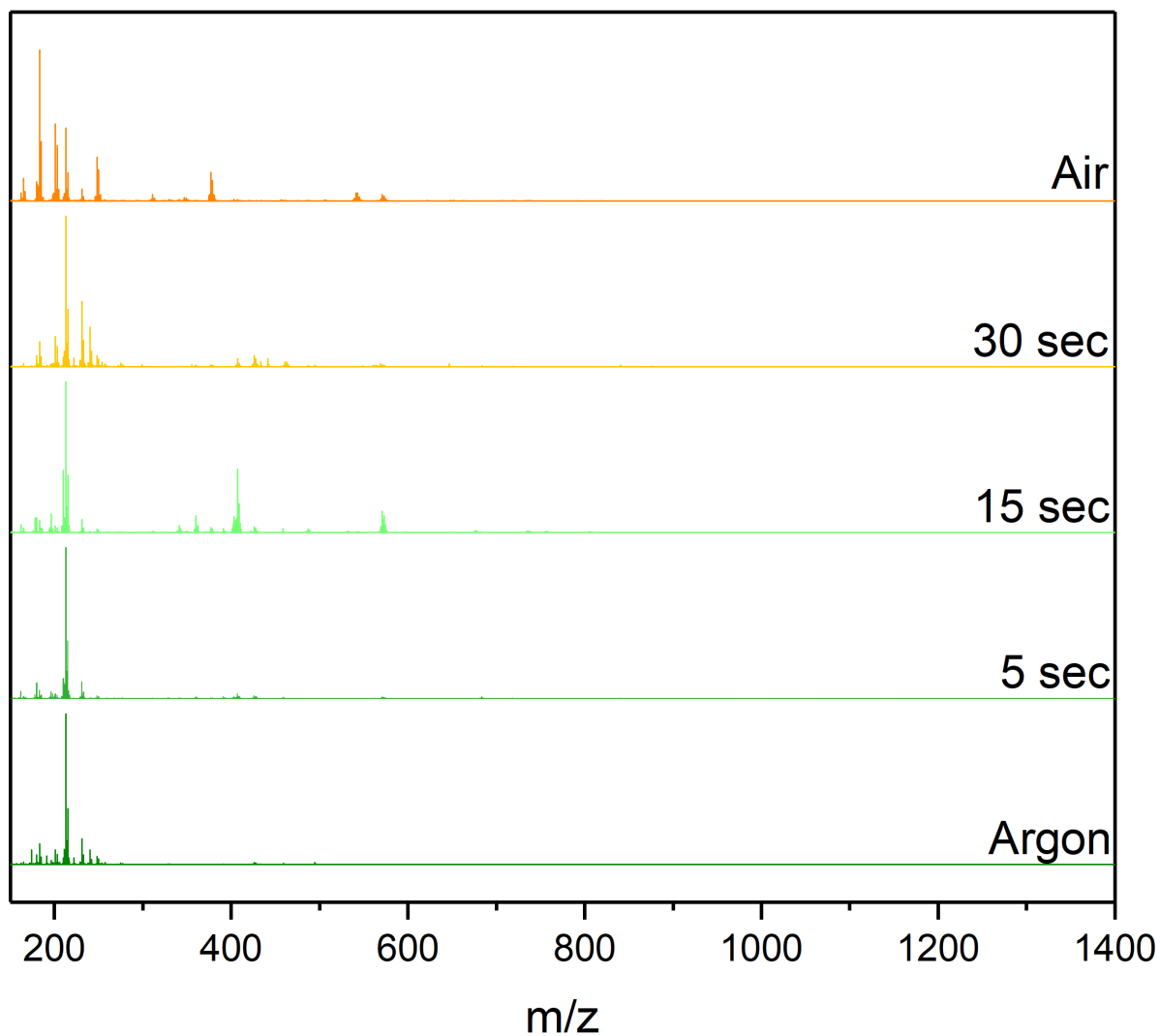


Figure S1: Full range LIFDI mass spectrum of $[(Cp)_2TiCl_2] + Zn$.

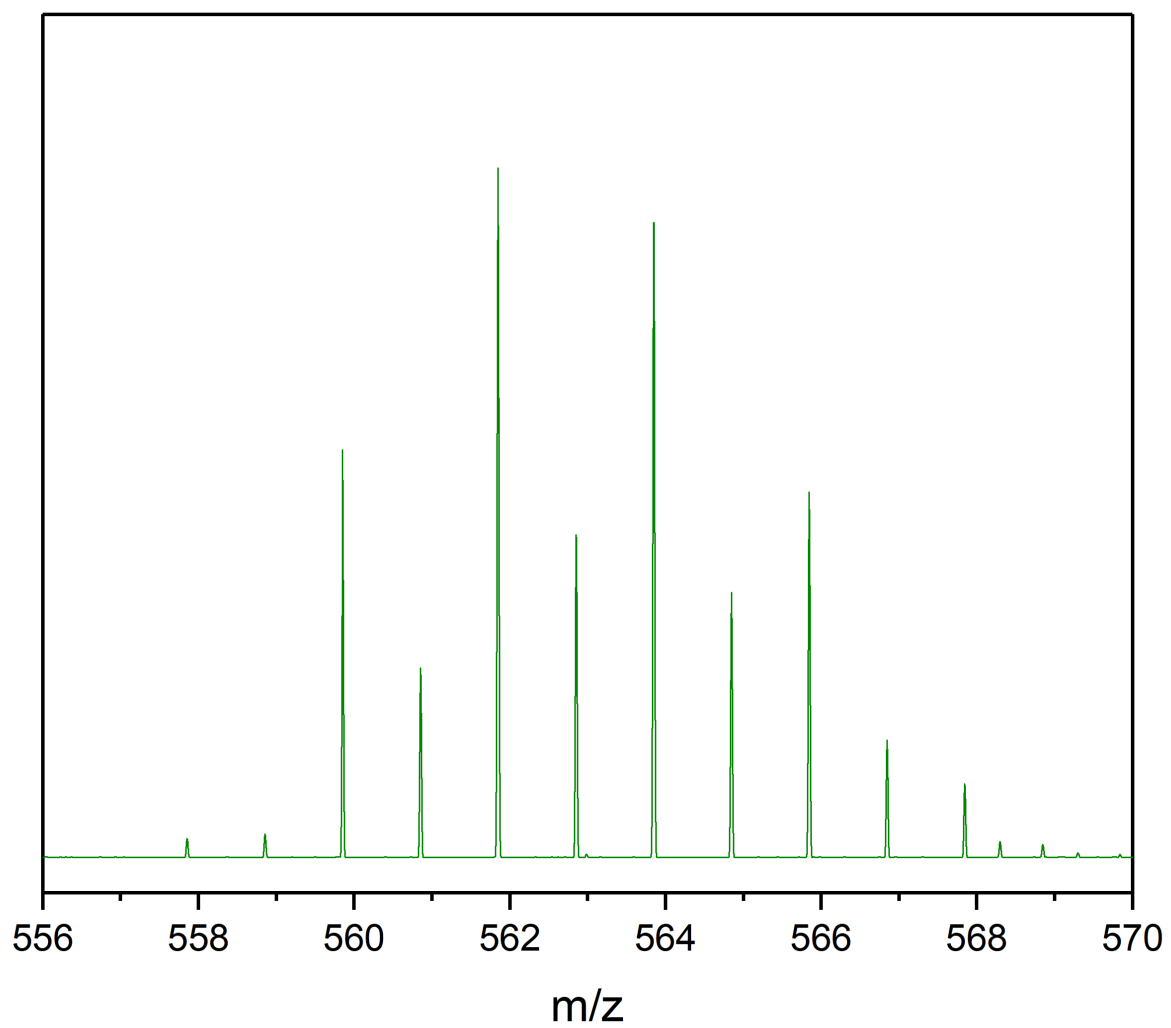


Figure S2: Molecular ion peak of $[(Cp)_2TiCl)_2ZnCl_2]^+$. The spectrum was recorded under inert conditions.

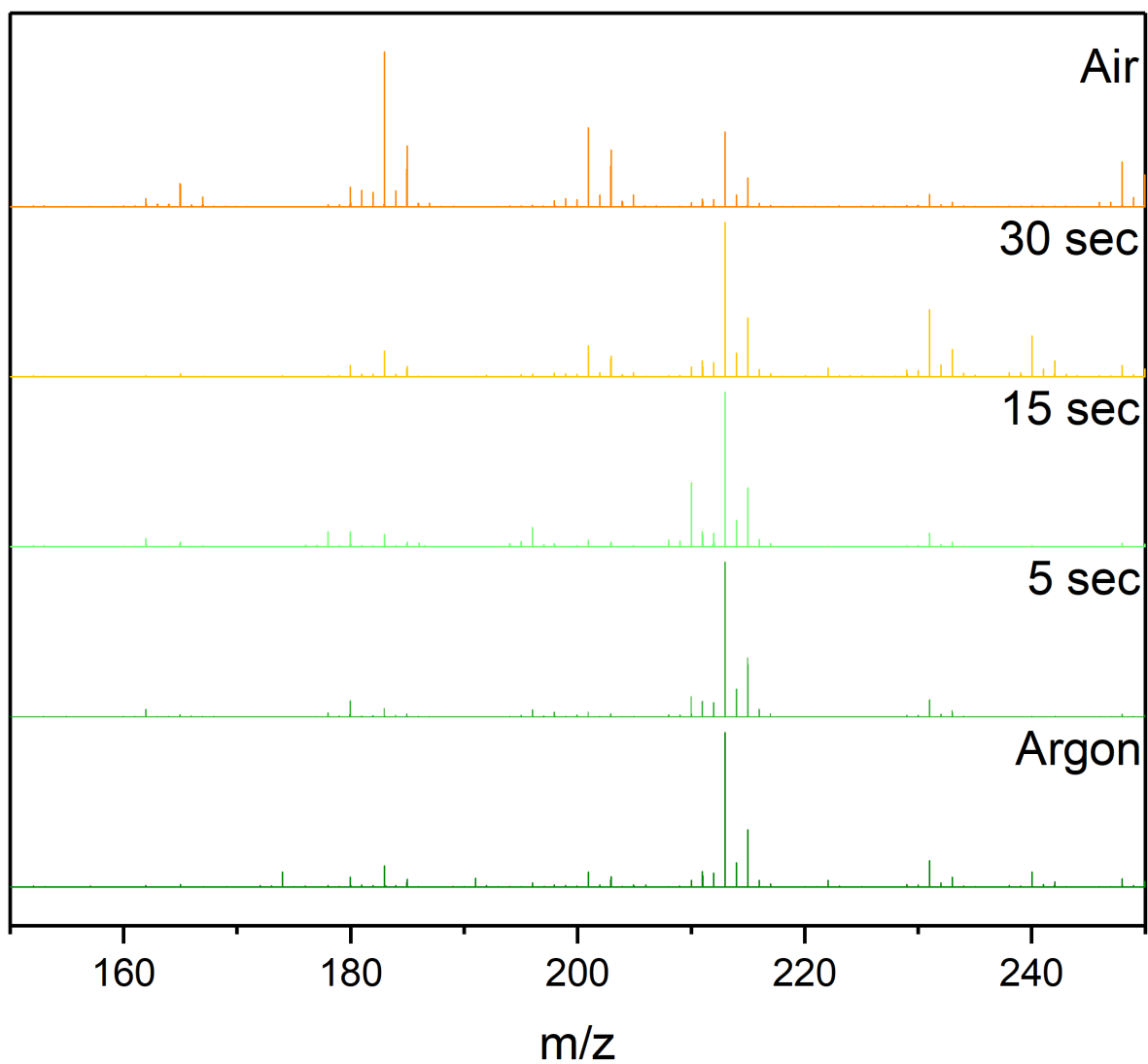


Figure S3: LIFDI mass spectrum of $[(Cp)_2TiCl_2] + Zn$, zoomed into m/z range of 150 – 250. Major peaks in increasing m/z order: 182.9680 $[(Cp)TiCl(OH)(OH_2)]^+$, 200.9354 $[(Cp)TiCl_2(OH_2)]^+$, 212.9936 $[(Cp)_2TiCl]^+$, 231.0054 $[(Cp)_2TiCl(OH_2)]^+$, 247.9632 $[(Cp)_2TiCl_2]^+$.

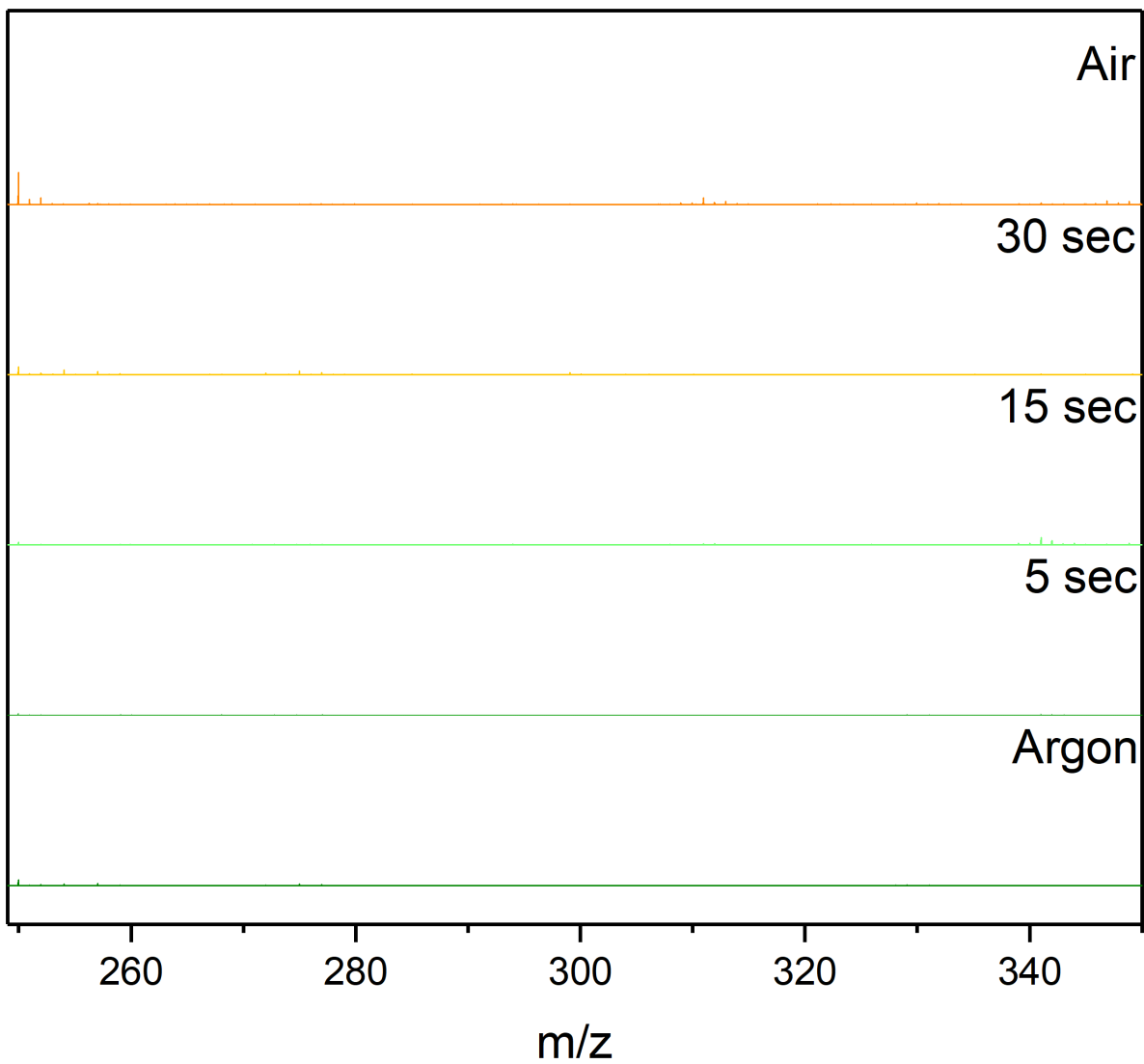


Figure S4: LIFDI mass spectrum of $[(Cp)_2TiCl_2] + Zn$, zoomed into m/z range of 250 – 350.

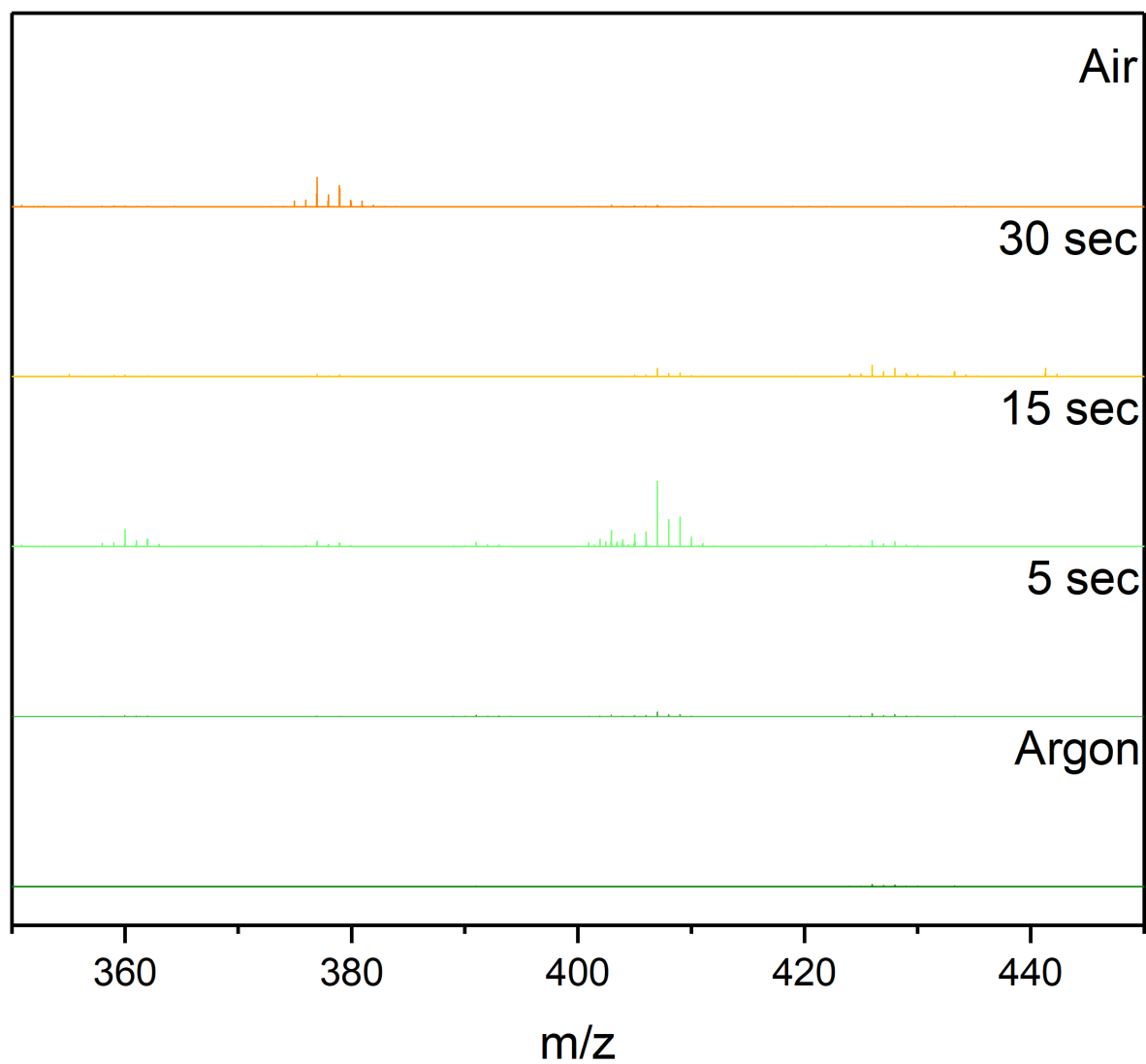


Figure S5: LIFDI mass spectrum of $[(Cp)_2TiCl_2] + Zn$, zoomed into m/z range of 350 - 450. Major peaks in increasing m/z order: 376.9465 $[(Cp)_3Ti_2Cl_2O]^+$, 407.0148 $[(Cp)_4Ti_2ClO]^+$.

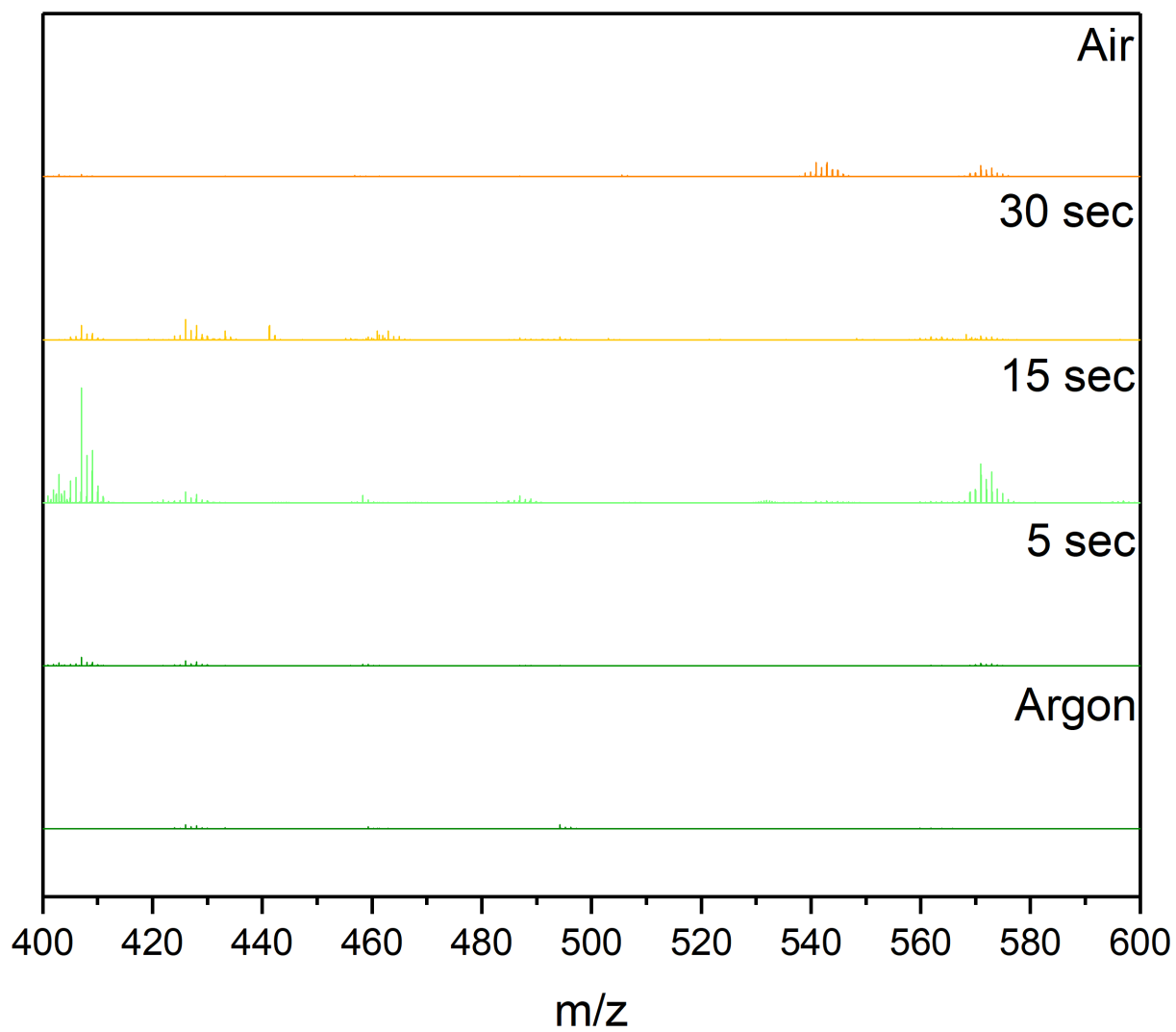


Figure S6: LIFDI mass spectrum of $[(Cp)_2TiCl_2] + Zn$, zoomed into m/z range of 400 - 600. Major peaks in increasing m/z order: 542.8914 $[(Cp)_4Ti_3ClO_2]^+$, 570.9646 $[(Cp)_5Ti_3Cl_2O_2]^+$.

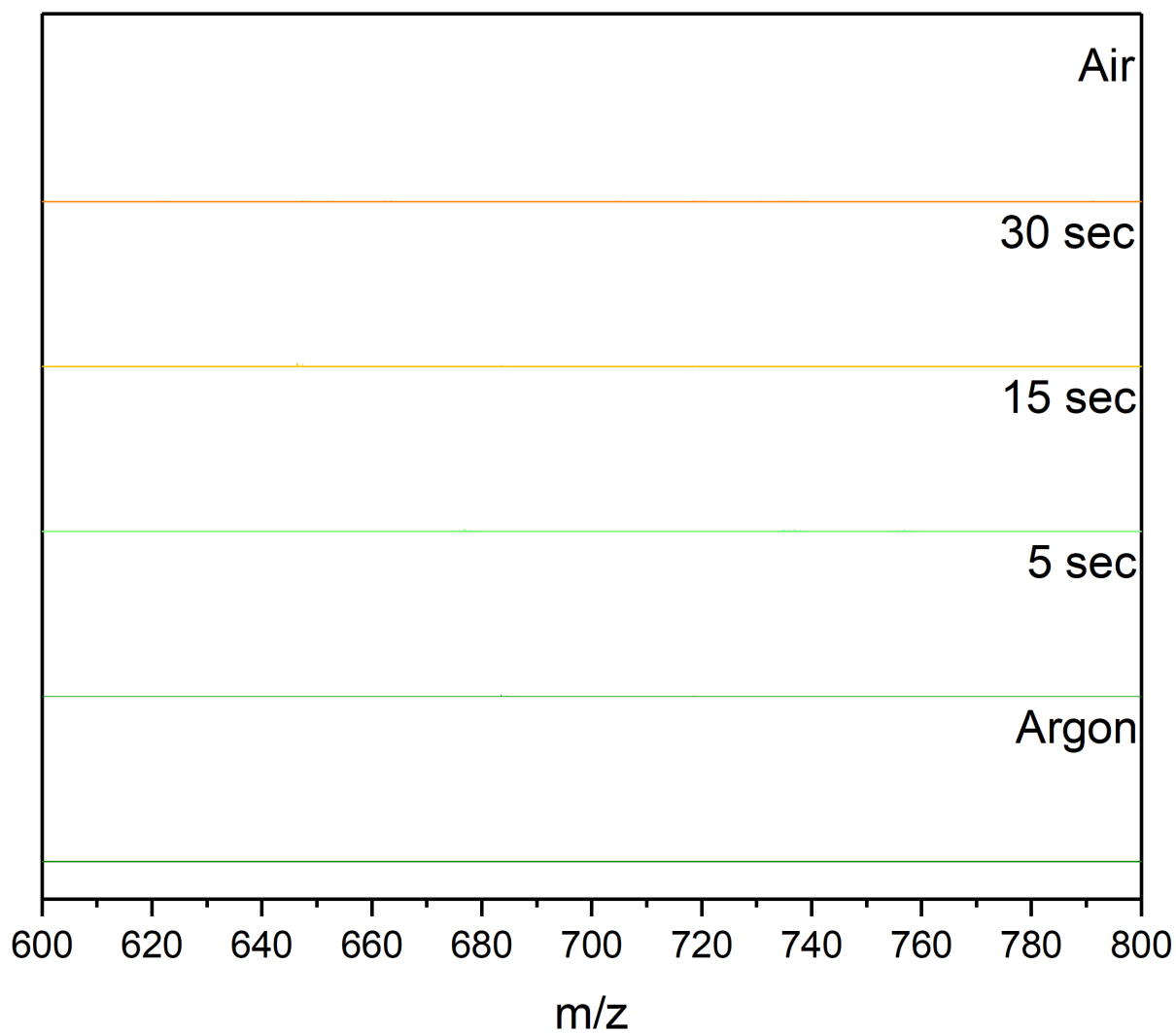


Figure S7: LIFDI mass spectrum of $[(Cp)_2TiCl_2] + Zn$, zoomed into m/z range of 600 - 800.

Full range spectra of [CuMes] + AlCp*

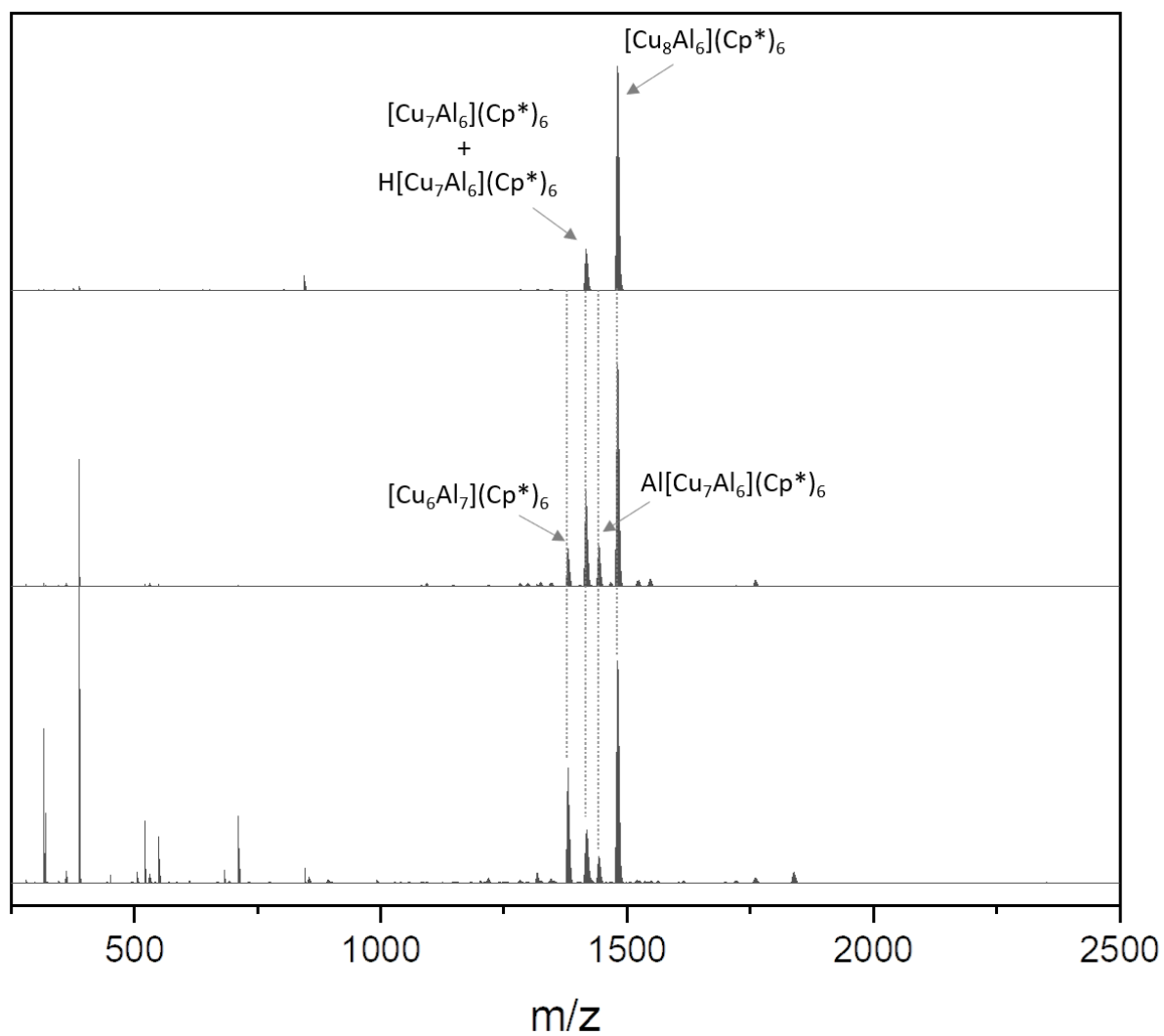


Figure S8: Full range LIFDI mass spectrum with peak labels of [CuMes] + 3.6 eq. of AlCp*.

2.7 Experimental Details

2.7.1 General Remarks

All manipulations were carried out using standard Schlenk techniques under inert atmospheres (Argon 4.6 from *Westphalen*), either in Schlenk flasks, tubes or an *UNILab* glovebox from *MBraun*. All glassware was flame dried in vacuum using heat guns and silylated prior to usage by refluxing small amounts of 1,1,1,3,3,3-hexamethyldisilazane (HMDS) in the reaction vessel. Residual HMDS was removed *in vacuo*. Solvents were dried using a *MBraun* Solvent Purification System and subsequent storage over molecular sieves (3 or 4 Å). The final H₂O content of all solvents was measured via Karl Fischer titration and was below 5 ppm. All chemicals and solvents were used as purchased from suppliers as *ABCR*, *ACROS Organics*, *Fisher Scientific* and *Sigma Aldrich*, if not stated otherwise. Precious metal salts (e.g., RuCl₃•xH₂O) were purchased from *Precious Metals Australia*. Deuterated solvents were bought from *Sigma Aldrich* and *Eurisotop*, stored over molecular sieves (3 and 4 Å) and degassed by freeze-pump-thaw.

2.7.2 Single Crystal X-Ray Diffraction

Data were collected on a single crystal x-ray diffractometer equipped with a CMOS detector (*Bruker APEX III*, κ-CMOS), a TXS rotating anode or an IMS microsource with MoK_α radiation ($\lambda = 0.71073$ Å) and a Helios optic using the APEX3 software package.¹ Measurements were performed on single crystals coated with perfluorinated ether. The crystals were fixed on top of a kapton micro sampler and frozen under a stream of cold nitrogen. A matrix scan was used to determine the initial lattice parameters. Reflections were corrected for Lorentz and polarisation effects, scan speed, and background using SAINT.² Absorption correction, including odd and even ordered spherical harmonics was performed using SADABS or TWINABS.^{2,3} Space group assignments were based upon systematic absences, E statistics, and successful refinement of the structures. The structures were solved using SHELXT with the aid of successive difference Fourier maps and were refined against all data using SHELXL-2014/2017 in conjunction with SHELXLE.^{4,5,6} For twinned crystals, the integration was performed for both domains and the structure was refined against hklf5 data. Hydrogen atoms were calculated in ideal positions as follows: Methyl hydrogen atoms were refined as part of rigid rotating groups, with a C–H distance of 0.98 Å and $U_{\text{iso(H)}} = 1.5 \cdot U_{\text{eq(C)}}$. Other H atoms were placed in calculated positions and refined using a riding model, with methylene and aromatic C–H distances of 0.99 Å and 0.95 Å, respectively, other C–H distances of 1.00 Å, all with $U_{\text{iso(H)}} = 1.2 \cdot U_{\text{eq(C)}}$. Non-hydrogen atoms were refined with anisotropic displacement parameters. Full-matrix least-squares refinements were carried out by minimizing $\sum w(F_o^2 - F_c^2)^2$ with the SHELXL weighting scheme.⁵ Neutral atom scattering factors for all atoms and anomalous dispersion corrections for the non-hydrogen atoms were taken from *International Tables for Crystallography*.⁷ A split layer refinement was used for disordered groups and additional

restraints on distances, angles and anisotropic displacement parameters were employed to ensure convergence within chemically reasonable limits, if necessary. Heavily disordered solvent molecules were treated as a diffuse contribution to the overall scattering without specific atom positions using the PLATON/SQUEEZE procedure.⁸ Images of the crystal structures were generated with PLATON and Mercury.^{9,10}

2.7.3 NMR Spectroscopy

NMR spectra were measured using Avance III NMR spectrometers (Bruker BioSpin GmbH) operating at spectrometer frequency of: 400 MHz (¹H), 101 MHz (¹³C) and 162 MHz (³¹P). Chemical shifts are given in ppm relative to tetramethyl silane, and spectra were referenced relative to the respective residual solvent signal. Abbreviations of the signal multiplicity: s: singlet, d: duplet, t: triplet, q: quartet, m: multiplet. NMR spectra were analyzed using the MestReNova software (version: 14.1.1-24571).

2.7.4 Mass Spectrometry

Liquid Injection Field Desorption Ionization Mass Spectrometry (LIFDI-MS) was measured directly from an inert atmosphere glovebox (*GS Gloveboxsystems*, E Line) with a *Thermo Fisher Scientific* Exactive Plus Orbitrap equipped with an ion source from *Linden CMS*. A detailed report on the setup was published in *Dalton Transactions*.¹¹

Electrospray Ionization Mass Spectrometry (ESI-MS) was measured with a *Thermo Fisher Scientific* Exactive Plus Orbitrap in the positive or negative mode respectively.

2.7.5 Infrared Spectroscopy

Infrared spectra were recorded with an Alpha FT-IR spectrometer from *Bruker*, equipped with an ATR (attenuated total reflection) accessory using a diamond ATR element. Samples were measured as powder under argon atmosphere in a glovebox. Spectral data was processed using the software OPUS 6.5 (*Bruker Optics GmbH*).

2.7.6 Raman Spectroscopy

The Raman spectra were recorded with a *Renishaw* InVia Raman Microscope equipped with a Newton EMCCD Camera. A frequency-doubled Nd:YAG laser (532 nm, 0.5–5 mW) and a 50x magnification micro-scope objective (*Leica* N PLAN EPI 50x/0.75 na) were used during the measurements. Samples were measured in glass capillaries under inert atmosphere.

2.7.7 UV-Vis Spectroscopy

UV-Vis spectra were recorded on an *Agilent Technologies* Cary 60 with a scan rate of 600 nm/min. Baseline correction was performed with the respective pure solvent. Each sample was measured in a Schlenk-modified 10.00 mm quartz glass cuvette from *Hellma* Analytics.

2.7.8 Elemental Analysis

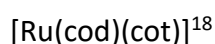
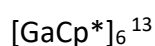
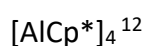
Elemental analysis and AAS measurements were performed by the Microanalytical Laboratory of the Technical University of Munich on a *HEKAtech* Euro EA CHNSO-Analyzer and for metal analysis a *Varian* AA280FS AAS spectrometer. Additional measurements were performed at the Microanalytical Laboratory Kolbe (Mülheim an der Ruhr) using an Elementar CHNOS-Analyzer (Vario-EL) and a *Perkin Elmer* AAS Analyst200.

2.7.9 Computational Methods

Computational details are given for the individual case.

2.7.10 Common starting reagents

The following compounds were prepared by literature procedures. For the literature known $[\text{GaTMP}]_4$ and $[\text{Ni}_2(\text{dvds})_3]$ novel accesses were developed and are stated in the respective addition information part.



2.7.11 References

1. APEX suite of crystallographic software, APEX 3, Version 2015-5.2, Bruker AXS Inc., Madison, Wisconsin, USA, **2015**.
2. SAINT, Version 8.34A and SADABS, Version 2014/5, Bruker AXS Inc., Madison, Wisconsin, USA, **2014**.
3. TWINABS, Version 2012/1, Bruker AXS Inc., Madison, Wisconsin, USA, **2012**.
4. G. M. Sheldrick, *Acta Crystallogr. Sect. A* **2015**, 71, 3–8.
5. G. M. Sheldrick, *Acta Crystallogr. Sect. C* **2015**, 71, 3–8.
6. C. B. Hübschle, G. M. Sheldrick, B. Dittrich, *J. Appl. Cryst.* **2011**, 44, 1281–1284
7. International Tables for Crystallography, Vol. C (Ed.: A. J. Wilson), Kluwer Academic Publishers, Dordrecht, The Netherlands, **1992**, Tables 6.1.1.4 (pp. 500–502), 4.2.6.8 (pp. 219–222), and 4.2.4.2 (pp. 193–199).
8. A. L. Spek, *Acta Crystallogr. Sect. C* **2015**, 71, 9–18.
9. A. L. Spek, *Acta Crystallogr. Sect. D* **2009**, 65, 148–155.
10. C. F. Macrae, I. J. Bruno, J. A. Chisholm, P. R. Edgington, P. McCabe, E. Pidcock, L. Rodriguez-Monge, R. Taylor, J. van de Streek, P. A. Wood, *J. Appl. Cryst.* **2008**, 41, 466–470.
11. M. Muhr, P. Heiß, M. Schütz, R. Bühler, C. Gemel, M. Linden, B. H. Linden, R. A. Fischer, *Dalton Trans.* **2021**, 50, 9031–9036.
12. C. Ganesamoorthy, S. Loerke, C. Gemel, P. Jerabek, M. Winter, G. Frenking, R. A. Fischer, *Chem. Commun.* **2013**, 49, 2858–2860.
13. P. Jutzi, B. Neumann, G. Reumann, H.-G. Stammler, *Organometallics* **1998**, 17, 1305–1314.
14. A. Seifert, G. Linti, *Eur. J. Inorg. Chem.* **2007**, 2007, 5080–5086.
15. D. J. Krysan, P. B. Mackenzie, *J. Org. Chem.* **1990**, 55, 4229–4230.
16. B. Bogdanović, M. Kröner, G. Wilke, *Liebigs Ann. Chem.* **1966**, 699, 1–23.
17. H. Maciejewski, B. Marciniak, I. Kownacki, *J. Organomet. Chem.* **2000**, 597, 175–181.
18. P. Pertici, G. Vitulli, M. Paci, L. Porri, *Dalton Trans.* **1980**, 1961–1964.
19. K. S. MacFarlane, S. J. Rettig, Z. Liu, B. R. James, *J. Organomet. Chem.* **1998**, 557, 213–219.

3. Conclusion

The conclusion from this work leads inevitably back to the three problems of cluster chemistry and its entanglement. Neither the problem of directed synthesis, nor structure prediction, nor controlled reactivity of clusters could of course be solved in the present work. What became apparent, however, is that these three problems cannot be solved separately at all. *In situ* mass spectrometry could be established as the backbone for successful predictive synthetic cluster chemistry. Identification and prediction of structures succeeds based on experimental data and density functional theory calculations.

The value of elucidating the composition of an inseparable mixture of closely related clusters by mass spectrometry in combination with the evaluation of the individual structure of each species by a DFT-based 'global optimization' approach lies mainly in the possible transferability of this strategy to similar problems in cluster chemistry. The approach is validated by various experimental spectroscopic techniques and forms the basis for a targeted reactivity study that elucidated key differences between individual clusters with slightly different core compositions. A further development of the methodology has already been successfully applied to the structural elucidation of various Cu/Zn clusters that are much less related to each other.

In the context of studying clusters in terms of their respective solid-phase analogues, it is essential to investigate cluster-substrate interactions in more detail, which requires freely accessible metal centers in cluster cores. The choice of the right GaR species as ligands proved to be crucial. Hampering transmetalation reactions can be prevented by using GaTMP instead of GaCp*, leading to a cluster with freely accessible Ni coordination sites. The reaction of such a cluster with H₂ leads to (poly)hydride species that are even active in hydrogenation catalysis reactions. Moreover, this example highlights the cooperative relationship between Ni and Ga: the Ga atoms act as a "storage site" for hydrides and are held responsible for the selective semihydrogenation catalysis of alkynes. The use of GaTMP is not limited to Ni. Treatment of TMs with 'high transmetalation potential' (e.g., Fe, Co) could lead to clusters with comparable active sites and eventually to the discovery of unprecedented reactivities.

The study of selective removal of ligands from clusters is based on a similar motivation - controlling the reactivity of reactive cluster species. Both presented RuGa examples illustrate the enhanced reactivity of undercoordinated cluster species, but also the challenges in controlling their competing reactivity (catalysis vs. cluster growth). Pioneering work in the field of photochemical activation of clusters potentially opens a novel strategy for selective formation of clusters with active sites: Undercoordinated species are produced under hydrogenolytic conditions and readily activate dummy substrates such as silanes, which in turn act as inorganic protecting groups that can be cleaved under mild conditions. It may be beneficial to apply the conceptual insights gained to the formation of clusters of interest and see if a unified approach can be found. Such a concept would allow for more predictable cluster synthesis and make subsequent reactivity more predictable.

4. Appendix

4.1 List of Abbreviations

ADF	Amsterdam Density Functional
AO	Atomic Orbital
ATR	Attenuated Total Reflection
C ₆ D ₆	Benzene- <i>d</i> ₆ (deuterated)
C ₆ D ₁₂	Cyclohexane- <i>d</i> ₁₂ (deuterated)
cdt	<i>trans,trans,trans</i> -1,5,9-cyclododecatriene
cod	1,5-Cyclododecadiene
Cp*	1,2,3,4,5-Pentamethylcyclopentadienyl
DFT	Density Functional Theory
dppbz	1,2-Bis(diphenylphosphino)benzene
dppe	1,2-Bis(diphenylphosphino)ethane
dvds	1,1,3,3-Tetramethyl-1,3-divinylsiloxane
EA	Elemental Analysis
EDA-NOCV	Energy Decomposition Analysis with the Natural Orbital for Chemical Valence extension
E-R	E = main group element, mainly group 13 (B, Al, Ga, In); R = organic group, mainly Cp*
EPR	Electron Paramagnetic Resonance
ESI	Electrospray Ionization
Et	Ethyl
FD	Field Desorption
HMBC	Heteronuclear Multiple Bond Correlation
HOMO	Highest Occupied Molecular Orbital
HR	Hume-Rothery
HSQC	Heteronuclear Single Quantum Coherence
IR	Infrared, mainly infrared spectroscopy
L	Ligand
LIFDI	Liquid Injection Field Desorption Ionization, mainly mass spectrometry
LUMO	Lowest Occupied Molecular Orbital

M	Metal
Me	Methyl
MO	Molecular Orbital
MS	Mass Spectrometry
NBO	Natural Bond Orbitals
NHC	<i>N</i> -Heterocyclic Carbene
MAS	Magic Angle Spinning (solid-state NMR)
NMR	Nuclear Magnetic Resonance
NOESY	Nuclear Overhauser Effect Spectroscopy
NP(s)	Nanoparticle(s)
ppm	Parts Per Million (chemical shift NMR)
PXRD	Powder X-Ray Diffraction
QTAIM	Quantum Theory of Atoms In Molecules
R	Organic Residue, mainly Cp*/TMP
ROESY	Rotating frame Overhauser Enhancement Spectroscopy
RT	Room Temperature (20-25 °C)
SC-XRD	Single Crystal X-Ray Diffraction
SQUID	Superconducting Quantum Interference Device
TDDFT	Time Dependent Density Functional Theory
THF	tetrahydrofuran
TIPSA	Triisopropylsilyl-acetylene
TM	Transition Metal
Tol- <i>d</i> ₈	Toluene- <i>d</i> ₈ (deuterated)
TMP	2,2,6,6-Tetramethylpiperidinyl
TZVPP	Valence triple-zeta with two sets of polarization functions
UV-Vis	Ultraviolet Visible, mainly spectroscopy
VE	Valence Electron
VT	Variable Temperature
WBI	Wiberg Bonding Index
XPS	X-Ray Photoelectron Spectroscopy

4.2 List of Publications

Thesis Relevant Publications:

1. M. Muhr⁺, J. Hornung⁺, J. Weßing, C. Jandl, C. Gemel, R. A. Fischer, *Inorg. Chem.* **2020**, *59*, 5086-5092.
2. M. Muhr⁺, P. Heiß⁺, M. Schütz, R. Bühler, C. Gemel, M. H. Linden, H. B. Linden, R. A. Fischer, *Dalton Trans.* **2021**, *50*, 9031-9036.
3. M. Muhr⁺, R. Bühler⁺, H. Liang, J. Gilch, C. Jandl, S. Kahlal, J.-Y. Saillard, C. Gemel, R. A. Fischer, *Chem. Eur. J.* **2022**, *28*, e202200887.

Subject Specific Publications:

1. J. Hornung, M. Muhr, C. Gemel, R. A. Fischer, *Dalton Trans.* **2019**, *48*, 11743-11748.
2. M. Schütz, M. Muhr, K. Freitag, C. Gemel, S. Kahlal, J.-Y. Saillard, A. C. H. Da Silva, J. L. F. Da Silva, T. F. Fässler, R. A. Fischer, *Inorg. Chem.* **2020**, *59*, 9077-9085.
3. M. Schütz, C. Gemel, M. Muhr, C. Jandl, S. Kahlal, J.-Y. Saillard, R. A. Fischer, *Chem. Sci.* **2021**, *12*, 6588-6599.
4. J. Mink, L. Staiger, M. Muhr, C. Gemel, M. Drees, L. Hajba, J. Mihály, C. Németh, B. V. Lokshin, K. Hemmer, M. Schütz, M. Cokoja, R. A. Fischer, *J. Raman Spectrosc.* **2021**, *52*, 2317-2337.

Mass Spectrometry related Publication:

1. A. Urstoeger, L. Zacherl, M. Muhr, Y. Selic, M. Wenisch, M. Klotz, M. Schuster, *Talanta* **2021**, *225*, 122028.
2. T. P. Schlachta, J. F. Schlagintweit, M. R. Anneser, E.-M. H. J. Esslinger, M. Muhr, S. Haslinger, F. E. Kühn, *Inorg. Chim. Acta* **2021**, *518*, 120228.
3. S. V. Hirmer, F. S. Tschernuth, F. Hanusch, R. Baierl, M. Muhr, S. Inoue, *Mendeleev Commun.* **2022**, *32*, 16-18.

[+] denotes equal contribution.

An updated list of all publication can be found though [ORCID](#).

4.3 Reprint Permissions

The screenshot shows a web browser window with the URL <https://s100.copyright.com/AppDispatchServlet>. The page header includes the CCC RightsLink logo and navigation links for Home, Help, Live Chat, and a user profile for Maximilian Muhr. The main content area displays the following information:

Tuning Nickel with Lewis Acidic Group 13 Metalloligands for Catalytic Olefin Hydrogenation
Author: Ryan C. Cammarota, Connie C. Lu
Publication: Journal of the American Chemical Society
Publisher: American Chemical Society
Date: Oct 1, 2015
Copyright © 2015, American Chemical Society

PERMISSION/LICENSE IS GRANTED FOR YOUR ORDER AT NO CHARGE

This type of permission/license, instead of the standard Terms and Conditions, is sent to you because no fee is being charged for your order. Please note the following:

- Permission is granted for your request in both print and electronic formats, and translations.
- If figures and/or tables were requested, they may be adapted or used in part.
- Please print this page for your records and send a copy of it to your publisher/graduate school.
- Appropriate credit for the requested material should be given as follows: "Reprinted (adapted) with permission from (COMPLETE REFERENCE CITATION). Copyright (YEAR) American Chemical Society." Insert appropriate information in place of the capitalized words.
- One-time permission is granted only for the use specified in your RightsLink request. No additional uses are granted (such as derivative works or other editions). For any uses, please submit a new request.

If credit is given to another source for the material you requested from RightsLink, permission must be obtained from that source.

Buttons: BACK, CLOSE WINDOW

The screenshot shows a web browser window with the URL <https://s100.copyright.com/AppDispatchServlet>. The page header includes the CCC RightsLink logo and navigation links for Home, Help, Live Chat, and a user profile for Maximilian Muhr. The main content area displays the following information:

A Bimetallic Nickel-Gallium Complex Catalyzes CO₂ Hydrogenation via the Intermediacy of an Anionic d10 Nickel Hydride
Author: Ryan C. Cammarota, Matthew V. Vollmer, Jing Xie, et al
Publication: Journal of the American Chemical Society
Publisher: American Chemical Society
Date: Oct 1, 2017
Copyright © 2017, American Chemical Society

PERMISSION/LICENSE IS GRANTED FOR YOUR ORDER AT NO CHARGE

This type of permission/license, instead of the standard Terms and Conditions, is sent to you because no fee is being charged for your order. Please note the following:

- Permission is granted for your request in both print and electronic formats, and translations.
- If figures and/or tables were requested, they may be adapted or used in part.
- Please print this page for your records and send a copy of it to your publisher/graduate school.
- Appropriate credit for the requested material should be given as follows: "Reprinted (adapted) with permission from (COMPLETE REFERENCE CITATION). Copyright (YEAR) American Chemical Society." Insert appropriate information in place of the capitalized words.
- One-time permission is granted only for the use specified in your RightsLink request. No additional uses are granted (such as derivative works or other editions). For any uses, please submit a new request.


If credit is given to another source for the material you requested from RightsLink, permission must be obtained from that source.

Buttons: BACK, CLOSE WINDOW

← → ↻ 🏠 🔒 https://s100.copyright.com/AppDispatchServlet

CCC RightsLink Home Help ▾ Email Support Maximilian Muhr ▾

Formation of a Propeller-Shaped Ni₄Ga₃ Cluster Supported by Transmetalation of Cp* from Ga to Ni

 **Author:** Maximilian Muhr, Julius Hornung, Jana Weßing, et al
Publication: Inorganic Chemistry
Publisher: American Chemical Society
Date: Apr 1, 2020
Copyright © 2020, American Chemical Society

PERMISSION/LICENSE IS GRANTED FOR YOUR ORDER AT NO CHARGE

This type of permission/license, instead of the standard Terms and Conditions, is sent to you because no fee is being charged for your order. Please note the following:

- Permission is granted for your request in both print and electronic formats, and translations.
- If figures and/or tables were requested, they may be adapted or used in part.
- Please print this page for your records and send a copy of it to your publisher/graduate school.
- Appropriate credit for the requested material should be given as follows: "Reprinted (adapted) with permission from {COMPLETE REFERENCE CITATION}. Copyright {YEAR} American Chemical Society." Insert appropriate information in place of the capitalized words.
- One-time permission is granted only for the use specified in your RightsLink request. No additional uses are granted (such as derivative works or other editions). For any uses, please submit a new request.

If credit is given to another source for the material you requested from RightsLink, permission must be obtained from that source.


[BACK](#) [CLOSE WINDOW](#)

Zur Suche Text hier eingeben 12:45 07.10.2022

← → ↻ 🏠 🔒 https://s100.copyright.com/AppDispatchServlet

CCC RightsLink Home ? Live Chat Maximilian Muhr ▾

Magnesium of Aryl Fluorides Catalyzed by a Rhodium–Aluminum Complex

 **Author:** Ikuya Fujii, Kazuhiko Semba, Qiao-Zhi Li, et al
Publication: Journal of the American Chemical Society
Publisher: American Chemical Society
Date: Jul 1, 2020
Copyright © 2020, American Chemical Society

PERMISSION/LICENSE IS GRANTED FOR YOUR ORDER AT NO CHARGE

This type of permission/license, instead of the standard Terms and Conditions, is sent to you because no fee is being charged for your order. Please note the following:

- Permission is granted for your request in both print and electronic formats, and translations.
- If figures and/or tables were requested, they may be adapted or used in part.
- Please print this page for your records and send a copy of it to your publisher/graduate school.
- Appropriate credit for the requested material should be given as follows: "Reprinted (adapted) with permission from {COMPLETE REFERENCE CITATION}. Copyright {YEAR} American Chemical Society." Insert appropriate information in place of the capitalized words.
- One-time permission is granted only for the use specified in your RightsLink request. No additional uses are granted (such as derivative works or other editions). For any uses, please submit a new request.

If credit is given to another source for the material you requested from RightsLink, permission must be obtained from that source.

[BACK](#) [CLOSE WINDOW](#)

Zur Suche Text hier eingeben 19:46 19.10.2022

JOHN WILEY AND SONS LICENSE
TERMS AND CONDITIONS

Sep 21, 2022

This Agreement between Maximilian Muhr ("You") and John Wiley and Sons ("John Wiley and Sons") consists of your license details and the terms and conditions provided by John Wiley and Sons and Copyright Clearance Center.

License Number 5393640518573

License date Sep 21, 2022

Licensed Content
Publisher John Wiley and SonsLicensed Content
Publication Angewandte Chemie International EditionLicensed Content Title Interconversion of Quadruply and Quintuply Bonded Molybdenum
Complexes by Reductive Elimination and Oxidative Addition of
DihydrogenLicensed Content
Author Ernesto Carmona, Santiago Alvarez, Eliseo Ruiz, et al

Licensed Content Date Feb 1, 2013

Licensed Content
Volume 52Licensed Content
Issue 11

Licensed Content Pages	5
Type of use	Dissertation/Thesis
Requestor type	University/Academic
Format	Print and electronic
Portion	Figure/table
Number of figures/tables	1
Will you be translating?	No
Title	Reactive sites generation at intermetallic clusters
Institution name	Technical University of Munich
Expected presentation date	Jan 2024
Portions	TOC
Requestor Location	Maximilian Muhr Lichtenbergstrasse 4 Garching, 85748 Germany Attn: Technical University Munich
Publisher Tax ID	EU826007151
Total	0.00 USD

Terms and Conditions

TERMS AND CONDITIONS

This copyrighted material is owned by or exclusively licensed to John Wiley & Sons, Inc. or one of its group companies (each a "Wiley Company") or handled on behalf of a society with which a Wiley Company has exclusive publishing rights in relation to a particular work (collectively "WILEY"). By clicking "accept" in connection with completing this licensing transaction, you agree that the following terms and conditions apply to this transaction (along with the billing and payment terms and conditions established by the Copyright Clearance Center Inc., ("CCC's Billing and Payment terms and conditions"), at the time that you opened your RightsLink account (these are available at any time at <http://myaccount.copyright.com>).

Terms and Conditions

- The materials you have requested permission to reproduce or reuse (the "Wiley Materials") are protected by copyright.
- You are hereby granted a personal, non-exclusive, non-sub licensable (on a stand-alone basis), non-transferable, worldwide, limited license to reproduce the Wiley Materials for the purpose specified in the licensing process. This license, **and any CONTENT (PDF or image file) purchased as part of your order**, is for a one-time use only and limited to any maximum distribution number specified in the license. The first instance of republication or reuse granted by this license must be completed within two years of the date of the grant of this license (although copies prepared before the end date may be distributed thereafter). The Wiley Materials shall not be used in any other manner or for any other purpose, beyond what is granted in the license. Permission is granted subject to an appropriate acknowledgement given to the author, title of the material/book/journal and the publisher. You shall also duplicate the copyright notice that appears in the Wiley publication in your use of the Wiley Material. Permission is also granted on the understanding that nowhere in the text is a previously published source acknowledged for all or part of this Wiley Material. Any third party content is expressly excluded from this permission.
- With respect to the Wiley Materials, all rights are reserved. Except as expressly granted by the terms of the license, no part of the Wiley Materials may be copied, modified, adapted (except for minor reformatting required by the new Publication), translated, reproduced, transferred or distributed, in any form or by any means, and no derivative works may be made based on the Wiley Materials without the prior permission of the respective copyright owner. **For STM Signatory Publishers clearing permission under the terms of the [STM Permissions Guidelines](#) only, the terms of the license are extended to include subsequent editions and for editions in other languages, provided such editions are for the work as a whole in situ and does not involve the separate exploitation of the permitted figures or extracts,** You may not alter, remove or suppress in any manner any copyright, trademark or other notices displayed by the Wiley Materials. You may not license, rent, sell, loan, lease, pledge, offer as security, transfer or assign the Wiley Materials on a stand-alone

basis, or any of the rights granted to you hereunder to any other person.

- The Wiley Materials and all of the intellectual property rights therein shall at all times remain the exclusive property of John Wiley & Sons Inc, the Wiley Companies, or their respective licensors, and your interest therein is only that of having possession of and the right to reproduce the Wiley Materials pursuant to Section 2 herein during the continuance of this Agreement. You agree that you own no right, title or interest in or to the Wiley Materials or any of the intellectual property rights therein. You shall have no rights hereunder other than the license as provided for above in Section 2. No right, license or interest to any trademark, trade name, service mark or other branding ("Marks") of WILEY or its licensors is granted hereunder, and you agree that you shall not assert any such right, license or interest with respect thereto
- NEITHER WILEY NOR ITS LICENSORS MAKES ANY WARRANTY OR REPRESENTATION OF ANY KIND TO YOU OR ANY THIRD PARTY, EXPRESS, IMPLIED OR STATUTORY, WITH RESPECT TO THE MATERIALS OR THE ACCURACY OF ANY INFORMATION CONTAINED IN THE MATERIALS, INCLUDING, WITHOUT LIMITATION, ANY IMPLIED WARRANTY OF MERCHANTABILITY, ACCURACY, SATISFACTORY QUALITY, FITNESS FOR A PARTICULAR PURPOSE, USABILITY, INTEGRATION OR NON-INFRINGEMENT AND ALL SUCH WARRANTIES ARE HEREBY EXCLUDED BY WILEY AND ITS LICENSORS AND WAIVED BY YOU.
- WILEY shall have the right to terminate this Agreement immediately upon breach of this Agreement by you.
- You shall indemnify, defend and hold harmless WILEY, its Licensors and their respective directors, officers, agents and employees, from and against any actual or threatened claims, demands, causes of action or proceedings arising from any breach of this Agreement by you.
- IN NO EVENT SHALL WILEY OR ITS LICENSORS BE LIABLE TO YOU OR ANY OTHER PARTY OR ANY OTHER PERSON OR ENTITY FOR ANY SPECIAL, CONSEQUENTIAL, INCIDENTAL, INDIRECT, EXEMPLARY OR PUNITIVE DAMAGES, HOWEVER CAUSED, ARISING OUT OF OR IN CONNECTION WITH THE DOWNLOADING, PROVISIONING, VIEWING OR USE OF THE MATERIALS REGARDLESS OF THE FORM OF ACTION, WHETHER FOR BREACH OF CONTRACT, BREACH OF WARRANTY, TORT, NEGLIGENCE, INFRINGEMENT OR OTHERWISE (INCLUDING, WITHOUT LIMITATION, DAMAGES BASED ON LOSS OF PROFITS, DATA, FILES, USE, BUSINESS OPPORTUNITY OR CLAIMS OF THIRD PARTIES), AND WHETHER OR NOT THE PARTY HAS BEEN ADVISED OF THE POSSIBILITY OF SUCH DAMAGES. THIS LIMITATION SHALL APPLY NOTWITHSTANDING ANY FAILURE OF ESSENTIAL PURPOSE OF ANY LIMITED REMEDY PROVIDED HEREIN.
- Should any provision of this Agreement be held by a court of competent jurisdiction to be illegal, invalid, or unenforceable, that provision shall be deemed amended to achieve as nearly as possible the same economic effect as the original provision, and the legality, validity and enforceability of the remaining provisions of this Agreement

shall not be affected or impaired thereby.

- The failure of either party to enforce any term or condition of this Agreement shall not constitute a waiver of either party's right to enforce each and every term and condition of this Agreement. No breach under this agreement shall be deemed waived or excused by either party unless such waiver or consent is in writing signed by the party granting such waiver or consent. The waiver by or consent of a party to a breach of any provision of this Agreement shall not operate or be construed as a waiver of or consent to any other or subsequent breach by such other party.
- This Agreement may not be assigned (including by operation of law or otherwise) by you without WILEY's prior written consent.
- Any fee required for this permission shall be non-refundable after thirty (30) days from receipt by the CCC.
- These terms and conditions together with CCC's Billing and Payment terms and conditions (which are incorporated herein) form the entire agreement between you and WILEY concerning this licensing transaction and (in the absence of fraud) supersedes all prior agreements and representations of the parties, oral or written. This Agreement may not be amended except in writing signed by both parties. This Agreement shall be binding upon and inure to the benefit of the parties' successors, legal representatives, and authorized assigns.
- In the event of any conflict between your obligations established by these terms and conditions and those established by CCC's Billing and Payment terms and conditions, these terms and conditions shall prevail.
- WILEY expressly reserves all rights not specifically granted in the combination of (i) the license details provided by you and accepted in the course of this licensing transaction, (ii) these terms and conditions and (iii) CCC's Billing and Payment terms and conditions.
- This Agreement will be void if the Type of Use, Format, Circulation, or Requestor Type was misrepresented during the licensing process.
- This Agreement shall be governed by and construed in accordance with the laws of the State of New York, USA, without regards to such state's conflict of law rules. Any legal action, suit or proceeding arising out of or relating to these Terms and Conditions or the breach thereof shall be instituted in a court of competent jurisdiction in New York County in the State of New York in the United States of America and each party hereby consents and submits to the personal jurisdiction of such court, waives any objection to venue in such court and consents to service of process by registered or certified mail, return receipt requested, at the last known address of such party.

WILEY OPEN ACCESS TERMS AND CONDITIONS

Wiley Publishes Open Access Articles in fully Open Access Journals and in Subscription journals offering Online Open. Although most of the fully Open Access journals publish open access articles under the terms of the Creative Commons Attribution (CC BY) License

only, the subscription journals and a few of the Open Access Journals offer a choice of Creative Commons Licenses. The license type is clearly identified on the article.

The Creative Commons Attribution License

The [Creative Commons Attribution License \(CC-BY\)](#) allows users to copy, distribute and transmit an article, adapt the article and make commercial use of the article. The CC-BY license permits commercial and non-

Creative Commons Attribution Non-Commercial License

The [Creative Commons Attribution Non-Commercial \(CC-BY-NC\)License](#) permits use, distribution and reproduction in any medium, provided the original work is properly cited and is not used for commercial purposes.(see below)

Creative Commons Attribution-Non-Commercial-NoDerivs License

The [Creative Commons Attribution Non-Commercial-NoDerivs License \(CC-BY-NC-ND\)](#) permits use, distribution and reproduction in any medium, provided the original work is properly cited, is not used for commercial purposes and no modifications or adaptations are made. (see below)

Use by commercial "for-profit" organizations

Use of Wiley Open Access articles for commercial, promotional, or marketing purposes requires further explicit permission from Wiley and will be subject to a fee.

Further details can be found on Wiley Online Library <http://olabout.wiley.com/WileyCDA/Section/id-410895.html>

Other Terms and Conditions:

v1.10 Last updated September 2015

Questions? customercare@copyright.com or +1-855-239-3415 (toll free in the US) or +1-978-646-2777.

JOHN WILEY AND SONS LICENSE
TERMS AND CONDITIONS

Oct 07, 2022

This Agreement between Maximilian Muhr ("You") and John Wiley and Sons ("John Wiley and Sons") consists of your license details and the terms and conditions provided by John Wiley and Sons and Copyright Clearance Center.

License Number 5403550022580

License date Oct 07, 2022

Licensed Content
Publisher John Wiley and SonsLicensed Content
Publication Chemistry - A European JournalLicensed Content Title C–H and Si–H Activation Reactions at Ru/Ga Complexes: A
Combined Experimental and Theoretical Case Study on the Ru–Ga
BondLicensed Content
Author Maximilian Muhr, Raphael Bühler, Hao Liang, et alLicensed Content
Date Aug 3, 2022Licensed Content
Volume 28Licensed Content
Issue 54

Licensed Content Pages	6
Type of use	Dissertation/Thesis
Requestor type	Author of this Wiley article
Format	Print and electronic
Portion	Full article
Will you be translating?	No
Title	Reactive sites generation at intermetallic clusters
Institution name	Technical University of Munich
Expected presentation date	Jan 2024
Requestor Location	Maximilian Muhr Lichtenbergstrasse 4 Garching, 85748 Germany Attn: Technical University Munich
Publisher Tax ID	EU826007151
Total	0.00 USD

Terms and Conditions

TERMS AND CONDITIONS

This copyrighted material is owned by or exclusively licensed to John Wiley & Sons, Inc. or

one of its group companies (each a "Wiley Company") or handled on behalf of a society with which a Wiley Company has exclusive publishing rights in relation to a particular work (collectively "WILEY"). By clicking "accept" in connection with completing this licensing transaction, you agree that the following terms and conditions apply to this transaction (along with the billing and payment terms and conditions established by the Copyright Clearance Center Inc., ("CCC's Billing and Payment terms and conditions"), at the time that you opened your RightsLink account (these are available at any time at <http://myaccount.copyright.com>).

Terms and Conditions

- The materials you have requested permission to reproduce or reuse (the "Wiley Materials") are protected by copyright.
- You are hereby granted a personal, non-exclusive, non-sub licensable (on a stand-alone basis), non-transferable, worldwide, limited license to reproduce the Wiley Materials for the purpose specified in the licensing process. This license, **and any CONTENT (PDF or image file) purchased as part of your order**, is for a one-time use only and limited to any maximum distribution number specified in the license. The first instance of republication or reuse granted by this license must be completed within two years of the date of the grant of this license (although copies prepared before the end date may be distributed thereafter). The Wiley Materials shall not be used in any other manner or for any other purpose, beyond what is granted in the license. Permission is granted subject to an appropriate acknowledgement given to the author, title of the material/book/journal and the publisher. You shall also duplicate the copyright notice that appears in the Wiley publication in your use of the Wiley Material. Permission is also granted on the understanding that nowhere in the text is a previously published source acknowledged for all or part of this Wiley Material. Any third party content is expressly excluded from this permission.
- With respect to the Wiley Materials, all rights are reserved. Except as expressly granted by the terms of the license, no part of the Wiley Materials may be copied, modified, adapted (except for minor reformatting required by the new Publication), translated, reproduced, transferred or distributed, in any form or by any means, and no derivative works may be made based on the Wiley Materials without the prior permission of the respective copyright owner. **For STM Signatory Publishers clearing permission under the terms of the [STM Permissions Guidelines](#) only, the terms of the license are extended to include subsequent editions and for editions in other languages, provided such editions are for the work as a whole in situ and does not involve the separate exploitation of the permitted figures or extracts**, You may not alter, remove or suppress in any manner any copyright, trademark or other notices displayed by the Wiley Materials. You may not license, rent, sell, loan, lease, pledge, offer as security, transfer or assign the Wiley Materials on a stand-alone basis, or any of the rights granted to you hereunder to any other person.
- The Wiley Materials and all of the intellectual property rights therein shall at all times remain the exclusive property of John Wiley & Sons Inc, the Wiley Companies, or their respective licensors, and your interest therein is only that of having possession of and the right to reproduce the Wiley Materials pursuant to Section 2 herein during the continuance of this Agreement. You agree that you own no right, title or interest in or

to the Wiley Materials or any of the intellectual property rights therein. You shall have no rights hereunder other than the license as provided for above in Section 2. No right, license or interest to any trademark, trade name, service mark or other branding ("Marks") of WILEY or its licensors is granted hereunder, and you agree that you shall not assert any such right, license or interest with respect thereto

- NEITHER WILEY NOR ITS LICENSORS MAKES ANY WARRANTY OR REPRESENTATION OF ANY KIND TO YOU OR ANY THIRD PARTY, EXPRESS, IMPLIED OR STATUTORY, WITH RESPECT TO THE MATERIALS OR THE ACCURACY OF ANY INFORMATION CONTAINED IN THE MATERIALS, INCLUDING, WITHOUT LIMITATION, ANY IMPLIED WARRANTY OF MERCHANTABILITY, ACCURACY, SATISFACTORY QUALITY, FITNESS FOR A PARTICULAR PURPOSE, USABILITY, INTEGRATION OR NON-INFRINGEMENT AND ALL SUCH WARRANTIES ARE HEREBY EXCLUDED BY WILEY AND ITS LICENSORS AND WAIVED BY YOU.
- WILEY shall have the right to terminate this Agreement immediately upon breach of this Agreement by you.
- You shall indemnify, defend and hold harmless WILEY, its Licensors and their respective directors, officers, agents and employees, from and against any actual or threatened claims, demands, causes of action or proceedings arising from any breach of this Agreement by you.
- IN NO EVENT SHALL WILEY OR ITS LICENSORS BE LIABLE TO YOU OR ANY OTHER PARTY OR ANY OTHER PERSON OR ENTITY FOR ANY SPECIAL, CONSEQUENTIAL, INCIDENTAL, INDIRECT, EXEMPLARY OR PUNITIVE DAMAGES, HOWEVER CAUSED, ARISING OUT OF OR IN CONNECTION WITH THE DOWNLOADING, PROVISIONING, VIEWING OR USE OF THE MATERIALS REGARDLESS OF THE FORM OF ACTION, WHETHER FOR BREACH OF CONTRACT, BREACH OF WARRANTY, TORT, NEGLIGENCE, INFRINGEMENT OR OTHERWISE (INCLUDING, WITHOUT LIMITATION, DAMAGES BASED ON LOSS OF PROFITS, DATA, FILES, USE, BUSINESS OPPORTUNITY OR CLAIMS OF THIRD PARTIES), AND WHETHER OR NOT THE PARTY HAS BEEN ADVISED OF THE POSSIBILITY OF SUCH DAMAGES. THIS LIMITATION SHALL APPLY NOTWITHSTANDING ANY FAILURE OF ESSENTIAL PURPOSE OF ANY LIMITED REMEDY PROVIDED HEREIN.
- Should any provision of this Agreement be held by a court of competent jurisdiction to be illegal, invalid, or unenforceable, that provision shall be deemed amended to achieve as nearly as possible the same economic effect as the original provision, and the legality, validity and enforceability of the remaining provisions of this Agreement shall not be affected or impaired thereby.
- The failure of either party to enforce any term or condition of this Agreement shall not constitute a waiver of either party's right to enforce each and every term and condition of this Agreement. No breach under this agreement shall be deemed waived or excused by either party unless such waiver or consent is in writing signed by the party granting such waiver or consent. The waiver by or consent of a party to a breach of

any provision of this Agreement shall not operate or be construed as a waiver of or consent to any other or subsequent breach by such other party.

- This Agreement may not be assigned (including by operation of law or otherwise) by you without WILEY's prior written consent.
- Any fee required for this permission shall be non-refundable after thirty (30) days from receipt by the CCC.
- These terms and conditions together with CCC's Billing and Payment terms and conditions (which are incorporated herein) form the entire agreement between you and WILEY concerning this licensing transaction and (in the absence of fraud) supersedes all prior agreements and representations of the parties, oral or written. This Agreement may not be amended except in writing signed by both parties. This Agreement shall be binding upon and inure to the benefit of the parties' successors, legal representatives, and authorized assigns.
- In the event of any conflict between your obligations established by these terms and conditions and those established by CCC's Billing and Payment terms and conditions, these terms and conditions shall prevail.
- WILEY expressly reserves all rights not specifically granted in the combination of (i) the license details provided by you and accepted in the course of this licensing transaction, (ii) these terms and conditions and (iii) CCC's Billing and Payment terms and conditions.
- This Agreement will be void if the Type of Use, Format, Circulation, or Requestor Type was misrepresented during the licensing process.
- This Agreement shall be governed by and construed in accordance with the laws of the State of New York, USA, without regards to such state's conflict of law rules. Any legal action, suit or proceeding arising out of or relating to these Terms and Conditions or the breach thereof shall be instituted in a court of competent jurisdiction in New York County in the State of New York in the United States of America and each party hereby consents and submits to the personal jurisdiction of such court, waives any objection to venue in such court and consents to service of process by registered or certified mail, return receipt requested, at the last known address of such party.

WILEY OPEN ACCESS TERMS AND CONDITIONS

Wiley Publishes Open Access Articles in fully Open Access Journals and in Subscription journals offering Online Open. Although most of the fully Open Access journals publish open access articles under the terms of the Creative Commons Attribution (CC BY) License only, the subscription journals and a few of the Open Access Journals offer a choice of Creative Commons Licenses. The license type is clearly identified on the article.

The Creative Commons Attribution License

The [Creative Commons Attribution License \(CC-BY\)](#) allows users to copy, distribute and transmit an article, adapt the article and make commercial use of the article. The CC-BY

license permits commercial and non-

Creative Commons Attribution Non-Commercial License

The [Creative Commons Attribution Non-Commercial \(CC-BY-NC\)License](#) permits use, distribution and reproduction in any medium, provided the original work is properly cited and is not used for commercial purposes.(see below)

Creative Commons Attribution-Non-Commercial-NoDerivs License

The [Creative Commons Attribution Non-Commercial-NoDerivs License](#) (CC-BY-NC-ND) permits use, distribution and reproduction in any medium, provided the original work is properly cited, is not used for commercial purposes and no modifications or adaptations are made. (see below)

Use by commercial "for-profit" organizations

Use of Wiley Open Access articles for commercial, promotional, or marketing purposes requires further explicit permission from Wiley and will be subject to a fee.

Further details can be found on Wiley Online Library <http://olabout.wiley.com/WileyCDA/Section/id-410895.html>

Other Terms and Conditions:

v1.10 Last updated September 2015

Questions? customercare@copyright.com or +1-855-239-3415 (toll free in the US) or +1-978-646-2777.



Order Confirmation

Thank you, your order has been placed. An email confirmation has been sent to you. Your order license details and printable licenses will be available within 24 hours. Please access Manage Account for final order details.

This is not an invoice. Please go to manage account to access your order history and invoices.

CUSTOMER INFORMATION

Payment by invoice: You can cancel your order until the invoice is generated by contacting customer service.

Billing Address

Maximilian Muhr
Lichtenbergstrasse 4
Garching, 85748
Germany

+49 8928954131
maximilian.muhr@tum.de

PO Number (optional)

N/A

Customer Location

Maximilian Muhr
Lichtenbergstrasse 4
Garching, 85748
Germany

Payment options

Invoice

PENDING ORDER CONFIRMATION

Confirmation Number: Pending

Order Date: 07-Oct-2022

1. Dalton transactions : an international journal of inorganic chemistry 0.00 USD

Article: Enabling LIFDI-MS measurements of highly air sensitive organometallic compounds: A combined MS/glovebox technique

Order License ID	Pending	Publisher	ROYAL SOCIETY
ISSN	1477-9226		OF CHEMISTRY
Type of Use	Republish in a thesis/dissertation	Portion	Chapter/article

LICENSED CONTENT

Publication Title	Dalton transactions : an international journal of inorganic chemistry	Rightholder	Royal Society of Chemistry
Article Title	Enabling LIFDI-MS measurements of highly air sensitive organometallic compounds: A combined MS/glovebox technique	Publication Type	Journal
		Start Page	9031
		End Page	9036
		Issue	26
		Volume	50
Author/Editor	Royal Society of Chemistry (Great Britain)		
Date	01/01/2003		
Language	English		
Country	United Kingdom of Great Britain and Northern Ireland		

REQUEST DETAILS

Portion Type	Chapter/article	Rights Requested	Main product
Page range(s)	1-7	Distribution	Worldwide
Total number of pages	7	Translation	Original language of publication
Format (select all that apply)	Print, Electronic	Copies for the disabled?	No
Who will republish the content?	Author of requested content	Minor editing privileges?	Yes
Duration of Use	Life of current edition	Incidental promotional use?	No
Lifetime Unit Quantity	Up to 499	Currency	USD

NEW WORK DETAILS

Title	Formation of reactivities sites at intermetallic clusters	Institution name	Technical University of Munich
Instructor name	Maximilian Muhr	Expected presentation date	2024-01-01

ADDITIONAL DETAILS

Order reference number	N/A	The requesting person / organization to appear on the license	Maximilian Muhr
------------------------	-----	---	-----------------

REUSE CONTENT DETAILS

Title, description or numeric reference of the portion(s)	Full article	Title of the article/chapter the portion is from	Enabling LIFDI-MS measurements of highly air sensitive organometallic compounds: A combined MS/glovebox technique
---	--------------	--	---

Firefox

<https://marketplace.copyright.com/rs-ui-web/mp/checkout/confirmation...>

Editor of portion(s)	Fischer, Roland A.; Muhr, Maximilian; Heiß, Patricia; Schütz, Max; Bühler, Raphael; Gemel, Christian; Linden, H. Bernhard; Linden, Mathias	Author of portion(s)	Fischer, Roland A.; Muhr, Maximilian; Heiß, Patricia; Schütz, Max; Bühler, Raphael; Gemel, Christian; Linden, H. Bernhard; Linden, Mathias
Volume of serial or monograph	50	Issue, if republishing an article from a serial	26
Page or page range of portion	9031-9036	Publication date of portion	2021-07-06

Total Items: 1

Total Due: 0.00 USD

Accepted: Marketplace Order General Terms and Conditions and any applicable Publisher Terms and Conditions

JOHN WILEY AND SONS LICENSE
TERMS AND CONDITIONS

Oct 19, 2022

This Agreement between Maximilian Muhr ("You") and John Wiley and Sons ("John Wiley and Sons") consists of your license details and the terms and conditions provided by John Wiley and Sons and Copyright Clearance Center.

License Number	5412620998665
License date	Oct 19, 2022
Licensed Content Publisher	John Wiley and Sons
Licensed Content Publication	Angewandte Chemie International Edition
Licensed Content Title	The Intermetalloid Cluster [(Cp*AlCu) ₆ H ₄], Embedding a Cu ₆ Core Inside an Octahedral Al ₆ Shell: Molecular Models of Hume–Rothery Nanophases
Licensed Content Author	Chelladurai Ganesamoorthy, Jana Weßing, Clarissa Kroll, et al
Licensed Content Date	Jun 24, 2014
Licensed Content Volume	53
Licensed Content Issue	30

Licensed Content Pages	5
Type of use	Dissertation/Thesis
Requestor type	University/Academic
Format	Print and electronic
Portion	Figure/table
Number of figures/tables	1
Will you be translating?	No
Title	Reactive sites generation at intermetallic clusters
Institution name	Technical University of Munich
Expected presentation date	Jan 2024
Portions	Figure 1
Requestor Location	Maximilian Muhr Lichtenbergstrasse 4 Garching, 85748 Germany Attn: Technical University Munich
Publisher Tax ID	EU826007151
Total	0.00 USD

Terms and Conditions

TERMS AND CONDITIONS

This copyrighted material is owned by or exclusively licensed to John Wiley & Sons, Inc. or one of its group companies (each a "Wiley Company") or handled on behalf of a society with which a Wiley Company has exclusive publishing rights in relation to a particular work (collectively "WILEY"). By clicking "accept" in connection with completing this licensing transaction, you agree that the following terms and conditions apply to this transaction (along with the billing and payment terms and conditions established by the Copyright Clearance Center Inc., ("CCC's Billing and Payment terms and conditions"), at the time that you opened your RightsLink account (these are available at any time at <http://myaccount.copyright.com>).

Terms and Conditions

- The materials you have requested permission to reproduce or reuse (the "Wiley Materials") are protected by copyright.
- You are hereby granted a personal, non-exclusive, non-sub licensable (on a stand-alone basis), non-transferable, worldwide, limited license to reproduce the Wiley Materials for the purpose specified in the licensing process. This license, **and any CONTENT (PDF or image file) purchased as part of your order**, is for a one-time use only and limited to any maximum distribution number specified in the license. The first instance of republication or reuse granted by this license must be completed within two years of the date of the grant of this license (although copies prepared before the end date may be distributed thereafter). The Wiley Materials shall not be used in any other manner or for any other purpose, beyond what is granted in the license. Permission is granted subject to an appropriate acknowledgement given to the author, title of the material/book/journal and the publisher. You shall also duplicate the copyright notice that appears in the Wiley publication in your use of the Wiley Material. Permission is also granted on the understanding that nowhere in the text is a previously published source acknowledged for all or part of this Wiley Material. Any third party content is expressly excluded from this permission.
- With respect to the Wiley Materials, all rights are reserved. Except as expressly granted by the terms of the license, no part of the Wiley Materials may be copied, modified, adapted (except for minor reformatting required by the new Publication), translated, reproduced, transferred or distributed, in any form or by any means, and no derivative works may be made based on the Wiley Materials without the prior permission of the respective copyright owner. **For STM Signatory Publishers clearing permission under the terms of the [STM Permissions Guidelines](#) only, the terms of the license are extended to include subsequent editions and for editions in other languages, provided such editions are for the work as a whole in situ and does not involve the separate exploitation of the permitted figures or extracts,** You may not alter, remove or suppress in any manner any copyright, trademark or other notices displayed by the Wiley Materials. You may not license, rent, sell, loan, lease, pledge, offer as security, transfer or assign the Wiley Materials on a stand-alone

basis, or any of the rights granted to you hereunder to any other person.

- The Wiley Materials and all of the intellectual property rights therein shall at all times remain the exclusive property of John Wiley & Sons Inc, the Wiley Companies, or their respective licensors, and your interest therein is only that of having possession of and the right to reproduce the Wiley Materials pursuant to Section 2 herein during the continuance of this Agreement. You agree that you own no right, title or interest in or to the Wiley Materials or any of the intellectual property rights therein. You shall have no rights hereunder other than the license as provided for above in Section 2. No right, license or interest to any trademark, trade name, service mark or other branding ("Marks") of WILEY or its licensors is granted hereunder, and you agree that you shall not assert any such right, license or interest with respect thereto
- NEITHER WILEY NOR ITS LICENSORS MAKES ANY WARRANTY OR REPRESENTATION OF ANY KIND TO YOU OR ANY THIRD PARTY, EXPRESS, IMPLIED OR STATUTORY, WITH RESPECT TO THE MATERIALS OR THE ACCURACY OF ANY INFORMATION CONTAINED IN THE MATERIALS, INCLUDING, WITHOUT LIMITATION, ANY IMPLIED WARRANTY OF MERCHANTABILITY, ACCURACY, SATISFACTORY QUALITY, FITNESS FOR A PARTICULAR PURPOSE, USABILITY, INTEGRATION OR NON-INFRINGEMENT AND ALL SUCH WARRANTIES ARE HEREBY EXCLUDED BY WILEY AND ITS LICENSORS AND WAIVED BY YOU.
- WILEY shall have the right to terminate this Agreement immediately upon breach of this Agreement by you.
- You shall indemnify, defend and hold harmless WILEY, its Licensors and their respective directors, officers, agents and employees, from and against any actual or threatened claims, demands, causes of action or proceedings arising from any breach of this Agreement by you.
- IN NO EVENT SHALL WILEY OR ITS LICENSORS BE LIABLE TO YOU OR ANY OTHER PARTY OR ANY OTHER PERSON OR ENTITY FOR ANY SPECIAL, CONSEQUENTIAL, INCIDENTAL, INDIRECT, EXEMPLARY OR PUNITIVE DAMAGES, HOWEVER CAUSED, ARISING OUT OF OR IN CONNECTION WITH THE DOWNLOADING, PROVISIONING, VIEWING OR USE OF THE MATERIALS REGARDLESS OF THE FORM OF ACTION, WHETHER FOR BREACH OF CONTRACT, BREACH OF WARRANTY, TORT, NEGLIGENCE, INFRINGEMENT OR OTHERWISE (INCLUDING, WITHOUT LIMITATION, DAMAGES BASED ON LOSS OF PROFITS, DATA, FILES, USE, BUSINESS OPPORTUNITY OR CLAIMS OF THIRD PARTIES), AND WHETHER OR NOT THE PARTY HAS BEEN ADVISED OF THE POSSIBILITY OF SUCH DAMAGES. THIS LIMITATION SHALL APPLY NOTWITHSTANDING ANY FAILURE OF ESSENTIAL PURPOSE OF ANY LIMITED REMEDY PROVIDED HEREIN.
- Should any provision of this Agreement be held by a court of competent jurisdiction to be illegal, invalid, or unenforceable, that provision shall be deemed amended to achieve as nearly as possible the same economic effect as the original provision, and the legality, validity and enforceability of the remaining provisions of this Agreement

SPRINGER NATURE LICENSE
TERMS AND CONDITIONS

Nov 10, 2022

This Agreement between Maximilian Muhr ("You") and Springer Nature ("Springer Nature") consists of your license details and the terms and conditions provided by Springer Nature and Copyright Clearance Center.

License Number	5413060454543
License date	Oct 20, 2022
Licensed Content Publisher	Springer Nature
Licensed Content Publication	Nature Reviews Chemistry
Licensed Content Title	Modern cluster design based on experiment and theory
Licensed Content Author	Takamasa Tsukamoto et al
Licensed Content Date	Mar 24, 2021
Type of Use	Thesis/Dissertation
Requestor type	academic/university or research institute
Format	print and electronic
Portion	figures/tables/illustrations
Number of figures/tables/illustrations	1

High-res required	no
Will you be translating?	no
Circulation/distribution	1 - 29
Author of this Springer Nature content	no
Title	Reactive sites generation at intermetallic clusters
Institution name	Technical University of Munich
Expected presentation date	Jan 2024
Portions	Figure 3a
	Maximilian Muhr Lichtenbergstrasse 4
Requestor Location	Garching, 85748 Germany Attn: Technical University Munich
Total	0.00 USD
Terms and Conditions	

Springer Nature Customer Service Centre GmbH
Terms and Conditions

This agreement sets out the terms and conditions of the licence (the **Licence**) between you and **Springer Nature Customer Service Centre GmbH** (the **Licensor**). By clicking 'accept' and completing the transaction for the material (**Licensed Material**), you also confirm your acceptance of these terms and conditions.

1. Grant of License

1.1. The Licensor grants you a personal, non-exclusive, non-transferable, world-wide licence to reproduce the Licensed Material for the purpose specified in your order

5. Eidesstattliche Erklärung

Ich, Maximilian Muhr, erkläre an Eides statt, dass ich die bei der promotionsführenden Einrichtung
TUM School of Natural Sciences, Department für Chemie, Lehrstuhl für Anorganische und Metallorganische
Chemie

der TUM zur Promotionsprüfung vorgelegte Arbeit mit dem Titel:
Accessible Sites at Bimetallic Complexes and Clusters

unter der Anleitung und Betreuung durch: Prof. Dr. Dr. h. c. Roland A. Fischer

ohne sonstige Hilfe erstellt und bei der Abfassung nur die gemäß § 7 Abs. 6 und 7 angegebenen Hilfsmittel benutzt habe.

- Ich habe keine Organisation eingeschaltet, die gegen Entgelt Betreuer*innen für die Anfertigung von Dissertationen sucht, oder die mir obliegenden Pflichten hinsichtlich der Prüfungsleistungen für mich ganz oder teilweise erledigt.
- Ich habe die Dissertation in dieser oder ähnlicher Form in keinem anderen Prüfungsverfahren als Prüfungsleistung vorgelegt.
- Teile der Dissertation wurden in u.a. Angew. Chem. Int. Ed.; Comm. Commun.; Nat. Commun.; veröffentlicht.
- Ich habe den angestrebten Doktorgrad noch nicht erworben und bin nicht in einem früheren Promotionsverfahren für den angestrebten Doktorgrad endgültig gescheitert.

Ich habe bereits am _____ bei der promotionsführenden Einrichtung
_____ der Hochschule
_____ unter Vorlage einer Dissertation mit dem Thema

die Zulassung zur Promotion beantragt mit dem Ergebnis:

- Ich habe keine Kenntnis über ein strafrechtliches Ermittlungsverfahren in Bezug auf wissenschaftsbezogene Straftaten gegen mich oder eine rechtskräftige strafrechtliche Verurteilung mit Wissenschaftsbezug.

Die öffentlich zugängliche Promotionsordnung sowie die Richtlinien zur Sicherung guter wissenschaftlicher Praxis und für den Umgang mit wissenschaftlichem Fehlverhalten der TUM sind mir bekannt, insbesondere habe ich die Bedeutung von § 27 PromO (Nichtigkeit der Promotion) und § 28 PromO (Entzug des Doktorgrades) zur Kenntnis genommen. Ich bin mir der Konsequenzen einer falschen Eidesstattlichen Erklärung bewusst.

Mit der Aufnahme meiner personenbezogenen Daten in die Alumni-Datei bei der TUM bin ich

- einverstanden, nicht einverstanden.

Maximilian Muhr

München, den 14.11.2022
